frontiers | Research Topics

Brain imaging relations through simultaneous recordings

Edited by
Waldemar Karwowski, Surjo R. Soekadar and
Aleksandra Dagmara Kawala-Sterniuk

Published in
Frontiers in Neuroscience

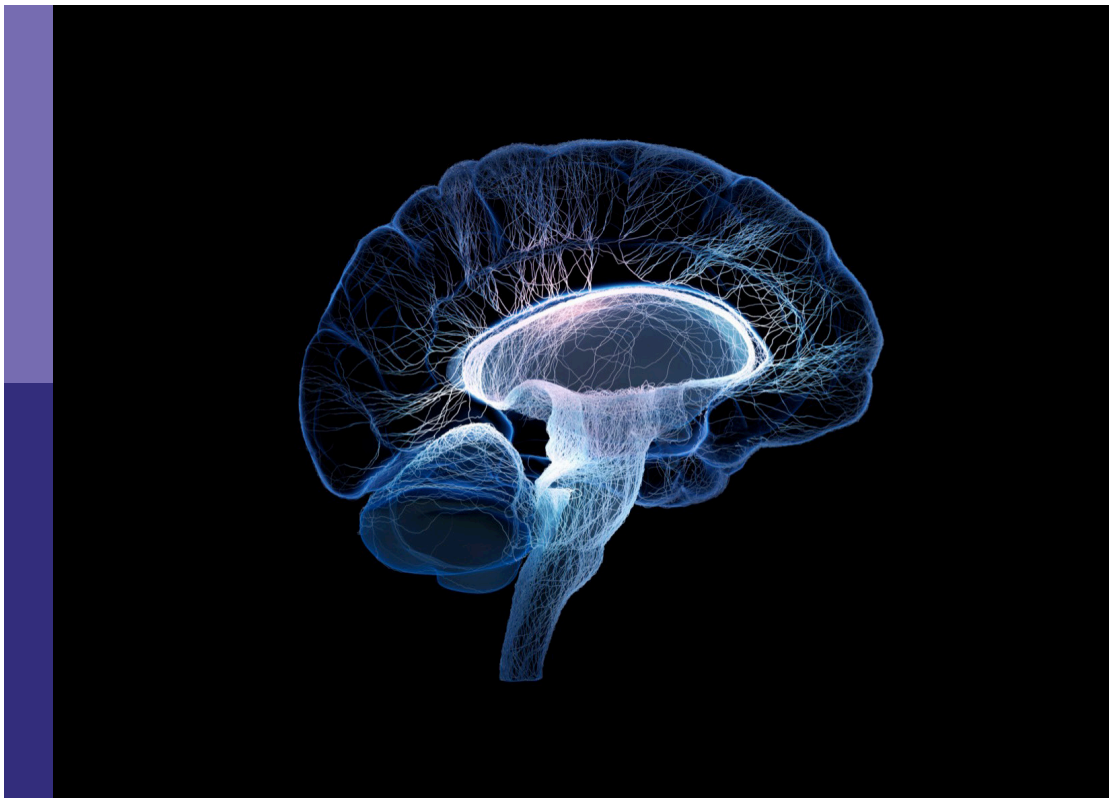

ISSN 1664-8714
ISBN 978-2-83251-725-3
DOI 10.3389/978-2-83251-725-3

About Frontiers

Frontiers is more than just an open access publisher of scholarly articles: it is a pioneering approach to the world of academia, radically improving the way scholarly research is managed. The grand vision of Frontiers is a world where all people have an equal opportunity to seek, share and generate knowledge. Frontiers provides immediate and permanent online open access to all its publications, but this alone is not enough to realize our grand goals.

Frontiers journal series

The Frontiers journal series is a multi-tier and interdisciplinary set of open-access, online journals, promising a paradigm shift from the current review, selection and dissemination processes in academic publishing. All Frontiers journals are driven by researchers for researchers; therefore, they constitute a service to the scholarly community. At the same time, the *Frontiers journal series* operates on a revolutionary invention, the tiered publishing system, initially addressing specific communities of scholars, and gradually climbing up to broader public understanding, thus serving the interests of the lay society, too.

Dedication to quality

Each Frontiers article is a landmark of the highest quality, thanks to genuinely collaborative interactions between authors and review editors, who include some of the world's best academicians. Research must be certified by peers before entering a stream of knowledge that may eventually reach the public - and shape society; therefore, Frontiers only applies the most rigorous and unbiased reviews. Frontiers revolutionizes research publishing by freely delivering the most outstanding research, evaluated with no bias from both the academic and social point of view. By applying the most advanced information technologies, Frontiers is catapulting scholarly publishing into a new generation.

What are Frontiers Research Topics?

Frontiers Research Topics are very popular trademarks of the *Frontiers journals series*: they are collections of at least ten articles, all centered on a particular subject. With their unique mix of varied contributions from Original Research to Review Articles, Frontiers Research Topics unify the most influential researchers, the latest key findings and historical advances in a hot research area.

Find out more on how to host your own Frontiers Research Topic or contribute to one as an author by contacting the Frontiers editorial office: frontiersin.org/about/contact

Brain imaging relations through simultaneous recordings

Topic editors

Waldemar Karwowski — University of Central Florida, United States
Surjo R. Soekadar — Charité Universitätsmedizin Berlin, Germany
Aleksandra Dagmara Kawala-Sterniuk — Opole University of Technology, Poland

Citation

Karwowski, W., Soekadar, S. R., Kawala-Sterniuk, A. D., eds. (2023). *Brain imaging relations through simultaneous recordings*. Lausanne: Frontiers Media SA.
doi: 10.3389/978-2-83251-725-3

Table of contents

frontiers | Frontiers in Neuroscience

TYPE Editorial
PUBLISHED 07 February 2023
DOI 10.3389/fnins.2023.1139336

OPEN ACCESS

EDITED AND REVIEWED BY
Anirban Dutta,
University of Lincoln, United Kingdom

*CORRESPONDENCE
Waldemar Karwowski
✉ wkar@ucf.edu
Surjo R. Soekadar
✉ surjo@gmx.de
Aleksandra Kawala-Sterniuk
✉ kawala84@gmail.com

SPECIALTY SECTION
This article was submitted to Neural Technology, a section of the journal Frontiers in Neuroscience

RECEIVED 06 January 2023
ACCEPTED 16 January 2023
PUBLISHED 07 February 2023

CITATION
Karwowski W, Soekadar SR and Kawala-Sterniuk A (2023) Editorial: Brain imaging relations through simultaneous recordings. *Front. Neurosci.* 17:1139336. doi: 10.3389/fnins.2023.1139336

Editorial: Brain imaging relations through simultaneous recordings

Waldemar Karwowski[1]*, Surjo R. Soekadar[2]* and Aleksandra Kawala-Sterniuk[3]*

[1]Department of Industrial and Systems Engineering, University of Central Florida, Orlando, FL, United States, [2]Clinical Neurotechnology Laboratory, Department of Psychiatry and Neurosciences, Charité Campus Mitte (CCM), Charité–Universitätsmedizin Berlin, Berlin, Germany, [3]Faculty of Electrical Engineering, Automatic Control and Informatics, Opole University of Technology, Opole, Poland

KEYWORDS

neural technology, MRI, EEG, fMRI, functional near-infrared spectroscopy, magnetoencephalography, simultaneous recordings

Editorial on the Research Topic
Brain imaging relations through simultaneous recordings

1. Introduction

Recent technological advancements in neuroscience and in particular neuroimaging has improved the understanding of brain functionality and connectivity—not only in animal but also in human brains (Kawala-Sterniuk et al., 2021; Saeidi et al., 2021; Simon et al., 2021). Today, we are not only able to identify, localize, and characterize brain pathologies, such as local infections, lesions, or tumors, but we are also able to study brain anatomy, functionality, development, neuronal networks, etc. with very high precision. Availability of sophisticated software and advanced algorithms improved the possibilities for the analysis of various biomedical signals and outputs (Ismail and Karwowski, 2020; Kawala-Sterniuk et al., 2021; Martinek et al., 2021).

Despite the above-mentioned rapid technological development in this field, certain machine-specific limitations have to be taken into consideration, as these affect our ability to fully understand the mechanisms underlying brain functions. The limitations include poor temporal and poor spatial resolution, as each respective neuroimaging technique is accompanied by some shortcomings. Hence, the recent shift in the field has led to hybrid methods, which are a combination of simultaneous neuroimaging methods such as electroencephalography (EEG) and magnet resonance imaging (MRI) or functional near-infrared spectroscopy (fNIRS). Such combined approaches overcome the limitations of single modalities and provide a fuller and more comprehensive picture of the brain. They also play an increasing role when interacting with the brain using stimulation techniques (e.g., transcranial electric or magnetic stimulation (TES/TMS), including closed-loop applications) (Nasr et al., 2022).

The Research Topic "*Brain Imaging Relations Through Simultaneous Recordings*" consists of a collection of 11 contributions discussing new methods and systems for various brain data recordings and analyses, and document the most recent advancements in the field of neural technology and simultaneous neuroimaging recordings.

The first article published by Żebrowska et al. titled "*Removal of the Sinusoidal Transorbital Alternating Current Stimulation Artifact From Simultaneous EEG Recordings: Effects of Simple Moving Average Parameters*" focuses on the analysis of electroencephalography (EEG) signals, which is a very challenging task—mostly due to the nature of these signals. This study states that alternating current stimulation can be a promising treatment method for various neurological disorders, but it causes numerous artifacts and disturbances in EEG signals. In order to remove

these artifacts, the authors proposed a simple moving average subtraction, which gave very promising and positive results. The authors of that paper based on a thorough literature background, proved that moving average filtering can be efficiently applied in EEG signals' processing.

The second article, entitled "*Reliability of MUSE 2 and Tobii Pro Nano at capturing mobile application users' real-time cognitive workload changes*," was written by Zhang and Cui. Unlike Żebrowska et al., this study focused on non-clinical, inexpensive equipment such as MUSE 2 in order to check if it could be a useful tool for obtaining high-quality EEG signals–potentially later applied for diagnostics purposes (Zhang and Cui). The article is also focused on a very broad topic—human omputer interaction (HCI), where the MUSE 2-EEG was combined with an eye-tracking device (Tobii Pro Nano). The obtained signals were of high quality and stable, making them useful in studies assessing the usability of smartphone applications. Despite some flaws, the authors have proven MUSE 2 to be a reliable device for cognitive workload detection and measurement.

Functional near-infrared spectroscopy (fNIRS) can be considered a less expensive alternative to fMRI functional magnetic resonance imaging). The use of fNRIS has been discussed in two articles: Deng et al. and Ma et al.. In the first article written by Deng et al., titled "*The analgesic effect of different interactive modes of virtual reality: A prospective functional near-infrared spectroscopy (fNIRS) study*," the authors focused on studying the analgesic effect of various virtual reality (VR) models with the use of fNIRS measurements. The obtained results proved VR to have the analgesic effect, which has been verified by the analysis of fNIRS signals. The second article written by Ma et al. and titled "*Increased cerebral cortex activation in patients with stroke during the electrical stimulation of cerebellar fastigial nucleus with functional near-infrared spectroscopy*" applied fNIRS data in order to detect any functional connectivity changes in patients affected by brain stroke and to study the cortical activation caused by fastigial nucleus (FNS) by measuring the cerebral cortex oxygenated hemoglobin concentration (HBO), which can be done with the fNIRS of both patients with stroke and healthy controls. This study proved that combining FNS and fNIRS techniques can help in choosing appropriate functional rehabilitation for patients with stroke.

Electroencephalography recordings can be efficiently combined with fNIRS as presented in article written by Chen et al. titled "*Amplitude of fNIRS resting-state global signal is related to EEG vigilance measures: A simultaneous fNIRS and EEG study*" describing fNIRS-EEG simultaneous recordings in healthy participants. The presented study consisted of two experiments, where the first one was carried out on patients in the supine, sitting, and standing positions; while the second experiment concerned the analysis of fluctuations between the epochs of a separate group of subjects. The authors found a negative temporal correlation between EEG vigilance measurements and global fNIRS signal amplitudes. According to the authors, this is the first study to reveal that vigilance as a neurophysiological factor modulates fNIRS dynamics at rest, which has important implications for understanding and processing noise in fNIRS signals.

Three studies using hybrid recording systems based on EEG and fMRI (functional magnetic resonance imaging) are also part of this special issue: Bhutada et al., Rusiniak et al., and Basedau et al.. The first article written by Bhutada et al., titled "*Semi-automated and direct localization and labeling of EEG electrodes using MR structural images for simultaneous fMRI-EEG*" describes both semi-automated and direct methods for standard EEG cap electrode localization and labeling. The data were obtained during simultaneous fMRI-EEG recordings. The authors proposed a novel, semi-automated method as a simple alternative for rapid electrodes labeling and localization with no need for using any additional equipment than the one already applied in a typical EEG-fMRI setup. Rusiniak et. al. wrote an article ("EEG-fMRI: Ballistocardiogram Artifact Reduction by Surrogate Method for Improved Source Localization"), where they focused on ballistocardiogram (BCG) removal from the brain signals obtained during EEG-fMRI recording. It is because the other biosignals are frequently acting and considered artifacts while present in brain recordings. Removal of such distorting biomedical signals is a very challenging task. Rusiniak et al. proposed a method based on surrogate source models applied for the purpose of artifact removal with the possible minimal distortion. In the third article written by Basedau et al.—"*High-density electroencephalography-informed multiband functional magnetic resonance imaging reveals rhythm-specific activations within the trigeminal nociceptive network*," the authors focused on using multi-modal non-invasive imaging techniques for the pain assessment purposes. The authors showed that changes in theta-band visible in EEG recordings are induced by trigeminal pain and these correlate with fMRI activation in the brainstem.

In another article, brain data obtained using imaging techniques were applied to assess the severity of pain Wang et al.. As cancer affects an increasing number of people, one of its most common symptoms is cancer pain (CP), which frequently reduces life quality. In an article written by Wang et al. titled "*Evaluation of the glymphatic system with diffusion tensor imaging-along the perivascular space in cancer pain*," the authors decided to apply diffusion tensor imaging along the perivascular space (DTI-ALPS) as a non-invasive method to detect the alteration of the caused by bone metastasis glymphatic function in patients affected with CP. Their findings can improve understanding not only the functional characteristics of the brain under cancer pain but also to evaluate it through brain function detection, which may play a crucial role in appropriate treatment formulation. Neuroimaging techniques described in that article may be considered biomarkers for cancer pain assessment.

Our special issue also contains a research article titled "Evaluating the Safety of Simultaneous Intracranial Electroencephalography and Functional Magnetic Resonance Imaging Acquisition Using a 3 Tesla Magnetic Resonance Imaging Scanner" by Fujita et al.. It presents a fMRI-based multi-modal system that was combined with invasive brain activity recordings–intracranial electroencephalography (icEEG). Due to the invasiveness of icEEG recording, both methods have never been carried out at the same time. The authors of this study decided to conduct both measurements simultaneously using a 3-Tesla scanner. The authors considered major risk factors and assessed safety rules. Their study proved that under appropriate conditions that health risks during such procedure are low.

The review article titled "*Vascular cognitive impairment after mild stroke: connectomic insights, neuroimaging, and knowledge translation*" written by Holguin et al. underlines that current stroke assessment protocols rarely detect vascular cognitive impairment (VCI), in particular among patients affected with lighter deficits. The authors emphasize the importance of screening for VCI because such screening provides information required for the rehabilitation and recovery process. In this article, the authors focused on the relationship between insult-induced connectome changes and

the VCI; and discussed the latest clinical approaches to identify disruptions in neural networks and white matter connectivity. It also outlines how occupational therapists can work to make significant clinical innovations and speed recovery for people affected by stroke.

As mentioned earlier, analysis of biomedical data, in particular brain signals, is a very challenging task, but this makes it very interesting. We hope that our Research Topic will be found interesting to readers and researchers in fields of medicine, biomedical engineering, or neuroscience.

Author contributions

All authors listed have made a substantial, direct, and intellectual contribution to the work and approved it for publication.

Conflict of interest

The authors declare that the research was conducted in the absence of any commercial or financial relationships that could be construed as a potential conflict of interest.

Publisher's note

All claims expressed in this article are solely those of the authors and do not necessarily represent those of their affiliated organizations, or those of the publisher, the editors and the reviewers. Any product that may be evaluated in this article, or claim that may be made by its manufacturer, is not guaranteed or endorsed by the publisher.

References

Ismail, L. E., and Karwowski, W. (2020). Applications of EEG indices for the quantification of human cognitive performance: a systematic review and bibliometric analysis. *PLoS ONE* 15, e0242857. doi: 10.1371/journal.pone.0242857

Kawala-Sterniuk, A., Browarska, N., Al-Bakri, A., Pelc, M., Zygarlicki, J., Sidikova, M., et al. (2021). Summary of over fifty years with brain-computer interfaces review. *Brain Sci.* 11, 43. doi: 10.3390/brainsci11010043

Martinek, R., Ladrova, M., Sidikova, M., Jaros, R., Behbehani, K., Kahankova, R., et al. (2021). Advanced bioelectrical signal processing methods: Past, present and future approach part II: brain signals. *Sensors* 21, 6343. doi: 10.3390/s21196343

Nasr, K., Haslacher, D., Dayan, E., Censor, N., Cohen, L. G., and Soekadar, S. R. (2022). Breaking the boundaries of interacting with the human brain using adaptive closed-loop stimulation. *Prog. Neurobiol.* 216, 102311. doi: 10.1016/j.pneurobio.2022.102311

Saeidi, M., Karwowski, W., Farahani, F. V., Fiok, K., Taiar, R., Hancock, P., et al. (2021). Neural decoding of eeg signals with machine learning: a systematic review. *Brain Sci.* 11, 1525. doi: 10.3390/brainsci11111525

Simon, C., Bolton, D. A., Kennedy, N. C., Soekadar, S. R., and Ruddy, K. L. (2021). Challenges and opportunities for the future of brain-computer interface in neurorehabilitation. *Front. Neurosci.* 15, 699428. doi: 10.3389/fnins.2021.699428

frontiers in Neuroscience

ORIGINAL RESEARCH
published: 29 July 2020
doi: 10.3389/fnins.2020.00735

Removal of the Sinusoidal Transorbital Alternating Current Stimulation Artifact From Simultaneous EEG Recordings: Effects of Simple Moving Average Parameters

Małgorzata Żebrowska[1,2]*, *Piotr Dzwiniel*[1]* and *Wioletta Joanna Waleszczyk*[1†]

[1] Laboratory of Visual Neurobiology, Nencki Institute of Experimental Biology of the Polish Academy of Sciences, Warsaw, Poland, [2] Faculty of Physics, Warsaw University of Technology, Warsaw, Poland

OPEN ACCESS

Edited by:
Hari S. Sharma,
Uppsala University, Sweden

Reviewed by:
Michael X. Cohen,
University of Amsterdam, Netherlands
Seaab Imad Sahib,
Middle Technical University, Iraq

***Correspondence:**
Małgorzata Żebrowska
m.zebrowska@nencki.edu.pl;
malgorzata.zebrowska.dokt@pw.edu.pl
Piotr Dzwiniel
p.dzwiniel@nencki.edu.pl

[†]Deceased on March 15, 2020

Specialty section:
This article was submitted to Neural Technology, a section of the journal Frontiers in Neuroscience

Received: 15 November 2019
Accepted: 22 June 2020
Published: 29 July 2020

Citation:
Żebrowska M, Dzwiniel P and Waleszczyk WJ (2020) Removal of the Sinusoidal Transorbital Alternating Current Stimulation Artifact From Simultaneous EEG Recordings: Effects of Simple Moving Average Parameters. Front. Neurosci. 14:735. doi: 10.3389/fnins.2020.00735

Alternating current stimulation is a promising method for the study and treatment of various visual neurological dysfunctions as well as progressive understanding of the healthy brain. Unfortunately, due to the current stimulation artifact, problems remain in the context of analysis of the electroencephalography (EEG) signal recorded during ongoing stimulation. To address this problem, we propose the use of a simple moving average subtraction as a method for artifact elimination. This method involves the creation of a template of the stimulation artifact from EEG signal recorded during non-invasive electrical stimulation with a sinusoidal alternating current. The present report describes results of the effects of a simple moving average filtration that varies based on averaging parameters; in particular, we varied the number of sinusoidal periods per segment of the recorded signal and the number of segments used to construct an artifact template. Given the ongoing lack of a mathematical model that allows for the prediction of the "hidden" EEG signal with the alternating current stimulation artifact, we propose performing an earlier simulation that is based on the addition of artificial stimulation artifact to the known EEG signal. This solution allows for the optimization of filtering parameters with detailed knowledge about the accuracy of artifact removal. The algorithm, designed in the MATLAB environment, has been tested on data recorded from two volunteers subjected to sinusoidal transorbital alternating current stimulation. Analysis of the percentage difference between the original and filtered signal in time and frequency domain highlights the advantage of 1-period filtration.

Keywords: EEG, non-invasive electrical stimulation, transorbital alternating current stimulation, sinusoidal stimulation, stimulation artifact, simple moving average, averaging parameters, artifact template removal

INTRODUCTION

Transorbital and transcorneal alternating current stimulation appear to be some of the most promising tools for studying and the rehabilitation of visual dysfunctions. As a result, there is a recent shift in the use of these methods from research laboratories to clinics (for review see Ota et al., 2018; Sabel et al., 2019). Detailed analysis of the brain activity during stimulation is

crucial for elucidating the processes underlying the generation of phenomena associated with mentioned stimulation.

There are few possible types of alternating current stimulation (ACS) wave shapes, including sinusoidal, triangle/sawtooth, and squared (Moreno-Duarte et al., 2014; Dowsett and Herrmann, 2016). In this work, we focus on the sinusoidal transorbital (to-) ACS given that the usefulness of this method (as well as other types and subtypes of ACS) in rehabilitation of visual dysfunction is unknown (Kanai et al., 2008; Brignani et al., 2013; Neuling et al., 2013; Vossen et al., 2015; Kasten et al., 2016). Our main concern is that analysis of the EEG signal recorded during stimulation is significantly impeded due to the presence of a stimulation artifact that completely obscures endogenous brain activity. A representation of this problem is provided in **Figure 1**, showing signal recorded during 40 μA 10 Hz sinusoidal toACS. The amplitude of the signal with toACS stimulation is much greater than the amplitude of the signal recorded prior to stimulation in both time (**Figure 1A**) and frequency domains (**Figures 1B,C**). This problem is complicated by the fact that the frequency of stimulation usually falls within the frequency of interest, which is crucial for the study of a given phenomenon. With regard to these problems, the conclusions about the impact of a particular stimulation protocol are usually drawn based on a comparison of the EEG signal recorded before and after stimulation. Knowledge about the EEG signal "hidden" under the artifact could provide additional information on the impact of stimulation on neural activity and thus enable scientists to extend and refine findings on the impact of stimulation. Therefore, a method of filtering the EEG signal is needed, allowing for the removal of artifact with the greatest possible accuracy while ensuring the smallest possible loss of information about endogenous brain activity.

The search for the most appropriate method of removing ACS artifacts initially begin in studies concerning functional magnetic resonance imaging (fMRI). The ACS artifact observed in the EEG signal is similar to the artifact recorded during fMRI with simultaneous stimulation. The previously proposed methods of filtration were based on a combination of average (i.e., template) artifact subtraction and other techniques, such as adaptive noise cancelation (Allen et al., 2000), principal component analysis (PCA; Niazy et al., 2005), or independent component analysis (ICA) with different filtering (Bénar et al., 2003). Some of these methods have already been used to remove the ACS artifact. Template subtraction and PCA have been adapted to remove 10 Hz sinusoidal tACS artifact (Helfrich et al., 2014) using a 2-step algorithm. This algorithm involves the calculation of an artifact template from artifact segments. Obtained artifact template is then subtracted from a segmented signal and the remaining artifact is subsequently removed with the use of a PCA. The combination of average template subtraction and PCA was also used by Kohli and Casson (2015). In this study, both techniques were used independently and their filtering results were compared.

Previous publications that discuss the removal of the ACS artifact have provided only brief explanations of the adopted filtration parameters. We have found insufficient explanation of the impact of mentioned filtration settings on the overall filtering procedure outcomes. These publications will be discussed briefly in the following. First, in Helfrich et al. (2014), the filtering approach was based on the use of 30 period segments, and then creating a template from 10 centered segments (i.e., 300 sinusoidal periods averaged to create 1-period artifact template). Other research (e.g., Kohli and Casson, 2015) suggests that individual segments should consist of the smallest possible number of oscillation periods and that the length of the segment (i.e., number of samples) should be an integer. The number of averaged segments was equal to 5% of all segments extracted from the signal. Given (1) the lack of a clear and well-established consensus regarding the choice of the optimal averaging parameters for satisfactory stimulation artifact removal, as well as (2) the need for analysis of the relation between those parameters and the removal method performance (Kohli and Casson, 2019), we decided to consider this issue.

The present study aimed to provide a comprehensive analysis of the effectiveness of the method for sinusoidal ACS artifact removal based on the subtraction of the artifact template created with the use of simple moving average (SMA). Our aim was to propose a guide for researchers using SMA method for cleaning EEG signals that have been contaminated with sinusoidal ACS artifacts. Although the algorithm used to create an average artifact template was applied in some of the aforementioned studies, our analysis of the literature revealed insufficient information about the values of the parameters used in the averaging procedure. Furthermore, this method is often used as the only filtration step or is used as the initial step before further filtration stages (e.g., PCA, ICA). Thus, the considerations discussed here are important for the accurate separation of the EEG signal of interest from contamination due to stimulation artifact. Therefore, this work focuses on illustrating the effects of various SMA parameters and their respective values on the performance of stimulation artifact removal from the EEG signal recorded during sinusoidal toACS. We included a quantitative analysis of the accuracy of the stimulation artifact removal and an assessment of the pros and cons of using SMA filtering in the EEG signal analysis.

MATERIALS AND METHODS

Ethical Approval

The study adhered to the Declaration of Helsinki and was approved by the Ethical Committee of the University of Warsaw. Participants provided written informed consent concerning their participation in the study.

Subjects

One healthy female (age 23 years) and one healthy male (age 30 years) participated in the study. The participants were co-authors of this article and were required to meet the following criteria: (1) age between 20 and 40 years old; (2) lack of myopia or other uncorrected visual acuity deficits; (3) lack of diagnosed mental disorders; (4) lack of diagnosed neurological diseases or disorders; (5) lack of history of epileptic seizures; (6) lack of history of head injury resulting in loss of consciousness and/or hospitalization with comorbid brain damage; (7) lack of intake

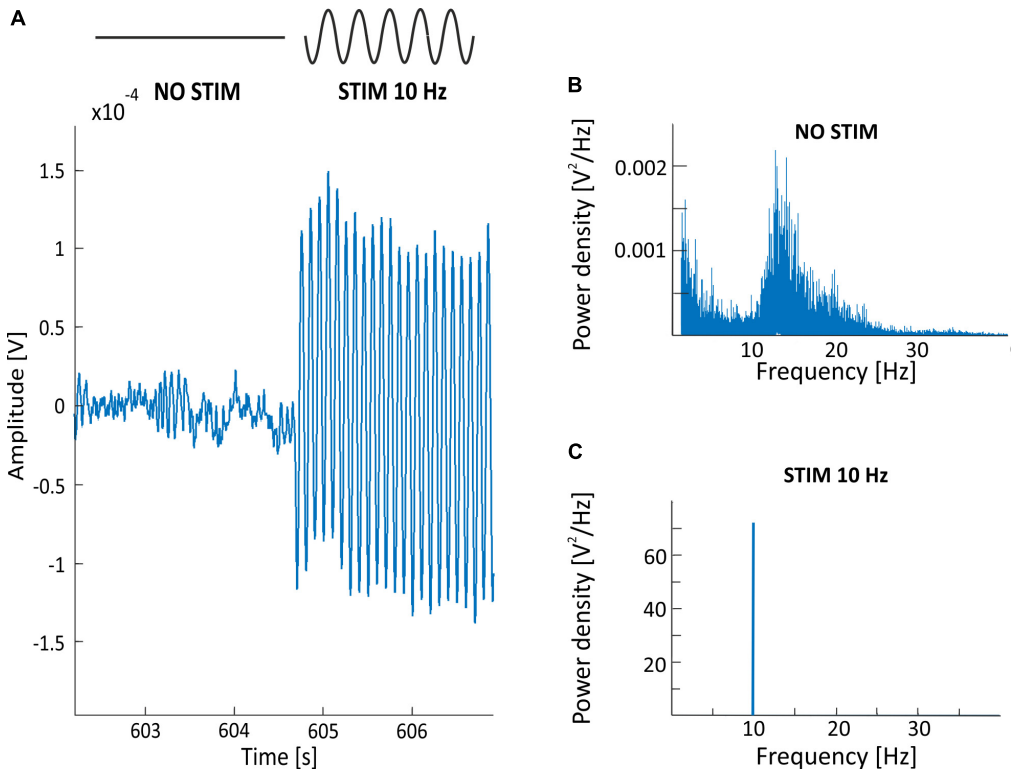

FIGURE 1 | (A) Example of the EEG recording (electrode O2; one exemplar participant) with a visible stimulation artifact starting around 604.5 s and resulting from an applied 40 μA 10 Hz sinusoidal to ACS. The EEG signal with superimposed stimulation artifact is 10 times greater in amplitude than the EEG signal recorded prior to stimulation. **(B)** Power spectrum density (PSD) before stimulation in a condition with an excitation in alpha band (i.e., closed eyes). The large intensity of artifact in 10 Hz during stimulation **(C)** doesn't allow for the analysis of the spectrum of endogenous brain activity in alpha band. PSD obtained from 5 min of signals, recorded at a 500 Hz sampling frequency.

of psychoactive substances including medical drugs; (8) lack of diagnosed addiction to any psychoactive substance; (9) lack of implanted electronic devices; (10) not pregnant.

Study Preparation

Prior to the experiment, each participant was appropriately prepared for the study. First, we applied the EEG cap on the participant's head. We ensured good contact between the EEG recording electrodes and the participant's skin via SuperVisc conductive gel (EASYCAP, Germany). Next, the participant's skin was cleaned and hydrated below and above both eyes with the use of 70% ethanol and Nuprep skin preparation gel (Weaver and Company, United States), respectively. Finally, self-adhesive current stimulation electrodes were placed in the prepared areas around the participant's eyes. The accepted impedance threshold between skin and electrodes was set to 10 kΩ.

Hardware Configuration and Experimental Design

Visual Stimulation and EEG Recording

The participant was situated in front of a laptop screen at a distance of 80 cm and was instructed to fixate on a white circular point (diameter: 0.3°, luminance: 207.5 cd/m^2) displayed on a homogenous black background (luminance: 0.3 cd/m^2). The experiment with the male participant consisted of two continuous 15-min blocks repeated over two subsequent days. On day one, EEG data were recorded while the participant's eyes were closed for the first block, and eyes open for the second block. On day two, toACS was applied during the middle 5 min of each block while performing simultaneous EEG recording. A 10-min break separated each block and EEG data was not recorded during the breaks (**Figure 3A**).

EEG data was recorded from the male subject using an actiCHamp EEG amplifier, an actiCAP EEG cap equipped with 32 active recording electrodes and one additional ground electrode, and recording software (Brain Products, Germany). The ground electrode was placed at the AFz electrode location and the software reference electrode was set at Cz. Thus, the raw EEG data consisted of 31 channels, given that the reference electrode was not included. Sampling frequency was set to 10 kHz. Low- and high-pass hardware filters were 2470 Hz and DC, respectively.

Detailed information about EEG data collection for the second subject (female) is presented in **Supplementary Materials**.

Electrical Stimulation

The generation and application of toACS was performed using DC-Stimulator MC (neuroConn, Germany). The stimulator has four stimulation output channels. The first two channels were used to apply toACS to the participant. The third channel carried the same information as the first two channels, but

instead of using the channel for stimulation, it was sent via opto-isolator to the EEG amplifier's AUX input and later used for EEG signal segmentation. Stimulation was applied via four 15 × 20 mm rectangular self-adhesive EMG electrodes (Spes Medica, Italy) connected with external cables to the stimulator and located directly below and above the participants' eyes, i.e., transorbitally (**Figure 2A**). Impedance between the stimulation electrodes and participants' skin never exceeded 100 kΩ. If the impedance exceeded 100 kΩ, the stimulator would automatically stop the procedure due to safety issues. Current stimulation was in a form of sinusoidal wave of 10 Hz frequency and 20 μA amplitude from peak-to-peak (**Figure 2B**). Maximum calculated current density of the applied current stimulation below each of the stimulating electrodes during stimulation peak was 0.066 $\mu A/mm^2$. Stimulation signal generated by the stimulator was prepared in Python programming language as *.mat file, and converted with a dedicated neuroConn's MATLAB toolbox into a *.bfs file, a file format used by the stimulator for stimulation. The sampling frequency of the stimulation signal was 16 kHz.

Data Pre-processing

Pre-processing of the recorded EEG data was performed with the use of custom-written scripts in Python programming language and MNE-Python package (Gramfort et al., 2013; Jas et al., 2018). First, the raw EEG data were filtered with a Butterworth 4th order biquadratic (i.e., second-order sections) IIR band-pass filter for the 0.1–100 Hz frequency range. Then, data were filtered with a zero-phase FIR notch filter of length 6.6 s for grid artifact frequency and associated harmonics removal, i.e., 50, 100, 150, 200, and 250 Hz. Of note, the filter type selection was motivated by the need to minimize edge artifacts around the current stimulation EEG artifacts.

Designed Algorithm for the Removal of the Sinusoidal ACS Artifact From EEG Signal

The algorithm that removes the sinusoidal ACS artifact from the simultaneous EEG data recording was implemented in the MATLAB environment. This algorithm is based on the coherent averaging technique, which is useful in digital signal processing to filter out noisy time series from repetitively applied stimuli (Rompelman and Ros, 1986). This method assumes that noise components are additive. Typically, during such filtration, the signal of interest is a periodic wave (e.g., a sinusoidal function) that is embedded in the noise. Averaging the corresponding noisy signal segments that are compatible in the phase causes the noise to be cleared, thus increasing the signal-to-noise ratio. In the case of EEG signal with embedded sinusoidal ACS artifact, the situation appears to be exactly the opposite (see **Figure 3B**).

The unwanted ACS component is a sinusoidal waveform of a specific frequency. Averaging the appropriate number of sinusoidal periods results in a filtered waveform. This waveform serves as a template for artifact that can later be subtracted from the recorded signal (**Figures 3A,B**). Due to the specificity of the EEG signal recorded during stimulation, the part of the signal that should be averaged to obtain the most comprehensive artifact template is not readily apparent. In fact, the artifact embedded in the signal may change over time due to possible impedance changes at the skin-electrode interface caused by sweating, peeling off the electrodes, or drying of the conductive gel. One possible solution to the progressive changes related to these potential fluctuations of the electric potential on the skin-electrode interface is the application of a coherent moving average (also called SMA) with a defined window that limits the range of the averaged signal. The algorithm, described in detail in the next paragraph, can be used to filter one-dimensional continuous time series; for example, recordings from a single EEG electrode.

Steps of the Algorithm

Division of the signal into segments

Knowing the sampling frequency of the signal F_s and the frequency of the stimulation *freqStim*, the number of samples corresponding to the length of the segment containing one full sine wave stimulation period can be calculated as follows:

$$segmentLength = \frac{F_s}{freqStim} \tag{1}$$

wherein *segmentLength* is the number of samples that corresponds to the length of one stimulation period.

Starting with the first sample that includes stimulation, the signal is divided into single-period segments (**Figure 4A**) or into segments of a total multiplicity of the period (**Figure 4B**). Each segment has the same length, corresponding to the same number of samples. As a result, the signal with the stimulation artifact, arising from one electrode (E), consists of segments $s(n)$ of the same length, according to the following rule:

$$E = [s(1),\ s(2),\ s(3), \ldots,\ s(N)] \tag{2}$$

wherein $s(n)$ represents successive segments, i.e., the sets of samples containing the total number of stimulus oscillations and $n \in < 1 : N >$, N is total number of segments.

Calculation of the artifact template

For each segment, $s(n)$, the artifact template *temp* is calculated on the basis of A. A refers to the number of averaged segments centered around the segment $s(n)$. In this process, the segment that is used to count the template is not used in averaging to avoid any possible later subtraction of information about the pure EEG. For this reason, the artifact template $temp(n)$ for the segment $s(n)$ is determined according to the following relationship:

$$temp(n) = \frac{1}{A}\left[\sum_{n+1-\frac{A}{2}}^{n+1+\frac{A}{2}} s(n)\right] \tag{3}$$

wherein $temp(n)$ represents an artifact template for segment $s(n)$, A represents an even number of averaged segments, $s(n)$ represents the segment, $n \in < 1 : N >$, and N refers to the total number of segments.

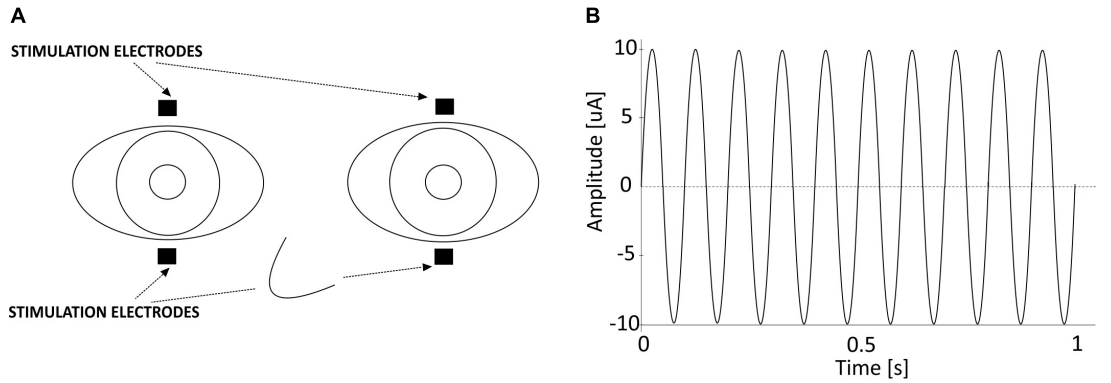

FIGURE 2 | (A) Location of the electrical stimulation electrodes used in the study. **(B)** One second of the 10 Hz 20 μA sinusoidal alternating current stimulation that was applied transorbitally.

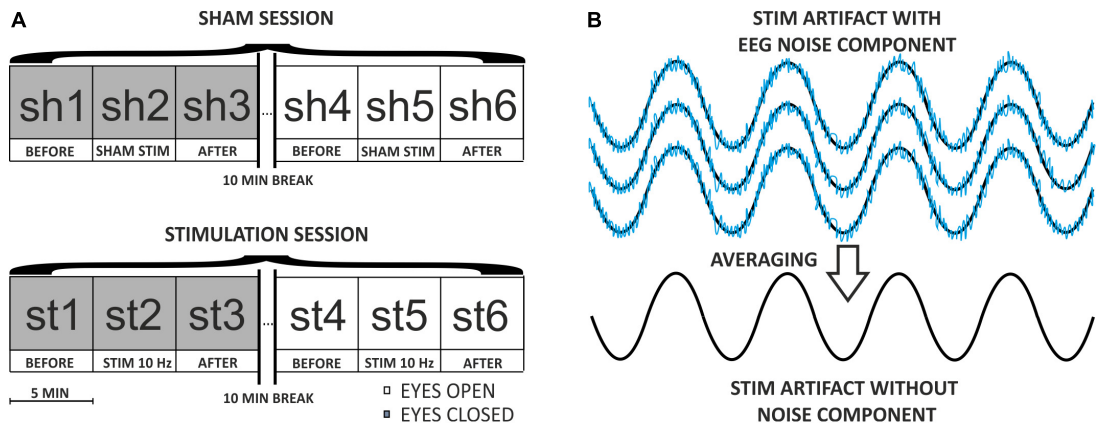

FIGURE 3 | (A) Diagram of the experimental procedure on the first participant. The procedure consisted of two continuous 15-min blocks (one with eyes closed, one with eyes open) repeated over the course of two subsequent days (SHAM and STIMULATION). A 10-min break separated each block, and EEG data were not recorded during the breaks. During every 15-min session, the stimulation lasted 5 min, and had a frequency of 10 Hz and an amplitude of 20 μA. **(B)** Diagram of the coherent averaging idea. In this example, four noisy sinusoidal segments compatible with phase are averaged resulting in a "pure" sinusoidal signal. The noise component with a low amplitude represents endogenous EEG activity embedded in a high-amplitude sinusoidal wave representing an ACS artifact. The noise after averaging is close to 0, which indicates that coherent averaging sets information about endogenous EEG activity to zero and thus allows for the acquisition of the ACS artifact template (i.e., sinusoidal component).

Subtraction of templates from segments

The last stage consists of subtracting the prepared templates from the corresponding segments. This operation results in a new segment, $newS\,(n)$, that is free of artifact and can be calculated as follows:

$$newS\,(n) = s\,(n) - temp\,(n) \tag{4}$$

wherein $newS\,(n)$ refers to a new segment without stimulation artifact, $s\,(n)$ represents the artifact segment, and $temp\,(n)$ represents the artifact template for segment $s\,(n)$.

Figure 5 presents three consecutive example segments. Each segment [i.e., $s\,(n)$, $s\,(n+1)$, and $s\,(n+2)$] (**Figures 5A–C**) was obtained from a signal with 10 Hz stimulation. Each segment was constructed from 10 sinusoidal periods. Thus, each segment is a 1-s recording and, due to the 500 Hz sample frequency, every $s\,(n)$ contains 500 samples. One period contains 50 samples according to the simple calculation $\frac{500\ Hz}{10\ Hz} = 50$. Three consecutive artifact templates [$temp\,(n)$, $temp\,(n+1)$, and $temp\,(n+2)$] were constructed from the average of 20 segments centered around the considered segment. The final effect of the filtering algorithm using the moving average method presents new filtered segments without artifact templates [$newS\,(n)$, $newS\,(n+1)$, and $newS\,(n+2)$], and with an amplitude that does not exceed 0.1 mV. The amplitude before and after the filtering has been changed more than 10 times.

Method for Selecting the Optimal Parameters of Filtration

Here, we analyzed the accuracy of artifact removal using the designed algorithm to verify, in detail, the effects of the two filtration parameters: (1) the number of periods per segment (i.e., in each artifact template) and (2) the number of averaged segments used to create each artifact template.

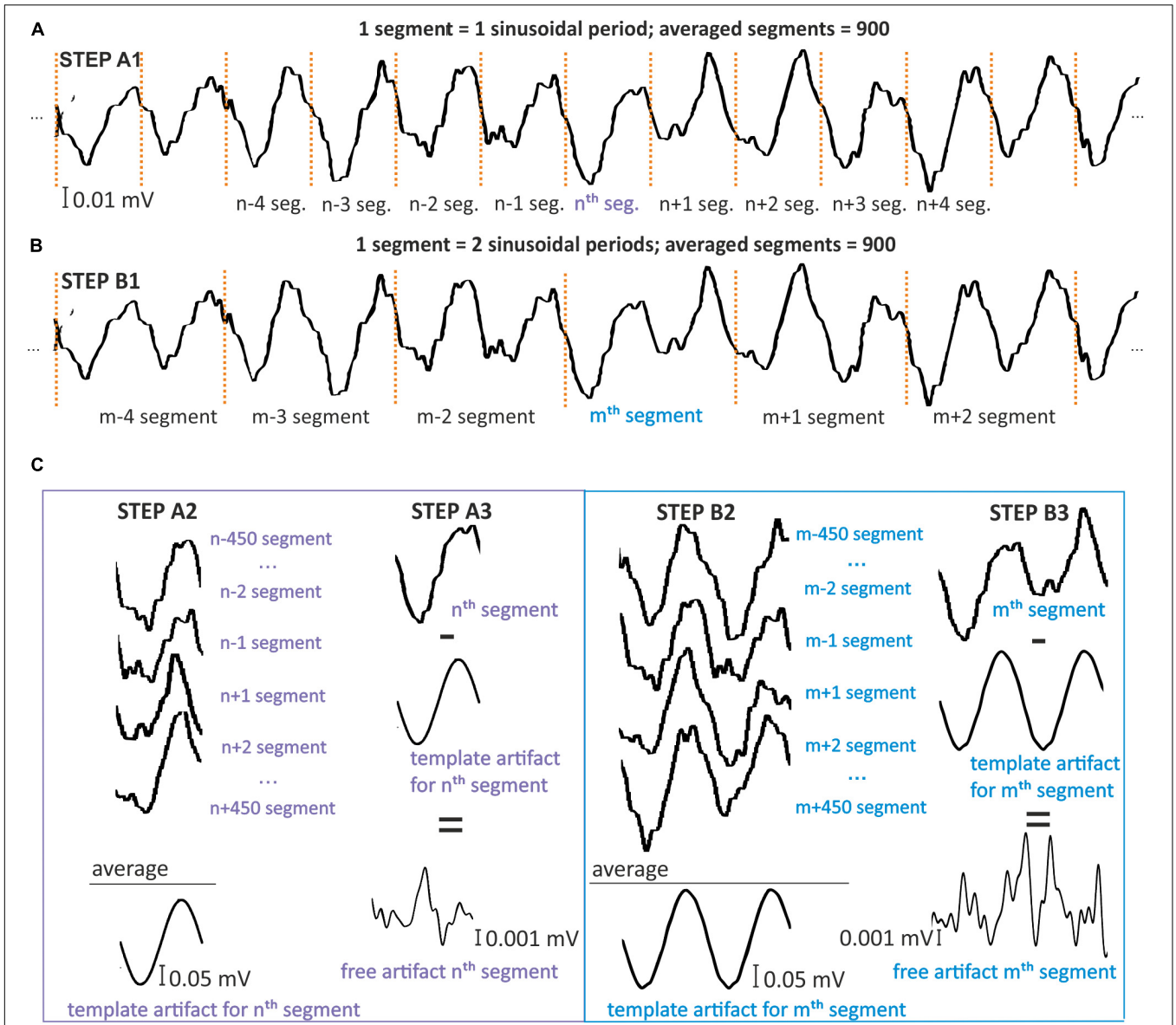

FIGURE 4 | Model for simple moving average filtration for 1- **(A)** and 2-period **(B)** segments. Simulation was prepared on signal STEP A1, B1, by dividing the signal for one or two period segments [s(n) and s(m)]. STEP A2, B2: To create an artifact template for the nth or mth segment, 900 other segments were selected that centered around the considered segments. The samples in the same phase were then averaged by columns. STEP A3,B3: The resulting artifact templates were then subtracted from the nth and mth segments that included artifact. This subtraction results in nth and mth segments that are free of artifact.

Verifying the effectiveness of artifact removal without simultaneously removing information about neural activity from the EEG signal is difficult due to the lack of a model that predicts the "real" EEG signal "hidden" under the artifact and lays in the middle of the inverse problem. To facilitate understanding the problem of removing stimulation artifact from EEG recordings, we present results of SMA filtering on signal recorded during eyes closed (**Figure 6A**) and eyes open (**Figure 6C**) conditions. These results are shown in time and frequency domains only, for one of several possible filtering settings (i.e., 900 1-period segments to create 1-period artifact template). Following filtration, a decrease in signal amplitude is observed in both time and frequency domains. Unfortunately, because we are unable to compare these results to a known stimulus signal, we have no information on the accuracy of removing the artifact and possible loss of information about neuronal activity. Therefore, it is important to identify the filtration conditions that would be most effective, and how to achieve a reliable assessment of the filtration algorithm.

Taking these factors into consideration, we adopted the following principle. First, a sinusoidal waveform interpolated and downsampled to simulate an undefined sinusoidal waveform in the actual EEG recording, EEG_S, was superimposed on pure *EEG* signal with a known power spectrum. Then, after applying the algorithm with different filtering parameters, the obtained signal

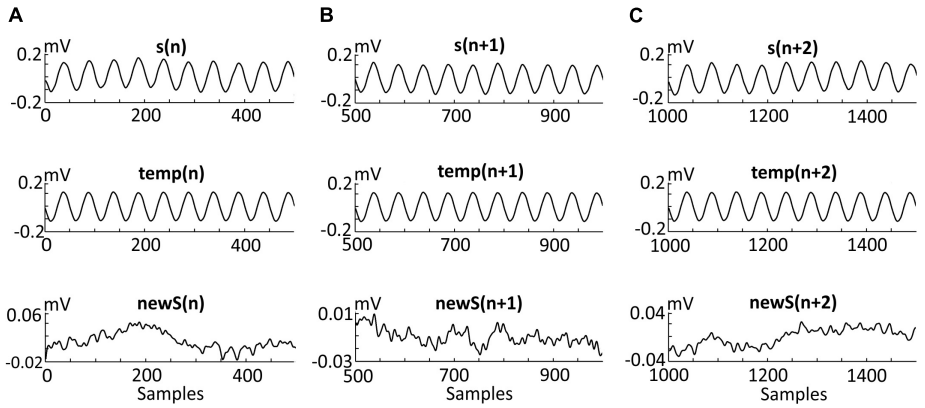

FIGURE 5 | Effects of the three steps of the algorithm. Three adjacent segments [s(n) **(A)**, s(n + 1) **(B)**, and s(n + 2) **(C)**] recorded during the stimulation of the second participant (details provided in the "Methods and Materials" section). Each segment contains 10 oscillations of a 10 Hz alternating current. Thus, each segment is a 1-s recording and, due to the 500 Hz sample frequency, every s(n) contains 500 samples. Of note, one period contains 50 samples according to the simple calculation (500 Hz)/(10 Hz) = 50. Each template [i.e., temp (n), temp(n + 1), and temp(n + 2)] was created by averaging 20 segments centered around segments s(n), s(n + 1), and s(n + 2). Three new segments [i.e., newS(n), newS(n + 1), and newS(n + 2)] were obtained after subtracting the artifact templates as follow: s(n)-temp(n) = newS(n).

($EEG_{removedArtifact}$) was compared with the original pure *EEG* signal. The described algorithm is as follows:

1. *EEG* + *SINUS* interpolated by the order of 10, then subjected to the downsampled by the order of 10 – (EEG_S).
2. EEG_S subjected to the sine artifact removal algorithm – ($EEG_{removedArtifact}$).
3. Compare *EEG* with $EEG_{removedArtifact}$.
   wherein *EEG* represents the EEG signal from the selected electrode, *SINUS* refers to the artificial stimulation in a form of sinusoidal function with a known frequency (*freqStim*), and amplitude (*Amp*).

Performing the simulation (see **Figures 6B,D**) using this approach allows for the determination of the optimal filtration parameters. These optimal parameters could then be used on the signal recorded during a real stimulation session. Upon application to real data, it is important that the EEG signal used in the simulation has the same sampling frequency and duration. Also, the artifact should be characterized by the frequency given in the actual stimulation. The number of averaged oscillations needed to create an artifact template is increased gradually until the signal is the closest to the original recorded signal. The resulting fixed length of the averaging window could then be used to remove the artifact in the stimulation signal.

To perform filtration of blocks *st2* (i.e., signal with eyes closed during stimulation, **Figure 3A**), a simulation needs to be prepared using a signal from block *sh2* (i.e., eyes closed during sham stimulation). The choice of signals is dictated by the need to preserve a similar condition of the subject from the real stimulation stage and the signal without the stimulation that is used to perform the simulation. For this reason, an analogous approach should be used to filter the block *st5* (i.e., signal with eyes open during stimulation). The reference signal for this case is block *sh5* (i.e., signal with eyes open during sham stimulation). In our opinion, it is important to keep the characteristics of the reference signals as close as possible to the signal from which the artifact should be removed. The simulation of artifact removal from block *sh2* contained the following components: (1) *EEG* (signal from the O2 electrode, block lasting 5 min, eyes closed during sham stimulation) and (2) *SINUS* (artificial stimulation, a sinusoidal function with *freqStim* = 10 Hz, and *Amp* = 0.0002 V (peak-to-peak of the sine wave).

To determine the optimal averaging parameters, we evaluated the percentage difference in the power spectrum (i.e., spectrum percentage difference, SPD) in the alpha band, and the difference in stimulation frequency between the original and filtered signal. The SPD was calculated as follow (5):

$$\textit{difference between spectra}\ (SPD) = \frac{\sum_{f=f}^{F} \left| P_{pureEEG} - P_{removedArtifact} \right|}{\sum_{f=f}^{F} \left| P_{pureEEG} \right|} * 100 \qquad (5)$$

wherein $P_{removedArtifact}$ is the power of the signal after filtration; $P_{pureEEG}$ is the power of the original signal; and f and F represent the minimum and maximum frequencies of the band, respectively.

The value of the signal's power in the given frequency band from f to F was determined using the following Formula (6):

$$P_{pureEEG/removedArtifact} = \left| FFT\ (df) \right|^2 \qquad (6)$$

where in $FFT\ (df)$ is the value of the signal amplitude calculated using the Fast Fourier Transform algorithm for frequencies from f to F with the frequency resolution df.

SPD in alpha band was calculated in the 8–12 Hz range, and in stimulation of 10 Hz frequency in the range of 9.5–10.5 Hz.

An analogous approach was used to analyze the differences in signals in the time domain by determining the differences in signal variances. Here, the variance of the time series is understood as a measure of the fluctuation of the signal amplitude

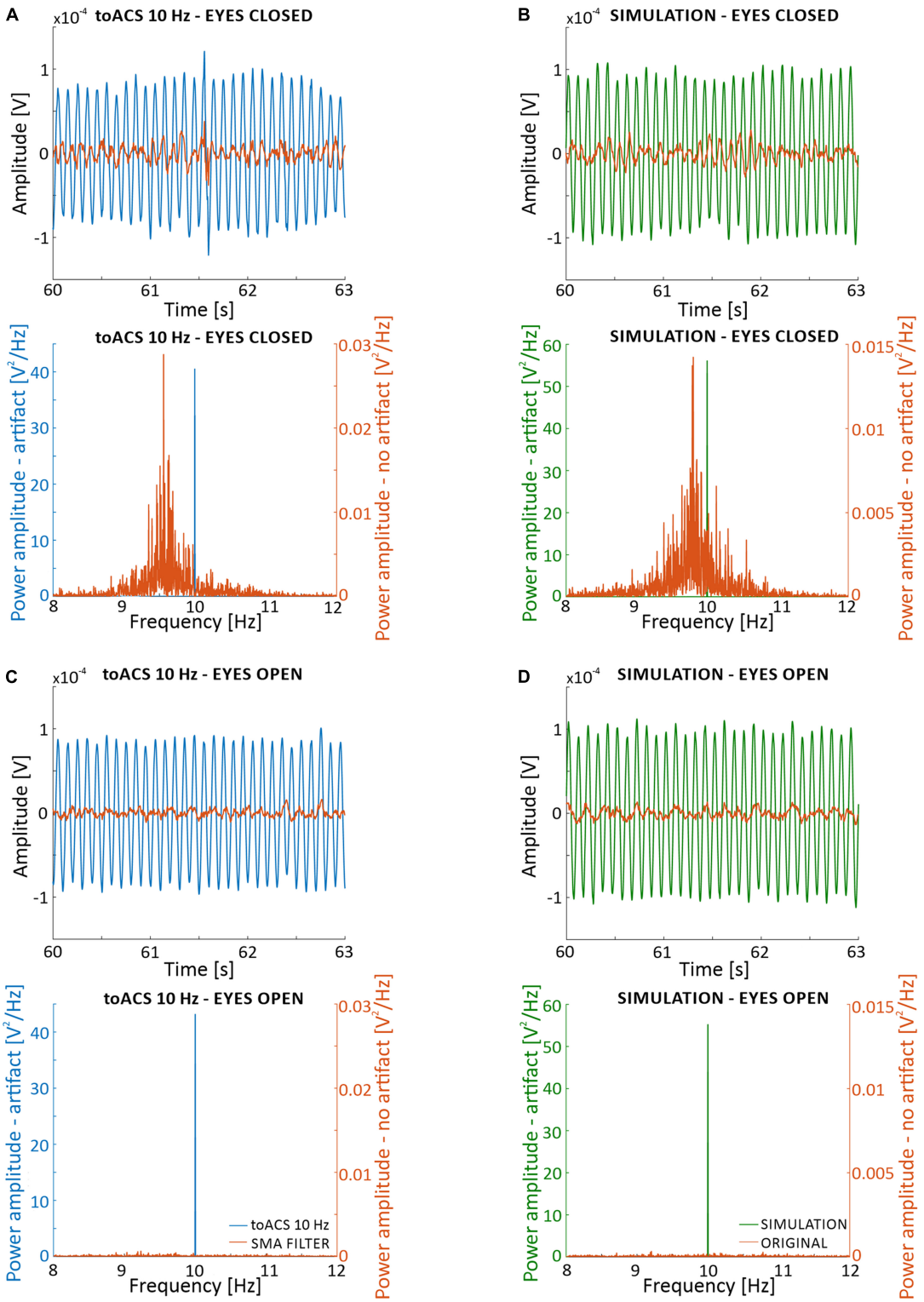

FIGURE 6 | Effects of simple moving average (SMA) filtration on 5-min of EEG signal recorded from the O2 electrode from the first participant with real stimulation artifact (i.e., blocks *st2* and *st5*) **(A,C)**, and with a superimposed artificial sinusoidal function (i.e., blocks *sh2* and *sh5*) **(B,D)**. Parameters of the filtration are: 1-period segments and 900-segment artifact templates. **(A)** Time and frequency analysis for the eyes closed condition with real stimulation artifact. **(B)** Time and frequency analysis for the eyes closed condition with superimposed artificial sinusoid. **(C)** Time and frequency analysis for the eyes open condition with real stimulation artifact. **(D)** Time and frequency analysis for the eyes open condition with superimposed artificial sinusoid. The superimposed artificial sinusoid used in **(B,D)** was of 10 Hz frequency and 0.0002 V amplitude.

values around the mean value. The variance, σ^2, of the time series $x(n)$ defines the following relationship (7):

$$\sigma^2 = \frac{1}{N}\sum_{n=1}^{N}(x(n) - x_{averaged})^2 \quad (7)$$

wherein N is the number of samples in $x(n)$, and $x_{averaged}$ is the average value of amplitude in $x(n)$.

The difference between signal variances was calculated according to the following relationship (8):

$$difference\ between\ variances = \frac{\sigma^2_{pureEEG} - \sigma^2_{removedArtifact}}{\sigma^2_{pureEEG}} * 100 \quad (8)$$

wherein $\sigma^2_{pureEEG}$ is the variance of the original signal, and $\sigma^2_{removedArtifact}$ is the variance of the signal after filtration.

RESULTS

Differences in the Frequency Domain

To show quantitative differences in the results more clearly, **Figure 7** report SPD values (defined in "Materials and Methods," section "Method for Selecting the Optimal Parameters of Filtration"). The percentage difference in alpha band power (see **Figure 7A**) between the primary and filtered signal depends on the number of averaged segments, and the number of periods in a given segment. To better illustrate the differences, the x-axis is shown on a logarithmic scale. Based on **Figure 7A**, the use of ten 1-period segments to calculate the artifact template for a 1-period segment results in an 80% change in alpha power as compared to the original signal recorded during the eyes closed condition. For the eyes open condition, there was a 60% alpha power change from the original signal. Increasing the number of 1-period segments used for averaging decreases these differences to the point at which the further extension of the averaging window does not significantly change the accuracy of removing the artifact (i.e., a plateau phase). In our opinion, the starting point of the plateau effect may indicate the most effective values of filtration parameters. Using multiperiod segments results in a similar relation, but the differences start a lower percentage value for short averaging windows (i.e., smaller than 300 segments). Due to the limited number of oscillations in the 5-min signal (i.e., 300 s $*$ 10 oscillations in every second = 3,000) and the selected number of periods in one segment, a limited number of segments were available for averaging. If the signal contains 3,000 oscillations, its division into two-periods segments results in 1,500 segments that can be used for averaging. Similarly, the division into 10-period segments will result in a relatively small number of segments for SMA (300). Taken together, we observed a relatively low difference in the spectrum, averaging for example at 400 segments for 1, 2, 3, etc. periodic division. This observation allows us to conclude that increasing the number of periods in a given segment forces the averaging of a longer signal fragment to obtain a satisfactorily low difference between signals.

As described in the "Materials and Methods" section, artifact may change over time due to several reasons, including progressive changes in the electric potential on the skin-electrode interface. It is therefore desirable to use the shortest possible portion of the signal with stimulation for averaging. It is also important to note that, as the number of periods per segment increases, the plateau effect becomes less apparent. For example, this effect can be seen in the zoomed-in charts shown in **Figure 7** without the logarithmic scale on the x-axis. Such property makes it difficult to identify the optimal filtration parameters. The percent values of changes in the spectrum for 10 Hz (see **Figure 7B**) show a similar trend as observed for the alpha band. In particular, starting from 10 to 600 segments, the power difference between signals at 10 Hz decreased from 97 to 7% in the eyes closed condition and decreased from 95 to 6% in the eyes open condition. Further extension of the averaging window does not significantly improve the filtration accuracy, i.e., the observed changes are on the order of 0.1%. Given the observed changes to the original spectrum induced by our applied algorithm, it seems reasonable to select the filtration parameters using 1-period segments that take into account ˜5% of the entire signal (i.e., 600 1-period segments from all 3000 oscillations).

In contrast to the above analyses, we checked for differences in the spectrum based on the length of signal taken for averaging (see **Figures 7C,D**). The approach was as follows: first, we selected the signal length [e.g., 1200 oscillations (120 s signal), 900 oscillations (90 s signal)]. Then, we determined the method for signal division (e.g., 1, 2, 3. periodic segments), and the SPD value was read for the number of averaged segments according to the following relationship:

$$periods\ in\ one\ segment * averaged\ segments = averaged\ oscillations \quad (9)$$

The data shown in **Figures 7C,D** indicate that the smallest possible difference in the obtained spectrum decreases with an increasing length of the averaged signal used to create the artifact template. In the case of 1200 averaged oscillations (i.e., 40% of 5 min signal), the smallest difference in the alpha band stops at 3–4%. However, for a smaller number of averaged oscillations, this value increases by 4–5% for 900 and 600 oscillations, and by 10% for 300 oscillations. The differences increase by 14 and 24% for 200 and 100 oscillations, respectively (**Figure 7C**). This effect is even stronger for the SPD in the 10 Hz; in particular, the smallest difference results in a 31% increase for the condition with 100 oscillations (**Figure 7D**). It is also interesting to note that the number of periods in each segment has more influence on the SPD value when a smaller number of averaged oscillations is used. As the number of periods in each segment increases together with a smaller number of averaged oscillations, the observed differences in the spectrum increase much faster. This is particularly true for 300, 200, and 100 oscillations. These results are similarly observed for the analysis of differences in the spectrum of the signal with open eyes, and with low power in the alpha band. In order to more accurately illustrate the effects of frequency domain filtration, power spectra for various averaging parameters are provided in **Supplementary Materials**.

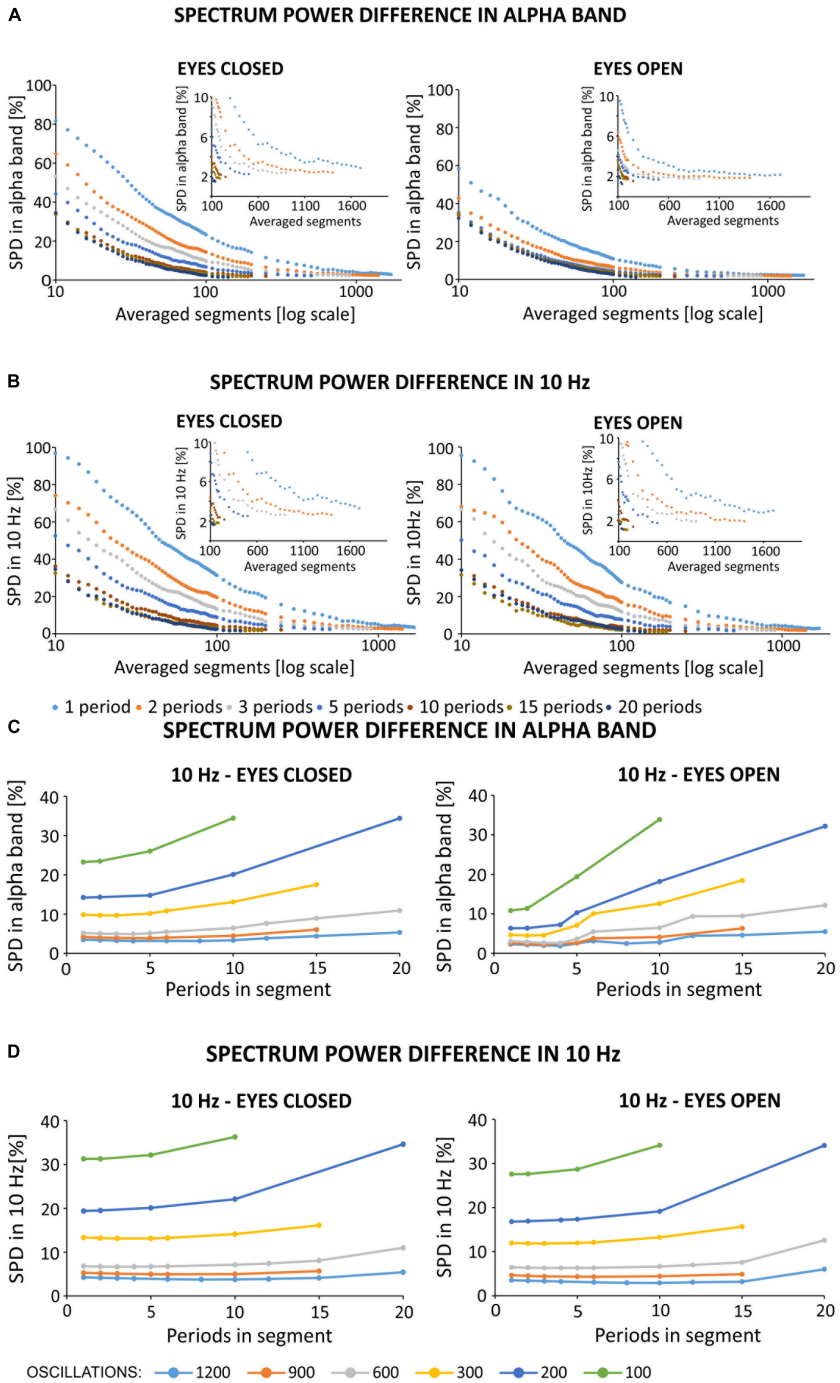

FIGURE 7 | (A,B) Spectrum percentage difference (SPD) between the original signal and the signal obtained after removing the simulated 10 Hz artifact. Simulated artifact was removed using different averaged segments that varied by the number of periods per segment. The zoomed-in portion of each chart highlights a limitation in the available number of averaged segments in different conditions (e.g., varying number of periods in each segment), and highlights the plateau phase. Due to the observed plateau phase, SPD values were determined for a range of 10–100 averaged segments in increments of 2, and in the range of 100–2000 in increments of 50. The original signal was obtained from the O2 electrode from the first participant, and downsampled to 500 Hz. **(A)** Results of SPD in the alpha band after simulated filtration prepared on block *sh2* (i.e., eyes closed) and *sh5* (i.e., eyes open). SPD in the alpha band was counted in the range of 8–12 Hz. **(B)** Results of SPD in 10 Hz after the simulated filtration prepared on block *sh2* (i.e., eyes closed) and *sh5* (i.e., eyes open). SPD in 10 Hz counted in the range of 9.5–10.5 Hz. **(C,D)** Spectrum percentage difference (SPD) between the original signal and the resulting signal after the removal of simulated 10 Hz artifact. Simulated artifact was removed using different averaged segments that varied by the number of periods per segment. The original signal was obtained from the O2 electrode from the first participant and was downsampled to 500 Hz. SPD values were determined according to the relationship described in Formula (9). The artifact template was created by storing the selected fixed number of oscillations to create an artifact template (i.e., 1200, 900, 600, . . .). Then, for a given number of periods in each segment, the appropriate number of averaged segments was selected. **(C)** SPD values in the alpha band (i.e., 8–12 Hz). **(D)** SPD values in 10 Hz (9.5–10.5 Hz).

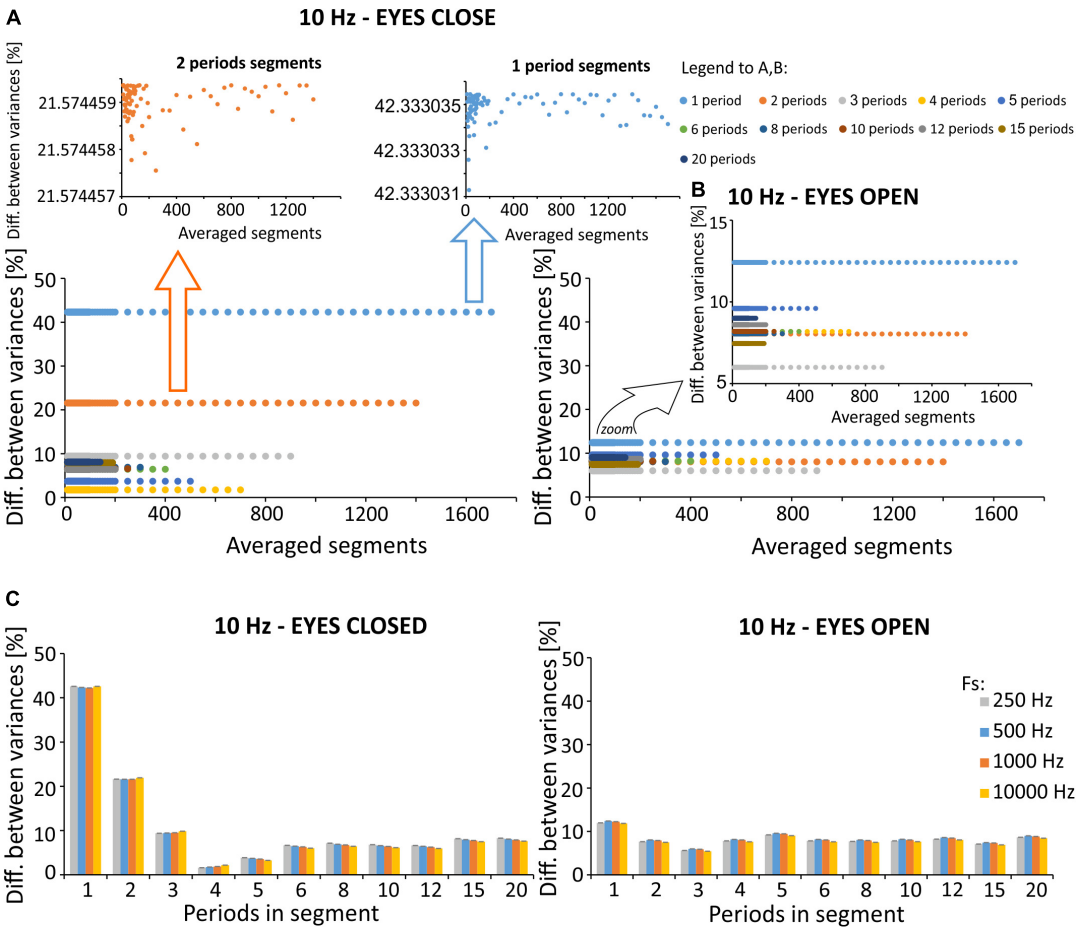

FIGURE 8 | Percent difference between signal variances for the various exemplar selected simulation, calculated according to the relationship described in Formula (8). **(A)** Difference in variance for a varying number of periods per segment, prepared using signal with excitation in the alpha band (eyes closed). Zoomed-in displays for 1- and 2-period segments were prepared to improve visibility of relatively small differences that vary based on averaged segments for the selected number of periods per segment. **(B)** Difference in variance for various number of periods per segment prepared using signal with inactivity in the alpha band (eyes open). **(C)** Averaged differences for various number of periods determined for different sampling frequencies. The original signal was recorded with a sampling frequency of 10 000 Hz, and downsampled in factors of 10, 20, and 40. This allowed us to analyze the signal with a sampling frequency of 1000 Hz, 500 Hz, and 250 Hz.

Differences in the Time Domain

We discovered changes (2–42%) in signal variation following SMA with different filtration parameters (see the 8th equation in the "Materials and Methods" section), as compared to the original signal variance (see **Figures 8A,B**). The eyes open condition is characterized by less pronounced changes in variance (6–13%) as compared to the eyes closed condition (2–42%). Of note, the effects of the number of periods per segment are larger than the number of average segments, when considering the difference in variance between the original and the filtered signals. Changes between signals with a varying number of periods per segment are significantly larger [condition: eyes closed, $p < 0.001$, $\chi^2 = 544.465$, df = (10, 539), Kruskal-Willis; condition: eyes open, $p < 0.001$, $\chi^2 = 544.465$, $df = (10, 539)$, Kruskal-Willis] than changes induced by a varying number of averaged segments [condition: eyes closed, $p = 1$, $\chi^2 = 0.371$, $df = (49, 500)$, Kruskal-Willis; condition: eyes open, $p = 1$, $\chi^2 = 0.574$, $df = (49, 500)$, Kruskal-Willis].

Due to the small differences in variance observed for a selected number of periods per segment, we also evaluated the effects of sampling frequency on the observed results in the time domain (**Figure 8C**). Registrations were made with the original sampling rate, which was equal to 10,000 Hz. To assess the effects of lower frequencies on changes in variances following SMA filtration, the signal was downsampled appropriately to 1000, 500, and 250 Hz. The analysis failed to identify the most effective sampling frequency for the removal of 10 Hz artifact.

Effects of SMA Filtering on the EEG Signal Recorded From Electrode F4

As described in previous studies (Fehér and Morishima, 2016), the amplitude of the stimulation artifact is not the same on all recording electrodes. Indeed, the amplitude has been shown to depend on the distance between the stimulation and recording electrodes. Given this known association, we investigated the effects of SMA filtration on electrode F4, using similar simulation

principles as applied above for O2. Compared to electrode O2, electrode F4 is characterized by a larger stimulation artifact amplitude. Thus, we added an artificial sinusoidal stimulation artifact to the uncontaminated EEG signal from the F4 electrode using an artificial sinusoid amplitude that is two times greater than the amplitude added to O2 (0.0004 V). **Figure 9** presents the SMA filtration effects in the frequency domain for a varying number of averaged 1-period segments on the signal obtained during the eyes closed (**Figure 9A**) and eyes open conditions (**Figure 9B**). These signals were recorded from the F4 electrode and downsampled to 500 Hz. The obtained spectra appear to be similar to the spectra observed for the O2 electrode. For the 10 1-period segments applied to the signal from the eyes closed condition, we observed strong notches in the power spectrum occurring at 10 Hz and for its harmonics. The use of a larger number of averaged segments was associated with a gradual approximation of the amplitude of the signal after filtration to the amplitude of the primary signal. The use of 10 1-period segments to calculate the artifact template for a 1-period segment results in a signal that differs from the original one by 74% in alpha power for the eyes closed condition (**Figure 9C**) and by 60% for the eyes open condition (**Figure 9D**). Increasing the number of 1-period segments used for averaging decreases these differences to the point at which the further extension of the averaging window does not significantly change the accuracy artifact removal (i.e., plateau phase). A similar pattern was observed for the analysis of the O2 electrode, with a smaller stimulation artifact.

Effects of SMA Filtration on EEG Signal With toACS Stimulation Artifact

We investigated the impact of SMA on real signal recorded during toACS from three different electrodes (F4, C3, and O2) recorded during both eyes open (**Figure 10A**) and eyes closed (**Figure 10B**) conditions. The original 5-min signals recorded during real 10 Hz stimulation were filtered with an SMA window that contained 600 1-period segments. Power spectra obtained from different electrodes allowed us to conclude that SMA filtration is useful for the general observation of different brain regions. This was despite the presence of neural activity or inactivity in the alpha band in the case of ∼10 Hz stimulation frequency, or any other frequency band that was identical to the stimulation frequency.

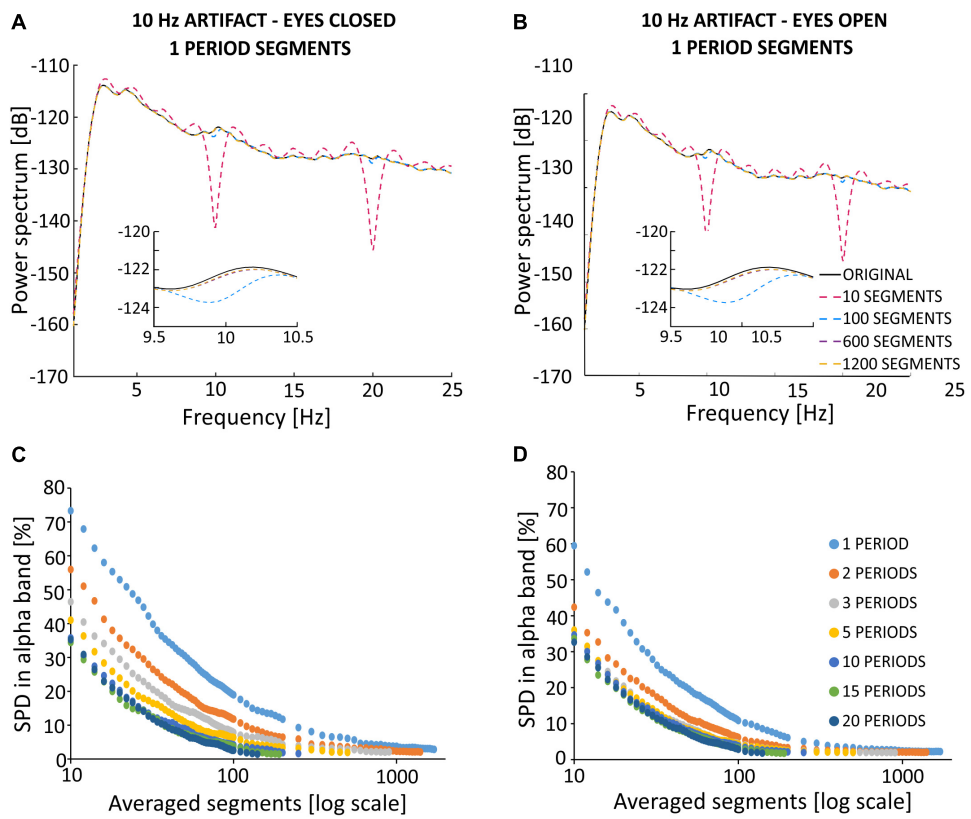

FIGURE 9 | Effects of SMA filtration on EEG signal recorded from the F4 electrode with superimposed artificial stimulation artifact. The F4 electrode is situated closer to the stimulation electrodes than the O2 electrode. Thus, the amplitude of contamination by the stimulation artifact is higher for F4 as compared to O2. **(A)** Results of simulated filtration prepared on block *sh2* (eyes closed). **(B)** Results of simulated filtration prepared on block *sh5* (eyes open). Blocks *sh2* and *sh5* cause the sham registration in the conditions with eyes closed and eyes open. Spectrum percentage difference (SPD) between the original signal and the signal obtained after removal of the simulated 10 Hz artifact, which varies depending on the averaged segments for a varying number of periods per segment for the eyes closed **(C)** and eyes open **(D)** conditions.

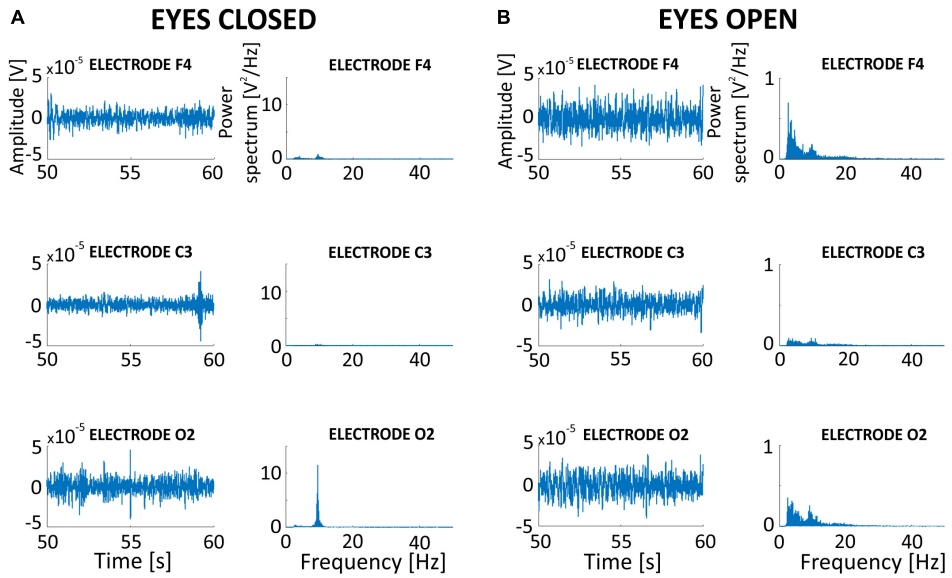

FIGURE 10 | Effects of SMA filtration on EEG signal recorded during 10 Hz sinusoidal toACS from three different electrodes (F4, C3, and O2) during both eyes open **(A)** and eyes closed **(B)** conditions. EEG signals were filtered with a moving window that consisted of 600 1-period segments.

DISCUSSION

Several studies report positive effects of different forms of ACS applied to the visual modality. In human studies of glaucoma or optic neuropathy, 10 days of toACS results in enhanced visual functions, enlarged visual fields, improved visual acuity, and decreased reaction time to visual stimuli, as well as improved vision-related quality of life (Fedorov et al., 2011; Gall et al., 2011; Sabel et al., 2011). A recent pilot clinical study shows similar effectiveness of long-term treatment (i.e., 4–6 years) with transcorneal(tco)ACS (Ota et al., 2018). Moreover, tcoACS has also proven to be useful in the treatment of retinitis pigmentosa, wherein recent clinical studies in humans demonstrate both structural and functional improvement (Schatz et al., 2011; Bittner and Seger, 2018; Bittner et al., 2018, however, see Wagner et al., 2017). Several other clinical studies demonstrate that tcoACS can improve visual function (i.e., visual acuity and/or visual field) in patients with various retinal diseases, including retinal artery occlusion, traumatic optic neuropathy, non-arteritic ischemic optic neuropathy, and Best vitelliform macular dystrophy (for a review, see Ota et al., 2018).

The mechanism of action of the various forms of ACS as a therapeutic method is still debated. Animal studies indicate that the therapeutic effects of toACS are due, in part, to neuroprotection of the retinal ganglion cells and decreased degeneration of photoreceptors (Hanif et al., 2016). Neuroprotective and pro-regenerative effects found in rodent models of optic neuropathies and retinal degeneration suggest that both toACS and tcoACS exert their effects via an upregulation of neurotrophic factors and a downregulation of pro-inflammatory pathways [for review, see Sehic et al., 2016; Antal et al., 2017 (submitted)]. Positive effects of toACS and tcoACS are not limited to the retina; indeed, the positive effects may also include changes in brain rhythms. Human and animal studies have shown that stimulation aftereffects also include modifications in neuronal oscillations (i.e., frequency, amplitude and phase), which are known as cortical entrainment (Sergeeva et al., 2015; Gall et al., 2016).

Considering the complexity of mentioned phenomena, there may be objections to whether examination of the acute effect can effectively help to understand the nature of processes related to toACS and tcoACS. There is a possibility, however, that therapeutic value of stimulation is related to brain plasticity. Despite this, observing brain activity during stimulation seems to be extremely helpful in understanding the mechanisms responsible for stable post-stimulation plastic changes.

The present study aimed to solve the problem of removing the EEG signal artifact that results from sinusoidal toACS. We designed an algorithm that allows the user to modify two parameters: (1) the number of sinusoidal periods present in each segment of the divided signal and (2) the number of segments (centered around the segment that included the artifact) used to calculate the artifact template for each segment. The selection of these parameters depends on the sampling frequency of the signal, the duration of the stimulation, and its frequency. Evaluation of the accuracy of artifact removal during real toACS is difficult due to the lack of relevant knowledge about the level to which brain oscillations are entrained by the electrical stimulus during simultaneous EEG recording. A reliable assessment of the accuracy of removing the stimulation artifact is currently possible only on simulation data, in which the information about the primary EEG signal is "hidden" under artificially superimposed sine wave representing sinusoidal toACS artifact. It is then possible to compare the original EEG signal with the EEG signal obtained after filtration in both time and frequency domains.

To choose the optimal parameter values of the SMA-based stimulation artifact removal, the approach we propose assumes that the correct pre-stimulation simulations are performed on the clean EEG signal (i.e., without real stimulation artifact). This approach involves applying a sinusoidal function to the known EEG signal (i.e., reference signal) that is similar in amplitude similar to the function that occurs during real stimulation. In addition, the frequency of the sinusoidal function should be the same as the frequency of the stimulation. The reference signal also should be the same length as the signal recorded during real stimulation and should reflect the condition that the subject was in during actual stimulation. For example, in a paradigm focused on alpha band activity excitation (via, for example, closing the eyes), the reference signal should also include an excitation in alpha band activity. The use of quantitative measures allows for the selection of appropriate filtering parameters, for example: (1) a difference in the power spectrum and/or (2) variance between the reference signal and the signal that resulted from the application of various filtering parameters.

When choosing the optimal averaging parameters, one should bear in mind the fact that in real stimulations, the electrical artifact changes progressively with time. Therefore, the length of the averaging window used to calculate the artifact template should be as short as possible, with minimal difference between the power of the reference signals and the filtered signals. As shown in **Figure 7** for the power domain, the difference between the filtered and the original signal decreases with an increase in the length of the averaged signal. A similar observation has been reported in the removal of deep brain stimulation artifact using an algorithm for creating a stimulation artifact template (Sun and Hinrichs, 2016). Analysis of the accuracy of artifact removal on artificial stimulation data showed power differences in the alpha band between the primary and filtered signals that range from 80 to 2% for different averaging window lengths on signal collected during an eyes closed condition. These differences range from 60 to 2% on signal collected during an eyes open condition. The dynamics of SPD can be characterized exponentially as follows: (1) SPD values decrease with an increase in the signal length used for artifact template creation and (2) the slope of the exponential curve decreases as the number of periods per segment increases. Considering the optimal filtration parameters, it is important to take into account the occurrence of the plateau phase, which is a reflection of the phenomenon that a progressive increase in the number of averaged segments does not substantially improve the accuracy of artifact removal. We predicted a positive effect of averaging the shortest possible signal to remove the artifact from real signals. This prediction allows to conclude that the plateau phase is a basis for inferring the correct choice of length of the averaged signal that is used in the creation of the artifact template. Our conclusions are consistent with previous work that has examined challenges related to removal of sinusoidal artifact. In particular, our results confirm the appropriateness of selecting an averaging window equal to 2.5% of the length of the full signal with stimulation (Helfrich et al., 2014). The approach involved creating an artifact template for a 30-period segment based on 10 neighboring segments centered on the segment that included the target artifact. In the case described by Helfrich and colleagues which included a 10 Hz stimulation that lasted 20 min, this means that 300 out of the total 12,000 oscillations are used for the template (i.e., 2.5% of the entire signal length). In our analysis, a 2.5% averaging window results in the selection of 750 1-period segments from a total of 3000 oscillations. This choice results in an ˜6% difference between the original and the filtered signal in the case of excitation or inactivity in the alpha band. The use of 2- and 3-period averages of 750 segments is in accordance with the results presented in **Figure 7**, and shows a more favorable difference between spectra. However, this approach requires using a larger portion of the signal. The second method proposed in the literature concerns the selection of a window that is 5% of the length of the entire signal and has the smallest possible number of oscillation periods. In our case, this approach would be an average of 150 1-period segments (Kohli and Casson, 2015). According to the simulation results, such averaging is associated with an error in the power spectrum in the alpha band that reaches almost 17% in the case of excitation (i.e., eyes closed) and 8% in the case of inactivity (i.e., eyes open). Under these parameters, the peak amplitude at 10 Hz reaches 22% in both states of activity. Due to the inability to observe the plateau phase for multiperiod data and under short stimulation times, the use of 1-period segments shows a clear plateau phase even in 5-min of signal.

Analysis of differences in the variance between the primary signal and signal after filtration showed that the SMA method induced large percentage changes. In particular, filtering the signal with increased power in the alpha band is characterized by a large percentage difference (42%) for the 1-period segment. This is a prerequisite for using SMA for signal analysis, primarily in the frequency domain. However, it is clear from the spectra obtained after SMA filtration that the algorithm partially removes the stimulation frequency from the spectrum. Adequate maneuvering with averaging parameters minimizes the removal effect.

Recently, an alternative solution has been proposed (Witkowski et al., 2016) to address the problem that the stimulation artifact obscures brain activity in the frequency range of interest: amplitude-modulated ACS (AM-ACS). This new method is based on stimulation with a specific wave created from two frequencies: (1) a high carrier frequency that is not related to brain oscillation and (2) a modulated low target frequency. The AM-ACS signal spectrum in the frequency range of interest is devoid of the large artifact observed during traditional non-modulated ACS. Unfortunately, although this is a relatively new and promising electrical stimulation paradigm, AM-ACS requires additional research to provide answers to many related issues. For example, a recent study compared the effects of ACS and AM-ACS on simulation data with modeled visual cortex (Negahbani et al., 2018). Results of this study indicate that, in the AM-ACS method, it is necessary to use a significantly larger amplitude of stimulation than in traditional ACS to observe similar effects in cortical activity. To the best of our knowledge, no studies using real EEG signals exist, which could prove in detail that AM-ACS and traditional ACS have the same effects on brain activity. Such evidence would be required for researchers to shift toward AM-ACS without negative effects and would

circumvent the problems associated with the ACS artifact. The algorithm we propose here for removing the sinusoidal toACS artifact may improve the accuracy of analyses using signals acquired during ACS and AM-ACS stimulation. This algorithm would allow one to verify and compare the usefulness and imperfections of both methods.

Considering the applicability of the proposed method, it is also worth paying attention to the alternative fMRI research option proposed in a number of papers (Vosskuhl et al., 2016; Chai et al., 2018; Kar et al., 2020). Compared to fMRI, EEG is commonly used in clinical practice and has a very good temporal resolution allowing observations of changes in the brain related to numerous deficits and diseases. Lower availability and much higher cost of the fMRI cannot completely replace the EEG-based research and its usefulness in clinics.

One unquestionable advantage of SMA filtration is the simplicity of the algorithm implementation, and presence of a clear operating principle. The two main parameters of the algorithm directly translate into periodic signal specificity with sinusoidal ACS. It is also important to note that the use of SMA filtration is associated with the assumption that the noise to be removed is additive. Previous research suggests the non-linear nature of the unwanted component in the signal, which may be a limitation to the applicability of the averaging algorithm to remove the ACS artifact (Noury et al., 2016). In response to these reports, Neuling et al. (2017) provided rationale for observing the non-linearity of the ACS artifact, which involved not exceeding the limits of technical stimulators. For this reason, in the present study we carefully monitored the impedance of the electrodes to ensure that the sidebands described in this study are not affected. Due to the aforementioned limitations in the use of SMA resulting from the non-linearity of the artifact caused by the hardware settings, the effect of SMA filtration on the signal from a different recording system was used in the main body of the article. These results are reported in **Supplementary Materials**. The analysis performed on the second signal did not reveal any changes in the effects of SMA filtration that significantly differ from the conclusions described herein. Despite mentioned discussion between research group, no final arrangements have been made about to what extent the artifact should be removed for the signal to be useful. There is a possibility that the proposed cleaning technique can remove some of the recorded ongoing neural activity. Due to this, we prepared detailed analysis in time and frequency domain for simulated data where we have 100% knowledge about original EEG information before adding stimulation artifact. This approach allows us to extract percentage value of accuracy of removing the artifact, which could be useful in planning protocol of stimulation and preprocessing step in EEG with simultaneous stimulation analysis.

DATA AVAILABILITY STATEMENT

The datasets generated for this study are available on request to the corresponding author.

ETHICS STATEMENT

The studies involving human participants were reviewed and approved by Ethical Committee of the University of Warsaw. The patients/participants provided their written informed consent to participate in this study.

AUTHOR CONTRIBUTIONS

MŻ: design and implementation of the filtration method in the Matlab environment and data analysis. MŻ, PD, and WW: writing and reviewing of the manuscript. PD and WW: study design. PD: data acquisition and EEG data pre-processing. WW: supervision. All authors contributed to the article and approved the submitted version.

FUNDING

This study was supported by statutory founding from the Nencki Institute of the Experimental Biology of the Polish Academy of Sciences (MŻ, PD, and WW), the National Centre for Research and Development grant REVIS ERA-NET NEURON/08/2012 (WW), and by the Polish National Science Centre grant 2016/23/N/HS6/02346 (PD).

ACKNOWLEDGMENTS

We would like to appreciate and thank our dear supervisor WW for her time, effort, and support in helping us to become better scientists then we would ever be without her wisdom, objectivity, and friendship. We also thank Thomas FitzGibbon for his comments on an earlier version of this manuscript.

SUPPLEMENTARY MATERIAL

The Supplementary Material for this article can be found online at: https://www.frontiersin.org/articles/10.3389/fnins.2020.00735/full#supplementary-material

REFERENCES

Allen, P. J., Josephs, O., and Turner, R. (2000). A method for removing imaging artifact from continuous EEG recorded during functional MRI. *Neuroimage* 12, 230–239. doi: 10.1006/nimg.2000.0599

Antal, A., Alekseichuk, I., Bikson, M., Brockmöller, J., Brunoni, A. R., Chen, R., et al. (2017). Low intensity transcranial electric stimulation: safety, ethical, legal regulatory and application guidelines. *Clin. Neurophysiol.* 128, 1774–1809. doi: 10.1016/j.clinph.2017.06.001

Bénar, C.-G., Aghakhani, Y., Wang, Y., Izenberg, A., Al-Asmi, A., Dubeau, F., et al. (2003). Quality of EEG in simultaneous EEG-fMRI for epilepsy. *Clin. Neurophysiol.* 114, 569–580. doi: 10.1016/S1388-2457(02)00383-8

Bittner, A. K., and Seger, K. (2018). Longevity of visual improvements following transcorneal electrical stimulation and efficacy of retreatment in three

individuals with retinitis pigmentosa. *Graefes Arch. Clin. Exp. Ophthalmol.* 256, 299–306. doi: 10.1007/s00417-017-3858-8

Bittner, A. K., Seger, K., Salveson, R., Kayser, S., Morrison, N., Vargas, P., et al. (2018). Randomized controlled trial of electro-stimulation therapies to modulate retinal blood flow and visual function in retinitis pigmentosa. *Acta Ophthalmol.* 96, e366–e376. doi: 10.1111/aos.13581

Brignani, D., Ruzzoli, M., Mauri, P., and Miniussi, C. (2013). Is transcranial alternating current stimulation effective in modulating brain oscillations? *PLoS One* 8:e56589. doi: 10.1371/journal.pone.0056589

Chai, Y., Sheng, J., Bandettini, P. A., and Gao, J.-H. (2018). Frequency-dependent tACS modulation of BOLD signal during rhythmic visual stimulation. *Hum. Brain Mapp.* 39, 2111–2120. doi: 10.1002/hbm.23990

Dowsett, J., and Herrmann, C. S. (2016). Transcranial alternating current stimulation with sawtooth waves: simultaneous stimulation and EEG recording. *Front. Hum. Neurosci.* 10:135. doi: 10.3389/fnhum.2016.00135

Fedorov, A., Jobke, S., Bersnev, V., Chibisova, A., Chibisova, Y., Gall, C., et al. (2011). Restoration of vision after optic nerve lesions with noninvasive transorbital alternating current stimulation: a clinical observational study. *Brain Stimul.* 4, 189–201. doi: 10.1016/j.brs.2011.07.007

Fehér, K. D., and Morishima, Y. (2016). Concurrent electroencephalography recording during transcranial alternating current stimulation (tACS). *J. Vis. Exp.* 22:e53527. doi: 10.3791/53527

Gall, C., Schmidt, S., Schittkowski, M. P., Antal, A., Ambrus, G. G., Paulus, W., et al. (2016). Alternating current stimulation for vision restoration after optic nerve damage: a randomized clinical trial. *PLoS One* 11:e0156134. doi: 10.1371/journal.pone.0156134

Gall, C., Sgorzaly, S., Schmidt, S., Brandt, S., Fedorov, A., and Sabel, B. A. (2011). Noninvasive transorbital alternating current stimulation improves subjective visual functioning and vision-related quality of life in optic neuropathy. *Brain Stimul.* 4, 175–188. doi: 10.1016/j.brs.2011.07.003

Gramfort, A., Luessi, M., Larson, E., Engemann, D. A., Strohmeier, D., Brodbeck, C., et al. (2013). MEG and EEG data analysis with MNE-Python. *Front. Neurosci.* 7:267. doi: 10.3389/fnins.2013.00267

Hanif, A. M., Kim, M. K., Thomas, J. G., Ciavatta, V. T., Chrenek, M., Hetling, J. R., et al. (2016). Whole-eye electrical stimulation therapy preserves visual function and structure in P23H-1 rats. *Exp. Eye Res.* 149, 75–83. doi: 10.1016/j.exer.2016.06.010

Helfrich, R. F., Schneider, T. R., Rach, S., Trautmann-Lengsfeld, S. A., Engel, A. K., and Herrmann, C. S. (2014). Entrainment of brain oscillations by transcranial alternating current stimulation. *Curr. Biol.* 24, 333–339. doi: 10.1016/j.cub.2013.12.041

Jas, M., Larson, E., Engemann, D. A., Leppäkangas, L., Taulu, S., Hämäläinen, M., et al. (2018). A reproducible MEG/EEG group study with the MNE software: recommendations, quality assessments, and good practices. *Front. Neurosci.* 12:530. doi: 10.3389/fnins.2018.00530

Kanai, R., Chaieb, L., Antal, A., Walsh, V., and Paulus, W. (2008). Frequency-dependent electrical stimulation of the visual cortex. *Curr. Biol.* 18, 1839–1843. doi: 10.1016/j.cub.2008.10.027

Kar, K., Ito, T., Cole, M. W., and Krekelberg, B. (2020). Transcranial alternating current stimulation attenuates BOLD adaptation, and increases functional connectivity. *J. Neurophysiol.* 123, 428–438. doi: 10.1152/jn.00376.2019

Kasten, F. H., Dowsett, J., and Herrmann, C. S. (2016). Sustained Aftereffect of α-tACS Lasts Up to 70 min after stimulation. *Front. Hum. Neurosci.* 10:245. doi: 10.3389/fnhum.2016.00245

Kohli, S., and Casson, A. J. (2015). "Removal of Transcranial a.c. Current Stimulation artifact from simultaneous EEG recordings by superposition of moving averages," in *Proceedings of the 2015 37th Annual International Conference of the IEEE Engineering in Medicine and Biology Society (EMBC). Presented at the 2015 37th Annual International Conference of the IEEE Engineering in Medicine and Biology Society (EMBC)* (Milan: IEEE), 3436–3439. doi: 10.1109/EMBC.2015.7319131

Kohli, S., and Casson, A. J. (2019). Removal of gross artifacts of transcranial alternating current stimulation in simultaneous EEG monitoring. *Sensors* 19:190. doi: 10.3390/s19010190 PMC6338981

Moreno-Duarte, I., Gebodh, N., Schestatsky, P., Guleyupoglu, B., Reato, D., Bikson, M., et al. (2014). "Transcranial Electrical Stimulation: transcranial Direct Current Stimulation (tDCS), Transcranial Alternating Current Stimulation (tACS), Transcranial Pulsed Current Stimulation (tPCS), and Transcranial Random Noise Stimulation (tRNS)," in *The Stimulated Brain*, Ed. R. C. Kadosh (Amsterdm: Elsevier), 35–59. doi: 10.1016/B978-0-12-404704-4.00002-8

Negahbani, E., Kasten, F. H., Herrmann, C. S., and Fröhlich, F. (2018). Targeting alpha-band oscillations in a cortical model with amplitude-modulated high-frequency transcranial electric stimulation. *Neuroimage* 173, 3–12. doi: 10.1016/j.neuroimage.2018.02.005

Neuling, T., Rach, S., and Herrmann, C. S. (2013). Orchestrating neuronal networks: sustained after-effects of transcranial alternating current stimulation depend upon brain states. *Front. Hum. Neurosci.* 7:161. doi: 10.3389/fnhum.2013.00161

Neuling, T., Ruhnau, P., Weisz, N., Herrmann, C. S., and Demarchi, G. (2017). Faith and oscillations recovered: on analyzing EEG/MEG signals during tACS. *Neuroimage* 147, 960–963. doi: 10.1016/j.neuroimage.2016.11.022

Niazy, R. K., Beckmann, C. F., Iannetti, G. D., Brady, J. M., and Smith, S. M. (2005). Removal of FMRI environment artifacts from EEG data using optimal basis sets. *Neuroimage* 28, 720–737. doi: 10.1016/j.neuroimage.2005.06.067

Noury, N., Hipp, J. F., and Siegel, M. (2016). Physiological processes non-linearly affect electrophysiological recordings during transcranial electric stimulation. *Neuroimage* 140, 99–109. doi: 10.1016/j.neuroimage.2016.03.065

Ota, Y., Ozeki, N., Yuki, K., Shiba, D., Kimura, I., Tsunoda, K., et al. (2018). The efficacy of transcorneal electrical stimulation for the treatment of primary open-angle glaucoma: a pilot study. *Keio J. Med.* 67, 45–53. doi: 10.2302/kjm.2017-0015-OA

Rompelman, O., and Ros, H. H. (1986). Coherent averaging technique: a tutorial review. Part 1: noise reduction and the equivalent filter. *J. Biomed. Eng.* 8, 24–29. doi: 10.1016/0141-5425(86)90026-9

Sabel, B. A., Fedorov, A. B., Naue, N., Borrmann, A., Herrmann, C., and Gall, C. (2011). Non-invasive alternating current stimulation improves vision in optic neuropathy. *Restor. Neurol. Neurosci.* 29, 493–505. doi: 10.3233/RNN-2011-0624

Sabel, B. A., Hamid, A. I. A., Borrmann, C., Speck, O., and Antal, A. (2019). Transorbital alternating current stimulation modifies BOLD activity in healthy subjects and in a stroke patient with hemianopia: a 7 Tesla fMRI feasibility study. *Int. J. Psychophysiol.* 154, 80–92. doi: 10.1016/j.ijpsycho.2019.04.002

Schatz, A., Röck, T., Naycheva, L., Willmann, G., Wilhelm, B., Peters, T., et al. (2011). Transcorneal electrical stimulation for patients with retinitis pigmentosa: a prospective, randomized, sham-controlled exploratory study. *Invest. Ophthalmol. Vis. Sci.* 52, 4485–4496. doi: 10.1167/iovs.10-6932

Sehic, A., Guo, S., Cho, K. S., Corraya, R. M., Chen, D. F., and Utheim, T. P. (2016). Electrical stimulation as a means for improving vision. *Am. J. Pathol.* 186, 2783–2797. doi: 10.1016/j.ajpath.2016.07.017

Sergeeva, E. G., Henrich-Noack, P., Gorkin, A. G., and Sabel, B. A. (2015). Preclinical model of transcorneal alternating current stimulation in freely moving rats. *Restor. Neurol. Neurosci.* 33, 761–769. doi: 10.3233/RNN-150513

Sun, L., and Hinrichs, H. (2016). Moving average template subtraction to remove stimulation artefacts in EEGs and LFPs recorded during deep brain stimulation. *J. Neurosci. Methods* 266, 126–136. doi: 10.1016/j.jneumeth.2016.03.020

Vossen, A., Gross, J., and Thut, G. (2015). Alpha Power Increase After Transcranial Alternating Current Stimulation at Alpha Frequency (α-tACS) Reflects Plastic Changes Rather Than Entrainment. *Brain Stimulat.* 8, 499–508. doi: 10.1016/j.brs.2014.12.004

Vosskuhl, J., Huster, R. J., and Herrmann, C. S. (2016). BOLD signal effects of transcranial alternating current stimulation (tACS) in the alpha range: a concurrent tACS–fMRI study. *Neuroimage* 140, 118–125. doi: 10.1016/j.neuroimage.2015.10.003

Wagner, S. K., Jolly, J. K., Pefkianaki, M., Gekeler, F., Webster, A. R., Downes, S. M., et al. (2017). Transcorneal electrical stimulation for the treatment of retinitis pigmentosa: results from the TESOLAUK trial. *BMJ Open Ophthalmol.* 2:e000096. doi: 10.1136/bmjophth-2017-000096

Witkowski, M., Garcia-Cossio, E., Chander, B. S., Braun, C., Birbaumer, N., Robinson, S. E., et al. (2016). Mapping entrained brain oscillations during transcranial alternating current stimulation (tACS). *Neuroimage* 140, 89–98. doi: 10.1016/j.neuroimage.2015.10.024

Conflict of Interest: The authors declare that the research was conducted in the absence of any commercial or financial relationships that could be construed as a potential conflict of interest.

frontiers in Neuroscience

ORIGINAL RESEARCH
published: 03 December 2020
doi: 10.3389/fnins.2020.560878

Amplitude of fNIRS Resting-State Global Signal Is Related to EEG Vigilance Measures: A Simultaneous fNIRS and EEG Study

*Yuxuan Chen[1], Julia Tang[2], Yafen Chen[2], Jesse Farrand[2], Melissa A. Craft[3], Barbara W. Carlson[3] and Han Yuan[2,4]**

[1] School of Electrical and Computer Engineering, University of Oklahoma, Norman, OK, United States, [2] Stephenson School of Biomedical Engineering, University of Oklahoma, Norman, OK, United States, [3] Fran and Earl Ziegler College of Nursing, University of Oklahoma Health Sciences Center, Oklahoma City, OK, United States, [4] Institute for Biomedical Engineering, Science, and Technology, University of Oklahoma, Norman, OK, United States

OPEN ACCESS

Edited by:
Waldemar Karwowski, University of Central Florida, United States

Reviewed by:
Vassiliy Tsytsarev, University of Maryland, College Park, United States
Aleksandra Dagmara Kawala-Sterniuk, Opole University of Technology, Poland

***Correspondence:**
Han Yuan
hanyuan@ou.edu

Specialty section:
This article was submitted to Neural Technology, a section of the journal Frontiers in Neuroscience

Received: *10 May 2020*
Accepted: *11 November 2020*
Published: *03 December 2020*

Citation:
Chen Y, Tang J, Chen Y, Farrand J, Craft MA, Carlson BW and Yuan H (2020) Amplitude of fNIRS Resting-State Global Signal Is Related to EEG Vigilance Measures: A Simultaneous fNIRS and EEG Study. Front. Neurosci. 14:560878. doi: 10.3389/fnins.2020.560878

Recently, functional near-infrared spectroscopy (fNIRS) has been utilized to image the hemodynamic activities and connectivity in the human brain. With the advantage of economic efficiency, portability, and fewer physical constraints, fNIRS enables studying of the human brain at versatile environment and various body positions, including at bed side and during exercise, which complements the use of functional magnetic resonance imaging (fMRI). However, like fMRI, fNIRS imaging can be influenced by the presence of a strong global component. Yet, the nature of the global signal in fNIRS has not been established. In this study, we investigated the relationship between fNIRS global signal and electroencephalogram (EEG) vigilance using simultaneous recordings in resting healthy subjects in high-density and whole-head montage. In Experiment 1, data were acquired at supine, sitting, and standing positions. Results found that the factor of body positions significantly affected the amplitude of the resting-state fNIRS global signal, prominently in the frequency range of 0.05–0.1 Hz but not in the very low frequency range of less than 0.05 Hz. As a control, the task-induced fNIRS or EEG responses to auditory stimuli did not differ across body positions. However, EEG vigilance plays a modulatory role in the fNIRS signals in the frequency range of less than 0.05 Hz: resting-state sessions of low EEG vigilance measures are associated with high amplitudes of fNIRS global signals. Moreover, in Experiment 2, we further examined the epoch-to-epoch fluctuations in concurrent fNIRS and EEG data acquired from a separate group of subjects and found a negative temporal correlation between EEG vigilance measures and fNIRS global signal amplitudes. Our study for the first time revealed that vigilance as a neurophysiological factor modulates the resting-state dynamics of fNIRS, which have important implications for understanding and processing the noises in fNIRS signals.

Keywords: electroencephalography, functional near-infrared spectroscopy, resting state, vigilance, global signal

INTRODUCTION

Functional near-infrared spectroscopy (fNIRS) is a non-invasive functional neuroimaging technique that can monitor concentration changes in oxygenated and deoxygenated hemoglobin (HbO and HbR) in the cerebral cortex. fNIRS measurement is based on the absorption of light in near-infrared spectrum from 700 to 1000 nm by biological tissues. Different chromophores, such as hemoglobin, myoglobin, and cytochrome aa3, have different absorptivity (Sood et al., 2015). With the advantage of low-cost, portability, and ease to co-register with other neural recording modalities, such as an EEG and fNIRS has become an attractive means for imaging and monitoring hemodynamic signals in the human brain, which complements the use of fMRI in versatile environment. fNIRS has been widely applied in functional neuroimaging (Torricelli et al., 2014; Chen et al., 2020), cerebral monitoring in neonates (Sood et al., 2015; Hu et al., 2020) and brain-computer interface (Naseer and Hong, 2015; Ahn and Jun, 2017; Shin et al., 2017). Unlike fMRI constraining subjects to lying down on a scanner bed, fNIRS poses fewer physical constraints on the participants, thereby permitting them to be studied at flexible body positions during recordings.

Particularly, imaging of resting-state functional connectivity (RSFC) in the human brain has been a recent focus for neuroimaging studies, including fNIRS (Mohammadi-Nejad et al., 2018; Pinti et al., 2018). The activity of the resting brain exhibits spontaneous and large-amplitude fluctuations, which have been observed in a number of imaging modalities such as fMRI (Biswal et al., 1995), positron emission tomography (Raichle et al., 2001; Watabe and Hatazawa, 2019), and direct measures of neuronal activity with electro- or magneto-encephalography (EEG or MEG) (Goldman et al., 2002; Mantini et al., 2007; Brookes et al., 2011; Yuan et al., 2012, 2016). The measures of resting-state cerebral hemodynamics, mostly using fMRI based on the blood-oxygenation-level dependent (BOLD) contrast, show fluctuations predominantly at a low frequency band of <0.1 Hz (Cordes et al., 2001). The temporal synchrony across brain regions have been revealed (Beckmann et al., 2005; Damoiseaux et al., 2006), and demonstrated to be important biomarkers for the brain at diseased conditions (Zhang and Raichle, 2010). Prior studies of RSFC in both healthy and diseased conditions can be influenced by the presence of a strong global component, which is usually observed throughout sampled voxels or sensors, thereby dominating the RSFC (Greicius et al., 2003; Fox et al., 2005, 2009). However, the approach of removing global signal has recently been shown to induce systematic biases and the anti-correlation enhanced by global signal regression (GSR) becomes the main concern (Fox et al., 2009; Murphy et al., 2009). Furthermore, evidences show that a neural component (Scholvinck et al., 2010; Wong et al., 2013, 2016) and even diagnostic information (Hahamy et al., 2014; Murphy and Fox, 2017; Yang et al., 2017) exist in the global signal, which challenges the assumption of removing it in the first place.

Like fMRI signals, fNIRS also offers the potential to examine the human brain at resting state by measuring concentration changes of HbO and HbR in the vasculature of the cortical tissues below sensing channels (Obrig and Villringer, 2003; Scholkmann et al., 2014). fNIRS has been effectively employed to characterize the resting-state brain in adults (Obrig et al., 2000; White et al., 2009; Lu et al., 2010; Mesquita et al., 2010; Zhang et al., 2010; Sasai et al., 2011; de Souza Rodrigues et al., 2019), infants or children (Homae et al., 2010; White et al., 2012; Molavi et al., 2013; Watanabe et al., 2017; Bulgarelli et al., 2019, 2020; Wang et al., 2020), and to assess differences between experimental groups (Keehn et al., 2013; Ieong et al., 2019; Arun et al., 2020). The most common RSFC analysis of fNIRS data involves evaluating the temporal relationship between time series of the preprocessed data from recording units, for example, through the Pearson's correlation. A global component has been observed in fNIRS measurements and commonly removed for the purpose of attenuating systematic noises at the resting state (White et al., 2009; Gregg et al., 2010; Mesquita et al., 2010; Eggebrecht et al., 2014; Tachtsidis and Scholkmann, 2016; Duan et al., 2018; Sherafati et al., 2020; Wyser et al., 2020). Whereas removing superficial contributions from short-distanced channels to fNIRS is increasingly employed to attenuate the systematic noises (Saager and Berger, 2005; Gagnon et al., 2011), data from both long-distanced and short-distanced channels commonly suggest a global component exist in fNIRS measurements and distribute across wide regions (Zhang et al., 2005, 2007, 2009; Kohno et al., 2007; Gregg et al., 2010; Tong and Frederick, 2010; Novi et al., 2016; Sato et al., 2016). However, the physiological nature of the fNIRS global signal has not been fully established, since the neurophysiological components in the resting-state global fNIRS signal have not been systematically investigated. Therefore, whether or not to remove the global signal in fNIRS-based RSFC analysis remains not clear.

In this study, we aimed to investigate the physiological underpinning of resting-state fNIRS global signal by concurrently acquiring fNIRS and EEG in whole-head, high-density montage. Previous studies using simultaneous EEG and fMRI recordings have revealed a negative association between the amplitude of resting state fMRI global signal and EEG vigilance level (Wong et al., 2013; Chang et al., 2016; Falahpour et al., 2018). These studies have shown that subjects at lower vigilance states are characteristic of higher global signal amplitudes, indicating that neurophysiological covariates exist in the global signal. Moreover, the temporal fluctuations of vigilance levels has been linked to the spontaneous activities in regions constituting the default mode network (DMN) (Olbrich et al., 2009) and also linked to the fluctuations of fMRI global signal (Chang et al., 2016; Falahpour et al., 2018), suggesting that regressing out the resting-state global signal could potentially impact the dynamic connectivity in resting state networks. Based on the prior studies using BOLD fMRI, in the current study we hypothesize that the fNIRS global signal has a neurological component and is related to the EEG vigilance. Two experiments were included: the 1st is a 10-min resting study from which we calculated the stationary metrics; the 2nd is a 45-min resting study from which we examined the epoch-to-epoch dynamics during the wakeful epochs. Furthermore, considering that fNIRS is a promising technology for imaging the human brain at versatile body positions, Experiment 1 also examined whether and how different

body positions affect the fNIRS global signal at resting state conditions and, as a control, the impact of body positions on evoked activities to auditory stimuli was studied. To our knowledge, our study is the first of its kind to examine the relationship between fNIRS global signal and EEG vigilance with an advanced simultaneous EEG and fNIRS system in high-density and whole-head montage.

MATERIALS AND METHODS

Protocol

All study procedures were completed according to the Declaration of Helsinki guidelines and approved by the Institutional Review Board at the University of Oklahoma Health Sciences Center.

Experiment 1: 10-min Resting at Different Body Positions

Twenty-four healthy subjects were recruited after giving informed consent. All subjects were right-handed. Two subjects were excluded due to excessive movements during the recording. Another three subjects were excluded due to high electrode impedance in recording sessions. Thus, nineteen subjects' data were included in the analysis (11 males and 8 females, aged 19 to 55 years old, average age ± STD = 30.8 ± 12.2 years). Each subject participated in two separate sessions, eyes-open (EO) and eyes-closed (EC), the order of which was randomized. For each subject, two sessions occurred on different days that were within a 4-week period (mean interval ± STD = 18.2 ± 29.5 days). Each session contained three recording blocks at different body positions: standing, sitting, and supine. The order of these blocks was randomized among all subjects but was kept the same for each subject at their consecutive visits. Each block contained a 10-min resting-state part and an auditory task part that lasted 6 min and 30 s. In the resting-state part, subjects were instructed to keep as still as possible and not fall asleep. Specifically, in EO resting condition, subjects were instructed to focus on a black cross on a white background. In the auditory task part, subjects were instructed to keep still and listen to the auditory stimuli from a pair of earbuds. In terms of the presentation, periods of 30-s stimuli on and 30-s stimuli off were interleaved. Within a period of stimuli on, subjects listened to a sequence of 15 brief one-kilohertz tones. One tone lased for 100 ms duration and sampled at 44.1 kHz. Tones within a stimuli-on period were separated by an inter-stimulus interval of 2 s. Six datasets (two eye conditions by three body positions) were obtained for each subject, yielding a total of 114 datasets in the current study, which included concurrent EEG and fNIRS data of both resting state and task conditions.

Experiment 2: 45-min Resting at Supine Position

Because Experiment 1 used a stationary design of 10-min resting study to investigate the fNIRS resting state signals, we further included Experiment 2 in the design of a 45-min resting study to examine the temporal dynamics in fNIRS global signal. Specifically, subjects were instructed to rest still and allowed to fall asleep during a 45-min recording, while subjects laid supine in an adjustable recliner. A total of 20 healthy subjects (sex: 12 females and 8 males; aged 28 to 63 years old; average age ± STD: 42.8 ± 11.7 years) were studied in Experiment 2 and no subjects overlapped in Experiments 1 and 2. The recording began and ended with bio-calibration, which were used to identify artifacts in the EEG recordings. The bio-calibration procedure was performed in a standard order of instructing subjects to (1) open and close their eyes, (2) blink, (3) perform lateral eye movements, (4) take deep breaths, (5) clench their teeth, and to (6) speak.

fNIRS Data Acquisition

An identical configuration of acquisition was used in Experiments 1 and 2. The fNIRS measurements were acquired with a NIRScout system (NIRx Medical Technologies, LLC, New York, United States). Thirty-two source probes and 32 detector probes were plugged into holders and arranged into a cap based on the international 10–5 system (Jasper, 1958). A total of 105 channels (i.e., 105 pairs of sources and detectors) were defined, covering the areas from the forehead to the occipital lobe. The inter-optode distance varied between 25, 27, and 30 mm, corresponding to three different sizes of caps (54, 58, and 60 cm). The intersection between the left and right tragus and the Nasion and Inion was the center of the cap, which was denoted by the Cz position. A dark black over-cap covered the cap to block external light luminance. The absorption of near-infrared light of two different wavelengths (760 and 850 nm) was measured with a sampling rate of 1.95 Hz.

EEG Data Acquisition

A 64-channel, fNIRS-compatible EEG system (BrainProducts, München, Germany) was utilized to record the EEG data. In order to couple the EEG signal with the fNIRS hemodynamic signal, the montage of the EEG electrodes was designed to match the fNIRS montage. Every EEG channel was crossed by an adjacent pair of light source and detector. Sixty-four EEG electrodes were also mounted onto corresponding holders. The electrode at FCz position was selected as the reference point. Two 32-channel amplifiers, which were powered by a rechargeable battery, were included in our EEG system. Electrically conductive gel was added to decrease the impedance between scalp and electrodes. The impedances of EEG electrodes were kept under 20 kΩ throughout the recordings. All the EEG datasets were digitized with a wide band of 0.1–250 Hz at a 500 Hz sampling rate.

fNIRS and EEG Data Pre-processing

Figure 1 shows the analysis flowchart of EEG and fNIRS data. EEGLAB (Delorme and Makeig, 2004) was used for pre-processing of EEG data. After loading the raw datasets, the data was re-referenced to the common average reference. A basic FIR bandpass filter from 0.1 Hz to 70 Hz was used to filter the data in addition to a notch filter of 60 Hz. Additional ocular and muscular artifacts were removed by the independent component analysis implemented in EEGLAB. The

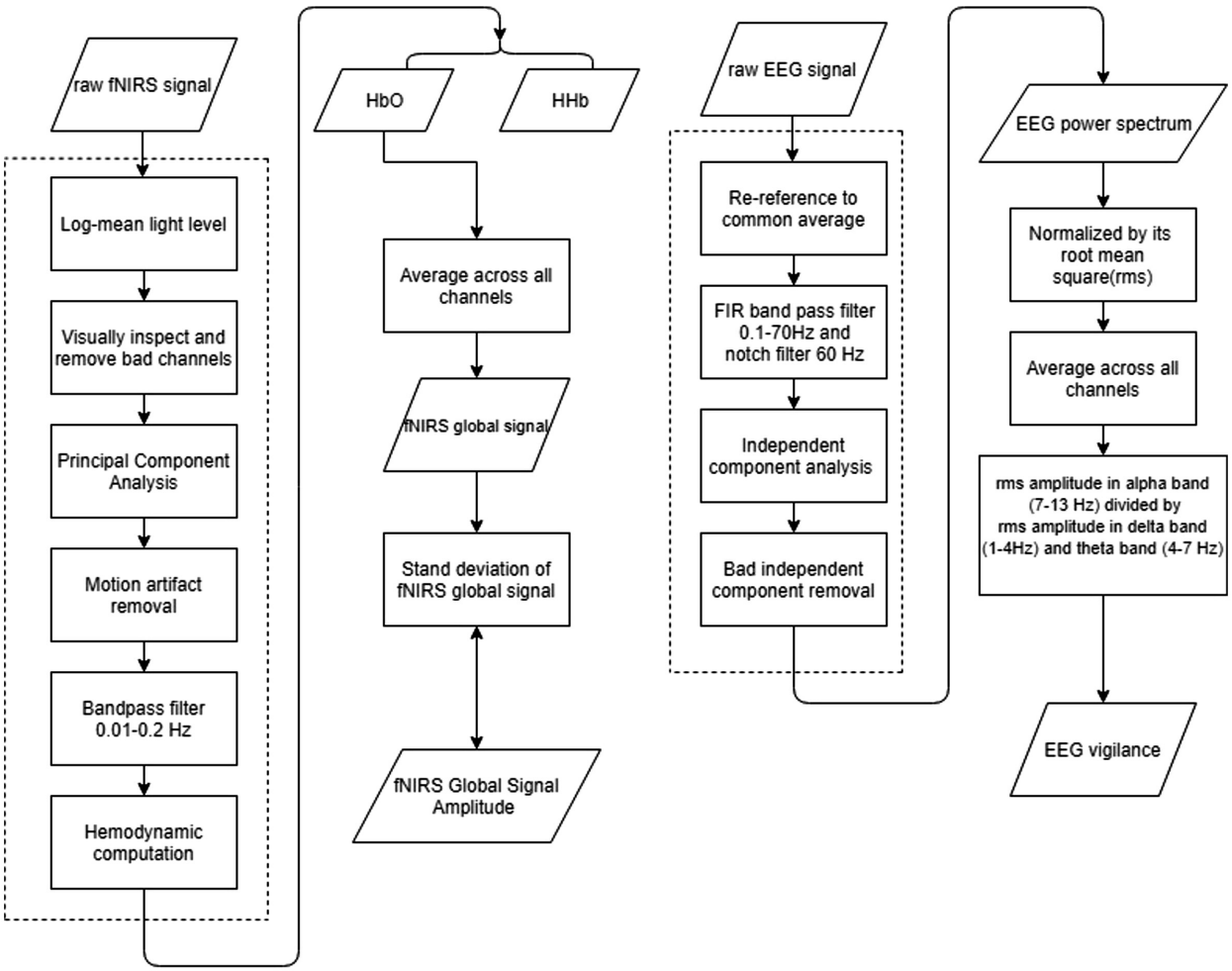

FIGURE 1 | Flowchart of the data processing flowchart. (Left) fNIRS signal processing procedures, and (Right) EEG signal processing procedures. Dashed line circles the pre-processing procedures.

ocular components, muscle movement components, and other artifacts were manually inspected and removed (Chaumon et al., 2015). Preprocessed EEG data were down-sampled to 250 Hz.

fNIRS data was pre-processed in HOMER2 (Huppert et al., 2009). Channels consisted of a source electrode and adjacent detector electrodes. Montages were created according to the setup of sources and detectors. Preprocessing of fNIRS data included converting raw light intensity to optical density, principle component analysis (PCA) removal, and motion artifact detection and correction. The PCA algorithm we performed here is to filter out the first principal component (Novi et al., 2016). Discontinuities and spikes existing in recordings were replaced by an average of its adjacent data segment. All channels were bandpass filtered from 0.01 to 0.2 Hz. The resulted time series were subject to hemodynamic computation via the modified Beer-Lambert law (Kocsis et al., 2006), yielding relative changes in concentrations of Oxy-Hemoglobin (HbO) and Deoxy-Hemoglobin (HbR) (Gratzer and Allison, 1960; Putze et al., 2014).

Calculation of Resting-State fNIRS Global Signal

After pre-processing, the fNIRS data became a measure of the relative concentration changes of HbO and HbR in units of μM. Then the preprocessed fNIRS were separated into two frequency bands: the lower range of <0.05 Hz and the upper range of >0.05 Hz that contains the Mayer wave (Julien, 2006), guided by inspection of power spectrum and analysis of variance (ANOVA) tests. To calculate the global signal, the time series of relative changes in HbO or HbR were averaged across all channels covering the whole brain. Then, the amplitude of the global signal was defined by the standard deviation of the global signal time series.

Quantification of EEG Vigilance Level

For EEG data, after removing artifacts, a spectrum was calculated by using Welch's power spectral density estimate with segments of 10 s and 50% overlap for each EEG channel. Then the spectrum

was divided by its overall root mean square (RMS) amplitude of all frequency bins, resulting in the relative amplitude spectrum. The relative amplitude spectrums were then averaged across all channels. Three frequency bands (delta: 1 – 4 Hz, theta: 4 – 7 Hz, alpha: 7 – 13 Hz) were delineated, and the RMS amplitudes were calculated separately for each band. A measure of EEG vigilance was defined as the RMS amplitude in the alpha band divided by the sum of RMS amplitudes in the delta and theta bands (Horovitz et al., 2008; Wong et al., 2013), which is equivalent to the alpha slow-wave index (ASI) (Jobert et al., 1994).

Auditory fNIRS and EEG Data

Whereas a key investigation of the Experiment 1 was to examine the impact of body position on resting-state neural recordings, we also included investigation of the body position on task-induced responses in EEG and fNIRS, in order to control systematic and environmental nuisances. A mixed block and event-related design were used for the concurrent EEG and fNIRS recordings. One session contained six task blocks and each block contained 15 auditory stimuli. The auditory stimuli were controlled by E-Prime software (Psychology Software Tools, Pennsylvania, United States). Stimuli was sent to earbuds by the stimulation computer. The trigger pulse corresponding to the sound then marked EEG and fNIRS synchronously via a parallel control box. There was a total of six task conditions (standing/sitting/supine body positions X EO/EC conditions).

For fNIRS analysis, block average was obtained after preprocessing in the same way described in resting data. The first marker of a task block was kept as the start of each task block. Based on all available auditory markers (as time 0 s), the time series were demeaned with reference to the time window from −5 to 0 s and averaged, resulting in the auditory response waveform. Segments containing detected motion artifacts were excluded from the average. To visualize the time courses of hemodynamic responses, the fNIRS auditory response was plotted from −10 to 50 s.

For EEG analysis, auditory evoked potentials (AEP) were obtained. Specifically, the recordings were band-pass filtered between 0.1 and 30 Hz, down sampled to 250 Hz, referenced to common average reference, and segmented into epochs from −100 to 500 ms. For every single segment, the $t = 0$ s denotes the onset of auditory stimuli. The mean of the baseline (averaged from −100 to 0 ms) was subtracted from the time series. Ocular and muscular artifacts were removed by the independent component analysis implemented in EEGLAB. Visual inspection further excluded the trials containing motion artifacts. Remaining trials of EEG epochs were averaged for each auditory task condition, resulting the AEP waveforms.

Sleep Stage Scoring

In Experiment 2, the 45-min recording was reviewed and manually scored into sleep stages by a certified expert (BWC), using standard scoring criteria by the American Academy of Sleep Medicine (Berry et al., 2017). Briefly, EEG data were first segmented into epochs of 30-s length. Based on the frequency and amplitude of the signal, each segment was assigned as awake, non-rapid-eye-movement sleep, Slow Wave Sleep, or rapid-eye-movement sleep. Only epochs of awake stages before first sleep onsite were included in the analysis.

Statistical Analysis

In Experiment 1, in order to explore the effect of body position on neural recordings (i.e., standing, sitting and supine), ANOVA was applied on the EEG or fNIRS quantities, separately for the EO and EC conditions. We performed the statistical test on each frequency bin along a continuous spectrum (**Figures 3**, **4**). Then, based on the delineation of frequencies, we segregated the quantities of the fNIRS global signal in two bands: $f < 0.05$ and $f > 0.05$ Hz.

Next, two-way repeated measures ANOVA (standing/sitting/supine body positions X EO/EC) was applied to assess if any main effect of body position or eye condition, or interaction between the body position and the eye condition, separately in the frequency range of <0.05 and >0.05 Hz and separately for HbO and HbR. Likewise, two-way repeated measures ANOVA (supine/sitting/standing body positions X EO/EC) was tested on the EEG vigilance scores. Furthermore, *post hoc* analysis assessed the difference between conditions using a paired, two-sided *t*-test. Bonferroni correction was used to correct the multiple comparison problem.

After delineating the position and eye effects, we assessed whether fNIRS global signal amplitudes were associated with the EEG vigilances. Particularly, motivated by a negative relationship between fMRI global signal and EEG vigilance reported in the literature, we tested whether higher fNIRS global signals are associated with lower vigilance. The analysis has excluded the frequency band of greater than 0.05 Hz that contains the Mayer wave. Also, the analysis only considered the eyes-open condition to exclude the body position factor on EEG or fNIRS. Then, per each individual, the EEG vigilance at three body positions was sorted into highest, medium and lowest levels; and the fNIRS global signal associated with the highest vigilance levels were compared to fNIRS global signals at the medium or lowest level using a paired, two-sample and one-sided *t*-test. Furthermore, for the purpose of determining whether vigilance variations underlie the fluctuations in fNIRS global signal, the co-variation was assessed in one eye condition at one body position across all subjects, because practically resting state experiments are conducted in a single experiment condition rather than combined. Partial correlations between global signal amplitude and vigilance measures were calculated, by controlling age and gender as confounding factors.

While Experiment 1 focused on the stationary properties of fNIRS and EEG, we further evaluated whether the epoch-by-epoch fluctuations in fNIRS global signal and EEG vigilance are associated in Experiment 2. For each subject, we calculated the fNIRS global signal amplitudes and EEG vigilance measures in 30-s epochs. Then the temporal correlation between the fNIRS global signal and EEG vigilance was calculated using Pearson's correlation coefficient across all epochs per each subject. To assess the temporal correlations at a group level, the correlation coefficients were converted

to z scores using the Fisher's transform. Afterward, a one-sample t-test against 0 was performed on all individuals' z scores to evaluate the significance of temporal correlation at a group level.

RESULTS

The aim of the study was to investigate the neurological basis of the fNIRS resting-state global signal, if any, and the impact of body positions on the resting-state signals. The results are organized as such: In Experiment 1, the frequency-dependent impact of body positions on fNIRS and EEG signals was explored, then the factors of body positions and eye conditions were assessed in fNIRS global signal in two delineated frequency bands, and finally, the co-variation in the amplitude of fNIRS global signal and EEG vigilance was analyzed. As control results, the fNIRS and EEG task responses to auditory stimuli were included. In Experiment 2, the epoch-to-epoch fluctuations of fNIRS global signal amplitudes and EEG vigilance measures across 30-s epochs were examined and their temporal correlation was reported.

Experiment 1: 10-Min Resting at Different Body Positions

Firstly, spontaneous fluctuations were observed in the fNIRS global signal when subjects rested with their eyes open and closed, without any external stimuli. Representative single-session traces of fNIRS global signals are shown in **Figure 2**, at an EC resting condition. Notably, the global signal at all three positions exhibit fluctuations with a peak frequency of ∼0.02 Hz. Meanwhile, the data acquired from these body positions exhibited different patterns of fluctuations in the time domain, i.e., slower fluctuations are observed in the supine position and faster fluctuations in the sitting and standing positions. In terms of the amplitude, we noted that the power spectrum at the supine position showed a lowest amplitude in the frequency range of 0.05 – 0.1 Hz than those at sitting and standing positions, in the representative subject.

Furthermore, the position-dependent profile of the resting-state fNIRS global signal is also prominent at the group level. **Figure 3** shows the grand average of the power spectrum of fNIRS global signal at various resting state conditions. Notably,

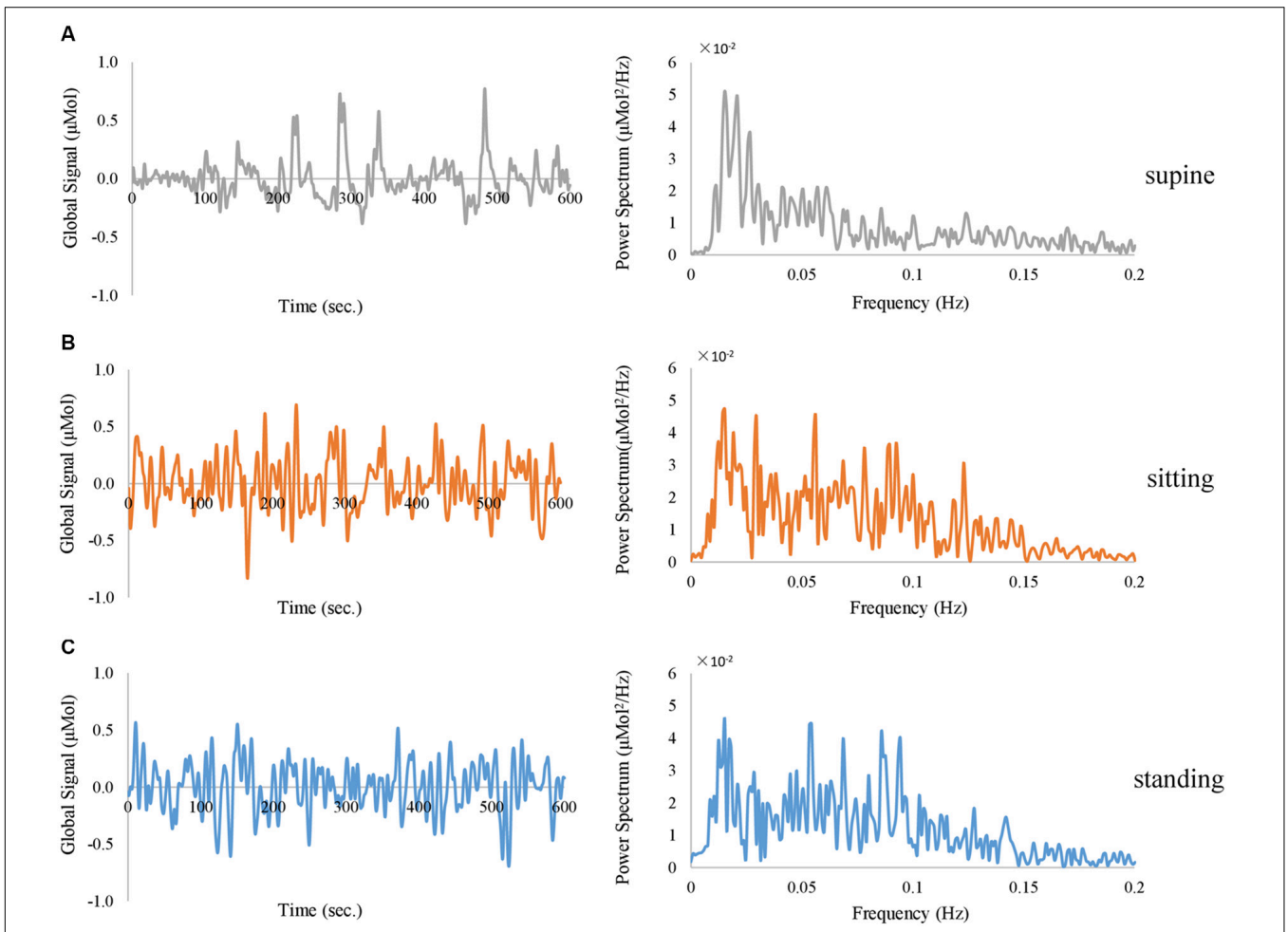

FIGURE 2 | Representative traces of fNIRS global signal derived from HbO signal when the subject closed the eyes and rested in **(A)** supine position (in gray color), **(B)** sitting position (in orange color), and **(C)** standing position (in blue color), exhibited in the time domain (left panel) and frequency domain (right panel).

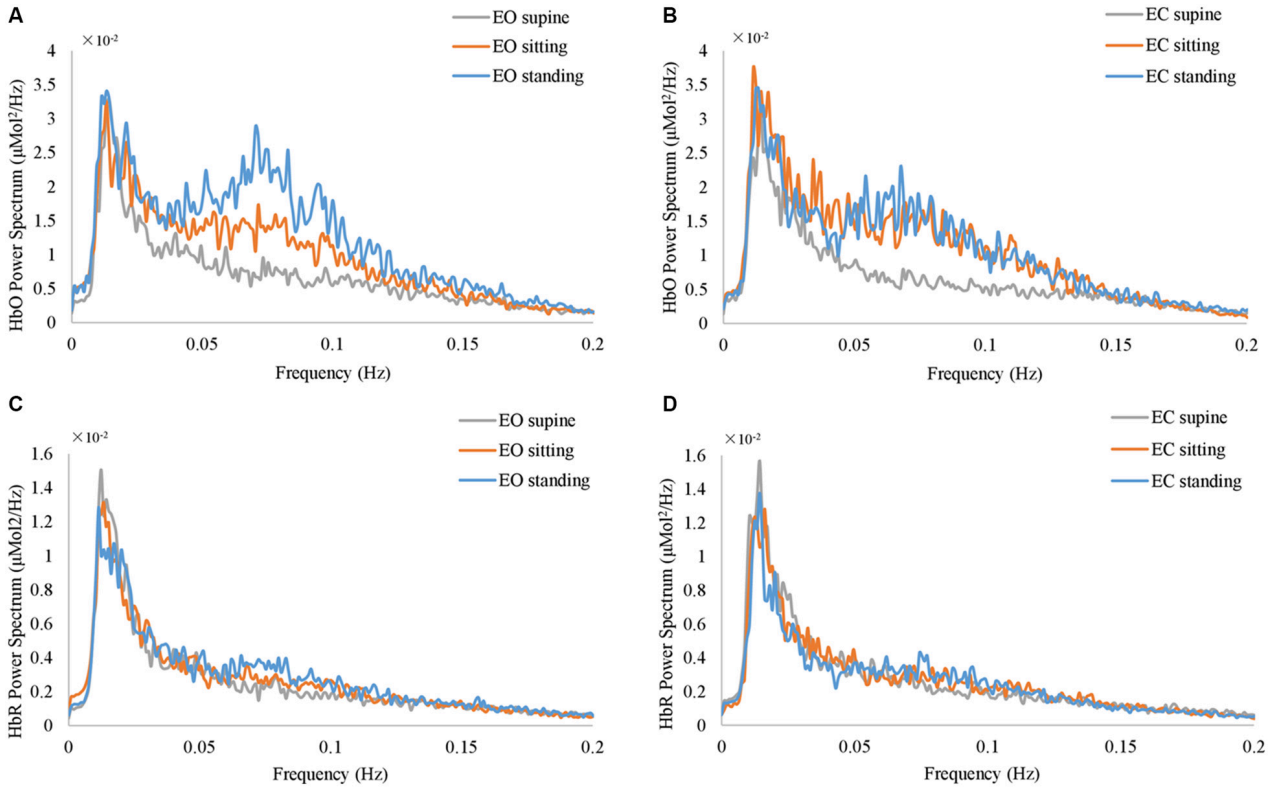

FIGURE 3 | The grand average of the power spectrum of fNIRS global signals at resting state. **(A)** and **(B)** show HbO signal at EO and EC conditions. **(C)** and **(D)** show HbR signal at EO and EC conditions, respectively. The gray, orange, and blue curves represent supine, sitting, and standing position, respectively, in all panels.

in the frequency range from 0.05 Hz to 0.1 Hz, the spectrums at three different body positions show largely different amplitudes. The spectrum at the standing position appears to be of highest amplitudes in 0.05 – 0.1 Hz, at both EO and EC conditions (**Figures 3A,B**) in blue curves, whereas spectrum at supine are of lowest amplitudes (**Figures 3A,B**) in gray curves. In order to delineate the frequency-dependent effect of body position, we performed one-way ANOVA on the amplitude of fNIRS global signal separately in each frequency bin. At the EO condition, between 0.05 and 0.09 Hz, the effect of body position was significant on HbO ($p < 0.05$, uncorrected). Similarly, at the EC condition, the effect of body position was significant in the range from 0.07 to 0.09 Hz on HbO ($p < 0.05$, uncorrected). Since the fNIRS signal in the frequency range of 0.05 – 0.1 Hz has been related to a physiological noise known as the Mayer wave (Julien, 2006), our later analysis of the fNIRS global signal then focused on two distinct frequency bands, i.e., $f < 0.05$ and $f > 0.05$ Hz, in order to distinguish a position-dependent impact that may be attributed to physiological noises. In HbR (**Figures 3C,D**), we used the same frequency bands as with HbO. Noteworthy, none of HbO or HbR data showed any significant effect of body positions in a frequency bin less than 0.05 Hz ($p > 0.05$, uncorrected).

Likewise, in the resting-state EEG, our analysis explored whether a position-dependent profile exists on the spectrum. **Figures 4A,B** show the grand average of the power spectrum at EC and EO conditions, respectively. ANOVA revealed that the body position was *not* significant in any of the frequency bins at either EO or EC conditions ($p > 0.05$, uncorrected). Notably, although the grand average at the EC conditions appears with different amplitudes for three different conditions, it did not reach a significance level ($p = 0.067$ at $f = 10.8$ Hz, uncorrected).

Next, we aggregated the fNIRS and EEG quantities as the amplitude of global signal and vigilance scores, respectively. In particular, we averaged the amplitude of the fNIRS global signal (as root-mean-square) in the range of $f < 0.05$ Hz, which excludes the Mayer wave, and then separately in the range of $f > 0.05$ Hz. Meanwhile, EEG vigilance scores were calculated based on the power spectrum of resting state EEG as the ratio of alpha-band RMS divided by the sum of delta- and theta-band RMS. Two-way Repeated Measures ANOVA (body positions × eye conditions) revealed that the effect of body positions was *not* significant on fNIRS global signal amplitude in the very low frequency range of $f < 0.05$ Hz ($q = 0.10$). Meanwhile, the effect of body position was significant on the fNIRS global signal in the range of $f > 0.05$ Hz ($q < 0.001$). Noteworthy, the interaction of body positions and eye condition was *not* significant in fNIRS global signal amplitude in either frequency range.

Post hoc comparison on HbO in the range of $f > 0.05$ Hz was then conducted to assess the difference between pairs of body positions (i.e., standing vs. supine, sitting vs. supine, and standing vs. sitting) (**Figure 5B**). Analysis showed that the amplitude

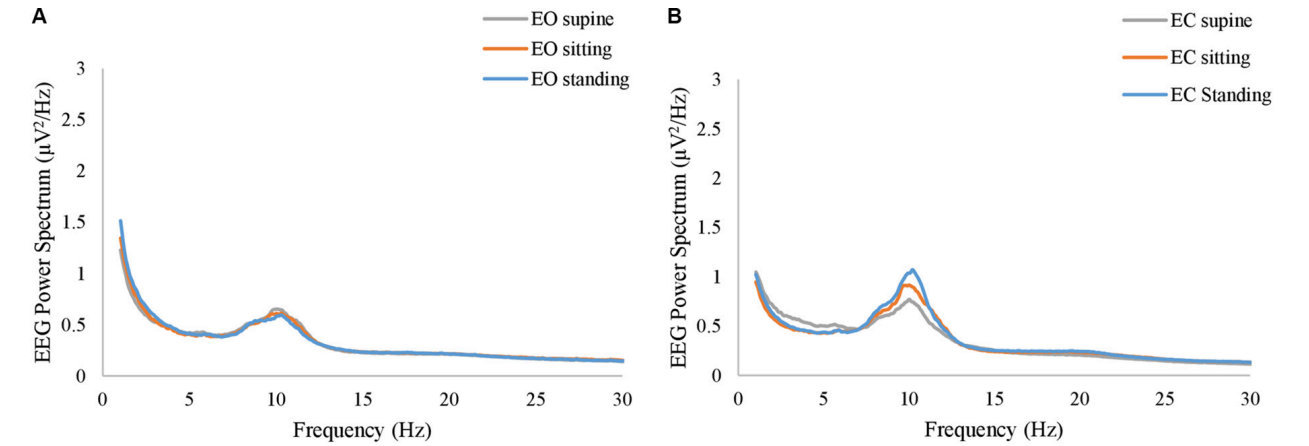

FIGURE 4 | The grand average of the power spectrum of EEG resting-state signals at **(A)** EO condition and **(B)** EC condition. The gray, orange, and blue curves represent supine, sitting, and standing position, respectively, in both panels.

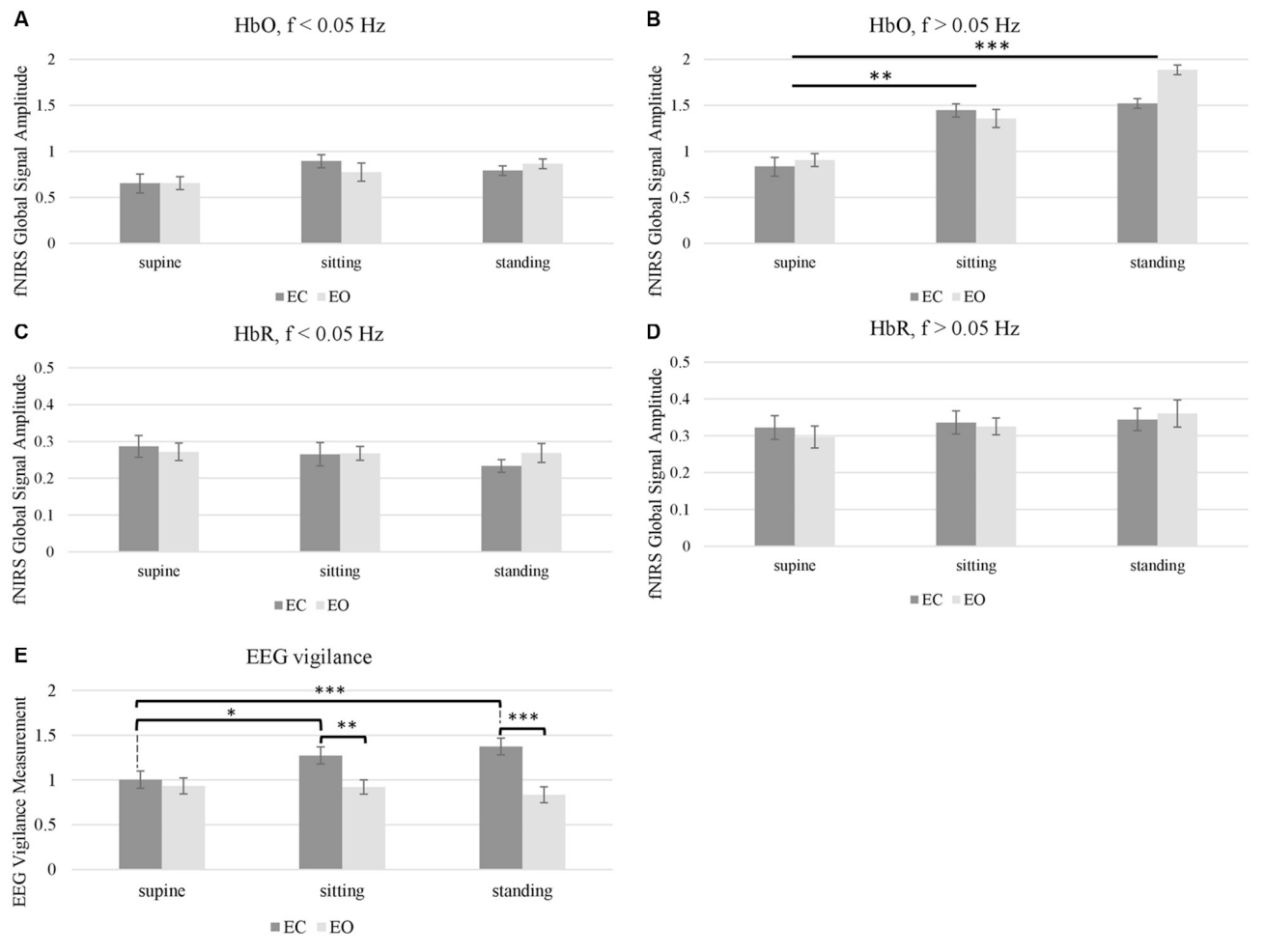

FIGURE 5 | Effects of body positions (supine, sitting, and standing) and eye conditions (EC and EO) on **(A–D)** fNIRS global signal amplitude, and **(E)** EEG vigilance measurement. The effect of body position was significant in HbO global signal amplitude, in the range of $f > 0.05$ Hz that contains Mayer wave **(B)**. EEG vigilance measurement showed significance in the effect of body position, the effect of eye conditions and the position-eye interaction **(E)**. Stars indicate *post hoc* significance after multiple comparison correction (* indicates $q < 0.05$, ** indicates $q < 0.01$, *** indicates $q < 0.001$). Error bars indicate standard error.

of fNIRS global signal for the supine position was significantly lower than the sitting position ($q < 0.01$) and standing position ($q < 0.001$), after multiple comparison correction. But amplitude of fNIRS global signal for sitting position did not differ from the standing position. Noteworthy, neither the eye factor or the eye-position interaction was significant in fNIRS HbO or HbR data.

In terms of EEG vigilance scores (**Figure 5E**), the two-way repeated measure ANOVA found that the effect of body position, the effect of eye condition and the eye-position interaction was all significant ($q < 0.001$). *Post hoc* comparisons on the EEG vigilance scores were then conducted to assess the differences. Informed by the significant interaction factor, we performed separate ANOVA analysis on the effect of body positions at separate eye condition and also performed separate *t*-test on pairs of body positions and eye conditions. Only under EC condition, the supine position had significant smaller EEG vigilance than sitting ($q < 0.05$) and standing position ($q < 0.001$). Furthermore, regarding the eye factor (EO vs. EC), the EEG vigilance showed significance at both sitting ($q < 0.01$) and standing positions ($q < 0.001$), but not in the supine position. However, under EO condition, there was no significant effect of body positions.

As a next step, we examined the relationship between the fNIRS global signal and the EEG at resting state. Firstly, we tested whether higher fNIRS global signals are associated with lower vigilance, which was motivated by a negative relationship between fMRI global signal and EEG vigilance reported in the literature. Particularly, we compared the amplitude of fNIRS global signal in the frequency range of $f < 0.05$ Hz against the EEG vigilance scores, only at EO state when either fNIRS or EEG quantities were *not* impacted by the factor of body positions. Results in **Figure 6** shows a reversed association was identified between EEG vigilance and fNIRS global signals. After sorting the vigilance measures within each individual, the resting sessions of lowest vigilance were associated with significantly higher HbO global signals [$t(18) = 2.02$, $p < 0.05$] and also higher HbR global signals [$t(18) = 2.98$, $p < 0.01$] than those of highest vigilance. Importantly, note that neither the vigilance nor the global signal differed between body positions at the eyes-open condition; nonetheless, a reversed association was still found between EEG and fNIRS.

In addition, we examined the co-variation between fNIRS global signal and EEG per each body position across individuals. Results showed a consistent negative trend such that higher global signals are associated with lower vigilance states. In particular, both HbO and HbR at the standing position significantly co-varied with the EEG vigilance after controlling age and gender as confounding factor (HbO: $r = -0.51$, $p < 0.05$; HbR: $r = -0.57$, $p < 0.05$), as shown in **Figure 7**. However, at other positions, the covariation did not reach significance after multiple comparison correction, although a negative trend in the association was consistently noted. HbR at the supine position showed a significance-approaching covariation with EEG vigilance ($r = -0.36$, $p = 0.1$) and HbO at the sitting position also approached significance ($r = -0.34$, $p = 0.1$). HbO at supine position ($r = -0.06$) and HbR at sitting position ($r = -0.20$) did not reach a significant covariation with EEG vigilance.

In order to control systematic and environmental nuisances, task-induced responses in EEG and fNIRS were investigated. **Figure 8** shows the grand average of EEG AEP curves at three different body positions, from the FCz electrode. In either EO and EC conditions, the AEP curves at three body positions followed a very similar profile: negative activities at the ∼100 ms (N1) and positive activities at the ∼200 ms (P2). The factor of body positions has *no* significant effect on N1 or P2 ($q > 0.1$). Furthermore, the eye-position interaction is not significant, either ($q > 0.1$).

Meanwhile, task-related fNIRS responses were averaged across the blocks after subtracting the activities between −5 s and 0 s, with time 0-s as the beginning of the block. **Figure 9** shows the grand average of fNIRS response to auditory stimuli. Representative time courses from the channels located over the left and right auditory cortex regions are shown in **Figure 9B**. When the auditory stimuli were on (shaded gray area in **Figure 9B**), relative changes of the HbO increased while the relative changes of the HbR decreased. In order to visualize the topography of auditory task responses, the block-average time series of fNIRS was selected from 10 to 30 s, averaged, and shown in **Figure 9A**. Positive activations of HbO are shown in left and

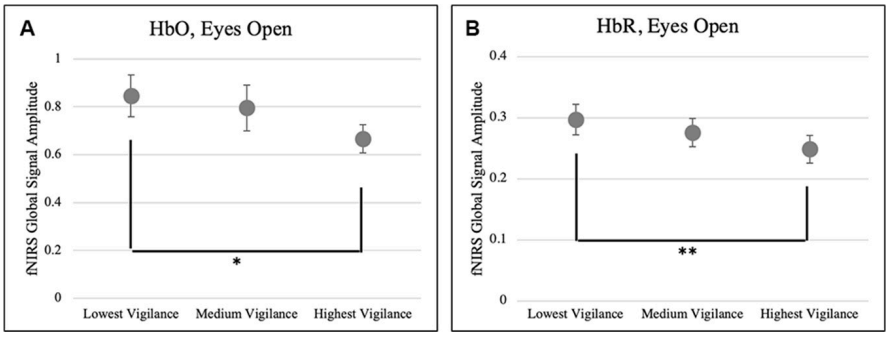

FIGURE 6 | A reversed association between EEG vigilance and fNIRS global signals. Resting state sessions of lowest vigilance measures were associated with significantly higher amplitudes of fNIRS global signals in the **(A)** HbO ($p < 0.05$) and **(B)** HbR ($p < 0.01$). *$p < 0.05$, **$q < 0.01$, and error bars indicate standard error.

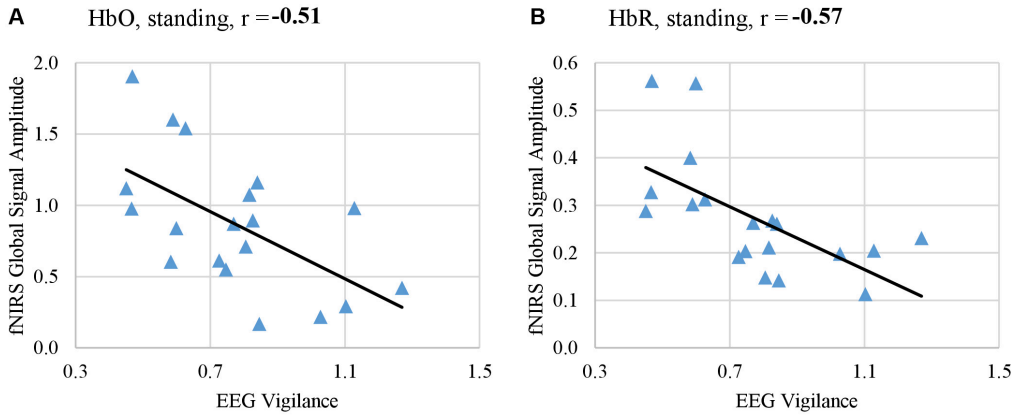

FIGURE 7 | Amplitude of fNIRS global signal in the range of $f < 0.05$ Hz co-varied with EEG-based measure of vigilance, when subjects rested in the standing position with their eyes open. fNIRS global signal amplitudes derived from HbO signal **(A)** and from HbR signal **(B)** both significantly co-varied with EEG vigilance after controlling age and gender as confounding factors (HbO: $r = -0.51$, $p < 0.05$, HbR: $r = -0.57$, $p < 0.05$).

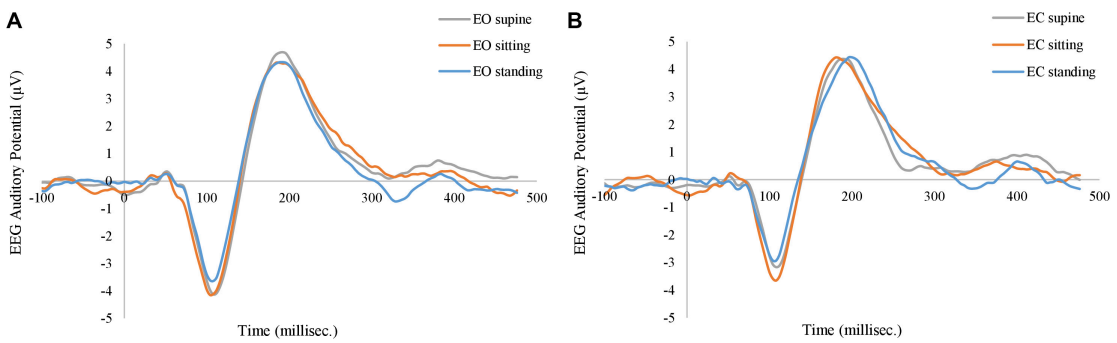

FIGURE 8 | Grand average of EEG auditory evoked potentials at **(A)** eyes-open (EO) condition, and at **(B)** eye-closed (EC) condition. The gray, orange, and blue curves represent supine, sitting, and standing positions in both panels.

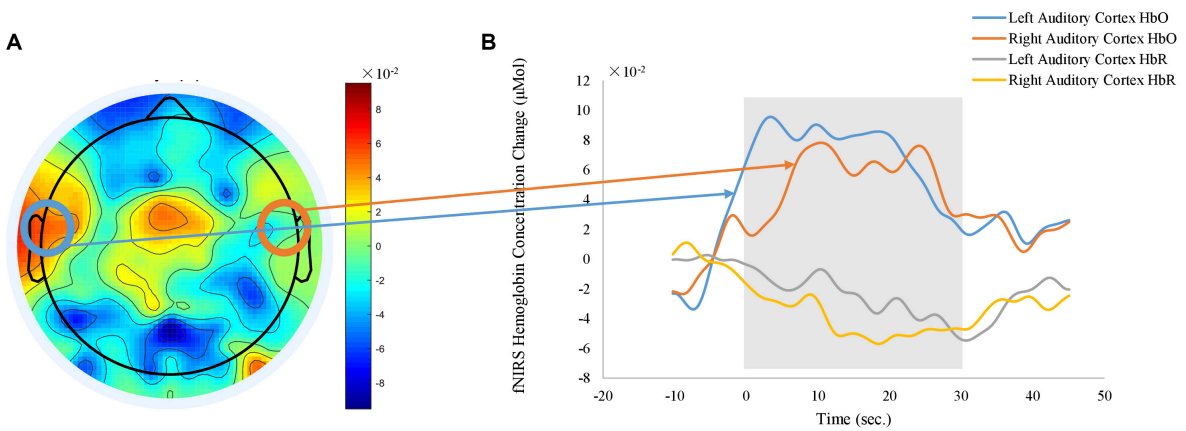

FIGURE 9 | Grand average of fNIRS auditory response derived from HbO signals. **(A)** shows the topography of averaged HbO responses between 10 to 30 s after the stimulus onsite). **(B)** plots the time courses of fNIRS auditory response obtained from representative channels over left and right auditory cortex (orange: left auditory cortex HbO, blue: right auditory cortex HbO, gray: left auditory cortex HbR, yellow: right auditory cortex HbR). Shaded gray area indicates the time window of auditory stimulus. Time zero is the onsite of stimulus.

right auditory cortex in the topography of HbO (**Figure 9B**). Results revealed *no* significant effect of body positions on the fNIRS auditory response.

Experiment 2: 45-Min Resting at Supine Position

In Experiment 2, subjects were instructed to rest for a total duration of 45 min while allowed to fall asleep. Sleep scoring found that all 19 were able to fall asleep. Only data at wakeful resting before any sleep were used in the current analysis (Mean ± SD = 711 ± 602 s, ranging from 150 to 2430 s). After quantifying vigilance and fNIRS global signal amplitude in 30-s epochs, temporal fluctuations were observed. The time courses of HbO, HbR, and EEG vigilance measurement in a representative subject are displayed in **Figure 10A**. Every dot represents the global signal amplitude calculated from a windowed 30-s fNIRS signal and vigilance measurement calculated from 30-s EEG in the same aligned time window. As the subject gradually fell into the sleep, the vigilance exhibited a slowly decreasing trend, in reversed synchrony with surges of increases in fNIRS global signal and temporal. In the same time course, scattered moments of rebounds in vigilance are also aligned with drops of global signals, especially toward the later duration before the subject fell into sleep. In the same subject (shown in **Figures 10B,C**), a negative temporal correlation was observed between fNIRS global signal amplitude and EEG vigilance measurement (HbO vs. vigilance: $r = -0.46$, p = 0.004; HbR vs. vigilance: $r = -0.61$, $p < 0.001$).

At the group level, all subjects exhibited temporal variations in EEG vigilance. Specifically, the standard derivation of EEG vigilance over the period of wakeful rest ranged from 0.07 to 0.46 across all subjects (Mean ± SD = 0.25 ± 0.13). In terms of association, analysis showed that there existed significant correlation between HbO global signal amplitude and vigilance [$t(19) = -2.57$, $p = 0.02$), as well as significant for HbR and vigilance [$t(19) = -2.80$, $p = 0.01$]. Despite that subjects had different durations of wakefulness, the window length of wakefulness was not associated with the temporal correlation between fNIRS global and vigilance ($p > 0.1$ for HbO and HbR). When restricting the wakeful epochs to be within the 10 min before falling into sleep, the temporal correlation was still significant between HbO and vigilance [$t(19) = -2.32$, $p = 0.03$], and also significant between HbR and vigilance [$t(19) = -2.83$, $p = 0.01$]. Furthermore, considering that individuals exhibited different levels of vigilance fluctuations (i.e., standard derivation of EEG vigilance ranged from 0.07 to 0.46), we examined whether the standard derivation of EEG vigilance modulated the association between EEG vigilance measures and fNIRS global signal; yet the analysis showed that the scale of vigilance fluctuation levels was not relevant ($p > 0.1$).

DISCUSSION

Our study has investigated the neurophysiological nature of the global signal of fNIRS measured at resting state. The results

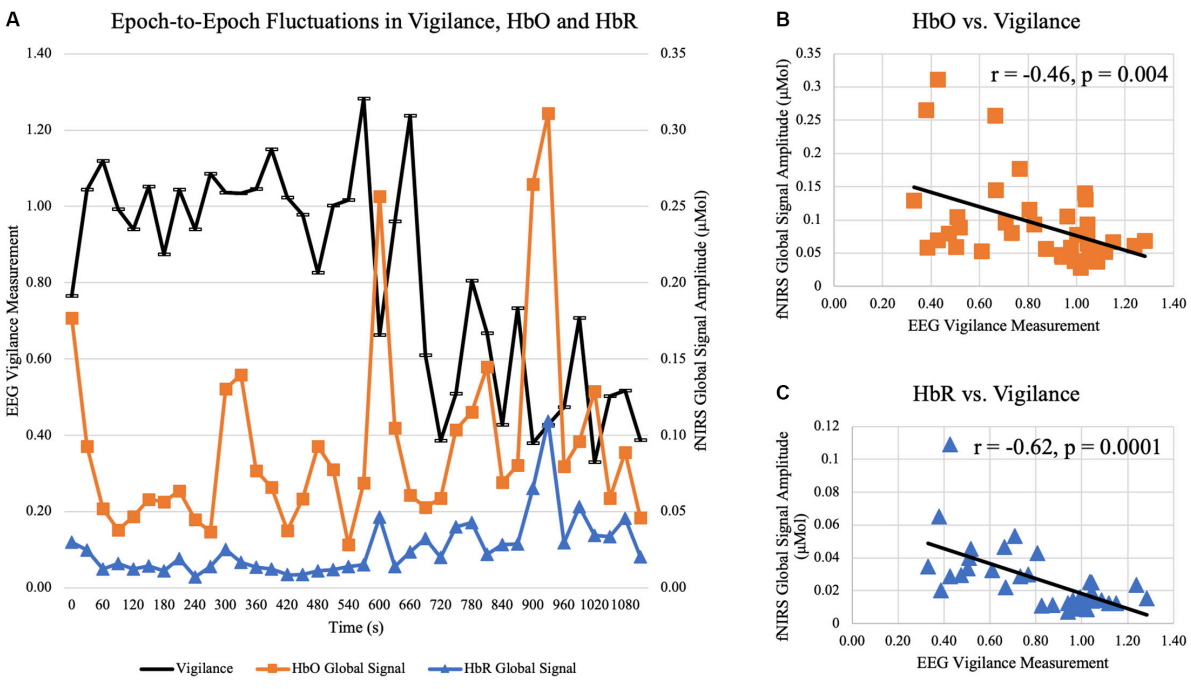

FIGURE 10 | Temporal correlation between epoch-to-epoch fluctuations of vigilance and fNIRS global signal in a representative subject at wakeful rest. **(A)** plots the time courses of EEG vigilance measure (black curve) and global signal amplitude of HbO (orange curve) and HbR (blue curve) calculated in 30-s epochs over 18 min. **(B)** shows the negative correlation between vigilance and HbO global signal amplitude is significant ($r = -0.46$, $p = 0.004$). **(C)** shows the negative correlation between vigilance and HbR global signal amplitude is significant ($r = -0.62$, $p < 0.001$).

for the first time have demonstrated that the amplitude of the fNIRS global signal, particularly in the frequency range of $0.01 < f < 0.05$ Hz, is reversely associated with EEG vigilance measures. The discovery of a neurological origin for fNIRS global signal has important implications for the processing of fNIRS signal acquired at resting state.

One of the most fundamental and critical issues in analyzing neuroimaging data is how to handle the global signal, which is defined as the time series of intensity averaged across imaging units in PET (Fox et al., 1988; Friston et al., 1990), fMRI (Desjardins et al., 2001; Macey et al., 2004), and more recently in fNIRS (Franceschini et al., 2006; Zeff et al., 2007; White et al., 2009; Mesquita et al., 2010). A strong presence of global signal in fMRI may lead to a massive and diffused activation pattern in task-based studies if the time series of the global signal is of similar profile with the task modulation (Kay et al., 2013; Power et al., 2015). Likewise, fNIRS studies of various tasks commonly removed a global component derived from the measurements to reveal focal activations, via linear regression or spatial filtering based on PCA/ICA decomposition (Zhang et al., 2005, 2007, 2016; Franceschini et al., 2006; Kohno et al., 2007; Zeff et al., 2007; Eggebrecht et al., 2012, 2014; Sato et al., 2016). Nonetheless, the impact of global signal is more problematic in task-free, resting state studies, as the global signal may lead to a perfusive connectivity pattern that is attributed to the global signal, no matter whichever seed region of interest is selected. Because region-specific connectivity is more desirable and because non-neuronal sources can dominantly contribute to the global signal (Glover et al., 2000; Wise et al., 2004; Birn et al., 2006; Yuan et al., 2013), the analysis of resting state fMRI data has commonly included steps to attenuate the impact of a global signal. For example, GSR removes an averaged signal of all recording units from the time series through linear regression. This procedure was originally developed for and applied to task-based fMRI data (Zarahn et al., 1997; Aguirre et al., 1998; Macey et al., 2004). Later, most resting-state fMRI studies have adopted GSR as a pre-processing approach: the global signal component is regressed out of preprocessed BOLD signals prior to computation of connectivity measures and therefore regionally focused connectivity patterns are reported (Fox et al., 2009). Similarly, in recent fNIRS studies of resting state brain, a global component has been recognized in the measurements from regularly distanced optodes (White et al., 2009; Mesquita et al., 2010; Tong and Frederick, 2010; Eggebrecht et al., 2014; Tachtsidis and Scholkmann, 2016; Duan et al., 2018; Wyser et al., 2020) and from short-distanced optodes (White et al., 2009; Gregg et al., 2010; Mesquita et al., 2010; Eggebrecht et al., 2014; Tachtsidis and Scholkmann, 2016; Duan et al., 2018; Sherafati et al., 2020; Wyser et al., 2020). To date, there is no well-established pre-processing routine in resting state fNIRS studies although multiple efforts are being made (Huppert et al., 2009; Ye et al., 2009; Xu et al., 2014; Santosa et al., 2018). Approaches such as GSR and spatial filtering via PCA and ICA decomposition that were used in task-based fNIRS studies are also commonly adapted in resting state fNIRS studies to remove the global component, yielding regionally focused connectivity pattern (Mesquita et al., 2010; Zhang et al., 2010, 2011; Sakakibara et al., 2016).

However, the removal of global signal in neuroimaging data has encountered controversial critiques, particularly in the studies of resting state functional connectivity. Because a global neurophysiological component may be present in direct neural recordings (Scholvinck et al., 2010; Wong et al., 2013, 2016), removing the global signal is shown to cause loss of such neural components, thereby confounding the resulted pattern of resting state functional connectivity. For example, Chen et al. (2012) found that the global signal is highly correlated with DMN component. Further evidences indicated that the global signal resembles the resting-state fMRI time courses of the largest cluster when the level of global noise is low (Chen et al., 2012). Under such circumstances, GSR could mathematically mandate the presence of anti-correlation network in fMRI studies (Murphy et al., 2009). Other studies have further linked the fluctuations of global signals to the varying levels of vigilance or arousal (Chang et al., 2016; Falahpour et al., 2018), which suggests that removing the global signal in those situations could remove an underlying behavioral factor. Therefore, the GSR should be very carefully applied when studying resting-state MRI (Murphy et al., 2009; Saad et al., 2012; Murphy and Fox, 2017). Until now, the nature of the fNIRS global signal has not been fully established since the neurophysiological components in the resting-state global fNIRS signal have not been systematically investigated. Our current study is the first of its kind to investigate the neuronal and non-neuronal sources in the fNIRS global signal by using concurrent fNIRS and EEG in whole-brain and high-density setup. Because both fNIRS and BOLD fMRI measure the cerebral hemodynamics, they carry similar substrates for neuronal activities while they also share common caveats due to non-neuronal sources, including respiration, cardiac pulsations, motion, etc. Like in the case of fMRI, removal of fNIRS global signal may lead to spurious results in the functional connectivity pattern, depending on whether or not there exists any neural component in the global signal of fNIRS and the amplitude level of global signal.

In this study, we have shown that fNIRS global signals acquired from the resting human brain are periodical oscillations. As shown in **Figures 2**, **3** at respective individual and group level, the resting-state fNIRS global signal resides in three ranges: dominantly less than 0.05 Hz with a peak component at ∼0.02 Hz, a second peak between 0.05 and 0.1 Hz (also known as the Mayer wave) and greater than 0.1 Hz. Furthermore, our study extended investigations of the fNIRS global signal at standing, sitting and supine positions. Indeed, periodic fluctuations were observed in the global signal at all body positions. The presence of a fluctuating fNIRS global signal with dominate activities of <0.1 Hz suggests that the RSFC pattern may be affected by the global signal. Comparing with intracranial neural recordings (Leopold et al., 2003; He et al., 2008; Shmuel and Leopold, 2008), fNIRS global signal and spontaneous neural activities overlap their peaks in the range of <0.1 Hz. Meanwhile, in comparison with fMRI, the fNIRS global signal shows a very similar spectral profile with those from BOLD fMRI. Especially, the spectrum of fNIRS at the supine position (**Figures 3A,B**) for both EO and EC conditions are almost identical to those reported in fMRI (e.g., Figure 1 in Biswal et al., 1995). Since

in our study the whole-head fNIRS montage were sampled at 1.95 Hz, which is a higher frequency than BOLD fMRI (usually 0.5 Hz), the spectrum of fNIRS global signal revealed a more accurate spectrum.

Importantly, for the first time our study reported a negative association between the amplitude of fNIRS global signal in the range of <0.05 Hz and the EEG vigilance based on the simultaneous recording in the Experiment 1 (**Figures 6,7**). Within individuals, the resting state sessions with lowest EEG vigilance measures were associated with significantly higher fNIRS global (HbO and HbR in **Figure 6**), which was observed at eyes open condition and neither EEG nor fNIRS was affected by body positions. Furthermore, in a single body position at eyes-open condition, a negative covariation between fNIRS global signal amplitude and EEG vigilance was also confirmed across individuals (HbO and HbR in **Figure 7**). The selection of frequencies $f < 0.05$ Hz for fNIRS is critical: it is within the range of resting state fMRI data but distinctly narrower to exclude the Mayer wave. Previous fMRI study has demonstrated that the functional connectivity in auditory, visual and sensorimotor cortices is characterized 90% by the low-frequency band from 0 to 0.1 Hz (Cordes et al., 2001). Meanwhile, the fractional amplitude of low-frequency fluctuation (fALFF) is defined as the ratio of power spectrum of 0.01 – 0.08 Hz to that of the whole frequency band (Zou et al., 2008). Noteworthy, one of the most studied networks – DMN – has significantly higher fALFF than other brain regions, which indicates DMN has higher intensity of regional spontaneous brain activity in the range of 0.01 – 0.08 Hz (Zou et al., 2008). More importantly, our fNIRS signal was further narrowed to the range of <0.05 Hz, in order to avoid the Mayor wave which is shown to depend on body positions. Because of a high sampling frequency, fNIRS was effective in preventing aliasing of high-frequencies related to pulse and respiration into the range of <0.05 Hz.

In addition, our results revealed that the power spectrum of HbO global signal depends on body positions in the range between 0.05 – 0.1 Hz, regardless eyes were opened and closed (shown in **Figures 2**, **3** at respective individual and group level). Data at the standing position show the largest amplitude than the others, while the supine position is associated with lowest amplitude. These findings are consistent with previous reports by Tachtsidis et al. (2004), who compared three different positions' effect on cerebral blood pressure with fNIRS. Their results showed that standing position has the highest mean blood pressure (MBP) and supine has the lowest MBP. They followed the Task Force of the European Society of Cardiology and the North American Society of Pacing and Electrophysiology (1994) to separate the frequency spectrum into three standard frequency bands: very low frequency (VLF: 0.02–0.04 Hz), low frequency (LF: 0.04–0.15 Hz) and high frequency (HF: 0.15–0.4 Hz). Although VLF did not reveal any significant impact of body position, their results reported that the magnitude of low frequency oscillation in HbO in the resting brain shows a significant difference between different postures in LF. Coincidentally, Mayer wave, i.e., the cyclic changes in arterial blood pressure, fall into this LF range (Muller et al., 2003; Julien, 2006). Mayer wave appears to have a close relationship with fNIRS global signal. It is observed as oscillations of arterial pressure at ∼0.1 Hz in conscious humans (Julien, 2006). Besides, it is positively related with the strength of the corresponding sympathetic nervous activity and the mean level of sympathetic nerve activity (Furlan et al., 2000). More importantly, prone, supine, and sitting have significantly different effect on autonomic regulation of cardiovascular function (Watanabe et al., 2007). One rational speculation is that different body positions, especially the up-tilt positions, significantly affect autonomic regulation includes SNA which set the level of sympathetic vasoconstrictor tone, hence contributing to sustain arterial pressure (Julien, 2006; Scholkmann et al., 2014; Mohammadi-Nejad et al., 2018). Therefore, we regarded position-dependent effect in the Mayer wave range to be of physiological origin and discarded them for comparison against EEG. Aside from the Mayer wave range, our analysis further eliminated the factor of body positions and revealed a negative association between the EEG vigilance and fNIRS global signal in the frequency range of <0.05 Hz (HbO and HbR in **Figures 6**, **7**). Such EEG-fNIRS association for the first time revealed a neurophysiological contribution to the fluctuations of fNIRS global signal (due to EEG vigilance), rather than a physiological factor (due to body positions). As control data in the Experiment 1, we conducted qualitative analysis and statistical analysis on auditory EEG and fNIRS responses. Our results did not observe the different body positions' effect on AEP of EEG data or task-related average of fNIRS data, at both EO and EC conditions. This excludes the concerns of environmental and systematic biases, such as the quality of data recording when subjects were positioned differently.

Our findings of a negative association between fNIRS global signal and EEG vigilance measures have important implications for the analysis and interpretation of fNIRS-based resting state functional connectivity. The reversed association between EEG vigilance and fNIRS global signal observed within individuals (**Figure 6**) indicates that removal of fNIRS global signal will also remove the neurological effect of vigilance in the signals. Therefore, in resting state functional connectivity studies using repeated fNIRS measures within an individual, especially if the subjects' conditions are related to the vigilance levels, global signal removal should not be performed. In addition, a negative covariation across individuals at the standing position (**Figure 7**) indicates that removal of global signal will also remove the neurological effect of vigilance in the signals. Therefore, in resting state studies using fNIRS (such as biomarkers of disease across individuals), especially when vigilance is an individual-level trait relevant to disease symptoms (Yang et al., 2017) or behaviors (Li et al., 2019), global signal removal could become problematic.

Furthermore, our study in the Experiment 2 for the first time reported a negative temporal correlation between the epoch-by-epoch fluctuations of fNIRS global signal and EEG vigilance, which further confirmed the negative association observed across subjects in Experiment 1. In wakeful rest periods that were verified by sleep scoring criteria, subjects exhibited momentary upsurges and drops of vigilance, as they stayed awake but were falling into sleep. Such vigilance fluctuations were then shown to be in reversed synchrony with the HbO and HbR

global signal: epochs of decreased vigilance were associated with surges in fNIRS global signal, and vice versa. Interestingly, such findings of negative association are consistent with other studies that have examined the BOLD fMRI signals and EEG or behavior measures of vigilance. For example, Olbrich et al. (2009) of simultaneous EEG and fMRI study have reported that decreased of EEG vigilance measures are associated with a perfusive increase of BOLD signals in widespread cortices (except the thalamus). Similarly, Liu and colleges have observed a negative temporal correlation between EEG vigilance and fMRI global signal calculated from whole-brain average, which was reported in 23 sessions out of the 25 sessions in total and ranged between 0 and −0.5 (Falahpour et al., 2018, **Figure 4**), which is similar with our observation. In another study performed in unanesthetized monkeys, Chang et al. (2016) investigated the behavior measure of vigilance, indicated as opening and closure of eyes, and reported again that the fluctuations of vigilance level have negative temporal correlation with BOLD signals in widespread cortices, in a similar spatial extent and consistent temporal manner with those observed in human studies (Olbrich et al., 2009; Falahpour et al., 2018). Our study, however, reported for the first time the negative temporal correlation exists in concurrent and whole-head fNIRS and EEG recordings in human. Our findings of the epoch-by-epoch association are important for the interpretation of dynamic resting state functional connectivity, which commonly used a windowed approach of 30-s to 120-s duration. While the resting state brain connectivity is increasingly recognized to possess rich information of dynamics (Hutchison et al., 2013), some studies removed the global signal (Allen et al., 2014) whereas other studies did not (Chang et al., 2013). By showing that the fNIRS global signal amplitude is negatively correlated with EEG vigilance, our findings suggest that the removal the global signal should not be performed in the investigation of dynamic connectivity using fNIRS, especially in conditions affected by vigilance fluctuations. Beyond that, DMN has been reported to be correlated with EEG vigilance scores (Olbrich et al., 2009). Removing fNIRS global signal therefore may attenuate activities of DMN that are related with vigilance fluctuations. Evidence has shown that the working memory plays a critical role in both visual rehearsal and vigilance performance (Baddeley et al., 1999). And age-related alterations and disease-related decrements (such as Alzheimer's disease) in DMN have significantly impacted working memory performance (Baddeley et al., 1999; Sambataro et al., 2010). Therefore, the fNIRS global signal should not be treated as non-neural confound, and its removal should be carefully considered via a frequency delineation.

Noteworthy, the calculation of the fNIRS global signal amplitude in our study is a reasonable adaption from the definition of global signal amplitude in previous fMRI study (Wong et al., 2013). Considering that the fNIRS optical density is converted to relative changes of HbO/HbR concentration in the stage of hemodynamic computation, the normalization in fNIRS equates the normalization in fMRI analysis (i.e., divided by the mean of fMRI time course), the calculation of fNIRS global signal in our study followed exactly the same definition in Wong et al. (2013). Our findings are consistent with previous findings on the relationship between fMRI global signal and EEG vigilance (Wong et al., 2013, 2016). Such discovery of a neurological component in fNIRS global in our study is novel. Importantly, our investigation adds findings from a unique perspective by showing a covariation relationship in a carefully constrained frequency range that has excluded the possible physiological noise of blood pressure regulation. Our studies of two experiment datasets have demonstrated the reversed association exiting in both static and dynamic manner.

Additionally, it is worthy to note that the quantification of EEG vigilance has limitations, due to interindividual variance in EEG activity that is commonly observed in many EEG studies (Jobert et al., 1994; de Munck et al., 2007; Olbrich et al., 2009). For example, certain subjects may exhibit almost no EEG alpha peak in the power spectrum of resting EEG at eyes open and sometimes, even at eyes closed states. In the meanwhile, there are subjects that show strong alpha peak power at both eyes open and eyes closed states. Here in our analysis we have taken multiple steps to mitigate the factor of interindividual variance in EEG activity. Firstly, we have calculated a normalized spectrum of EEG accounting all frequency bins; and the vigilance measures was calculated as the ration between the alpha-band amplitude divided by the sum of amplitudes in the delta and theta bands based on the normalized spectrum. Then, in Experiment 1, we accounted the interindividual variance by contrasting between the lowest vigilance condition and higher vigilance conditions within individuals, at which subjects' eyes were all open. Moreover, in Experiment 2, we examined the temporal fluctuations to determine the association between EEG vigilance and fNIRS, while we concluded that the levels of vigilance fluctuations did not affect the temporal association. Nonetheless, because we also examined the across-individual covariation (**Figure 7**), the observation of the association between EEG vigilance and fNIRS global signal could be attributed to interindividual variance in EEG activities rather than the neurological factor of vigilance, although removal the global signal under such situation could still introduce confounds to the fNIRS resting state functional connectivity analysis.

CONCLUSION

With the advantage of economic efficiency and portability, fNIRS has been proposed as a complementary option to fMRI, especially to be used in populations with contraindications to MRI scanner and in challenged environment (such as brain monitoring at bed-side or during surgery). The current study for the first time revealed a negative relationship between fNIRS global signal amplitudes and EEG vigilance in human participants, based on concurrent EEG and fNIRS recordings at high-density and whole-head montage. Our results stressed the significant effect of body positions on the fNIRS resting-state global signal, primarily in the frequency range of greater than 0.05 Hz yet not in the range of less than 0.05 Hz. However, EEG vigilance plays a modulatory role in the fNIRS signals in the frequency range of less than 0.05 Hz: resting-state sessions of low EEG vigilance measures

are associated with high amplitudes of fNIRS global signals. Moreover, the epoch-by-epoch fluctuations of EEG vigilance and fNIRS global signals are significantly correlated in a negative manner at a wakeful resting period. The findings of a neural component, i.e., EEG vigilance, in fNIRS global signal suggests that such global signal should not be removed as non-neural physiological signal, especially in studies and conditions where vigilance and related brain networks are of interest.

DATA AVAILABILITY STATEMENT

The raw data supporting the conclusions of this article will be made available by the authors, without undue reservation.

ETHICS STATEMENT

The studies involving human participants were reviewed and approved by the Institutional Review Board at the University of Oklahoma Health Sciences Center. The patients/participants provided their written informed consent to participate in this study.

AUTHOR CONTRIBUTIONS

YC contributed to data collection, the data analysis, and manuscript writing. JT, YC, and MC contributed to data collection. JF and BC contributed to data analysis. HY contributed to study design, the data analysis, and the manuscript writing. All authors contributed to the article and approved the submitted version.

FUNDING

This study was supported by NSF RII Track-2 FEC 1539068, Oklahoma Center for the Advancement of Science and Technology HR16-057, and Institute for Biomedical Engineering, Science, and Technology at University of Oklahoma.

ACKNOWLEDGMENTS

The authors would like to thank Dr. Lei Ding, Dr. Guofa Shou, Johnny O'Keeffe, Josiah Rippetoe, and Junwei Ma for their assistance in the data collection.

REFERENCES

Aguirre, G. K., Zarahn, E., and D'Esposito, M. (1998). The variability of human. BOLD hemodynamic responses. *Neuroimage* 8, 360–369. doi: 10.1006/nimg.1998.0369

Ahn, S., and Jun, S. C. (2017). Multi-Modal Integration of EEG-fNIRS for brain-computer interfaces - current limitations and future directions. *Front. Hum. Neurosci.* 11:503. doi: 10.3389/fnhum.2017.00503

Allen, E. A., Damaraju, E., Plis, S. M., Erhardt, E. B., Eichele, T., and Calhoun, V. D. (2014). Tracking whole-brain connectivity dynamics in the resting state. *Cereb. Cortex* 24, 663–676. doi: 10.1093/cercor/bhs352

Arun, K. M., Smitha, K. A., Sylaja, P. N., and Kesavadas, C. (2020). Identifying resting-state functional connectivity changes in the motor cortex using fNIRS during recovery from stroke. *Brain Topogr.* 33, 710–719. doi: 10.1007/s10548-020-00785-782

Baddeley, A., Cocchini, G., Della Sala, S., Logie, R. H., and Spinnler, H. (1999). Working memory and vigilance: evidence from normal aging and Alzheimer's disease. *Brain Cogn.* 41, 87–108. doi: 10.1006/brcg.1999.1097

Beckmann, C. F., DeLuca, M., Devlin, J. T., and Smith, S. M. (2005). Investigations into resting-state connectivity using independent component analysis. *Philos. Trans. R. Soc. Lond. B Biol. Sci.* 360, 1001–1013. doi: 10.1098/rstb.2005.1634

Berry, R. B., Brooks, R., Gamaldo, C., Harding, S. M., Lloyd, R. M., Quan, S. F., et al. (2017). AASM scoring manual updates for 2017 (version 2.4). *J. Clin. Sleep Med.* 13, 665–666. doi: 10.5664/jcsm.6576

Birn, R. M., Diamond, J. B., Smith, M. A., and Bandettini, P. A. (2006). Separating respiratory-variation-related fluctuations from neuronal-activity-related fluctuations in fMRI. *Neuroimage* 31, 1536–1548. doi: 10.1016/j.neuroimage.2006.02.048

Biswal, B., Yetkin, F. Z., Haughton, V. M., and Hyde, J. S. (1995). Functional connectivity in the motor cortex of resting human brain using echo-planar MRI. *Magn. Reson. Med.* 34, 537–541. doi: 10.1002/mrm.1910340409

Brookes, M. J., Woolrich, M., Luckhoo, H., Price, D., Hale, J. R., Stephenson, M. C., et al. (2011). Investigating the electrophysiological basis of resting state networks using magnetoencephalography. *Proc. Natl. Acad. Sci. U.S.A.* 108, 16783–16788. doi: 10.1073/pnas.1112685108

Bulgarelli, C., Blasi, A., de Klerk, C., Richards, J. E., Hamilton, A., and Southgate, V. (2019). Fronto-temporoparietal connectivity and self-awareness in 18-month-olds: a resting state fNIRS study. *Dev. Cogn. Neurosci.* 38:100676. doi: 10.1016/j.dcn.2019.100676

Bulgarelli, C., de Klerk, C., Richards, J. E., Southgate, V., Hamilton, A., and Blasi, A. (2020). The developmental trajectory of fronto-temporoparietal connectivity as a proxy of the default mode network: a longitudinal fNIRS investigation. *Hum. Brain Mapp.* 41, 2717–2740. doi: 10.1002/hbm.24974

Chang, C., Leopold, D. A., Scholvinck, M. L., Mandelkow, H., Picchioni, D., Liu, X., et al. (2016). Tracking brain arousal fluctuations with fMRI. *Proc. Natl. Acad. Sci. U.S.A.* 113, 4518–4523. doi: 10.1073/pnas.1520613113

Chang, C., Liu, Z., Chen, M. C., Liu, X., and Duyn, J. H. (2013). EEG correlates of time-varying BOLD functional connectivity. *NeuroImage* 72, 227–236. doi: 10.1016/j.neuroimage.2013.01.049

Chaumon, M., Bishop, D. V., and Busch, N. A. (2015). A practical guide to the selection of independent components of the electroencephalogram for artifact correction. *J. Neurosci. Methods* 250, 47–63. doi: 10.1016/j.jneumeth.2015.02.025

Chen, G., Chen, G., Xie, C., Ward, B. D., Li, W., Antuono, P., et al. (2012). A method to determine the necessity for global signal regression in resting-state fMRI studies. *Magn. Reson. Med.* 68, 1828–1835. doi: 10.1002/mrm.24201

Chen, W. L., Wagner, J., Heugel, N., Sugar, J., Lee, Y. W., Conant, L., et al. (2020). Functional near-infrared spectroscopy and its clinical application in the field of neuroscience: advances and future directions. *Front. Neurosci.* 14:724. doi: 10.3389/fnins.2020.00724

Cordes, D., Haughton, V. M., Arfanakis, K., Carew, J. D., Turski, P. A., Moritz, C. H., et al. (2001). Frequencies contributing to functional connectivity in the cerebral cortex in "resting-state" data. *AJNR Am. J. Neuroradiol.* 22, 1326–1333.

Damoiseaux, J. S., Rombouts, S. A., Barkhof, F., Scheltens, P., Stam, C. J., Smith, S. M., et al. (2006). Consistent resting-state networks across healthy subjects. *Proc. Natl. Acad. Sci. U.S.A.* 103, 13848–13853. doi: 10.1073/pnas.0601417103

de Munck, J. C., Gonçalves, S. I, Huijboom, L., Kuijer, J. P. A., Pouwels, P. J. W., Heethaar, R. M., et al. (2007). The hemodynamic response of the alpha rhythm: an EEG/fMRI study. *NeuroImage* 35, 1142–1151. doi: 10.1016/j.neuroimage.2007.01.022

de Souza Rodrigues, J., Ribeiro, F. L., Sato, J. R., Mesquita, R. C., and Júnior, C. E. B. (2019). Identifying individuals using fNIRS-based cortical connectomes. *Biomed. Opt. Express* 10, 2889–2897. doi: 10.1364/boe.10.002889

Delorme, A., and Makeig, S. (2004). EEGLAB: an open source toolbox for analysis of single-trial EEG dynamics including independent component analysis. *J. Neurosci. Methods* 134, 9–21. doi: 10.1016/j.jneumeth.2003.10.009

Desjardins, A. E., Kiehl, K. A., and Liddle, P. F. (2001). Removal of confounding effects of global signal in functional MRI analyses. *Neuroimage* 13, 751–758. doi: 10.1006/nimg.2000.0719

Duan, L., Zhao, Z., Lin, Y., Wu, X., Luo, Y., and Xu, P. (2018). Wavelet-based method for removing global physiological noise in functional near-infrared spectroscopy. *Biomed. Opt. Express* 9, 3805–3820. doi: 10.1364/BOE.9.003805

Eggebrecht, A. T., Ferradal, S. L., Robichaux-Viehoever, A., Hassanpour, M. S., Dehghani, H., Snyder, A. Z., et al. (2014). Mapping distributed brain function and networks with diffuse optical tomography. *Nat. Photonics* 8, 448–454. doi: 10.1038/nphoton.2014.107

Eggebrecht, A. T., White, B. R., Ferradal, S. L., Chen, C., Zhan, Y., Snyder, A. Z., et al. (2012). A quantitative spatial comparison of high-density diffuse optical tomography and fMRI cortical mapping. *Neuroimage* 61, 1120–1128. doi: 10.1016/j.neuroimage.2012.01.124

Falahpour, M., Chang, C., Wong, C. W., and Liu, T. T. (2018). Template-based prediction of vigilance fluctuations in resting-state fMRI. *Neuroimage* 174, 317–327. doi: 10.1016/j.neuroimage.2018.03.012

Fox, M. D., Snyder, A. Z., Vincent, J. L., Corbetta, M., Van Essen, D. C., and Raichle, M. E. (2005). The human brain is intrinsically organized into dynamic, anticorrelated functional networks. *Proc. Natl. Acad. Sci. U.S.A.* 102, 9673–9678. doi: 10.1073/pnas.0504136102

Fox, M. D., Zhang, D., Snyder, A. Z., and Raichle, M. E. (2009). The global signal and observed anticorrelated resting state brain networks. *J. Neurophysiol.* 101, 3270–3283. doi: 10.1152/jn.90777.2008

Fox, P. T., Mintun, M. A., Reiman, E. M., and Raichle, M. E. (1988). Enhanced detection of focal brain responses using intersubject averaging and change-distribution analysis of subtracted PET images. *J. Cereb. Blood Flow Metab.* 8, 642–653. doi: 10.1038/jcbfm.1988.111

Franceschini, M. A., Joseph, D. K., Huppert, T. J., Diamond, S. G., and Boas, D. A. (2006). Diffuse optical imaging of the whole head. *J. Biomed. Opt.* 11:054007. doi: 10.1117/1.2363365

Friston, K. J., Frith, C. D., Liddle, P. F., Dolan, R. J., Lammertsma, A. A., and Frackowiak, R. S. (1990). The relationship between global and local changes in PET scans. *J. Cereb. Blood Flow Metab.* 10, 458–466. doi: 10.1038/jcbfm.1990.88

Furlan, R., Porta, A., Costa, F., Tank, J., Baker, L., Schiavi, R., et al. (2000). Oscillatory patterns in sympathetic neural discharge and cardiovascular variables during orthostatic stimulus. *Circulation* 101, 886–892. doi: 10.1161/01.cir.101.8.886

Gagnon, L., Perdue, K., Greve, D. N., Goldenholz, D., Kaskhedikar, G., and Boas, D. A. (2011). Improved recovery of the hemodynamic response in diffuse optical imaging using short optode separations and state-space modeling. *Neuroimage* 56, 1362–1371. doi: 10.1016/j.neuroimage.2011.03.001

Glover, G. H., Li, T. Q., and Ress, D. (2000). Image-based method for retrospective correction of physiological motion effects in fMRI: RETROICOR. *Magn. Reson. Med.* 44, 162–167. doi: 10.1002/1522-2594(200007)44:1<162::aid-mrm23>3.0.co;2-e

Goldman, R. I., Stern, J. M., Engel, J. Jr., and Cohen, M. S. (2002). Simultaneous EEG and fMRI of the alpha rhythm. *Neuroreport* 13, 2487–2492. doi: 10.1097/01.wnr.0000047685.08940.d0

Gratzer, W. B., and Allison, A. C. (1960). Multiple haemoglobins. *Biol. Rev.* 35, 459–503. doi: 10.1111/j.1469-185X.1960.tb01523.x

Gregg, N. M., White, B. R., Zeff, B. W., Berger, A. J., and Culver, J. P. (2010). Brain specificity of diffuse optical imaging: improvements from superficial signal regression and tomography. *Front. Neuroenerget.* 2:14. doi: 10.3389/fnene.2010.00014

Greicius, M. D., Krasnow, B., Reiss, A. L., and Menon, V. (2003). Functional connectivity in the resting brain: a network analysis of the default mode hypothesis. *Proc. Natl. Acad. Sci. U.S.A.* 100, 253–258. doi: 10.1073/pnas.0135058100

Hahamy, A., Calhoun, V., Pearlson, G., Harel, M., Stern, N., Attar, F., et al. (2014). Save the global: global signal connectivity as a tool for studying clinical populations with functional magnetic resonance imaging. *Brain Connect.* 4, 395–403. doi: 10.1089/brain.2014.0244

He, B. J., Snyder, A. Z., Zempel, J. M., Smyth, M. D., and Raichle, M. E. (2008). Electrophysiological correlates of the brain's intrinsic large-scale functional architecture. *Proc. Natl. Acad. Sci. U.S.A.* 105, 16039–16044. doi: 10.1073/pnas.0807010105

Homae, F., Watanabe, H., Otobe, T., Nakano, T., Go, T., Konishi, Y., et al. (2010). Development of global cortical networks in early infancy. *J. Neurosci.* 30, 4877–4882. doi: 10.1523/JNEUROSCI.5618-09.2010

Horovitz, S. G., Fukunaga, M., de Zwart, J. A., van Gelderen, P., Fulton, S. C., Balkin, T. J., et al. (2008). Low frequency BOLD fluctuations during resting wakefulness and light sleep: a simultaneous EEG-fMRI study. *Hum. Brain Mapp.* 29, 671–682. doi: 10.1002/hbm.20428

Hu, Z., Liu, G., Dong, Q., and Niu, H. (2020). Applications of resting-state fNIRS in the developing brain: a review from the connectome perspective. *Front. Neurosci.* 14:476. doi: 10.3389/fnins.2020.00476

Huppert, T. J., Diamond, S. G., Franceschini, M. A., and Boas, D. A. (2009). HomER: a review of time-series analysis methods for near-infrared spectroscopy of the brain. *Appl. Opt.* 48, D280–D298.

Hutchison, R. M., Womelsdorf, T., Allen, E. A., Bandettini, P. A., Calhoun, V. D., Corbetta, M., et al. (2013). Dynamic functional connectivity: promise, issues, and interpretations. *NeuroImage* 80, 360–378. doi: 10.1016/j.neuroimage.2013.05.079

Ieong, H. F., Gao, F., and Yuan, Z. (2019). Machine learning: assessing neurovascular signals in the prefrontal cortex with non-invasive bimodal electro-optical neuroimaging in opiate addiction. *Sci. Rep.* 9:18262. doi: 10.1038/s41598-019-54316-54316

Jasper, H. H. (1958). The ten-twenty electrode system of the international federation. *Electroencephalogr. Clin. Neurophysiol.* 10, 371–375.

Jobert, M., Schulz, H., Jahnig, P., Tismer, C., Bes, F., and Escola, H. (1994). A computerized method for detecting episodes of wakefulness during sleep based on the alpha slow-wave index (ASI). *Sleep* 17, 37–46.

Julien, C. (2006). The enigma of Mayer waves: facts and models. *Cardiovasc. Res.* 70, 12–21. doi: 10.1016/j.cardiores.2005.11.008

Kay, K. N., Rokem, A., Winawer, J., Dougherty, R. F., and Wandell, B. A. (2013). GLMdenoise: a fast, automated technique for denoising task-based fMRI data. *Front. Neurosci.* 7:247. doi: 10.3389/fnins.2013.00247

Keehn, B., Wagner, J. B., Tager-Flusberg, H., and Nelson, C. A. (2013). Functional connectivity in the first year of life in infants at-risk for autism: a preliminary near-infrared spectroscopy study. *Front. Hum. Neurosci.* 7:444. doi: 10.3389/fnhum.2013.00444

Kocsis, L., Herman, P., and Eke, A. (2006). The modified Beer-Lambert law revisited. *Phys. Med. Biol.* 51, N91–N98. doi: 10.1088/0031-9155/51/5/N02

Kohno, S., Miyai, I., Seiyama, A., Oda, I., Ishikawa, A., Tsuneishi, S., et al. (2007). Removal of the skin blood flow artifact in functional near-infrared spectroscopic imaging data through independent component analysis. *J. Biomed. Opt.* 12:062111. doi: 10.1117/1.2814249

Leopold, D. A., Murayama, Y., and Logothetis, N. K. (2003). Very slow activity fluctuations in monkey visual cortex: implications for functional brain imaging. *Cereb. Cortex* 13, 422–433. doi: 10.1093/cercor/13.4.422

Li, J., Bolt, T., Bzdok, D., Nomi, J. S., Yeo, B. T. T., Spreng, R. N., et al. (2019). Topography and behavioral relevance of the global signal in the human brain. *Sci. Rep.* 9:14286. doi: 10.1038/s41598-019-50750-50758

Lu, C.-M., Zhang, Y.-J., Biswal, B. B., Zang, Y.-F., Peng, D.-L., and Zhu, C.-Z. (2010). Use of fNIRS to assess resting state functional connectivity. *J. Neurosci. Methods* 186, 242–249. doi: 10.1016/j.jneumeth.2009.11.010

Macey, P. M., Macey, K. E., Kumar, R., and Harper, R. M. (2004). A method for removal of global effects from fMRI time series. *Neuroimage* 22, 360–366. doi: 10.1016/j.neuroimage.2003.12.042

Mantini, D., Perrucci, M. G., Del Gratta, C., Romani, G. L., and Corbetta, M. (2007). Electrophysiological signatures of resting state networks in the human brain. *Proc. Natl. Acad. Sci. U.S.A.* 104, 13170–13175. doi: 10.1073/pnas.0700668104

Mesquita, R. C., Franceschini, M. A., and Boas, D. A. (2010). Resting state functional connectivity of the whole head with near-infrared spectroscopy. *Biomed. Opt. Express* 1, 324–336. doi: 10.1364/BOE.1.000324

Mohammadi-Nejad, A. R., Mahmoudzadeh, M., Hassanpour, M. S., Wallois, F., Muzik, O., Papadelis, C., et al. (2018). Neonatal brain resting-state functional connectivity imaging modalities. *Photoacoustics* 10, 1–19. doi: 10.1016/j.pacs.2018.01.003

Molavi, B., May, L., Gervain, J., Carreiras, M., Werker, J. F., and Dumont, G. A. (2013). Analyzing the resting state functional connectivity in the human language system using near infrared spectroscopy. *Front. Hum. Neurosci.* 7:921. doi: 10.3389/fnhum.2013.00921

Muller, T., Reinhard, M., Oehm, E., Hetzel, A., and Timmer, J. (2003). Detection of very low-frequency oscillations of cerebral haemodynamics is influenced by data detrending. *Med. Biol. Eng. Comput.* 41, 69–74. doi: 10.1007/bf02343541

Murphy, K., Birn, R. M., Handwerker, D. A., Jones, T. B., and Bandettini, P. A. (2009). The impact of global signal regression on resting state correlations: are anti-correlated networks introduced? *Neuroimage* 44, 893–905. doi: 10.1016/j.neuroimage.2008.09.036

Murphy, K., and Fox, M. D. (2017). Towards a consensus regarding global signal regression for resting state functional connectivity MRI. *Neuroimage* 154, 169–173. doi: 10.1016/j.neuroimage.2016.11.052

Naseer, N., and Hong, K. S. (2015). fNIRS-based brain-computer interfaces: a review. *Front. Hum. Neurosci.* 9:3. doi: 10.3389/fnhum.2015.00003

Novi, S. L., Rodrigues, R. B., and Mesquita, R. C. (2016). Resting state connectivity patterns with near-infrared spectroscopy data of the whole head. *Biomed. Opt. Express* 7, 2524–2537. doi: 10.1364/BOE.7.002524

Obrig, H., Neufang, M., Wenzel, R., Kohl, M., Steinbrink, J., Einhaupl, K., et al. (2000). Spontaneous low frequency oscillations of cerebral hemodynamics and metabolism in human adults. *Neuroimage* 12, 623–639. doi: 10.1006/nimg.2000.0657

Obrig, H., and Villringer, A. (2003). Beyond the visible–imaging the human brain with light. *J. Cereb. Blood Flow Metab.* 23, 1–18. doi: 10.1097/01.WCB.0000043472.45775.29

Olbrich, S., Mulert, C., Karch, S., Trenner, M., Leicht, G., Pogarell, O., et al. (2009). EEG-vigilance and BOLD effect during simultaneous EEG/fMRI measurement. *Neuroimage* 45, 319–332. doi: 10.1016/j.neuroimage.2008.11.014

Pinti, P., Tachtsidis, I., Hamilton, A., Hirsch, J., Aichelburg, C., Gilbert, S., et al. (2018). The present and future use of functional near-infrared spectroscopy (fNIRS) for cognitive neuroscience. *Ann. N. Y. Acad. Sci.* 1464, 5–29. doi: 10.1111/nyas.13948

Power, J. D., Schlaggar, B. L., and Petersen, S. E. (2015). Recent progress and outstanding issues in motion correction in resting state fMRI. *Neuroimage* 105, 536–551. doi: 10.1016/j.neuroimage.2014.10.044

Putze, F., Hesslinger, S., Tse, C.-Y., Huang, Y., Herff, C., Guan, C., et al. (2014). Hybrid fNIRS-EEG based classification of auditory and visual perception processes. *Front. Neurosci.* 8:373–373. doi: 10.3389/fnins.2014.00373

Raichle, M. E., MacLeod, A. M., Snyder, A. Z., Powers, W. J., Gusnard, D. A., and Shulman, G. L. (2001). A default mode of brain function. *Proc. Natl. Acad. Sci. U.S.A.* 98, 676–682. doi: 10.1073/pnas.98.2.676

Saad, Z. S., Gotts, S. J., Murphy, K., Chen, G., Jo, H. J., Martin, A., et al. (2012). Trouble at rest: how correlation patterns and group differences become distorted after global signal regression. *Brain Connect.* 2, 25–32. doi: 10.1089/brain.2012.0080

Saager, R. B., and Berger, A. J. (2005). Direct characterization and removal of interfering absorption trends in two-layer turbid media. *J. Opt. Soc. Am. A Opt. Image Sci. Vis.* 22, 1874–1882. doi: 10.1364/josaa.22.001874

Sakakibara, E., Homae, F., Kawasaki, S., Nishimura, Y., Takizawa, R., Koike, S., et al. (2016). Detection of resting state functional connectivity using partial correlation analysis: a study using multi-distance and whole-head probe near-infrared spectroscopy. *Neuroimage* 142, 590–601. doi: 10.1016/j.neuroimage.2016.08.011

Sambataro, F., Murty, V. P., Callicott, J. H., Tan, H. Y., Das, S., Weinberger, D. R., et al. (2010). Age-related alterations in default mode network: impact on working memory performance. *Neurobiol. Aging* 31, 839–852. doi: 10.1016/j.neurobiolaging.2008.05.022

Santosa, H., Zhai, X., Fishburn, F., and Huppert, T. (2018). The NIRS Brain AnalyzIR Toolbox. *Algorithms* 11:73. doi: 10.3390/a11050073

Sasai, S., Homae, F., Watanabe, H., and Taga, G. (2011). Frequency-specific functional connectivity in the brain during resting state revealed by NIRS. *Neuroimage* 56, 252–257. doi: 10.1016/j.neuroimage.2010.12.075

Sato, T., Nambu, I., Takeda, K., Aihara, T., Yamashita, O., Isogaya, Y., et al. (2016). Reduction of global interference of scalp-hemodynamics in functional near-infrared spectroscopy using short distance probes. *Neuroimage* 141, 120–132. doi: 10.1016/j.neuroimage.2016.06.054

Scholkmann, F., Kleiser, S., Metz, A. J., Zimmermann, R., Mata Pavia, J., Wolf, U., et al. (2014). A review on continuous wave functional near-infrared spectroscopy and imaging instrumentation and methodology. *Neuroimage* 85(Pt 1), 6–27. doi: 10.1016/j.neuroimage.2013.05.004

Scholvinck, M. L., Maier, A., Ye, F. Q., Duyn, J. H., and Leopold, D. A. (2010). Neural basis of global resting-state fMRI activity. *Proc. Natl. Acad. Sci. U.S.A.* 107, 10238–10243. doi: 10.1073/pnas.0913110107

Sherafati, A., Snyder, A. Z., Eggebrecht, A. T., Bergonzi, K. M., Burns-Yocum, T. M., Lugar, H. M., et al. (2020). Global motion detection and censoring in high-density diffuse optical tomography. *Hum. Brain Mapp.* doi: 10.1002/hbm.25111 [Online ahead of print]

Shin, J., Kwon, J., Choi, J., and Im, C. H. (2017). Performance enhancement of a brain-computer interface using high-density multi-distance NIRS. *Sci. Rep.* 7:16545. doi: 10.1038/s41598-017-16639-16630

Shmuel, A., and Leopold, D. A. (2008). Neuronal correlates of spontaneous fluctuations in fMRI signals in monkey visual cortex: Implications for functional connectivity at rest. *Hum. Brain Mapp.* 29, 751–761. doi: 10.1002/hbm.20580

Sood, B. G., McLaughlin, K., and Cortez, J. (2015). Near-infrared spectroscopy: applications in neonates. *Semin. Fetal Neonatal Med.* 20, 164–172. doi: 10.1016/j.siny.2015.03.008

Tachtsidis, I., Elwell, C. E., Leung, T. S., Lee, C. W., Smith, M., and Delpy, D. T. (2004). Investigation of cerebral haemodynamics by near-infrared spectroscopy in young healthy volunteers reveals posture-dependent spontaneous oscillations. *Physiol. Meas.* 25, 437–445. doi: 10.1088/0967-3334/25/2/003

Tachtsidis, I., and Scholkmann, F. (2016). False positives and false negatives in functional near-infrared spectroscopy: issues, challenges, and the way forward. *Neurophotonics* 3:031405. doi: 10.1117/1.NPh.3.3.031405

Tong, Y., and Frederick, B. D. (2010). Time lag dependent multimodal processing of concurrent fMRI and near-infrared spectroscopy (NIRS) data suggests a global circulatory origin for low-frequency oscillation signals in human brain. *Neuroimage* 53, 553–564. doi: 10.1016/j.neuroimage.2010.06.049

Torricelli, A., Contini, D., Pifferi, A., Caffini, M., Re, R., Zucchelli, L., et al. (2014). Time domain functional NIRS imaging for human brain mapping. *Neuroimage* 85(Pt 1), 28–50. doi: 10.1016/j.neuroimage.2013.05.106

Wang, M., Hu, Z., Liu, L., Li, H., Qian, Q., and Niu, H. (2020). Disrupted functional brain connectivity networks in children with attention-deficit/hyperactivity disorder: evidence from resting-state functional near-infrared spectroscopy. *Neurophotonics* 7:015012. doi: 10.1117/1.NPh.7.1.015012

Watabe, T., and Hatazawa, J. (2019). Evaluation of functional connectivity in the brain using positron emission tomography: a mini-review. *Front. Neurosci.* 13:775. doi: 10.3389/fnins.2019.00775

Watanabe, H., Shitara, Y., Aoki, Y., Inoue, T., Tsuchida, S., Takahashi, N., et al. (2017). Hemoglobin phase of oxygenation and deoxygenation in early brain development measured using fNIRS. *Proc. Natl. Acad. Sci. U.S.A.* 114, E1737–E1744. doi: 10.1073/pnas.1616866114

Watanabe, N., Reece, J., and Polus, B. I. (2007). Effects of body position on autonomic regulation of cardiovascular function in young, healthy adults. *Chiropr. Osteopat.* 15:19. doi: 10.1186/1746-1340-15-19

White, B. R., Liao, S. M., Ferradal, S. L., Inder, T. E., and Culver, J. P. (2012). Bedside optical imaging of occipital resting-state functional connectivity in neonates. *Neuroimage* 59, 2529–2538. doi: 10.1016/j.neuroimage.2011.08.094

White, B. R., Snyder, A. Z., Cohen, A. L., Petersen, S. E., Raichle, M. E., Schlaggar, B. L., et al. (2009). Resting-state functional connectivity in the human brain revealed with diffuse optical tomography. *Neuroimage* 47, 148–156. doi: 10.1016/j.neuroimage.2009.03.058

Wise, R. G., Ide, K., Poulin, M. J., and Tracey, I. (2004). Resting fluctuations in arterial carbon dioxide induce significant low frequency variations in BOLD signal. *Neuroimage* 21, 1652–1664. doi: 10.1016/j.neuroimage.2003.11.025

Wong, C. W., DeYoung, P. N., and Liu, T. T. (2016). Differences in the resting-state fMRI global signal amplitude between the eyes open and eyes closed states are related to changes in EEG vigilance. *Neuroimage* 124(Pt A), 24–31. doi: 10.1016/j.neuroimage.2015.08.053

Wong, C. W., Olafsson, V., Tal, O., and Liu, T. T. (2013). The amplitude of the resting-state fMRI global signal is related to EEG vigilance measures. *Neuroimage* 83, 983–990. doi: 10.1016/j.neuroimage.2013.07.057

Wyser, D., Mattille, M., Wolf, M., Lambercy, O., Scholkmann, F., and Gassert, R. (2020). Short-channel regression in functional near-infrared spectroscopy is more effective when considering heterogeneous scalp hemodynamics. *Neurophotonics* 7:035011. doi: 10.1117/1.NPh.7.3.035011

Xu, Y., Graber, H. L., and Barbour, R. L. (2014). "nirsLAB: a Computing(Environment)for fNIRS Neuroimaging Data Analysis," in *Proceedings of the conference Biomedical Optics 2014* (Washington, DC: Optical Society of America).

Yang, G. J., Murray, J. D., Glasser, M., Pearlson, G. D., Krystal, J. H., Schleifer, C., et al. (2017). Altered Global Signal Topography in Schizophrenia. *Cereb. Cortex* 27, 5156–5169. doi: 10.1093/cercor/bhw297

Ye, J. C., Tak, S., Jang, K. E., Jung, J., and Jang, J. (2009). NIRS-SPM: statistical parametric mapping for near-infrared spectroscopy. *NeuroImage* 44, 428–447. doi: 10.1016/j.neuroimage.2008.08.036

Yuan, H., Ding, L., Zhu, M., Zotev, V., Phillips, R., and Bodurka, J. (2016). Reconstructing large-scale brain resting-state networks from high-resolution EEG: spatial and temporal comparisons with fMRI. *Brain Connect.* 6, 122–135. doi: 10.1089/brain.2014.0336

Yuan, H., Zotev, V., Phillips, R., and Bodurka, J. (2013). Correlated slow fluctuations in respiration, EEG, and BOLD fMRI. *Neuroimage* 79, 81–93. doi: 10.1016/j.neuroimage.2013.04.068

Yuan, H., Zotev, V., Phillips, R., Drevets, W. C., and Bodurka, J. (2012). Spatiotemporal dynamics of the brain at rest–exploring EEG microstates as electrophysiological signatures of BOLD resting state networks. *Neuroimage* 60, 2062–2072. doi: 10.1016/j.neuroimage.2012.02.031

Zarahn, E., Aguirre, G., and D'Esposito, M. (1997). A trial-based experimental design for fMRI. *Neuroimage* 6, 122–138. doi: 10.1006/nimg.1997.0279

Zeff, B. W., White, B. R., Dehghani, H., Schlaggar, B. L., and Culver, J. P. (2007). Retinotopic mapping of adult human visual cortex with high-density diffuse optical tomography. *Proc. Natl. Acad. Sci. U.S.A.* 104, 12169–12174. doi: 10.1073/pnas.0611266104

Zhang, D., and Raichle, M. E. (2010). Disease and the brain's dark energy. *Nat. Rev. Neurol.* 6, 15–28. doi: 10.1038/nrneurol.2009.198

Zhang, H., Duan, L., Zhang, Y. J., Lu, C. M., Liu, H., and Zhu, C. Z. (2011). Test-retest assessment of independent component analysis-derived resting-state functional connectivity based on functional near-infrared spectroscopy. *Neuroimage* 55, 607–615. doi: 10.1016/j.neuroimage.2010.12.007

Zhang, H., Zhang, Y.-J., Lu, C.-M., Ma, S.-Y., Zang, Y.-F., and Zhu, C.-Z. (2010). Functional connectivity as revealed by independent component analysis of resting-state fNIRS measurements. *Neuroimage* 51, 1150–1161. doi: 10.1016/j.neuroimage.2010.02.080

Zhang, Q., Brown, E. N., and Strangman, G. E. (2007). Adaptive filtering to reduce global interference in evoked brain activity detection: a human subject case study. *J. Biomed. Opt.* 12:064009. doi: 10.1117/1.2804706

Zhang, Q., Strangman, G. E., and Ganis, G. (2009). Adaptive filtering to reduce global interference in non-invasive NIRS measures of brain activation: how well and when does it work? *Neuroimage* 45, 788–794. doi: 10.1016/j.neuroimage.2008.12.048

Zhang, X., Noah, J. A., and Hirsch, J. (2016). Separation of the global and local components in functional near-infrared spectroscopy signals using principal component spatial filtering. *Neurophotonics* 3:015004. doi: 10.1117/1.NPh.3.1.015004

Zhang, Y., Brooks, D. H., Franceschini, M. A., and Boas, D. A. (2005). Eigenvector-based spatial filtering for reduction of physiological interference in diffuse optical imaging. *J. Biomed. Opt.* 10:11014. doi: 10.1117/1.1852552

Zou, Q. H., Zhu, C. Z., Yang, Y., Zuo, X. N., Long, X. Y., Cao, Q. J., et al. (2008). An improved approach to detection of amplitude of low-frequency fluctuation (ALFF) for resting-state fMRI: fractional ALFF. *J. Neurosci. Methods* 172, 137–141. doi: 10.1016/j.jneumeth.2008.04.012

Conflict of Interest: The authors declare that the research was conducted in the absence of any commercial or financial relationships that could be construed as a potential conflict of interest.

frontiers in Neuroscience

METHODS
published: 22 December 2020
doi: 10.3389/fnins.2020.558981

Semi-Automated and Direct Localization and Labeling of EEG Electrodes Using MR Structural Images for Simultaneous fMRI-EEG

Abhishek S. Bhutada[1†], Pradyumna Sepúlveda[2†], Rafael Torres[3], Tomás Ossandón[3,4], Sergio Ruiz[3,4] and Ranganatha Sitaram[3,4,5*]*

[1] Department of Molecular and Cellular Biology, University of California, Berkeley, Berkeley, CA, United States, [2] Institute of Cognitive Neuroscience, University College London, London, United Kingdom, [3] Department of Psychiatry, Faculty of Medicine, Interdisciplinary Center for Neuroscience, Pontificia Universidad Católica de Chile, Santiago, Chile, [4] Laboratory for Brain–Machine Interfaces and Neuromodulation, Pontificia Universidad Católica de Chile, Santiago, Chile, [5] Institute for Biological and Medical Engineering, Pontificia Universidad Católica de Chile, Santiago, Chile

OPEN ACCESS

Edited by:
Surjo R. Soekadar,
Charité – Universitätsmedizin Berlin, Germany

Reviewed by:
Aleksandra Dagmara Kawala-Sterniuk,
Opole University of Technology, Poland
Vassiliy Tsytsarev,
University of Maryland, College Park, United States

***Correspondence:**
Ranganatha Sitaram
rasitaram@uc.cl
Sergio Ruiz
sruiz@uc.cl

[†] These authors have contributed equally to this work

Specialty section:
This article was submitted to Neural Technology, a section of the journal Frontiers in Neuroscience

Received: 04 May 2020
Accepted: 08 October 2020
Published: 22 December 2020

Citation:
Bhutada AS, Sepúlveda P, Torres R, Ossandón T, Ruiz S and Sitaram R (2020) Semi-Automated and Direct Localization and Labeling of EEG Electrodes Using MR Structural Images for Simultaneous fMRI-EEG. Front. Neurosci. 14:558981. doi: 10.3389/fnins.2020.558981

Electroencephalography (EEG) source reconstruction estimates spatial information from the brain's electrical activity acquired using EEG. This method requires accurate identification of the EEG electrodes in a three-dimensional (3D) space and involves spatial localization and labeling of EEG electrodes. Here, we propose a new approach to tackle this two-step problem based on the simultaneous acquisition of EEG and magnetic resonance imaging (MRI). For the step of spatial localization of electrodes, we extract the electrode coordinates from the curvature of the protrusions formed in the high-resolution T1-weighted brain scans. In the next step, we assign labels to each electrode based on the distinguishing feature of the electrode's distance profile in relation to other electrodes. We then compare the subject's electrode data with template-based models of prelabeled distance profiles of correctly labeled subjects. Based on this approach, we could localize EEG electrodes in 26 head models with over 90% accuracy in the 3D localization of electrodes. Next, we performed electrode labeling of the subjects' data with progressive improvements in accuracy: with ∼58% accuracy based on a single EEG-template, with ∼71% accuracy based on 3 EEG-templates, and with ∼76% accuracy using 5 EEG-templates. The proposed semi-automated method provides a simple alternative for the rapid localization and labeling of electrodes without the requirement of any additional equipment than what is already used in an EEG-fMRI setup.

Keywords: electroencephalography, magnetic resonance imaging, EEG/fMRI, source localization, electrode positioning, electrode labeling

INTRODUCTION

Despite the usefulness of electroencephalography (EEG) to study the dynamic changes in brain signal, one of its historical weaknesses has been its restricted spatial resolution. An approach to tackle this issue has been to analyze EEG signals with an inverse mathematical model and trace brain activity through a method called EEG source reconstruction (Michel et al., 2004). By using

models of the brain's structure, the inverse model allows us to locate regions that are activated over time from the information given by the voltage measurements of the electrodes. EEG source reconstruction serves many clinical and neuroscientific purposes such as epileptic seizure mapping and understanding neurovascular coupling (Gavaret et al., 2004; Vulliemoz et al., 2010; Yuan et al., 2010; Hanslmayr et al., 2011; De Ciantis and Lemieux, 2013; Lei et al., 2015). On the other hand, another way to deal with EEG drawbacks has been relying on multimodal approaches. The development of EEG-fMRI has resulted in an interesting symbiosis of two techniques that allow a richer and more comprehensive understanding of brain dynamics in a non-invasive way (Goebel and Esposito, 2009; Huster et al., 2012).

For a successful source reconstruction analysis of EEG signals, it is necessary to precisely obtain three-dimensional (3D) coordinates of the location of each electrode for each individual subject (Dalal et al., 2014). Although some previous approaches have relied on a standard positioning of electrodes in the EEG cap, the personalization of electrode mapping for each experimental subject improves the accuracy of the observed results by taking into consideration the differences in head shape and size across subjects. Although some external devices and methods have been proposed to obtain electrode locations (see below), in the present work we propose one method to use the standard EEG-fMRI experimental setup, i.e., MR-compatible EEG system with and electrode cap using conductive gel plus a magnetic resonance imaging (MRI) scanner, without further additions or extra MR-sequences to obtain EEG positions and labeling, facilitating a more accurate analysis of EEG in a multimodal environment.

The process of spatial localization of EEG electrodes involves two major steps: (1) correctly localizing and obtaining the 3D coordinates of each electrode, and (2) distinguishing each electrode by finding its proper label. There have been attempts to solve these two steps of the problem (De Munck et al., 1991; Steddin and Botzel, 1995; Yoo et al., 1997; Le et al., 1998; Koessler et al., 2007; Péchaud et al., 2007); however, there are only a few approaches that have automated this process of mapping electrodes. In the following paragraphs, we summarize the existing manual, semi-automated, and automated methods of EEG localization and labeling.

Manual Localization and Labeling

The most rudimentary methods are based on direct manual measurements (e.g., calipers or compass) of the distances between each electrode and particular landmarks to later calculate the Cartesian coordinates using a system of equations (De Munck et al., 1991). Recent methods through the use of digitizers, cameras, or external devices allow for manual localization of electrodes on the standard cap (Koessler et al., 2007). Electromagnetic digitization utilizes an electromagnetic field transmitter and multiple receivers across the subject's head in order to create a model. Another stylus receiver is then used as a way to manually localize electrodes on the head (Le et al., 1998). An ultrasound digitizer uses a similar method for digitizing the subject's head and for localizing EEG electrodes by using sound impulses (Steddin and Botzel, 1995). A photogrammetry system, also known as geodesic photogrammetry system (GPS), uses a system of multiple cameras placed in a polyhedron-based structure around the subject's head and allows for 3D reconstruction of a head model and localization of the electrodes through method of triangulation (Russel et al., 2005; Clausner et al., 2017). The photogrammetry method still involves manual selection of points on each of the pictures taken. While these methods are useful in visually generating a head model, the process of localizing and labeling each of the electrodes is still manual and time-consuming. Some methods have taken advantage of the manual digitization and they have co-registered it with MRI volumes, using fiducial points and surface matching (Brinkmann et al., 1998; Lamm et al., 2001).

Semi-Automated Localization and Labeling

Initial attempts to make visible electrodes in MR have considered the inclusion of additional tags e.g., inclusion of gadolinium capsules, and manual segmentation of the electrodes from the images (Yoo et al., 1997). However, other methods have relied on the fact that electrodes are visible thanks to the conductive gel in some structural brain images acquired using MRI (see **Figure 1**). Using this feature, a semi-automated method of localizing electrodes, the Pancake View Method, has been implemented (De Munck et al., 2011). In this method, a flat pancake view of the head can be derived from T1-weighted (T1W) structural images. Each electrode artifact can be visualized in a single two-dimensional (2D) view. Later, locations and labels have to be selected manually for each electrode, generating a grid with known vertices. Using the template grid, the electrodes can be labeled automatically on other subjects using the same cap. Finally, the 2D coordinates of the pancake view are transformed to obtain the 3D coordinates of each one of the electrodes in the MRI coordinate frame. Another method based on MR, allows the localization of electrodes without relying on the presence of conductive gel, but using additional MR-sequences ultra-short echo time sequences (UTE) exclusively sensitive to the polymer material of the electrodes (Butler et al., 2017).

The combinatorial optimization and self-calibration is a different semi-automated approach to localizing electrode positions (Péchaud et al., 2007). In this method, the 3D coordinates of each electrode are reconstructed with a photogrammetry-based method of ten different pictures of the subject's head from various angles. The 3D coordinates are used to generate a template head with labels. To label the electrodes on a test subject, a minimization algorithm is then applied on the coordinates of the subject's head and the previously prepared template head in order to automatically provide labels for each of the electrodes.

These methods are closer to fully automatic approaches to solving the two-step problem; however, a limitation to these techniques is that they both require manual selection of points to localize the electrodes which can be quite time-consuming.

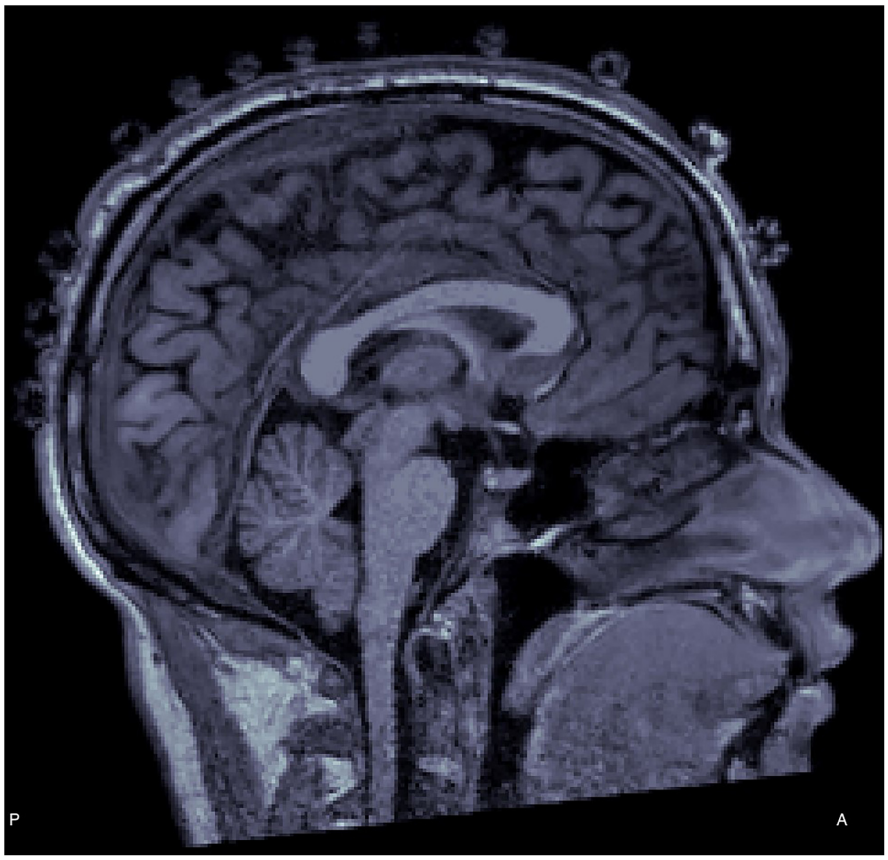

FIGURE 1 | T1-weighted (T1W) structural image with electrode protrusions appearing over the scalp.

Fully-Automated Localization and Labeling

A method for automated localization and labeling of electrodes also exploits the protrusions pertaining to EEG electrodes that appear in MR structural images (Koessler et al., 2008). In this method, structural MR images are pre-processed to enhance the clarity of the electrode protrusions so that they are more clearly visible as high-intensity voxels. With this approach, electrodes can be localized more effectively by segmenting the different layers of the head and identifying the voxels with the highest intensity across the scalp of the subject. After the electrodes are localized, a point drift method is used to register and label each electrode (Koessler et al., 2008). Although this approach results in automated localization and labeling, it requires specific sensors for detection of EEG electrodes in MR anatomical images. These sensors are not commonly used on a standard 64 channel EEG cap and must be externally glued on the subject's scalp.

Marino et al. (2016) reported an automatic method devised for high-density electrode caps, which extracts the electrode position through image processing and labels the electrodes using a transformation of the candidate position to MNI space to be matched with a template of the desired EEG positions. Another method (Fleury et al., 2019) allows the localization of electrodes without relying on the presence of conductive gel (although it uses additional UTE sequences, mentioned above) and implements automatic labeling using the iterative Closest Point algorithm, over a template of the electrode cap. These approaches again rely on the use of specialized electrodes for localization.

In another recent study, the same high-density electrode caps used in Marino's study were localized with the use of 3D scanners (Taberna et al., 2019). The approach used in Taberna's study was accurate in localization and used Closest Point algorithm to label the electrodes. Another study shows how 3D scanners have improved EEG source modeling due to a more reliable electrode localization (Homölle and Oostenveld, 2019). Yet, these approaches require the additional hardware (i.e., 3D scanner) in order to localize electrodes.

The Proposed Approach

Our MR-based method provides a direct way of solving this two-step problem of localization and labeling of the electrodes in a simultaneous EEG/MRI setup. With our approach, the user does not have the need for additional equipment (e.g., digitizers and cameras) or the need for specialized MR sequences (e.g., UTE sequences) to solve this two-step problem (Steddin and Botzel, 1995; Yoo et al., 1997; Le et al., 1998; Russel et al., 2005; Koessler et al., 2007; Péchaud et al., 2007; Marino et al., 2016;

Butler et al., 2017; Clausner et al., 2017; Fleury et al., 2019; Homölle and Oostenveld, 2019; Taberna et al., 2019). We take advantage of the fact that standard EEG electrodes can be seen in the standard high-resolution MRI structural images. A surface model of the head is first generated from the T1 images and electrodes are localized in the Cartesian coordinate system by considering the fact that each electrode protrusion in the MRI images possesses relatively higher curvature than the surrounding scalp in the generated head mesh (see **Figure 2**). In order to isolate the specific 3D coordinate value of a particular electrode, we consider the centroid of groups of points with maximal curvature to obtain the electrode location. The locations of all electrodes are determined in this manner first. In the next step, electrodes are labeled based on the idea that each electrode has a particular set of distances to all of the other electrodes. The set of all distances from each electrode to all other electrodes is called the Distance Profile (see **Figure 4**). The approach is based on the assumption that for a given EEG cap configuration, distance profiles should be constant despite changes in the point of reference of the coordinates system or in the shape of experimental subject heads. In this way we present an approach that provides a simple solution to the problem of localizing and labeling electrodes.

MATERIALS AND METHODS

Our method involves pre-processing of the T1W structural images in order to create a head model that can be used to extract the electrode positions. Next, the localization of electrodes is performed by finding vertices in the head mesh which have maximal curvature. The final step involves utilizing the distance profile criterion in order to assign labels to each of the electrode positions. An approximate duration of applying our method to localize and label electrodes is around 10 min per electrode set (participant), mostly giving time required for human intervention (i.e., indicating fiducial points in MR, pruning any extraneous electrodes located, etc.). Our study considers 26 T1W structural scans (subjects' ages: 22.86 ± 1.54) acquired during real-time fMRI neurofeedback study during simultaneous acquisition of EEG signals fMRI results from that study can be found in Sepulveda et al. (2016). The experimental protocol was approved by the ethics committee of Pontificia Universidad Católica de Chile. Each participant signed a written informed consent during the study. More details on the approach are available in the **Supplementary Methods**.

MR and EEG Acquisition

MR acquisition was done using a Philips Achieva 1.5T MR scanner (Philips Healthcare, Best, Netherlands) at the Pontificia Universidad Católica de Chile. A standard 8-channel head coil was used. Structural T1W brain volumes were acquired using T1W-3D Turbo Field Echo (TFE, magnetization prepared gradient echo also known as MPRAGE) sequence with TR/TE = 7.4/3.4 ms, matrix size = 208 × 227, $\alpha = 8°$, 317 partitions, voxels size = 1.1 mm × 1.1 mm × 0.6 mm, TI = 868.7 ms. To prevent discomfort during MRI sessions, pads and air cushions were used to fix subject heads.

MR-compatible EEG caps with 64 electrodes (Compumedics Neuroscan Quik-Cap) were used for the entire experiment. In particular, the MR structural scan was acquired at the end of the neurofeedback experiment. Therefore, it should be noted that participants were inside the scanner (wearing the EEG cap) for around 1 h before extracting the MR volumes.

Generating the Head Model

From T1W structural images each electrode can be seen directly as small bumps or protrusions over the scalp of the subject (see **Figure 1**). These protrusions are generated by the material of the EEG electrode and gel. Therefore, generating a head model which will include these protrusions is fundamental to localize the position of the electrodes. FreeSurfer (version 3.19; Dale et al., 1999)[1] and Brainstorm software (version 5.30; Tadel et al., 2011) can be used to generate a head model directly from the

[1]http://surfer.nmr.mgh.harvard.edu/

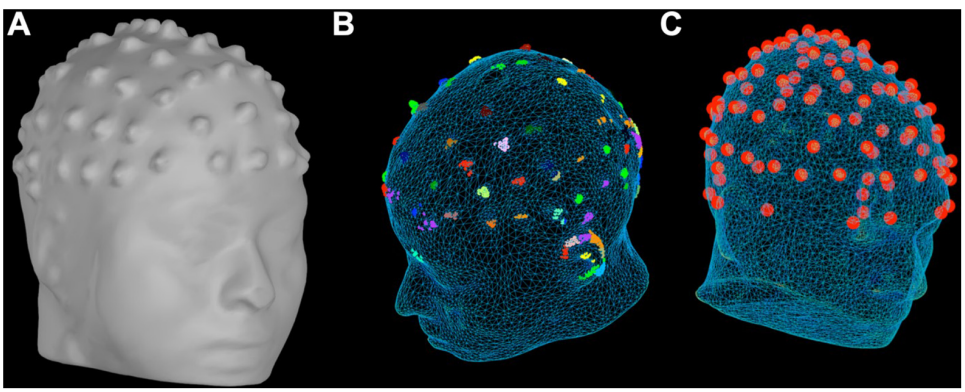

FIGURE 2 | Head Models. **(A)** Head model generated from the T1W structural scan of a subject using Free Surfer. Each protrusion on the scalp is an EEG electrode. **(B)** Clusters of vertices with high curvature are used to generate the position of the potential electrodes. Different clusters are depicted using different colors. **(C)** Using the curvature information of the head model, we can identify electrodes using the proposed method.

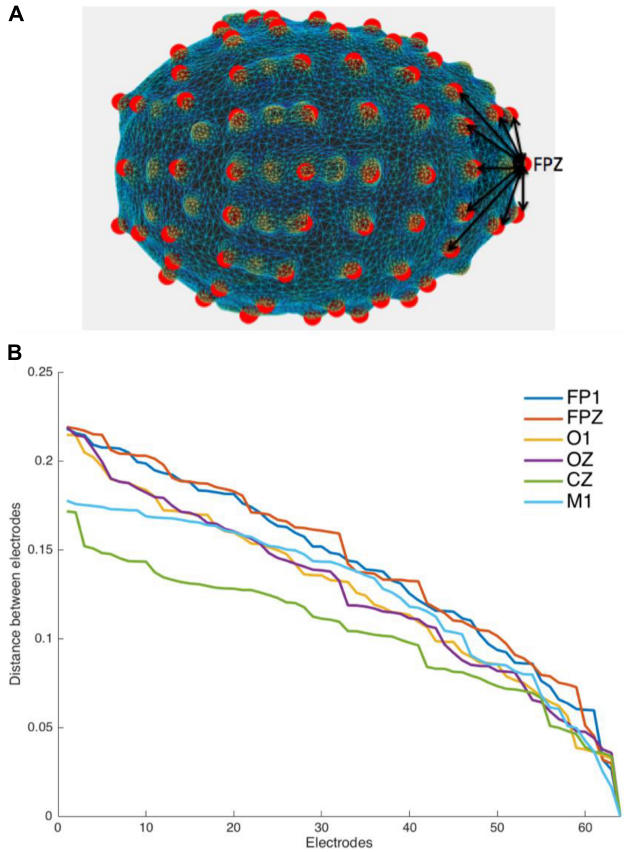

FIGURE 3 | Distance Profile. **(A)** Distances from one electrode to other electrodes form a particular pattern that could be utilized in identifying and labeling electrodes. **(B)** The distance profiles for six of the 64 electrodes of a subject (frontal: FP1 and FPZ, occipital: O1 and OZ, and central: CZ and M1). To construct the distance profile, we set the Euclidean distances between the electrode of interest and the rest of the 63 electrodes in a descending order. Comparing the distance profiles of FPZ and OZ the total distance of FPZ from all other electrodes would decrease slower than in the case of OZ. This profile is used to individualize the electrode for the assignment of labels to each electrode by comparison with electrodes with known position and label (Note: Distance values were extracted from the units available through Brainstorm from the MRI volumes).

anatomical MRI volume (**Figure 2A**). More importantly, when using Brainstorm this process is fast (less than 1 min to generate the head surface mesh using 10,000 vertices, erode factor = 0, and fill holes factor = 2). However, this step requires manual selection of fiducial points on the anatomical MRI volume to align the head model. This selection was done by an experienced user through the Brainstorm graphical interface.

Electrode Positioning

The head model, available in Brainstorm, contains information about the curvature for each vertex in the 3D mesh. The position of the electrodes was found by isolating vertices with high curvature on the surface mesh of the head model. Using the coordinate system assigned by Brainstorm, we restricted a search space $z > 0$ in the axial plane. Since the coordinate system is based on fiducial points from the MRI image, by limiting our search to $z > 0$ we were able to exclude the vertices located on the nose, cheeks or lips of the head model. Next, we identified the 2,000 highest curvature vertices across the remaining mesh. This value considers the number of electrodes and characteristics of the EEG cap used in Sepulveda et al. (2016) experiment and may need to be changed to work in other systems (e.g., using more vertices to cover a higher number of electrodes). Due to the resolution of the mesh, there were groups of vertices with high curvature contained within the area corresponding to one single electrode. Therefore, from the group of 2,000 vertices selected above, we clustered the vertices whose distances from each other were within 1 cm (estimated diameter for the used electrode). Assuming that clusters containing the greatest number of vertices represent an electrode, we selected all the clusters that contained at least 10 vertices (**Figure 2B**). The centroid of each cluster was calculated to represent the position of the potential electrode (**Figure 2C**). A matrix containing the position of the potential electrodes was generated. Given that this step was not completely accurate (see section "Results"), a manual check of the potential electrodes were required. In most cases, an excess of points on the scalp was generated in the matrix; therefore, a manual removal of these extra points was performed by an experienced human analyzer on our team. Before moving onto the next step, a matrix of precisely 64 (unlabeled) electrodes was required. Please see the section "Localization" in the **Supplementary Methods** for more details on this stage. Custom MATLAB scripts were used for electrode positioning.

Electrode Labeling Using the Distance Profile Method

The next step was to correctly identify the labels of each of the 64 points that we located in the 3D head space. We hypothesized that each of the electrodes can be distinguished from one another based on their relative distances. For example, frontal electrodes like FPZ, FP1, or FP2 might have a greater number of electrodes far away from them than the number of electrodes close to them. In contrast, an electrode like CZ may have more electrodes closer to it than farther from it (**Figure 3**). This is mainly due to the general shape of the head and how the electrodes are arranged on the cap. For this reason, each electrode has a unique collection of Euclidean distances to all the other electrodes, otherwise referred to in this paper as their distance profile.

For each electrode, a distance profile was determined. To do this, we calculated the distances from an electrode to all the others, and we sorted these distances in a vector from the highest to the lowest (**Figure 3**). A crucial requirement for this step is having at least one template (i.e., a set of localized and labeled electrodes) with extracted reference distance profiles. Using this template, a Pearson correlation was calculated between the distance profiles of the unlabeled and template electrodes. The label of the template electrode was given to the unlabeled electrode with the highest correlated distance profile.

It should be noted that the distance profiles of electrodes located in symmetrical positions in the left and right hemispheres with respect to the central electrode axis (e.g., FP1 and FP2, C1 and C2, etc.,) might be identical. This created confounds for

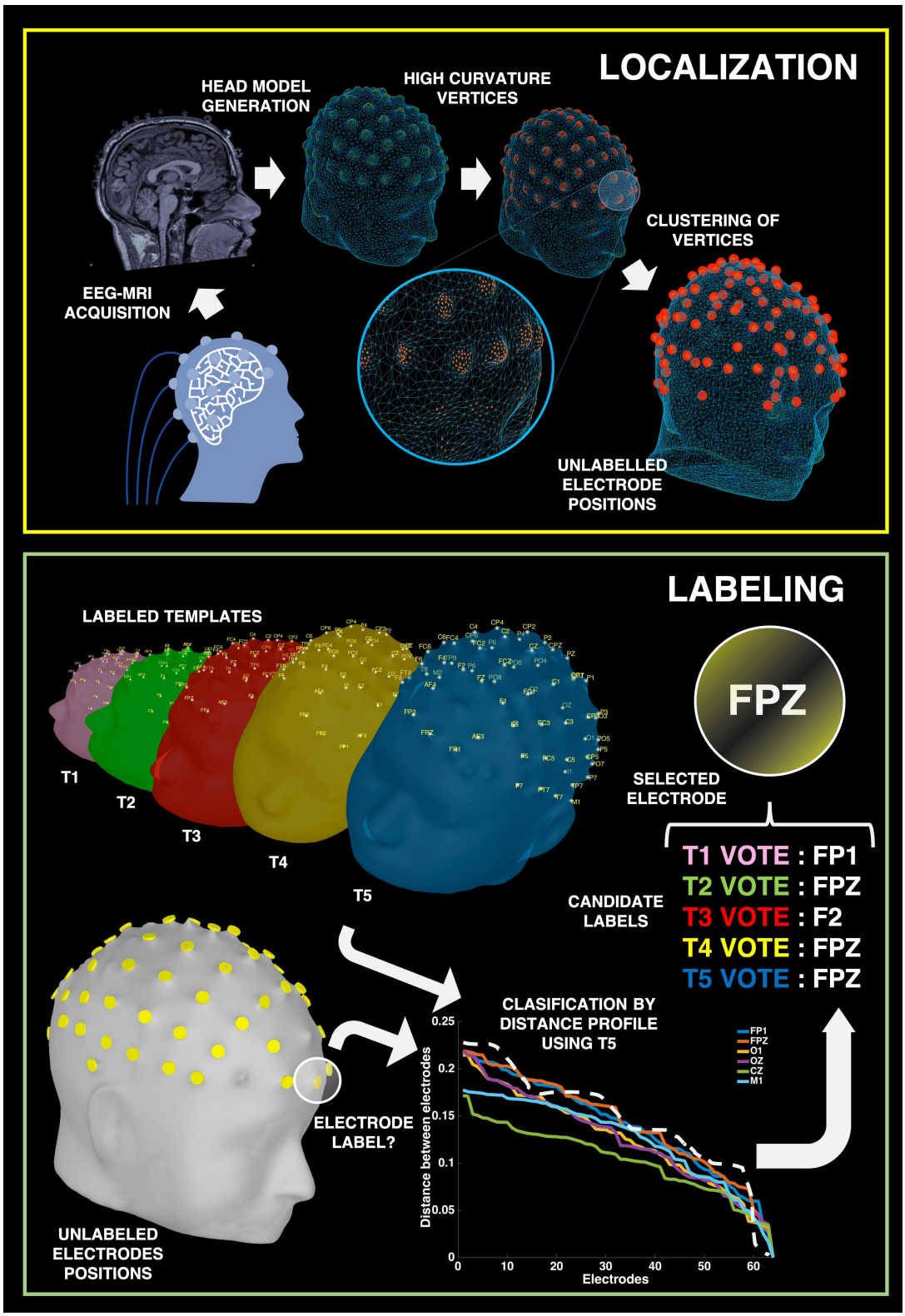

FIGURE 4 | Processing Pipeline. Summary of processing pipeline for electrode localizations and labeling. Top: During EEG-fMRI acquisition, we extrapolate the location of each electrode by looking for protrusions across the subject's scalp. Bottom: Through the use of labeled templates, we can classify the electrode by comparing the distance profiles for each unlabeled electrode (white dashed line) to the distance profiles of labeled electrodes of each template. The template analysis successfully votes to give the correct label of FPZ by 3 out of the 5 template votes.

accurate labeling. To avoid this problem, we picked the electrodes labeled as FPZ and OZ to define a central plane. All electrodes that were located in symmetrical positions were compared against this central plane. A list with the pair of electrodes that are located in symmetrical positions with respect to the central plane was defined to run this comparison (e.g., FP1–FP2, F1–F2, and C1–C2, etc.). Once the unlabeled electrodes were each assigned a label using distance profile comparison, we checked if the hemisphere (right or left) was correctly assigned. For example, an electrode labeled as C1 could be C1 or C2. Since both C1 and C2 electrodes are in symmetrical positions, they should ideally have identical distance profile. If we found that this electrode was actually to the left side of the central plane, we kept its label as C1; however, if we found that it was actually to the right side of the central plane, we labeled it C2, the other symmetrical label. If pairs of electrodes are given the same label, the relative position of the electrodes are compared to determine which ones are located at the right and left hemisphere. In cases when more than three unlabeled electrodes receive the same name, a label was not assigned.

In order to properly automate the process of labeling the electrodes, it is critical to use templates that are robust in defining the distance profiles for all the electrodes. However, given the wide variability between participants' head shape, the use of a unique template may be inappropriate to arrive at correct electrode labeling. In our method, we used multiple templates for the labeling of individual electrodes to account for this variability. To estimate the improvement that the inclusion of additional templates provides to the labeling performance, we tested using 1, 3, and 5 templates. When multiple templates were used, we implemented a voting system for the definition of the final electrode label: Every template "proposes" a label for the unlabeled electrode and the label with most votes is assigned (see **Figure 4**). If there is no majority in the voting, the label that comes first in the sequential order of electrodes is assigned (e.g., the sequence for a 64-electrode Neuroscan Quik-Cap is presented in **Supplementary Material**). If none of the templates was able to identify a label for the electrode, the electrode remains unlabeled. For more details about this stage, please check "Labeling" section in the **Supplementary Methods**. Custom MATLAB scripts were used for electrode labeling.

Detection Rate of Electrode Localization

To estimate the detection rate of our electrode localization method, we compared the results of our curvature positing algorithm with the true electrode positions. In our case, since we did not have access to digitizers or any other mechanism to extract the location of the electrodes, we determined the true position of electrodes by visual inspection of the locations in the MRI volume. In this way, points that did not correspond to electrodes [e.g., around eyes or ears, and electrooculogram (EOG) electrodes] were taken out. We used 26 structural T1W brain volumes for the purpose of testing the proposed method. We computed the detection rate of the method (i.e., true electrodes identified / 64) for each volume. A heat map was generated using EEGLAB, containing the information about the mean detection rate for the localization of electrodes across participants (Delorme and Makeig, 2004).

Accuracy Analysis of Electrode Labeling

In order to check the accuracy of the distance profile method, we compare the labels assigned to the 64 electrodes by the algorithm with the true labels. To assess the performance of the method, we determined the value for true positives (TP, electrodes correctly labeled), false positives (FP, electrodes mislabeled), and false negatives (FN, electrodes for which no label was assigned).

We used the same 26 sets of 64 electrodes again as either templates or unlabeled electrode sets in order to test the accuracy of the labeling step. To test the accuracy and robustness of the multiple template approach, we considered different combinations of each of the 26 sets to generate variations of template groups. In other words, we ran multiple simulations in which we defined one of the electrodes sets as unlabeled, and picked 1, 3, or 5 of the remaining sets as templates. The vote system described above was used in each of the simulations for 3 and 5 templates. In the 5-template approach, due to the high number of possible combinations we selected only a subset to test (i.e., 30% of the total number of combinations was randomly selected). We calculated the TP, FP, and FN for every electrode set that was labeled using 1, 3, or 5 templates.

RESULTS

Detection Rate of Electrode Localization Method

From the structural MRI volume, we extracted the positioning of electrodes using curvature information from the vertices in the head model mesh. The centroid of the clusters of high curvature vertices were used to obtain the location of potential electrodes. Overall, the analysis of 26 different head models showed that our method was able to detect 93.99% of the electrodes [standard deviation (SD) = 0.0882] (**Figure 5**). From further inspection, we observed that the frontal and central electrodes were accurately identified by the algorithm (electrode detection over 90%). However, the localization of some occipital (e.g., OZ, I1, and I2) and lateral electrodes (e.g., T7 and T8) appeared to have a lower detection rate (electrode detection $<$80% accuracy).

On average, the algorithm identified 20.307 extra electrodes (SD = 3.8447), i.e., points indicated as electrode positions but without correspondence to real labeled electrodes. Considering that the caps had 64 labeled electrodes in total, this means the algorithm detects around 30% of excess points. This may be due to either artifacts in the MR-structural image, empty electrode holders in the EEG cap (dummy electrodes) or additional (e.g., REF, GND, and oculomotor electrodes). Importantly, the caps used in the experiment (Compumedics Quik-Cap) contained around 15 dummy or additional electrodes. Extra electrodes were removed manually to leave only 64 electrodes for the labeling step.

Accuracy Analysis of Electrode Labeling

After locating the electrodes in the 3D head space, the Distance Profile method was employed to assign the labels. We used various templates (1, 3, and 5) to compare the electrodes' distance

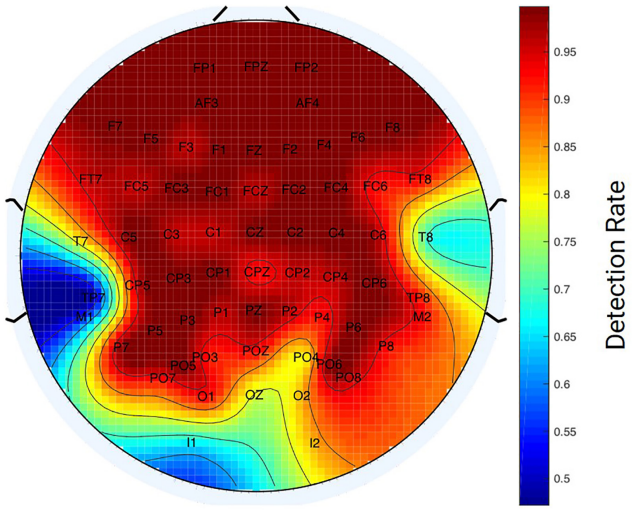

FIGURE 5 | Detection Rate of Electrode Localization Method. Heat map of the mean accuracy for the localization of electrodes across 26 structural MRI scans. Areas indicated in red reflect high detection rate, while areas in blue reflect low detection rate for identifying electrodes.

profiles, as a way of generating more accurate and robust labeling. In the cases of 3 and 5 templates, a voting system determined the label to be assigned to each electrode. Due to a problem in determining the middle plane in the cap (missed labeling of FPZ and OZ), we were unable to run the algorithm in 2.314% of all the simulated unlabeled-labeled combinations set for one template approach (15 pairs out of 650 possible pairs). These pairs were excluded and TP, FP, and FN were calculated for the remaining combinations in the cases for 1, 3, and 5 templates. From the results of our simulations, we obtained the mean value for TP, FP, and FN for each one of the 26 electrode sets available (**Figure 6** and **Table 1**).

The results in **Table 1** show that as the number of templates increases there is a corresponding increase in the number of true positive electrodes and decrease in FN. Adding more templates increases the accuracy of labeling by enabling the cross-checking of labels and filling in of missing labels. Another trend that must be noted is that the number of FP remains at a constant value of about 20% despite increasing the number of templates.

Additionally, we evaluated the accuracy of our distance profile algorithm by analyzing each electrode, pointing to identify the ones that are more difficult to label through this method. We generated spatial maps to display the accuracy of the method using 1, 3, and 5 templates (**Figure 7**). In this case, it appears that occipital electrodes are labeled with higher accuracy (>80% accuracy) while some fronto-lateral electrodes present more difficulties for identification (e.g., FP1 labeling accuracy <50%).

DISCUSSION

Localization and labeling of EEG electrodes are critical for the analysis of EEG data, especially for source reconstruction. Functional imaging in clinical applications (e.g., epileptic foci detection), neurofeedback and brain-computer interfaces (BCI) can greatly benefit from an accurate representation of the spatial location of the electrodes. Many methods have been proposed so far (Steddin and Botzel, 1995; Yoo et al., 1997; Le et al., 1998; Russel et al., 2005; Koessler et al., 2007; Péchaud et al., 2007; Marino et al., 2016; Butler et al., 2017; Clausner et al., 2017; Fleury et al., 2019; Homölle and Oostenveld, 2019; Taberna et al., 2019). However, most approaches require laborious manual intervention to prepare for the experiment or the use of special digitization devices.

The proposed approach enables the direct localization and labeling of EEG electrodes without the requirement of external devices (e.g., digitizers) in a context of simultaneous EEG-MRI experiments. Simultaneous EEG-fMRI experiments are already time-consuming and tedious for participants. The use of additional equipment (Steddin and Botzel, 1995; Brinkmann et al., 1998; Le et al., 1998; Lamm et al., 2001; Russel et al., 2005; Koessler et al., 2007; Clausner et al., 2017) and special protocols (Yoo et al., 1997; De Munck et al., 2011; Marino et al., 2016; Butler et al., 2017; Homölle and Oostenveld, 2019; Taberna et al., 2019) may increase setup time and cost, and cause fatigue and extra burden on the participants. Additionally, misplacement problems may arise between the electrode digitization (using external devices) outside the scanner and the later positioning of the participant inside the scanner. Also, our method does not rely on special MR acquisition sequences (Butler et al., 2017; Fleury et al., 2019), which may not be available in standard research or clinical setups. By using the spatial data provided from the individual MR structural volumes, it is possible to identify the electrodes on the head of a subject wearing a standard EEG cap. The MR structural volumes are required in any fMRI study for pre-processing. In this way, we were able to preserve the position in which the fMRI experiment was performed without incurring any extra time and cost than required for the standard fMRI procedure.

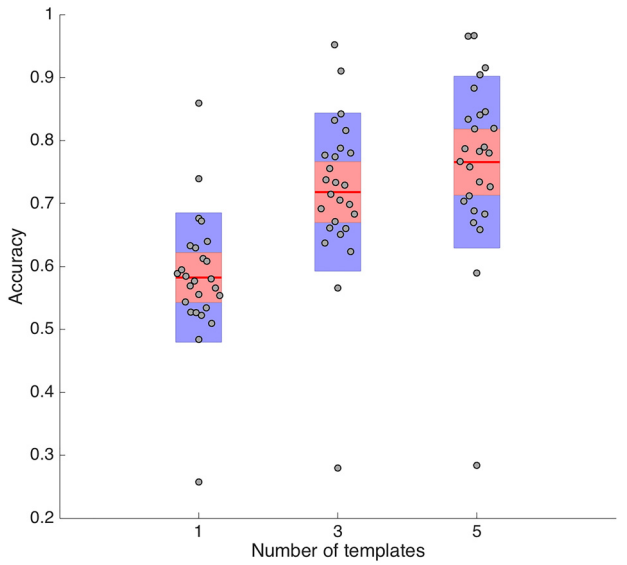

FIGURE 6 | Electrode Labeling Accuracy. Box plots of the TP values for the different number of template(s): one template (left), 3 templates (middle), and 5 templates (right). The red line represents the mean value. Dots correspond to the accuracy obtained for each electrode set (26 in total). As the number of templates increases the mean accuracy also increases.

TABLE 1 | Summary of accuracy analysis with the distance profile method.

Number of templates		True positives (%)	False positives (%)	False negatives (%)
1	Mean value	58.23	20.05	21.72
	Standard deviation	10.27	9.05	3.96
3	Mean value	71.79	20.81	7.40
	Standard deviation	12.56	11.60	2.70
5	Mean value	76.55	20.83	2.62
	Standard deviation	13.65	13.21	2.12

In the initial step of localization of the electrodes, we utilized the curvature data given by the head model to find the Cartesian coordinates of the electrodes. Protrusions with high curvature are formed in the surface of 3D reconstruction of structural scans, due to the volume of gel contained between the electrode and the scalp. Using this method over 90% of the electrodes were accurately localized in our simulations. Our results found that the occipital and temporal electrodes were more difficult to localize than electrodes in other regions. This outcome could be due to a decrease in the MR signal resulting from the gels in those electrodes. It should be noted that the structural MR volumes were acquired at the end of the experiment; thus, the subjects had been inside the scanner in a supine position for around 1 h. Since the EEG electrodes were prepared by gelling at the earliest time in the preparation for the experiment, it is possible that the gel would have dried considerably by the time of the MR acquisition. The regions with poorer localization are the ones in the posterior electrodes, which coincidentally are the electrodes over the which the participant's head rests during the experiment. One cause for this might be that these regions are drying faster because they may experience higher temperatures during the experiment. Another potential cause is that the gravitational force can displace the gel away from the scalp in these posterior electrodes when the subject is in the supine position. Additionally, hair presence may increase the space between the electrodes and the scalp, causing the gel to spread out from the electrode capsule. By detaching part of the volume off of the scalp surface, these complications decrease the signal observed in those particular electrodes. These changes in the electrode gel throughout the course of the scan can lead to variation in the localization across subjects. Such errors may lead to mislabeling problems, as a result of variability in the distance profiles of the electrodes. To overcome the above problems, we propose that the MR structural images are acquired at the beginning of the experiment when the gel is fresh and is contained in all electrodes to an equal extent.

During automated labeling, our method distinguishes each electrode based on its particular distance profile: The descending ordering of the distances between each electrode and the other 63 electrodes in the cap. Given that each electrode has a distinct location, the distance profile of each will be different from other electrodes in the same hemisphere to allow for proper labeling. To carry out the labeling, we used the distance profiles of previously labeled electrodes as templates for comparison. As observed above, the use of multiple templates results in higher accuracy of the labeling: From an average of 58% of electrodes correctly labeled for 1 template to a 76% for 5 templates. Through the use of multiple templates, many of the false negative electrodes were reduced. Interestingly, although the number of FN reduces with the use of multiple templates, the number of FP (i.e., electrodes that were mislabeled) did not reduce significantly. Since this number seems to be independent of the number of templates we are using, it may be related to a particular weakness of our distance profile comparison. A higher similarity of the distance profile in a particular subgroup of electrodes might make it difficult to distinguish electrode identity using correlations; thus, hindering successful classification. Therefore, the same label would be assigned indistinctly to different electrodes, generating mismatches. We think this is the case for the lateral frontal electrodes.

Despite the increase in the accuracy of labeling with templates, it is observed that lateral frontal electrodes are the most difficult to identify using this method. As mentioned above, similar distance profiles between the electrodes in this region may generate FP (e.g., FC1 has a very similar profile to C1, making them prone to labeling mismatch). Additionally, we think this problem may arise from the way our method deals with symmetry of electrode locations on left and right hemispheres (e.g., F1 and F2 electrodes). In our method, to identify electrodes that are located at symmetrical positions on the cap we define the midplane using frontal and occipital electrodes located in the center. In the case that two electrodes are assigned the same label we assumed that they may correspond to a symmetrical pair (e.g., two electrodes labeled as C1 when they actually should be C1 and C2). To distinguish them, we considered the location of each one of them relative to the midplane. However, if we have three electrodes assigned with the same label, we decided to keep them

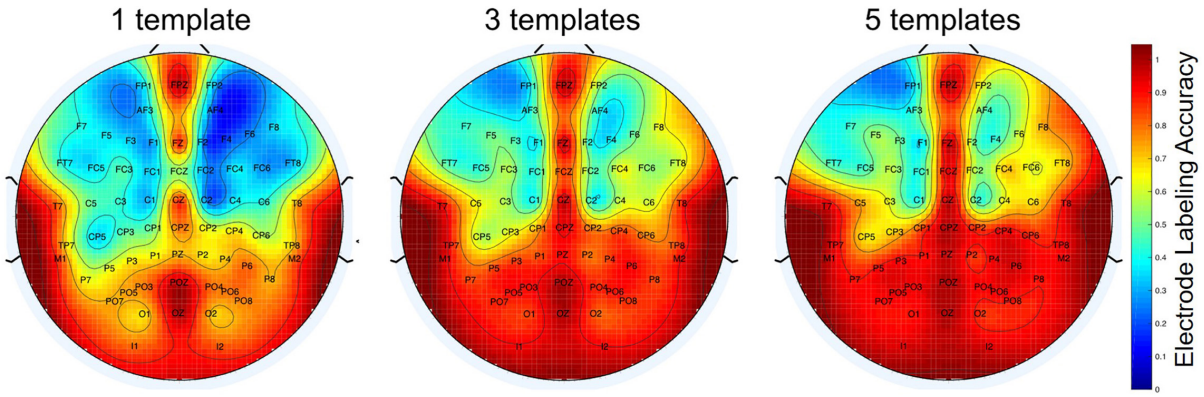

FIGURE 7 | Electrode Labeling. Heat maps of the mean value of TP in the labeling of individual electrodes using the distance profile algorithm with 1, 3, and 5 templates. Red corresponds to a high accuracy of labeling while blue corresponds to a low accuracy. There is a positive relationship between the number of templates to the accuracy of labeling.

unlabeled. The reason for this was to avoid having electrodes with the same name in the cap since it would cause confusion as to which of the three electrodes belong to the symmetrical pair. Therefore, it is possible that if the frontal electrodes have similar distance profiles, they might be given the same label (more than twice). This would cause those electrodes to remain unlabeled.

We can compare our values on detection rate and labeling accuracy to the most recent methods that use EEG-fMRI system-based approaches. When looking at Fleury et al. (2019) and Butler et al. (2017), who present an approach that does not require any additional devices, we see that they report a detection rate around 94%. Our detection rate is similar to their results. One disadvantage of their approach is that they did not contribute to solving the problem of labeling and relied on using De Munck's Pancake model (2011). For this reason, these papers did not present any values on localization accuracy; thus, we could not compare our results with those. We also compared our results with Marino et al. (2016) and De Munck et al. (2011), whose papers present a semi-automated method to solve the two-step problem. When comparing our results to De Munck et al. (2011), we saw that their approach had a manual selection process for localization of electrodes. This is decidedly a big limitation since it requires relatively more time and an experienced user to manually select each electrode. In our study, the localization step is automated, although in practical terms minor human intervention is required to correct detection errors. Marino et al. (2016) presents an automated approach that has a very good detection rate and labeling accuracy. While their approach had very few FN detected in the localization step (<0.5%), they also had FP detected (∼16% of 256 electrode set, which is even further reduced using additional filtering). Our false positive rate was higher than theirs (∼30% of 64 electrode set). However, please note that our false positive rate for detection does not take into account the fact that some of these FP are caused by DUMMY or REF electrodes (i.e., extra electrodes physically present in the cap). Their labeling step notably yielded no FP or FN. We found that our labeling accuracy was ∼77% when using 5 templates. While Marino et al. (2016) present a more accurate approach for solving this two-step problem, it is based on the use of high-density electrodes (HydroCel Geodesic Sensor Net, Electrical Geodesics) for proper localization and labeling, which is not a standard EEG system in EEG-fMRI studies.

The labeling accuracy of our method relies on the following assumptions: (1) head shapes and distance profiles are similar across the subject population and (2) the localization of the electrodes is performed using the standard 10–20 system. However, it is known that head morphology is variable across humans, e.g., relationship between head circumference and height (Bushby et al., 1992). Additionally, the use of the same EEG caps in heads of variable shapes unavoidably will lead to discrepancies in electrode positions. We must also consider that our method uses individual head models as templates, making the identification even more idiosyncratic. To ameliorate these variabilities, one might consider using average head models or probabilistic head models. Furthermore, the method might be improved by generating a more sophisticated voting system when multiple templates are used. Statistical measures such as t-maps can be used. Also, to avoid assigning the same label to different electrodes, it might be useful to utilize the information of nearby electrodes to help characterize an electrode's identity more precisely (e.g., include in the comparison of distance profiles not only the electrode to label but also neighboring electrodes).

In our method, the localization and labeling steps are designed as automated procedures. However, between localization and labeling user supervision is required to remove (or add) localized positions from the electrode matrix when more (or less) than 64 points are reported. As mentioned earlier, the identification of high curvature areas around the ears or additional electrodes (e.g., REF electrodes) are some of the reasons for these FP. In our experiments, empty electrode holders were located mostly in the occipital region to distribute head weight. The inclusion of these electrodes as part of the labeling step (e.g., as DUMMY or REF) may be a solution to reduce the human intervention required at this stage.

In conclusion, here we have presented a semi-automated and direct method for localizing and labeling electrodes on a standard EEG cap, from MR structural images, acquired during simultaneous fMRI-EEG experiments. We used elements required for standard EEG-fMRI studies (i.e., T1W structural scans and standard MRI-compatible EEG caps using conductive electrode gel), presenting a more economical approach to the two-step problem of labeling and localizing electrodes. The method exploits data that is already available (MR structural scans); thus, avoiding the extra time and cost that is otherwise involved in the use of external digitization devices and cumbersome manual processes or extra modifications to the standard EEG-fMRI procedure. Our future work will conduct comparisons of this method with other existing approaches.

DATA AVAILABILITY STATEMENT

The code used for the localization and labeling of electrodes is available in GitHub: https://github.com/pradysepulveda/EEG_Loc_Label_2020. Example electrodes sets are also available.

ETHICS STATEMENT

The experimental protocol was approved by the ethics committee of Pontificia Universidad Católica de Chile. Each participant signed a written informed consent during the study.

AUTHOR CONTRIBUTIONS

AB, PS, SR, and RS designed the study and methodology. PS acquired MRI scans of participants. PS and AB analyzed the data. AB, PS, SR, RT, TO, and RS worked on the discussion and wrote the manuscript. All authors contributed to the article and approved the submitted version.

FUNDING

This work was supported by Comisión Nacional de Investigación Científica y Tecnológica de Chile (Conicyt) through Fondo Nacional de Desarrollo Científico y Tecnológico, Fondecyt (project numbers 1171320 and 1171313), CONICYT-PIA Anillo ACT1416, ACT1414, ACT172121, and CONICYT PFCHA/DOCTORADO BECAS CHILE/2017 (72180193).

SUPPLEMENTARY MATERIAL

The Supplementary Material for this article can be found online at: https://www.frontiersin.org/articles/10.3389/fnins.2020.558981/full#supplementary-material

REFERENCES

Brinkmann, B. H., O'Brien, T. J., Dresner, M. A., Lagerlund, T. D., Sharbrough, F. W., and Robb, R. A. (1998). Scalp-recorded EEG localization in MRI volume data. *Brain Topogr. Summer* 10, 245–253. doi: 10.1023/a:1022266822252

Bushby, K., Cole, T., Matthews, J., and Goodship, J. (1992). Centiles for adult head circumference. *Arch. Dis. Childhood* 67, 1286–1287. doi: 10.1136/adc.67.10.1286

Butler, R., Gilbert, G., Descoteaux, M., Bernier, P. M., and Whittingstall, K. (2017). Application of polymer sensitive MRI sequence to localization of EEG electrodes. *J. Neurosci. Methods* 278, 36–45. doi: 10.1016/j.jneumeth.2016.12.013

Clausner, T., Dalal, S. S., and Crespo-García, M. (2017). Photogrammetry-based head digitization for rapid and accurate localization of EEG electrodes and MEG fiducial markers using a single digital SLR camera. *Front. Neurosci.* 11:264. doi: 10.3389/fnins.2017.00264

Dalal, S. S., Rampp, S., Willomitzer, F., and Ettl, S. (2014). Consequences of EEG electrode position error on ultimate beamformer source reconstruction performance. *Front. Neurosci.* 8:42. doi: 10.3389/fnins.2014.00042

Dale, A. M., Fischl, B., and Sereno, M. I. (1999). Cortical surface-based analysis. I. Segmentation and surface reconstruction. *Neuroimage* 9, 179–194. doi: 10.1006/nimg.1998.0395

De Ciantis, A., and Lemieux, L. (2013). Localisation of epileptic foci using novel imaging modalities. *Curr. Opin. Neurol.* 26, 368–373. doi: 10.1097/wco.0b013e328363372c

De Munck, J. C., Houdt, P. J., Verdaasdonk, R. M., and Ossenblok, P. P. W. (2011). A semi-automatic method to determine electrode positions and labels from gel artifacts in EEG/fMRI-studies. *NeuroImage* 59, 399–401.

De Munck, J. C., Vijn, P. C. M., and Spekreijse, H. (1991). A practical method for determining electrode positions on the head. *Electroencaphogr. Clin. Neurophysiol.* 78, 85–87. doi: 10.1016/0013-4694(91)90023-w

Delorme, A., and Makeig, S. (2004). EEGLAB: an open source toolbox for analysis of single-trial EEG dynamics including independent component analysis. *J. Neurosci. Methods* 134, 9–21. doi: 10.1016/j.jneumeth.2003.10.009

Fleury, M., Barillot, C., Mano, M., Bannier, E., and Maurel, P. (2019). Automated electrodes detection during simultaneous EEG/fMRI. *Front. ICT* 5:31. doi: 10.3389/fict.2018.00031

Gavaret, M., Badier, J. M., Marquis, P., Bartolomei, F., and Chauvel, P. (2004). Electrical source imaging in temporal lobe epilepsy. *Clin. Neurophysiol.* 21, 267–282.

Goebel, R., and Esposito, F. (2009). *The Added Value of EEG-fMRI in Imaging Neuroscience. EEG-fMRI*. Berlin: Springer, 97–112.

Hanslmayr, S., Volberg, G., Wimber, M., Raabe, M., Greenlee, M. W., and Bäuml, K. T. (2011). The relationship between brain oscillations and BOLD signal during memory formation: a combined EEG-fMRI study. *J. Neurosci.* 31, 15674–15680. doi: 10.1523/JNEUROSCI.3140-11.2011

Homölle, S., and Oostenveld, R. (2019). Using a structured-light 3D scanner to improve EEG source modeling with more accurate electrode positions. *J. Neurosci. Methods* 326, 108378. doi: 10.1016/j.jneumeth.2019.108378

Huster, R. J., Debener, S., Eichele, T., and Herrmann, C. S. (2012). Methods for simultaneous EEG-fMRI: an introductory review. *J. Neurosci.* 32, 6053–6060. doi: 10.1523/jneurosci.0447-12.2012

Koessler, L., Benhadid, A., Maillard, L., Vignal, J. P., Felblinger, J., Vespignani, H., et al. (2008). Automatic localization and labeling of EEG sensors (ALLES) in MRI volume. *NeuroImage* 41, 914–923. doi: 10.1016/j.neuroimage.2008.02.039

Koessler, L., Maillard, L., Benhadid, A., Vignal, J. P., Braun, M., and Vespignani, H. (2007). Spatial localization of EEG electrodes. *Clin. Neurophysiol.* 37, 97–102. doi: 10.1016/j.neucli.2007.03.002

Lamm, C., Windischberger, C., Leodolter, U., Moser, E., and Bauer, H. (2001). Co-registration of EEG and MRI data using matching of spline interpolated and MRI-segmented reconstructions of the scalp surface. *Brain Topogr. Winter* 14, 93–100. doi: 10.1023/a:1012988728672

Le, J., Lu, M., Pellouchoud, E., and Gevins, A. (1998). A rapid method for determining standard 10/10 electrode positions for high-resolution EEG studies. *Electroencephalogr. Clin. Neurophysiol.* 106, 554–558. doi: 10.1016/s0013-4694(98)00004-2

Lei, X., Wu, T., and Valdes-Sosa, P. A. (2015). Incorporating priors for EEG source imaging and connectivity analysis. *Front. Neurosci.* 9:284. doi: 10.3389/fnins.2015.00284

Marino, M., Liu, Q., Brem, S., Wenderoth, N., and Mantini, D. (2016). Automated detection and labeling of high-density EEG electrodes from structural MR images. *J. Neural Eng.* 13:056003. doi: 10.1088/1741-2560/13/5/056003

Michel, C. M., Murray, M. M., Lantz, G., Gonzalez, S., Spinelli, L., and Grave de Peralta, R. (2004). EEG source imaging. *Clin. Neurophysiol.* 115, 2195–2222.

Péchaud, M., Keriven, R., Papadopoulo, T., and Badier, J. M. (2007). "Automatic labeling of EEG electrodes using combinatorial optimization," in *Proceedings of the Annual International Conference of the IEEE Engineering in Medicine and Biology Society*, (Piscataway, NJ: IEEE Engineering in Medicine and Biology Society), 4398–4401.

Russel, G. S., Eriksen, K. J., Poolman, P., Luu, P., and Tucker, D. M. (2005). Geodesic photogrammetry for localizing sensor positions in dense-array EEG. *Clin. Neurophysiol.* 116, 1130–1140. doi: 10.1016/j.clinph.2004.12.022

Sepulveda, P., Sitaram, R., Rana, M., Montalba, C., Tejos, C., and Ruiz, S. (2016). How feedback, motor imagery, and reward influence brain self-regulation using real-time fMRI. *Hum. Brain Mapp.* 37, 3153–3171. doi: 10.1002/hbm.23228

Steddin, S., and Botzel, K. (1995). A new device for scalp electrode localization with unrestrained head. *J. Neurol.* 242:65.

Taberna, G. A., Marino, M., Ganzetti, M., and Mantini, D. (2019). Spatial localization of EEG electrodes using 3D scanning. *J. Neural Eng.* 16:026020. doi: 10.1088/1741-2552/aafdd1

Tadel, F., Baillet, S., Mosher, J. C., Pantazis, D., and Leahy, R. (2011). Brainstorm: a user-friendly application for MEG/EEG analysis. *Comput. Intellig. Neurosci.* 2011:879716.

Vulliemoz, S., Lemieux, L., Daunizeau, J., Michel, C. M., and Duncan, J. S. (2010). The combination of EEG Source Imaging and EEG-correlated functional MRI to map epileptic networks. *Epilepsia* 51, 491–505. doi: 10.1111/j.1528-1167.2009.02342.x

Yoo, S. S., Guttmann, C. R., Ives, J. R., Panych, L. P., Kikinis, R., Schomer, D. L., et al. (1997). 3D localization of surface 10-20 EEG electrodes on high resolution anatomical MR images Electroencephalogr. *Clin. Neurophysiol.* 102, 335–339. doi: 10.1016/s0013-4694(96)95088-9

Yuan, H., Liu, T., Szarkowski, R., Rios, C., Ashe, J., and He, B. (2010). Negative covariation between task-related responses in alpha/beta-band activity and BOLD in human sensorimotor cortex: an EEG and fMRI study of motor imagery and movements. *NeuroImage* 49, 2596–2606. doi: 10.1016/j.neuroimage.2009.10.028

Conflict of Interest: The authors declare that the research was conducted in the absence of any commercial or financial relationships that could be construed as a potential conflict of interest.

frontiers in Neuroscience

ORIGINAL RESEARCH
published: 04 March 2022
doi: 10.3389/fnins.2022.823701

Evaluation of the Glymphatic System With Diffusion Tensor Imaging-Along the Perivascular Space in Cancer Pain

*Aibo Wang[1,2,3,4], Lei Chen[2,3,4,5], Can Tian[6], Xiaoyu Yin[1,2,3,4], Xinyue Wang[7], Yize Zhao[7], Miao Zhang[7], Lili Yang[8] and Zhaoxiang Ye[1,2,3,4]**

[1] Department of Radiology, Tianjin Medical University Cancer Institute and Hospital, Tianjin, China, [2] National Clinical Research Center for Cancer, Tianjin, China, [3] Tianjin's Clinical Research Center for Cancer, Tianjin, China, [4] The Key Laboratory of Cancer Prevention and Therapy, Tianjin, China, [5] Department of Cancer Pain Management, Tianjin Medical University Cancer Institute and Hospital, Tianjin, China, [6] Department of Pathology, Tianjin Third Central Hospital, Tianjin, China, [7] College of Medical Imaging, Dalian Medical University, Dalian, China, [8] Zhejiang MedicalTech Therapeutics Company Co., Ltd., Wenzhou, China

OPEN ACCESS

Edited by:
Surjo R. Soekadar,
Charité Universitätsmedizin Berlin, Germany

Reviewed by:
Susana Vacas,
UCLA Health System, United States
Youngkyoo Jung,
University of California, Davis, United States

***Correspondence:**
Zhaoxiang Ye
yezhaoxiang@163.com

Specialty section:
This article was submitted to Brain Imaging Methods, a section of the journal Frontiers in Neuroscience

Received: 28 November 2021
Accepted: 27 January 2022
Published: 04 March 2022

Citation:
Wang A, Chen L, Tian C, Yin X, Wang X, Zhao Y, Zhang M, Yang L and Ye Z (2022) Evaluation of the Glymphatic System With Diffusion Tensor Imaging-Along the Perivascular Space in Cancer Pain. Front. Neurosci. 16:823701. doi: 10.3389/fnins.2022.823701

Cancer pain (CP) is one of the most common symptoms affecting life quality, and there is considerable variation in pain experience among patients with malignant tumors. Previously, it has been found that the fluid drainage function in the brain can be regulated by peripheral pain stimulation. However, the relationship between cancer pain and functional changes of the glymphatic system (an important pathway for fluid drainage in the brain) remains unclear. In this study, 97 participants were enrolled, which included 40 participants in the cancer pain (CP) group, 27 participants in the painless cancer (PLC) group and 30 participants in the control (NC) group. Differences in glymphatic system function among the three groups and between before and after pain pharmacological intervention were analyzed by measuring diffusivity and the index along the perivascular space (ALPS index) using diffusion tensor imaging. We found that diffusivity and the ALPS index were significantly lower in the CP group than in the PLC and NC group and increased following intervention with pain relief. Moreover, the ALPS index was negatively correlated with the degree of pain in the CP group. The present study verified that alterations in glymphatic function are closely related to cancer pain, and the quantification of functional changes reflects pain severity. Our findings support the use of neuroimaging biomarkers for cancer pain assessment and indicate that pain can be alleviated by regulating brain function status.

Keywords: cancer pain, glymphatic system, MRI, DTI, ALPS

INTRODUCTION

Cancer pain (CP) is a general term for pain caused by tissue and nerve invasion due to a primary tumor or metastasis as well as pain caused by tumor-related treatment and is one of the most common symptoms in cancer patients, and incidence of pain accounts for 40–70% of all cancer patients (Neufeld et al., 2017; Yang et al., 2021). CP not only causes significant physical and

psychological pain to patients, impacting quality of life, but also presents difficulties in cancer treatment (Ham et al., 2017). Thus, active and effective control of CP and improving life quality of cancer patients through the accurate assessment of the pain are considered important tasks during cancer treatment. The mechanism of CP is complex, and pain perception varies considerably among cancer patients (Loffler et al., 2018; Caraceni and Shkodra, 2019). Currently, clinical assessment of the degree of CP is primarily based on a patient's subjective pain score, dose of pain medication, and observation of status by physicians (Jeter et al., 2018; Caraceni and Shkodra, 2019). However, patients' subjective cognition and expression ability and doctors' subjective misjudgment may result in the pain assessment to deviate from actual pain status, which may lead to inaccurate drug dosages, delayed pain control (Neufeld et al., 2017; Sato et al., 2017), unsatisfactory pain relief, or even drug overuse during CP interventions (Preuss et al., 2021). Therefore, the objective quantification of CP will help in the formulation of effective pain intervention plans and adjustment of treatment plans based on corresponding changes in indicators caused by pain.

The glymphatic system is a recently discovered effective drainage and exchange pathway between the cerebrospinal fluid (CSF) in subarachnoid space and the interstitial fluid (ISF) in the brain parenchyma. It is composed of the perivascular space and the water channel aquaporin-4 (AQP4), localized on the endfeet of astrocytes (Iliff et al., 2012; Nycz and Mandera, 2021), and is active during deep sleep (Anzai and Minoshima, 2021). The glymphatic system, the extracellular space (ECS) in the deep brain, the subarachnoid space, the lymphatic vessels in the dural sinuses, and the ventricular system together constitute the intracerebral fluid circulation pathway (Louveau et al., 2015; Lei et al., 2017; Nycz and Mandera, 2021). Fluid drainage in the brain is crucial for maintaining the homeostasis of the brain microenvironment (Lei et al., 2017). Increasingly, studies have shown that impairment of the drainage and clearance function of the glymphatic system is closely related to several mental and neurodegenerative diseases, such as depression, Alzheimer's disease (AD), and Parkinson's disease (PD) (Lei et al., 2017; Rasmussen et al., 2018; Hablitz and Nedergaard, 2021; Yan et al., 2021). Furthermore, several studies have reported that peripheral pain stimulation induces spatial structural alterations and decreased drainage function of the ECS in the deep brain (Goldman et al., 2020; Li et al., 2020). More importantly, chronic pain is a vital risk factor for depression and cognitive impairment (Jenny Wei et al., 2021). Therefore, CP may also cause alterations in glymphatic system function. However, whether glymphatic system function is altered in patients with CP and whether pain and glymphatic system function are correlated remain unclear. This knowledge will help gain a deeper understanding of brain changes under CP and whether changes in brain functional parameters have potential value for the quantitative evaluation of CP.

Previous studies on the glymphatic system have been based primarily on the observation of tracer drainage, diffusion, and distribution following invasive tracer introduction (Lei et al., 2017; Benveniste et al., 2021). A non-invasive method to assess glymphatic system function will offer significant value in clinical settings. Diffusion tensor imaging (DTI)-along the perivascular space (DTI-ALPS) was proposed by Taoka et al. (2017) as a non-invasive measurement method, which is now widely used in studies on the glymphatic system of the human brain. This method assumes the following: in the white matter near the lateral ventricles, the medullary veins run in the right-left direction (x-axis), which is perpendicular to the lateral ventricular wall. In contrast, at this level, the projection fibers run predominantly in the head-foot direction (z-axis), mainly adjacent to the lateral ventricle, and the association fibers (the superior longitudinal fascicles) run in the anterior-posterior direction (y-axis), outside of the projection fibers (Taoka et al., 2017). Thus, the perivascular space is orthogonal to the major fibers at this level (Taoka et al., 2017). In our previous study, we found that myelinated fibers in the deep brain play a crucial role in regulating ISF drainage (Wang et al., 2019). The application of a high b-value (e.g., b = 1000 s/mm^2) to DTI suppresses the flowing venous blood, which allows independent analysis of the diffusivity along the x-direction in perivascular space (Taoka et al., 2017; **Figure 1**).

By DTI-ALPS, Taoka et al. (2017) found that the ALPS index was significantly negatively correlated with the Mini-Mental State Exam score in AD patients when b = 1000 s/mm^2, which indicated lower water diffusivity along the perivascular space in relation to AD severity. One study in 2020 on glymphatic system alterations in patients with type two diabetes showed that diffusivity in different fiber areas and the ALPS index were associated with the severity of diabetes; moreover, the ALPS index reflected the damage of the glymphatic system (Yang et al., 2020). Recently, McKnight et al. (2021) reported that the ALPS index in PD patients was significantly lower than that in patients with essential tremor, which may be related to changes in the transport environment in the glymphatic system due to abnormal protein aggregation in PD. Furthermore, they found correlations between the ALPS index and age and T2-weighted white matter hyperintensity (McKnight et al., 2021). Taken together these findings demonstrate that DTI-ALPS is feasible in detecting functional changes of the glymphatic system. In the present study, we applied DTI-ALPS to the analysis of ALPS index changes in participants experiencing CP and investigated the relationship between the ALPS index and CP to determine the potential value of the ALPS index as a biological indicator of CP conditions.

MATERIALS AND METHODS

Informed Consent, Participant Recruitment, and Criterion

The study was approved by the ethics committee of Tianjin Medical University Cancer Institute and Hospital, and all participants provided informed consent, adhering to the ethical standards stipulated by the Declaration of Helsinki and its amendments.

Ninety seven participants were enrolled, which included Forty participants in the CP group, Twenty seven participants in the PLC group and Thirty participants in the NC group (**Table 1**). All subjects were right-handed. After enrollment, we acquired brain magnetic resonance imaging (MRI) data, which included axial

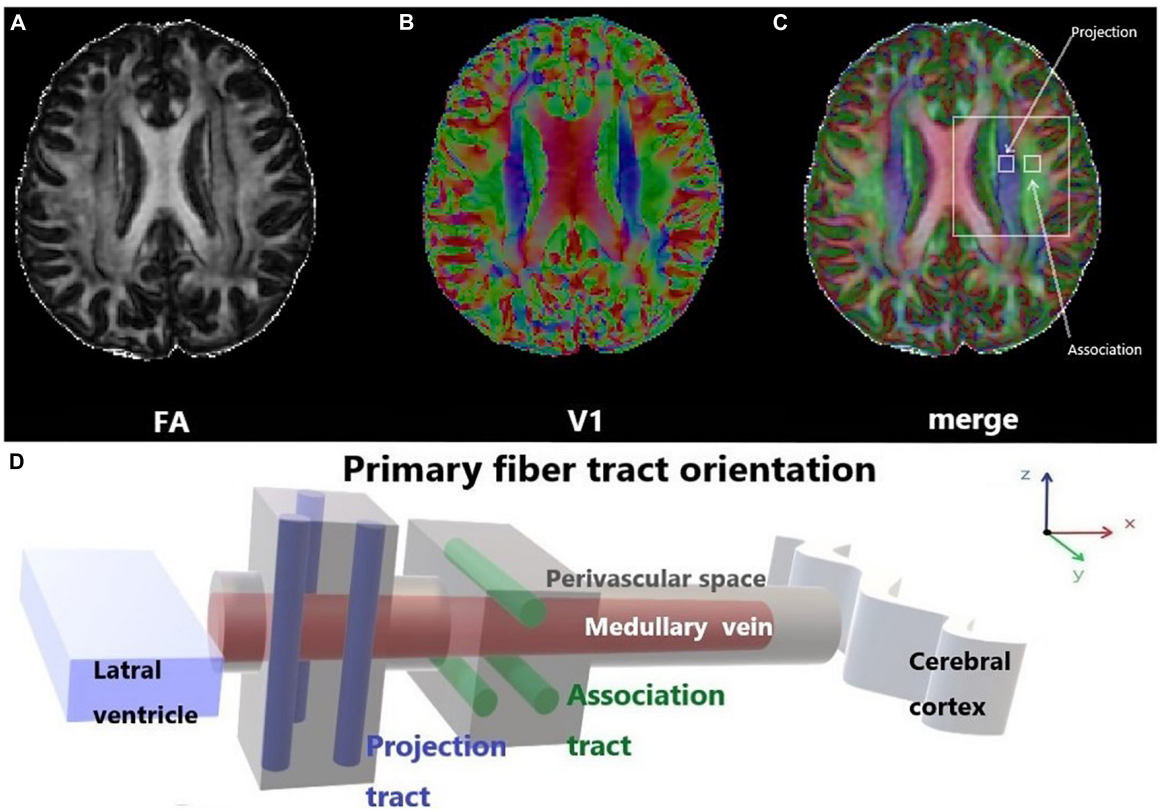

FIGURE 1 | Diffusion tensor imaging-along the perivascular space (DTI-ALPS). **(A)** The DTI fractional anisotraphy (FA) map shows the maximum level of the lateral ventricle for anatomical location. **(B)** The DTI V1 map shows the direction and distribution of the different types of fiber tracts: projection fibers (*z*-axis: blue), association fibers (*y*-axis: green), and subcortical fibers (*x*-axis: red). **(C)** The merged image of the FA and V1 maps and two regions of interest (ROIs) were set onto the projection and association fibers, and diffusivity within the ROIs in the three directions was measured. **(D)** Schematic of the positional relationship between the perivascular space of the medullary vein and adjacent fibers at the same level. The perivascular space of the medullary vein is parallel to the *x*-axis and orthogonal to the projection fibers in the *z*-axis and the association fibers in the *y*-axis.

T2-fluid attenuated inversion recovery (FLAIR) images and DTI on a 3.0-Tesla magnetic resonance scanner (Discovery MR750, General Electric, Milwaukee, WI, United States) to evaluate T2-weighted hyperintensities in the deep white matter (DWM) and obtain ALPS indices. The self-rating anxiety (SAS) and self-rating depression scales (SDS) were used to evaluate the emotional states of the two groups. The numeric rating (NRS) and visual analog scales (VAS) were used to evaluate the degree of pain in the CP group. The mini-mental state examination (MMSE) was used to evaluate the cognitive function. Sixteen participants in the CP group were included in the follow-up group, after CP pharmacological intervention, according to the 'three-stage' treatment plan and treatment for primary tumors for 1 month without other treatments, such as nerve block and physiotherapy. Patients' degree of pain, emotional state, and brain MRI were assessed using the same methods as those used at baseline. None of the 16 participants were on antidepressants or anti-anxiety drugs during the study period (**Figure 2**).

Cancer Pain Group

Forty participants were recruited into the CP group, which included 19 males (47.5%) and 21 females (53.5%), with an average age of 54.33 $\pm$ 7.28 years. All participants in the CP group had a confirmed history of spinal bone metastasis, and primary tumors included lung cancer (19 cases), breast cancer (14 cases), prostatic carcinoma (3 cases), renal carcinoma (2 cases), rectum carcinoma (1 case), and thyroid carcinoma (1 case). All participants in the CP group have no obvious pain feeling in any other parts of the body except for the confirmed back pain related to spinal bone metastasis diagnosed via various imaging examinations, which included patients who had not taken any pain treatment medicine (15 participants) as some of these participants were diagnosed with tumor for the first time and some of these participants were focusing on treatment of the primary tumor by systemic chemotherapy or targeted therapy and did not yet undergo intervention targeting the pain as well as those who did not respond well to pain medication before enrollment (25 participants). Some participants showed the symptoms related to primary tumor such as cough, blood in the sputum, chest tightness, malnutrition and enlarged axillary lymph nodes, those did not affect the nervous system directly. Pain duration of each participant was $\geq$ 1 month. The average pain duration time before hospitalization was 6.46 $\pm$ 4.50 months. All participants in the CP group have no acute symptoms and no invasive treatment in the last month.

TABLE 1 | Demographic and clinical information of each group.

	CP group (n = 40)	PLC group (n = 27)	NC group (n = 30)
Recruitment criteria	• confirmed pain related to spinal bone metastasis • pain duration ≥ 1 month • no obvious pain feeling in any other parts of the body • no acute symptoms of tumor in the last month • no invasive treatment in the last month • no cognitive impairment • no mental illness or serious consciousness disturbance • no drug abuse or alcohol addiction • no heart, liver or kidney failure • expected survival time > 2 months	• confirmed tumor history • no obvious pain feeling • no acute symptoms of tumor • no invasive treatment in the last month • no cognitive impairment • no mental illness or serious consciousness disturbance • no drug abuse or alcohol addiction • no heart, liver or kidney failure • expected survival time > 2 months	• healthy adult • no chronic pain • no chronic diseases • no invasive treatment in the last month • no anxiety or depression • no cognitive • impairment • no mental illness or serious consciousness disturbance • no drug abuse or alcohol addiction • no heart, liver or kidney failure • expected survival time > 2 months
Primary tumor	• lung cancer (19 cases) • breast cancer (14 cases) • prostatic carcinoma (3 cases) • renal carcinoma (2 cases) • rectum carcinoma (1 case) • thyroid carcinoma (1 case)	• lung cancer (19 cases) • breast cancer (8 cases)	
Primary tumor treatment	• systemic chemotherapy (15 participants) • targeted therapy (12 participants) • chemotherapy combined with targeted therapy (7 participants) • no treatment as first diagnosed (6 participants)	• systemic chemotherapy (10participants) • targeted therapy (6 participants) • chemotherapy combined with targeted therapy (8 participants) • no treatment as first diagnosed (3 participants)	
Pain intervention	• no pain treatment as first diagnosed (6 participants) • did not undergo pain intervention as focusing on primary tumor treatment (9 participants) • did not respond well to pain medication (25 participants)		
Age (years)	54.33 ± 7.28	56.30 ± 6.31	52.77 ± 10.34
Age composition			
≥ 65	4 (10%)	2 (8%)	6 (20%)
≥ 45, < 65	32 (80%)	23 (92%)	17 (56.67%)
≥ 30	4 (10%)	1 (4%)	7 (23.33%)
Sex			
Male	19 (47.5%)	12 (44.4%)	18 (60%)
Female	21 (53.5%)	15 (55.6%)	12 (40%)
SAS	58.98 ± 8.22	52.07 ± 4.66	44.80 ± 3.55
SDS	58.80 ± 7.79	56.77 ± 6.83	48.10 ± 2.66
MMSE	28.4 ± 1.21	29.4 ± 1.13	28.8 ± 1.17
Fazekas score			
0	14 (35%)	9 (33.3%)	9 (30%)
1	12 (30%)	9 (33.3%)	13 (43.3%)
2	12 (30%)	9 (33.3%)	7 (23.3%)
3	2 (5%)	0	1 (3.3%)

SAS, self-report anxiety scale; SDS, self-report depression scale; MMSE, mini mental state examination.

Painless Cancer Group

Twenty seven participants were recruited into the PLC group, which included 19 males (44.4%) and 21 females (55.6%), with an average age of 56.30 ± 6.31 years. All participants in the PLC group had a confirmed history of tumor including lung cancer (19 cases), breast cancer (8 cases). All participants in the PLC group have no obvious pain feeling in any parts of the body except for the symptoms related to primary tumor such as cough, blood in the sputum, chest tightness, malnutrition and enlarged axillary lymph nodes, those did not affect the nervous system directly. Except for three participants whose tumors were first diagnosed, the rest of the participants in the PLC were receiving systematic chemotherapy or targeted therapy for tumors. All participants in the PLC group have no acute symptoms and no invasive treatment in the last month.

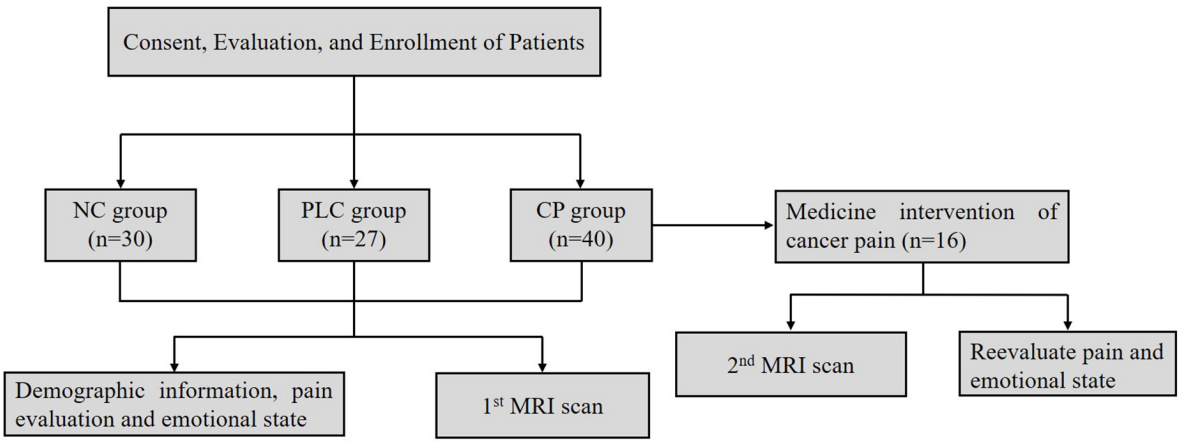

FIGURE 2 | Procedures and data used for the study.

Normal Control Group

Thirty participants were recruited into the control (NC) group, which included 18 males (60%) and 12 females (40%), with an average age of 52.78 ± 10.34 years. All participants in the NC group were healthy people without chronic pain or chronic diseases or anxiety or depression in the past and have no acute symptoms and no invasive treatment in the last month.

Assessment of Pain Level

The NRS and VAS were used to quantify the degree of pain in the CP group. The NRS is an 11-point scale from 0 to 10. A higher number indicates greater pain: 0 indicates "no pain," and 10 indicates the "worst imaginable pain." Participants selected a number that best represented their pain. The VAS is a reliable, valid, responsive, and frequently used scale to measure pain outcomes. It consists of a bidirectional straight 10-cm line with two labels at each end of the line: "no pain" and "worst possible pain." Patients were instructed to draw a vertical mark on the line that indicated their pain level (Hjermstad et al., 2011).

Emotional State Evaluation

The SDS and SAS were used to evaluate the emotional states of the NC and CP groups. The SDS is a self-report instrument designed to detect symptoms related to depression and measure the severity of depression. The SAS is designed to detect symptoms related to anxiety. The two scales are similar in the items and specific methods in scale assessment. Both the SDS and SAS comprise 20 items, each of which is scored on a scale of 1–4, ranging from the absence of the symptom (score of 1) to maximal symptoms (score of 4), and a higher score indicates greater severity of depression or anxiety. Standard scores of 53 (equal to the original raw score of 41) for the SAS and 50 (equal to the original raw score of 40) for the SDS were used as the cut-off scores for Chinese clinical significance, where the higher the score, the more severe the depressive or anxious mood (Zhang et al., 2021).

Cognitive Evaluation

The MMSE is a screening instrument to acquire a global impression of cognitive function. It was administered as the first instrument in a comprehensive fitness-to-drive assessment in a clinical setting (see Piersma et al. (2016) for the full protocol). The sum score of the MMSE (range 0–30) was used.

Brain Magnetic Resonance Imaging

Image Acquisition

For the axial T2-FLAIR image, we used the following scanning protocols: repetition time [TR]/echo time [TE] = 8000/120 ms; inversion time [TI] = 2100 ms; flip angle = 90°; section thickness = 5 mm; field of view [FOV] = 26; number of excitations = 1. The scanning protocols for the DTI were: b = 0 and b = 1000 s/mm^2, echo-planer sequence, TR = 6600 ms, TE = 89 ms, motion probing gradient (MPG) = 60 directions, FOV = 230 mm, matrix = 94 × 94, slice thickness = 3 mm.

Image Analysis

White Matter Lesion Assessment

Brain axial T2-FLAIR images were assessed by two radiologists with more than 5 years of diagnostic experience. DWM T2-weighted hyperintensity was graded on a 0–3-point scale according to the Fazekas score standard: absence (score of 0); punctate lesions (score of 1); punctate lesions beginning to merge (score of 2); large lesion fusion (score of 3) (Morotti et al., 2020).

Diffusion Tensor Imaging Analysis and Along the Perivascular Space Calculation

The FMRIB Software Library (FSL) toolkit (version 6.0)[1] was used to process and reconstruct the DTI images. First, the BET toolkit (version 2.0) was used to extract the brain, and the fractional intensity threshold was set to 0.3. Images were then motion-corrected and eddy current-corrected using the eddy function in the FDT diffusion toolkit (version 2.0). The processed DTI images were used to fit the tensor using the FDT diffusion toolkit

[1]https://fsl.fmrib.ox.ac.uk/fsl/fslwiki/

(version 2.0), and the parameter images were generated to allow measurements of FA, tensor, diffusivity, and vector. The locations of projection and association fibers adjacent to the left lateral ventricular were confirmed by two radiologists with more than 5 years of diagnostic experience. Two 3 mm × 3 mm regions of interest (ROIs) were set in each of the two fibers in FSLeyes. Diffusivity of the three directions in the ROIs was measured and the mean ALPS index was calculated according to the following formula:

Along the perivascular space index = mean (Dxproj, Dxassoc)/mean (Dyproj, Dzassoc) (1),

where Dxproj and Dxassoc are the *x*-axis diffusivities in the area of the projection and association fibers, respectively, Dyproj is the *y*-axis diffusivity in the area of the projection fibers, and Dzassoc is the z-axis diffusivity in the area of the association fibers (**Figure 3**).

Statistical Analysis

The SPSS version 21.0 software (Inc., Chicago, IL, United States) was used for the statistical analysis. NRS, VAS, SAS, and SDS scores, diffusivity, and the ALPS index are expressed as means ± standard deviations. Bland-Altman plot analysis was used to analyze the consistency of results between NRS and VAS pain assessment methods. Kruskal-wallis analysis was used to test for differences in diffusivity, ALPS index, MMSE, SAS, and SDS scores among the three groups. Wilcoxon rank-sum analysis was used to test for differences in diffusivity, and ALPS index in participants in the CP group from before to after pain treatment. Changes in SAS and SDS scores in the CP group before and after pain treatment were compared using paired-samples t-test. Chi-square tests were used to analyze differences in sex ratio, age composition, and Fazekas score among the three groups. Pearson's correlation was used to analyze correlations between diffusivity and the ALPS index and age, Fazekas score, NRS score, VAS score, pain duration, SAS score, and SDS score. Statistical significance was set to $p < 0.05$.

RESULTS

Demographic and Clinical Features

Because glymphatic system function can be influenced by age, sex, white matter lesions, and emotional state (Nedergaard and Goldman, 2020; Gertje et al., 2021), we firstly compared the age and sex compositions and brain white matter T2-hyperintensity among the CP, PLC and NC group. After analysis, no significant differences were found among groups in age (54.33 ± 7.28 years vs. 56.30 ± 6.31 years vs. 52.77 ± 10.34 years, $p = 0.387$), age composition ($p = 0.069$), or sex composition ($p = 0.444$). The Fazekas scores of the three groups were as follows: CP group: score of 0, 14 (35%); score of 1, 12 (30%); score of 2, 12 (30%);

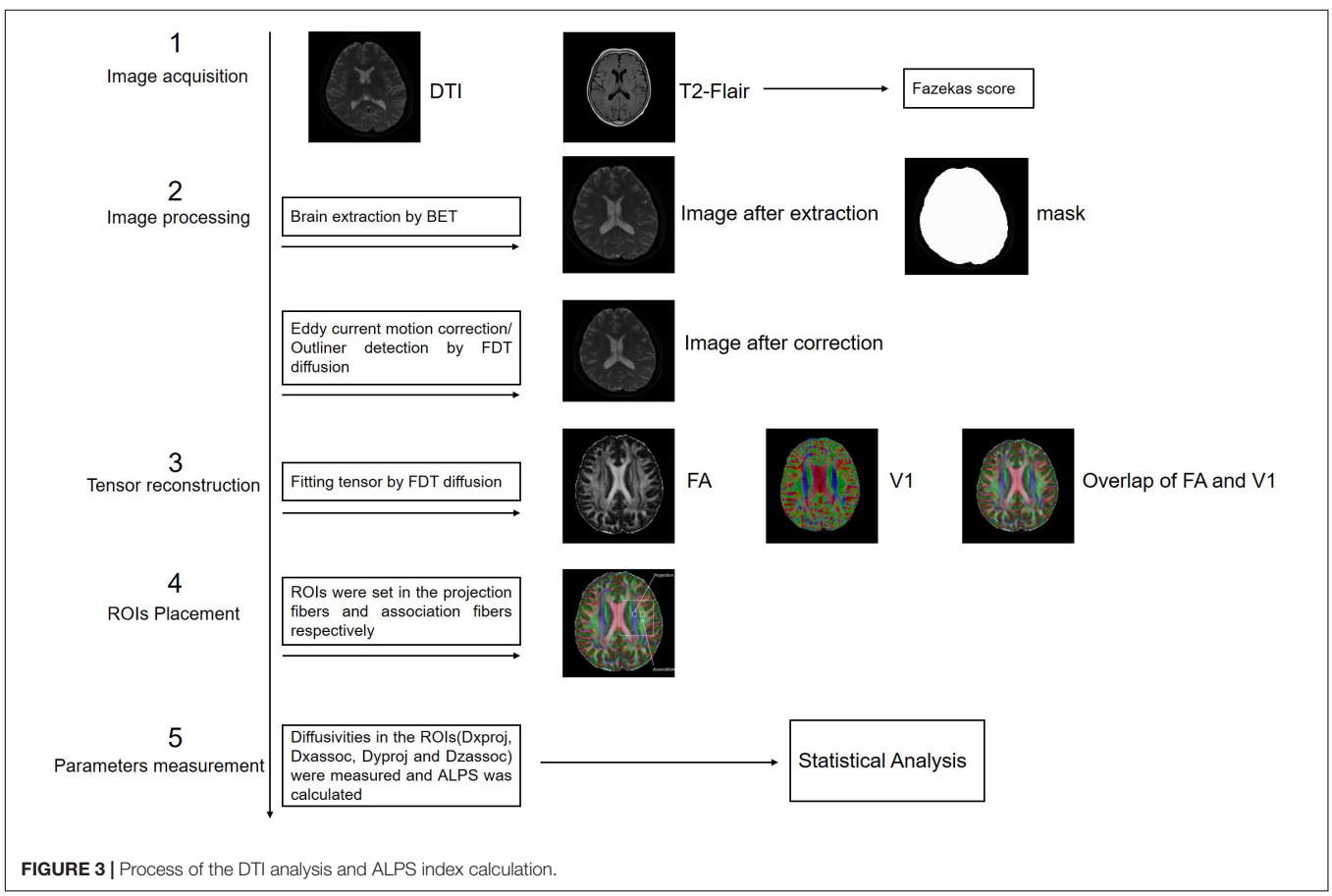

FIGURE 3 | Process of the DTI analysis and ALPS index calculation.

score of 3, 2 (5%). PLC group: score of 0, 9 (33.3%); score of 1, 9 (33.3%); score of 2, 9 (33.3%); score of 3, 0.NC group: score of 0, 9 (30%); score of 1, 13 (43.3%); score of 2, 7 (23.3%); score of 3, 1 (3.33%). No significant difference was found among groups for the Fazekas score ($p = 0.876$). SAS and SDS scores were both higher in the CP group than in the NC group (SAS: 58.98 ± 8.22 vs. 44.80 ± 3.55, $p < 0.001$; SDS: 58.80 ± 7.79 vs. 48.10 ± 2.66, $p < 0.001$). And no significant difference was found between CP group and PLC group for SAS and SDS scores, although CP group showed higher scores ($p = 0.134$). No significant difference was found among groups for MMSE score ($p = 0.249$).

The Consistency of the Numeric Rating and Visual Analog Scales Scores

Results of Bland-Altman plot analysis showed that the two methods had high consistency in evaluating the degree of CP. The deviation value of the two methods was −0.175, the standard deviation was 0.873, the limits of agreement = −1.888, 1.5376, and the 95% bias confidence interval (CI) = −0.454, 0.104. The lower limit of agreement 95% CI = −2.371, −1.40, and the upper limit of agreement 95% CI = 1.054, 2.021 (**Figure 4**).

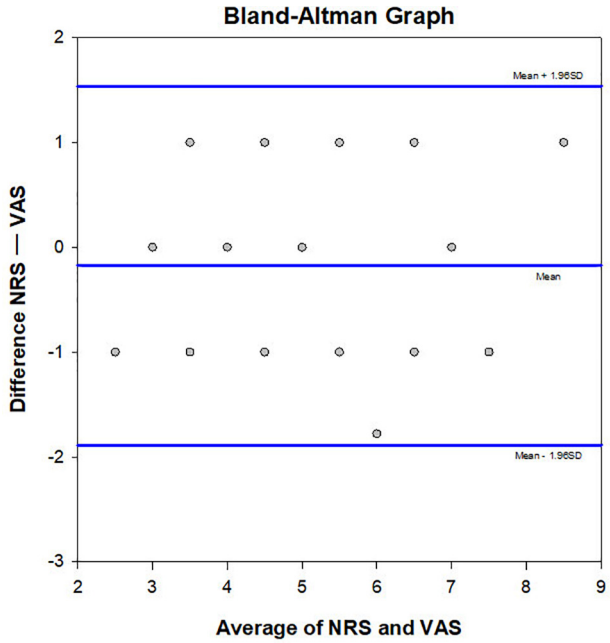

FIGURE 4 | Bland Altman plot. Consistency of the NRS and VAS methods was verified ($n = 40$). The averages of the two scores were compared and plotted. The central line represents the mean difference, and the upper and lower lines indicate the 95% limits of agreement.

Alterations in Diffusivity and Along the Perivascular Space Index in Cancer Pain

Compared with the NC group, Dxproj (0.541 ± 0.054 vs. 0.629 ± 0.083, $p < 0.001$), Dzproj (1.066 ± 0.150 vs. 1.238 ± 0.112, $p < 0.001$), Dxassoc (0.521 ± 0.051 vs. 0.793 ± 0.089, $p < 0.001$), Dyassoc (1.070 ± 0.124 vs. 1.249 ± 0.080, $p < 0.001$), and Dzassoc (0.239 ± 0.095 vs. 0.345 ± 0.103, $p < 0.001$) were significantly lower in the CP group. However, there was no difference in Dyproj between the NC and CP groups (0.543 ± 0.009 vs. 0.566 ± 0.009, $p = 0.355$). Compared with the PLC group, Dxassoc (0.521 ± 0.051 vs. 0.624 ± 0.067, $p < 0.001$) was significantly lower in the CP group ($p < 0.001$) (**Figures 5A,B**). No significant differences were found for Dxproj (0.541 ± 0.054 vs. 0.559 ± 0.095, $p = 0.453$), Dyproj (0.543 ± 0.009 vs. 0.558 ± 0.065, $p = 0.859$), Dzproj (1.066 ± 0.150 vs. 1.141 ± 0.063, $p = 0.488$), Dyassoc (1.070 ± 0.124 vs. 1.150 ± 0.102, $p = 0.070$), and Dzassoc (0.239 ± 0.095 vs. 0.222 ± 0.119, $p = 0.999$) between CP and PLC group. In the NC group, Dxproj ($r = -0.698$, $p < 0.001$) and Dzproj ($r = -0.661$, $p < 0.001$) were negatively correlated with the Fazekas score. In the CP group, Dxproj was negatively correlated with NRS and VAS scores ($r_{NRS} = -0.463$, $p_{NRS} = 0.003$, $r_{VAS} = -0.586$, $p_{VAS} < 0.001$) and Dzassoc was negatively correlated with pain duration ($r = -0.360$, $p = 0.023$) (**Table 2** and **Table 3**).

Results of the ALPS index analysis showed that the ALPS index in the CP group was significantly lower than that in the PLC and NC group (1.571 ± 0.153 vs. 1.526 ± 0.103 vs. 1.386 ± 0.207, $p = 0.0002$; **Figure 5C**). The ALPS index was negatively correlated with age and Fazekas score in the NC group ($r_{age} = -0.675$, $p_{age} = 0.000$; $r_{Fazekas} = -0.626$, $p_{Fazekas} = 0.012$), which is consistent with previous research (**Figures 5D,H**; McKnight et al., 2021). However, the ALPS index was not correlated with age or Fazekas score in the CP group ($r_{age} = -0.230$, $p_{age} = 0.056$; $r_{Fazekas} = -0.190$, $p_{Fazekas} = 0.242$; **Figure 5I**). The ALPS index in the CP group was negatively correlated with NRS and VAS scores ($r_{NRS} = -0.716$, $p_{NRS} = 0.013$; $r_{VAS} = -0.603$, $p_{VAS} = 0.027$; **Figures 5E,F,I**). In addition, we found that the ALPS index in the CP group was negatively correlated with pain duration ($r = -0.568$, $p = 0.043$; **Figures 5G,I**). Finally, we did not find any significant correlations between diffusivity in any x, y or z direction, ALPS index and emotional scores in either the CP or NC group ($p > 0.05$). Besides, no significant correlation was found in PLC group between diffusivity, ALPS index and other parameters ($p > 0.05$) (**Tables 2**, **3**).

Diffusivity and Along the Perivascular Space Index Changes in the Cancer Pain Group After Pain Intervention

In the CP group, there was no significant difference in diffusivity or ALPS index between participants who had been treated with drugs before recruitment and those who had not ($p > 0.05$). The 16 participants in the CP group who were enrolled in the follow-up group were treated with pain medication for 1 month. NRS, VAS, SAS, and SDS scores of these 16 participants decreased after the intervention (NRS: 4.50 ± 1.317 vs. 1.88 ± 0.619, $p < 0.001$; VAS: 4.38 ± 1.409 vs. 1.88 ± 0.696, $p = 0.000$; SDS: 59.64 ± 9.014 vs. 58.45 ± 7.258, $p = 0.001$; SAS: 59.73 ± 6.784 vs. 58.91 ± 7.409, $p = 0.001$). Dxproj (0.535 ± 0.057 vs. 0.586 ± 0.030, $p = 0.002$), Dxassoc (0.513 ± 0.044 vs. 0.584 ± 0.057, $p < 0.001$), Dzproj (1.070 ± 0.123 vs. 1.166 ± 0.045, $p = 0.018$), Dxassoc (0.513 ± 0.044 vs.

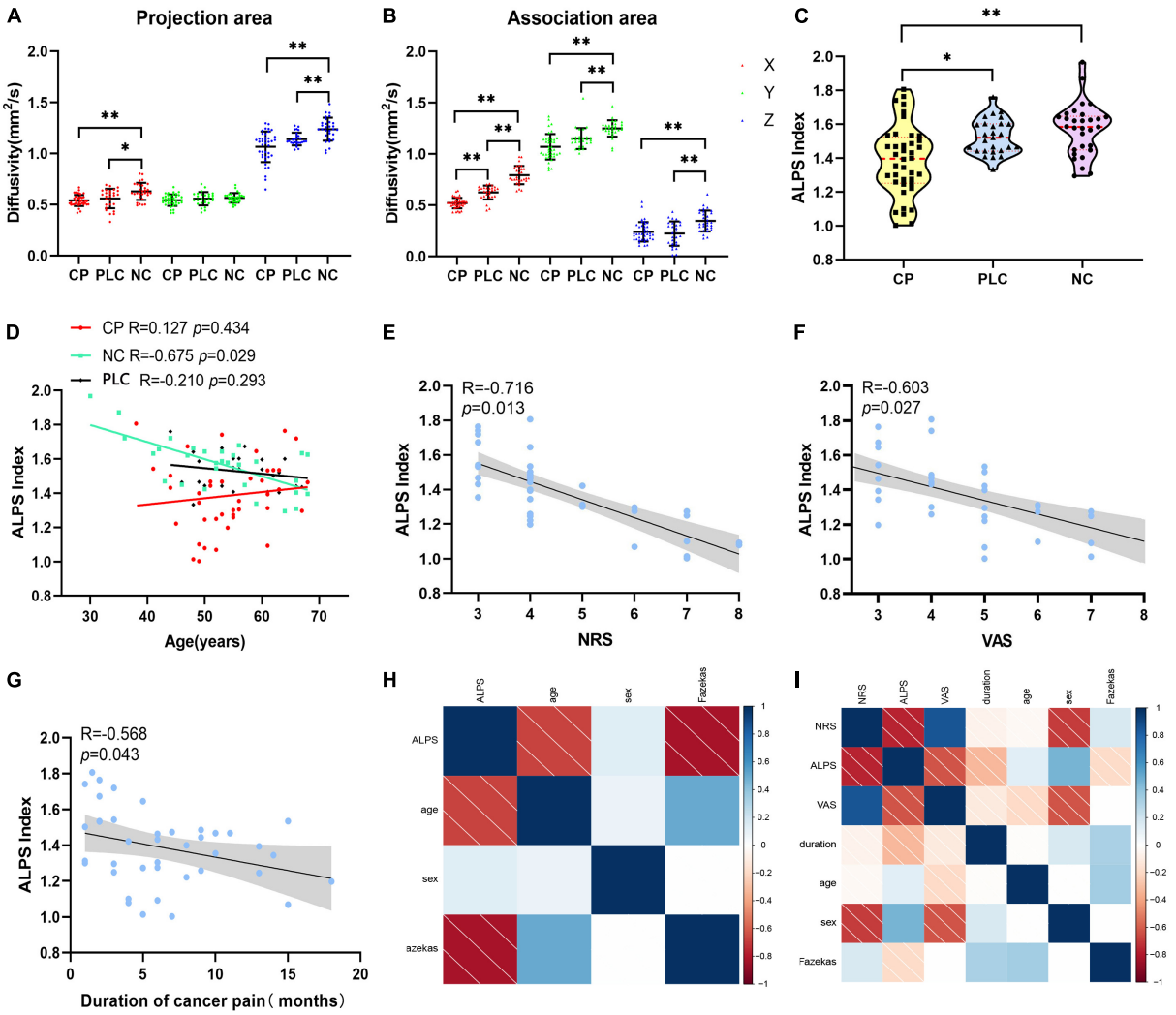

FIGURE 5 | Differences in diffusivity and ALPS index among the CP, PLC, and NC groups. **(A,B)** Comparisons of Dx, Dz, Dy of the projection and association fibers among the CP, PLC and NC groups. Diffusivity in the CP group was lower than that in the NC group, except for Dyproj. And Dxassoc in the CP group was lower than that in the PLC group. **(C)** Violin plot showing the comparison of the ALPS index among the NC, PLC and CP groups. The ALPS index of the CP group was significantly lower than that in the PLC and NC groups. **(D)** Correlation between ALPS index and age in the NC (green), PLC (black) and CP groups (red). In the NC group, the ALPS index was negatively correlated with age. However, in the CP and PLC groups, there were no correlations between the ALPS index and age. **(E,F)** The ALPS index was negatively correlated with NRS and VAS scores in the CP group. **(G)** Negative correlation between the ALPS index and pain duration. **(H,I)** The correlation factor matrices of the NC and CP groups; darker colors where the two factors converge indicate higher correlations. $^{*}p < 0.05$, $^{**}p < 0.01$.

0.584 ± 0.057, $p < 0.001$), Dyassoc (1.077 ± 0.143 vs. 1.156 ± 0.071, $p = 0.003$), and ALPS index (1.412 ± 0.193 vs. 1.528 ± 0.119, $p = 0.012$) were significantly higher after the intervention (**Figure 6**). No significant alterations were found for Dyproj (0.544 ± 0.053 vs. 0.565 ± 0.044, $p = 0.231$) and Dzassoc (0.232 ± 0.091 vs. 0.204 ± 0.065, $p = 0.489$) after intervention. Although diffusivity and the ALPS index showed an increasing trend with decreases in NRS and VAS scores after pain intervention, there was no correlation between these measures ($p > 0.05$). Moreover, there were no significant correlations among diffusivity, ALPS index, and emotional scores after treatment ($p > 0.05$) (**Table 4**).

DISCUSSION

In this study, DTI-ALPS was used as a non-invasive method to detect the alteration of glymphatic function in CP caused by bone metastasis, which is the most common forms of persistent and severe CP (Hong et al., 2020; Yoneda et al., 2021). We firstly found the alteration of glymphatic function under CP. Furthermore, the relationship between glymphatic function and CP was revealed. Our findings are helpful to further understand the functional characteristics of brain under cancer pain, and also has important hints for the evaluation of cancer pain through brain function detection.

TABLE 2 | Correlation analysis of CP group.

	NRS		VAS		Pain duration		Age		Fazekas score		SDS		SAS	
Dxproj	r = −0.463	$p = 0.003$	r = −0.586	$p < 0.001$	$r = 0.184$	$p = 0.255$	$r = 0.211$	$p = 0.192$	$r = -0.050$	$p = 0.761$	$r = 0.065$	$p = 0.692$	r = −0.138	$p = 0.396$
Dyproj	r = −0.099	$p = 0.542$	r = −0.263	$p = 0.101$	$r = 0.023$	$p = 0.886$	$r = -0.060$	$p = 0.713$	$r = 0.286$	$p = 0.073$	$r = 0.290$	$p = 0.069$	r = −0.006	$p = 0.971$
Dzproj	r = −0.081	$p = 0.617$	r = −0.111	$p = 0.494$	$r = -0.082$	$p = 0.616$	$r = -0.064$	$p = 0.696$	$r = -0.063$	$p = 0.701$	$r = 0.020$	$p = 0.902$	r = −0.080	$p = 0.623$
Dxassoc	r = −0.407	$p = 0.063$	r = −0.349	$p = 0.059$	$r = -0.360$	$p = 0.023$	$r = 0.201$	$p = 0.215$	$r = -0.052$	$p = 0.749$	$r = 0.090$	$p = 0.580$	r = −0.222	$p = 0.169$
Dyassoc	r = 0.267	$p = 0.096$	r = 0.203	$p = 0.210$	$r = -0.123$	$p = 0.449$	$r = -0.070$	$p = 0.666$	$r = -0.163$	$p = 0.314$	$r = 0.215$	$p = 0.182$	r = 0.009	$p = 0.956$
Dzassoc	r = 0.562	$p = 0.000$	r = 0.462	$p = 0.003$	$r = 0.242$	$p = 0.133$	$r = -0.197$	$p = 0.222$	$r = 0.040$	$p = 0.807$	$r = -0.020$	$p = 0.905$	r = 0.259	$p = 0.107$
ALPS index	r = −0.876	$p = 0.013$	r = −0.793	$p = 0.027$	$r = -0.322$	$p = 0.043$	$r = -0.230$	$p = 0.056$	$r = -0.190$	$p = 0.242$	$r = -0.036$	$p = 0.826$	r = −0.261	$p = 0.104$

To date, although there are various methods to treat CP, such as three-stage analgesics, nerve blocks, and Chinese acupuncture point stimulation, 50% of patients continue to experience CP. In addition, some patients experience side effects, such as increased drug tolerance or even addiction due to drug abuse during the treatment process; this is because the CP experience is subjective, with no objective indicator for CP evaluation in clinical pain management (Gallagher et al., 2017; Neufeld et al., 2017). Therefore, an objective biomarker that reflects the status of CP will help to accurately quantify CP in the clinic and will be highly valuable for the formulation of effective treatment plans for CP.

In chronic pain stimulation, numerous microstructural and functional changes occur in the brain, such as synaptic plasticity, blood perfusion, and connectivity properties of the functional and structural networks (Kuner and Flor, 2017; Iwabuchi et al., 2020; Barroso et al., 2021). These changes are closely related to the onset of pain, which may not only be adaptive changes in response to peripheral pain stimulation but also a key intermediate link to pain perception (Prinsloo et al., 2014). Han et al. found using tracer-based MRI that peripheral pain stimulation induces changes in ISF drainage and the spatial structure of ECS in the deep brain (Li et al., 2020). Excitation of neurons decreased the volume fraction (α) of the ECS in the deep brain and the clearance rate of ISF toward the superficial cortex (Li et al., 2020).

In our study, we found that diffusivity of the CP group decreased in the primary directions of the projection and association fibers and perivascular space was significantly lower than that in the NC group; moreover, the ALPS index in the CP group was also significantly lower than that in the PLC and NC group, which indicated that ISF drainage in both the brain parenchyma and perivascular space was impaired. We speculate that these drainage alterations were caused by the following mechanisms: (1) in our previous research, we found that myelinated fiber tracts regulated ISF drainage in the deep brain, and the ISF drained into the superficial cortex along the myelinated fiber tracts, which constitutes the upstream structure of the glymphatic system in the cortex (Wang et al., 2019). As previously reported by Han et al., peripheral pain stimulation leads to morphological changes of brain cells, which results in spatial structure changes of the ECS in the deep brain, obstructing ISF drainage into the cortex and affecting the function of the glymphatic system downstream. This results in a decrease in diffusivity, which reflects the drainage directions of the myelinated fiber tracts and perivascular space (Li et al., 2020). (2) The release of neurotransmitters, such as norepinephrine, increases under chronic pain stimulation, which may cause arteries in the brain to contract and decrease pulsation, affecting the function of the glymphatic system (Xie et al., 2013; IsHak et al., 2018; Goldman et al., 2020). Norepinephrine promotes the activation of microglia, which interact with other brain cells, such as neurons and astrocytes, via 'crosstalk,' causing changes in the activity and metabolism of cells, further affecting the function of the glymphatic system (Malcangio, 2019). (3) Because chronic pain is a risk factor for depression and neurodegenerative diseases, such as AD, pain stimulation may also affect brain waste clearance and the drainage function of perivascular spaces

TABLE 3 | Correlation analysis of PLC and NC groups.

	Age		Fazekas score		SDS		SAS	
PLC group								
Dxproj	r = −0.171	p = 0.394	r = 0.316	p = 0.109	r = 0.143	p = 0.814	r = 0.134	p = 0.444
Dyproj	r = 0.112	p = 0.577	r = 0.346	p = 0.587	r = 0.262	p = 0.612	r = 0.078	p = 0.873
Dzproj	r = 0.192	p = 0.336	r = 0.044	p = 0.827	r = 0.168	p = 0.604	r = −0.110	p = 0.661
Dxassoc	r = 0.461	p = 0.066	r = 0.063	p = 0.757	r = 0.304	p = 0.173	r = 0.236	p = 0.489
Dyassoc	r = 0.794	p = 0.207	r = 0.270	p = 0.173	r = 0.311	p = 0.114	r = 0.117	p = 0.542
Dzassoc	r = 0.095	p = 0.638	r = 0.437	p = 0.063	r = 0.226	p = 0.501	r = 0.007	p = 0.603
ALPS index	r = −0.210	p = 0.293	r = 0.447	p = 0.019	r = 0.141	p = 0.441	r = 0.163	p = 0.563
NC group								
Dxproj	r = −0.273	p = 0.144	r = −0.698	p < 0.001	r = 0.074	p = 0.697	r = −0.127	p = 0.503
Dyproj	r = −0.194	p = 0.304	r = −0.024	p = 0.900	r = −0.432	p = 0.064	r = −0.157	p = 0.407
Dzproj	r = −0.448	p = 0.060	r = −0.661	p < 0.001	r = −0.183	p = 0.332	r = −0.085	p = 0.654
Dxassoc	r = 0.693	p = 0.244	r = −0.366	p = 0.543	r = 0.042	p = 0.826	r = −0.143	p = 0.451
Dyassoc	r = 0.233	p = 0.216	r = −0.041	p = 0.829	r = 0.688	p = 0.248	r = 0.084	p = 0.661
Dzassoc	r = 0.627	p = 0.102	r = 0.304	p = 0.103	r = 0.253	p = 0.178	r = −0.044	p = 0.818
ALPS index	r = −0.675	p < 0.001	r = −0.826	p < 0.001	r = 0.045	p = 0.813	r = −0.319	p = 0.840

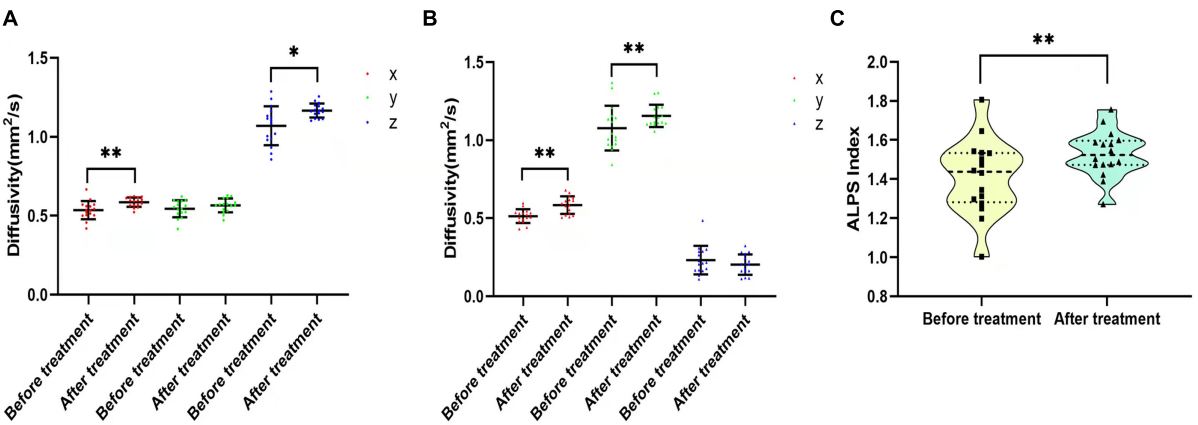

FIGURE 6 | Diffusivity and ALPS index changes before and after pain intervention. **(A,B)** Comparisons of Dx, Dy, and Dz in the projection and association fibers between before and after pain treatment. Diffusivity increased after treatment, except for Dyproj and Dzassoc. **(C)** Violin plot shows the comparison of the ALPS index between before and after pain treatment. The ALPS index increased significantly after pain treatment. *$p < 0.05$, **$p < 0.01$.

TABLE 4 | Correlation analysis of diffusivity and ALPS index after pain intervention.

	NRS		VAS		SDS		SAS	
Dxproj	r = −0.103	p = 0.705	r = −0.105	p = 0.388	r = 0.140	p = 0.682	r = −0.061	p = 0.859
Dyproj	r = −0.056,	p = 0.837	r = 0.202	p = 0.453	r = 0.497	p = 0.120	r = 0.157	p = 0.644
Dzproj	r = 0.041	p = 0.880	r = −0.091	p = 0.737	r = 0.348	p = 0.294	r = 0.406	p = 0.215
Dxassoc	r = −0.010	p = 0.969	r = −0.084	p = 0.756	r = 0.382	p = 0.246	r = −0.025	p = 0.942
Dyassoc	r = 0.293	p = 0.272	r = 0.325	p = 0.220	r = 0.182	p = 0.591	r = 0.174	p = 0.610
Dzassoc	r = −0.017	p = 0.951	r = 0.009	p = 0.975	r = −0.225	p = 0.505	r = −0.320	p = 0.338
ALPS index	r = −0.008	p = 0.978	r = −0.288	p = 0.279	r = 0.278	p = 0.408	r = 0.226	p = 0.504

(IsHak et al., 2018). All of these mechanisms can influence the overall ISF drainage in the brain.

Moreover, we found that the ALPS index was correlated with age and Fazekas score in the NC group, which is consistent with previous studies (McKnight et al., 2021). However, this was not observed in the CP group, which showed a negative correlation between the ALPS index and degree of pain, where the higher the level of pain, the lower the ALPS index. Following pain intervention, the ALPS index increased with pain relief, which suggested that the glymphatic system is mainly affected by pain stimulation under CP, and the ALPS index is a parameter that reflects the function of the glymphatic system and has a

certain indication function on CP. Additionally, the ALPS index in the CP group was negatively correlated with the duration of pain, which suggested that the longer the pain duration, the more serious the impairment to the glymphatic system. However, whether there is an interaction between the degree of pain and pain duration on drainage function remains to be elucidated in a larger sample. It is worth noting that there was no correlation between the ALPS index and degree of pain after pain intervention. We speculate that this is because the low degree of pain before the intervention in the participants who were enrolled in the follow-up, and their pain was effectively controlled after intervention, and the change in the ALPS index of them was not significant.

Our study has the following shortcomings. Firstly, the method we applied only describes ISF drainage in the paravalvular space at the level of the lateral ventricle via a mathematical formula; thus, it lacks intuition compared with that of the tracer-based method. Moreover, ISF drainage in the brain may be regionalized (Wang et al., 2019; Harrison et al., 2020), which means that the functions and spatial structures may be different among difference brain regions, and the measurement of drainage function for one region may not reflect the functional alteration of the whole brain. Secondly, a larger sample is needed to investigate influencing factors, such as analgetic dosage, of glymphatic system changes in patients with CP.

In conclusion, by applying DTI-ALPS, we found a correlation between glymphatic system function and CP and that the ALPS index may have potential value for evaluating CP. In the future, the ALPS index, combined with biological indicators, such as gene polymorphisms, may allow more objective and individualized CP assessments. Furthermore, the association between the glymphatic system and pain stimulation may help in the development of non-pharmaceutical interventions for pain, where pain may be alleviated via the regulation of glymphatic function (Goldman et al., 2020).

DATA AVAILABILITY STATEMENT

The original contributions presented in the study are included in the article/supplementary material, further inquiries can be directed to the corresponding author/s.

ETHICS STATEMENT

The studies involving human participants were reviewed and approved by Ethics Committee of Tianjin Medical University Cancer Institute and Hospital. The patients/participants provided their written informed consent to participate in this study. Written informed consent was obtained from the individual(s) for the publication of any potentially identifiable images or data included in this article.

AUTHOR CONTRIBUTIONS

AW and ZY designed the study. LC collected the patients. XY collected the images. AW and LY processed the date and images. CT, MZ, XW, and YZ analyzed date and contributed to the original draft. AW, CT, and ZY reviewed and edited the manuscript. All authors contributed to the article and approved to the submitted version.

REFERENCES

Anzai, Y., and Minoshima, S. (2021). Why We Need to Sleep: glymphatic Pathway and Neurodegenerative Disease. *Radiology* 300, 669–670.

Barroso, J., Wakaizumi, K., Reis, A. M., Baliki, M., Schnitzer, T. J., Galhardo, V., et al. (2021). Reorganization of functional brain network architecture in chronic osteoarthritis pain. *Hum. Brain Mapp.* 42, 1206–1222. doi: 10.1002/hbm.25287

Benveniste, H., Lee, H., Ozturk, B., Chen, X., Koundal, S., Vaska, P., et al. (2021). Glymphatic Cerebrospinal Fluid and Solute Transport Quantified by MRI and PET Imaging. *Neuroscience* 474, 63–79. doi: 10.1016/j.neuroscience.2020.11.014

Caraceni, A., and Shkodra, M. (2019). Cancer Pain Assessment and Classification. *Cancers* 11:510. doi: 10.3390/cancers11040510

Gallagher, E., Rogers, B. B., and Brant, J. M. (2017). Cancer-Related Pain Assessment: monitoring the Effectiveness of Interventions. *Clin. J. Oncol. Nurs.* 21, 8–12. doi: 10.1188/17.CJON.S3.8-12

Gertje, E. C., van Westen, D., Panizo, C., Mattsson-Carlgren, N., and Hansson, O. (2021). Association of Enlarged Perivascular Spaces and Measures of Small Vessel and Alzheimer Disease. *Neurology* 96, e193–e202. doi: 10.1212/WNL.0000000000011046

Goldman, N., Hablitz, L. M., Mori, Y., and Nedergaard, M. (2020). The Glymphatic System and Pain. *Med. Acupunct.* 32, 373–376. doi: 10.1089/acu.2020.1489

Hablitz, L. M., and Nedergaard, M. (2021). The Glymphatic System: a Novel Component of Fundamental Neurobiology. *J. Neurosci.* 41, 7698–7711. doi: 10.1523/JNEUROSCI.0619-21.2021

Ham, O. K., Chee, W., and Im, E. O. (2017). The Influence of Social Structure on Cancer Pain and Quality of Life. *West. J. Nurs. Res.* 39, 1547–1566. doi: 10.1177/0193945916672663

Harrison, I. F., Ismail, O., Machhada, A., Colgan, N., Ohene, Y., Nahavandi, P., et al. (2020). Impaired glymphatic function and clearance of tau in an Alzheimer's disease model. *Brain* 143, 2576–2593. doi: 10.1093/brain/awaa179

Hjermstad, M. J., Fayers, P. M., Haugen, D. F., Caraceni, A., Hanks, G. W., Loge, J. H., et al. (2011). "Studies comparing Numerical Rating Scales, Verbal Rating Scales, and Visual Analogue Scales for assessment of pain intensity in adults: a systematic literature review. *J. Pain Symptom Manage.* 41, 1073–1093. doi: 10.1016/j.jpainsymman.2010.08.016

Hong, S., Youk, T., Lee, S. J., Kim, K. M., and Vajdic, C. M. (2020). Bone metastasis and skeletal-related events in patients with solid cancer: a Korean nationwide health insurance database study. *PLoS One* 15:e0234927. doi: 10.1371/journal.pone.0234927

Iliff, J. J., Wang, M., Liao, Y., Plogg, B. A., Peng, W., Gundersen, G. A., et al. (2012). A paravascular pathway facilitates CSF flow through the brain parenchyma and the clearance of interstitial solutes, including amyloid beta. *Sci. Transl. Med.* 4:147ra111. doi: 10.1126/scitranslmed.3003748

IsHak, W. W., Wen, R. Y., Naghdechi, L., Vanle, B., Dang, J., Knosp, M., et al. (2018). Pain and Depression: a Systematic Review. *Harv. Rev. Psychiatry* 26, 352–363.

Iwabuchi, S. J., Xing, Y., Cottam, W. J., Drabek, M. M., Tadjibaev, A., Fernandes, G. S., et al. (2020). Brain perfusion patterns are altered in chronic knee pain: a spatial covariance analysis of arterial spin labelling MRI. *Pain* 161, 1255–1263. doi: 10.1097/j.pain.0000000000001829

Jenny Wei, Y. J., Chen, C., Fillingim, R. B., DeKosky, S. T., Schmidt, S., Pahor, M., et al. (2021). Uncontrolled Pain and Risk for Depression and Behavioral Symptoms in Residents With Dementia. *J. Am. Med. Dir. Assoc.* 22, 2079–2086.e5. doi: 10.1016/j.jamda.2021.05.010

Jeter, K., Blackwell, S., Burke, L., Joyce, D., Moran, C., Conway, E. V., et al. (2018). Cancer symptom scale preferences: does one size fit all? *BMJ Support. Palliat. Care* 8, 198–203. doi: 10.1136/bmjspcare-2015-001018

Kuner, R., and Flor, H. (2017). Structural plasticity and reorganisation in chronic pain. *Nat. Rev. Neurosci.* 18:113. doi: 10.1038/nrn.2017.5

Lei, Y., Han, H., Yuan, F., Javeed, A., and Zhao, Y. (2017). The brain interstitial system: anatomy, modeling, in vivo measurement, and applications. *Prog. Neurobiol.* 157, 230–246. doi: 10.1016/j.pneurobio.2015.12.007

Li, Y., Han, H., Shi, K., Cui, D., Yang, J. I, Alberts, L., et al. (2020). The Mechanism of Downregulated Interstitial Fluid Drainage Following Neuronal Excitation. *Aging Dis.* 11, 1407–1422. doi: 10.14336/AD.2020.0224

Loffler, M., Kamping, S., Brunner, M., Bustan, S., Kleinbohl, D., Anton, F., et al. (2018). Impact of controllability on pain and suffering. *Pain Rep.* 3:e694. doi: 10.1097/PR9.0000000000000694

Louveau, A., Smirnov, I., Keyes, T. J., Eccles, J. D., Rouhani, S. J., Peske, J. D., et al. (2015). Structural and functional features of central nervous system lymphatic vessels. *Nature* 523, 337–341. doi: 10.1038/nature14432

Malcangio, M. (2019). Role of the immune system in neuropathic pain. *Scand. J. Pain* 20, 33–37. doi: 10.1515/sjpain-2019-0138

McKnight, C. D., Trujillo, P., Lopez, A. M., Petersen, K., Considine, C., Lin, Y. C., et al. (2021). Diffusion along perivascular spaces reveals evidence supportive of glymphatic function impairment in Parkinson disease. *Parkinsonism Relat. Disord.* 89, 98–104. doi: 10.1016/j.parkreldis.2021.06.004

Morotti, A., Shoamanesh, A., Oliveira-Filho, J., Schlunk, F., Romero, J. M., Jessel, M., et al. (2020). White Matter Hyperintensities and Blood Pressure Lowering in Acute Intracerebral Hemorrhage: a Secondary Analysis of the ATACH-2 Trial. *Neurocrit. Care* 32, 180–186. doi: 10.1007/s12028-019-00761-0

Nedergaard, M., and Goldman, S. A. (2020). Glymphatic failure as a final common pathway to dementia. *Science* 370, 50–56. doi: 10.1126/science.abb8739

Neufeld, N. J., Elnahal, S. M., and Alvarez, R. H. (2017). Cancer pain: a review of epidemiology, clinical quality and value impact. *Future Oncol.* 13, 833–841. doi: 10.2217/fon-2016-0423

Nycz, B., and Mandera, M. (2021). The features of the glymphatic system. *Auton. Neurosci.* 232:102774. doi: 10.1016/j.autneu.2021.102774

Piersma, D., Fuermaier, A. B., de Waard, D., Davidse, R. J., de Groot, J., Doumen, M. J., et al. (2016). Prediction of Fitness to Drive in Patients with Alzheimer's Dementia. *PLoS One* 11:e0149566. doi: 10.1371/journal.pone.0149566

Preuss, C. V., Kalava, A., and King, K. C. (2021). *Prescription of Controlled Substances: benefits and Risks*. Treasure Island (FL): StatPearls.

Prinsloo, S., Gabel, S., Lyle, R., and Cohen, L. (2014). Neuromodulation of cancer pain. *Integr. Cancer Ther.* 13, 30–37. doi: 10.1177/1534735413477193

Rasmussen, M. K., Mestre, H., and Nedergaard, M. (2018). The glymphatic pathway in neurological disorders. *Lancet Neurol.* 17, 1016–1024. doi: 10.1016/S1474-4422(18)30318-1

Sato, J., Mori, M., Nihei, S., Takeuchi, S., Kashiwaba, M., and Kudo, K. (2017). Objective evaluation of chemotherapy-induced peripheral neuropathy using quantitative pain measurement system (Pain Vision((R))), a pilot study. *J. Pharm. Health Care Sci.* 3:21. doi: 10.1186/s40780-017-0089-4

Taoka, T., Masutani, Y., Kawai, H., Nakane, T., Matsuoka, K., Yasuno, F., et al. (2017). Evaluation of glymphatic system activity with the diffusion MR technique: diffusion tensor image analysis along the perivascular space (DTI-ALPS) in Alzheimer's disease cases. *Jpn. J. Radiol.* 35, 172–178. doi: 10.1007/s11604-017-0617-z

Wang, A., Wang, R., Cui, D., Huang, X., Yuan, L., Liu, H., et al. (2019). The Drainage of Interstitial Fluid in the Deep Brain is Controlled by the Integrity of Myelination. *Aging Dis.* 10, 937–948. doi: 10.14336/AD.2018.1206

Xie, L., Kang, H., Xu, Q., Chen, M. J., Liao, Y., Thiyagarajan, M., et al. (2013). Sleep drives metabolite clearance from the adult brain. *Science* 342, 373–377. doi: 10.1126/science.1241224

Yan, T., Qiu, Y., Yu, X., and Yang, L. (2021). Glymphatic Dysfunction: a Bridge Between Sleep Disturbance and Mood Disorders. *Front. Psychiatry* 12:658340. doi: 10.3389/fpsyt.2021.658340

Yang, G., Deng, N., Liu, Y., Gu, Y., and Yao, X. (2020). Evaluation of Glymphatic System Using Diffusion MR Technique in T2DM Cases. *Front. Hum. Neurosci.* 14:300. doi: 10.3389/fnhum.2020.00300

Yang, J., Wahner-Roedler, D. L., Zhou, X., Johnson, L. A., Do, A., Pachman, D. R., et al. (2021). Acupuncture for palliative cancer pain management: systematic review. *BMJ Support. Palliat. Care* 11, 264–270. doi: 10.1136/bmjspcare-2020-002638

Yoneda, T., Hiasa, M., Okui, T., and Hata, K. (2021). Sensory nerves: a driver of the vicious cycle in bone metastasis? *J. Bone Oncol.* 30:100387. doi: 10.1016/j.jbo.2021.100387

Zhang, Y., Wang, Z., Du, J., Liu, J., Xu, T., Wang, X., et al. (2021). Regulatory Effects of Acupuncture on Emotional Disorders in Patients With Menstrual Migraine Without Aura: a Resting-State fMRI Study. *Front. Neurosci.* 15:726505. doi: 10.3389/fnins.2021.726505

Conflict of Interest: LY was employed by Zhejiang MedicalTech Therapeutics Company Co., Ltd.

The remaining authors declare that the research was conducted in the absence of any commercial or financial relationships that could be construed as a potential conflict of interest.

Publisher's Note: All claims expressed in this article are solely those of the authors and do not necessarily represent those of their affiliated organizations, or those of the publisher, the editors and the reviewers. Any product that may be evaluated in this article, or claim that may be made by its manufacturer, is not guaranteed or endorsed by the publisher.

frontiers in Neuroscience

ORIGINAL RESEARCH
published: 10 March 2022
doi: 10.3389/fnins.2022.842420

EEG-fMRI: Ballistocardiogram Artifact Reduction by Surrogate Method for Improved Source Localization

Mateusz Rusiniak[1], Harald Bornfleth[1], Jae-Hyun Cho[1], Tomasz Wolak[2], Nicole Ille[1], Patrick Berg[1] and Michael Scherg[1]*

[1] Research Department, BESA GmbH, Gräfelfing, Germany, [2] Bioimaging Research Center, World Hearing Center of the Institute of Physiology and Pathology of Hearing, Warsaw, Poland

For the analysis of simultaneous EEG-fMRI recordings, it is vital to use effective artifact removal tools. This applies in particular to the ballistocardiogram (BCG) artifact which is difficult to remove without distorting signals of interest related to brain activity. Here, we documented the use of surrogate source models to separate the artifact-related signals from brain signals with minimal distortion of the brain activity of interest. The artifact topographies used for surrogate separation were created automatically using principal components analysis (PCA-S) or by manual selection of artifact components utilizing independent components analysis (ICA-S). Using real resting-state data from 55 subjects superimposed with simulated auditory evoked potentials (AEP), both approaches were compared with three established BCG artifact removal methods: Blind Source Separation (BSS), Optimal Basis Set (OBS), and a mixture of both (OBS-ICA). Each method was evaluated for its applicability for ERP and source analysis using the following criteria: the number of events surviving artifact threshold scans, signal-to-noise ratio (SNR), error of source localization, and signal variance explained by the dipolar model. Using these criteria, PCA-S and ICA-S fared best overall, with highly significant differences to the established methods, especially in source localization. The PCA-S approach was also applied to a single subject Berger experiment performed in the MRI scanner. Overall, the removal of BCG artifacts by the surrogate methods provides a substantial improvement for the analysis of simultaneous EEG-fMRI data compared to the established methods.

Keywords: simultaneous EEG and fMRI, artifact removal, optimal basis set (OBS), blind source separation (BSS), multimodal imaging, spatial filter (SF), independent component analysis (ICA), pulse artifact (PA)

OPEN ACCESS

Edited by:
Surjo R. Soekadar, Charité – Universitätsmedizin Berlin, Germany

Reviewed by:
Joao Miguel Castelhano, University of Coimbra, Portugal
Vlastimil Koudelka, National Institute of Mental Health, Czechia

****Correspondence:***
Mateusz Rusiniak
mateusz.rusiniak@besa.de

Specialty section:
This article was submitted to Brain Imaging Methods, a section of the journal Frontiers in Neuroscience

Received: *23 December 2021*
Accepted: *16 February 2022*
Published: *10 March 2022*

Citation:
Rusiniak M, Bornfleth H, Cho J-H, Wolak T, Ille N, Berg P and Scherg M (2022) EEG-fMRI: Ballistocardiogram Artifact Reduction by Surrogate Method for Improved Source Localization. Front. Neurosci. 16:842420. doi: 10.3389/fnins.2022.842420

INTRODUCTION

Interest in simultaneous electroencephalogram (EEG) and functional magnetic resonance imaging (fMRI) experiments has grown, ever since Logothetis et al. (2001) showed a clear relationship between EEG and the blood oxygenation level-dependent (BOLD) signal. Over the years, it has become clear that multimodal data acquisition, in particular EEG-fMRI, provides new insights into

neurocognitive functions (Laufs, 2012; Manganas and Bourbakis, 2017). Simultaneous EEG-fMRI recordings benefit from the advantages of both methods—delivering high spatial and temporal precision, and observation of electric and hemodynamic changes at the same time (Mulert and Lemieux, 2010; Rosenkranz and Lemieux, 2010).

The utility of simultaneous EEG-fMRI recordings is limited by three main interconnected factors: (1) the effectiveness of fMRI-related artifact reduction from EEG recording; (2) the usability of analytical tools; (3) the examination cost. Here, effective methods for artifact reduction are of highest importance and a prerequisite for generating useful results. Two types of artifacts are predominant in the EEG signal recorded during fMRI acquisition. The first type is an imaging artifact induced by the magnetic gradient coils (Allen et al., 2000). The second type, the so-called ballistocardiogram (BCG), is related to the heartbeat (Debener et al., 2008) or pulse artifact (Yan et al., 2010). While there is general agreement that the adaptive average subtraction method proposed by Allen et al. (2000) with further improvement from Moosmann et al. (2009) is a sufficient solution for imaging artifact removal, the BCG artifact is still not treated efficiently. The BCG artifact is a complex signal distortion that originates from multiple physical phenomena. As described by the Maxwell equations, the changing magnetic field induces a changing electric field. Therefore, even microscopic head movements in a strong magnetic field generate a strong electrical current. The heartbeat and related blood flow cause whole-body movements when a subject is in supine position (Niazy et al., 2005; Debener et al., 2008). In addition, when an electrode is located near a vein, the skin pulsation can generate another component of artifact (Bonmassar et al., 2002; Yan et al., 2010). Since blood is a conductive fluid, it can generate electrical potential changes over the scalp due to the Hall effect (Müri et al., 1998; Mullinger et al., 2013). Moreover, the BCG artifact can vary over the duration of a recording (Marino et al., 2018a) because of various factors (i.e., position change in MRI, blood pressure change, etc.).

Over the past few years, multiple data processing approaches have been proposed to reduce the BCG artifact (see for review: Grouiller et al., 2007; Vanderperren et al., 2010). Three main trends of BCG artifact reduction can be distinguished: (1) channel-wise subtraction of a BCG artifact template; (2) blind source separation (BSS) based on independent component analysis (ICA); (3) the combination of both methods. The first method evolved from the original work of Allen et al. (1998) and was significantly improved by Niazy et al. (2005). In this approach, the artifact template is created and then subtracted from the data using the optimal basis set (OBS)—the combination of the principal components obtained from the averaged artifact template and the template itself. Further improvements to the OBS were recently proposed by Oh et al. (2014) and Marino et al. (2018b). Most of the changes, however, focus on QRS complex detection and BCG template creation, where the correction procedure is based on artifact signal subtraction which can introduce distortion that mostly manifests itself in topography malformation (Ille et al., 2002). The second approach—Blind Source Separation (BSS)—is of a different nature (Jung et al., 2000). The signal is first decomposed to select artifact-related components. Then, the signal is projected back to the sensor space leaving out these components. The BSS approach usually makes use of ICA algorithms for decomposition as initially proposed by Bénar et al. (2003). Nowadays, there is a vast number of ICA algorithms and many different approaches for component selection (see Vanderperren et al., 2010), which were applied for BCG artifact reduction. Among others, the Infomax (Bell and Sejnowski, 1995; Lee et al., 1999) and the FastICA (Hyvarinen, 1999) have been shown to be successful in reducing the BCG artifact (Infomax: Bénar et al., 2003; Srivastava et al., 2005; Debener et al., 2007, FastICA: Mantini et al., 2007). Nonetheless, the BSS approach could be questioned due to the complex nature of the BCG artifact (Grouiller et al., 2007; Abreu et al., 2016). The independency criterion for ICA might not be fulfilled since the BCG artifact originates from multiple phenomena which result from the same physiological process. One attempt to overcome this limitation is to combine ICA with QRS detection of an EKG electrode either by performing ICA on the epoched data relative to R-peak (Debener et al., 2007) or by clustering approach (Wang et al., 2018). Yet still, the separation between the components of the artifact, as well as the separation of artifact and brain signals, might be insufficient. To address these problems of the mentioned methods, a third approach that is a combination of both methods (OBS-ICA or ICA-OBS) has been proposed (Debener et al., 2007; Abreu et al., 2016; Marino et al., 2018b). Despite the rationality of such an idea, one should consider that the pitfalls of both methods can also propagate to this approach, resulting in high signal distortion when not used carefully (Vanderperren et al., 2010).

To deal with the BCG artifact, there are also hardware-based solutions like reference layer (Chowdhury et al., 2014; Luo et al., 2014) or carbon wire loops (Masterton et al., 2007; Abbott et al., 2015; van der Meer et al., 2016). In those approaches, the BCG artifact is reduced by the subtraction of a referential signal obtained from additional layers/electrodes/loops which record the currents induced by the movement and not the brain activity. It was already shown that this approach can reduce the BCG artifact efficiently (Bullock et al., 2021), however it requires additional hardware and a setup procedure, and also cannot be applied to data already recorded.

In the present paper, we propose a semi-automated BCG artifact reduction method based on surrogate spatial filtering (Berg and Scherg, 1994a). The measured signal is a superposition of brain and artifact activities. In the surrogate method, it is assumed that the artifact signals and the signals originating from the brain can be separated if their spatial distributions over the scalp are known. The artifact topographies can be obtained either by principal component analysis (PCA) performed on an averaged artifact template (Ille et al., 2002) (similarly to the OBS method) or by ICA (like in the BSS method). The brain signals are estimated using a surrogate model consisting of a set of regional dipole sources distributed over the brain to describe most of the EEG signal. Therefore, the BCG reduction procedure should not introduce substantial distortions of the brain signals and separate out the artifact components sufficiently at the same time. In this study, the proposed approaches were compared

with the most commonly used OBS, BSS, and OBS-ICA methods described above.

MATERIALS AND METHODS

Subjects

EEG data were collected from 55 young male adults (mean age 27 years). One additional male subject (27 years) was recruited for the Berger experiment. This subject data was part of a previous study (Rusiniak et al., 2018).

All subjects had no history of neuropsychiatric disorders or head injury. Subjects provided written informed consent prior to participation. EEG data processing was performed using BESA Research software (version 7.1 March 2021, BESA GmbH, Gräfelfing, Germany) unless otherwise stated.

Data Acquisition

Data was collected using an MRI compatible 64-channel EEG system (SynAmps2, Neuroscan, Texas, United States). EEG recordings were performed in a 3 T MR scanner (Magnetom Trio, Siemens, Erlangen, Germany) simultaneously with an fMRI sequence (TR = 3 s, TE = 30 ms, 47 slices, slice thickness = 3 mm, no gap, pixel spacing = 2 × 2 mm). The EEG recording was sampled with 10 kHz frequency starting before the fMRI session and ending after finishing the image acquisition. The EEG sampling clock was synchronized with the MRI machine. Simultaneous EEG-fMRI sessions lasted 6 min (120 volumes). Subjects were asked to observe a black screen (resting-state paradigm) and remain calm. Each fMRI volume acquisition was marked by a trigger event in the EEG data.

A second experiment designed to evoke alpha rhythm in occipital cortex [Berger, 1929 experiment (1929)] was conducted using the same EEG and MRI setup. The subject was asked to open his eyes (when the beep sound was presented) or close them (when the screen was switched to black). Each block lasted for 30 s and the whole recording lasted 6 min.

Superimposition of Simulated Auditory Evoked Potentials Data

To analyze the efficiency of BCG artifact reduction, simulated auditory evoked potentials (AEP) were added to each resting-state EEG recording using BESA Simulator (version 1.4.0, BESA GmbH, Gräfelfing, Germany). 200 replications of the same simulated AEP signal were added to the original EEG to mimic an auditory EEG-fMRI experiment (inter-stimulus interval = 1.5 s with jitter = 0.2 s) prior to artifact correction or any other signal processing. Two dipoles, oriented perpendicular to the right and left Sylvian fissure, were used to generate the AEP. Source activities were simulated as near-to synchronous monophasic Cz-negative deflections (2 ms time lag, parameters detailed in **Table 1**) and some noise was added with a signal-to-noise ratio (SNR) of 6.

Figure 1 illustrates the locations, waveforms and topographies of the two-dipole AEP simulation (the plots were created using BESA Plot, Version 1.2.3, BESA GmbH, Gräfelfing, Germany).

TABLE 1 | Description of the dipolar model used for auditory ERP simulation.

Source	Location in Talairach coordinates			Orientation			N100 peak
	X	Y	Z	X	Y	Z	Latency
Left	−49	−18	12	−0.17	−0.25	−0.95	101 ms
Right	49	−15	13	0.15	−0.24	−0.96	103 ms

Using this model, the scalp AEP distribution was generated at the 64 recording electrodes and overlapped with the original EEG at the 200 predefined trigger times as specified above. This overlap of AEP and EEG served as the same, identical input for each pipeline of artifact correction to evaluate the differences between methods and to observe the specific distortions of the AEP introduced by each method.

The resulting signal $d_k(t)$ at electrode k can be described as the sum of the measured electrical potential $u_k(t)$ and simulated $AEP_k(t)$:

$$d_k(t) = u_k(t) + AEP_k(t). \quad (1)$$

Since the measured electrical potential $u_k(t)$ is a mixture of the brain signal $b_k(t)$, imaging artifact $IMG_k(t)$, BCG artifact $BCG_k(t)$, and noise $n_k(t)$, Eq. 1 can be formulated as follows:

$$d_k(t) = b_k(t) + IMG_k(t) + BCG_k(t) + n_k(t) + AEP_k(t). \quad (2)$$

Pipeline of Artifact Processing

The pipeline of removing artifacts and retrieving the superimposed, averaged AEP consisted of several steps. First, the imaging artifact $IMG_k(t)$ was estimated and removed from the data $d_k(t)$, as described in the fMRI artifact removal section. Second, different BCG artifact reduction approaches were applied to reduce $BCG_k(t)$. Third, bad trials were rejected, and the accepted N AEP trials were averaged as detailed below. The number of rejections depends on the noise level of the EEG, as described in the Evaluation metrics section. Finally, the averaging enhanced the time-locked AEP while minimizing $b_k(t)$ and $n_k(t)$. Leaving away the latter terms, this leads to the formula of the averaged AEP:

$$\overline{AEP}_k(t) = \sum_{n=1}^{N} AEP_{n,k}(t) \cong \sum_{n=1}^{N} (d_{n,k}(t) - IMG_{n,k}(t) - BCG_{n.k}(t)). \quad (3)$$

Thus, an optimal IMG and BCG artifact reduction should result in an averaged AEP similar to the simulated AEP.

Functional Magnetic Resonance Imaging Artifact Removal

The imaging artifact $IMG_k(t)$ was removed from $d_k(t)$ by applying the realignment parameter informed moving average

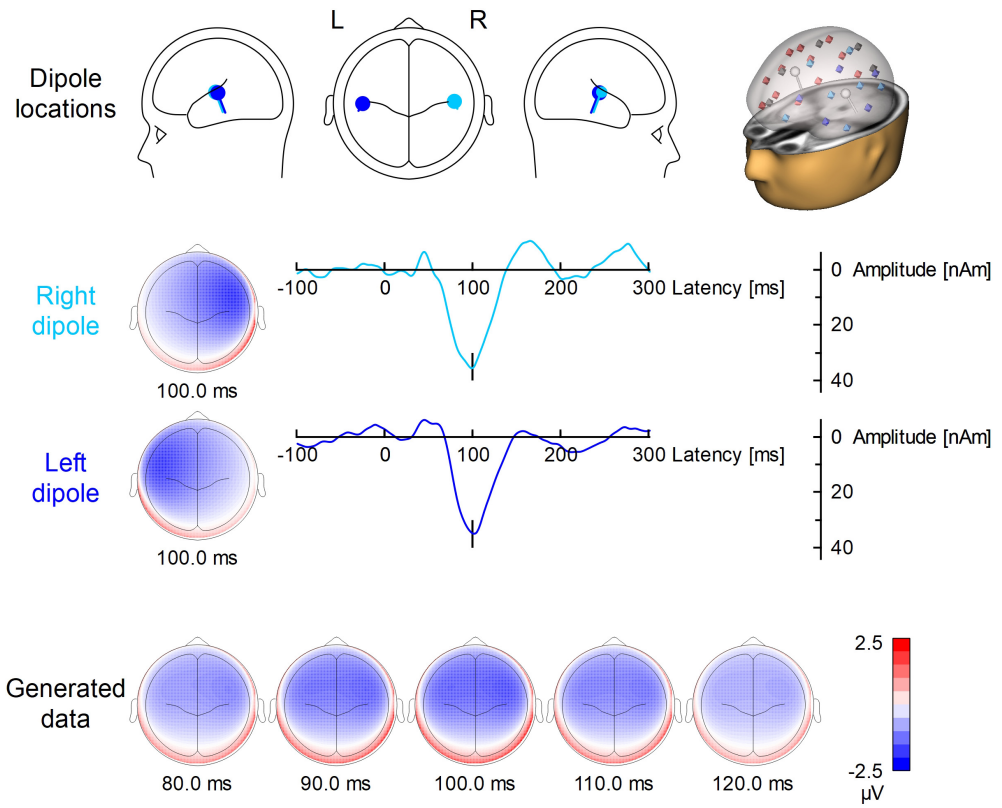

FIGURE 1 | Dipole model used for the simulation of auditory ERP. In the first row, the locations and orientations of the two dipoles are depicted in the head scheme. On the right, the modeled dipoles are shown in the presence of the surrogate model used for BCG artifact correction. The 29 regional sources for surrogate brain model are color-coded (red for right hemisphere, blue for left hemisphere, gray for midline). The modeled sources (which are not part of surrogate brain activity model) are shown in white. The second and third row show the left and right dipole source waveforms along with their topographies. Below, the evolution of the N100 topography from 80 to 120 ms is depicted.

artifact subtraction method as described by Moosmann et al. (2009). We used 16 averages as a parameter for moving template creation and a realignment threshold of 0.5 mm. The realignment information was obtained from fMRI preprocessing using Statistical Parametric Mapping software (version SPM12, the Wellcome Centre for Human Neuroimaging, London, United Kingdom) in MATLAB (version 2007, MathWorks, United States). After fMRI artifact removal, EEG data were down-sampled to 1 kHz.

Ballistocardiogram Artifact Removal

To reduce the BCG artifact, five different approaches were used independently as described below and illustrated in **Figure 2**.

Ballistocardiogram Artifact Removal by the PCA Surrogate Method

The PCA Surrogate method (PCA-S) consisted of the following steps: First, for the purpose of creating an averaged template of the artifact, EEG data were band-pass filtered in the frequency range of BCG (1–20 Hz) and re-referenced to the average reference. Then, one representative occurrence of the BCG artifact was manually selected from the EEG data based on visual inspection of all channel waveforms and used for automated pattern search (Scherg et al., 2002; Bast et al., 2004) to create an averaged template of the artifact. Each detected pattern that had a spatio-temporal correlation with the template higher than 60% was accepted. In the next step, a PCA was performed on the averaged template. All principal components accounting for more than 0.5% of the artifact template signal variance were used for spatial filtering. The number of components varied between 4 and 8 (mean 5.7). The accepted artifact-related principal components were combined with predefined regional sources (surrogate model) distributed evenly throughout the brain to calculate a spatial filter that separated the BCG artifact from brain activity as described by Berg and Scherg (1994a). We used a brain surrogate model that included 29 regional sources. A regional source in EEG consists of 3 dipoles at the same location with orthogonal orientations to describe the surrounding brain activity in any direction. Thus, the brain activity was approximated with high goodness-of-fit (>99%) by 87 dipoles (Beniczky et al., 2016). The surrogate model (together with simulated sources which are not part of it) are shown in the first row of **Figure 1**. By combining the artifact-related principal components and brain-related source components, the inverse spatial filter of PCA-S was created. When applying this linear filter to the original, unfiltered EEG signals, source waveforms

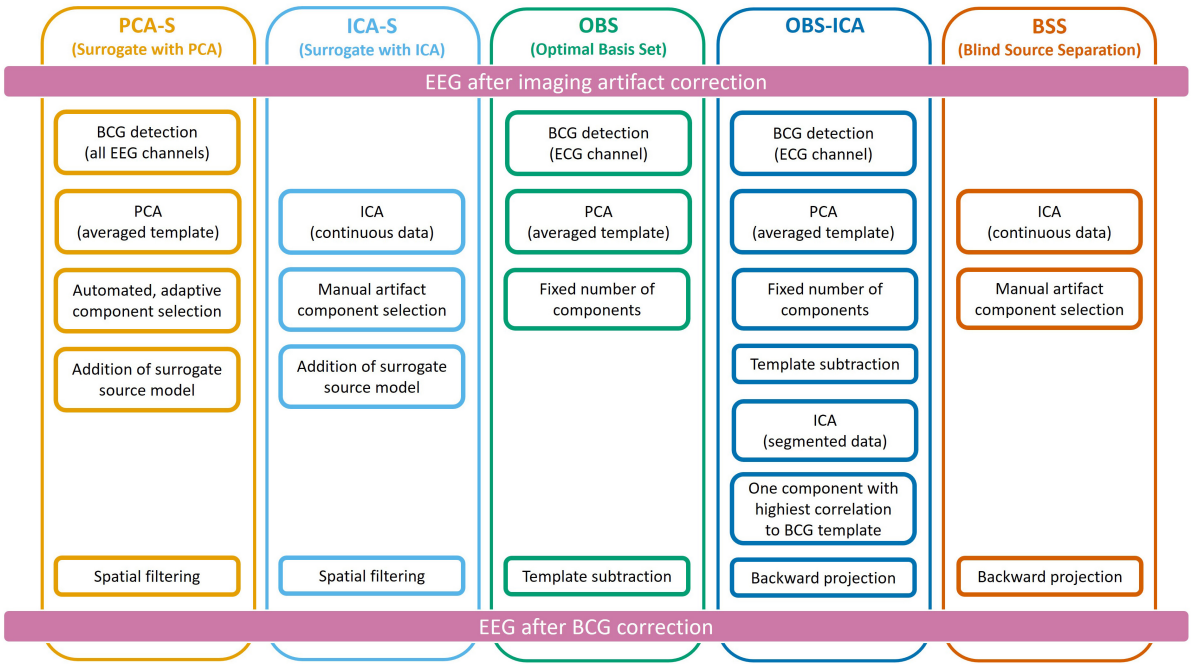

FIGURE 2 | Schematic representation of all five methods used for Ballistocardiogram (BCG) artifact reduction. Data processing was performed from top to bottom, each column represents one method.

with BCG artifact were calculated. Then, data can be projected back onto the scalp EEG using only non-BCG-related data to reconstruct the BCG artifact corrected EEG in sensor space. The brain surrogate model was applied with regularization of 2% and artifact coefficients were applied without regularization.

Ballistocardiogram Artifact Removal by ICA Surrogate

The ICA surrogate (ICA-S) method is comparable to the PCA-S method. Instead of using PCA topographies, the BCG artifact components were determined by ICA using the same manual selection as described for BSS (section Ballistocardiogram Artifact Removal by Optimal Basis Set). Then, the spatial components of the ICA traces that were identified as artifact were combined with the 87 spatial brain source components as described for PCA-S (cf. **Figure 2**).

Ballistocardiogram Artifact Removal by Optimal Basis Set

The OBS approach of BCG artifact reduction (Niazy et al., 2005) was used as implemented in the FMRIB plug-in (version 2.0, Nuffield Department of Clinical Neuroscience, Medical Sciences Division, Oxford, United Kingdom) for the EEGLAB toolbox (version 13.6.5.b, Swartz Center for Computational Neuroscience, San Diego, United States). After removing the fMRI imaging artifact, EEG was exported from the BESA Research software into European Data Format (EDF) and loaded into EEGLAB. First, QRS complexes were detected in the ECG channel by the FMRIB plugin (combined algorithms of Christov, 2004; Kim et al., 2004). Second, by averaging the epochs around the detected QRS complexes, an averaged template of the BCG artifact was created. Finally, using the OBS approach, the principal components of the averaged artifact template were subtracted from the EEG. The number of removed components was fixed to 4 which is the default value in the FMRIB plugin. After BCG artifact reduction, EEG data were converted to EDF and reloaded into the BESA Research software for further analysis.

Ballistocardiogram Artifact Removal by Optimal Basis Set and ICA

The OBS-ICA method used the outcome of the procedure above (OBS) followed by ICA. This computation was performed in the EEGLAB toolbox following the Debener et al. (2007) processing pipeline. First data was filtered in the range of 0.3–40 Hz and epoched around each detected BCG event (in a range of −50 to −750 ms). Then ICA was computed on concatenated epochs using the Extended Infomax approach (Lee et al., 1999). The component that had the highest spatial correlation with the topography of maximum signal of BCG template was removed during back projection of scalp EEG.

Ballistocardiogram Artifact Removal by Blind Source Separation

The BSS approach (Jung et al., 2000) is based on ICA. After filtering with a time-constant filter (low cutoff 0.1 Hz) and a high cutoff filter (30 Hz), a 40 s block of data with clearly visible BCG artifact was selected to perform ICA using the Extended Infomax algorithm (Lee et al., 1999). The largest components were displayed for inspection, and the following

visual cues were used to manually identify and mark traces with BCG artifact: waveform shape, and temporal relationship to the electrocardiography (ECG) channel. The number of marked components varied from 3 to 9 (mean 5.5), depending on data. Finally, the BCG artifact corrected scalp EEG was calculated by back projecting only the unmarked ICA components.

Auditory Evoked Potentials Averaging

Using the artifact-corrected EEG, identical analysis steps were performed for all BCG artifact correction methods. First, bad epochs with residual artifacts like movement or blink were rejected using the automated rejection tool of BESA Research. Epochs with peak-to-peak amplitudes greater than 120 μV and signal gradients greater than 75 μV/sample were excluded. For the detection of bad epochs, data were filtered from 0.3 Hz (forward phase-shift, 6 dB/Oct) to 30 Hz (zero phase-shift, 24 dB/Oct). Second, after rejecting bad epochs, filters were turned off to average the AEP in a window of −300 to +800 ms around the accepted triggers. The averaged signal was filtered using the same filter settings as previously. Finally, EEG data were re-referenced to the average reference of the 64 channels of the artifact-corrected EEG. The grand average AEP was created using the AEPs averages of all subjects.

Evaluation Metrics

We compared the BCG artifact reduction methods by using the following evaluation criteria: First, for each data correction method that was applied, we compared the number of events that passed the amplitude and gradient acceptance thresholds for averaging. Second, the SNR values of the averaged AEP resulting after applying each method were compared. SNR per channel was computed using the root mean square value of pre-stimulus interval (−300 to 0 ms) as baseline and the root mean square value of the first 300 ms of post-stimulus data as the signal of interest. The mean SNR value across all channels was computed. Third, the averaged AEP waveforms were examined by comparing the latency and amplitude at Cz as detected automatically by the peak detection algorithm of BESA Research in the time range from 0 to 200 ms.

We examined the accuracy of source reconstruction after each BCG artifact reduction method. Since the AEP had been generated by fixed simulated bilateral dipoles (**Figure 1** and **Table 1**), we assessed how much of the averaged signal after BCG correction was explained by the initial AEP model. For this, explained variance was calculated both for the grand average AEP and individual AEP in the full width of half maximum (FWHM) range (81–114 ms). This would amount to 100% if data variance over all channels was fully explained by the model. Lower values indicate higher distortion of the AEP topography.

We also evaluated the location and angle error from single subject source localization. For this purpose we computed a source solution containing two symmetric dipoles for every subject. Dipole locations and orientations were fitted to the artifact corrected averaged ERP using the Nelder-Mead optimization algorithm (Nelder and Mead, 1965) in the range 81–114 ms. A 4-shell ellipsoidal head model was used (the same as for the ERP simulation) (Berg and Scherg, 1994b). The localization error was computed as a norm of difference between obtained and seeded dipole position (c.f. **Figure 1** and **Table 1**). The difference angle was computed as scalar product between dipole orientations. Since in each model there was exactly two dipoles, to simplify further analysis we computed the average error for each pair of dipoles.

None of the tested variables showed normal distribution as tested by Shapiro-Wilk test in the SPSS software (version 21.0, IBM, New York, United States). Therefore, the Kruskal-Wallis (K-W) test was applied followed by Dunn-Bonferroni *post-hoc* pairwise comparison in SPSS.

Alpha Rhythm Data Analysis (Single Subject)

We compared the eyes-closed state with the eyes-opened state from Berger experiment session using mean fast Fourier transform (FFT). The mean FFT was computed in overlapping blocks (2.05 s) over combined periods of each condition (c.a. 180 s per condition). To investigate the difference, we evaluated the spatial distribution in the alpha range as well as an FFT heat map representing mean amplitude per frequency for each channel, sub-divided into channel groups (frontal, central, left temporal, right temporal, and occipital). In addition, for this data set we compared BCG waveforms from the beginning of the recording with ones from the end of the recording, to evaluate the BCG variability. For this purpose, two different epochs of raw EEG signal after average referencing and filtering (0.3–30 Hz) were sent to the source analysis module of BESA Research. We compared two epochs—one from the eyes-opened state at the beginning of the recording (10 s) and one from the eyes-closed state at the end of the recording (355 s). The epochs were time-locked to the R-peak and the epoch interval was −100 to 600 ms. For both epochs the same model (spatial filtering) was applied, replicating the PCA-S artifact reduction—29 brain regional sources (with 2% regularization) extended with 4 BCG coefficients (with no regularization) obtained from PCA. These were the same components that we used for artifact correction.

RESULTS

Mean Trial Number

As an initial measurement of BCG artifact reduction efficiency, we assessed the number of accepted events after rejecting bad epochs. The more accepted events, the higher the quality of the data (fewer residual artifacts).

In **Figure 3** (left), the mean numbers of accepted trials were compared. The highest mean value was observed for the PCA-S method ($\bar{x} = 178 \pm 16$). Lower values were obtained for ICA-S ($\bar{x} = 155 \pm 41$), OBS ($\bar{x} = 120 \pm 44$) and OBS-ICA ($\bar{x} = 126 \pm 45$) while the BSS method showed the lowest numbers ($\bar{x} = 93 \pm 62$). There was a statistically significant difference between these methods as determined by K-W test [$H(4) = 101.1$, $p < 0.001$] with a mean rank trial number of 215 for PCA-S, 171 for ICA-S, 106 for OBS, 115 for OBS-ICA and 82 for BSS. *Post-hoc* testing (**Table 2**) revealed that the higher number of accepted epochs was

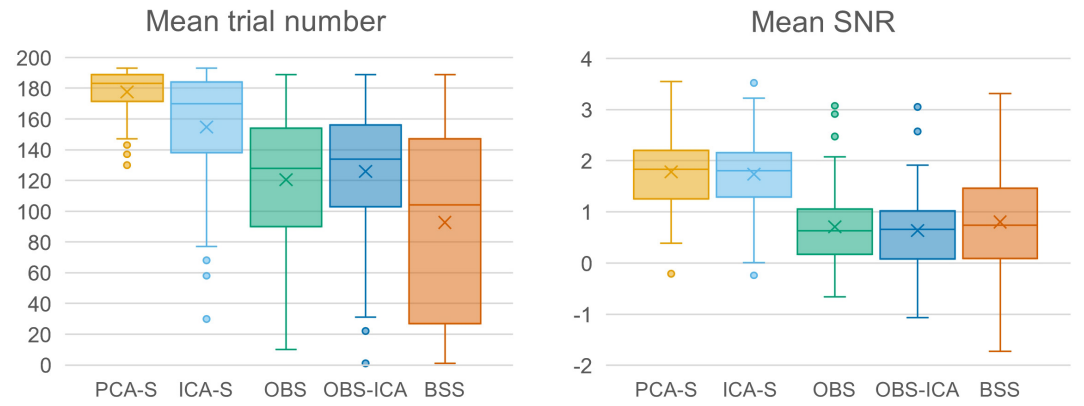

FIGURE 3 | Comparison charts of mean trial number and mean SNR for different BCG artifact reduction methods. Boxes show the medians and 1st and 3rd quartiles, whiskers denote the 1.5 interquartile range, crosses indicate mean values, and outliers are represented by dots.

statistically significant when PCA was compared with all other methods ($p < 0.001$ for OBS, OBS-ICA, BSS and $p < 0.05$ for ICA-S). Similarly, ICA-S outperformed OBS ($p < 0.001$), BSS ($p < 0.001$), and OBS-ICA ($p < 0.05$). There was no significant difference between OBS and OBS-ICA ($p = 1.000$), OBS and BSS ($p = 1.000$) and between OBS-ICA and BSS ($p = 0.307$).

Signal-To-Noise

SNR is a good indicator of the averaged data quality. Higher SNR value indicates a cleaner and less noisy baseline. When the five BCG artifact reduction methods (**Figure 3**, right) were compared, the highest SNR values were observed for PCA-S ($\bar{x} = 3.45 \pm 1.60$) and ICA-S ($\bar{x} = 3.42 \pm 1.77$). OBS, OBS-ICA and BSS had much smaller values (OBS: $\bar{x} = 1.33 \pm 3.14$, OBS-ICA: $\bar{x} = 1.11 \pm 3.29$, BSS: $\bar{x} = 1.43 \pm 2.08$). The K-W test showed statistically significant differences between these methods [$H(4) = 81.4$, $p < 0.001$]. The mean rank SNR was 193, 188, 100, 96, 112 for PCA-S, ICA-S, OBS, OBS-ICA, and BSS, respectively. *Post-hoc* pairwise comparison (see **Table 2**) revealed that the higher SNR value observed for both PCA-S and ICA-S was significantly higher ($p < 0.001$) than for OBS, OBS-ICA and BSS.

TABLE 2 | Dunn-Bonferroni *post-hoc* results of pairwise comparison between BCG artifact reduction methods for trial number and SNR.

Pair	Trial number	SNR
PCA-S vs. ICA-S	**0.035***	1.000
PCA-S vs. OBS	**0.000****	**0.000****
PCA-S vs. OBS-ICA	**0.000****	**0.000****
PCA-S vs. BSS	**0.000****	**0.000****
ICA-S vs. OBS	**0.000****	**0.000****
ICA-S vs. OBS-ICA	**0.002***	**0.000****
ICA-S vs. BSS	**0.000****	**0.000****
OBS vs. OBS-ICA	1.000	1.000
OBS vs. BSS	1.000	1.000
OBS-ICA vs. BSS	0.307	1.000

*Statistically significant values are indicated in bold print, *$p < 0.05$, **$p < 0.001$.*

The difference in SNR between PCA-S and ICA-S, as well as between OBS, OBS-ICA, and BSS was not significant ($p = 1.000$).

Auditory Evoked Potentials Waveform Properties

To reflect typical ERP evaluation, we compared the averaged AEP signals resulting from the different methods (**Figure 4A**). The overall waveforms for grand average after BCG artifact reduction were similar to the modeled ones. However, the AEP amplitudes after BCG reduction were slightly reduced as compared to the simulated model for all the methods. Peak latency and amplitude differences between BCG artifact reduction methods were evaluated for N100 at the central electrode (Cz) but no significant differences were found. [K-W test for amplitude: $H(4) = 3.0$, $p = 0.553$, K-W test for latency: $H(4) = 1.3$, $p = 0.866$]. Despite of no difference in amplitude and latency at Cz electrode, some differences in the scalp topography of the grand-mean AEP averaged over the latency range of 81–114 ms were observed (**Figure 4B**). This could affect source localization which was furtherly evaluated.

Explained Variance

The quality of source reconstruction as defined by the explained variance of the grand average data was highest with PCA-S (97.3%) and ICA-S (96.9%), whereas it was reduced for OBS (93.8%) and OBS-ICA (94.0%), as well as for BSS (90.3%), as shown in **Figure 5** (left). Due to the noise of the corrected individual AEPs the mean values of explained variance were lower when considering the mean values over all subjects (**Figure 5**, right). They were still considerably smaller in OBS ($\bar{x} = 67.3\% \pm 16.0$), OBS-ICA ($\bar{x} = 62.8\% \pm 21.1$), and BSS ($\bar{x} = 40.5\% \pm 23.8$) as compared to PCA-S ($\bar{x} = 80.0\% \pm 9.9$) and ICA-S ($\bar{x} = 77.3\% \pm 12.9$). The statistical evaluation by the K-W test showed a significant difference between the five BCG reduction methods [$H(4) = 102.0$, $p < 0.001$] with a mean rank explained variance of 194 for PCA-S, 182 for ICA-S, 133 for OBS, 132 for OBS-ICA, and 58 for BSS. The *post-hoc* pairwise comparison is depicted in **Table 3**. The explained variance

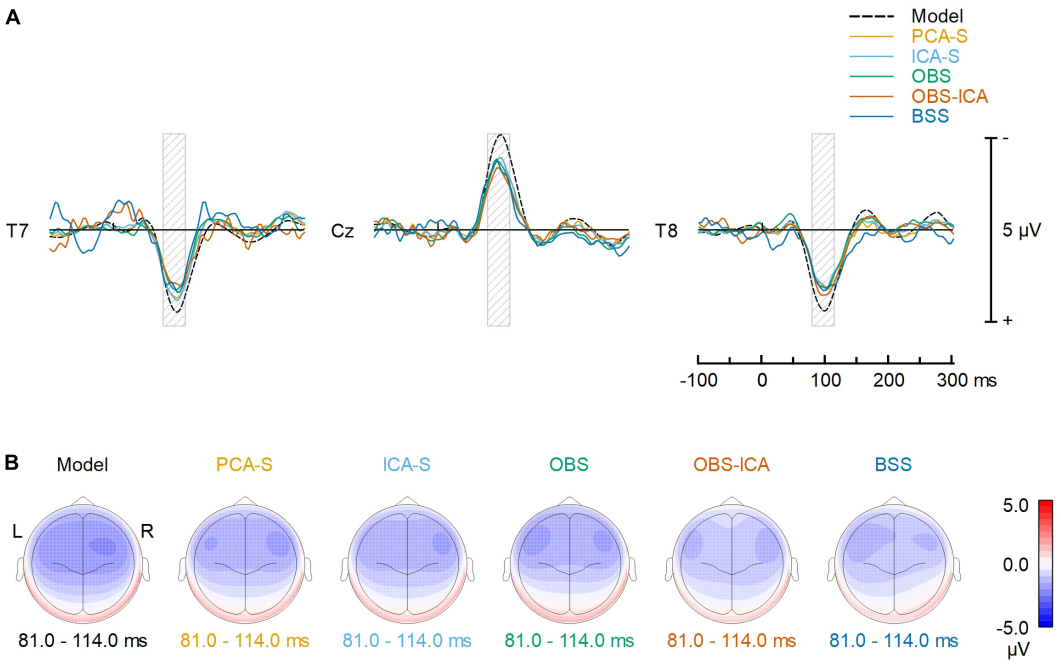

FIGURE 4 | Comparison of the BCG artifact reduction methods. **(A)** The signals recovered at T7, Cz and T8 electrodes (virtually re-referenced to the average reference) are compared to the noise-free, simulated AEP signal. Each solid color line represents one of the 5 different BCG artifact reduction methods; the dashed line (Model) represents the simulated AEP signal. **(B)** Topographic plots of averaged ERP response for the simulated AEP signal and the BCG artifact reduction methods in the range 81–114 ms (full width at half maximum of the modeled signal power, as illustrated by the gray shaded areas in the top row).

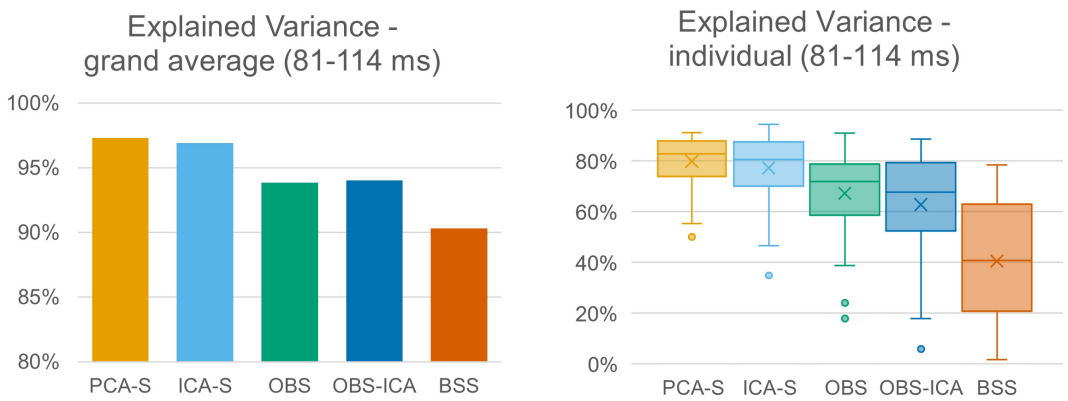

FIGURE 5 | Explained variance of grand averaged data and individual data. Explained variance was averaged across the full width at half maximum of modeled signal power for the different BCG artifact reduction methods. For individual data the boxes show the medians and 1st and 3rd quartiles, whiskers denote the 1.5 interquartile range, crosses indicate mean values, and outliers are represented by dots.

obtained for PCA-S was significantly higher than any other non-surrogate-based methods: OBS ($p < 0.05$), OBS-ICA ($p < 0.001$) and BSS ($p < 0.001$). Similarly, ICA-S values were significantly higher in comparison to non-surrogate-based methods, but the difference was slightly smaller ($p < 0.05$ for OBS and OBS-ICA, $p < 0.001$ for BSS). BSS had significantly lower explained variance as compared to both OBS and OBS-ICA ($p < 0.001$). There was no statistical difference between PCA-S and ICA-S and between OBS and OBS-ICA.

Localization Error and Angle Error

Furthermore, we evaluated how the observed difference in explained variance translates to source analysis efficiency. To measure this, we verified the deviation between source model fitted to the artifact corrected data and the seeded model (see **Figure 1** and **Table 1**). As shown in **Figure 6**, PCA-S and ICA-S had most of the dipoles located around the auditory cortex (where the seeded dipoles were located). For the OBS, and even more so for OBS-ICA, more outliers can be observed.

TABLE 3 | Dunn-Bonferroni *post-hoc* results of pairwise comparison between BCG artifact reduction methods for explained variance, localization error and angle error.

Pairwise comparison	Explained variance	Localization error	Angle error
PCA-S vs. ICA-S	1.000	1.000	1.000
PCA-S vs. OBS	**0.001***	**0.016***	**0.040***
PCA-S vs. OBS-ICA	**0.000****	**0.002***	**0.002***
PCA-S vs. BSS	**0.000****	**0.000****	**0.000****
ICA-S vs. OBS	**0.013***	0.073	0.264
ICA-S vs. OBS-ICA	**0.001***	**0.012***	**0.026***
ICA-S vs. BSS	**0.000****	**0.000****	**0.000****
OBS vs. OBS-ICA	1.000	1.000	1.000
OBS vs. BSS	**0.000****	**0.000****	**0.000****
OBS-ICA vs. BSS	**0.000****	**0.001***	**0.006***

*Statistically significant values are indicated in bold print, *p < 0.05, **p < 0.001.*

The BSS method resulted in dipoles widely distributed over the whole brain volume. This observation is supported by the numerical verification of localization and angle error, as shown in **Figure 7**. The localization and angle error were smallest for PCA-S (localization error: $\bar{x}$ = 17.2 mm ± 10.4, angle error: $\bar{x}$ = 22.5° ± 9.8) and ICA-S (localization error: $\bar{x}$ = 18.2 mm ± 11.3, angle error: $\bar{x}$ = 24.0° ± 10.7). A larger error was observed for both OBS (localization error: $\bar{x}$ = 27.6 mm ± 18.4, angle error: $\bar{x}$ = 28.9° ± 11.2) and OBS-ICA (localization error: $\bar{x}$ = 29.0 mm ± 18.5, angle error: $\bar{x}$ = 31.1° ± 11.9). The largest deviation from simulated model was observed for BSS (localization error: $\bar{x}$ = 49.6 mm ± 24.9, angle error: $\bar{x}$ = 43.0° ± 16.3). Further statistical evaluation confirmed that these differences were statistically significant [$H(4) = 76.2$, $p < 0.001$ for localization error, $H(4) = 63.8$, $p < 0.001$ for angle error]. The mean rank values for localization error were 92.3, 99.6, 140.2, 148.8, 209.2 for PCA-S, ICA-S, OBS, OBS-ICA, and BSS, respectively. The mean rank values for angle error were 94.5, 104.5, 138.2, 150.2, 202.6 for PCA-S, ICA-S, OBS, OBS-ICA, and BSS, respectively. The pairwise comparison showed that both localization and angle error for PCA-S was lower than for OBS and OBS-ICA ($p < 0.05$), as well as for BSS ($p < 0.001$). Similarly, ICA-S had lower localization and angle error than OBS-ICA ($p < 0.05$) and BSS ($p < 0.001$). Also, BSS was outperformed by OBS ($p < 0.001$) and by OBS-ICA ($p < 0.05$). There were no statistical differences between PCA-S and ICA-S ($p = 1.000$), ICA-S and OBS ($p = 0.073$ for localization error, $p = 0.264$ for angle error), OBS and OBS-ICA ($p = 1.000$).

The Evaluation of Single Subject Recording (Berger Experiment)

No BCG artifact was visible in the data after PCA-S artifact correction, as shown in **Figure 8**. The blink related to the closing of the eyes is clearly visible in the middle of the shown interval, followed by prominent alpha rhythmical activity. No such activity can be observed before the closing of the eyes. In raw data the blink is also visible, yet due to high contamination with BCG artifact no other data features can be distinguished, even when investigating heat maps and topography maps which are shown below the data interval in **Figure 8**. Conversely, after correcting data using the PCA-S method, the heat maps depicted a strong differentiation between eyes-opened and eyes-closed states—the activity in the alpha frequency range can be noted, especially in occipital channels. Importantly, in both heat maps, no other atypical oscillatory activity can be observed. The alpha rhythm topography also reflected the normal topography typically observed for the Berger experiment—strong activity in the occipital lobe in eyes-closed state, which is absent during the eyes-opened state.

Ballistocardiogram Variability Evaluation in a Single Subject Recording (Berger Experiment)

In **Figure 9** the waveforms for four components of BCG obtained at the beginning (10 s) and at the end of the recording (355 s) are shown. In addition, the first sample was obtained during eyes-opened state, the second during eyes-closed state. While all waveforms are similar, some minor differences can be observed, especially for the second component.

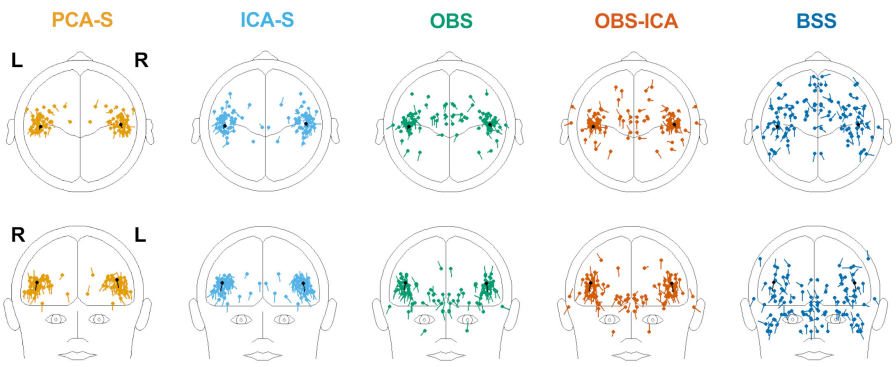

FIGURE 6 | Distribution of source localization obtained by fitting two symmetric dipoles to individual data, for the different BCG artifact reduction methods. In each image the seeded dipole model in the right and left Sylvian fissure is depicted in black.

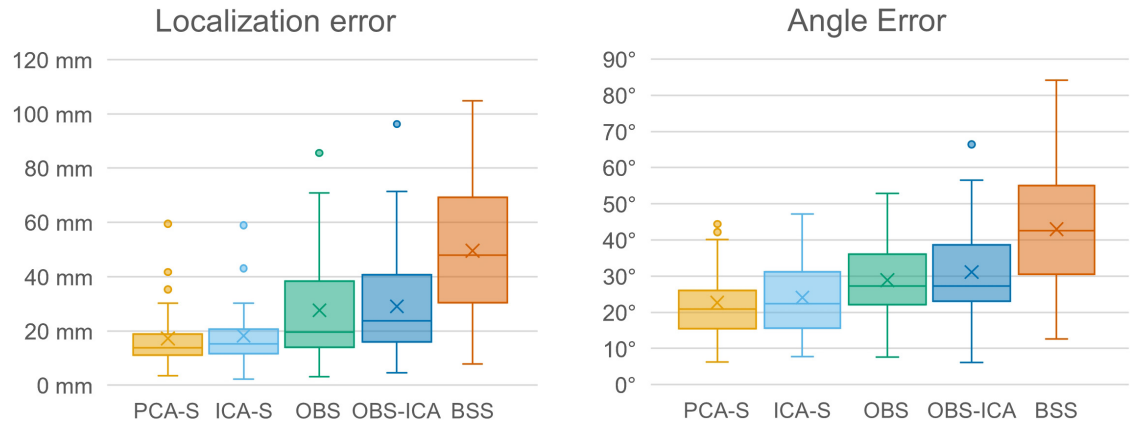

FIGURE 7 | Localization error and angle error for individual model fitting for the different BCG artifact reduction methods. Boxes show the medians and 1st and 3rd quartiles, whiskers denote the 1.5 interquartile range, crosses indicate mean values, and outliers are represented by dots.

DISCUSSION

In this study, we applied the spatial filtering method (Berg and Scherg, 1994a) to EEG data measured during fMRI acquisition using a standard surrogate source model in order to reduce the BCG artifact. To compare this approach with the established methods of OBS, OBS-ICA, and BBS, we combined real resting-state EEG data measured during fMRI acquisition with simulated AEPs. Thus, we could evaluate the strength of artifact reduction and signal distortions introduced by the different methods. This approach is justified by the assumption that the fMRI environment introduces only contaminations of the EEG signal and does not influence the brain signals themselves. Importantly, we evaluated our method using auditory ERPs. This bilateral, synchronous activity with tangential dipolar orientation makes the source analysis challenging (Scherg et al., 2019) and highly dependent on SNR. Also, as shown by Shams et al. (2015), the auditory ERPs are more troublesome for BCG artifact correction when compared to e.g., visual ERPs, due to differences in the BCG characteristic across different channels since the generators lie on distant and opposite sites relative to the to head center.

While there was no significant difference between methods for AEP waveform properties, both surrogate-based BCG artifact reduction methods—PCA-S and ICA-S—outperformed the OBS, OBS-ICA, and BSS approaches in the following evaluation metric: the basic signal features (number of events accepted for averaging and SNR), the quality of source reconstruction for the grand average, and source localization error for single subjects. The method used to estimate the artifact topography in the surrogate methods (PCA or ICA) did not have an impact on the AEP outcome, apart from a higher mean trial number accepted for ERP averaging when the PCA method was used.

The number of events accepted for averaging was significantly higher when comparing PCA-S with ICA-S ($p < 0.05$) and OBS, OBS-ICA, BSS ($p < 0.001$, **Figure 3**, left). A higher number of accepted events for averaging is of major importance since it may lead to shorter experiments and allow for more sophisticated methods of data analysis, for example, the comparison of the first and second part of an experiment, single-trial analysis, time-frequency analysis (Castelhano et al., 2014), or EEG-driven fMRI analysis (Abreu et al., 2018). Furthermore, the higher the number of averaged events, the less biological noise contaminates the waveforms, which can be evaluated using SNR and peak amplitudes.

The highest SNR was observed for PCA-S, followed by ICA-S (**Figure 3**, right). The significant reduction of SNR in the OBS, OBS-ICA, and BSS methods was mainly due to increased noise introduced before and after the AEP. These findings are in general agreement with the observations of Debener et al. (2007) and explain why the number of detected events was significantly reduced both in OBS and BSS. Interestingly, a slightly lower SNR value was observed when OBS-ICA was compared to OBS, while the number of mean number of trials showed the opposite relationship. This observation stands in contrast to Debener et al. (2007), yet it was not statistically significant here.

Amplitude reduction was observed in all BCG artifact reduction methods, but we did not notice any significant difference between tested methods for single (central) electrode amplitude and latency evaluation. For the first time, this study showed this effect is clearly a product of data processing, as the testing procedure combined modeled AEP activity with real EEG resting state data instead of using test-retest comparisons. However, the cause of this reduction is unclear since it might be due either to the specific BCG artifact reduction process or to the fMRI artifact removal. For simultaneous EEG-fMRI studies, it is widely accepted that signal quality and amplitude is decreased to some extent (i.e., Rusiniak et al., 2013; Marino et al., 2018b). Yet, it is crucial that the MR environment and EEG post-processing do not distort signal topography, in order to minimize the bias of statistical comparisons and source localization. The stability of the signal distribution after BCG correction is also of major importance for a direct comparison of the AEP within and outside of the magnetic resonance device, as well as for longitudinal experiments apart from the documented

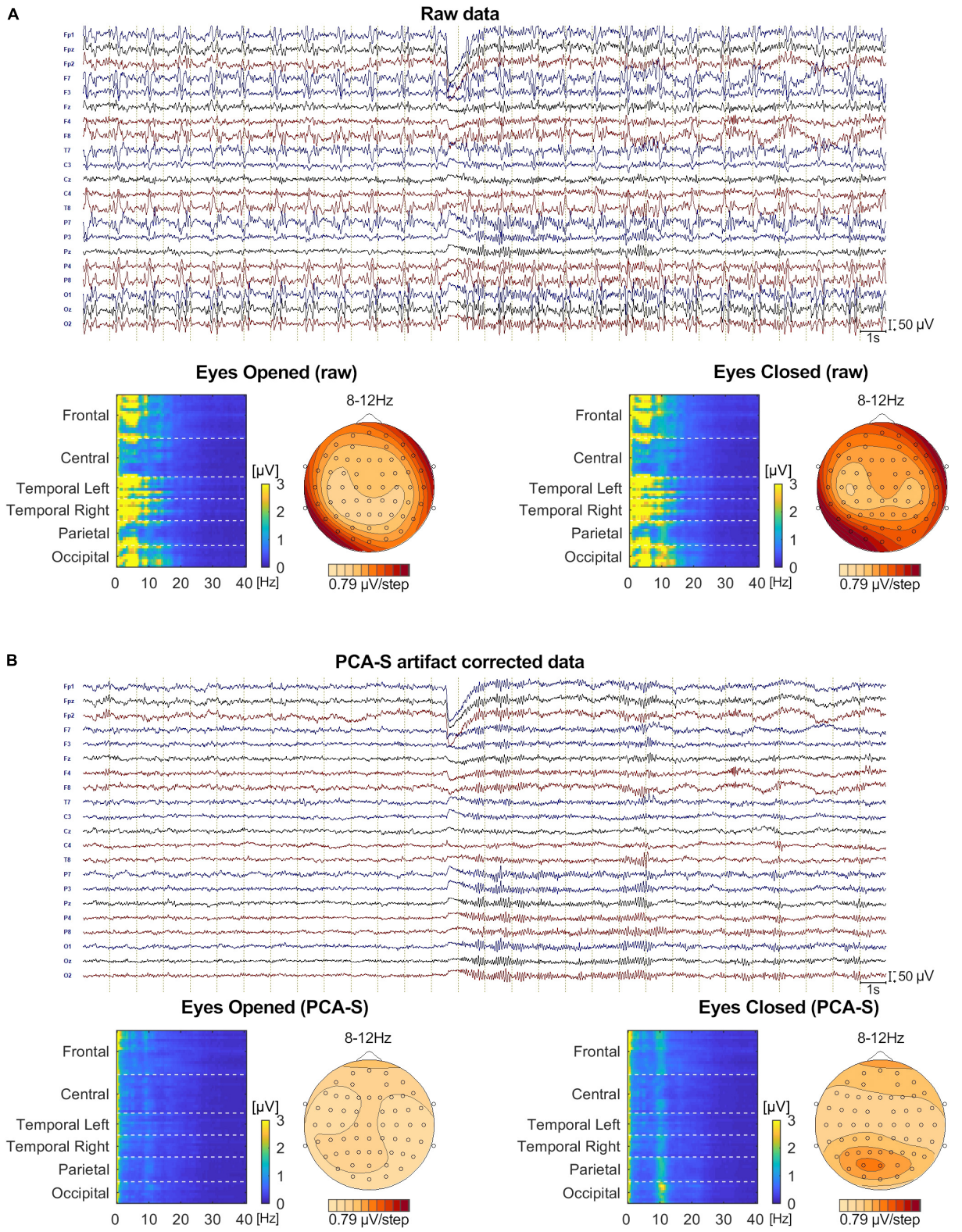

FIGURE 8 | The comparison of Eyes-Opened and Eyes-Closed state for both raw **(A)** and PCA-S artifact corrected data **(B)**. At the top of each sub-figure an example of the same 30 s of recording is shown, in which the transition from eyes-opened to eyes-closed state occurs in the middle. 20 electrodes are shown (every second channel from the 64-channel montage that was used). Below, an FFT heat map for both states, respectively, is shown, showing each recorded channel (grouped by brain lobes) along with the alpha rhythm topography.

amplitude reduction. Inspecting topographies obtained on the grand average level for all the methods (**Figure 4B**) it can be noted that each method affected the topography, yet the outcome of PCA-S and ICA-S reassembled the modeled signal, whereas it looks like the OBS and OBS-ICA introduced some frontal shift in the map. The topography after BSS artifact correction seems to be distorted most.

The differences in topography may likely translate into a distortion of source localization. Therefore, we checked the explained variance of the corrected AEP data when using the simulated AEP source as model. The percentage of explained variance was significantly higher using PCA-S and ICA-S as compared to the OBS, OBS-ICA, and BSS methods. For both surrogate methods the explained variance was around 97%. This value clearly indicates that most of the signal was explained, and that the model is adequate for data explanation. The lower the value, the larger the risk that the model might be considered not sufficient for the data, leading to a perceived need to introduce additional sources to the model. This observation was investigated in more detail by performing analysis on the individual subject level. Obviously, due to much larger noise contamination compared to the grand average, the explained variance at the single subject level was lower in general. The difference between surrogate methods and other methods was even more prominent in this case. For PCA-S as well as for ICA-S, we obtained a mean value around 80% with very low inter-subject variability, while the other methods performed much worse, especially BSS. This indicated the need for a larger number of cases for non-surrogate-based methods to achieve trust-worthy grand average generation. Furthermore, source analysis on a single subject level analysis might not be fully trust-worthy for these methods.

To investigate the reproducibility of single subject source analysis we performed the source fitting procedure on single subjects and evaluated how far from the modeled sources the results were. The source distribution shown for every method in **Figure 6**, followed by the statistical analysis of localization and angle error shown in **Figure 7** and **Table 3**, clearly indicated that PCA-S, as well as ICA-S provided robust and focused results close to the modeled signal (with mean error values around 20 mm and 20°). Most importantly, these methods successfully located activity in the temporal lobe, with just sparse outliers. The OBS and OBS-ICA seem to also lead to correct localization of sources in the vicinity of the modeled sources, yet the high number of outliers as visible in **Figure 6** indicate that both methods distort the signal in many cases. The BSS method did not allow for trust-worthy source localization at single subject level at all.

Finally, we verified if the PCA-S method works also for non-ERP data. The Berger experiment is clinically relevant and by far the oldest procedure for evaluation of a non-dipolar, rhythmical signal on continuous data level. In **Figure 8** we show that the PCA-S method proposed here allowed for successful BCG artifact reduction and signal evaluation on both visual and computational level (FFT heat maps, alpha rhythm topography). No signal distortion and residual artifacts were observed.

Using this dataset, we also evaluated how PCA-S approach handles BCG variability (**Figure 9**). Due to changes in cardiac rhythm and blood pressure the artifact changes over time (Oh et al., 2014; Marino et al., 2018a). However, unless the subject changes head position in the MR machine, the spatial distribution is not affected by the aforementioned changes that only impact the temporal aspects of BCG. In this regards the spatial filtering

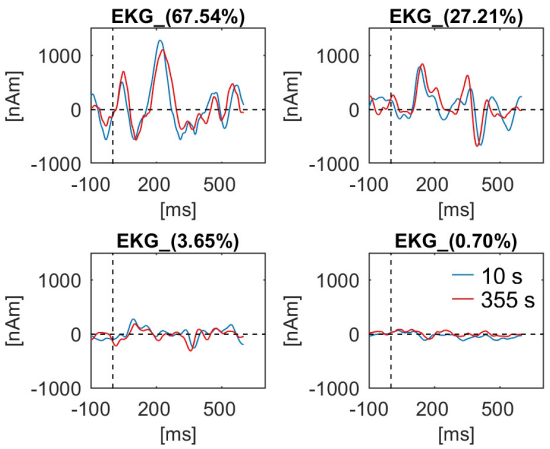

FIGURE 9 | BCG waveforms from a single subject (Berger experiment) for all four artifact components used for artifact correction. Waveforms at the beginning of the recording (10 s, blue line) and at the end of the recording (355 s, red line) are shown. For each component the percentage value of explained variance in the BCG template is indicated in the waveform caption.

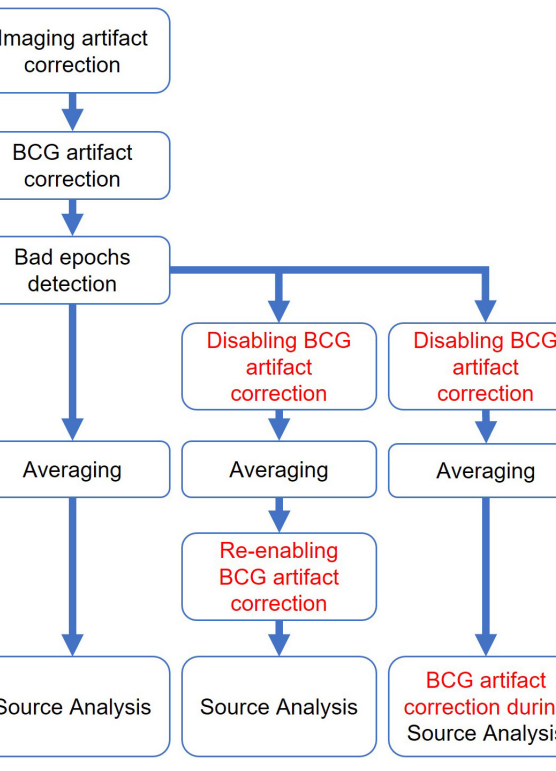

FIGURE 10 | Different BCG artifact reduction pipelines for surrogate artifact reduction methods.

should be unaffected by the physiological artifact variation. The artifact waveforms extracted by spatial filter from data at the beginning and at the end were reviewed. There is a noticeable difference in the waveforms that proved adaptation of data correction to changes in temporal aspects of the artifact. Also, even though first data block was extracted during the eyes-opened state and the second during eyes-closed state, there is no prominent oscillatory activity visible in any of the waveforms. Furthermore, PCA-S, as well as ICA-S, can be easily extended to account for spatial changes by applying regularization to the artifact components, however, that could introduce a risk of data distortion. Here it is worth adding that subject movement in the MR machine is an even bigger issue for fMRI gradient artifact removal, which is based on moving average artifact subtraction, and happens prior to BCG artifact correction in simultaneous EEG-fMRI data processing. Therefore, subject movement should be avoided.

The surrogate approach presented here was already successfully applied in our previous study where simultaneous EEG-fMRI was used for time-frequency analysis of the relationship between alpha rhythm and default mode network in a group of adults (Rusiniak et al., 2018). Recently Plaska et al. (2021, Preprint) applied this approach to evaluate interhemispheric connectivity in working memory during a visual stimulation task.

The classical implementation of the OBS method requires an additional ECG electrode to create the BCG artifact template. Moreover, the OBS method assumes a fixed delay (210 ms) of the BCG artifact relative to the R-wave of the ECG (Niazy et al., 2005). As mentioned before the recent findings show that this value varies with blood transverse time (Oh et al., 2014; Marino et al., 2018a). This problem was partially solved by deriving the triggers for template averaging from the EEG (Marino et al., 2018b), similarly to the creation of the averaged template in PCA-S. In both approaches, the additional ECG channel is no longer required, and the QRS-BCG timing difference is not an issue. However, if no trigger is detected in the OBS-based methods, the BCG artifact will not be subtracted from the signal at this time point. Moreover, in the OBS approach there is no brain signal modeling and artifact components are simply subtracted from the data. In contrast, PCA-S and ICA-S provide a stationary spatial filter (as defined by the inverse separating BCG and surrogate components) that projects out all BCG-artifact components from the EEG at each time point when an artifact occurs. A potential disadvantage of spatial filtering is that a sufficient number of recording channels is needed, amounting to at least the number of artifact and brain source components to enable their separation (Berg and Scherg, 1994a; Scherg et al., 2002). In contrast, a subtraction procedure as used in OBS can be used even for a single channel dataset. However, this limitation is of minor importance in recent studies which use at least 32 EEG channels.

The BSS method uses a stationary spatial filter derived from ICA. The ICA approach implemented here is prone to human error as incorrect components may be selected, or selected components may contain small parts of the ERP activities that are removed with the artifact (Marino et al., 2018a). It is worth mentioning that automatic and semi-automatic approaches do exist (i.e., Srivastava et al., 2005; Mantini et al., 2007; Debener et al., 2008), yet they suffer from the same ICA method limitations. Since ERP signals are typically much smaller than the background EEG, ICA rarely creates independent components for the whole ERP that would be spatially orthogonal to the removed ICA components. Thus, any part of the ERP spatially correlated with the removed components will result in ERP amplitude reduction and distortion if not modeled by another component. In contrast, both PCA-S and ICA-S were specifically designed to remove the correlation between artifact and brain source components, based on the spatial filtering method of Berg and Scherg (1994a). Since the BSS approach is based on ICA and is independent of QRS detection, it acts as a spatial filter on the whole EEG similarly to the surrogate model approaches. However, the BSS approach is fully based on ICA requiring perfect visual selection and separation of the BCG artifact components. An additional problem with ICA-based approaches is the vast amount of possible options for ICA computation (Vanderperren et al., 2010). The BCG artifact is a complex multi-dimensional signal due to the head movement in the strong static magnetic field (translation and rotation in any direction) caused by ballistic forces generated by the heart as well as single electrode movements due to skin pulsation and the Hall effect (Debener et al., 2008; Marino et al., 2018a). It might be scattered over multiple independent components or might not be well separated from another activity. While the manual BCG-related components selection conducted here might be sub-optimal, it is worth to underline that the same selection of ICA artifact components was used in our BSS and ICA-S applications and ICA-S outperformed BSS as well as OBS and OBS-ICA. The fundamental difference of ICA-S is that these components are not simply projected out by the spatial filter (potentially together with some relevant brain activity), but instead they are used as a model of the artifact when separating artifact and brain surrogate components by the inverse filter. Thus, the brain activities are preserved to a large extent in ICA-S as well as by the PCA-S method.

Considering the basic problems of both approaches (OBS and BSS) as shown and discussed here, this combination does not solve the essential problem of subtracting out brain signal together with the artifact in both approaches. While OBS-ICA delivered slightly higher number of mean trial number accepted for averaging, the decrease in all other parameters (SNR, explained variance and localization error) was observed as well. There was no statistical difference between OBS and OBS-ICA but the distortion introduced by the additional ICA step made the difference between OBS-ICA and both surrogate methods (PCA-S and ICA-S) more significant. It is likely that careful manual trimming of OBS and OBS-ICA parameters could improve the efficiency of these methods, but this can be stated for all other methods as well.

BCG artifact reduction is one of the major problems limiting broader usage of simultaneous EEG-fMRI. Taking the above into consideration, the big advantage of the OBS method is its automation and ease of use as implemented in the FMRIB plug-in

for the EEGLAB toolbox. As shown here, the PCA-S approach has also been automated apart from the initial selection of one good sample of the BCG artifact. This step could also be automated for future applications (Marino et al., 2018b). Both PCA-S and OBS use PCA to obtain the spatial topographies of the artifact. PCA-S adjusts the number of components using a cutoff criterion based on the variance of each component but does not subtract these components directly from the EEG. In contrast, OBS needs to limit the number of orthogonal PCA components, typically to four, in order not to subtract too much other activity from the EEG due to limited separation from the brain signal.

OBS, OBS-ICA, and BSS BCG artifact correction have to be performed prior to the rejection of other artifacts, averaging, and source analysis. Contrary to this, the spatial filter defined by contrasting artifact and surrogate model components is a linear operator which leads to other advantages: It can be applied for the first time prior to the detection of other artifacts and averaging (**Figure 10**). In addition, the averaging can be done using the uncorrected EEG and the filter is then reapplied to the averaged data prior to source analysis, since averaging and filtering are linear operations and thus commutative (2nd column in **Figure 10**). The last combination (3rd column in **Figure 10**) would add the spatial artifact components to the source model of the ERP in order to separate artifact and ERP source activities. Thus, the impact of the number of artifact components and their topographies can be assessed at each stage of data processing in PCA-S and ICA-S and adjusted if required.

In this study, a standard surrogate model of 29 regional sources equally distributed over the brain was used in order to: (a) allow for an automated application of the PCA-S approach and (b) investigate the potential benefit of the surrogate approach even in cases where the source model is not a perfect match of the underlying ERP (e.g., in AEPs), plus for rhythmical non-focal activity. The general surrogate brain activity model might not fit perfectly to every brain data and could lead to some minor distortion, but still the impact of this is less severe than for any other method presented here. Please note that the used surrogate model does not have a source overlap with the seeded model as shown in **Figure 1**. The adequate choice of an individually generated surrogate model can further improve the rendering of an undistorted ERP when spatial filtering is used for the separation of artifact and brain source components (Berg and Scherg, 1994a). For example, Siniatchkin et al. (2007) used an individual surrogate model of interictal epileptiform discharges recorded outside of the magnet and averaged previously. However, as they pointed out, the limitation of such an approach is to procedures where test-retest can be performed.

While in this paper the focus was on a broad evaluation of source analysis improvement resulting from usage of PCA-S and ICA-S, further assessment of this approach is needed especially for time-frequency and single trial data analysis. The high number of retained events for averaging (**Figure 3**) might suggest that this approach might be effective for these application types as well. Also, since the surrogate approach is based on spatial filtering and does not need extensive computing it potentially could be used for real-time data processing, after preparing a BCG artifact template during a training phase at the beginning of the recording. Here we performed the evaluation using simulated ERPs superimposed on real EEG-fMRI data. While this allowed for precise assessment of the artifact correction quality there is a need for further evaluation of this approach with real data tests, even though some positive outcomes were already shown (Rusiniak et al., 2018; Plaska et al., 2021, Preprint).

The present study demonstrates that BCG artifact reduction techniques provide more reliable results when surrogate-based spatial filtering is used to correct simultaneous EEG-fMRI recordings especially for source analysis. While for simple ERP evaluation all methods gave similar results, the proposed methods of PCA-S and ICA-S successfully reduced BCG artifacts and preserved the simulated brain signals much better than the established methods of OBS, OBS-ICA, and BBS. This finding was independent of the artifact modeling approach used (PCA or ICA). We also showed that the approach proposed here can be used for evaluation of continuous EEG (Berger experiment) and is unaffected by temporal variation of the BCG artifact. Therefore, the surrogate model approaches can be automated and applied to all types of cognitive EEG-fMRI studies. They have already been implemented in the BESA Research 7.1 software package, and a detailed whole EEG-fMRI pipeline description is available (BESA, 2022).

DATA AVAILABILITY STATEMENT

The raw data supporting the conclusions of this article will be made available by the authors, without undue reservation.

ETHICS STATEMENT

The studies involving human participants were reviewed and approved by the Ethics Committee of the Institute of Physiology and Pathology of Hearing. The patients/participants provided their written informed consent to participate in this study.

AUTHOR CONTRIBUTIONS

MR conceptualized the study, collected funds, performed data analysis, and wrote the first draft of the manuscript. MR, HB, NI, PB, and MS contributed to the methodology. MR, HB, J-HC, NI, and PB worked on algorithms and their implementation. MR and TW collected data and administered the project. MS supervised the project. All authors contributed to manuscript revision, read, and approved the submitted version.

FUNDING

EEG-fMRI data used in this manuscript was collected as part of a grant from the Polish National Science Center no. 2011/01/N/NZ4/04985.

REFERENCES

Abbott, D. F., Masterton, R. A. J., Archer, J. S., Fleming, S. W., Warren, A. E. L., and Jackson, G. D. (2015). Constructing carbon fiber motion-detection loops for simultaneous EEG–fMRI. *Front. Neurol.* 5:260. doi: 10.3389/fneur.2014.00260

Abreu, R., Leal, A., and Figueiredo, P. (2018). EEG-informed fMRI: a review of data analysis methods. *Front. Hum. Neurosci.* 12:29. doi: 10.3389/fnhum.2018.00029

Abreu, R., Leite, M., Jorge, J., Grouiller, F., van der Zwaag, W., Leal, A., et al. (2016). Ballistocardiogram artifact correction taking into account physiological signal preservation in simultaneous EEG-fMRI. *Neuroimage* 135, 45–63. doi: 10.1016/j.neuroimage.2016.03.034

Allen, P. J., Josephs, O., and Turner, R. (2000). A method for removing imaging artifact from continuous EEG recorded during functional MRI. *Neuroimage* 12, 230–239. doi: 10.1006/nimg.2000.0599

Allen, P. J., Polizzi, G., Krakow, K., Fish, D. R., and Lemieux, L. (1998). Identification of EEG Events in the MR scanner: the problem of pulse artifact and a method for its subtraction. *Neuroimage* 8, 229–239. doi: 10.1006/nimg.1998.0361

Bast, T., Oezkan, O., Rona, S., Stippich, C., Seitz, A., Rupp, A., et al. (2004). EEG and MEG source analysis of single and averaged interictal spikes reveals intrinsic epileptogenicity in focal cortical dysplasia. *Epilepsia* 45, 621–631. doi: 10.1111/j.0013-9580.2004.56503.x

Bell, A. J., and Sejnowski, T. J. (1995). An information-maximization approach to blind separation and blind deconvolution. *Neural Comput.* 7, 1129–1159. doi: 10.1162/neco.1995.7.6.1129

Bénar, C.-G., Aghakhani, Y., Wang, Y., Izenberg, A., Al-Asmi, A., Dubeau, F., et al. (2003). Quality of EEG in simultaneous EEG-fMRI for epilepsy. *Clin. Neurophysiol.* 114, 569–580. doi: 10.1016/S1388-2457(02)00383-8

Beniczky, S., Duez, L., Scherg, M., Hansen, P. O., Tankisi, H., Sidenius, P., et al. (2016). Visualizing spikes in source-space: rapid and efficient evaluation of magnetoencephalography. *Clin. Neurophysiol.* 127, 1067–1072. doi: 10.1016/j.clinph.2015.07.017

Berg, P., and Scherg, M. (1994a). A multiple source approach to the correction of eye artifacts. *Electroencephalogr. Clin. Neurophysiol.* 90, 229–241. doi: 10.1016/0013-4694(94)90094-9

Berg, P., and Scherg, M. (1994b). A fast method for forward computation of multiple-shell spherical head models. *Electroencephalogr. Clin. Neurophysiol.* 90, 58–64. doi: 10.1016/0013-4694(94)90113-9

Berger, P. D. H. (1929). Über das elektrenkephalogramm des menschen. *Arch. Psychiatr. Nervenkrankh.* 87, 527–570. doi: 10.1007/BF01797193

BESA (2022). *Pipeline for Simultaneous EEG-fMRI Recording.* Available online at: http://wiki.besa.de/index.php?title=Pipeline_for_simultaneous_EEG-fMRI_recording (accessed February 7, 2022).

Bonmassar, G., Purdon, P. L., Jääskeläinen, I. P., Chiappa, K., Solo, V., Brown, E. N., et al. (2002). Motion and ballistocardiogram artifact removal for interleaved recording of EEG and EPs during MRI. *Neuroimage* 16, 1127–1141. doi: 10.1006/nimg.2002.1125

Bullock, M., Jackson, G. D., and Abbott, D. F. (2021). Artifact reduction in simultaneous EEG-fMRI: a systematic review of methods and contemporary usage. *Front. Neurol.* 12:622719. doi: 10.3389/fneur.2021.622719

Castelhano, J., Duarte, I. C., Wibral, M., Rodriguez, E., and Castelo-Branco, M. (2014). The dual facet of gamma oscillations: separate visual and decision making circuits as revealed by simultaneous EEG/fMRI. *Hum. Brain Mapp.* 35, 5219–5235. doi: 10.1002/hbm.22545

Chowdhury, M. E. H., Mullinger, K. J., Glover, P., and Bowtell, R. (2014). Reference layer artefact subtraction (RLAS): a novel method of minimizing EEG artefacts during simultaneous fMRI. *Neuroimage* 84, 307–319. doi: 10.1016/j.neuroimage.2013.08.039

Christov, I. I. (2004). Real time electrocardiogram QRS detection using combined adaptive threshold. *Biomed. Eng. Online* 3:28. doi: 10.1186/1475-925X-3-28

Debener, S., Mullinger, K. J., Niazy, R. K., and Bowtell, R. W. (2008). Properties of the ballistocardiogram artefact as revealed by EEG recordings at 1.5, 3 and 7 T static magnetic field strength. *Int. J. Psychophysiol.* 67, 189–199. doi: 10.1016/j.ijpsycho.2007.05.015

Debener, S., Strobel, A., Sorger, B., Peters, J., Kranczioch, C., Engel, A. K., et al. (2007). Improved quality of auditory event-related potentials recorded simultaneously with 3-T fMRI: removal of the ballistocardiogram artefact. *Neuroimage* 34, 587–597. doi: 10.1016/j.neuroimage.2006.09.031

Grouiller, F., Vercueil, L., Krainik, A., Segebarth, C., Kahane, P., and David, O. (2007). A comparative study of different artefact removal algorithms for EEG signals acquired during functional MRI. *Neuroimage* 38, 124–137. doi: 10.1016/j.neuroimage.2007.07.025

Hyvarinen, A. (1999). Fast and robust fixed-point algorithms for independent component analysis. *IEEE Trans. Neural Netw.* 10, 626–634. doi: 10.1109/72.761722

Ille, N., Berg, P., and Scherg, M. (2002). Artifact correction of the ongoing EEG using spatial filters based on artifact and brain signal topographies. *J. Clin. Neurophysiol.* 19, 113–124. doi: 10.1097/00004691-200203000-00002

Jung, T.-P., Makeig, S., Humphries, C., Lee, T.-W., McKeown, M. J., Iragui, V., et al. (2000). Removing electroencephalographic artifacts by blind source separation. *Psychophysiology* 37, 163–178. doi: 10.1111/1469-8986.3720163

Kim, K. H., Yoon, H. W., and Park, H. W. (2004). Improved ballistocardiac artifact removal from the electroencephalogram recorded in fMRI. *J. Neurosci. Methods* 135, 193–203. doi: 10.1016/j.jneumeth.2003.12.016

Laufs, H. (2012). A personalized history of EEG–fMRI integration. *Neuroimage* 62, 1056–1067. doi: 10.1016/j.neuroimage.2012.01.039

Lee, T.-W., Girolami, M., and Sejnowski, T. J. (1999). Independent component analysis using an extended infomax algorithm for mixed Subgaussian and Supergaussian Sources. *Neural Comput.* 11, 417–441. doi: 10.1162/089976699300016719

Logothetis, N. K., Pauls, J., Augath, M., Trinath, T., and Oeltermann, A. (2001). Neurophysiological investigation of the basis of the fMRI signal. *Nature* 412, 150–157. doi: 10.1038/35084005

Luo, Q., Huang, X., and Glover, G. H. (2014). Ballistocardiogram artifact removal with a reference layer and standard EEG cap. *J. Neurosci. Methods* 233, 137–149. doi: 10.1016/j.jneumeth.2014.06.021

Manganas, S., and Bourbakis, N. (2017). "A Comparative Survey on Simultaneous EEG-fMRI Methodologies," in *Proceedings of the 2017 IEEE 17th International Conference on Bioinformatics and Bioengineering (BIBE)*, Washington, DC, 1–8. doi: 10.1109/BIBE.2017.00-87

Mantini, D., Perrucci, M. G., Cugini, S., Ferretti, A., Romani, G. L., and Del Gratta, C. (2007). Complete artifact removal for EEG recorded during continuous fMRI using independent component analysis. *Neuroimage* 34, 598–607. doi: 10.1016/j.neuroimage.2006.09.037

Marino, M., Liu, Q., Del Castello, M., Corsi, C., Wenderoth, N., and Mantini, D. (2018a). Heart–Brain Interactions in the MR Environment: characterization of the Ballistocardiogram in EEG Signals Collected During Simultaneous fMRI. *Brain Topogr.* 31, 337–345. doi: 10.1007/s10548-018-0631-1

Marino, M., Liu, Q., Koudelka, V., Porcaro, C., Hlinka, J., Wenderoth, N., et al. (2018b). Adaptive optimal basis set for BCG artifact removal in simultaneous EEG-fMRI. *Sci. Rep.* 8:8902. doi: 10.1038/s41598-018-27187-6

Masterton, R. A. J., Abbott, D. F., Fleming, S. W., and Jackson, G. D. (2007). Measurement and reduction of motion and ballistocardiogram artefacts from simultaneous EEG and fMRI recordings. *Neuroimage* 37, 202–211. doi: 10.1016/j.neuroimage.2007.02.060

Moosmann, M., Schönfelder, V. H., Specht, K., Scheeringa, R., Nordby, H., and Hugdahl, K. (2009). Realignment parameter-informed artefact correction for simultaneous EEG–fMRI recordings. *Neuroimage* 45, 1144–1150. doi: 10.1016/j.neuroimage.2009.01.024

Mulert, C., and Lemieux, L. (eds) (2010). *EEG - fMRI: Physiological Basis, Technique, and Applications*. Berlin: Springer-Verlag. doi: 10.1007/978-3-540-87919-0

Mullinger, K. J., Havenhand, J., and Bowtell, R. (2013). Identifying the sources of the pulse artefact in EEG recordings made inside an MR scanner. *Neuroimage* 71, 75–83. doi: 10.1016/j.neuroimage.2012.12.070

Müri, R. M., Felblinger, J., Rösler, K. M., Jung, B., Hess, C. W., and Boesch, C. (1998). Recording of electrical brain activity in a magnetic resonance environment: distorting effects of the static magnetic field. *Magn. Reson. Med.* 39, 18–22. doi: 10.1002/mrm.1910390105

Nelder, J. A., and Mead, R. (1965). A simplex method for function minimization. *Comput. J.* 7, 308–313. doi: 10.1093/comjnl/7.4.308

Niazy, R. K., Beckmann, C. F., Iannetti, G. D., Brady, J. M., and Smith, S. M. (2005). Removal of FMRI environment artifacts from EEG data using optimal basis sets. *Neuroimage* 28, 720–737. doi: 10.1016/j.neuroimage.2005.06.067

Oh, S. S., Han, Y., Lee, J., Yun, S. D., Kang, J. K., Lee, E. M., et al. (2014). A pulse artifact removal method considering artifact variations in the simultaneous

recording of EEG and fMRI. *Neurosci. Res.* 81–82, 42–50. doi: 10.1016/j.neures.2014.01.008

Plaska, C. R., Ortega, J., Gomes, B. A., and Ellmore, T. M. (2021). Interhemispheric connectivity supports load-dependent working memory maintenance for complex visual stimuli. *bioRixv* [Preprint]. doi: 10.1101/2021.03.24.436845

Rosenkranz, K., and Lemieux, L. (2010). Present and future of simultaneous EEG-fMRI. *Magn. Reson. Mater. Phys. Biol. Med.* 23, 309–316. doi: 10.1007/s10334-009-0196-9

Rusiniak, M., Lewandowska, M., Wolak, T., Pluta, A., Milner, R., Ganc, M., et al. (2013). A modified oddball paradigm for investigation of neural correlates of attention: a simultaneous ERP–fMRI study. *Magn. Reson. Mater. Phys. Biol. Med.* 26, 511–526. doi: 10.1007/s10334-013-0374-7

Rusiniak, M., Wróbel, A., Cieśla, K., Pluta, A., Lewandowska, M., Wojcik, J., et al. (2018). The relationship between alpha burst activity and the default mode network. *Acta Neurobiol. Exp.* 78, 92–13. doi: 10.21307/ane-2018-010

Scherg, M., Berg, P., Nakasato, N., and Beniczky, S. (2019). Taking the EEG back into the brain: the power of multiple discrete sources. *Front. Neurol.* 10:855. doi: 10.3389/fneur.2019.00855

Scherg, M., Ille, N., Bornfleth, H., and Berg, P. (2002). Advanced Tools for Digital EEG review:: virtual source montages, whole-head mapping, correlation, and phase analysis. *J. Clin. Neurophysiol.* 19, 91–112. doi: 10.1097/00004691-200203000-00001

Shams, N., Alain, C., and Strother, S. (2015). Comparison of BCG artifact removal methods for evoked responses in simultaneous EEG–fMRI. *J. Neurosci. Methods* 245, 137–146. doi: 10.1016/j.jneumeth.2015.02.018

Siniatchkin, M., Moeller, F., Jacobs, J., Stephani, U., Boor, R., Wolff, S., et al. (2007). Spatial filters and automated spike detection based on brain topographies improve sensitivity of EEG–fMRI studies in focal epilepsy. *Neuroimage* 37, 834–843. doi: 10.1016/j.neuroimage.2007.05.049

Srivastava, G., Crottaz-Herbette, S., Lau, K. M., Glover, G. H., and Menon, V. (2005). ICA-based procedures for removing ballistocardiogram artifacts from EEG data acquired in the MRI scanner. *Neuroimage* 24, 50–60. doi: 10.1016/j.neuroimage.2004.09.041

van der Meer, J. N., Pampel, A., Van Someren, E. J. W., Ramautar, J. R., van der Werf, Y. D., Gomez-Herrero, G., et al. (2016). Carbon-wire loop based artifact correction outperforms post-processing EEG/fMRI corrections—A validation of a real-time simultaneous EEG/fMRI correction method. *Neuroimage* 125, 880–894. doi: 10.1016/j.neuroimage.2015.10.064

Vanderperren, K., De Vos, M., Ramautar, J. R., Novitskiy, N., Mennes, M., Assecondi, S., et al. (2010). Removal of BCG artifacts from EEG recordings inside the MR scanner: a comparison of methodological and validation-related aspects. *Neuroimage* 50, 920–934. doi: 10.1016/j.neuroimage.2010.01.010

Wang, K., Li, W., Dong, L., Zou, L., and Wang, C. (2018). Clustering-Constrained ICA for ballistocardiogram artifacts removal in simultaneous EEG-fMRI. *Front. Neurosci.* 12:59. doi: 10.3389/fnins.2018.00059

Yan, W. X., Mullinger, K. J., Geirsdottir, G. B., and Bowtell, R. (2010). Physical modeling of pulse artefact sources in simultaneous EEG/fMRI. *Hum. Brain Mapp.* 31, 604–620. doi: 10.1002/hbm.20891

Conflict of Interest: MR, HB, J-HC, NI, and PB were employees of BESA GmbH, a company which develops and provides software tools for EEG and MEG data analysis. MS was employee and shareholder of BESA GmbH.

The remaining author declares that the research was conducted in the absence of any commercial or financial relationships that could be construed as a potential conflict of interest.

Publisher's Note: All claims expressed in this article are solely those of the authors and do not necessarily represent those of their affiliated organizations, or those of the publisher, the editors and the reviewers. Any product that may be evaluated in this article, or claim that may be made by its manufacturer, is not guaranteed or endorsed by the publisher.

frontiers | Frontiers in Neuroscience

ORIGINAL RESEARCH
published: 16 May 2022
doi: 10.3389/fnins.2022.802239

High-Density Electroencephalography-Informed Multiband Functional Magnetic Resonance Imaging Reveals Rhythm-Specific Activations Within the Trigeminal Nociceptive Network

*Hauke Basedau, Kuan-Po Peng, Arne May and Jan Mehnert**

Department of Systems Neuroscience, University Medical Center Hamburg-Eppendorf, Hamburg, Germany

The interest in exploring trigeminal pain processing has grown in recent years, mainly due to various pathologies (such as migraine) related to this system. However, research efforts have mainly focused on understanding molecular mechanisms or studying pathological states. On the contrary, non-invasive imaging studies are limited by either spatial or temporal resolution depending on the modality used. This can be overcome by using multimodal imaging techniques such as simultaneous functional magnetic resonance imaging (fMRI) and electroencephalography (EEG). Although this technique has already been applied to neuroscientific research areas and consequently gained insights into diverse sensory systems and pathologies, only a few studies have applied EEG-fMRI in the field of pain processing and none in the trigeminal system. Focusing on trigeminal nociception, we used a trigeminal pain paradigm, which has been well-studied in either modality. For validation, we first acquired stand-alone measures with each imaging modality before fusing them in a simultaneous session. Furthermore, we introduced a new, yet simple, non-parametric correlation technique, which exploits trial-to-trial variance of both measurement techniques with Spearman's correlations, to consolidate the results gained by the two modalities. This new technique does not presume a linear relationship and needs a few repetitions per subject. We also showed cross-validation by analyzing visual stimulations. Using these techniques, we showed that EEG power changes in the theta-band induced by trigeminal pain correlate with fMRI activation within the brainstem, whereas those of gamma-band oscillations correlate with BOLD signals in higher cortical areas.

Keywords: simultaneous EEG-fMRI, trial-to-trial variance, beta time-series, correlation, validation, brain rhythms

OPEN ACCESS

Edited by:
Aleksandra Dagmara Kawala-Sterniuk, Opole University of Technology, Poland

Reviewed by:
Mariusz Pelc, University of Greenwich, United Kingdom
Grzegorz Marcin Wójcik, Maria Curie-Skłodowska University, Poland

***Correspondence:**
Jan Mehnert
j.mehnert@uke.de

Specialty section:
This article was submitted to Brain Imaging Methods, a section of the journal Frontiers in Neuroscience

Received: *26 October 2021*
Accepted: *30 March 2022*
Published: *16 May 2022*

Citation:
Basedau H, Peng K-P, May A and Mehnert J (2022) High-Density Electroencephalography-Informed Multiband Functional Magnetic Resonance Imaging Reveals Rhythm-Specific Activations Within the Trigeminal Nociceptive Network. Front. Neurosci. 16:802239. doi: 10.3389/fnins.2022.802239

INTRODUCTION

The human trigeminal nociceptive system is the origin of numerous pathologies such as headaches and facial pain syndromes (Stankewitz et al., 2010; Schulte et al., 2016, 2017; Goadsby et al., 2017; Mehnert et al., 2017). Most studies on humans are limited by either spatial or temporal resolution, depending on the modality used. While electroencephalography (EEG) provides the high temporal

resolution needed for casual interference such as coupling measures, it lacks spatial resolution. In contrast, functional magnetic resonance imaging (fMRI) can provide a spatial resolution of up to 1 mm^3, yet it suffers from poor temporal resolution. The idea of combining both non-invasive techniques through simultaneous measurements thus has unique potential (Mulert and Lemieux, 2010) because it may overcome the spatial constrain of the EEG and the temporal limitation of fMRI. However, it is methodologically demanding and although neuroimaging of trigeminal nociception has made substantial progress in understanding trigeminal processing and related pathophysiology (May, 2013), simultaneous EEG-fMRI has not yet been established for trigeminal nociception. Here, we explored simultaneous EEG-fMRI as an intriguing tool to enhance insights into the human trigeminal nervous system.

Simultaneous EEG-fMRI has not yet been established to research the human trigeminal pain system. Nevertheless, a few studies using EEG-fMRI offer insights into the pain processing of other parts of the body (Iannetti and Mouraux, 2010). These studies mostly used heat delivered either by thermode (Roberts et al., 2008; Mayhew et al., 2013) or laser (Iannetti et al., 2005; Mobascher et al., 2009a,b; Brinkmeyer et al., 2010) on the hand, arm, or leg. One study applied painful electrical stimulation (Christmann et al., 2007), but the stimulations mentioned in these studies are not easily transferable to investigate the trigeminal nociception and furthermore exploit event-related potentials (ERP) rather than event-related synchronization (ERS) and desynchronization (ERD) of individual frequency bands, which are more robust to shifts of the stimulation onset in the millisecond range.

To investigate the spatiotemporal mechanisms of physiological trigeminal pain processing non-invasively in humans, we used a standardized and well-published experimental study design, eliciting trigeminal pain by applying gaseous ammonia into the nostril. Further conditions include visual stimuli as well as rose odor and simple air puffs as control conditions (Stankewitz et al., 2010; Schulte et al., 2016). We acquired high-density EEG using 64 channels (Scarff et al., 2004) and simultaneously fMRI with a brainstem optimized protocol (Schulte et al., 2016) that was extended through multiband acquisition techniques (Uji et al., 2018) to cover also all cortical areas of the brain. Our data fusion of both measurement modalities (EEG and fMRI) reveals new insights into the spatiotemporal dynamics of the trigeminal nociceptive system (May et al., 2020).

The aim of the study was twofold. First, we aimed to verify a novel analytical routine for fusing fMRI and EEG data. To this end, we used non-parametric Spearman's correlations between single-trial EEG power changes and single-trial blood oxygen level-dependent (BOLD) changes from the fMRI. This validation was used in the visual condition first, as a correlation between the induced steady-state evoked potential and the occipital regions of the brain is rather robust. In a second step, we aimed to gain deeper insight into trigeminal nociception by using the aforementioned analytical routine to correlate evoked EEG features with the fMRI during painful trigeminal input.

For the visual control condition, we aimed to replicate an (early) event-related potential (ERP), decreased alpha event-related synchronization (ERS), and, most prominently, a steady-state evoked potential (SSEP) and its higher harmonics (Mehnert et al., 2019) in the time-frequency representation of the central occipital electrode (Oz) of the EEG. The SSEP should correlate with BOLD changes in occipital regions in the fMRI.

The painful stimulation is estimated to reproduce the previously presented results in EEG. This refers to an ERP representation in the theta-/delta-band (Ploner et al., 2006; Huart et al., 2012; Taesler and Rose, 2016; Mehnert et al., 2019), a decrease in the alpha-band (Mehnert et al., 2019), and an increase in gamma ERS (Bader, 2019), all at the central-parietal electrode Pz.

We further hypothesized that correlations between power changes of the theta frequency and hemodynamics of the fMRI are present in areas in the brainstem pertinent to the trigeminal nociceptive system, including the spinal trigeminal nucleus (STN), the rostral ventromedial medulla (RVM), and eventually the periaqueductal gray (Stankewitz et al., 2010). We further expected gamma ERS to correlate with cortical areas of the pain matrix (Zhang et al., 2012).

MATERIALS AND METHODS

Subjects

In total, 35 healthy volunteers (18 women, age: 28.03 $\pm$ 3.94 years) participated in a standardized experiment on trigeminal pain processing. The study was approved by the Local Ethics Committee in Hamburg, Germany (PV 4896) and was conducted in accordance with the Declaration of Helsinki. We obtained written informed consent before the initiation of the first study session. The volunteers underwent a two-session pilot study consisting of (i) acquisition of EEG solely and (ii) acquisition of fMRI solely. Of these 35 participants, 18 volunteers were recruited for a final third session of (iii) simultaneous acquisition of EEG-fMRI. One was excluded due to inadequate data quality and prominent fMRI-artifact residuals in the EEG. The criteria for insufficient data quality are described in the section "Preprocessing of Electroencephalography Data." Therefore, the final group of combined EEG-fMRI consisted of 17 (9 women, age: 28.29 $\pm$ 3.51 years) datasets.

Experimental Design

The stimulus design is well-established and has been published multiple times elsewhere (Stankewitz et al., 2010; Schulte et al., 2016; Mehnert et al., 2017, 2018, 2019; Mehnert and May, 2019). In short, the volunteers received four different stimuli (ammonia, rose scent, or air into the left nostril, and a repetitive visual stimulation at 8 Hz) with an interstimulus interval of 46 $\pm$ 9 s, where the ammonia elicits a short-lasting, stinging, or stabbing painful sensations (Hummel and Kobal, 1992; Stankewitz et al., 2010). Refer to **Figure 1** for an overview of the experimental timeline. For all experimental sessions (EEG alone, fMRI alone, EEG-fMRI), the experiment was divided into three blocks, in which each condition was randomly presented

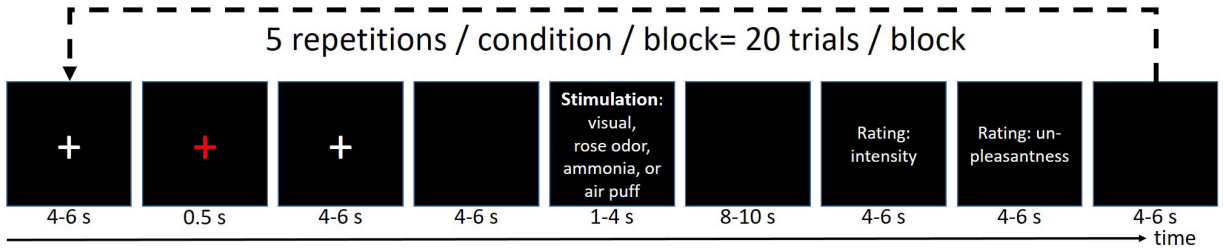

FIGURE 1 | Experimental design. Each run was repeated three times resulting in 15 stimuli/condition/participant.

five times, corresponding to 15 presentations of each condition for each participant in total. The subject rated the intensity and unpleasantness after each stimulus using a visual analog scale ranging from 0 to 100 for the intensity rating, where 0 means no pain at all while 100 refers to the worst imaginable pain. The unpleasantness was rated between −50 (extremely pleasant) and 50 (extremely unpleasant).

Stand-Alone Acquisition of Electroencephalography (First Session)

During the first session of the experiment, we acquired fast (5,000 Hz), high-density EEG (BrainAmp MR plus, Brain Products, Munich, Germany) with 59 channels, as well as echocardiogram (ECG) and 4 electrooculogram (EOG) channels, in a shielded EEG recording chamber. We used a custom-built photoionization detector (PID) (Bentekk, Hamburg, Germany) to track the gaseous stimulation boli of the ammonia with high-temporal resolution (100 Hz) necessary to identify the precise stimulus onset for the EEG analysis and to control the concentration and amount of ammonia given at a single-trial level.

Stand-Alone Acquisition of Functional Magnetic Resonance Imaging (Second Session)

During a second appointment, high-resolution structural images using an MPRAGE sequence (voxel size 1 mm × 1 mm × 1 mm) were initially recorded, along with field maps (74 slices, 3 mm × 3 mm × 2 mm resolution, FOV 222 mm, TR 0.814 s) for the correction of inhomogeneities in the magnetic field. The participants subsequently underwent high resolution (1.25 mm × 1.25 mm × 2 mm), multiband BOLD fMRI [echo-planar imaging, TR 3.173 s, TE 35 ms, 74 slices, 2 slices at a time (i.e., multiband), FOV 225 mm] covering the brainstem from foramen magnum up to all cortical areas using a 3T MR scanner (PRISMA, Siemens, Erlangen, Germany).

Acquisition of Simultaneous Electroencephalography and Functional Magnetic Resonance Imaging (Third Session)

For those participating in the third session, simultaneous EEG and fMRI were recorded using the parameters already described for the EEG and fMRI stand-alone sessions. Additionally, a second ECG and pulse and breathing were acquired with a supplementary device (Expression MR-Monitor, PHILIPS Corporation, Massachusetts, United States) to correct for cardiovascular artifacts. The timing of the EEG and the MR scanner was synchronized using a SyncBox (Brain Products, Munich, Germany), and triggers occurring at each radiofrequency pulse (RF-pulse) were passed from the MR to the EEG. All settings followed the protocol provided by the EEG manufacturer (sampling rate = 5,000 Hz; resolution: 0.5 μV; low cutoff = 10 s; high cutoff = 250 Hz; series resistor values = 10 kΩ) (Brain Products, Munich, Germany). During the acquisition, the helium compressor was turned off to avoid vibrations and, therefore, electrical noise for optimizing data quality. An overview of the complete setup is sketched in **Supplementary Figure 1**.

Preprocessing of Electroencephalography Data

Electroencephalography data were re-referenced to the average, cut into epochs between −500 and 3,000 ms time-locked to stimulus onset, and high-pass filtered at 0.5 Hz using the FieldTrip toolbox (Oostenveld et al., 2011). Power line artifacts were reduced by a notch filter at 50 Hz. Eye movement and blinking artifacts were automatically eliminated by regressing the difference in the signal between the two vertical as well as the two horizontal EOG channels using the procedure described by Parra et al. (2005). Thereafter, all trials passed the automated muscle detection routine of FieldTrip (version 22-02-2017)[1] using the *ft_artifact_muscle* routine with default parameters (bandpass-filter: Butterworth at 110–140 Hz, filter order 8, Hilbert transform, and a boxcar of 0.2) and an overall z-score higher than 5 using the *ft_artifact_zvalue* routine, which thresholds the *z*-transformed value of the preprocessed raw data at a z-score of 5. Furthermore, for the investigation of gamma oscillations, it was necessary to filter residual saccades. For this purpose, an algorithm developed by Hassler et al. (2011) was used, which detects transient saccades by an automated decomposition of saccades and removes them from the remaining data by interpolation. All identified artifact-loaded trials were completely excluded from further analysis, leaving 96.38% of the trials (90.7% in ammonia condition, 98.7% in rose, 96.6% in checker, and 99.6% in air condition) for the analysis.

[1]https://www.fieldtriptoolbox.org/

Time-frequency transformation of the individual trials was calculated using the multitaper method (Thomson, 1982; Mitra and Pesaran, 1999; Litvak et al., 2011) for frequencies of 2–100 Hz with frequency steps of 1 Hz and frequency resolution of 1–10 Hz, depending on the frequency under observation {higher resolution for higher frequencies created with MATLAB's *linspace* [1, 10 length (frequencies)] routine} using the implementation of the SPM12 toolbox[2]. Temporal resolution was set to 800 ms and the temporal steps to 50 ms. The resulting time-frequency spectra were—on a single-trial level—recalculated as relative changes to baseline (defined as 500–0 ms before stimulus onset) by division, logarithmically transformed, and then averaged within the individuals showing the induced responses (David et al., 2006) following the robust averaging protocol within SPM12. Then, the individual averages were cropped to a temporal window from 0 to 2,500 ms regarding stimulus onset.

For comparability reasons, the same approach was chosen for the simultaneous data. Given the synchronization between EEG and fMRI, as stated before and markers for each RF pulse, gradient artifact were corrected using the software provided by the EEG manufacturer (Brain Vision Analyzer 2, Brain Products, Munich, Germany) using 111 gradient template averages (three times the 37 slices) before any other preprocessing step. This algorithm in principle uses an average of several EEG periods as a template for a scanner artifact and subtracts this curve from the data as described in the study by Allen et al. (2000). Cardiobalistic artifacts were also corrected with the aforementioned software using the pulse signal acquired by the Expression® monitor for the detection of heartbeats. Again, this algorithm uses averages of several pulses used as templates to correct the EEG signals (Allen et al., 1998). In addition, we used a band-stop filter to denoise the remaining artifacts of the fMRI in the frequency range between 11.17 and 12.16 Hz (0.5 Hz around the repetition frequency of the RF pulses, i.e., number of slices/TR). The artifact correction of the preprocessing routine for the simultaneous with fMRI acquired EEG data left 94.0% of the trials (88.2% in ammonia condition, 96.1% in rose, 95.3% in checker, and 96.5% in air condition) for the analysis.

For the visual condition, we extracted trial-wise averages at the stimulation frequency of 8 Hz in the temporal window between 100 and 2,000 ms at the central occipital electrode, where the SSEP is expected. This was previously reported to show a significant increase for the current experimental design (Mehnert et al., 2019). For the nociceptive condition, we extracted trial-wise averages for four time-frequency windows at the central parietal electrode (Pz), which is a representation of the ERP in the theta-/delta-band (Ploner et al., 2006; Huart et al., 2012; Taesler and Rose, 2016; Mehnert et al., 2019), a decrease in the alpha-band (Mehnert et al., 2019) signifying a rise in attention, as well as an increase in gamma ERS (Bader, 2019) as stated in the section "Introduction." The details of the time-frequency windows are presented in **Table 1** and have previously been reported to contain significant changes in response to trigeminal nociception (Grosser et al., 2000; Bader, 2019; Mehnert et al., 2019). Averages of the time-frequency windows used for the nociceptive condition were also tested for the control condition (air puffs). The significance of these derived features is tested by a two-sided *t*-test against 0 with an alpha level of 0.05 in the stand-alone EEG session and for the EEG in the simultaneous EEG-fMRI session.

Preprocessing of Functional Magnetic Resonance Imaging Data

All fMRI images in the second and third sessions were first denoised using the spatially adaptive non-local mean algorithm (Manjón et al., 2010) implemented in the CAT12 extension of SPM12. Field maps were preprocessed and used for realignment and unwarping of the fMRI data. The data were further corrected for slice time, taking the multiband acquisition into account. Subsequently, functional images were co-registered to the anatomical images; the latter was then used to normalize all data to MNI space with a non-linear approach and smoothed with a 4 mm^3 isotropic Gaussian kernel (Schulte et al., 2016) for the trigeminal nociception but 6 mm for the repetitive visual stimulation. Data from the three acquired runs were combined into a single general linear model (GLM). In the GLM, we modeled the four conditions (ammonia, visual, rose, and air puffs) as well as the evaluations (ratings) in separate regressors. The GLM further included the run-wise movement parameters calculated in the realignment as regressors of no interest. In a similar fashion, 18–20 regressors per session inferred the cardiac and breathing characteristics of each image using the approach provided by Deckers et al. (2006). Group level statistics were calculated using SPM12: The main effects of the repetitive visual stimulation and the trigeminal nociception (beta images) were statistically tested with a *t*-test at a voxel-wise FWE-corrected

[2]http://www.fil.ion.ucl.ac.uk/spm/

TABLE 1 | Time-frequency windows of interest derived from the study by Bader (2019) and Mehnert et al. (2019).

Electrode	Frequency	Time	*t*-value for EEG-standalone/EEG in EEG-fMRI (df = 34/df = 16)	*p* for EEG-standalone/EEG in EEG-fMRI
Repetitive visual stimulation				
Oz	8 Hz (flicker, SSVEP)	100–2000 ms	6.16/4.34	<0.0001/<0.0001
Trigeminal nociception				
Pz	3–6 Hz (theta/delta)	350–1150 ms	3.72/1.53	0.0007/0.0028
Pz	9–10 (alpha)	1250–2000 ms	−6.10/n.s.	<0.0001/0.2551
Pz	33–43 Hz (low gamma)	100–2000 ms	4.05/2.44	0.0003/0.0266
Pz	57–100 Hz (high gamma)	300–2000 ms	6.13/3.43	<0.0001/0.0034

threshold of $p < 0.05$ with a minimal cluster extent of 30 voxels in the stand-alone fMRI session. This high statistical threshold was used to ensure the reproductive capacity of the experimental design used.

Simultaneous Electroencephalography-Functional Magnetic Resonance Imaging Data Fusion

To perform our analytical approach on correlations of trial-to-trial variability in the spirit of Iannetti and Mouraux (2010), we calculated one GLM where each painful, each visual, and each air puff trial were individually modeled with a HRF and included as regressors of interest in a trial-by-trial GLM (Rissman et al., 2004; Abdulrahman and Henson, 2016), while rose scent stimulation was included as a single, condition-wise regressor. As for the stand-alone analysis of the fMRI, further regressors were implemented to account for movement and breathing as well as pulse-related artifacts. The resulting so-called beta time-series (Abdulrahman and Henson, 2016) of each participant was then normalized to MNI space using the SPM12 standard procedure (Ashburner and Friston, 2005) with an isotropic voxel size of 2 mm^3 using the segmentation of the participants' structural image. The images were then z-transformed within each subject and concatenated across subjects for visual stimulation, trigeminal nociception, and the control condition (air puffs), respectively.

Trial-wise averages of EEG data from one time-frequency window for the visual condition were extracted [the flicker frequency of 8 Hz known to produce an SSVEP (Norcia et al., 2015)] at the central occipital electrode Oz and averages within four time-frequency windows for the trigeminal nociception and the control condition (air puffs) at the central-parietal electrode Pz. The time-frequency windows and electrode positions extracted are listed in **Table 1** and marked in **Figure 2** and **Supplementary Figures 2, 3**. Trial-wise averages of EEG power modulations were z-transformed within each subject and concatenated across subjects. After this process, each EEG time-frequency window and each fMRI voxel contains a time course with one entry for each trial (i.e., trial-wise averages of time-frequency windows for the EEG and beta time-series for the fMRI). We then correlated EEG and fMRI by non-parametric Spearman's correlation in the temporal dimension in a searchlight manner (Kriegeskorte et al., 2006). For each voxel, we extracted the beta time-series of all neighbors within a sphere of 6 mm radius, which were part of a gray and white matter mask. The resulting beta time-series were then averaged and correlated with the individual time-frequency window of the EEG data. We repeated this approach for each voxel, resulting in an image of correlation coefficients (and p-values) in MNI space for each time-frequency window of interest.

To evaluate our approach, we first tested it using the data from the repetitive visual stimulation to locate the 8 Hz time-frequency window of the EEG within the primary visual cortical areas (which therefore were masked). Presented results are FDR corrected for the number of the voxel at a threshold of $p < 0.05$ (one-sided). We used the more general FDR correction instead of FWE correction because the latter is based on random field theory, which might not be applicable to this specific type of non-parametric correlation.

Our primary hypothesis of correlations between trial-wise average power changes in the theta-band time-frequency window and trial-wise BOLD changes in the brainstem was tested using a lower threshold of $p < 0.005$ (one-sided, uncorrected). The latter was chosen because EEG measures only superficial signals, as neuronal activity of the brainstem will be overlaid by cortical activation. Therefore, activity from the brainstem is only represented indirectly and in a minor part of the EEG signal. Furthermore, the nuclei in the brainstem are rather small in comparison to cortical areas. The main source of EEG is derived from the pyramidal cells on the cortex, and the direct contribution from the gray matter in the brainstem is rather small (Olejniczak, 2006). All other trial-to-trial correlations of EEG average power from the selected time-frequency windows and fMRI beta time-series were tested at an FDR-corrected (for the number of the voxel of the gray and white matter mask) threshold of $p < 0.05$ (one-sided).

Furthermore, we included a comparison of correlations between the trigeminal nociception and the control condition. As for the trigeminal nociception, we first calculated correlations between the single-trial beta values of the air puffs and the single-trial EEG responses for the air puffs in the same time-frequency windows as for the nociceptive condition. In a second step, we performed a comparison between the correlation results of the nociception and the air puffs using a permutation approach. For each voxel and time-frequency window, we compared the (Fisher z-transformed) difference of the correlation values of the air puffs and the correlation value of the nociception to a null distribution stemming from the difference of correlation between randomized orders of nociception and control calculated for 50,000 permutations of the randomly selected voxel. As for the main fusion analysis, gamma-band correlation differences were again FDR corrected at an alpha of 0.05, while theta-band correlation differences had to pass a statistical threshold of $p < 0.005$ (uncorrected).

Correlation With Ratings

In addition, we correlated the subjects' z-scored single-trial intensity ratings of the nociceptive condition with the aforementioned z-scored and trial-wise averages of the EEG's time-frequency windows mentioned in **Table 1** using the Pearson correlation coefficient at an alpha level of 0.05 (two-sided).

Similar to our analyses on the fusion of fMRI and EEG, we used z-scored trial-wise intensity ratings (instead of the EEG features) to correlate pain intensity and fMRI beta time-series. Here again, we used an FDR-corrected threshold $p < 0.05$.

RESULTS

Behavior

The ratings for the painful stimulation of the first trigeminal branch (ammonia) showed significant higher intensity (EEG

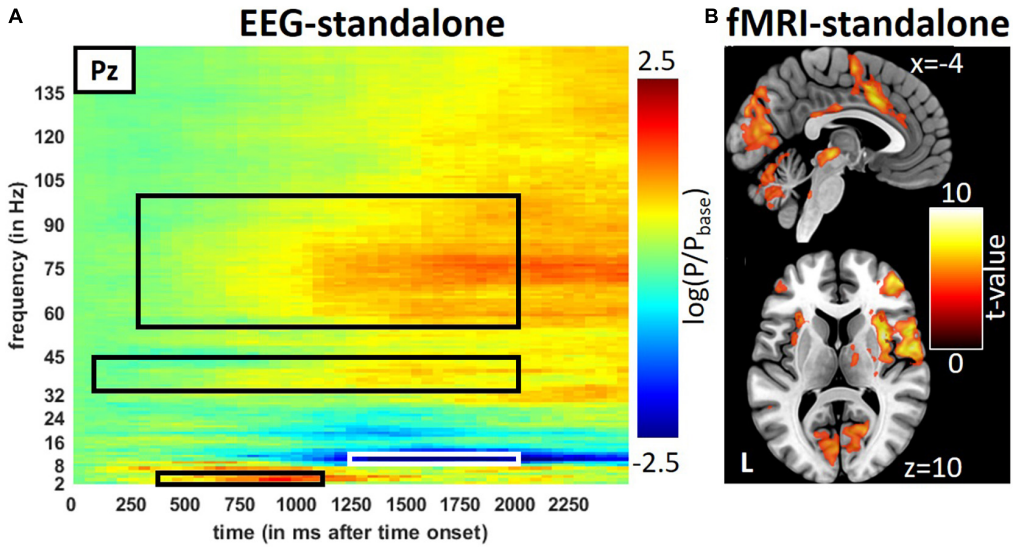

FIGURE 2 | Result from the stand-alone measurements during trigeminal nociception in EEG and fMRI. **(A)** Averages of stimulus induce power changes in time-frequency bands of trigeminal nociception in the EEG and **(B)** activity seen by the fMRI. Results of the fMRI are presented at a visualization threshold of $p < 0.001$ (uncorrected). Time-frequency windows of interest are framed in black or white.

stand-alone: 53.05 ± 18.12, fMRI stand-alone: 46.26 ± 17.47, EEG-fMRI: 45.69 ± 17.48, with an intensity scale ranging from 0 to 100) and unpleasantness (EEG stand-alone: 7.33 ± 17.17, fMRI stand-alone: 0.95 ± 15.85, EEG-fMRI: 2.02 ± 15.06, with ratings ranging from −50 to 50) ratings than the control condition (air puffs) in each of the three sessions ($p < 0.01$, Wilcoxon signed-rank tests).

Electroencephalography Features

Extracted EEG features were normally distributed (KS-test) and showed significant differences from 0 for the visual and nociceptive but not for the control condition (air). This applies to both EEG sessions (EEG stand-alone and EEG combined with fMRI), except for the alpha-band after nociception, which became insignificant in the combined session and was therefore dismissed from the fusion analyses between EEG and fMRI. The results are presented in **Table 1**. The results of the EEG for all 35 subjects in the EEG-only session, the subgroup, which also participated in the EEG-fMRI session, and the EEG-fMRI session are displayed in **Supplementary Figure 2**.

Neuroimaging

The repetitive visual stimulation revealed the expected outcome: high activity in primary visual areas and correlations between the SSEP of the EEG and occipital area activation (**Figure 3A**). Details on the results for the visual stimulation can be found in the **Supplementary Section** "Results for the Repetitive Visual Stimulation" and **Supplementary Figures 2, 3** and **Supplementary Tables 2, 3**. Similar to the visual stimulation, the trigeminal-nociceptive stimulation also replicated previously published results (Mehnert et al., 2019) on power changes in time-frequency bands of the EEG in the stand-alone session (**Figure 2A**) as well as during the simultaneous EEG-fMRI measurements (**Supplementary Figure 2**). Like with visual stimulation, painful stimulation showed an ERS in the frequency band of 3–6 Hz in the parietal-central (Pz) channel ranging from 350 to 1,150 ms after onset. The expected ERD in the alpha frequency range (8–13 Hz) follows. Simultaneously, a wide-ranging synchronization in gamma oscillations occurred, which can be separated into a lower and higher frequency range (Bader, 2019).

In the fMRI stand-alone session, the activation for trigeminal-nociceptive stimulation was similar to previously published results, i.e., FWE-corrected ($p < 0.05$) bilateral activation of pain-related cortical areas (insula, operculum, cerebellum, and somatosensory cortex) and midbrain areas (thalamus) with the dominance of the contralateral hemisphere (**Figure 2B** and **Supplementary Table 2**). An activation of the ipsilateral STN, the first relay of the trigeminal nerve in the central nervous

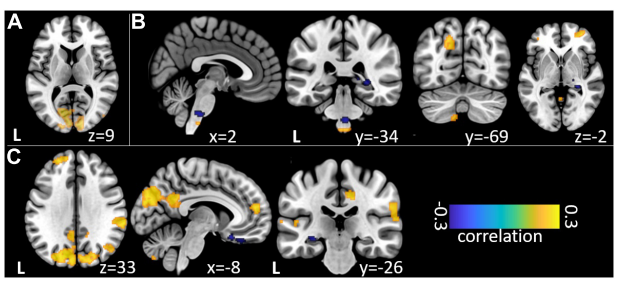

FIGURE 3 | Non-parametric correlations of trial-to-trial variance between EEG event-related band-power changes and fMRI beta time-series. **(A)** Relation of EEG SSVEP and fMRI during repetitive visual stimulation. **(B)** Relation of theta/delta and **(C)** high gamma EEG time-frequency windows during trigeminal nociception.

system, became significant at a small-volume FWE-corrected ($p < 0.05$) threshold within a sphere of 4 mm around previously published coordinates [MNI coordinates (−6, −39, −45), Stankewitz et al., 2010].

Our analysis of correlations between EEG power changes in specific time-frequency windows and beta time-series of the fMRI revealed positive relationships between the EEG theta-/delta-band (3–6 Hz) and the bilateral STN ($r = 0.20$), as well as the cerebellum (right: $r = -0.21$; left: $r = -0.18$). The frontal medial gyrus ($r = 0.23$) also showed significant positive correlations between EEG and fMRI. A negative correlation was observed in structures such as the RVM ($r = -0.21$), the entering area of the trigeminal nerve ($r = -0.22$) (Stankewitz et al., 2010), and the entorhinal area ($r = -0.34$). These results are shown in **Figure 3B** and presented detail in **Table 2**. These results persist when comparing them to the control condition of air puffs (**Supplementary Figure 4** and **Supplementary Table 4**). Additionally, the strength of these nociceptive stimulus-associated synchronizations was significantly positively correlated with the intensity evaluation of painful stimuli ($r = 0.151$, $p = 0.023$, two-sided test, **Figure 4A**).

Event-related synchronization in the high gamma-band (57–100 Hz) showed positive correlations in bilateral secondary visual association areas (right: $r = 0.25$; left: $r = 0.29$) and in somatosensory areas such as the contralateral SII ($r = 0.27$), middle cingulate cortex ($r = 0.25$), and insula ($r = 0.23$). In addition, negative correlation was found bilaterally in the primary visual cortex (right: $r = -0.24$; left: $r = -0.20$) and in the ipsilateral insula ($r = -0.23$). These results are presented in **Figure 3C** and **Table 3**. No significant correlation between fMRI beta time-series and EEG power changes in the alpha and low gamma range were observed at the chosen statistical threshold. These results persist when comparing them to the control condition of air puffs (**Supplementary Figure 4** and **Supplementary Table 4**). We further found a significantly positive correlation between the gamma-band and the individual intensity ratings ($r = 0.25$, $p < 0.001$, two-sided test, **Figure 4B**). Correlations of intensity ratings and fMRI beta time-series were not significant at an FDR-corrected threshold of $p < 0.05$.

DISCUSSION

The simultaneous recording of EEG and fMRI has received increased attention in basic research and clinical translation (Debener et al., 2006; Ullsperger and Debener, 2010; Huster et al., 2012) since it has the potency to overcome a fundamental problem in neuroimaging: the imbalance between the temporal and spatial resolution of electrophysiological and hemodynamic responses. This study serves as a bridge to translate our well-studied experimental paradigm on trigeminal nociception induced by gaseous ammonia (Stankewitz et al., 2010) to non-invasive simultaneous EEG-fMRI to gain further insights into trigeminal pain processing in humans. For this purpose, the primary goal of this study is to validate and evaluate this approach together with a novel way of fusing EEG and fMRI data.

As a first step, we reevaluated our paradigm in two stand-alone sessions of separate EEG and fMRI measurements. For both modalities, we were able to reproduce previously published results for trigeminal nociception and also for repetitive visual stimulation. We used the latter to validate our analytical approach by fusing data from both modalities during the simultaneous experimental session. Regarding trigeminal nociceptive stimuli, we observed in fMRI, in both stand-alone and simultaneous sessions, activations in areas such as the thalamus, primary and secondary somatosensory cortices, insula, and cingulate cortex. These results (**Supplementary Table 2**) are in line with previous studies dealing with the central processing of painful, in particular, trigeminal nociceptive stimuli (Peyron et al., 2000; Treede et al., 2000; Apkarian et al., 2005; Tracey and Mantyh, 2007; Stankewitz et al., 2010). The results of the time-frequency analyses in the EEG of the EEG stand-alone session reproduced previously published findings (Bader, 2019; Mehnert et al., 2019) despite a smaller cohort size (**Table 1**). The EEG results from the stand-alone session were further used as a reference to confirm the reliability of the extensive cleaning of artifacts caused by influences of EEG signals on MRI during the simultaneous collection of both modalities. In the combined EEG-fMRI session, we observed a slight reduction in the induced power, although the previously observed stimulus-associated effects were rather robust in explicit time-frequency bands (**Supplementary Figure 2**).

Non-parametric Correlation of Intertrial Variation in Electroencephalography and Functional Magnetic Resonance Imaging

In addition to the reevaluation of our results for simultaneous EEG-fMRI, we carefully validated our analytical approach for fusing both modalities with the repetitive visual stimulation,

TABLE 2 | Trial-to-trial correlations between EEG and fMRI for the trigeminal nociception for the theta/delta frequency band at electrode Pz using a statistical threshold of $p < 0.005$ (uncorrected).

Anatomical region (direction of correlation)	Left (ipsilateral)					Right (contralateral)				
	Cluster size	*x*	*y*	*z*	*r*	Cluster size	*x*	*y*	*z*	*r*
Spinal trigeminal nucleus (+)	16	−7	−36	−58	0.198	13	8	−36	−58	0.198
Cerebellum (+)	13	−12	−72	−56	0.182	13	48	−54	−54	0.216
Middle frontal gyrus (+)						156	30	48	4	0.230
Transition zone of sensory trigeminal nerve fibers (–)	30	−14	−18	−30	−0.222					
Rostral ventromedial medulla (–)		–	–	–		53	2	−34	−46	−0.211
Entorhinal area/Parahippocampus (–)		–	–	–		228	20	0	−40	−0.343

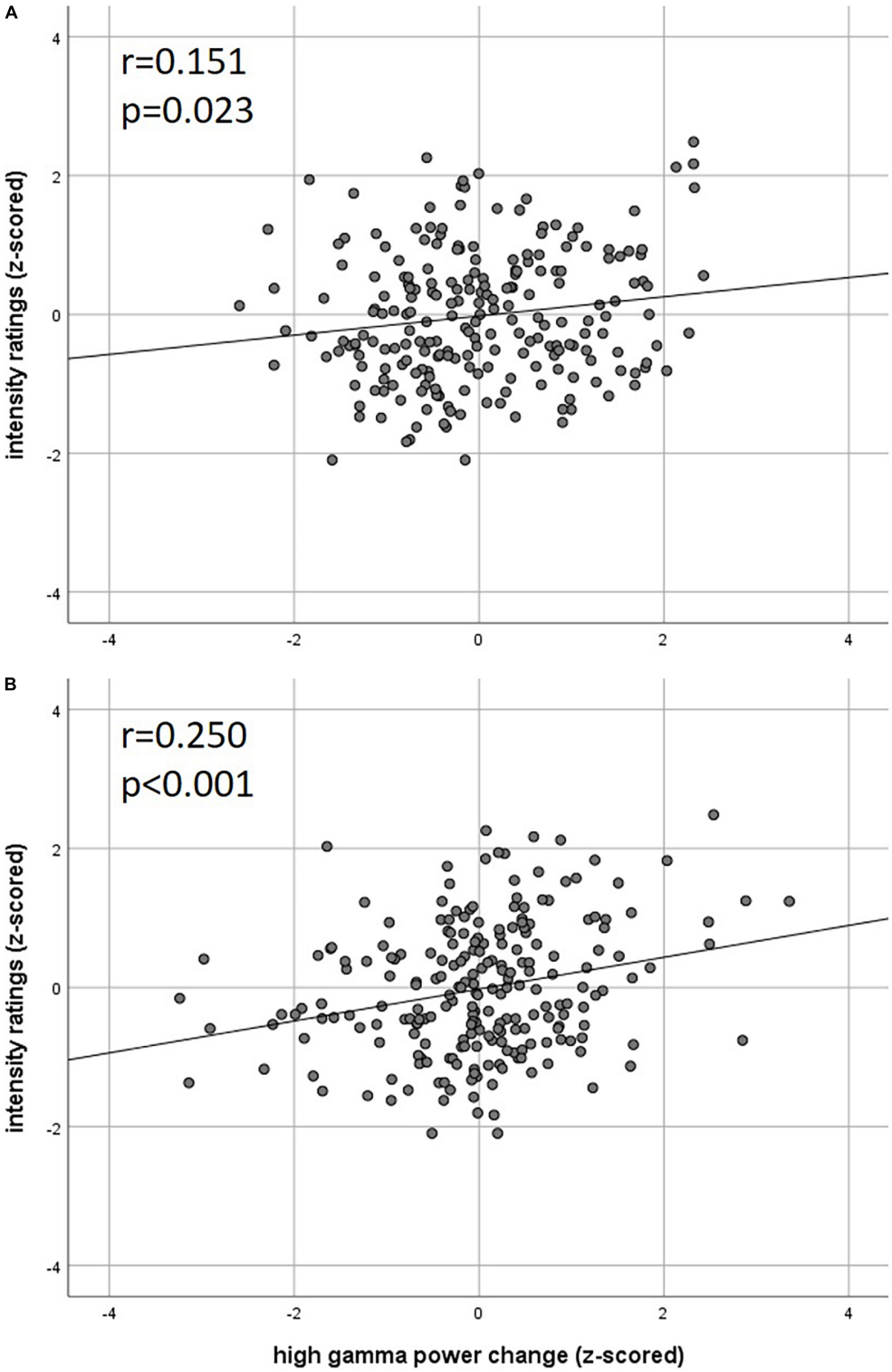

FIGURE 4 | Correlation of intensity ratings with EEG **(A)** theta power and **(B)** high gamma power (*z*-scored rating and power, two-sided Pearson's correlation).

as here the hypothesis is clear: a strong correlation between trial-to-trial variations in the fMRI of the primary visual cortex and the SSEP in the EEG. Several approaches to fuse EEG and fMRI exist (Mulert and Lemieux, 2010; Abreu et al., 2018), and they all have their advantages and disadvantages. Early EEG-fMRI studies aimed at correlating the raw (but temporally shifted

TABLE 3 | Trial-to-trial correlations between EEG and fMRI for the trigeminal nociception for the high gamma frequency band at electrode Pz using a statistical threshold of $p < 0.05$ (FDR corrected for the considered number of the voxel).

Anatomical region (direction of correlation)	Left (ipsilateral)					Right (contralateral)				
	Cluster size	x	y	z	r	Cluster size	x	y	z	r
Visual cortex (–)	22	−22	−100	−12	−0.204	148	16	−100	−12	−0.247
Insula (–)	35	−42	0	20	−0.234					
Orbital gyri (–)	235	−10	18	−24	−0.264	58	10	28	−26	−0.237
Middle temporal gyrus (+)	1907	−56	−64	14	0.299	295	52	−46	8	0.253
Insula (+)						29	36	−6	12	0.225
Middle cingulate cortex (+)						78	14	−22	36	0.246
SII (+)						356	66	−34	30	0.265
Middle occipital gyrus (+)						197	46	−68	26	0.205
Cuneus/Precuneus (+)	636	−16	−76	28	0.258	734	18	−76	28	0.217

or convolved by a hemodynamic response function) time courses of both modalities (Moosmann et al., 2003; Ritter et al., 2009), presuming a quasi-linear relationship and artifact-free data. Later approaches mostly used ERP components, which are less stable than the power changes of time-frequency bands (Varela et al., 2001). As a result, they need a high number of repetitions, which are subsequently used as an additional regressor for the fMRI analysis, mostly as a parametric modulator, which also assumes linearity (Andreou et al., 2017). Notably, EEG and fMRI measure different signals of activation, and an assumption of linearity might be misleading to research their relationship. To overcome this issue, there are multiple ways to use multivariate approaches (Dähne et al., 2015), which fuse multimodal data with the disadvantage of the need for a high number of repetitions for adequate cross-validation (Dähne et al., 2013) or a high number of conditions exploiting the function of interest (Cichy et al., 2016). Thus, these approaches seem only possible for higher cognitive functions.

As the number of repetitions and the number of conditions to deliver trigeminal pain are limited, we decided to examine non-linear rank correlations of trial-to-trial variations of both modalities in an EEG-informed fMRI fashion, where the z-transformed single-trial responses of the individual participants were concatenated. To achieve this, the stimulation-associated responses in the EEG of previously published time-frequency windows were correlated with estimates of the hemodynamic responses of the individual stimuli from the fMRI. Our approach has the advantage that relatively few trials are necessary, and it is easily extendable to a multivariate fashion, e.g., by using a support vector regression (Bogler et al., 2014) during the searchlight approach (Allefeld and Haynes, 2014).

Trigeminal Nociception in Electroencephalography-Informed Functional Magnetic Resonance Imaging

Our main finding during trigeminal nociception is a significant relationship between the theta/delta frequency bands, which corresponds to the time-frequency equivalent of a nociceptive evoked potential (Makeig et al., 2004) and is also correlated to the individually perceived intensity of the painful stimulation and the STN as well as the RVM. As hypothesized, this time-frequency window shows a significant correlation with the corresponding activation estimates in certain brainstem regions (see **Figure 3B** and **Table 2**) including the STN, the first relay station of the trigeminal peripheral nerve (Borsook et al., 2003; Stankewitz et al., 2010; Schulte et al., 2016). The result is that the variability of the EEG signal is more covariant with STN activation than with other somatosensory discriminating regions of the pain matrix, such as SI or SII, which could lead to the conclusion that the ascending pain signal is processed independently of the somatotopic assignment in SI (Petrovic et al., 2004). The negative relation with the RVM, which is part of the descending antinociceptive system (Heinricher et al., 1989; Ossipov et al., 2010), contrasts this positive relation. This negative association might reflect the results of the animal study by Heinricher et al. (1989): they showed that the spontaneous activity of "on" and "off" cells in the RVM is modulated by painful stimuli at a very early stage of central pain processing. An opposite correlation of the nociceptive signal from the STN to the RVM with decreasing strength of the EP suggests that, in addition to nociception, antinociceptive modulation is initiated simultaneously to (pro)nociceptive ascending pain processing. In conclusion, the strength of the pain-induced early evoked synchronizations in the theta/delta frequency band, which is the time-frequency equivalent of the nociceptive evoked potential, indicates an early trial-to-trial modulation of trigeminal nociceptive stimuli already at the brainstem level.

In the gamma frequency range, we observed a correlation between EEG and fMRI in numerous cortical structures. In addition to positive correlations with regions generally associated with the pain matrix, such as the contralateral insula, middle cingulate cortex, and SII, extra-sensory cortical structures such as visual (cuneus/precuneus) and visual-associative areas (temporal gyrus, occipital medial gyrus) also showed a positive correlation between the gamma power modulation in EEG and the single-trial activation in fMRI (**Figure 3C** and **Table 3**). This can be explained by the full range of neuronal structures for processing extrinsic stimuli that are inevitably obtained by extending the time window of observation (Senkowski et al., 2014). Furthermore, it has been shown that fMRI results and gamma power changes after nociceptive input are not specific to pain and can also be induced by other attentive paradigms (Legrain et al., 2011) and hence reflect a more general salience system, which can also explain the correlation to visual and frontal areas. However, the individual variability in the strength of nociceptive-evoked

gamma oscillations suggests that central sensory processing occurs at both motivational-affective and purely sensory discriminatory levels. Consequently, power changes in this time-frequency window are significantly positively correlated with individuals' intensity ratings (**Figure 4B**), echoing the previous findings (Gross et al., 2007; Hauck et al., 2007; Schulz et al., 2012; Zhang et al., 2012; Tu et al., 2016). This is corroborated by the positive correlations of this gamma oscillation with BOLD signals in areas of the lateral as well as the medial pain pathway. Interestingly, the contralateral and ipsilateral insula correlate in opposite directions with the EEG's power changes. This might be explained by feedback transmission, which could be dependent on the stimulated side. In conclusion, the gamma frequency range might not exclusively indicate the processing of nociceptive-sensory stimuli but reveals associations to a wide range of structures, suggesting both motivational-affective and sensory-discriminative processing recruiting associative areas (secondary visual cortex, medial occipital gyrus, temporal gyrus), while primary structures (primary visual cortex) show an opposite direction of influence on both signals.

Conclusion

Our study validates an experimental trigeminal nociceptive paradigm for simultaneous EEG-fMRI and a novel approach for EEG-informed fMRI analysis. While our findings on the experimental side should be extended to clinical cohorts such as migraine or cluster headache patients, our analytical approach may be adapted to any multimodal data analysis and possibly extended to a multivariate approach.

DATA AVAILABILITY STATEMENT

The raw data supporting the conclusions of this article will be made available by the authors, to the researchers meeting the criteria to access the confidential data.

ETHICS STATEMENT

The studies involving human participants were reviewed and approved by the Ärztekammer Hamburg, PV 4896. The patients/participants provided their written informed consent to participate in this study.

AUTHOR CONTRIBUTIONS

JM and AM designed the experiment. HB and K-PP collected the data. JM and HB analyzed the data. All authors wrote and reviewed the final manuscript.

FUNDING

This study was supported by the Deutsche Forschungsgemeinschaft (DFG, German Research Foundation) – SFB936-178316478 – A5 (AM).

ACKNOWLEDGMENTS

We thank our volunteers for participating and our MRI assistants Kathrin Bergholz, Katrin Wendt, and Waldemar Schwarz for their help with this study.

SUPPLEMENTARY MATERIAL

The Supplementary Material for this article can be found online at: https://www.frontiersin.org/articles/10.3389/fnins.2022.802239/full#supplementary-material

REFERENCES

Abdulrahman, H., and Henson, R. N. (2016). Effect of trial-to-trial variability on optimal event-related fMRI design: implications for beta-series correlation and multi-voxel pattern analysis. *Neuroimage* 125, 756–766. doi: 10.1016/j.neuroimage.2015.11.009

Abreu, R., Leal, A., and Figueiredo, P. (2018). EEG-informed fMRI: a review of data analysis methods. *Front. Hum. Neurosci.* 12:29. doi: 10.3389/fnhum.2018.00029

Allefeld, C., and Haynes, J.-D. (2014). Searchlight-based multi-voxel pattern analysis of fMRI by cross-validated MANOVA. *NeuroImage* 89, 345–357. doi: 10.1016/j.neuroimage.2013.11.043

Allen, P. J., Josephs, O., and Turner, R. (2000). A method for removing imaging artifact from continuous EEG recorded during functional MRI. *Neuroimage* 12, 230–239. doi: 10.1006/nimg.2000.0599

Allen, P. J., Polizzi, G., Krakow, K., Fish, D. R., and Lemieux, L. (1998). Identification of EEG events in the MR scanner: the problem of pulse artifact and a method for its subtraction. *Neuroimage* 8, 229–239. doi: 10.1006/nimg.1998.0361

Andreou, C., Frielinghaus, H., Rauh, J., Mußmann, M., Vauth, S., Braun, P., et al. (2017). Theta and high-beta networks for feedback processing: a simultaneous EEG–fMRI study in healthy male subjects. *Transl. Psychiatry* 7:e1016. doi: 10.1038/tp.2016.287

Apkarian, A. V., Bushnell, M. C., Treede, R.-D., and Zubieta, J.-K. (2005). Human brain mechanisms of pain perception and regulation in health and disease. *Eur. J. Pain* 9, 463–484. doi: 10.1016/j.ejpain.2004.11.001

Ashburner, J., and Friston, K. J. (2005). Unified segmentation. *Neuroimage* 26, 839–851. doi: 10.1016/j.neuroimage.2005.02.018

Bader, D. (2019). *Raum, Zeit und Frequenz: EEG-Dynamiken der Migräne*. Available online at: http://ediss.sub.uni-hamburg.de/volltexte/2019/9885 (accessed August 26, 2019).

Bogler, C., Mehnert, J., Steinbrink, J., and Haynes, J.-D. (2014). Decoding vigilance with NIRS. *PLoS one* 9:e101729. doi: 10.1371/journal.pone.0101729

Borsook, D., DaSilva, A. F. M., Ploghaus, A., and Becerra, L. (2003). Specific and somatotopic functional magnetic resonance imaging activation in the trigeminal ganglion by brush and noxious heat. *J. Neurosci.* 23, 7897–7903.

Brinkmeyer, J., Mobascher, A., Warbrick, T., Musso, F., Wittsack, H.-J., Saleh, A., et al. (2010). Dynamic EEG-informed fMRI modeling of the pain matrix using 20-ms root mean square segments. *Hum Brain Mapp* 31, 1702–1712. doi: 10.1002/hbm.20967

Christmann, C., Koeppe, C., Braus, D. F., Ruf, M., and Flor, H. (2007). A simultaneous EEG–fMRI study of painful electric stimulation. *NeuroImage* 34, 1428–1437. doi: 10.1016/j.neuroimage.2006.11.006

Cichy, R. M., Pantazis, D., and Oliva, A. (2016). Similarity-based fusion of MEG and fMRI reveals spatio-temporal dynamics in human cortex during

visual object recognition. *Cereb Cortex* 26, 3563–3579. doi: 10.1093/cercor/bhw135

Dähne, S., Bießmann, F., Meinecke, F. C., Mehnert, J., Fazli, S., and Müller, K. R. (2013). Integration of multivariate data streams with bandpower signals. *IEEE Transac. Multimedia* 15, 1001–1013. doi: 10.1109/TMM.2013.2250267

Dähne, S., Bießmann, F., Samek, W., Haufe, S., Goltz, D., Gundlach, C., et al. (2015). Multivariate machine learning methods for fusing multimodal functional neuroimaging data. *Proc. IEEE* 103, 1507–1530. doi: 10.1109/JPROC.2015.2425807

David, O., Kilner, J. M., and Friston, K. J. (2006). Mechanisms of evoked and induced responses in MEG/EEG. *NeuroImage* 31, 1580–1591. doi: 10.1016/j.neuroimage.2006.02.034

Debener, S., Ullsperger, M., Siegel, M., and Engel, A. K. (2006). Single-trial EEG–fMRI reveals the dynamics of cognitive function. *Trends Cogn. Sci.* 10, 558–563. doi: 10.1016/j.tics.2006.09.010

Deckers, R. H. R., van Gelderen, P., Ries, M., Barret, O., Duyn, J. H., Ikonomidou, V. N., et al. (2006). An adaptive filter for suppression of cardiac and respiratory noise in MRI time series data. *NeuroImage* 33, 1072–1081. doi: 10.1016/j.neuroimage.2006.08.006

Goadsby, P. J., Holland, P. R., Martins-Oliveira, M., Hoffmann, J., Schankin, C., and Akerman, S. (2017). Pathophysiology of migraine: a disorder of sensory processing. *Physiol. Rev.* 97, 553–622. doi: 10.1152/physrev.00034.2015

Gross, J., Schnitzler, A., Timmermann, L., and Ploner, M. (2007). Gamma oscillations in human primary somatosensory cortex reflect pain perception. *PLoS Biol.* 5:e133. doi: 10.1371/journal.pbio.0050133

Grosser, K., Oelkers, R., Hummel, T., Geisslinger, G., Brune, K., Kobal, G., et al. (2000). Olfactory and trigeminal event-related potentials in migraine. *Cephalalgia* 20, 621–631.

Hassler, U., Trujillo Barreto, N., and Gruber, T. (2011). Induced gamma band responses in human EEG after the control of miniature saccadic artifacts. *NeuroImage* 57, 1411–1421. doi: 10.1016/j.neuroimage.2011.05.062

Hauck, M., Lorenz, J., and Engel, A. K. (2007). Attention to painful stimulation enhances γ-band activity and synchronization in human sensorimotor cortex. *J. Neurosci.* 27, 9270–9277. doi: 10.1523/JNEUROSCI.2283-07.2007

Heinricher, M. M., Barbaro, N. M., and Fields, H. L. (1989). Putative nociceptive modulating neurons in the rostral ventromedial medulla of the rat: firing of on- and off-cells is related to nociceptive responsiveness. *Somatosens. Mot. Res.* 6, 427–439. doi: 10.3109/08990228909144685

Huart, C., Legrain, V., Hummel, T., Rombaux, P., and Mouraux, A. (2012). Time-frequency analysis of chemosensory event-related potentials to characterize the cortical representation of odors in humans. *PLoS One* 7:e33221. doi: 10.1371/journal.pone.0033221

Hummel, T., and Kobal, G. (1992). Differences in human evoked potentials related to olfactory or trigeminal chemosensory activation. *Electroencephalogr. Clin. Neurophysiol.* 84, 84–89. doi: 10.1016/0168-5597(92)90070-r

Huster, R. J., Debener, S., Eichele, T., and Herrmann, C. S. (2012). Methods for simultaneous EEG-fMRI: an introductory review. *J. Neurosci.* 32, 6053–6060. doi: 10.1523/JNEUROSCI.0447-12.2012

Iannetti, G. D., and Mouraux, A. (2010). "Combining EEG and fMRI in pain research," in *EEG - fMRI: Physiological Basis, Technique, and Applications*, eds C. Mulert and L. Lemieux (Berlin: Springer), 365–384. doi: 10.1007/978-3-540-87919-0_18

Iannetti, G. D., Niazy, R. K., Wise, R. G., Jezzard, P., Brooks, J. C. W., Zambreanu, L., et al. (2005). Simultaneous recording of laser-evoked brain potentials and continuous, high-field functional magnetic resonance imaging in humans. *NeuroImage* 28, 708–719. doi: 10.1016/j.neuroimage.2005.06.060

Kriegeskorte, N., Goebel, R., and Bandettini, P. (2006). Information-based functional brain mapping. *Proc. Natl. Acad. Sci. U.S.A.* 103, 3863–3868. doi: 10.1073/pnas.0600244103

Legrain, V., Iannetti, G. D., Plaghki, L., and Mouraux, A. (2011). The pain matrix reloaded: a salience detection system for the body. *Progr. Neurobiol.* 93, 111–124. doi: 10.1016/j.pneurobio.2010.10.005

Litvak, V., Mattout, J., Kiebel, S., Phillips, C., Henson, R., Kilner, J., et al. (2011). EEG and MEG data analysis in SPM8. *Compu. Intell. Neurosci.* 2011:e852961. doi: 10.1155/2011/852961

Makeig, S., Debener, S., Onton, J., and Delorme, A. (2004). Mining event-related brain dynamics. *Trends Cogn. Sci.* 8, 204–210. doi: 10.1016/j.tics.2004.03.008

Manjón, J. V., Coupé, P., Martí-Bonmatí, L., Collins, D. L., and Robles, M. (2010). Adaptive non-local means denoising of MR images with spatially varying noise levels. *J. Magn. Reson. Imaging* 31, 192–203. doi: 10.1002/jmri.22003

May, A. (2013). Pearls and pitfalls: neuroimaging in headache. *Cephalalgia* 33, 554–565. doi: 10.1177/0333102412467513

May, A., Schulte, L. H., Nolte, G., and Mehnert, J. (2020). Partial similarity reveals dynamics in brainstem-midbrain networks during trigeminal nociception. *Brain Sci.* 10:603. doi: 10.3390/brainsci10090603

Mayhew, S. D., Hylands-White, N., Porcaro, C., Derbyshire, S. W. G., and Bagshaw, A. P. (2013). Intrinsic variability in the human response to pain is assembled from multiple, dynamic brain processes. *NeuroImage* 75, 68–78. doi: 10.1016/j.neuroimage.2013.02.028

Mehnert, J., and May, A. (2019). Functional and structural alterations in the migraine cerebellum. *J. Cereb. Blood Flow Metab.* 39, 730–739. doi: 10.1177/0271678X17722109

Mehnert, J., Bader, D., Nolte, G., and May, A. (2019). Visual input drives increased occipital responsiveness and harmonized oscillations in multiple cortical areas in migraineurs. *NeuroImage Clin.* 23:101815. doi: 10.1016/j.nicl.2019.101815

Mehnert, J., Hebestreit, J., and May, A. (2018). Cortical and subcortical alterations in medication overuse headache. *Front. Neurol.* 9:499. doi: 10.3389/fneur.2018.00499

Mehnert, J., Schulte, L., Timmann, D., and May, A. (2017). Activity and connectivity of the cerebellum in trigeminal nociception. *NeuroImage* 150, 112–118.

Mitra, P. P., and Pesaran, B. (1999). Analysis of dynamic brain imaging data. *Biophys. J.* 76, 691–708. doi: 10.1016/S0006-3495(99)77236-X

Mobascher, A., Brinkmeyer, J., Warbrick, T., Musso, F., Wittsack, H. J., Saleh, A., et al. (2009a). Laser-evoked potential P2 single-trial amplitudes covary with the fMRI BOLD response in the medial pain system and interconnected subcortical structures. *NeuroImage* 45, 917–926. doi: 10.1016/j.neuroimage.2008.12.051

Mobascher, A., Brinkmeyer, J., Warbrick, T., Musso, F., Wittsack, H. J., Stoermer, R., et al. (2009b). Fluctuations in electrodermal activity reveal variations in single trial brain responses to painful laser stimuli — A fMRI/EEG study. *NeuroImage* 44, 1081–1092. doi: 10.1016/j.neuroimage.2008.09.004

Moosmann, M., Ritter, P., Krastel, I., Brink, A., Thees, S., Blankenburg, F., et al. (2003). Correlates of alpha rhythm in functional magnetic resonance imaging and near infrared spectroscopy. *Neuroimage* 20, 145–158. doi: 10.1016/S1053-8119(03)00344-6

Mulert, C., and Lemieux, L. (eds) (2010). *EEG - fMRI: Physiological Basis, Technique, and Applications*. Berlin: Springer-Verlag. doi: 10.1007/978-3-540-87919-0

Norcia, A. M., Appelbaum, L. G., Ales, J. M., Cottereau, B. R., and Rossion, B. (2015). The steady-state visual evoked potential in vision research: a review. *J. Vis.* 15:4. doi: 10.1167/15.6.4

Olejniczak, P. (2006). Neurophysiologic basis of EEG. *J. Clin. Neurophysiol.* 23, 186–189.

Oostenveld, R., Fries, P., Maris, E., and Schoffelen, J.-M. (2011). FieldTrip: open source software for advanced analysis of MEG, EEG, and invasive electrophysiological data. *Comput. Intell. Neurosci.* 2011:156869. doi: 10.1155/2011/156869

Ossipov, M. H., Dussor, G. O., and Porreca, F. (2010). Central modulation of pain. *J. Clin. Invest.* 120, 3779–3787. doi: 10.1172/JCI43766

Parra, L. C., Spence, C. D., Gerson, A. D., and Sajda, P. (2005). Recipes for the linear analysis of EEG. *Neuroimage* 28, 326–341. doi: 10.1016/j.neuroimage.2005.05.032

Petrovic, P., Petersson, K. M., Hansson, P., and Ingvar, M. (2004). Brainstem involvement in the initial response to pain. *NeuroImage* 22, 995–1005. doi: 10.1016/j.neuroimage.2004.01.046

Peyron, R., Laurent, B., and García-Larrea, L. (2000). Functional imaging of brain responses to pain. a review and meta-analysis (2000). *Neurophysiol. Clin.* 30, 263–288. doi: 10.1016/S0987-7053(00)00227-6

Ploner, M., Gross, J., Timmermann, L., Pollok, B., and Schnitzler, A. (2006). Pain suppresses spontaneous brain rhythms. *Cereb. Cortex* 16, 537–540. doi: 10.1093/cercor/bhj001

Rissman, J., Gazzaley, A., and D'Esposito, M. (2004). Measuring functional connectivity during distinct stages of a cognitive task. *Neuroimage* 23, 752–763. doi: 10.1016/j.neuroimage.2004.06.035

Ritter, P., Moosmann, M., and Villringer, A. (2009). Rolandic alpha and beta EEG rhythms' strengths are inversely related to fMRI-BOLD signal in primary somatosensory and motor cortex. *Hum. Brain Mapp.* 30, 1168–1187. doi: 10.1002/hbm.20585

Roberts, K., Papadaki, A., Gonçalves, C., Tighe, M., Atherton, D., Shenoy, R., et al. (2008). Contact heat evoked potentials using simultaneous EEG and fMRI and their correlation with evoked pain. *BMC Anesthesiol.* 8:8. doi: 10.1186/1471-2253-8-8

Scarff, C. J., Reynolds, A., Goodyear, B. G., Ponton, C. W., Dort, J. C., and Eggermont, J. J. (2004). Simultaneous 3-T fMRI and high-density recording of human auditory evoked potentials. *NeuroImage* 23, 1129–1142. doi: 10.1016/j.neuroimage.2004.07.035

Schulte, L. H., Allers, A., and May, A. (2017). Hypothalamus as a mediator of chronic migraine: evidence from high-resolution fMRI. *Neurology* 88, 2011–2016. doi: 10.1212/WNL.0000000000003963

Schulte, L. H., Sprenger, C., and May, A. (2016). Physiological brainstem mechanisms of trigeminal nociception: an fMRI study at 3T. *NeuroImage* 124, 518–525. doi: 10.1016/j.neuroimage.2015.09.023

Schulz, E., Zherdin, A., Tiemann, L., Plant, C., and Ploner, M. (2012). Decoding an individual's sensitivity to pain from the multivariate analysis of EEG Data. *Cereb. Cortex* 22, 1118–1123. doi: 10.1093/cercor/bhr186

Senkowski, D., Höfle, M., and Engel, A. K. (2014). Crossmodal shaping of pain: a multisensory approach to nociception. *Trends Cogn. Sci.* 18, 319–327. doi: 10.1016/j.tics.2014.03.005

Stankewitz, A., Voit, H. L., Bingel, U., Peschke, C., and May, A. (2010). A new trigemino-nociceptive stimulation model for event-related fMRI. *Cephalalgia* 30, 475–485. doi: 10.1111/j.1468-2982.2009.01968.x

Taesler, P., and Rose, M. (2016). Prestimulus theta oscillations and connectivity modulate pain perception. *J. Neurosci.* 36, 5026–5033. doi: 10.1523/JNEUROSCI.3325-15.2016

Thomson, D. J. (1982). Spectrum estimation and harmonic analysis. *Proc. IEEE* 70, 1055–1096. doi: 10.1109/PROC.1982.12433

Tracey, I., and Mantyh, P. W. (2007). The cerebral signature for pain perception and its modulation. *Neuron* 55, 377–391. doi: 10.1016/j.neuron.2007.07.012

Treede, R.-D., Apkarian, V. A., Bromm, B., Greenspan, J. D., and Lenz, F. A. (2000). Cortical representation of pain: functional characterization of nociceptive areas near the lateral sulcus. *Pain* 87, 113–119. doi: 10.1016/S0304-3959(00)00350-X

Tu, Y., Zhang, Z., Tan, A., Peng, W., Hung, Y. S., Moayedi, M., et al. (2016). Alpha and gamma oscillation amplitudes synergistically predict the perception of forthcoming nociceptive stimuli. *Hum. Brain Mapp.* 37, 501–514. doi: 10.1002/hbm.23048

Uji, M., Wilson, R., Francis, S. T., Mullinger, K. J., and Mayhew, S. D. (2018). Exploring the advantages of multiband fMRI with simultaneous EEG to investigate coupling between gamma frequency neural activity and the BOLD response in humans. *Hum. Brain Mapp.* 39, 1673–1687. doi: 10.1002/hbm.23943

Ullsperger, M., and Debener, S. (2010). *Simultaneous EEG and fMRI: Recording, Analysis, and Application*. Oxford: Oxford University Press.

Varela, F., Lachaux, J.-P., Rodriguez, E., and Martinerie, J. (2001). The brainweb: phase synchronization and large-scale integration. *Nat. Rev. Neurosci.* 2, 229–239. doi: 10.1038/35067550

Zhang, Z. G., Hu, L., Hung, Y. S., Mouraux, A., and Iannetti, G. D. (2012). Gamma-band oscillations in the primary somatosensory cortex—a direct and obligatory correlate of subjective pain intensity. *J. Neurosci.* 32, 7429–7438. doi: 10.1523/JNEUROSCI.5877-11.2012

Conflict of Interest: The study was funded by the Deutsche Forschungsgemeinschaft (DFG, German Research Foundation) – SFB936-178316478 – A5 (AM). The funder was not involved in the study design, collection, analysis, interpretation of data, the writing of this article or the decision to submit it for publication.

The remaining authors declare that the research was conducted in the absence of any commercial or financial relationships that could be construed as a potential conflict of interest.

frontiers | Frontiers in Neuroscience

ORIGINAL RESEARCH
published: 23 June 2022
doi: 10.3389/fnins.2022.921922

Evaluating the Safety of Simultaneous Intracranial Electroencephalography and Functional Magnetic Resonance Imaging Acquisition Using a 3 Tesla Magnetic Resonance Imaging Scanner

Yuya Fujita[1], Hui Ming Khoo[1], Miki Hirayama[2], Masaaki Kawahara[2], Yoshihiro Koyama[2], Hiroyuki Tarewaki[2], Atsuko Arisawa[3], Takufumi Yanagisawa[1], Naoki Tani[1], Satoru Oshino[1], Louis Lemieux[4] and Haruhiko Kishima[1]*

[1] Department of Neurosurgery, Osaka University Graduate School of Medicine, Suita, Japan, [2] Department of Radiology, Osaka University Hospital, Suita, Japan, [3] Department of Radiology, Osaka University Graduate School of Medicine, Suita, Japan, [4] Department of Clinical and Experimental Epilepsy, UCL Queen Square Institute of Neurology, London, United Kingdom

OPEN ACCESS

Edited by:
Surjo R. Soekadar, Charité – Universitätsmedizin Berlin, Germany

Reviewed by:
Soumyajit Mandal, Brookhaven National Laboratory (DOE), United States
Elias Ebrahimzadeh, Institute for Research in Fundamental Sciences (IPM), Iran

***Correspondence:**
Hui Ming Khoo
khoo@nsurg.med.osaka-u.ac.jp

Specialty section:
This article was submitted to Brain Imaging Methods, a section of the journal Frontiers in Neuroscience

Received: 16 April 2022
Accepted: 25 May 2022
Published: 23 June 2022

Citation:
Fujita Y, Khoo HM, Hirayama M, Kawahara M, Koyama Y, Tarewaki H, Arisawa A, Yanagisawa T, Tani N, Oshino S, Lemieux L and Kishima H (2022) Evaluating the Safety of Simultaneous Intracranial Electroencephalography and Functional Magnetic Resonance Imaging Acquisition Using a 3 Tesla Magnetic Resonance Imaging Scanner. Front. Neurosci. 16:921922. doi: 10.3389/fnins.2022.921922

Background: The unsurpassed sensitivity of intracranial electroencephalography (icEEG) and the growing interest in understanding human brain networks and ongoing activities in health and disease have make the simultaneous icEEG and functional magnetic resonance imaging acquisition (icEEG-fMRI) an attractive investigation tool. However, safety remains a crucial consideration, particularly due to the impact of the specific characteristics of icEEG and MRI technologies that were safe when used separately but may risk health when combined. Using a clinical 3-T scanner with body transmit and head-receive coils, we assessed the safety and feasibility of our icEEG-fMRI protocol.

Methods: Using platinum and platinum-iridium grid and depth electrodes implanted in a custom-made acrylic-gel phantom, we assessed safety by focusing on three factors. First, we measured radio frequency (RF)-induced heating of the electrodes during fast spin echo (FSE, as a control) and the three sequences in our icEEG-fMRI protocol. Heating was evaluated with electrodes placed orthogonal or parallel to the static magnetic field. Using the configuration with the greatest heating observed, we then measured the total heating induced in our protocol, which is a continuous 70-min icEEG-fMRI session comprising localizer, echo-planar imaging (EPI), and magnetization-prepared rapid gradient-echo sequences. Second, we measured the gradient switching-induced voltage using configurations mimicking electrode implantation in the frontal and temporal lobes. Third, we assessed the gradient switching-induced electrode movement by direct visual detection and image analyses.

Results: On average, RF-induced local heating on the icEEG electrode contacts tested were greater in the orthogonal than parallel configuration, with a maximum increase of 0.2°C during EPI and 1.9°C during FSE. The total local heating was below the 1°C safety limit across all contacts tested during the 70-min icEEG-fMRI session. The induced voltage was within the 100-mV safety limit regardless of the configuration. No gradient switching-induced electrode displacement was observed.

Conclusion: We provide evidence that the additional health risks associated with heating, neuronal stimulation, or device movement are low when acquiring fMRI at 3 T in the presence of clinical icEEG electrodes under the conditions reported in this study. High specific absorption ratio sequences such as FSE should be avoided to prevent potential inadvertent tissue heating.

Keywords: MRI, simultaneous intracranial EEG-fMRI, subdural electrode, depth electrode, 3 tesla, fMRI, epilepsy, safety

INTRODUCTION

There are several modalities used to analyze brain activity. Scalp electroencephalography (EEG) is a simple method for measuring brain signals with high temporal resolution. However, EEG source localization is generally difficult for the superficial activity that EEG can actually detect, in particular if the generator is widespread and complex. Functional magnetic resonance imaging (fMRI) focuses on the changes in cerebral blood flow, using blood oxygen level-dependent contrast for probing brain activity, regardless of the coverage and indifference to the extent and complexity of the source. By effectively combining their advantages, simultaneous EEG and fMRI measurement (EEG-fMRI) is an attractive investigation tool for those who are interested in understanding the relationship between the two modalities. For example, EEG-fMRI is used in epilepsy to understand the mechanisms underlying the generation of epileptic activities, spontaneous brain activities that are unpredictable (Gotman et al., 2006; Khoo et al., 2017). It is also used in the field of neuroscience to study the hemodynamic correlates of event-related potentials and to study neurofeedback (Mele et al., 2019). However, activities in the high-frequency band, markers of most cognitive neuronal activities, are difficult to record on scalp EEG, and the information gained from these activities are also limited for the following reasons. (1) Spectral power follows a 1/f distribution across frequencies and thus high gamma activities are generally lower in amplitude than that of low frequency activities (Baranauskas et al., 2012; Jaspers-Fayer et al., 2012; Li et al., 2019). (2) The skull further attenuates the amplitude of EEG, generally resulting in a low signal-to-noise ratio especially in the high-frequency band. (3) High-frequency activities overlap the spectral bandwidth of muscle activities. (4) Scalp EEG has low sensitivity to activity generated deep in the brain as it detects mostly neocortical activity (Wennberg et al., 2011). Intracranial EEG (icEEG) electrodes, implanted to delineate the epileptogenic zone of patients with drug-resistant epilepsy prior to resection, provide increased sensitivity to activities in the high-frequency range, while allowing detection of low amplitude activities in a lower frequency range (i.e., epileptiform activities). Hence, the sensitivity of icEEG acquired simultaneously with fMRI provides a good opportunity to study neuronal activities more substantively (Vulliemoz et al., 2011; Cunningham et al., 2012; Tehrani et al., 2021).

There are three potential hazards associated with the introduction of icEEG electrodes to the magnetic resonance imaging (MRI) environment (Carmichael et al., 2010; Boucousis et al., 2012): radiofrequency (RF)-induced heating of brain tissue surrounding the electrodes, in which the temperature increase of a device is conservatively limited to within 1°C of the surrounding tissue according to current safety standards (IEC, 2015); neural stimulation or tissue damage caused by induced currents in low-resistance circuits generated by magnetic field fluctuations such as gradient switching (Georgi et al., 2004; Wang et al., 2018), in which a voltage exceeding 100 mV at a frequency less than 10 kHz can cause neural stimulation (Georgi et al., 2004); and tissue damage due to uncontrolled electrode movement caused by forces or torques induced by the static or dynamic magnetic field on the electrode.

Although deep brain stimulation (DBS) electrode (MRI-conditional for 3 T) and icEEG electrodes from a specific manufacturer (DIXI medical, MRI-conditional for 1.5–3 T) are allowed for MRI under the restrictive guidelines of manufacturers, most commercial icEEG electrodes have yet to be formally approved for MRI (Ciumas et al., 2014; Hawsawi et al., 2017). Nevertheless, structural imaging of icEEG electrodes has been well documented in both clinical and research settings without adverse events at 1.5 T (Davis et al., 1999; Carmichael et al., 2007, 2008; Larson et al., 2008; Nazzaro et al., 2010; Weise et al., 2010; Vulliemoz et al., 2011; Zrinzo et al., 2011; Hawsawi et al., 2017, 2020; Erhardt et al., 2018; Hall and Khoo, 2018; Yazdani et al., 2021). Imaging of DBS electrodes at 3 T has also been documented in 10 patients with a mild temperature increase and concluded to be potentially safe (Sammartino et al., 2017). Due to the potential of increased risk, clinical imaging of icEEG electrodes at 3 T has never been documented (Hawsawi et al., 2017). Nonetheless, simultaneous acquisition of icEEG and fMRI (icEEG-fMRI) has been documented in a few human studies at 1.5 T performed in two institutions (Vulliemoz et al., 2011;

Carmichael et al., 2012; Chaudhary et al., 2016; Ridley et al., 2017; Saignavongs et al., 2017; Liu et al., 2022) and at 3 T in another (Aghakhani et al., 2015; Tehrani et al., 2021), using a local imaging protocol developed in each institution for research, without reports of significant adverse events to date. Hence, icEEG-fMRI appears to pose a low health risk to patients provided that site-specific precautions are taken.

However, findings of the icEEG-fMRI safety studies that justified the choice of MRI field strength by two of the aforementioned institutions, appeared to be conflicting: significant RF-induced heating at 3 T was documented in one (Carmichael et al., 2008) but not in the other (Boucousis et al., 2012) even though the same type of electrodes (platinum-iridium electrodes from Ad-Tech Medical, Racine, WI, United States) has been used. This difference can be attributed to various factors given the difference in the equipment and conditions used in each institution and thus imaging of icEEG electrodes at 3 T remains controversial. The logical conclusion on the safety of any icEEG-fMRI acquisition is that it is dependent on specific conditions and a careful assessment must be made for any significant deviation from the tested conditions, including electrode implantation and wiring configurations, scanner type and field strength, type of RF coil (body or head transmit), MRI scanning protocol and sequences (Carmichael et al., 2008, 2010).

In this study, we assessed the feasibility of performing icEEG-fMRI over the entire course of a typical prolonged acquisition that lasted for approximately 70 min in a GE Signa Architect UPG 3 T MRI scanner with a body transmit head-receive coil, using grid and depth electrodes commercially available in Japan. To this effect, following previous work on the safety of icEEG-fMRI (Carmichael et al., 2008, 2010; Boucousis et al., 2012), we performed temperature, voltage, and electrode movement measurements on a standard gel and acrylic phantom. If proven feasible, the findings may serve as a guidance for developing clinical combined icEEG-fMRI protocols at 3 T and provide another piece of evidence regarding the feasibility of icEEG-fMRI at 3 T, an MRI field strength that is becoming the standard in clinical and research settings due to the improved signal-to-noise ratio that it offers.

MATERIALS AND METHODS

Phantom Preparation

To better reflect actual icEEG-fMRI acquisitions, we used a phantom made of two elements: a spherical head and a rectangular torso with electrical conductivity and thermal characteristics similar to those of human tissue. The head part of the phantom was made by combining two custom-made hollow hemispherical acrylic shells (diameter = 150 mm), in which one of them had an opening (diameter = 50 mm) on the top. We used a commercially available polypropylene box (42 L: width 362 mm, length 617 mm, height 185 mm) as the container for the body part of the phantom. The containers were then filled up with a semi-liquid gel comprising distilled water, poly-acrylic acid partial sodium salt (A9799; Sigma-Aldrich, St. Louis, MO, United States) and sodium chloride (008-71265; Kishida Chemical Co., Ltd., Osaka, Japan). The gel had an electrical conductivity of 0.26 S m^{-1} and limited thermal convection to mimic those of human tissue (Carmichael et al., 2010). The gels for the head and torso were made by adding sodium chloride (1.4 g for the head, 28 g for the torso) to distilled water (2 L for the head, 40 L for the torso) heated to 40°C to prevent air bubbles forming in the gel. Then we gradually added poly-acrylic acid partial sodium salt (16 g for the head, 320 g for the torso) while slowly stirring the solutions. We pre-implanted the electrodes in the head phantom from the top opening and from the gap between the two hemispheres. To mimic how the electrodes are placed in real human subjects, we fixed the grid electrodes tangential to the inner surface of the acrylic container with the electrode contact exposure facing the center, and placed the depth electrodes perpendicular to the surface of the acrylic container with all of the contacts embedded within the gel (**Figure 1A**). Then the gap was sealed with a polymer clay made of polyvinyl (Super Sculpey® Beige, Polyform Products Company, Elk Grove Village, IL, United States).

We tested two types of commercially available intracranial grid and depth electrodes: the first type was from Unique Medical (Tokyo, Japan), which we are currently using at our center; the second type was from Ad-Tech Medical (Racine, WI, United States), which has been used in previous safety studies (Carmichael et al., 2010; Boucousis et al., 2012). The grid electrodes have 20 disk-shaped contacts, and the depth electrodes have six contacts (**Figure 1B**) connected via lead wires to connector terminals. **Table 1** summarizes the composition and dimension of each electrode type.

The Unique Medical electrodes were implanted on one side and the Ad-Tech electrodes on the contralateral in the same head phantom to allow fair comparisons between the two types of electrodes. The two grid electrodes were placed at the bottom side of the acrylic container. For Unique Medical, two depth electrodes were implanted: one was placed quasi-perpendicular (depth electrode A) and one quasi-parallel (depth electrode B) to the grid electrode (**Figures 1A,C**). For Ad-Tech, only one depth electrode was implanted (depth electrode A) quasi-perpendicular to the grid electrode (**Figures 1A,C**). In total, two grid electrodes and three depth electrodes were placed in the head phantom. Since the head phantom was not attached to the body phantom, we rotated the head phantom accordingly to achieve the configurations needed in each experiment during either the temperature or voltage measurement (see "*The Experiments: Electrode and phantom configurations*" section below for details).

Temperature Measurement Methodology

The temperature was measured continuously and simultaneously from four locations using a four-channel, fiber-optic thermometry system (MultiSens; Opsens Solutions, Quebec, QC, Canada) connected to four fiber optic MRI-compatible temperature sensors (OTP-M; Opsens Solutions, Quebec, QC, Canada, accuracy ± 0.30°C) with a sampling rate of 1/1.4 s. We placed the temperature sensors at the electrode tip, the location most likely to demonstrate the largest temperature change as shown in previous studies (Boucousis et al., 2012; Carmichael et al., 2012), as follows: the most distal contact (#1) of the 6-contact depth electrode A, the corner or edge of

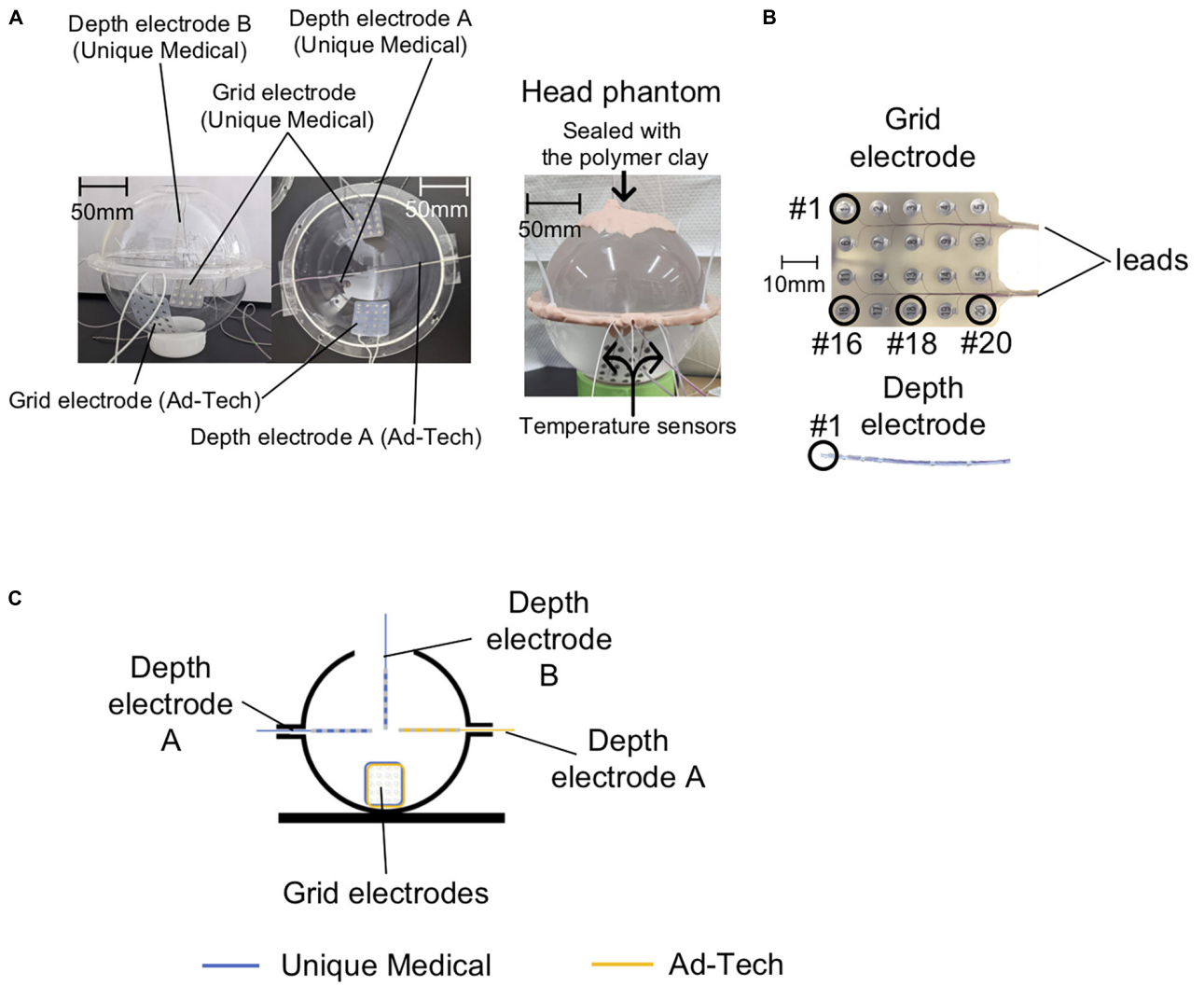

FIGURE 1 | Phantom preparation. **(A)** Left panel: Photos of the empty acrylic shells are shown here to clarify the position of each electrode in the head phantom. Two Unique Medical depth electrodes were placed in the acrylic shells: one was quasi-perpendicular (depth electrode A) and the other was quasi-parallel (depth electrode B) to the grid electrode. Only one Ad-Tech depth electrode was implanted, which was quasi-perpendicular to the grid electrode (depth electrode A). Right panel: photo of the head phantom that was ready for use in experiments of both the temperature and voltage measurements. **(B)** Electrode contact numbering. In the case of grid electrodes, #1 represents the contact at the right corner and the most distal from the leads, and #20 represents the contact at the left corner and the most proximal to the leads. In the case of depth electrodes, #1 represents the contact at the tip. **(C)** The head phantom as represented in a two-dimensional line drawing.

the grid (#16 or #18) (**Figure 1B**). A temperature sensor was placed at the middle of the head phantom, distanced from all electrodes to serve as a control (**Figure 2A**). In the case of grid electrodes, the temperature sensors were laid in a transverse position on the surface of the disk contact and held in place using a silk suture through the silicon. In the case of depth electrodes, the sensor was laid parallel, and tied to the electrode contact using a silk thread. Then the sensors were connected via optical fibers to the thermometry system placed outside the MRI room (**Figure 2B**). To mimic concurrent icEEG-fMRI acquisitions, the electrodes were connected to the EEG amplifiers (Brain Products, Gilching, Germany) via connector cables (180 cm, Tech-Attach Connection System; Ad-Tech Medical) attached to a 64-channel touch-proof electrode input box (EIB64; Brain Products). The connector cables were folded (with 10 cm folds, as previously reported; Carmichael et al., 2012) and placed straight at the center of the MRI bore to minimize the MRI-induced current. To avoid movement due to machinery-induced vibration, the external portion of the leads of the electrodes (between the phantom head and the connector cables) were sandwiched between memory foam cushions that were placed around the phantom head inside the head coil. MRI-compatible sandbags were used to immobilize the cables between the head coil and the EEG amplifiers, which were connected via optic fibers to the recording computer placed outside the MRI room. The signals from the implanted electrodes were recorded during temperature measurements to mimic an actual icEEG-fMRI acquisition on human subjects.

Voltage Measurement Methodology

Voltages were measured using a balanced coaxial probe connected to a 350-MHz digital oscilloscope (MDO3034; Tektronix Inc., Beaverton, OR, United States) placed in the MRI control room. The balanced coaxial probe consisted of two 10-m long 50-ohm coaxial cables (RG-58/U) in which the shields were soldered together, and a 950-ohm resistor attached in series to each cable's end (AKA 20:1 'low impedance' probe) (Smith, 1993; Lemieux et al., 1997). The two probes of the balanced coaxial probe were connected to the icEEG electrodes via a connector block and a 10-cm connector cable (Tech-Attach Connection System; Ad-Tech Medical) modified for the voltage measurement to ensure electrical isolation between electrode tails and between contacts (**Figures 3A,B**).

TABLE 1 | Materials and dimension of the electrodes used.

	Unique Medical Co. Ltd.	**Ad-Tech Medical Instrument Co.**
Grid electrode	**UZN C1-20-05-10-2-A**	**FG20C-SP10X-000**
Dimension		
Number of contacts	20 (4 × 5)	20 (4 × 5)
Center-to-center contact spacing (mm)	10	10
Contact diameter/exposure (mm)	5/3	4/2.3
Lead wire diameter (mm)	0.08	0.0635
Total length (mm)	465	430
Materials		
Contacts	Platinum	Platinum–iridium
Imbedding sheet	Silicon	Silicon
Lead wire	Stainless steel	Stainless steel
Lead tubing	Silicon	Silicon
Connector terminal	Stainless steel	Nickel–chromium
Depth Electrode	**UZN D4-06-054-151-101-A**	**SD06R-SP10X-000**
Dimension		
Number of contacts	6	6
Center-to-center contact spacing (mm)	5 between the first four contacts from the tip 15 between contact #4 and #5 10 between contact #5 and #6	10
Contact length (mm)	1.0	1.32
Electrode diameter (mm)	1.5	1.1
Lead wire diameter (mm)	0.08	0.0635
Total length (mm)	450	380
Materials		
Contacts	Platinum	Platinum
Lead wire	Platinum	Nickel–chromium
Lead tubing	Silicon	Polyurethane
Connector terminal	Stainless steel	Nickel–chromium

Movement Measurement Methodology

We assessed the potential electrode movement induced by the magnetic field's gradients switching during the scan using two different approaches: visual assessment and image analyses. For visual assessment, an echo-planar imaging (EPI) scan was acquired (see sequence parameters below) with the electrodes placed in the head coil without the gel head phantom because the gel was not completely transparent (**Figure 4**). For image analyses, we used one of the 200-volume EPI scan images acquired during the RF-induced heating experiments (experiment B as described in the section "*The Experiments: Electrode and phantom configurations*" below). We evaluated the displacement of the electrode tip between two consecutive EPI volumes using the following steps (**Figure 5**). (1) We identified the tip of each depth electrode and contact #1 of each grid electrode (see **Figure 1B** for the position). (2) For each electrode, we extracted a three-dimensional (3D) region of interest (ROI) of 10 × 10 × 10 voxels containing either the tip of a depth electrode or the contact #1 of a grid (voxel size of EPI = 3.7 × 3.7 × 3.7 mm). This resulted in five 3D ROIs, each containing one of the five electrodes implanted in the head phantom. (3) We calculated the cross-correlation between two consecutive EPI volumes within the 3D ROI to look for dissimilarity using an FSL tool (*fslcc*[1]). This was repeated for each 3D ROI extracted in step (2). Cross-correlation value was 1.00000 between two identical 3D ROI and the mean cross-correlation value among nine 3D ROIs extracted at random location from the EPI volume (resulted in nine dissimilar ROI-restricted EPI volumes) was 0.36396 (range 0.10098-0.84291). Thus, any cross-correlation value lower than 1.00000 indicates dissimilarity and possible electrode displacement. (4) For each 3D ROI, the pair of consecutive volumes with the lowest correlation value was considered the most dissimilar and identified as the pair with the greatest electrode displacement. We visually examined the tip of a depth electrode or contact #1 of a grid between the pair of consecutive volumes identified and physically measured the displacement if there was any.

Scanning Sequences

All measurements were performed in a 3.0 T MRI scanner (GE 3 T MRI Signa Architect, No. EM0219; GE Medical Systems, Milwaukee, WI, United States) using the standard RF body transmit and head-receive coils, the latter with an opening at the back to allow the wires to pass straight to the back of the MRI bore. In RF-induced heating, switching gradient-induced voltage and electrode movement experiments described in the section "*The Experiments: Electrode and phantom configurations*" below, the parameters of the scanning sequences used were as follows: localizer (two-dimensional gradient-recalled steady state) acquired in sagittal, coronal, and axial separately {sagittal: echo time [TE] = 5.6 ms, repetition time [TR] = 20 ms, flip angle = 30°, field of view (FOV) = 28 cm, matrix = 256 × 256, five 5-mm-thick slices; coronal: TE = 7.6 ms, TR = 20 ms, flip angle = 30°, FOV = 28 cm, matrix = 256 × 256, five 5-mm-thick slices; axial: TE = 10 ms, TR = 20 ms, flip angle = 30°,

[1]https://fsl.fmrib.ox.ac.uk/

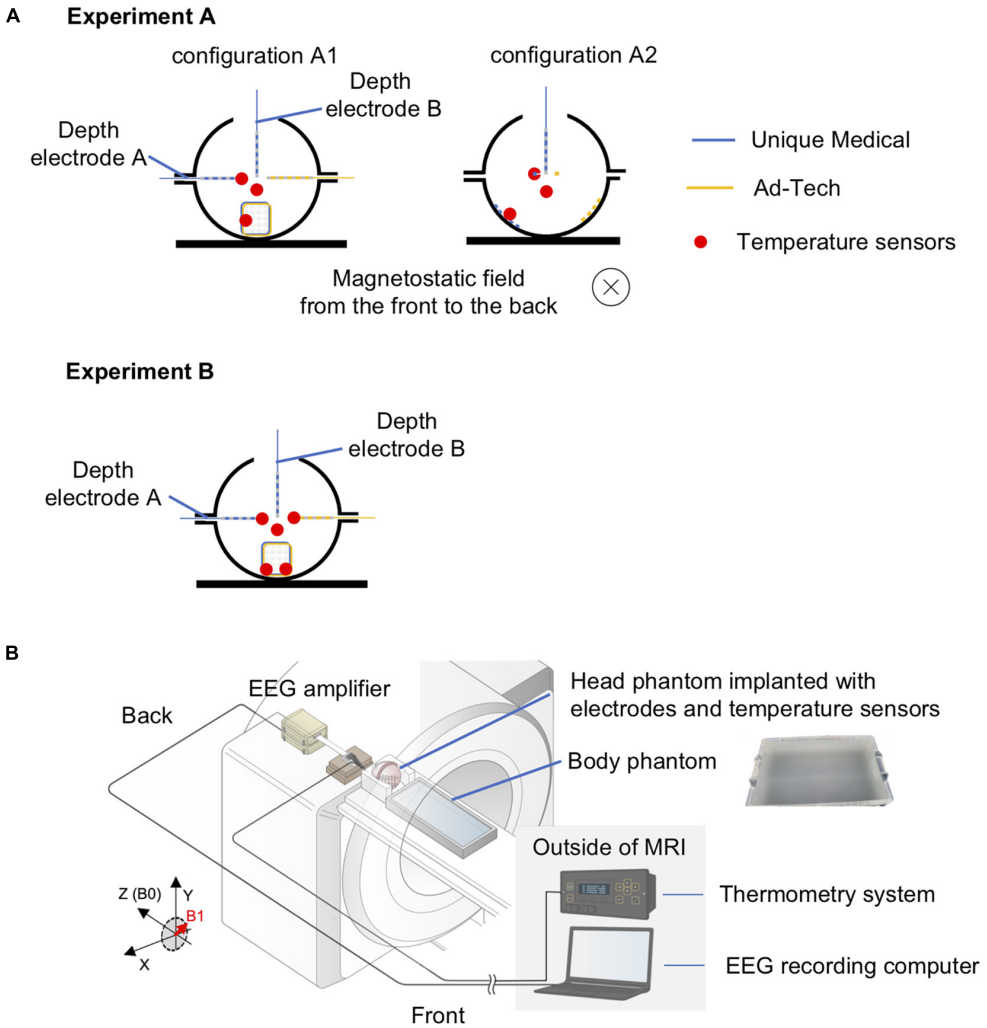

FIGURE 2 | Experimental setup for temperature measurement of radiofrequency-induced heating. **(A)** Orientation of the head phantom and the location of temperature sensors during experiment A (upper panel) and experiment B (lower panel). In experiment A, two conditions were tested: configuration A1 – electrodes placed orthogonal to the direction of the static magnetic field; configuration A2 – electrodes placed parallel to the direction of the static magnetic field. The blue electrodes were Unique Medical electrodes, and the yellow electrodes were Ad-Tech. The location of a temperature sensor was indicated as red dot. The red dot distanced from all electrodes represents the sensor placed within the gel to serve as control. Experiment B was performed twice: two sensors were placed on Unique Medical electrodes during the first and on Ad-Tech electrodes during the second time. **(B)** Layout of the phantoms and all of the equipment during experiments for temperature measurement. The head and body phantoms were placed in the magnetic resonance imaging (MRI) scanner with the head at the isocenter to emulate an actual simultaneous acquisition of icEEG and fMRI (icEEG-fMRI). The electrodes implanted in the head phantom were connected to the EEG amplifier placed at the "back" of the MRI bore, with exactly the same configuration as an actual icEEG-fMRI acquisition in human subject. The electrodes were secured using memory foam cushions in the head coil and cables were secured using sandbags to prevent movements resulted from mechanical vibration of the MRI scanners during the experiment. The fiber optic MRI-compatible temperature sensors, fixed to the intracranial electrodes, were connected via optical fibers to the thermometry system placed outside the MRI in the control room.

FOV = 28 cm, matrix = 256 × 256, five 5-mm thick slices}; EPI (T2*-weighted gradient-recalled echo planar, TE = 22 ms, TR = 1900 ms, flip angle = 70°, FOV = 23 cm, matrix = 64 × 64, 33 3.7-mm-thick slices) acquired as a 200-volume image per scan (total scan time = 6 min 20 s) and scans were repeated if required; magnetization-prepared rapid gradient-echo (MP-RAGE) (3D T1-weighted inversion recovery, TE = 2.5 ms, TR = 2500 ms, flip angle = 9°, FOV = 25.6 cm, matrix = 256 × 256 × 166, 1-mm-thick slices); and fast spin echo (FSE) (two-dimensional T2-weighted spin echo, TE = 102 ms, TR = 4000 ms, flip angle = 180°, FOV = 22 cm, matrix = 512 × 256, 24 5-mm-thick slices).

The Experiments: Electrode and Phantom Configurations

Since the mechanism underlying RF-induced heating and switching gradient-induced voltage differs (see below), the electrode and phantom were configured differently for temperature and voltage measurements to maximize the effects

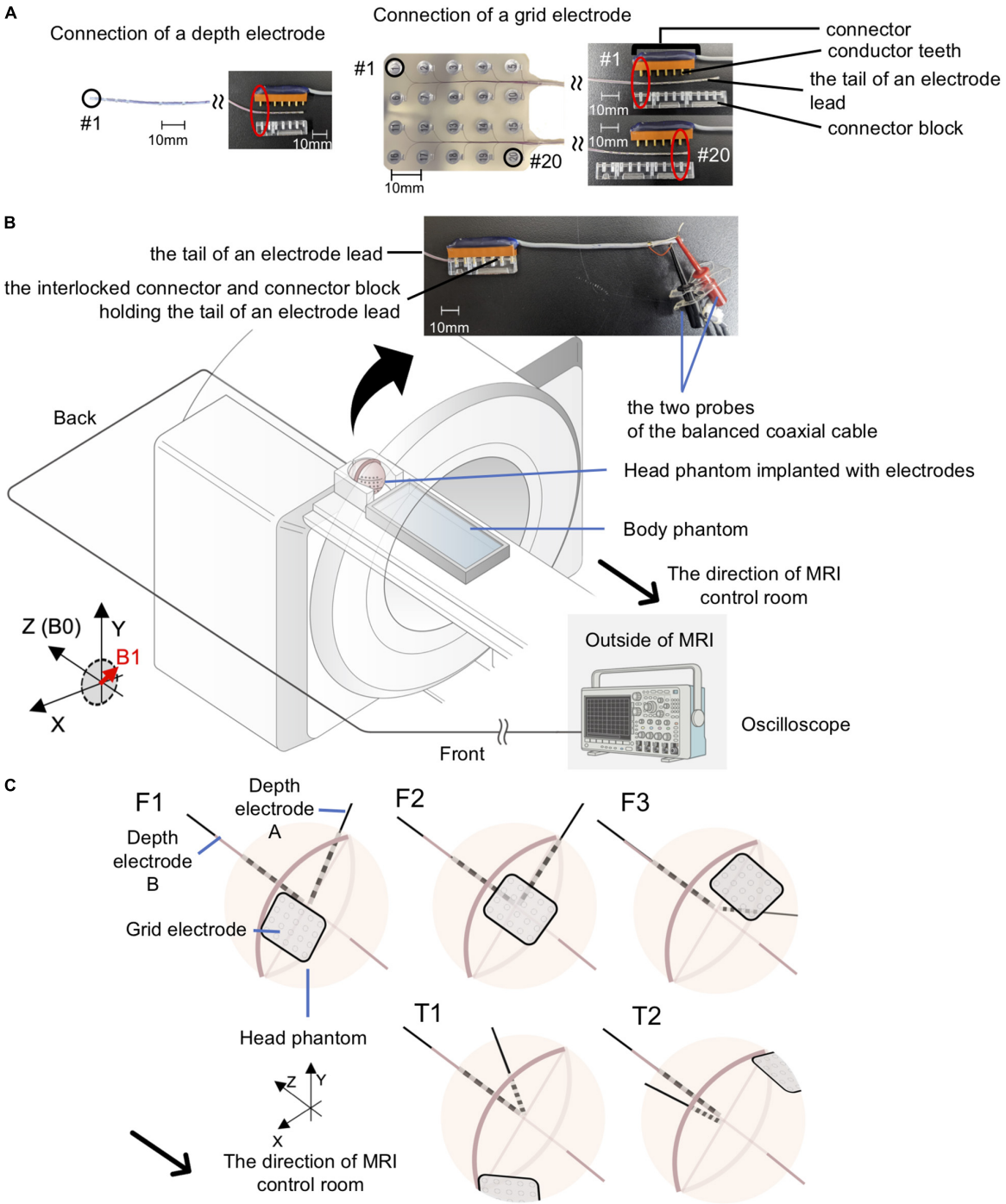

FIGURE 3 | Experimental setup for gradient switching-induced voltage measurement. **(A)** Modified Ad-Tech connector cables and the electrodes. An Ad-Tech connector cable was cut at 10 cm away from the connector and 2 cm of the cable outer sheath was removed to expose the wires embedded within the cable. Each wire corresponds to one pair of conductor tooth on the connector; connection to an electrode contact can be established by connecting the probe of the balanced coaxial cable to one of these wires. The electrode was connected to the connector via a connector block; connection to any of the contacts on a grid electrode can be achieved by adjusting the relative position of the conductor tooth (on the connector) and the connector block. **(B)** Layout of the phantoms and all of the equipment during experiments for voltage measurement. Each electrode was connected via a modified Ad-Tech connecter cable (as in A) and a custom-made balanced coaxial cable to the oscilloscope placed outside the magnetic resonance imaging (MRI) in the control room. The electrodes were secured using memory foam cushions (not shown) in the head coil. The portion of electrode leads outside the head coil and the connector were placed at the center of the MRI bore as far away from the head coil as possible and firmly secured using sandbags (not shown). **(C)** Electrode configurations for voltage measurements. Upper panel – electrode configuration emulating frontal lobe implantation on the right (F1), center (F2), and left (F3). Lower panel – electrode configuration emulating temporal lobe implantation on the right (T1) and left (T2). See **Table 2** for electrode contact pairs used for the measurement. Only the Unique medical electrodes are shown for illustrative purpose.

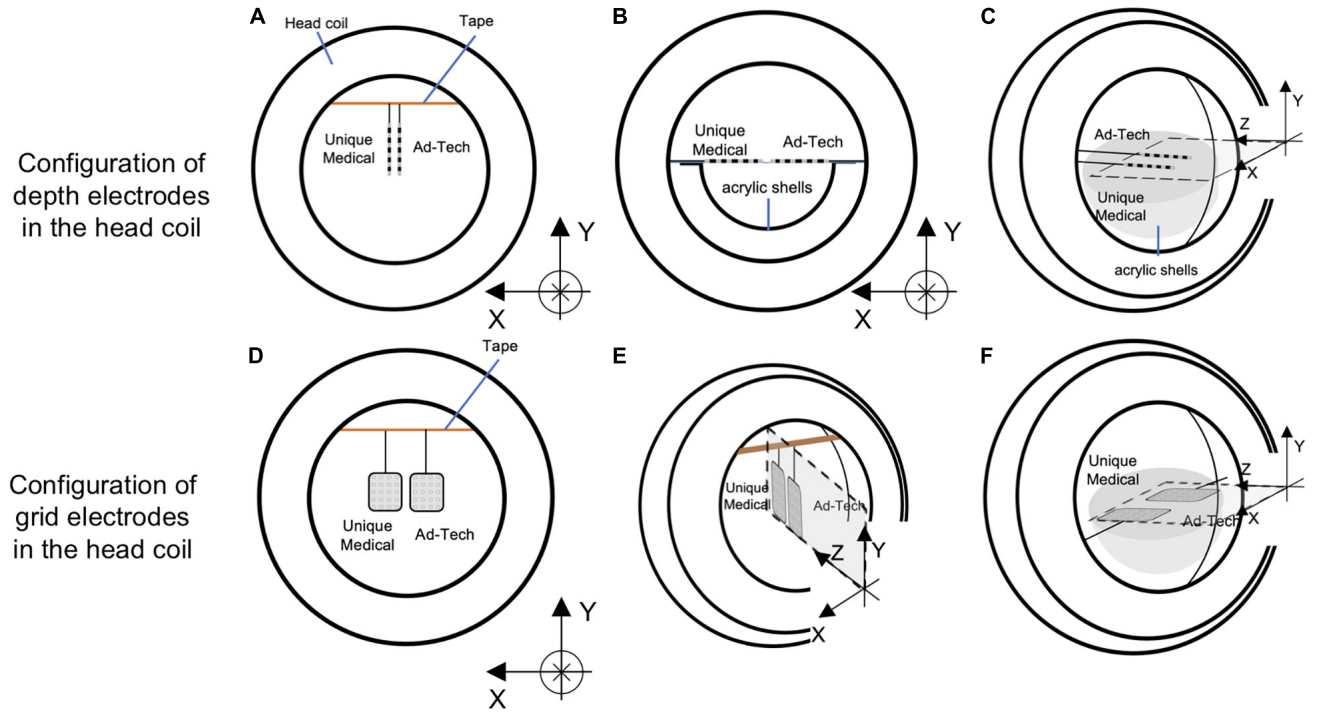

FIGURE 4 | Configurations of the electrodes in the head coil during experiments for detecting gradient switching-induced electrode movement by visual assessment. Configurations of depth electrodes were shown in the upper panel and grid electrodes in the lower panel. Two depth electrodes (one Unique Medical and another Ad-Tech) were placed parallel to the *Y*-axis **(A)**, *X*-axis **(B)**, or *Z*-axis **(C)**. Two grid electrodes (one Unique Medical and another Ad-Tech) were placed in the XY-plane **(D)**, YZ-plane **(E)**, or ZX-plane **(F)**. In **(A,D,E)**, the electrodes were hanged down from a surgical tape (indicated as orange line) that was placed across the head coil parallel to the *X*-axis, with the end taped to the head coil. Each electrode was taped to the surgical tape at a point 7.5 cm from the tip. In **(B,C,F)**, the electrodes were placed on an isometric graph paper attached on the acrylic shell (that was used for preparing the head phantom). In all **(A–F)**, the electrodes were placed as close as possible to the center of the head coil (without touching each other), which was then placed at the isocenter of the magnetic resonance imaging scanner bore while running scans of EPI sequence.

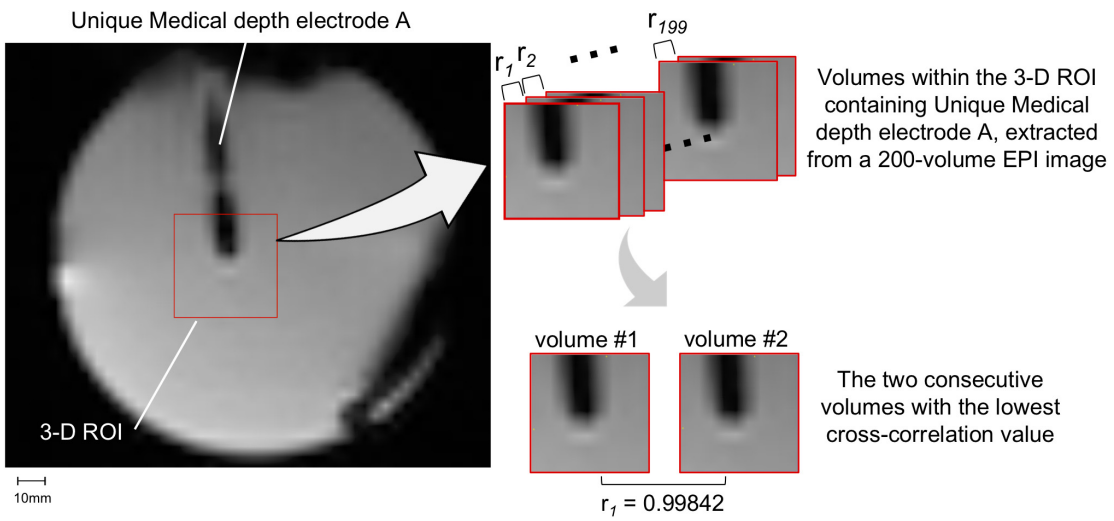

FIGURE 5 | Movement measurement methodology – using image analysis. A three-dimensional (3D) region-of-interest (ROI) of 10 × 10 × 10 voxels containing either the tip of a depth electrode or contact #1 of a grid was extracted. Only Unique Medical depth electrode A and its 3D ROI are shown **(left panel)**. The cross-correlation value (r_i) between two consecutive EPI volumes within the 3D ROI was calculated **(right upper panel)**: the lower the correlation value, the more dissimilar the pair of volumes were and thus the more likely the electrode was displaced. The pair of consecutive volumes with the lowest correlation coefficient were visually examined and any visible displacement of the electrode tip was physically measured. The two consecutive volumes within the 3D ROI containing Unique Medical depth electrode A with the lowest cross-correlation value was shown in the **right lower panel**.

of each factor (worst-case scenarios). **Table 2** summarizes the MRI sequences tested in each experiment below.

Radio Frequency-Induced Heating

For temperature measurements, since the RF-induced heating may vary depending on the orientation of the electrodes relative to the scanner static magnetic field (B_0) (Nordbeck et al., 2008; Winter et al., 2020), temperature change was first recorded during a scan of each MRI sequence to identify the worst case (experiment A, shorter recording), and then recorded during a scan using all MRI sequences over a total scan period of approximately 70 min (experiment B, longer recording), to mimic a typical icEEG-fMRI acquisition. In experiment A, measurements were performed using two configurations as follows: electrodes oriented perpendicularly to B_0 (A1) and electrodes parallel to B_0 (A2). Experiment B was performed using the configuration found in experiment A that resulted in most heating (which corresponded to A1, see **Table 3**) with MRI sequences in the following order: localizer, EPI (200-volume image × 10, total scan time approximately 63 min), and MP-RAGE (scan time ∼8 min). Experiment B was repeated three times for Unique Medical electrodes. Repeated measurement has been well-documented previously using Ad-Tech electrodes (Boucousis et al., 2012) and thus not repeated here.

Switching Gradient-Induced Voltage

For voltage measurements, since the gradient field amplitude varies as a function of location along the scanner's long axis (Schaefer et al., 2000) and to maximize the effect (worst case scenarios), measurements were performed with electrodes configured in orientations mimicking either frontal lobe or temporal lobe implantations (see **Table 4** and **Figure 3C**). For frontal lobe implantation configurations, electrodes were placed to mimic either implantation in the right (configuration F1), center (configuration F2), or left (configuration F3) aspects of the frontal lobe. Two temporal lobe implantation configurations were used: right (configuration T1) and left (configuration T2).

According to Maxwell's equation, the larger the circuit within the electrodes and leads perpendicular to the magnetic field, the larger the induced voltage (Georgi et al., 2004). Based on this equation and previous studies (Carmichael et al., 2010; Boucousis et al., 2012), we measured the gradient-induced voltage between two most distant electrode contacts aiming

TABLE 3 | Results of Experiment A.

		Depth	Grid	Control
Measurement	B_{1+}RMS	ΔT(°C)	ΔT(°C)	ΔT(°C)
Configuration A1: Orthogonal				
A1.1 (EPI)	0.77	0.2	0.1	0.1
A1.2 (MP-RAGE)	0.72	0.1	0.1	0.1
A1.3 (FSE)	2.57	1.9	0.7	0.2
Configuration A2: Parallel				
A2.1 (EPI)	0.77	0.1	0.1	0.1
A2.2 (MP-RAGE)	0.72	0.1	0.1	0.1
A2.3 (FSE)	2.57	0.6	0.4	0.1

Temperature measurements for the Unique Medical electrodes.
EPI, echo-planar imaging; MP-RAGE, magnetization-prepared rapid gradient-echo; FSE, fast spin echo; B_{1+}RMS, root mean square value of B_{1+} averaged over a period of 10 s; Depth, depth electrode; Grid, grid electrode; △ T, maximum change in temperature.

TABLE 2 | MRI sequences tested in the radio frequency-induced heating, switching gradient-induced voltage and electrode movement experiments.

Experiments	Measurement #	MRI sequences tested
Radio frequency-induced heating		
• Only low B_{1+}RMS or SAR sequences (localizer, EPI, MP-RAGE) were used when the EEG amplifiers were placed in the scanner. These are the sequences required to complete a typical icEEG-fMRI experiment at our center.		
• A high B_{1+}RMS sequence or SAR (FSE) that causes substantial heating was used as a positive control, after the amplifiers were removed from the scanner. This sequence would not be used during a typical icEEG-fMRI experiment.		
Experiment A – shorter recording (separate scan of each MRI sequence)		
Configuration A1 – electrodes oriented perpendicular to B_0	A1.1	EPI
	A1.2	MP-RAGE
	A1.3	FSE
Configuration A2 – electrodes oriented parallel to B_0	A2.1	EPI
	A2.2	MP-RAGE
	A2.3	FSE
Experiment B – longer recording (continuous scan of all MRI sequences)	B	Localizer + 10 consecutive EPI scans + MP-RAGE
Switching gradient-induced voltage		
• Nerve stimulation is likely caused by induced currents and voltages resulted from a time-varying gradient magnetic field of less than 10 kHz.		
	See **Table 4**	EPI
Electrode movement		
• Rapidly switching gradient field may cause rapid movement of implants because implants are subjected to mechanical force when exposed to gradient field.		
	See **Figure 4**	EPI

B_{1+}RMS, root mean square value of B_{1+} averaged over a period of 10 s; EPI, echo-planar imaging; FSE, fast spin echo; icEEG-fMRI, simultaneous acquisition of icEEG and fMRI; MP-RAGE, magnetization-prepared rapid gradient-echo; MRI, magnetic resonance imaging; SAR, specific absorption ratio.

TABLE 4 | Electrode configurations for voltage measurement.

Configuration	Location	Voltage measurement #	First contact (see Figure 1B for electrode type and contact numbering)	Location of the first contact in relation to the phantom	Second contact (see Figure 1B for electrode type and contact numbering)	Location of the first contact in relation to the phantom
Frontal lobe						
F1	Right	F1.1	Grid #1	Inner surface	Grid #20	Inner surface
		F1.2	Grid #1	Inner surface	Depth A #1	Near center
F2	Middle	F2.1	Grid #1	Inner surface	Grid #20	Inner surface
F3	Left	F3.1	Grid #1	Inner surface	Grid #20	Inner surface
		F3.2	Grid #1	Inner surface	Depth A#1	Near center
Temporal lobe						
T1	Right	T1.1	Grid #1	Inner surface	Grid #20	Inner surface
		T1.2	Grid #1	Inner surface	Depth A #1	Near center
		T1.3	Depth A #1	Near center	Depth B #1	Near center
T2	Left	T2.1	Grid #1	Inner surface	Grid #20	Inner surface
		T2.2	Grid #1	Inner surface	Depth A #1	Near center
		T2.3	Depth A #1	Near center	Depth B #1	Near center

*Grid, grid electrode; Depth, depth electrode; Depth A, the depth electrode that was implanted quasi-perpendicular to the grid electrode; Depth B, depth electrode that was implanted quasi-parallel to the grid (see **Figures 1A,C**).*

at maximizing the loop area (representing the worst-case condition). The measurement was performed with either of the following electrode contact combinations: between contact #1 and #20 of a grid electrode, between contact #1 of a depth electrode and contact #1 of a grid electrode, or between contact #1 of two depth electrodes (the third combination was only available for depth electrodes from Unique Medical). Electrodes that were not used during each measurement were electrically shorted at the tails/cable terminations. The last four columns of **Table 4** summarize the electrode contact combinations used in each configuration and the location of each electrode contact in relation to the phantom. The orientation of each electrode contact relative to the MRI bore axis is shown in **Figure 3C**.

Electrode Movement

For visual assessment of electrode movement, the electrodes were oriented either parallel to the *X*-, *Y*- or *Z*-axis of the MRI bore (**Figure 4**). For the orientation parallel to the *Y*-axis configuration, the electrodes were fixed at a point 75 mm away from the tip of a depth electrode or the distal edge of a grid electrode using a surgical tape; the tip or edge of the electrodes was hanging freely. An isometric graph paper was placed at the back to facilitate detection of any possible movement, without touching the electrodes. For the orientation parallel to the *X*- or *Z*-axis configuration, the electrodes were placed on a piece of isometric graph paper, held at the same point as above-mentioned. Movement was assessed under both direct visual observation and through video recording taken during the experiment.

RESULTS

Temperature Measurements

Table 3 and **Figure 6** summarize temperature changes for each sequence used in our icEEG-fMRI protocol, and a high specific absorption rate (SAR) sequence (FSE). For configuration A1, the observed maximum temperature increases were 0.2, 0.1, and 1.9°C during EPI, MP-RAGE, and FSE, respectively, for the depth electrode; and 0.1, 0.1, and 0.7°C during EPI, MP-RAGE, and FSE, respectively, for the grid electrode. For configuration A2, the observed maximum temperature increases were 0.1, 0.1, and 0.6°C during EPI, MP-RAGE, and FSE, respectively, for the depth electrode; and 0.1, 0.1, and 0.4°C during EPI, MP-RAGE, and FSE, respectively, for the grid electrode. **Figure 7** shows the results of Experiment B. For Unique Medical electrodes, the observed total median temperature increases were 0.4 and 0.6°C for the grid and depth electrodes, respectively. For Ad-Tech electrodes, the observed total temperature increases were 0.7 and 0.6°C for grid and depth electrodes, respectively. The temperature increased monotonically with time at all electrodes throughout the course, although a more rapid increase on depth electrodes was observed upon the start of MP-RAGE.

Voltage Measurements

Under frontal lobe implantation configurations, the greatest mean gradient-induced voltage was 43.5 (standard deviation, SD 0.5) mV for Unique Medical and 64.0 (SD 1.4) mV for Ad-Tech electrodes. Under temporal lobe implantation configurations, the greatest mean gradient-induced voltage was 79.3 (SD 1.6) mV for Unique Medical and 86.6 (SD 1.1) mV for Ad-Tech electrodes. A larger voltage was induced under the left temporal lobe implantation configurations. The results are shown in **Table 5**.

Movement Measurements

Under visual assessment, no movement was detected under all tested conditions. Using EPI image analyses, the lowest cross-correlation value of each 3D ROI containing a depth electrode tip or grid electrode contact #1 was shown in **Table 6**. Visual inspection revealed no displacement even between the volume pairs with the lowest cross-correlation value (see **Figure 5** for an example). The variation in cross-correlation values were due to

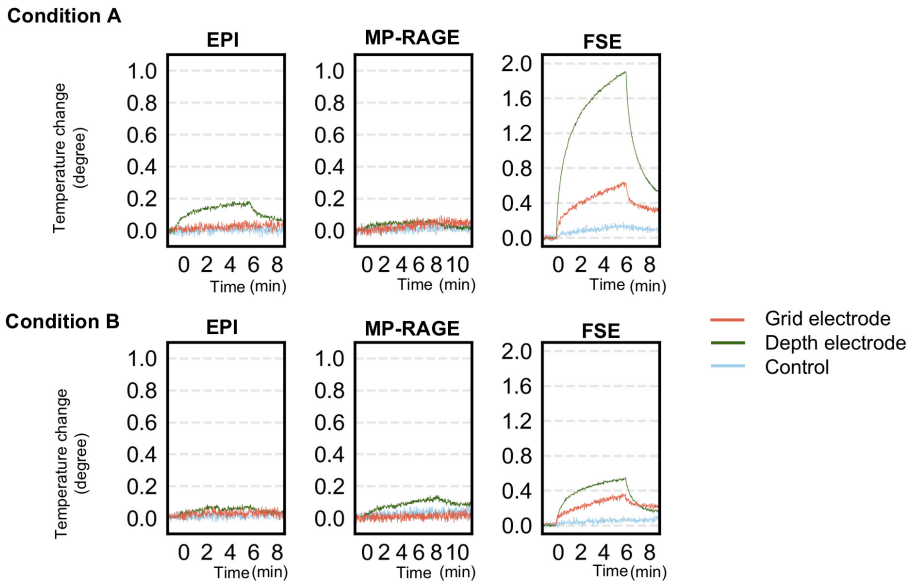

FIGURE 6 | Temperature changes observed during a scan of each sequence for simultaneous acquisition of icEEG and fMRI (EPI, MP-RAGE), and a high-SAR sequence (FSE) as control in experiment A. The **upper panel** shows the changes at each electrode when oriented perpendicularly to B_0 (configuration A1). The **lower panel** shows the changes at each electrode when oriented parallel to B_0 (configuration A2). The temperature change was generally larger in configuration A1 except for MP-RAGE. SAR, specific absorption rate; EPI, echo planar imaging; FSE, fast spin echo; MP-RAGE, magnetization-prepared rapid gradient-echo.

slight changes in global intensity between EPI volumes instead of a visible displacement.

DISCUSSION

This study addressed the safety of performing icEEG-fMRI at 3 T using depth and grid electrodes available in Japan, under conditions tested in this study. For all conditions tested, the gradient-induced voltages were within 100 mV and the maximum temperature increase was within 1°C, both fulfilling the criteria according to current safety standards (Georgi et al., 2004; IEC, 2015). A prolonged acquisition that lasted approximately 70 min under the worst-case scenario also did not result in a temperature increase exceeding 1°C in the vicinity of the electrodes. Despite the difference in the combination of electrodes and scanner used in our study, the results were comparable to studies reported on the feasibility of icEEG-fMRI. For example, Carmichael et al. (2010) and Boucousis et al. (2012) reported temperature changes within 1°C, induced voltages within 100 mV and no significant implant movements using Ad-Tech electrodes in a 1.5 T Siemens scanner and a 3 T GE scanner, respectively. The findings of our study may serve as a guidance for safety precaution to centers intending to perform MRI imaging for post-implantation localization of icEEG electrodes. MP-RAGE sequence is rather safe but not high SAR sequence such as FSE; however, a local safety protocol should be developed in each center because a slight difference in MRI scanner, coils, electrode and leads configuration may result in considerable differences in the safety profile of implants in an MRI (Carmichael et al., 2008).

Radio frequency-induced heating can result from implanted electrodes acting as a resonating linear antenna. The high electrical resistance of the tissue causes local resistive heating and increases temperature (Mattei et al., 2008). RF-induced heating can cause neuronal damage when prolonged increases of 5°C above body temperature occur (Dewhirst et al., 2003; Georgi et al., 2004; Boucousis et al., 2012). Current safety standards have further limited the acceptable heating of a device more conservatively to within 1°C (IEC, 2015). In our experiments, the temperature increase during the prolonged 70-min acquisition was well below this limit. Our observations provide evidence that the risk of excessive heating is manageable in the specific circumstances tested; namely a 3 T GE MRI scanner with body RF coil, grid, and depth electrodes configured to mimic implantation in the frontal and temporal lobes. We found that RF-induced heating was more prominent with the electrodes placed orthogonal to the static magnetic field. Previous studies have shown that the closer the distance between an electrode and the RF transmitter coil, the higher the temperature of the induced heating (Mattei et al., 2008; Bhusal et al., 2018). For this reason, the temperature increased more when an electrode was placed orthogonal, in which the electrode has been inserted from the side and thus closer to the transmitter coil. These observations along with ours are in line with the observations of some early case reports on the adverse effects potentially resulting from RF-heating in the MRI. These include a transient dystonic and ballistic movements following a head MRI (Spiegel et al., 2003) and a peri-electrode hemorrhage following a lumbar spine MRI (Henderson et al., 2005) both performed at 1.0 T on patients with Parkinson's disease that was implanted with bilateral DBS. The difference in severity of the adverse effects

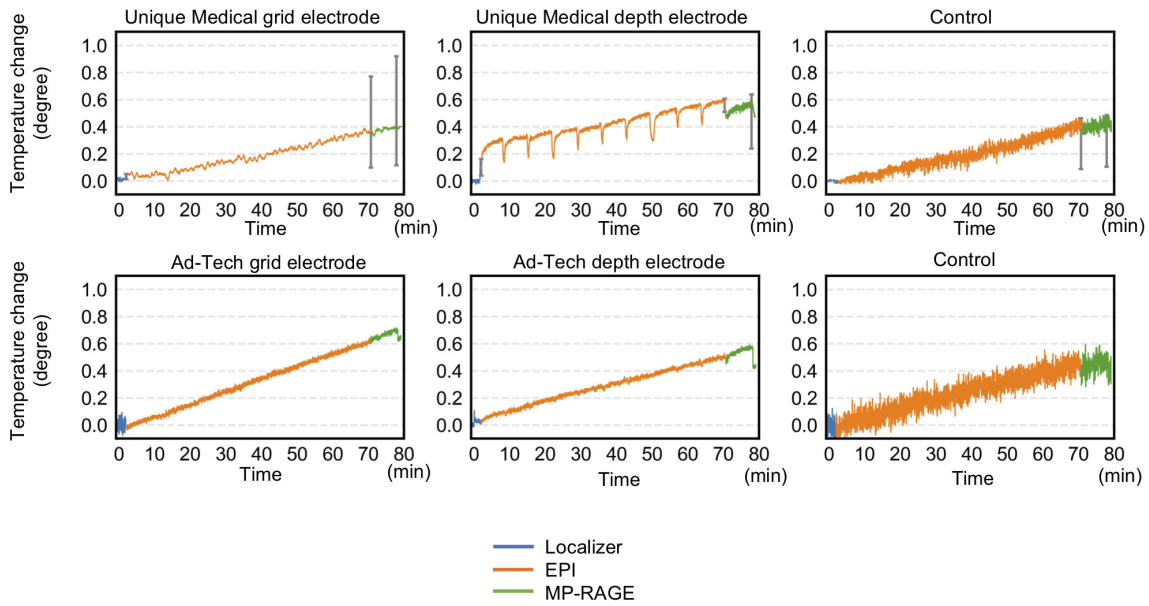

FIGURE 7 | Temperature changes throughout the 70-min acquisition using all sequences of a typical simultaneous acquisition of icEEG and fMRI experiment. Radio frequency-induced heating on grid and depth electrodes placed orthogonal to the static magnetic field were shown. For Unique Medical electrodes, each trace represents the median temperature changes from three measurements. Error bars show the interquartile range of the measured temperature at the end of each sequence. The total temperate increase was within 1°C regardless of electrode type. Compared to Ad-Tech, Unique Medical electrodes showed a more abrupt temperature decrease between images.

in these reports suggested the potential impact of electrodes' orientation, length, and configuration on RF-induced heating. Indeed, a study on a cardiac pacemaker implant showed the impact of lead pathway and device position on RF-heating during MRI (Nordbeck et al., 2009).

Gradient switching during EPI causes polarity of the magnetic field to change rapidly and results in an induced current. The induced current is dependent on the frequency and the cross-sectional area of the electrode contacts. In general, stimuli above 10 kHz such as those generated by RF pulse do not evoke action potentials in neuronal cells (Patrick Reilly, 2016; Ziegelberger et al., 2020). Therefore, only the effect of gradient switching below 10 kHz are considered in terms of induced voltage that

TABLE 5 | Observed gradient-induced voltages.

Configuration	Measurement #	Peak voltage (mV)			
		Unique Medical		Ad-Tech	
		Mean	*SD*	Mean	*SD*
F1	F1.1	43.5	0.5	14.6	0.9
	F1.2	7.2	1.0	55.7	0.6
F2	F2.1	22.3	0.4	64.0	1.4
F3	F3.1	29.0	0.9	14.6	0.8
	F3.2	26.0	0.5	21.1	1.3
T1	T1.1	55.5	1.0	66.3	0.9
	T1.2	19.6	0.9	51.8	1.1
	T1.3	41.5	0.6	NA	
T2	T2.1	64.9	5.1	10.7	0.4
	T2.2	55.9	1.8	86.6	1.1
	T2.3	79.3	1.6	NA	

Depth, depth electrode; Grid, grid electrode; NA, not applicable;
*Depth A, the depth electrode that was implanted quasi-perpendicular to the grid electrode; Depth B, the depth electrode that was implanted quasi-parallel to the grid electrode (see **Figures 1A,C**).*
Mean and standard deviation of 10 peak voltages were shown. Note that only one Ad-Tech depth electrode was implanted in the phantom, and thus the voltage measurement was not applicable for the combination of the two Ad-Tech depth electrodes. NA, not applicable; SD, standard deviation.

TABLE 6 | The lowest cross-correlation value between two consecutive EPI images acquired during a 200-volume EPI scan.

Electrode	The lowest cross-correlation value	The corresponding pair of EPI volumes (image #)
Unique Medical grid electrode contact #1	0.99996	1/2
Unique Medical depth electrode A tip	0.99912	1/2
Unique Medical depth electrode B tip	0.99842	1/2
Ad-Tech grid electrode contact #1	0.99994	1/2
Ad-Tech depth electrode A tip	0.99976	1/2

*Depth electrode A, the depth electrode that was implanted quasi-perpendicular to the grid electrode; depth electrode B, the depth electrode that was implanted quasi-parallel to the grid electrode (see **Figures 1A,C**). EPI, echo-planar imaging.*

could result in inadvertent neuronal stimulation or brain tissue damage, which has been suggested to occur at voltage exceeding 100 mV (Georgi et al., 2004). In this study, neither implantation mimicking frontal nor temporal lobe exceeded this limit, thus confirming the safety of icEEG-fMRI using these implantation schemes, which predominate at our center.

Implants such as intracranial electrodes can be subjected to mechanical force when exposed to magnetic gradient, depending on their orientation. The resultant force may lead to movement of implants against the surrounding tissue (Erhardt et al., 2018). Our study showed that gradient switching during the EPI sequence did not cause any visible movement by direct visual inspection and analysis of the EPI images. We did not perform a formal measurement of static magnetic field-induced forces according to the American Society for Testing of Materials because these were previously reported to be insignificant for non-ferromagnetic platinum-iridium electrode contacts (Carmichael et al., 2010; Boucousis et al., 2012).

This study showed that the total temperature increase during a 70-min acquisition that included all MRI sequences used in a typical icEEG-fMRI experiment at our center was below the established safety limit of 1°C. Nevertheless, as the increase was summative following each scan, a sufficient interval should be placed in between scans if more scans are needed. We did not evaluate the difference in electrode heating between the left and right side of the scanner because our MRI scanner uses multiple RF transmissions in parallel (multidrive RF transmission technology) that minimizes the RF non-uniformity especially around the isocenter, where the electrodes were placed. Therefore, our findings should not be extrapolated to MRI scanners without this technology. The minimal increase in temperature recorded in this study may well be attributed to the configuration of the connecting cables placed along the central axis of the coil because the closer the cable is placed to the transmitter coil, the more heat is generated (Carmichael et al., 2010; Bhusal et al., 2018). Although we did not evaluate the effect of cable length in this study, it should also be carefully considered and optimized to the strength of the magnetic field; the temperature increase is greatest when the cable length is one fourth or half the RF wavelength (Yeung et al., 2007). Although we expect the effect of brain perfusion to mitigate RF-induced heating in living human subjects and therefore our heating measurements can be taken to reflect a worst-case scenario in this specific sense, the utmost care and attention to detail is recommended when considering performing icEEG-fMRI in patients; specifically, a local safety assessment and experiments such as those presented here, are recommended as a minimum. Our findings are not generalizable to other MRI scanners, RF-transmit coils, or electrodes from other manufacturers (Carmichael et al., 2008).

DATA AVAILABILITY STATEMENT

The original contributions presented in this study are included in the article, further inquiries can be directed to the corresponding author.

AUTHOR CONTRIBUTIONS

YF and HMK were responsible for the conception and design of the study under the advice of LL. YF, HMK, MH, MK, YK, and HT were responsible for data acquisition. YF and HMK were responsible for data analyses, drafting a significant portion of the manuscript and figures. YF conducted the statistical analyses under the supervision of HMK. All authors were responsible for interpreting the findings, contributed toward subsequent revisions, and approved the submitted manuscript.

FUNDING

This study was sponsored by the National Institute of Information and Communications Technology of Japan (NICT Grant No. 21301); Grant-in-Aid for Scientific Research (No. 20K09368) from the Ministry of Education, Culture, Sports, Science and Technology of Japan; and AMED Brain/Minds Beyond (Grant No. JP19dm0307103). Open access publication of this study was supported by UCB Japan (publication support grant).

ACKNOWLEDGMENTS

The authors thank the MRI physicists and technologists at Osaka University Hospital and the Center for Information and Neural Networks (CiNet) for their technical advice and support during the conduction of the study.

REFERENCES

Aghakhani, Y., Beers, C. A., Pittman, D. J., Gaxiola-Valdez, I., Goodyear, B. G., and Federico, P. (2015). Co-localization between the bold response and epileptiform discharges recorded by simultaneous intracranial eeg-fmri at 3 T. *Neuroimage Clin.* 7, 755–763. doi: 10.1016/j.nicl.2015.03.002

Baranauskas, G., Maggiolini, E., Vato, A., Angotzi, G., Bonfanti, A., Zambra, G., et al. (2012). Origins of 1/f2 scaling in the power spectrum of intracortical local field potential. *J. Neurophysiol.* 107, 984–994. doi: 10.1152/jn.00470.2011

Bhusal, B., Bhattacharyya, P., Baig, T., Jones, S., and Martens, M. (2018). Measurements and simulation of RF heating of implanted stereo-electroencephalography electrodes during MR scans. *Magn. Reson. Med.* 80, 1676–1685. doi: 10.1002/mrm.27144

Boucousis, S. M., Beers, C. A., Cunningham, C. J. B., Gaxiola-Valdez, I., Pittman, D. J., Goodyear, B. G., et al. (2012). Feasibility of an intracranial EEG-Fmri protocol at 3 T: risk assessment and image quality. *Neuroimage* 63, 1237–1248. doi: 10.1016/j.neuroimage.2012.08.008

Carmichael, D. W., Pinto, S., Limousin-Dowsey, P., Thobois, S., Allen, P. J., Lemieux, L., et al. (2007). Functional Mri with active, fully implanted, deep brain stimulation systems: safety and experimental confounds. *Neuroimage* 37, 508–517.

Carmichael, D. W., Thornton, J. S., Rodionov, R., Thornton, R., Mcevoy, A., Allen, P. J., et al. (2008). Safety of Localizing Epilepsy Monitoring Intracranial Electroencephalograph Electrodes Using Mri: radiofrequency-Induced Heating. *J. Magn. Reson. Imaging* 28, 1233–1244. doi: 10.1002/jmri.21583

Carmichael, D. W., Thornton, J. S., Rodionov, R., Thornton, R., Mcevoy, A. W., Ordidge, R. J., et al. (2010). Feasibility of simultaneous intracranial Eeg-fmri in humans: a safety study. *Neuroimage* 49, 379–390. doi: 10.1016/j.neuroimage.2009.07.062

Carmichael, D. W., Vulliemoz, S., Rodionov, R., Thornton, J. S., Mcevoy, A. W., and Lemieux, L. (2012). Simultaneous intracranial Eeg-fmri in humans: protocol considerations and data quality. *NeuroImage* 63, 301–309. doi: 10.1016/j.neuroimage.2012.05.056

Chaudhary, U. J., Centeno, M., Thornton, R. C., Rodionov, R., Vulliemoz, S., Mcevoy, A. W., et al. (2016). Mapping human preictal and ictal haemodynamic networks using simultaneous intracranial Eeg-fmri. *Neuroimage Clin.* 11, 486–493. doi: 10.1016/j.nicl.2016.03.010

Ciumas, C., Schaefers, G., Bouvard, S., Tailhades, E., Perrin, E., Comte, J. C., et al. (2014). A phantom and animal study of temperature changes during fmri with intracerebral depth electrodes. *Epilepsy Res.* 108, 57–65. doi: 10.1016/j.eplepsyres.2013.10.016

Cunningham, C. B. J., Goodyear, B. G., Badawy, R., Zaamout, F., Pittman, D. J., Beers, C. A., et al. (2012). Intracranial Eeg-fmri analysis of focal epileptiform discharges in humans. *Epilepsia* 53, 1636–1648. doi: 10.1111/j.1528-1167.2012.03601.x

Davis, L. M., Spencer, D. D., Spencer, S. S., and Bronen, R. A. (1999). Mr imaging of implanted depth and subdural electrodes: is it safe? *Epilepsy Res.* 35, 95–98. doi: 10.1016/s0920-1211(99)00007-8

Dewhirst, M. W., Viglianti, B. L., Lora-Michiels, M., Hanson, M., and Hoopes, P. J. (2003). Basic principles of thermal dosimetry and thermal thresholds for tissue damage from hyperthermia. *Int. J. Hyperth.* 19, 267–294. doi: 10.1080/0265673031000119006

Erhardt, J. B., Fuhrer, E., Gruschke, O. G., Leupold, J., Wapler, M. C., Hennig, J., et al. (2018). Should patients with brain implants undergo Mri? *J. Neural Eng.* 15:041002. doi: 10.1088/1741-2552/aab4e4

Georgi, J. C., Stippich, C., Tronnier, V. M., and Heiland, S. (2004). Active Deep Brain Stimulation during Mri: a Feasibility Study. *Magn. Reson. Med.* 51, 380–388. doi: 10.1002/mrm.10699

Gotman, J., Kobayashi, E., Bagshaw, A. P., Bénar, C. G., and Dubeau, F. (2006). Combining Eeg and fmri: a multimodal tool for epilepsy research. *J. Magn. Reson. Imaging* 23, 906–920. doi: 10.1002/jmri.20577

Hall, J. A., and Khoo, H. M. (2018). Robotic-Assisted and Image-Guided Mri-Compatible Stereoelectroencephalography. *Can. J. Neurol. Sci.* 45, 35–43. doi: 10.1017/cjn.2017.240

Hawsawi, H. B., Carmichael, D. W., and Lemieux, L. (2017). Safety of Simultaneous Scalp or Intracranial Eeg during Mri: a Review. *Front. Phys.* 5:42. doi: 10.3389/fphy.2017.00042

Hawsawi, H. B., Papadaki, A., Thornton, J. S., Carmichael, D. W., and Lemieux, L. (2020). Temperature Measurements in the Vicinity of Human Intracranial Eeg Electrodes Exposed to Body-Coil Rf for Mri at 1.5T. *Front. Neurosci.* 14:429. doi: 10.3389/fnins.2020.00429

Henderson, J. M., Tkach, J., Phillips, M., Baker, K., Shellock, F. G., and Rezai, A. R. (2005). Permanent Neurological Deficit Related to Magnetic Resonance Imaging in a Patient with Implanted Deep Brain Stimulation Electrodes for Parkinson's Disease: case Report. *Neurosurgery* 57, E1063–E1063. doi: 10.1227/01.neu.0000180810.16964.3e

IEC (2015). *Particular Requirements for Basic Safety and Essential Performance of Magnetic Resonance Equipment for Medical Diagnosis. Iec 60601-2-33 Edition 3 Amendment 2*. Geneva, Switzerland: IEC.

Jaspers-Fayer, F., Ertl, M., Leicht, G., Leupelt, A., and Mulert, C. (2012). Single-trial Eeg-fmri coupling of the emotional auditory early posterior negativity. *Neuroimage* 62, 1807–1814. doi: 10.1016/j.neuroimage.2012.05.018

Khoo, H. M., Von Ellenrieder, N., Zazubovits, N., Dubeau, F., and Gotman, J. (2017). Epileptic networks in action: synchrony between distant hemodynamic responses. *Ann. Neurol.* 82, 57–66. doi: 10.1002/ana.24973

Larson, P. S., Richardson, R. M., Starr, P. A., and Martin, A. J. (2008). Magnetic resonance imaging of implanted deep brain stimulators: experience in a large series. *Stereotact Funct. Neurosurg.* 86, 92–100. doi: 10.1159/000112430

Lemieux, L., Allen, P. J., Franconi, F., Symms, M. R., and Fish, D. R. (1997). Recording of Eeg during fmri experiments: patient safety. *Magn. Reson. Med.* 38, 943–952. doi: 10.1002/mrm.1910380614

Li, Q., Liu, G., Yuan, G., Wang, G., Wu, Z., and Zhao, X. (2019). Single-trial Eeg-fmri reveals the generation process of the mismatch negativity. *Front. Hum. Neurosci.* 13:168. doi: 10.3389/fnhum.2019.00168

Liu, J. Y. W., Hawsawi, H. B., Sharma, N., Carmichael, D. W., Diehl, B., Thom, M., et al. (2022). Safety of intracranial electroencephalography during functional electromagnetic resonance imaging in humans at 1.5 tesla using a head transmit Rf coil: histopathological and heat-shock immunohistochemistry observations. *NeuroImage* 254:119129. doi: 10.1016/j.neuroimage.2022.119129

Mattei, E., Triventi, M., Calcagnini, G., Censi, F., Kainz, W., Mendoza, G., et al. (2008). Complexity of Mri induced heating on metallic leads: experimental measurements of 374 configurations. *BioMed. Eng. Online* 7, 1–16. doi: 10.1186/1475-925X-7-11

Mele, G., Cavaliere, C., Alfano, V., Orsini, M., Salvatore, M., and Aiello, M. (2019). Simultaneous Eeg-fmri for Functional Neurological Assessment. *Front. Neurol.* 10:848. doi: 10.3389/fneur.2019.00848

Nazzaro, J. M., Lyons, K. E., Wetzel, L. H., and Pahwa, R. (2010). Use of brain Mri after deep brain stimulation hardware implantation. *Int. J. Neurosci.* 120, 176–183. doi: 10.3109/00207450903389156

Nordbeck, P., Fidler, F., Weiss, I., Warmuth, M., Friedrich, M. T., Ehses, P., et al. (2008). Spatial distribution of Rf-induced E-fields and implant heating in Mri. *Magn. Reson. Med.* 60, 312–319. doi: 10.1002/mrm.21475

Nordbeck, P., Weiss, I., Ehses, P., Ritter, O., Warmuth, M., Fidler, F., et al. (2009). Measuring Rf-induced currents inside implants: impact of device configuration on Mri safety of cardiac pacemaker leads. *Magn. Reson. Med.* 61, 570–578. doi: 10.1002/mrm.21881

Patrick Reilly, J. (2016). Survey of numerical electrostimulation models. *Phys. Med. Biol.* 61, 4346–4363. doi: 10.1088/0031-9155/61/12/4346

Ridley, B., Wirsich, J., Bettus, G., Rodionov, R., Murta, T., Chaudhary, U., et al. (2017). Simultaneous Intracranial Eeg-fmri Shows Inter-Modality Correlation in Time-Resolved Connectivity Within Normal Areas but Not Within Epileptic Regions. *Brain Topogr.* 30, 639–655. doi: 10.1007/s10548-017-0551-5

Saignavongs, M., Ciumas, C., Petton, M., Bouet, R., Boulogne, S., Rheims, S., et al. (2017). Neural Activity Elicited by a Cognitive Task can be Detected in Single-Trials with Simultaneous Intracerebral Eeg-fmri Recordings. *Int. J. Neural Syst.* 27:1750001. doi: 10.1142/S0129065717500010

Sammartino, F., Krishna, V., Sankar, T., Fisico, J., Kalia, S. K., Hodaie, M., et al. (2017). 3-Tesla Mri in patients with fully implanted deep brain stimulation devices: a preliminary study in 10 patients. *J. Neurosurg.* 127, 892–898. doi: 10.3171/2016.9.JNS16908

Schaefer, D. J., Bourland, J. D., and Nyenhuis, J. A. (2000). Review of patient safety in time-varying gradient fields. *J. Magn. Reson. Imaging* 12, 20–29. doi: 10.1002/1522-2586(200007)12:1<20::aid-jmri3>3.0.co;2-y

Smith, D. C. (1993). *High Frequency Measurements and Noise in Electronic Circuits*. Berlin: Springer.

Spiegel, J., Fuss, G., Backens, M., Reith, W., Magnus, T., Becker, G., et al. (2003). Transient dystonia following magnetic resonance imaging in a patient with deep brain stimulation electrodes for the treatment of Parkinson disease. Case Rep. *J. Neurosurg.* 99, 772–774. doi: 10.3171/jns.2003.99.4.0772

Tehrani, N., Wilson, W., Pittman, D. J., Mosher, V., Peedicail, J. S., and Aghakhani, Y. (2021). Localization of interictal discharge origin: a simultaneous intracranial electroencephalographic-functional magnetic resonance imaging study. *Epilepsia* 62, 1105–1118. doi: 10.1111/epi.16887

Vulliemoz, S., Carmichael, D. W., Rosenkranz, K., Diehl, B., Rodionov, R., Walker, M. C., et al. (2011). Simultaneous intracranial Eeg and fmri of interictal epileptic discharges in humans. *Neuroimage* 54, 182–190. doi: 10.1016/j.neuroimage.2010.08.004

Wang, T. R., Dallapiazza, R. F., Moosa, S., Huss, D., Shah, B. B., and Elias, W. J. (2018). Thalamic Deep Brain Stimulation Salvages Failed Focused Ultrasound Thalamotomy for Essential Tremor: a Case Report. *Stereotactic Funct. Neurosurg.* 96, 60–64. doi: 10.1159/000486646

Weise, L. M., Schneider, G. H., Kupsch, A., Haumesser, J., and Hoffmann, K. T. (2010). Postoperative Mri examinations in patients treated by deep brain stimulation using a non-standard protocol. *Acta Neurochir.* 152, 2021–2027. doi: 10.1007/s00701-010-0738-y

Wennberg, R., Valiante, T., and Cheyne, D. (2011). Eeg and Meg in mesial temporal lobe epilepsy: where do the spikes really come from? *Clin. Neurophysiol.* 122, 1295–1313. doi: 10.1016/j.clinph.2010.11.019

Winter, L., Seifert, F., Zilberti, L., Murbach, M., and Ittermann, B. (2020). Mri-Related Heating of Implants and Devices: a Review. *J. Magn. Reson. Imaging* 53, 1646–1665. doi: 10.1002/jmri.27194

Yazdani, M., Reagan, J., Kocher, M., Antonucci, M., Taylor, J., Edwards, J., et al. (2021). Safety of Mri in the localization of implanted intracranial electrodes for refractory epilepsy. *J. Neuroimaging* 31, 551–559. doi: 10.1111/jon.12848

Yeung, C. J., Karmarkar, P., and Mcveigh, E. R. (2007). Minimizing Rf heating of conducting wires in Mri. *Magn. Reson. Med.* 58, 1028–1034. doi: 10.1002/mrm.21410

Ziegelberger, G., Croft, R., Feychting, M., Green, A. C., Hirata, A., and D'inzeo, G. (2020). Guidelines for limiting exposure to electromagnetic fields (100 kHz to 300 Ghz). *Health Phys.* 118, 483–524. doi: 10.1097/HP.0000000000001210

Zrinzo, L., Yoshida, F., Hariz, M. I., Thornton, J., Foltynie, T., Yousry, T. A., et al. (2011). Clinical safety of brain magnetic resonance imaging with implanted deep brain stimulation hardware: large case series and review of the literature. *World Neurosurg.* 76, 164–172. doi: 10.1016/j.wneu.2011.02.029

Conflict of Interest: The authors declare that the research was conducted in the absence of any commercial or financial relationships that could be construed as a potential conflict of interest.

frontiers | Frontiers in Neuroscience

REVIEW
published: 07 July 2022
doi: 10.3389/fnins.2022.905979

Vascular Cognitive Impairment After Mild Stroke: Connectomic Insights, Neuroimaging, and Knowledge Translation

Jess A. Holguin[1], John L. Margetis[1], Anisha Narayan[2], Grant M. Yoneoka[3] and Andrei Irimia[4,5]**

[1] T.H. Chan Division of Occupational Science and Occupational Therapy, University of Southern California, Los Angeles, CA, United States, [2] Tulane University School of Medicine, Tulane University, New Orleans, LA, United States, [3] John A. Burns School of Medicine, University of Hawai'i at Mānoa, Honolulu, HI, United States, [4] Leonard Davis School of Gerontology, Ethel Percy Andrus Gerontology Center, University of Southern California, Los Angeles, CA, United States, [5] Corwin D. Denney Research Center, Department of Biomedical Engineering, Viterbi School of Engineering, University of Southern California, Los Angeles, CA, United States

OPEN ACCESS

Edited by:
Aleksandra Dagmara Kawala-Sterniuk, Opole University of Technology, Poland

Reviewed by:
Mario Versaci, Mediterranea University of Reggio Calabria, Italy
Timothy Michael Ellmore, City College of New York, United States

***Correspondence:**
Jess A. Holguin
jess.holguin@med.usc.edu
Andrei Irimia
irimia@usc.edu

Specialty section:
This article was submitted to Brain Imaging Methods, a section of the journal Frontiers in Neuroscience

Received: *28 March 2022*
Accepted: *20 June 2022*
Published: *07 July 2022*

Citation:
Holguin JA, Margetis JL, Narayan A, Yoneoka GM and Irimia A (2022) Vascular Cognitive Impairment After Mild Stroke: Connectomic Insights, Neuroimaging, and Knowledge Translation. Front. Neurosci. 16:905979. doi: 10.3389/fnins.2022.905979

Contemporary stroke assessment protocols have a limited ability to detect vascular cognitive impairment (VCI), especially among those with subtle deficits. This lesser-involved categorization, termed mild stroke (MiS), can manifest compromised processing speed that negatively impacts cognition. From a neurorehabilitation perspective, research spanning neuroimaging, neuroinformatics, and cognitive neuroscience supports that processing speed is a valuable proxy for complex neurocognitive operations, insofar as inefficient neural network computation significantly affects daily task performance. This impact is particularly evident when high cognitive loads compromise network efficiency by challenging task speed, complexity, and duration. Screening for VCI using processing speed metrics can be more sensitive and specific. Further, they can inform rehabilitation approaches that enhance patient recovery, clarify the construct of MiS, support clinician-researcher symbiosis, and further clarify the occupational therapy role in targeting functional cognition. To this end, we review relationships between insult-derived connectome alterations and VCI, and discuss novel clinical approaches for identifying disruptions of neural networks and white matter connectivity. Furthermore, we will frame knowledge translation efforts to leverage insights from cutting-edge structural and functional connectomics research. Lastly, we highlight how occupational therapists can provide expertise as knowledge brokers acting within their established scope of practice to drive substantive clinical innovation.

Keywords: stroke, neuroimaging, occupational therapy, neurorehabilitation, cognitive dysfunction, neurocognitive function, translational medical research, connectomics

INTRODUCTION

Stroke is the most frequent cause of disability in the United States (Ovbiagele and Nguyen-Huynh, 2011), a fact that spurs investigation into the nature and variability of infarct-related deficits along a continuum of impairment. The literature is replete with widely accepted functional characterizations of moderate through severe stroke (Murphy et al., 2001; Hodics et al., 2012; Rost et al., 2016), with less clarity available on mild clinical presentations

(Brott et al., 1989; Roberts et al., 2020). This uncertainty stems from the absence of a precise taxonomy for characterizing the mild stroke (MiS) population (Roberts et al., 2020). In clinical practice, the lack of a consensus definition precludes consistency in evaluation and treatment approaches and obscures understanding of this population's needs.

Ongoing work to develop an accord on MiS codification can benefit both research and clinical practice. In their systematic review on downstream effects of inconsistent MiS classification, Roberts et al. (2020) discuss 10 distinct definitions present in the literature. This lack of diagnostic and taxonomic uniformity potentiates knowledge translation efforts targeting the depth and breadth of understanding within this important stroke practice and research area. However, even a robust consensus definition cannot explain mechanisms that drive variation in post-stroke disability, especially regarding shared and distinct underpinnings among each NIH Stroke Scale (NIHSS) severity level (National Institute of Neurological Disorders and Stroke, 2011).

Within this review, we address MiS-relevant associations between vascular cognitive impairment (VCI), processing speed (PS), and neural network efficiency, as informed by insights from neuroimaging and connectomics research. We present evidence suggesting that established norms for key neurocognitive assessments can be used as proxies for detecting potentially overlooked VCI. Infusing emerging theoretical perspectives from multiple academic disciplines, we review approaches that can fuel substantial clinical innovation. In particular, we focus on using proxy-defined, threshold-specific instances of dysfunction that are scalable according to premorbid capacities and inherent daily routine demands. Drawing from neuroimaging-informed models employed to predict and monitor stroke recovery, we argue that performance capacity can be quantified by the degree of dissociation between available and necessary performance skills. Such quantification could empower clinicians and MiS survivors to more strategically consider interrelationships between current abilities and requisite progress along an ecologically valid, individualized recovery timeline.

We also examine three intersecting themes that provide a framework for early MiS care innovation and highlight paths to advance clinical investigation targeting health and wellbeing. After providing background on essential considerations of stroke and associated cognitive sequelae, we first review the problem of MiS-associated-VCI (MiS-VCI) underdetection and clarify the consequences of imprecisely characterizing stroke-derived neurocognitive dysfunction. Secondly, we examine the promise of knowledge translation efforts to improve stroke care and address priorities articulated by healthcare systems and research funding agencies. Thirdly, we overview and delineate knowledge relevant to MiS-VCI rehabilitation that derives from cutting-edge neuroanatomic, structural, and functional connectomics research. These studies employ advanced neuroimaging technologies plus conventional computed tomography (CT) and magnetic resonance imaging (MRI). Importantly, we focus on PS as a proxy for the integrity of neural networks and neurocognitive capacities. Lastly, we highlight clinical implications and future directions by providing evidence and arguments supporting more comprehensive MiS-VCI screening in early stroke care and emphasize the pivotal role of occupational therapy (OT) in addressing functional cognition.

While calling attention to the valuable confluence of contemporary research findings and clinical stroke rehabilitation practices, we will discuss literature ranging from the acute to more chronic phases of recovery. Beyond temporal considerations, foundational links between network theory and neurological insults are influenced by a broad range of factors such as demographic characteristics, lesion laterality, and even mechanisms of injury (e.g., ischemic vs. hemorrhagic stroke vs. traumatic brain injury). Herein, we do not focus on such differentiating factors, as it would far exceed the scope of this endeavor and is the likely purview of future prospective data-analytic studies. We do, however, discuss in detail the findings from conceptual and applied perspectives on an overarching construct poised to drive innovation in clinical practice. Please see **Table 1**. for a summary of constructs and interrelationships.

BACKGROUND

Stroke Diagnosis and Classification

Currently, stroke is diagnosed based on neuroimaging and clinical examinations. Aberrant clinical examinations often reflect ischemia-associated fragmentation of neural networks and are highly correlated with abnormal findings on CT or MRI (Jadhav et al., 2020). More severe levels of stroke are typically accompanied by overt motor, sensory, and neurocognitive impairments. By contrast, MiS often involves a small ischemic lesion that may go undetected even when employing standard CT imaging. Detecting subtle deficits is further complicated by an upstream dearth of information concerning MiS-VCI. Lacking a consensus taxonomy for MiS, clinicians often rely on imprecise or inadequate categorizations of symptoms and sequelae. Such conceptualizations are frequently derived from routine neurological assessment protocols which quantify post-stroke severity and functional impairment but fall short of informing rehabilitation approaches (Hajek et al., 1997; Wolf and Rognstad, 2013). Importantly, many of these metrics quantify interrelationships between motor deficits and patients' daily functioning by focusing on the ability to perform activities of daily living (ADL), bed mobility, transfers, and ambulation, rather than neurocognitive capacities (Wolf and Rognstad, 2013; Lee et al., 2015). Within this review, we use the overarching TREAT definition of MiS (Spokoyny et al., 2015) (i.e., NIHSS 0-5, and the absence of visual field deficits, aphasia, pronounced weakness, or other disabling deficits).

Neurocognitive Function, Vascular Cognitive Impairment, and Functional Cognition

"Neurocognitive" refers to the interrelated domains of perceptual-motor function, language, social cognition, complex attention, executive function (EF), learning, and memory (Ganguli et al., 2011). VCI refers to the broad spectrum of neurocognitive impairment associated with vascular pathology,

TABLE 1 | Summary of overarching constructs, themes, and seminal works within the reviewed sources.

References	Summary Points
MiS classification and VCI underdetection	
Roberts et al., 2020	Highlights inconsistencies in MiS classification linked to contemporary methods of assessment, imaging, and outcomes. Discusses 10 different definitions present in the literature.
Fischer et al., 2010	Examined six MiS definitions and outcomes, testing their validity in stroke patient subgroups. Determined that definitions best suited for this population were: (a) those with a score of 1 or less on every NIHSS item and normal consciousness; or (b) an NIHSS score of three or less.
Burns et al., 2018	Presents findings from The Health and Wellness Task Force that emphasize return to work and driving as being key aspects of community reintegration following stroke. Discusses "mild stroke" as a misnomer in light of the persistent challenges experienced by MiS survivors. Notes the disconnect between patients' needs and available services to address them. Proposes an interdisciplinary MiS practice model to assist those described as frequently being discharged from the hospital without appropriate rehabilitation services targeting complex life activities.
Wolf and Rognstad, 2013	Study with findings indicating ".performance on standardized cognitive testing in the early phases of mild stroke remained stable over a 6-month period. These results help justify the necessity and ability to assess cognition immediately post-mild stroke in order to make accurate and appropriate rehabilitation recommendations." p. 256
Hajek et al., 1997	Examined patients' performance on 11 multifaceted stroke assessments. Determined. . . "cognitive functions are frequently affected in stroke patients, cognitive impairment needs to be more seriously considered when describing and/or predicting a patient's level of independence." p. 1331
Yakhkind et al., 2016	Reviews current evidence and standard of care for MiS patients. "A majority of patients with ischemic stroke present with mild deficits for which aggressive management is not often pursued. Comprehensive work-up and appropriate intervention for minor strokes and transient ischemic attacks (TIAs) point toward better patient outcomes, lower costs, and fewer cases of disability. Imaging is a key modality to guide treatment and predict stroke recurrence." p. 86
Balasooriya-Smeekens et al., 2016	"Stroke and transient ischemic attack (TIA) survivors reported residual impairments that for many had impact on work. Most impairments were 'invisible', including fatigue, problems with concentration, memory and personality changes. . . .Despite having been able to return to work after a stroke, people may still experience difficulties in staying in work and risking losing their job."
Adamit et al., 2015	Prospective cohort study of interrelationships among cognition, participation and quality of life (QoL) among MiS survivors. Participants experienced neurocognitive impairments negatively impacting participation and QoL. Health care systems and rehabilitation programs neglect the rehabilitation needs of MiS patients as they are seemingly independent with basic daily tasks. MiS has long-term effects impacting patients and their family members.
Barbay et al., 2018	Systematic review and meta-analysis of prevalence in post-stroke neurocognitive disorders (NCD) found 36% prevalence among MiS survivors. Argued that "Harmonization of stroke assessment and cognitive score thresholds is urgently needed to allow more accurate estimation of post-stroke NCD prevalence, especially mild post-stroke NCD." P. 322
Neurocognitive Function and VCI	
de Haan et al., 2006	Cognitive and emotional outcomes are linked to: (a) focal damage causing selective impairments from gray matter dysfunction; (b) diffuse neuronal dysfunction compromising mental speed, memory, and executive functioning; and (c) outcomes being modulated by age, sex, premorbid level of functioning, and comorbidity. Modern neuropsychological assessment can facilitate patient classification, intervention selection, and creation of prognostic models.
Irimia et al., 2014	Reviews the state of the art in structural and connectomic neuroimaging targeting brain atrophy, alterations in morphometry, and inter-regional connectivity post injury. Discusses monitoring of clinical condition and evolution of status, including the potential for translational impact when coupled with neuropsychological measures.
Irimia and Van Horn, 2015b	Summarizes the use of functional magnetic resonance imaging, diffusion tensor imaging, positron emission tomography, magnetic resonance spectroscopy, and electroencephalography for studying TBI-related brain dysfunction and improving rehabilitation. Neurocognitive aspects discussed include consciousness, attention, memory, higher cognition, personality, and affect. Provides recommendations for future neuroimaging research.
Bullmore and Sporns, 2009	Highly influential review of complex brain networks in diverse experimental modalities (e.g., structural and functional MRI, diffusion tensor imaging, magnetoencephalography and electroencephalography).
Turken et al., 2008	Demonstrated correlation between Digit-Symbol performance and fractional anisotropy of white matter in bilateral parietal and temporal lobes and the left middle frontal gyrus. Assessed the effect of white matter damage on processing speed using voxel-based lesion-symptom mapping. Results indicated that cognitive processing speed is correlated with the structural integrity of white matter tracts associated with parietal and temporal cortices, left middle frontal gyrus, and the superior longitudinal fasciculus.
Gawryluk et al., 2014	Study employing 4T fMRI and an adapted Symbol Digit Modalities Test to identify white matter activation in either the corpus callosum or internal capsule in 88% of participants. "A key step in linking neuroimaging advances to the evaluation of clinical disorders is to examine whether WM activation can be detected at the individual level during clinical tests associated with WM function."
Adleman et al., 2002	". . . the first developmental fMRI investigation of the Stroop interference task, provides a template with which normal development and neurodevelopmental disorders of prefrontal cortex function can be assessed."

(Continued)

TABLE 1 | (Continued)

References	Summary Points
Neuroimaging and Neuroinformatics	
Lim and Kang, 2015	Outlines the basic concepts of structural and functional connectivity, and the connectome. Explores current evidence regarding how stroke lesions cause changes in connectivity and network architecture parameters. Discusses clinical implications of perspectives on the connectome in relation to the cognitive and behavioral sequela of stroke. p. 256
Eckert, 2011	Neuroimaging morphometry study on neurobiological predictors of age-related changes in processing speed. Declines in specific neural systems compromise processing speed. "Future studies of processing speed – dependent neural systems will be important for identifying the etiologies for processing speed change and the development of interventions that mitigate gradual age-related declines in cognitive functioning and enhance healthy cognitive aging." p. 25
MiS-VCI rehabilitation and links to neuroanatomic, structural, and functional connectomics research	
Park and Friston, 2013	Context-sensitive integration during cognition tasks entails a divergence between structural and functional networks. Function-structure mapping is crucial for understanding the nature of brain networks. The emergence of dynamic functional networks from static structural connections calls for a formal (computational) approach to neuronal information processing that may resolve this dialectic between structure and function. p. 579
Petersen and Sporns, 2015	". . .network science offers a theoretical framework for approaching brain structure and function as a multi-scale system comprised of networks of neurons, circuits, nuclei, cortical areas and systems of areas. This paper views large-scale networks at the level of areas and systems, mostly based on data from human neuroimaging, and how this view of network structure and function has begun to illuminate our understanding of the biological basis of cognitive architectures." p. 207
Kuceyeski et al., 2016	Demonstrated that "measures of baseline connectome disruption, acquired using only routinely collected MRI scans, can predict 6-month post-stroke outcomes in various functional domains including cognition, motor function and daily activities." p. 2587
Liew et al., 2020	". . . outlines the efforts taken by the ENIGMA Stroke Recovery working group to develop neuroinformatics protocols and methods to manage multisite stroke brain magnetic resonance imaging, behavioral and demographics data. Specifically, the processes for scalable data intake and preprocessing, multisite data harmonization, and large-scale stroke lesion analysis are described, and challenges unique to this type of big data collaboration in stroke research are discussed. Finally, future directions and limitations, as well as recommendations for improved data harmonization through prospective data collection and data management, are provided." p. 129
Lopes et al., 2021	"Prediction accuracy was evaluated in four domains (memory, attention/executive, language and visuospatial functions) and compared with clinical data and other functional networks. . . A machine learning model based on the post-stroke cognitive impairment network can predict the long-term cognitive outcome after stroke." p. E1167
Knowledge translation approach to improving stroke care	
Austin, 2021	"The mission of translational science is to bring predictivity and efficiency to the development and dissemination of interventions that improve human health. . . Reviews the origins of translational science and advances to this point." p. 1629
Meyer, 2010	"Knowledge brokers are people or organizations that move knowledge around and create connections between researchers and their various audiences. This commentary reviews some of the literature on knowledge brokering and lays out some thoughts on how to analyze and theorize this practice." p. 118
Chaudoir et al., 2013	Systematic review of structural, organizational, provider, patient, and innovation level measures affecting implementation of health innovations. ". . .discussion centers on strategies that researchers can utilize in order to identify, adapt, and improve extant measures for use in their own implementation research. In total, our literature review and resulting measures compendium increases the capacity of researchers to conceptualize and measure implementation-related constructs in their ongoing and future research." p. 1

foregrounding working memory, PS, and EF as sensitive categorical impairment indicators (Hachinski et al., 2006). VCI is arguably a key defining characteristic of MiS and a robust predictor of successful participation in normal daily routines (Khatri et al., 2010; Spokoyny et al., 2015; Overdorp et al., 2016). Nevertheless, VCI is often overlooked in acute clinical settings despite multilevel implications for patients, health care systems, and society (Tellier and Rochette, 2009; Ovbiagele et al., 2013; Adamit et al., 2015). This disconnection stems from insufficient MiS diagnostic criteria, with underdeveloped characterizations impeding deficit identification and remediation (Fischer et al., 2010; Roberts et al., 2020). Even using the term *mild,* in this context, can inadequately represent the persistent obstacles within post-stroke daily functioning (Burns et al., 2018). Lastly, "functional cognition" relates to OT's focus on "clients" and their capacity to perform essential tasks given the totality of their abilities, including their use of strategies, habits/routines, and contextual/environmental resources (Giles et al., 2017). Although functional cognition requires looking beyond discrete skills, we contend that initially employing a sound, generalized proxy for network dysfunction can increase access to more specific, comprehensive, and ecologically valid types of intervention currently missing from MiS care.

Neurorehabilitation research and practice are moving toward performance-based assessment tools, such as the Executive Function Performance Test (Baum et al., 2008), the Menu Task (Al-Heizan et al., 2020), and the Kettle Test (Hartman-Maeir et al., 2009). Yet, traditional instruments such as the

Trail Making Test (Reitan, 1958), Symbol-Digit Modalities Test (SDMT) (Smith, 1973), and Stroop Color-Word Test (SCWT) (Golden and Freshwater, 2002) remain part of the gold standard for validating newer instruments. Despite newer tools achieving higher ecological validity by evaluating real-world task performance, their administration requirements often strain clinician capacities given time and environmental limitations inherent to practice, especially in fast-paced hospital settings.

In this review, we highlight the use of PS to detect compromised connectome integrity. We further explore how assessing VCI via the select, psychometrically robust instruments discussed herein can significantly improve early stroke care services. In particular, circumscribing and formalizing early MiS-VCI detection protocols can help identify subtle deficits that may be otherwise overlooked. Further, more uniform, sensitive, and specific assessments can potentiate greater access to subsequent performance-based OT evaluations emphasizing functional cognition.

Mild Stroke-Vascular Cognitive Impairment Underdetection

Uncertainty surrounding the concept of MiS-VCI derives in part from inadequate in-place assessment protocols (Roberts et al., 2020). This shortcoming is troubling given that VCI is common among MiS survivors (Chung et al., 2013; Spokoyny et al., 2015; Overdorp et al., 2016) and involves subtle—yet persistent—deficits in working memory and EF. Importantly, PS (i.e., "the rapidity with which a patient processes simple or routine information without making errors of either omission or commission," Weiss et al., 2010) can sensitively detect MiS-VCI. Improper or inadequate computation within neural networks can significantly impact patients' ability to undertake daily life tasks, especially when required speed, complexity, and duration amount to high cognitive loads (Khatri et al., 2010; Wolf and Rognstad, 2013; Spokoyny et al., 2015). To offset such potential issues, we wish to extend the scope of care available to the underserved MiS population.

Building on existing literature, we aim to advance MiS-VCI knowledge translation targeting clinical research. To this end, we discuss MiS-relevant scope, implications, and opportunities afforded by structural neuroimaging and connectomics research, though without deeply exploring overarching MiS and VCI associations that are thoroughly reviewed elsewhere (Brodaty et al., 2010; Spitzer et al., 2011; Li et al., 2012; Wolf and Rognstad, 2013; Spokoyny et al., 2015; Sensenbrenner et al., 2020). More concretely, we propose a novel course of action informed by neuroimaging, connectomics, network science, and OT that quantifies covert VCI and highlights the mechanistic link to connectopathies. Our central thesis holds that, in light of technological innovation and advances in neuroimaging and neuroinformatics, PS has emerged as an underutilized—yet essential—indicator of compromised neural network integrity, and thus as a viable MiS-VCI biomarker.

Acute stroke screening protocols lack the ability to consistently detect subtle MiS-VCI. Not having sensitive indicators of potential VCI can potentiate patients being ill-prepared to resume full participation in their daily routine. Being unaware of possible neurocognitive deficits, MiS survivors may prematurely recommence complex tasks such as driving, employment, and caregiving. Therefore, we support using robust capacity indicators to quantify potential discrepancies between pre- and post-stroke levels of functioning.

Mild stroke survivors experience less sensorimotor and VCI than those with moderate-to-severe strokes (Tellier and Rochette, 2009). Yet, they have similar rates of disability (19%, Cucchiara et al., 2019) as all stroke severity classifications as a whole (22%, Mu et al., 2017). Current methodological approaches for understanding and quantifying the nuances of MiS-VCI cannot explain the mechanisms that underlie these findings. Therefore, a critical question is: What is the source of MiS survivors' documented disability?

Even subtle VCI can manifest a profound functional disconnection between past and present capacities when individuals undertake complex tasks (Stephens et al., 2005). In practice, there are widely accepted measures of motor function such as the Fugl-Meyer assessment (Fugl-Meyer et al., 1975) and the Action Research Arm Test (Lyle, 1981; Santisteban et al., 2016). Yet, uncertainty regarding the measurement and classification of MiS-VCI persists. In this context, focusing on MiS-VCI may yield promising etiological insights (de Haan et al., 2006) via ecologically valid perspectives on daily task proficiency (Stephens et al., 2005).

Profound VCI unquestionably contributes to stroke-associated disability (Spitzer et al., 2011; Wolf and Rognstad, 2013; Sensenbrenner et al., 2020). Yet, there is an absence of research examining the influence of PS thresholds on the likelihood and severity of post-stroke disability. This knowledge gap stems from the widespread practice of classifying stroke by heavily weighting the degree of motor impairment, leading to estimates that 88% of stroke cases acquire notable motor deficiencies, with 71% failing to regain motor function within 6 months of onset (Bonita and Beaglehole, 1988). Among those with TREAT-defined MiS, 29-35.6% reportedly experience residual deficits (Spokoyny et al., 2015). Regarding MiS-VCI, focusing on the degradation of network efficiency to better understand post-stroke disability reveals a path to move beyond the circumscribed utility of primarily motor-driven assessments.

Impact of Underdetection

Stroke survivors with less pronounced impairments are more likely to resume participation in complex activities that offer little margin for error (Hofgren et al., 2007). This tendency may help explain how MiS survivors that lack overt deficits ultimately file for disability at relatively similar rates to those with higher degrees of documented impairment (Mu et al., 2017). To a potentially detrimental degree, decisions regarding activity participation are likely scaled according to patients' perceived residual capacity. This perspective derives from individuals' reflections on their lived experience, combined with the degree to which healthcare providers have endorsed their overarching capacities. Though predominantly missing from discussions in contemporary practice, PS provides a sound framework for assessing the integrity of neurocognitive operations in a way that can bridge the gap between actual and perceived abilities.

As detailed in subsequent sections, PS can provide a valuable, quantifiable proxy for neurocognitive function. Moreover, it can drive cutting-edge knowledge translation efforts targeting stroke severity characterization and recovery prediction.

Stroke survivors discharging from the acute hospital setting with unrecognized MiS-VCI face considerable challenges in resuming safe and independent daily routine participation (Balasooriya-Smeekens et al., 2016; Camicia et al., 2016). Unfortunately, there is a dearth of literature coalescing clinical evidence to compel early, highly sensitive neurocognitive assessment that could prompt referrals to essential outpatient therapy services following hospitalization. Without improved, neurocognitively focused early stroke care screening protocols, MiS will remain inconsistently detected, incompletely understood, and MiS survivors will continue to struggle in silence (Barbay et al., 2018).

Despite unequivocal evidence linking functional cognition to successful ADL performance (Chung et al., 2013; Fride et al., 2015; Overdorp et al., 2016), widely used stroke assessments lack the sensitivity to detect subtle VCI (Wolf and Rognstad, 2013; Yakhkind et al., 2016; Burns et al., 2018). Concerns about the limited scope of diagnostic instruments are compounded by the frequent suspicion that some MiS patients are incorrectly perceived as lacking deficits (Yakhkind et al., 2016). As a result, MiS patients are often discharged with unrecognized VCI after brief hospital admissions (Balasooriya-Smeekens et al., 2016; Camicia et al., 2016), and are likely to experience threshold-dependent VCI.

Broadly conceived, threshold-dependent VCI involves diminished neurocognitive functioning linked to activity-dependent increases in cognitive load. Daily living involves fluctuating requirements in speed, complexity, and duration inherent to activity engagement. PS metrics can quantify maladaptive responses to variable, multifocal task demands (Leavitt et al., 2011). Thus, increased cognitive load, reflecting greater requisite mental effort during task performance (Calvillo and Irimia, 2020), is linked to diminished task performance quality (Hajek et al., 1997; Fischer et al., 2010). Clinical stroke protocols can benefit from incorporating elements informed by responses to cognitive load and likely individual-specific performance variability.

Knowledge Translation

Entrenched disconnections between research discovery and carry over into clinical practice reinforce a longstanding barrier to mutually beneficial exchanges of ideas (Austin, 2021). Previous efforts targeting top-down, direct-translation of knowledge to end-users have attempted to rectify this issue, with recent trends favoring intricate, multilevel stakeholder collaborations. Within a knowledge translation framework, OT is highly qualified to incorporate innovative approaches into multidisciplinary care collaboratively. Such ends can be accomplished by OT occasionally acting as the knowledge broker, a designation characterizing persons that "facilitate the creation, sharing, and use of knowledge" (Meyer, 2010).

Given OT's expertise in addressing functional cognition within dynamic, real-world contexts, practitioners can facilitate valuable MiS-VCI research collaborations mobilizing neuroimaging and connectomics-based knowledge. In particular, they can lend insight into the multifaceted nature of patients' impairments, an essential component of innovative predictive models, patient care delivery, and communications with various stakeholders. Among allied health professions in acute care settings, OT is the only one to have demonstrated a statistically significant association between healthcare spending and lower readmission rates (Rogers et al., 2017). In line with NIH's emphasis on innovation and developing evidence-based treatment, OT's established expertise, in-place representation within acute care teams, and cost-effective services provide strong support for its potential to broker knowledge toward those ends effectively (Chaudoir et al., 2013).

Neuroimaging-Based Perspectives and Future Mild Stroke Care

Neuroimaging and Neuroinformatics for Mild Stroke Care

Neuroimaging technologies have added unprecedented scope and precision to our understanding of neurological disorders. Unfortunately, current advances in neuroimaging and neuroinformatics outpace translational efforts targeting MiS care. Given the symbiotic nature of translational research and clinical practice, such delays have hindered ongoing innovation in both domains. Although evidence-based protocols guiding early stroke care have improved recovery trajectories, common metrics quantifying MiS characteristics do not reflect recent insights into complex neural processes underlying observable clinical deficits. Instead, contemporary early stroke clinical assessments inordinately focus on motor capacity over cognitive function (Bonita and Beaglehole, 1988; Hodics et al., 2012), endorsing an underdeveloped representation of MiS sequelae.

Connectomics is the field of study concerned with the systematic mapping of neural connections. It provides a unique framework for analyzing neural network disruptions by combining graph theory methodology with neuroimaging (Irimia et al., 2014). Specifically, by conceptualizing brain regions as nodes with structural or functional properties connected by white matter (WM) fibers, connectomics can bridge the gap between mapping neural networks and understanding their functions (Bullmore and Sporns, 2009). Neural network analysis involves focusing on both functional and structural connectivity (Irimia and Van Horn, 2015b). Employing diffusion tensor imaging (DTI) and diffusion spectrum imaging, *structural* connectomics uses spatial topography data to construct a physical map of neural activity and infer WM anatomic organization along with neurological insult-derived connectivity damage (Irimia et al., 2014).

Using functional MRI (fMRI) (Irimia and Van Horn, 2015b), magnetoencephalography (MEG) (Irimia and Van Horn, 2015a), and electroencephalography (EEG) (Lima et al., 2006; Irimia and Van Horn, 2015a) *functional* connectomics involves the study of neural network activity via: (a) temporal dynamics; (b) maps representing information exchange between nodes and modules;

(c) resting states; and (d) responses to exogenous stimuli (Halgren et al., 2011). Such studies facilitate the measurement of network integrity following neurological insults, including stroke. Additionally, brain activity can be further understood mechanistically through activation patterns identified within the functional connectome. This lens can be useful when cognitive abilities, behavior, or network PS modulate neural responses (Craddock et al., 2015).

Ischemic insults can compromise information processing within and across neural networks. In worst-case scenarios, this ability is lost. In more moderate cases, neuroplasticity can facilitate the preservation of intended operational outputs in a lesioned network. Importantly, this type of recovery has been studied more thoroughly in sensorimotor than neurocognitive domains (Gray et al., 1989; Wang et al., 2010; Lee et al., 2015). With neurocognitive demands, however, negative consequences of ischemic insults may manifest as sub-optimal neural processing, producing operations that are detrimental to the desired outcome or are inadequately timed. Such imprecision gives rise to alternative neural pathway use during network activation sequences to meet specific PS demands (Honey and Sporns, 2008; Wang et al., 2010). By integrating connectomics insights into practice and knowledge translation initiatives, rehabilitation professionals can better identify, isolate, and subsequently target alternative pathways within patient-tailored therapeutic activities.

Consistent with previously discussed trends comparing VCI across stroke severity levels, the ubiquity of WM damage and compromised neurocognitive function is well-documented among severe cases (Zinn et al., 2007), and significantly less so among those with lower degrees of functional impairment (Wolf and Rognstad, 2013). Using innovative PS measures can more sensitively detect MiS-VCI than standard assessment protocols. The following two sections review evidence linking common processing efficiency metrics to emerging insights from connectomics. Such evidence, we propose, can aid the formulation of novel, concrete guidelines for utilizing such knowledge in clinical rehabilitation practice and knowledge translation endeavors.

Insights From Structural Connectomics

Previous studies have highlighted relationships between PS and the modulation of WM connections. For example, Turken et al. (2008) demonstrated that damage to the structural integrity of WM axons correlates with diminished performance in PS tasks. Specifically, posterior parietal lesions often lead to compromised PS and associated changes in the integrity of water diffusion anisotropy along WM fibers. Additional evidence suggests that brain activity recruiting temporo-occipital WM structures, such as the inferior longitudinal fasciculi, also modulates PS (Turken et al., 2008). There is robust support for the use of well-studied, psychometrically sound neurocognitive assessments targeting processing efficiency. For example, the SDMT evaluates PS and efficiency and is sensitive to WM disruptions (Gawryluk et al., 2014), whereas the SCWT includes a useful event-related cognitive task that can measure PS sensitively even in the presence of subtle VCI (Adleman et al., 2002).

DTI techniques like WM tractography facilitate the modeling and visualization of neural pathways (Basser and Pierpaoli, 2011). This method has been used to employ compromised processing efficiency as a metric for impairment magnitude across various neurocognitive domains. Action potentials propagating along WM axons enable information exchange across neural networks, often by synchronizing the firing of neuronal populations (Assaf and Pasternak, 2008; Turken et al., 2008; Basser and Pierpaoli, 2011). Thus, WM insults can substantially alter information processing across network nodes, disrupting neurocognitive capacities (Assaf and Pasternak, 2008; Turken et al., 2008; Basser and Pierpaoli, 2011). At the microscale, such insults often involve dendritic or synaptic loss and inflammation modulated by microglia, both phenomena being able to interfere with local network function (Lim and Kang, 2015).

In addition to applications for MiS-VCI, given DTI's ability to identify subtle WM abnormalities, it can assist in predicting functional outcomes in other cases involving less severe neurological insults. In particular, there is support for this technology addressing WM changes associated with cerebral hemorrhages and mild traumatic brain injury (Irimia et al., 2014), as well as those linked to the neuro-invasion potential of SARS-CoV-2 during the recovery from COVID-19 (Lu et al., 2020). Importantly, standard structural MRI cannot always detect WM changes (Lim and Helpern, 2002; Assaf and Pasternak, 2008). Thus, DTI can be leveraged to assist the diagnosis and classification of MiS, and help researchers elucidate the relationship between structural WM damage and MiS-VCI. Additionally, because DTI-based network analysis can provide quantitative measures of brain dysfunction, this strategy can complement in-place behavioral diagnostic methods. For these reasons, we propose that insights obtained by combining quantitative descriptions of structural network integrity and insult location can have utility for improving diagnostic accuracy while facilitating MiS characterization and targeted treatment-approach development.

Insights From Functional Connectomics

In its own right, functional connectivity can substantially assist MiS diagnosis and classification. Research suggests that the brain can be modeled as a small-world network with extensive local clustering, which facilitates efficient information processing (Lim and Kang, 2015). Global communication, by contrast, relies on long-range connections between network nodes. This ranged approach enables further information processing and integration across neuroanatomically or functionally distinct regions. The extent of network impairment following stroke is highly dependent upon lesion location and can alter both local and global network efficiencies (Wang et al., 2010; Lim and Kang, 2015). For example, Wang et al. (2010) studied patients with focal subcortical motor pathway damage and found that, compared to healthy volunteers, motor execution networks exhibited lower efficiency of local information transfer between homotopic brain network regions. Similarly, reductions in global network efficiency due to nodal damage have been demonstrated by both computational models and MRI studies (Honey and Sporns, 2008; Alstott et al., 2009; Wang et al., 2010). Therefore,

interpretations and clinical applications of connectomic measures require careful consideration.

While stroke may compromise local network efficiency, distal network modules can assume the roles of injured regions in response to rehabilitation (Biernaskie et al., 2005; Nomura et al., 2010; Grefkes and Fink, 2011). Given structural redundancies within the brain, these networks can be recruited during recovery from stroke, potentiating functional improvement. Whereas local network efficiency can decrease following stroke, there can also be simultaneous, compensatory functional connectivity increases throughout the brain. Compensation may involve rerouting information between nodes using indirectly connected uninjured regions, increasing the amount of neural processing commensurate with task demands.

Researchers can harness functional connectomics to enhance investigations of cortical information exchange and network integrity since connectomic analysis can sensitively detect subtle MiS-VCI. Furthermore, functional connectivity methods can facilitate the investigation of task-related, inter-regional coupling (Wang et al., 2010), phenomena that are essential considerations in conceptualizing VCI. Incorporating these insights into MiS care can bolster clinical assessment methods and improve the detection of subtle network inefficiencies associated with context-driven impairment.

PS: A Proxy for Complex Neurocognitive Function

To assess network processing efficiency and quantify the adequacy of mental operations indelible to neurocognitive function, clinical assessments should account for patient-specific factors that facilitate or hinder performance. Replicating stressors that fuel context-driven impairment can be impractical in acute care settings. In this light, there is utility in identifying a sound proxy to screen core neurocognitive capacities. One crucial factor that varies in response to context-driven cognitive demands is PS. Task-specific demands governing speed, complexity, and duration parameters influence the degree of perceived difficulty associated with any given neurocognitive operation.

Distractions and unexpected changes in the scope of a given task can negatively impact processing efficiency by increasing the cognitive load. Such challenges increase demands upon working memory and EF. Given the nuanced nature of daily living, difficulties may still ensue after reducing competing stimuli and prioritizing task resources. Within the literature, there are examples linking compromised PS to deficient saccadic eye movements and oculomotor impairment to neurocognitive dysfunction (Barnett and Singman, 2015). Similarly, the SCWT and the SDMT are gold-standard assessments of PS (Smith, 1973; Golden and Freshwater, 2002). Importantly, results from these instruments derive from large normative statistical samples and allow subject stratification according to age and educational attainment peers. These tests have also been used to measure neurocognitive function under heightened cognitive load (Siegle et al., 2008) and detect deficits ranging from subtle to profound impairment. In conclusion, using PS as a proxy to assess connectomic integrity and subsequent neurocognitive capacities provides a central organizing principle to inform MiS-VCI detection protocols, drive knowledge translation efforts, and refine treatment approaches.

DISCUSSION

Clinical Applications and Considerations

Building on the Human Connectome Project's body of knowledge, current conceptualizations of intact network processing (Sporns et al., 2005), generalized linear models of neurocognitive function (Park and Friston, 2013; Petersen and Sporns, 2015), and studies of damaged network integrity due to focal or diffuse injuries (Lim and Kang, 2015), the potential benefit of incorporating connectomic methods into MiS care protocols is compelling. Work toward this end involves creating functional connectivity models, plus calculating network clustering coefficients and characteristic path lengths (Bullmore and Sporns, 2009). Thus, improved MiS-VCI detection could involve quantifying neural network efficiency or the extent of network reorganization following injury. Such strategies offer the potential to stratify MiS presentations with substantial sensitivity and specificity based on the severity of functional network impairments. This approach has already been demonstrated in proof-of-concept studies involving moderate-to-severe stroke (Wang et al., 2010), suggesting that extending this method to more accurately characterize MiS-VCI should be a future research priority.

While clinical neuroimaging modalities critically inform medical management decisions following moderate and severe stroke (Wintermark et al., 2013), multimodal imaging and network theory research have substantially advanced our current understanding of structural and functional connectivity disturbances underlying MiS (Silasi and Murphy, 2014). Such progress has enabled clinicians and researchers to better characterize stroke lesions and their impact on structural and functional connectivity. In practice, neuroimaging localizes lesions topographically to construct a predictive framework for cognitive outcomes after stroke (Hope et al., 2013). However, most topographic models do not account for stroke severity (van Meer et al., 2012; Hope et al., 2013). Thus, aiming beyond topography-based lesion analysis (e.g., studying stroke-driven structural connectome alterations) can potentially help predict MiS-VCI incidence and identify associated biomarkers (Kuceyeski et al., 2016). To improve MiS care, clinician scientists, OT, and other allied health professions should acquire and incorporate findings from standard structural and multimodal imaging technologies. Employing aggregate, atlas-informed (Liew et al., 2020) neuroimaging biomarkers can aid MiS classification, reducing uncertainty stemming from absent consensus on best practices governing detection and diagnosis. Although MiS and brain network heterogeneity may be limiting factors in this respect, incorporating knowledge from VCI-associated deficit atlases can refine clinical evaluations (Wang et al., 2010). Insights from these data-driven approaches may inform the development and selection of MiS-VCI rehabilitation approaches rooted in daily living contexts.

However, what is the best way to employ multimodal approaches in quantifying network efficiency and PS while also deriving more sensitive and specific MiS-VCI characterizations? One process could involve the creation or refinement of resting-state fMRI atlases and mapping MiS-associated functional network impairments. This type of development would be akin to MR fingerprinting techniques (Ma et al., 2013) and the Virtual Brain Project, where neuroinformatics drives personalized medical care (Falcon et al., 2016).

Advances in network theory and neuroimaging applications can help clinicians develop innovative, evidence-based, early MiS care. For example, the literature supports the utility of studying compromised network efficiency linked to damaged neuroanatomical structures (Honey and Sporns, 2008). Due to stroke-related increases in average neural network path lengths, information relayed across these structures takes longer to reach intended destinations. This insult-derived change supports screening for MiS-VCI using PS metrics (Turken et al., 2008; Eckert, 2011), as PS is a key variable predicting overall cognition-based stroke outcomes (Su et al., 2015).

As previously discussed, VCI can be reliably measured at the bedside by OT using robust instruments like the SDMT and SCWT (Smith, 1973; Golden and Freshwater, 2002). Additionally, compromised PS can disrupt essential visual-motor skills such as pursuits and saccades. These foundational visual-motor abilities are sensitive to mild cortical insults and can reflect the integrity of core neurocognitive capacities at risk for context-driven impairment (Barnett and Singman, 2015). Therefore, healthcare providers should integrate this information into early stroke care protocols to increase MiS-VCI detection and subsequent access to services (e.g., outpatient OT targeting functional cognition and post-stroke quality of life).

Looking beyond applications within *acute* MiS care, neuroimaging advances could inform more effective functional cognition protocols for *chronic* insult recovery. Historically, clinicians have relied heavily upon assessment batteries or subjective measures to determine intervention efficacy (Hajek et al., 1997). However, research suggests that technology such as DTI can be employed to bolster predictions regarding motor responses to restorative stroke therapies (Cassidy et al., 2018). The validity of such approaches targeting MiS-VCI would be further strengthened by in-depth analyses of network disruptions within specific regions of interest, quantified by measures like connectivity strength (Sporns and Zwi, 2004; Park and Friston, 2013).

Future Directions

In addition to improving detection and service provision for stroke patients, emerging practices involving multimodal neuroimaging are being employed to model and predict clinical outcomes. For example, recent studies have successfully predicted aspects of post-stroke cognitive recovery by examining DTI-based connectivity measures and employing machine learning analysis of resting-state network fMRI data (Aben et al., 2021; Lopes et al., 2021). Unfortunately, these studies focus on long-term timelines, using measures acquired 6 months after stroke to predict function at 3-years, or 5 weeks post onset being used to predict 1-year status. We contend that, while such studies are important to advance our overarching understanding of stroke, we must also look pointedly at immediately pressing issues. Specifically, steps should be promptly taken to improve triaging and care for individuals experiencing MiS.

The clinical and neuroimaging communities should undertake sustained knowledge translation efforts to develop theory-driven, practice-based treatment models addressing the paucity of knowledge regarding MiS-VCI. As exemplified in the examples below, integrating neuroimaging protocols with clinical rehabilitation insights can enhance our understanding of this understudied condition. For instance, bolstering functional cognition assessments to consider network strain under high cognitive loads can improve MiS-VCI characterization. Also, positron emission tomography (PET) or MR spectroscopy (MRS) can potentiate improved post-stroke functional mapping and pharmacological targeting of performance-specific neurotransmitters and blood-borne molecules (Schlosser, 2000). Further, evidence supports that incorporating neuroimaging insights into pharmaceutical development protocols can improve early post-stroke medication effectiveness (Faingold and Blumenfeld, 2015). One potentially beneficial general consideration regarding MRI segmentation, as the accuracy of its scheme relies on the ability to differentiate between tissue classes (Madhukumar and Santhiyakumari, 2015) is that the use of fuzzy preprocessors can account for tissue geometry and reduce computational load (Versaci et al., 2015). Lastly, promising MEG/EEG mapping research supports that *temporal* network patterns reflect resource shifts pre, during, and post task performance (Irimia and Van Horn, 2015b). Studies such as these, examined within large samples, could elucidate high-frequency, time-dependent characteristics of network activity, against which deficient MiS-VCI dynamics can be compared. However, considerable work remains to clarify interrelationships between MiS-driven electrophysiological changes during neural activity and links to clinical parameters.

CONCLUSION

Subtle stroke-associated neurocognitive impairment is an under-examined condition that impacts patients, health care systems, and society overall (Sun et al., 2014). Though two-thirds of stroke survivors experience minor deficits (Yaghi et al., 2017), and the emerging recognition that VCI is a potential hallmark of MiS (Lim and Kang, 2015), conventional assessments often mischaracterize or inadequately detect MiS. Existing diagnostic and rehabilitation paradigms would benefit from incorporating current perspectives from neuroimaging and connectomics. Such inclusion would illustrate research and practice symbiosis, via knowledge translation efforts, targeting improved MiS-VCI construct clarification and clinical service provision.

Incorporating connectomics and network theory into existing clinical perspectives may require further innovation targeting the acquisition, analysis, and interpretation of neuroimaging data. Nevertheless, structural and functional neuroimaging methods

offer unique opportunities for scientific discovery and clinical advances in MiS care whether employed individually or together (Silasi and Murphy, 2014). Available literature supports two key approaches for developing and refining current perspectives: (a) quantify interrelationships between MiS-VCI and network dysfunction via existing neurocognitive assessments; and (b) atlas MiS-derived neural damage to bolster interdependence of MiS research and clinical practice (Liew et al., 2020). These and other strategic knowledge-translation efforts should be pursued in the understudied yet epidemiologically significant area of MiS-VCI.

Finally, considering the MiS-survivor experience, returning to prior routines can be fraught with challenges. Performing complex activities with neurocognitive deficits can be complicated by a narrow margin of error separating success from failure. Consider the prospect of resuming employment with undiagnosed MiS-VCI. A VCI-fueled unsuccessful return to work scenario is easy to envision without access to sensitive assessment and treatment. Despite legal protections available through the Americans with Disabilities Act (n.d.), there is still an inordinate risk for performance-based termination if MiS-VCI has not been identified.

Every day, lapses in judgment and substandard quality of work drives job loss among neurologically intact individuals. In this light, how are MiS-VCI survivors likely to fare given an increased probability of substandard complex task performance in conjunction with potential overestimations of their capacities? Without sensitive MiS-VCI assessments and established access to ecologically valid functional cognition interventions, MiS survivors are often ill-equipped to fully participate in the context of daily living. They are also likely to struggle in negotiating the impact of multifaceted functional disconnections from their baseline capacities. Such deficiencies can be life-changing, significantly altering their ability to perform other complex tasks such as driving and caregiving. In response to such potentialities, clinicians and researchers should proactively infuse cutting-edge neuroimaging technology, neuroinformatics, and connectomics perspectives into rehabilitative approaches to positively influence MiS survivors' neurocognitive recovery trajectories.

AUTHOR CONTRIBUTIONS

All authors listed have made a substantial, direct, and intellectual contribution to the work, and approved it for publication.

FUNDING

This study was supported by the National Institutes of Health grants R01 NS 100973 and RF1 AG 054443 to AI, by the U.S. Department of Defense contract W81XWH-18-1-0413, a Hanson-Thorell Family Research Scholarship, the James J. and Sue Femino Foundation, and the University of Southern California through the Undergraduate Research Associates Program (URAP) and the Center for Undergraduate Research in Viterbi Engineering (CURVE).

REFERENCES

Aben, H. P., De Munter, L., Reijmer, Y. D., Spikman, J. M., Visser-Meily, J. M. A., Biessels, G. J., et al. (2021). Prediction of Cognitive Recovery After Stroke: The Value of Diffusion-Weighted Imaging-Based Measures of Brain Connectivity. *Stroke* 52, 1983–1992. doi: 10.1161/STROKEAHA.120.032033

Adamit, T., Maeir, A., Ben Assayag, E., Bornstein, N. M., Korczyn, A. D., and Katz, N. (2015). Impact of first-ever mild stroke on participation at 3 and 6 month post-event: the TABASCO study. *Disabil. Rehabil.* 37, 667–673. doi: 10.3109/09638288.2014.923523

Adleman, N. E., Menon, V., Blasey, C. M., White, C. D., Warsofsky, I. S., Glover, G. H., et al. (2002). A developmental fMRI study of the Stroop color-word task. *Neuroimage* 16, 61–75. doi: 10.1006/nimg.2001.1046

Americans with Disabilities Act. (n.d.). Springer Reference. doi: 10.1007/springerreference_44126

Al-Heizan, M. O., Giles, G. M., Wolf, T. J., and Edwards, D. F. (2020). The construct validity of a new screening measure of functional cognitive ability: The menu task. *Neuropsychol. Rehabil.* 30, 961–972. doi: 10.1080/09602011.2018.1531767

Alstott, J., Breakspear, M., Hagmann, P., Cammoun, L., and Sporns, O. (2009). Modeling the Impact of Lesions in the Human Brain. *PLoS Comput. Biol.* 5:e1000408. doi: 10.1371/journal.pcbi.1000408

Assaf, Y., and Pasternak, O. (2008). Diffusion tensor imaging (DTI)-based white matter mapping in brain research: a review. *J. Mol. Neurosci.* 34, 51–61. doi: 10.1007/s12031-007-0029-0

Austin, C. P. (2021). Opportunities and challenges in translational science. *Clin. Transl. Sci.* 14, 1629–1647. doi: 10.1111/cts.13055

Balasooriya-Smeekens, C., Bateman, A., Mant, J., and De Simoni, A. (2016). Barriers and facilitators to staying in work after stroke: insight from an online forum. *BMJ Open* 6:e009974. doi: 10.1136/bmjopen-2015-009974

Barbay, M., Diouf, M., Roussel, M., and Godefroy, O. (2018). Systematic Review and Meta-Analysis of Prevalence in Post-Stroke Neurocognitive Disorders in Hospital-Based Studies. *Dement Geriatr. Cogn. Disord.* 46, 322–334. doi: 10.1159/000492920

Barnett, B. P., and Singman, E. L. (2015). Vision concerns after mild traumatic brain injury. *Curr. Treat. Options Neurol.* 17:329. doi: 10.1007/s11940-014-0329-y

Basser, P. J., and Pierpaoli, C. (2011). Microstructural and physiological features of tissues elucidated by quantitative-diffusion-tensor MRI. *J. Magn. Reson.* 213, 560–570. doi: 10.1016/j.jmr.2011.09.022

Baum, C. M., Connor, L. T., Morrison, T., Hahn, M., Dromerick, A. W., and Edwards, D. F. (2008). Reliability, validity, and clinical utility of the Executive Function Performance Test: a measure of executive function in a sample of people with stroke. *Am. J. Occup. Ther.* 62, 446–455. doi: 10.5014/ajot.62.4.446

Biernaskie, J., Szymanska, A., Windle, V., and Corbett, D. (2005). Bi-hemispheric contribution to functional motor recovery of the affected forelimb following focal ischemic brain injury in rats. *Eur. J. Neurosci.* 21, 989–999. doi: 10.1111/j.1460-9568.2005.03899.x

Bonita, R., and Beaglehole, R. (1988). Recovery of motor function after stroke. *Stroke* 19, 1497–1500. doi: 10.1161/01.STR.19.12.1497

Brodaty, H., Altendorf, A., Withall, A., and Sachdev, P. S. (2010). Mortality and institutionalization in early survivors of stroke: the effects of cognition, vascular mild cognitive impairment, and vascular dementia. *J. Stroke Cerebrovasc. Dis.* 19, 485–493. doi: 10.1016/j.jstrokecerebrovasdis.2009.09.006

Brott, T., Adams, H. P. Jr., Olinger, C. P., Marler, J. R., Barsan, W. G., Biller, J., et al. (1989). Measurements of acute cerebral infarction: a clinical examination scale. *Stroke* 20, 864–870. doi: 10.1161/01.STR.20.7.864

Bullmore, E., and Sporns, O. (2009). Complex brain networks: graph theoretical analysis of structural and functional systems. *Nat. Rev. Neurosci.* 10, 186–198. doi: 10.1038/nrn2575

Burns, S. P., Schwartz, J. K., Scott, S. L., Devos, H., Kovic, M., Hong, I., et al. (2018). Interdisciplinary Approaches to Facilitate Return to Driving and Return

to Work in Mild Stroke: A Position Paper. *Arch. Phys. Med. Rehabil.* 99, 2378–2388. doi: 10.1016/j.apmr.2018.01.032

Calvillo, M., and Irimia, A. (2020). Neuroimaging and Psychometric Assessment of Mild Cognitive Impairment After Traumatic Brain Injury. *Front. Psychol.* 11:1423. doi: 10.3389/fpsyg.2020.01423

Camicia, M., Wang, H., DiVita, M., Mix, J., and Niewczyk, P. (2016). Length of Stay at Inpatient Rehabilitation Facility and Stroke Patient Outcomes. *Rehabil. Nurs.* 41, 78–90. doi: 10.1002/rnj.218

Cassidy, J. M., Tran, G., Quinlan, E. B., and Cramer, S. C. (2018). Neuroimaging Identifies Patients Most Likely to Respond to a Restorative Stroke Therapy. *Stroke* 49, 433–438. doi: 10.1161/STROKEAHA.117.018844

Chaudoir, S. R., Dugan, A. G., and Barr, C. H. (2013). Measuring factors affecting implementation of health innovations: a systematic review of structural, organizational, provider, patient, and innovation level measures. *Implement. Sci.* 8:22. doi: 10.1186/748-5908-8-22

Chung, C., Pollock, A., Campbell, T., Durward, B., and Hagen, S. (2013). Cognitive rehabilitation for executive dysfunction in adults with stroke or other adult nonprogressive acquired brain damage. *Stroke.* 44:e77–e78. doi: 10.1161/STROKEAHA.113.002049

Craddock, R. C., Tungaraza, R. L., and Milham, M. P. (2015). Connectomics and new approaches for analyzing human brain functional connectivity. *Gigascience* 4:13. doi: 10.1186/s13742-015-0045-x

Cucchiara, B., George, D. K., Kasner, S. E., Knutsson, M., Denison, H., Ladenvall, P., et al. (2019). Disability after minor stroke and TIA: A secondary analysis of the SOCRATES trial. *Neurology* 93, e708–e716. doi: 10.1212/WNL.0000000000007936

de Haan, E. H., Nys, G. M., and Van Zandvoort, M. J. (2006). Cognitive function following stroke and vascular cognitive impairment. *Curr. Opin. Neurol.* 19, 559–564. doi: 10.1097/01.wco.0000247612.21235.d9

Eckert, M. A. (2011). Slowing down: age-related neurobiological predictors of processing speed. *Front. Neurosci.* 5:25. doi: 10.3389/fnins.2011.00025

Faingold, C. L., and Blumenfeld, H. (2015). Targeting Neuronal Networks with Combined Drug and Stimulation Paradigms Guided by Neuroimaging to Treat Brain Disorders. *Neuroscientist* 21, 460–474. doi: 10.1177/1073858415592377

Falcon, M. I., Jirsa, V., and Solodkin, A. (2016). A new neuroinformatics approach to personalized medicine in neurology: The Virtual Brain. *Curr. Opin. Neurol.* 29, 429–436. doi: 10.1097/WCO.0000000000000344

Fischer, U., Baumgartner, A., Arnold, M., Nedeltchev, K., Gralla, J., De Marchis, G. M., et al. (2010). What is a minor stroke? *Stroke* 41, 661–666. doi: 10.1161/STROKEAHA.109.572883

Fride, Y., Adamit, T., Maeir, A., Ben Assayag, E., Bornstein, N. M., Korczyn, A. D., et al. (2015). What are the correlates of cognition and participation to return to work after first ever mild stroke? *Top. Stroke Rehabil.* 22, 317–325. doi: 10.1179/1074935714Z.0000000013

Fugl-Meyer, A. R., Jääskö, L., Leyman, I., Olsson, S., and Steglind, S. (1975). The post-stroke hemiplegic patient. 1. a method for evaluation of physical performance. *Scand. J. Rehabil. Med.* 7, 13–31.

Ganguli, M., Blacker, D., Blazer, D. G., Grant, I., Jeste, D. V., Paulsen, J. S., et al. (2011). Classification of neurocognitive disorders in DSM-5: a work in progress. *Am. J. Geriatr. Psychiatr.* 19, 205–210. doi: 10.1097/JGP.0b013e3182051ab4

Gawryluk, J. R., Mazerolle, E. L., Beyea, S. D., and D'Arcy, R. C. (2014). Functional MRI activation in white matter during the Symbol Digit Modalities Test. *Front. Hum. Neurosci.* 8:589. doi: 10.3389/fnhum.2014.00589

Giles, G. M., Edwards, D. F., Morrison, M. T., Baum, C., and Wolf, T. J. (2017). Screening for Functional Cognition in Postacute Care and the Improving Medicare Post-Acute Care Transformation (IMPACT) Act of 2014. *Am. J. Occup. Ther.* 71, 7105090010p1–7105090010p6 doi: 10.5014/ajot.2017.715001

Golden, C., and Freshwater, S. M. (2002). *The Stroop Color and Word Test: a Manual for Clinical and Experimental Uses*. Chicago, IL: Stoelting.

Gray, C. S., French, J. M., Bates, D., Cartlidge, N. E., Venables, G. S., and James, O. F. (1989). Recovery of visual fields in acute stroke: homonymous hemianopia associated with adverse prognosis. *Age Ageing* 18, 419–421. doi: 10.1093/ageing/18.6.419

Grefkes, C., and Fink, G. R. (2011). Reorganization of cerebral networks after stroke: new insights from neuroimaging with connectivity approaches. *Brain* 134(Pt 5), 1264–1276. doi: 10.1093/brain/awr033

Hachinski, V., Iadecola, C., Petersen, R. C., Breteler, M. M., Nyenhuis, D. L., Black, S. E., et al. (2006). National Institute of Neurological Disorders and Stroke-Canadian Stroke Network vascular cognitive impairment harmonization standards. *Stroke* 37, 2220–2241. doi: 10.1161/01.STR.0000237236.88823.47

Hajek, V. E., Gagnon, S., and Ruderman, J. E. (1997). Cognitive and functional assessments of stroke patients: an analysis of their relation. *Arch. Phys. Med. Rehabil.* 78, 1331–1337. doi: 10.1016/S0003-9993(97)90306-3

Halgren, E., Sherfey, J., Irimia, A., Dale, A. M., and Marinkovic, K. (2011). Sequential temporo-fronto-temporal activation during monitoring of the auditory environment for temporal patterns. *Hum. Brain Mapp.* 32, 1260–1276. doi: 10.1002/hbm.21106

Hartman-Maeir, A., Harel, H., and Katz, N. (2009). Kettle test–a brief measure of cognitive functional performance. Reliability and valdity in stroke rehabilitation. *Am. J. Occup. Ther.* 63, 592–599. doi: 10.5014/ajot.63.5.592

Hodics, T. M., Nakatsuka, K., Upreti, B., Alex, A., Smith, P. S., and Pezzullo, J. C. (2012). Wolf Motor Function Test for characterizing moderate to severe hemiparesis in stroke patients. *Arch. Phys. Med. Rehabil.* 93, 1963–1967. doi: 10.1016/j.apmr.2012.05.002

Hofgren, C., Björkdahl, A., Esbjörnsson, E., and Sunnerhagen, K. S. (2007). Recovery after stroke: cognition, ADL function and return to work. *Acta Neurol. Scand.* 115, 73–80. doi: 10.1111/j.1600-0404.2006.00768.x

Honey, C. J., and Sporns, O. (2008). Dynamical consequences of lesions in cortical networks. *Hum. Brain Mapp.* 29, 802–809. doi: 10.1002/hbm.20579

Hope, T. M., Seghier, M. L., Leff, A. P., and Price, C. J. (2013). Predicting outcome and recovery after stroke with lesions extracted from MRI images. *Neuroimage Clin.* 2, 424–433. doi: 10.1016/j.nicl.2013.03.005

Irimia, A., and Van Horn, J. D. (2015b). Functional neuroimaging of traumatic brain injury: advances and clinical utility. *Neuropsychiatr. Dis. Treat.* 11, 2355–2365. doi: 10.2147/NDT.S79174

Irimia, A., and Van Horn, J. D. (2015a). Epileptogenic focus localization in treatment-resistant post-traumatic epilepsy. *J. Clin. Neurosci.* 22, 627–631. doi: 10.1016/j.jocn.2014.09.019

Irimia, A., Goh, S. Y., Torgerson, C. M., Vespa, P., and Van Horn, J. D. (2014). Structural and connectomic neuroimaging for the personalized study of longitudinal alterations in cortical shape, thickness and connectivity after traumatic brain injury. *J. Neurosurg. Sci.* 58, 129–144.

Jadhav, A. P., Desai, S. M., Liebeskind, D. S., and Wechsler, L. R. (2020). Neuroimaging of Acute Stroke. *Neurol. Clin.* 38, 185–199. doi: 10.1016/j.ncl.2019.09.004

Khatri, P., Kleindorfer, D. O., Yeatts, S. D., Saver, J. L., Levine, S. R., Lyden, P. D., et al. (2010). Strokes with minor symptoms: an exploratory analysis of the National Institute of Neurological Disorders and Stroke recombinant tissue plasminogen activator trials. *Stroke* 41, 2581–2586. doi: 10.1161/STROKEAHA.110.593632

Kuceyeski, A., Navi, B. B., Kamel, H., Raj, A., Relkin, N., Toglia, J., et al. (2016). Structural connectome disruption at baseline predicts 6-months post-stroke outcome. *Hum. Brain Mapp.* 37, 2587–2601. doi: 10.1002/hbm.23198

Leavitt, V. M., Lengenfelder, J., Moore, N. B., Chiaravalloti, N. D., and DeLuca, J. (2011). The relative contributions of processing speed and cognitive load to working memory accuracy in multiple sclerosis. *J. Clin. Exp. Neuropsychol.* 33, 580–586. doi: 10.1080/13803395.2010.541427

Lee, K. B., Lim, S. H., Kim, K. H., Kim, K. J., Kim, Y. R., Chang, W. N., et al. (2015). Six-month functional recovery of stroke patients: a multi-time-point study. *Int. J. Rehabil. Res.* 38, 173–180. doi: 10.1097/MRR.0000000000000108

Li, W., Cheng, Y. H., and Yu, X. G. (2012). [Observation on therapeutic effect of acupuncture combined with medicine on mild cognition disorders in patients with post-stroke]. *Zhongguo Zhen Jiu* 32, 3–7.

Liew, S. L., Zavaliangos-Petropulu, A., Jahanshad, N., Lang, C. E., Hayward, K. S., Lohse, K. R., et al. (2020). The ENIGMA Stroke Recovery Working Group: Big data neuroimaging to study brain-behavior relationships after stroke. *Hum. Brain Mapp.* 43, 129–148. doi: 10.1002/hbm.25015

Lim, J. S., and Kang, D. W. (2015). Stroke Connectome and Its Implications for Cognitive and Behavioral Sequela of Stroke. *J. Stroke* 17, 256–267. doi: 10.5853/jos.2015.17.3.256

Lim, K. O., and Helpern, J. A. (2002). Neuropsychiatric applications of DTI-a review. *NMR Biomed.* 15, 587–593. doi: 10.1002/nbm.789

Lima, E. A., Irimia, A., and Wikswo, J. P. (2006). "*The magnetic inverse problem*". *The SQUID Handbook: Applications of SQUIDs and SQUID Systems*.(eds) J. Clarke, and A. I. Braginski (Hoboken, NJ: John Wiley & Sons) doi: 10.1002/9783527609956.ch10

Lopes, R., Bournonville, C., Kuchcinski, G., Dondaine, T., Mendyk, A. M., Viard, R., et al. (2021). Prediction of Long-term Cognitive Functions after Minor Stroke, Using Functional Connectivity. *Neurology*. [Epub ahead of print] doi: 10.1212/WNL.0000000000011452

Lu, Y., Li, X., Geng, D., Mei, N., Wu, P. Y., Huang, C. C., et al. (2020). Cerebral Micro-Structural Changes in COVID-19 Patients-An MRI-based 3-month Follow-up Study. *EClin. Med.* 25:100484. doi: 10.1016/j.eclinm.2020.100484

Lyle, R. C. (1981). A performance test for assessment of upper limb function in physical rehabilitation treatment and research. *Int. J. Rehabil. Res.* 4, 483–492. doi: 10.1097/00004356-198112000-00001

Ma, D., Gulani, V., Seiberlich, N., Liu, K., Sunshine, J. L., Duerk, J. L., et al. (2013). Magnetic resonance fingerprinting. *Nature* 495, 187–192. doi: 10.1038/nature11971

Madhukumar, S., and Santhiyakumari, N. (2015). Evaluation of k-Means and fuzzy C-means segmentation on MR images of brain. *Egyptian J. Radiol. Nuclear Med.* 46, 475–479. doi: 10.1016/j.ejrnm.2015.02.008

Meyer, M. (2010). The rise of the knowledge broker. *Sci. Commun.* 32, 118–127. doi: 10.1177/1075547009359797

Mu, F., Hurley, D., Betts, K. A., Messali, A. J., Paschoalin, M., Kelley, C., et al. (2017). Real-world costs of ischemic stroke by discharge status. *Curr. Med. Res. Opin.* 33, 371–378. doi: 10.1080/03007995.2016.1257979

Murphy, R., Sackley, C. M., Miller, P., and Harwood, R. H. (2001). Effect of experience of severe stroke on subjective valuations of quality of life after stroke. *J. Neurol. Neurosurg. Psychiatr.* 70, 679–681. doi: 10.1136/jnnp.70.5.679

National Institute of Neurological Disorders and Stroke (2011). *NIH stroke scale. Bethesda, Md.?: National Institute of Neurological Disorders and Stroke*. Washington, DC: Dept. of Health and Human Services.

Nomura, E. M., Gratton, C., Visser, R. M., Kayser, A., Perez, F., and D'Esposito, M. (2010). Double dissociation of two cognitive control networks in patients with focal brain lesions. *Proc. Natl. Acad. Sci. U.S.A.* 107, 12017–12022. doi: 10.1073/pnas.1002431107

Ovbiagele, B., and Nguyen-Huynh, M. N. (2011). Stroke epidemiology: advancing our understanding of disease mechanism and therapy. *Neurotherapeutics* 8, 319–329. doi: 10.1007/s13311-011-0053-1

Ovbiagele, B., Goldstein, L. B., Higashida, R. T., Howard, V. J., Johnston, S. C., Khavjou, O. A., et al. (2013). Forecasting the future of stroke in the United States: a policy statement from the American Heart Association and American Stroke Association. *Stroke* 44, 2361–2375. doi: 10.1161/STR.0b013e31829734f2

Overdorp, E. J., Kessels, R. P., Claassen, J. A., and Oosterman, J. M. (2016). The Combined Effect of Neuropsychological and Neuropathological Deficits on Instrumental Activities of Daily Living in Older Adults: a Systematic Review. *Neuropsychol. Rev.* 26, 92–106. doi: 10.1007/s11065-015-9312-y

Park, H. J., and Friston, K. (2013). Structural and functional brain networks: from connections to cognition. *Science* 342:1238411. doi: 10.1126/science.1238411

Petersen, S. E., and Sporns, O. (2015). Brain Networks and Cognitive Architectures. *Neuron* 88, 207–219. doi: 10.1016/j.neuron.2015.09.027

Reitan, R. M. (1958). Validity of the Trail Making Test as an Indicator of Organic Brain Damage. *Perceptual. Motor Skills* 8, 271–276. doi: 10.2466/pms.1958.8.3.271

Roberts, P. S., Krishnan, S., Burns, S. P., Ouellette, D., and Pappadis, M. R. (2020). Inconsistent Classification of Mild Stroke and Implications on Health Services Delivery. *Arch. Phys. Med. Rehabil.* 101, 1243–1259. doi: 10.1016/j.apmr.2019.12.013

Rogers, A. T., Bai, G., Lavin, R. A., and Anderson, G. F. (2017). Higher Hospital Spending on Occupational Therapy Is Associated With Lower Readmission Rates. *Med. Care Res. Rev.* 74, 668–686. doi: 10.1177/1077558716666981

Rost, N. S., Bottle, A., Lee, J. M., Randall, M., Middleton, S., Shaw, L., et al. (2016). Stroke Severity Is a Crucial Predictor of Outcome: An International Prospective Validation Study. *J. Am. Heart Assoc.* 5:e002433. doi: 10.1161/JAHA.115.002433

Santisteban, L., Térémetz, M., Bleton, J. P., Baron, J. C., Maier, M. A., and Lindberg, P. G. (2016). Upper Limb Outcome Measures Used in Stroke Rehabilitation Studies: A Systematic Literature Review. *PLoS One* 11:e0154792.

Schlosser, R. (2000). [Detection of neurotransmitter interactions with PET and SPECT by pharmacological challenge paradigms]. *Nervenarzt* 71, 9–18. doi: 10.1007/s001150050002

Sensenbrenner, B., Rouaud, O., Graule-Petot, A., Guillemin, S., Piver, A., Giroud, M., et al. (2020). High Prevalence of Social Cognition Disorders and Mild Cognitive Impairment Long Term After Stroke. *Alzheimer Dis. Assoc. Dis.* 34, 72–78. doi: 10.1097/WAD.0000000000000355

Siegle, G. J., Ichikawa, N., and Steinhauer, S. (2008). Blink before and after you think: blinks occur prior to and following cognitive load indexed by pupillary responses. *Psychophysiology* 45, 679–687. doi: 10.1111/j.1469-8986.2008.00681.x

Silasi, G., and Murphy, T. H. (2014). Stroke and the connectome: how connectivity guides therapeutic intervention. *Neuron* 83, 1354–1368. doi: 10.1016/j.neuron.2014.08.052

Smith A. (1973). Symbol Digit Modalities Test (SDMT), Manual. Los Angeles, CA: Western Psychological Services.

Spitzer, J., Tse, T., Baum, C. M., and Carey, L. M. (2011). Mild impairment of cognition impacts on activity participation after stroke in a community-dwelling Australian cohort. *OTJR* 31, S8–S15.

Spokoyny, I., Raman, R., Ernstrom, K., Khatri, P., Meyer, D. M., Hemmen, T. M., et al. (2015). Defining mild stroke: outcomes analysis of treated and untreated mild stroke patients. *J. Stroke Cerebrovasc. Dis.* 24, 1276–1281. doi: 10.1016/j.jstrokecerebrovasdis.2015.01.037

Sporns, O., and Zwi, J. D. (2004). The small world of the cerebral cortex. *Neuroinformatics* 2, 145–162. doi: 10.1385/NI:2:2:145

Sporns, O., Tononi, G., and Kotter, R. (2005). The human connectome: A structural description of the human brain. *PLoS Comput. Biol.* 1:e42. doi: 10.1371/journal.pcbi.0010042

Stephens, S., Kenny, R. A., Rowan, E., Kalaria, R. N., Bradbury, M., Pearce, R., et al. (2005). Association between mild vascular cognitive impairment and impaired activities of daily living in older stroke survivors without dementia. *J. Am. Geriatr. Soc.* 53, 103–107. doi: 10.1111/j.1532-5415.2005.53019.x

Su, C. Y., Wuang, Y. P., Lin, Y. H., and Su, J. H. (2015). The role of processing speed in post-stroke cognitive dysfunction. *Arch. Clin. Neuropsychol.* 30, 148–160. doi: 10.1093/arclin/acu057

Sun, J. H., Tan, L., and Yu, J. T. (2014). Post-stroke cognitive impairment: epidemiology, mechanisms and management. *Ann. Transl. Med.* 2:80.

Tellier, M., and Rochette, A. (2009). Falling through the cracks: a literature review to understand the reality of mild stroke survivors. *Top. Stroke Rehabil.* 16, 454–462. doi: 10.1310/tsr1606-454

Turken, A., Whitfield-Gabrieli, S., Bammer, R., Baldo, J. V., Dronkers, N. F., and Gabrieli, J. D. (2008). Cognitive processing speed and the structure of white matter pathways: convergent evidence from normal variation and lesion studies. *Neuroimage* 42, 1032–1044. doi: 10.1016/j.neuroimage.2008.03.057

van Meer, M. P., Otte, W. M., van der Marel, K., Nijboer, C. H., Kavelaars, A., van der Sprenkel, J. W., et al. (2012). Extent of bilateral neuronal network reorganization and functional recovery in relation to stroke severity. *J. Neurosci.* 32, 4495–4507. doi: 10.1523/JNEUROSCI.3662-11.2012

Versaci, M., Calcagno, S., and Morabito, F. C. (2015). *Image Contrast Enhancement by Distances Among Points in Fuzzy Hyper-Cubes. Computer Analysis of Images and Patterns*. Berlin: Springer International Publishing.

Wang, L., Yu, C., Chen, H., Qin, W., He, Y., Fan, F., et al. (2010). Dynamic functional reorganization of the motor execution network after stroke. *Brain* 133, 1224–1238. doi: 10.1093/brain/awq043

Weiss, L., Saklofske, D. H., Coalson, D. L., and Raiford, S. E. (2010). Theoretical, empirical and clinical foundations of the WAIS-IV index scores. *WAIS IV Clin. Use Interp.* 61–94. doi: 10.1016/B978-0-12-375035-8.10003-5

Wintermark, M., Sanelli, P. C., Albers, G. W., Bello, J. A., Derdeyn, C. P., Hetts, S. W., et al. (2013). Imaging recommendations for acute stroke and transient ischemic attack patients: a joint statement by the American Society

of Neuroradiology, the American College of Radiology and the Society of NeuroInterventional Surgery. *J. Am. Coll. Radiol.* 10, 828–832. doi: 10.1016/j.jacr.2013.06.019

Wolf, T. J., and Rognstad, M. C. (2013). Changes in cognition following mild stroke. *Neuropsychol. Rehabil.* 23, 256–266. doi: 10.1080/09602011.2012.748672

Yaghi, S., Herber, C., Boehme, A. K., Andrews, H., Willey, J. Z., Rostanski, S. K., et al. (2017). The Association between Diffusion MRI-Defined Infarct Volume and NIHSS Score in Patients with Minor Acute Stroke. *J. Neuroimaging* 27, 388–391. doi: 10.1111/jon.12423

Yakhkind, A., McTaggart, R. A., Jayaraman, M. V., Siket, M. S., Silver, B., and Yaghi, S. (2016). Minor Stroke and Transient Ischemic Attack: Research and Practice. *Front. Neurol.* 7:86. doi: 10.3389/fneur.2016.00086

Zinn, S., Bosworth, H. B., Hoenig, H. M., and Swartzwelder, H. S. (2007). Executive function deficits in acute stroke. *Arch. Phys. Med. Rehabil.* 88, 173–180.

Conflict of Interest: The authors declare that the research was conducted in the absence of any commercial or financial relationships that could be construed as a potential conflict of interest.

frontiers | Frontiers in Neuroscience

TYPE Original Research
PUBLISHED 18 August 2022
DOI 10.3389/fnins.2022.895237

OPEN ACCESS

EDITED BY
Aleksandra Dagmara Kawala-Sterniuk,
Opole University of Technology,
Poland

REVIEWED BY
Fengmei Lu,
Chengdu No. 4 People's Hospital,
China
Eugene Golanov,
Houston Methodist Hospital,
United States

*CORRESPONDENCE
Shaoling Wu
wushl@mail.sysu.edu.cn
Chao Ma
machao@mail.sysu.edu.cn

†These authors have contributed equally to this work and share first authorship

SPECIALTY SECTION
This article was submitted to Brain Imaging Methods, a section of the journal Frontiers in Neuroscience

RECEIVED 13 March 2022
ACCEPTED 25 July 2022
PUBLISHED 18 August 2022

CITATION
Ma H, Zhai Y, Xu Z, Fan S, Wu X, Xu J, Wu S and Ma C (2022) Increased cerebral cortex activation in stroke patients during electrical stimulation of cerebellar fastigial nucleus with functional near-infrared spectroscopy. *Front. Neurosci.* 16:895237. doi: 10.3389/fnins.2022.895237

Increased cerebral cortex activation in stroke patients during electrical stimulation of cerebellar fastigial nucleus with functional near-infrared spectroscopy

Haiyun Ma†, Yujia Zhai†, Zhen Xu, Shengnuo Fan, Xian Wu, Jing Xu, Shaoling Wu* and Chao Ma*

Department of Rehabilitation Medicine, Sun Yat-sen Memorial Hospital, Sun Yat-sen University, Guangzhou, China

Background: Electrical stimulation of the cerebellar fastigial nucleus (FNS) has been shown to protect animals against cerebral ischemic injury. However, the changes in cortical activation as a response to FNS have not been illustrated in humans.

Objective: This study aims to detect functional connectivity changes in the brain of stroke patients, and investigate the cortical activation caused by FNS through measuring the oxygenated hemoglobin concentration (HBO) in the cerebral cortex of stroke patients and healthy controls (HCs).

Methods: This study recruited 20 patients with stroke and 20 HCs with all the following factors matched: age, gender and BMI. The experiment session was made up of the pre-task baseline, FNS task period, and post-task baseline. FNS task period contains 5 blocks, each block encompassing the resting state (30 s) and the FNS state (30 s). HBO signals were acquired by functional near-infrared spectroscopy (fNIRS) from the Prefrontal Cortex (PFC), the Motor Cortex (MC) and the Occipital Cortex (OC) throughout the experiment. The Pearson correlation coefficient was used to calculate the resting-state functional connectivity strength between the two groups, and the general linear model (GLM) was used to calculate the activation of 39 fNIRS channels during FNS in stroke patients and HCs, respectively.

Results: The coupling strength of stroke patients were significantly decreased in the following regions: right MC and left MC ($t = 4.65$, $p = 0.0007$), right MC and left OC ($t = 2.93$, $p = 0.04$), left MC and left OC ($t = 2.81$, $p = 0.04$). In stroke patients, the changes in cerebral oxygenated hemoglobin (ΔHBO) among 12 channels (CH) in the bilateral PFC and bilateral MC regions were significantly increased during the FNS state (FDR corrected $p < 0.05$) compared with the resting state. In HCs, only 1 channel was increased (FDR corrected $p < 0.05$) in the left PFC during FNS.

Conclusion: By using the FNS and fNIRS techniques, the characteristics of functional connectivity were found to decrease in stroke patients. It was also noticed that FNS activates the PFC and MC regions. These findings may help to guide functional rehabilitation in stroke patients.

KEYWORDS

cerebellar fastigial, electrical stimulation, cortical activation, oxygenated hemoglobin concentration, functional near infrared spectroscopy

Introduction

Four pairs of nuclei (fastigial nuclei, emboliform nuclei, globose nuclei and the dentate nuclei) exist in the cerebellum. The cerebellar fastigial nucleus (FNS) is located at the top of the fourth ventricle. According to one MRI study, the FN is approximately 3 × 3 × 3 mm in size (in width, height and length, respectively) (Dimitrova et al., 2002). The FN is well known for its essential role in motor control and the non-motor system (Al-Afif et al., 2019; Zhang X. Y. et al., 2016). It carries out extensive projections to many motor structures, which control the body's movement by projecting to the reticular structure of the medulla oblongata/brainstem and the primary motor cortex (MC). Eye movement, for example, is governed by the projection of the cranial nucleus in the brainstem. The FN also regulates the cardiovascular system by sending projection fibers to the solitary tract and the paramedian reticular nucleus. In the 1990s, a study discovered a fastigial pressor response (FPR) in cats, whereby the arterial pressure was observed to increase upon stimulation of the FN (Miura and Reis, 1969).

Electrical stimulation of the cerebellar FNS has been proven to improve brain cortical blood perfusion effectively (Golanov and Reis, 1996). It is also effective against cerebral ischemia. Cerebral ischemia can evoke an inflammatory response and secondary brain injury. Researchers found that FNS contributes to decreased infarction volumes, elicits suppression of periinfarction depolarizing waves, promoting axonal regeneration, and inhibiting inflammatory response (Golanov and Reis, 1999; Wang et al., 2019; Xia et al., 2019). Xia et al. (2019) observed that FNS treatment could affect the expression of some inflammatory factors such as caspase-1 and interleukin 1β, besides inhibiting cell apoptosis and promoting neuronal repair and regeneration (Wang et al., 2019). Several basic animal experiments have proven that FNS is involved in regulating activity in other brain regions and modulate vascular activity (Zhang C. et al., 2016; Golanov et al., 2017; Gao et al., 2018). However, clinical applications of this treatment are relatively few, and relevant clinical treatment evidence are still lacking.

Functional imaging technology can be applied to detect brain metabolism, cerebral blood flow (CBF) and other indicators to determine the level of cerebral cortex activity, thus providing a clear image of a person's state of brain function. Traditional functional imaging methods include functional magnetic resonance imaging (fMRI) (Buxton, 2013) and positron emission tomography (PET) (Hooker and Carson, 2019). Nevertheless, these techniques cannot provide dynamic observation of brain function changes during electrical stimulation. Recently, functional near-infrared spectroscopy (fNIRS) has been widely used in the evaluation of brain function because of its portability, repeatability, and for being non-radiation. fNIRS is a hemodynamics-based neuroimaging technique that provides a non-invasive method for the detection of relative changes in cerebral oxygenated hemoglobin (ΔHBO) at the cortical surface (Lloyd-Fox et al., 2010; Obrig, 2014; Scholkmann et al., 2014). This method is commonly used to detect changes in cerebral hemodynamics during electrical stimulation and rehabilitation tasks in stroke, depression, Parkinson's and various mental diseases (Noda et al., 2012; Wang et al., 2020; Conceição et al., 2021; Zhang et al., 2021). Kozel et al. (2009) and Li et al. (2019) acquired fNIRS when their subjects were receiving transcranial magnetic stimulation, and they found decreased levels of activation and functional connectivity within the cerebrum. In addition, the simultaneous application of transcranial electrical stimulation or peripheral nerve electrical stimulation combined with fNIRS to explore the mechanism of CBF is an essential innovation in therapeutic interventions (Di Rosa et al., 2019; Huo et al., 2019). The integration of fNIRS and transcranial electrical stimulation therapy also brings great potential for neuroscience research and clinical application of the brain related diseases. All these advantages make fNIRS a suitable technique for detecting activity changes in the brain cortex during FNS.

FNS is a non-invasive brain stimulation technique that transmits bionic low-frequency biological current to the cerebellar FNS through a bilateral mastoid process to modulate CBF and brain function (Hu et al., 2017). This study aims to detect brain functional connectivity changes in stroke patients, and investigate the cortical activation caused by FNS through measuring the concentration of HBO in the cerebral cortex of stroke patients and healthy controls (HCs), respectively.

Materials and methods

This study was conducted at the Rehabilitation Medicine Department of Sun Yat-sen Memorial Hospital. This study was performed adhering to the Declaration of Helsinki on biomedical research involving stroke patients and healthy subjects. The research protocol was approved by the Sun Yat-sen Memorial Hospital Ethics Committee (SYSEC-KY-KS-2021-251). All participants provided written informed consent before their inclusion in this study. The comprehensive testing lasted for 10 min, including resting and stimulation.

Participants

Forty right-handed participants comprised of 20 patients with stroke (3 females, 17 males) and 20 sex, age-matched HCs with no history of mental or neurological disorders were recruited from the local community to participate in this fNIRS study. The patients with stroke were recruited from the Department of Rehabilitation Medicine, Sun Yat-sen Memorial Hospital, Guangzhou, China, while the HCs were enrolled from the society. For the patients with stroke, the inclusion criteria for stroke group were as follows: (1) Right-handed; (2) an ischemic stroke as confirmed by imaging (the magnetic resonance imaging or computed tomography) outcomes; (3) unilateral lesions; and (4) more than 4 weeks after the onset of stroke. Meanwhile, the exclusion criteria were as follows: (1) unstable medical condition; (2) any neurological disease except stroke; (3) unable to cooperate with the examination due to depression, anxiety, mania, schizophrenia and/or other mental disorders; (4) skin infections, lesions and/or sensitive tingling in the areas of stimulation; and (5) informed consent could not be obtained from patients or their family members.

The Modified Rankin Scale (MRS), National Institutes of Health Stroke Scale (NIHSS), and Modified Barthel index (MBI) were evaluated by trained attending physicians to assess patients's neurological and motor functional recovery. The Body mass index (BMI) and blood pressure were extracted from the electronic medical records of patients in hospital.

Study design

The experimental section consisted of a 40-s pre-task baseline, a 300-s FNS task period, and a 20-s post-task baseline (**Figure 1A**). The 300-s FNS task period was made up of 5 block sets, with each block containing an FNS condition (30 s) and a resting condition (30 s). Participants were asked to sit in a quiet, dark environment to avoid noise and light interference, and the order of tasks was not revealed before the experiment. The fNIRS measurements were taken through the whole experimental process. During the FNS condition, electrodes of the FNS electrical stimulator (CVFT-201, QianKang electrical stimulator, ShangHai, China) were attached to the bilateral mastoid (**Figure 1B**). FNS was performed using model 3 (136 Hz, strength: 45–90%) according to the manufacturer's instructions.

Functional near-infrared spectroscopy

A continuous-wave, multi-channel fNIRS system (NirSmart, Danyang Huichuang Medical Equipment Co., Ltd.) was used to measure HBO and deoxygenated hemoglobin (HBR) with a sampling rate of 11 Hz. The wavelengths of light for this measurement system were between 730 and 850 nm. As shown in **Figure 1C**, 39 fNIRS channels were positioned over the PFC (LPFC/RPFC), MC (LMC/RMC) and OC (LOC/ROC) regions. The fNIRS measured light intensity signals through 19 light source probes and 15 detector probes. Concentration changes of HBO were calculated by the light intensity obtained from fNIRS.

Data preprocessing

The data recorded from fNIRS were preprocessed and analyzed using the NirSpark software package, which runs in MATLAB (Mathworks, United States). Data preprocessing included several steps. The raw light intensity was converted to optical density according to the modified Beer-Lambert Law (Kocsis et al., 2006). Remove both baseline shifts and spike artifacts by using parameter-free motion correction method (Hou et al., 2021). The band-pass filtering of the optical density signals was set between 0.01 and 0.2 Hz to remove baseline drift and physiological noise (Zheng et al., 2019; Si et al., 2021). The optical density transformed to HBO and HBR concentrations (Tak and Ye, 2014). Because the HBO has a better signal-to-noise ratio than HBR, we choose the HBO as our primary indicator in the following analysis. The hemodynamic response function (HRF) initial time was set to –5 s while the end time was set to 50 s (with "–5 to 0 s" as the baseline state and "0–50 s" as the state for a block paradigm). With the FNS duration set to 30 s, the HBO of each five-block paradigm were superimposed and averaged to produce an average block result.

Analysis of functional near-infrared spectroscopy data

For each participant, functional connectivity was calculated by conducting the Pearson correlation analyses between time series of each pair channel. The Pearson correlation was calculated for the pre-task baseline between any two channels to generate a 39 × 39 correlation matrix for each participant. Furthermore, the 39 channels were divided into six regions

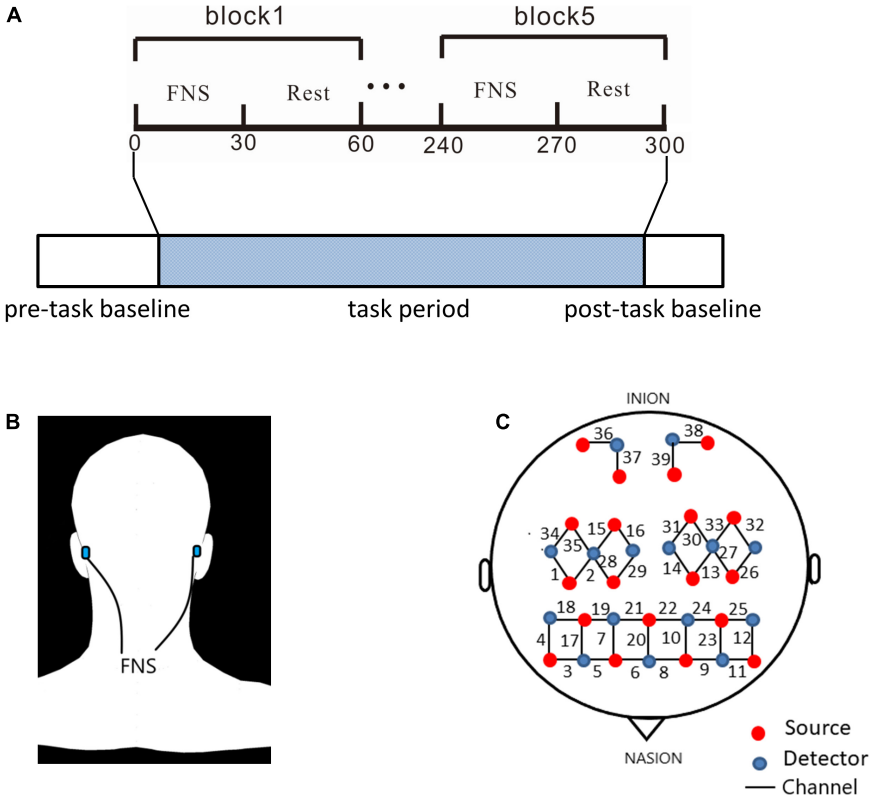

FIGURE 1
Experiment equipment and procedures. **(A)** The experimental process consisted pre-task baseline, task period, and post-task baseline. The block design in task period is made up of 5 cycles of 2 states: 30 s of FNS and 30 s of rest. **(B)** Location of electrodes for FNS: bionic low-frequency biological current from 2 transcutaneous electrodes is transmitted along the mastoid process to the fastigial nucleus. **(C)** The source optodes, detector optodes and channels: 39 Channels according to the 10/10 system. 6 cerebral areas were measured: LPFC, RPFC, LMC, RMC, LOC, and ROC.

of interest (ROI), including LPFC, RPFC, LMC, RMC, LOC, and ROC. We calculated the functional connection matrix between the six ROI in the same way. For any two ROI, the mean value of the functional connection value of all channel pairs between them is used as the functional connection value between the two ROI.

The mean time course for one subject is expressed as X = [xi(t)t = 1,2,3,....N], where xi(t)t = 1,2,3,....N is the mean time series of the region. The formula for calculation is as follows: $\bar{x}$

xi = the average of xi

$$r\left(x_i, x_j\right) = \frac{\sum_{t=1}^{N}\left[x_i\left(t\right) - \bar{x}_i\right]\ \left[x_j\left(t\right) - \bar{x}_j\right]}{\sqrt{\sum_{t=1}^{N}\ \left[x_i\left(t\right) - \bar{x}_i\right]^{\ 2}}\sqrt{\sum_{t=1}^{N}\ \left[\left[x_j\left(t\right) - \bar{x}_j\right]\right]^{\ 2}}} \quad (1)$$

According to the waveforms of individuals in all 39 channels, each channel' s averaged waveforms of HBO and HBR changes of all participants in the stroke groups were obtained. The general linear model (GLM) (Uga et al., 2014) was used to analyze the preprocessed HBO data of each channel for each subject to identify cerebral areas that were significantly activated by FNS. GLM establishes an ideal HRF for each subject task, allowing the calculation of beta values that reflect the level of cerebral cortex activation according to the matching degree of actual HRF and excellent HRF values. The results of this study are based on beta values.

Statistical analysis

Data normality was tested by the Shapiro-Wilk test. The Mann-Whitney *U*-test was used for age and height difference in stroke and HCs, while gender was tested by the chi-square test. A two-sample *t*-test was used to compare the characteristics such as weight, BMI and BP between the stroke group and the HCs.

In the activation analysis, the beta values of the stroke group and the HCs were analyzed with a single sample *t*-test and two-sample *t*-test on each channel by using the NirSpark software. Statistical results were corrected by FDR correction ($p < 0.05$).

To find the difference in functional connectivity between the HCs and the stroke group, two-sample *t*-tests were performed between groups to identify correlation in each ROI, and the results were corrected by FDR multiple hypothesis tests.

Results

Demographic and characteristics

The demographic characteristics comparisons of the two groups are listed in Table 1. The stroke group included 17 males and 3 females. The HCs included 16 males and 4 females. Participants with stroke and HCs showed no difference in age ($z = 1.93$, $p > 0.05$), gender (chi-square = 0.17, $p > 0.05$), BMI ($t = 1.18$, $p > 0.05$), or blood pressure ($t = 0.73$, $p > 0.05$; $t = -0.55$, $p > 0.05$). Among them, 11 patients had unilateral basal ganglia infarction, 5 patients had brainstem infarction (Supplementary Table 1). The mean time after stroke of stroke group was 4 months (*SD* = 2.1), the mean MRS, NIHSS and MBI scores of patients were 3 (*SD* = 0.7), 10 (*SD* = 4.5) and 45 (*SD* = 12), respectively.

Decreased functional connectivity in stroke patients

Figure 2A employs a 39 × 39 matrix figure to show averaged connectivity strength during FNS by group. Data

TABLE 1 Characteristics comparison between stroke group and HCs.

	Stroke ($n = 20$)	HCs ($n = 20$)	T/Z/χ^2	*p*
Age (years)	42 (30.0, 49.75)	30 (28.39)	1.93	0.056
Gender (M/F)	17/3	16/4	0.17	0.677
Weight (kg)	63 (8.9)	58 (8.4)	1.77	0.085
Height (cm)	173 (162.5, 175.8)	165.5 (160.3, 172.3)	1.66	0.096
BMI (kg/m^2)	22 (2.3)	21 (1.8)	1.18	0.242
Systolic blood pressure (mmHg)	126 (17.9)	123 (9.6)	0.73	0.473
Diastolic blood pressure (mmHg)	82 (13.2)	84 (6.1)	−0.55	0.584
Time poststroke (month)	4 (2.1)	–	–	–
MRS	3 (0.7)	–	–	–
NIHSS	10 (4.5)	–	–	–
MBI	45 (12)	–	–	–

HCs, Healthy controls; BMI, Body mass index; MRS, Modified Rankin Scale; NIHSS, National Institutes of Health Stroke Scale; MBI, Modified Barthel index.

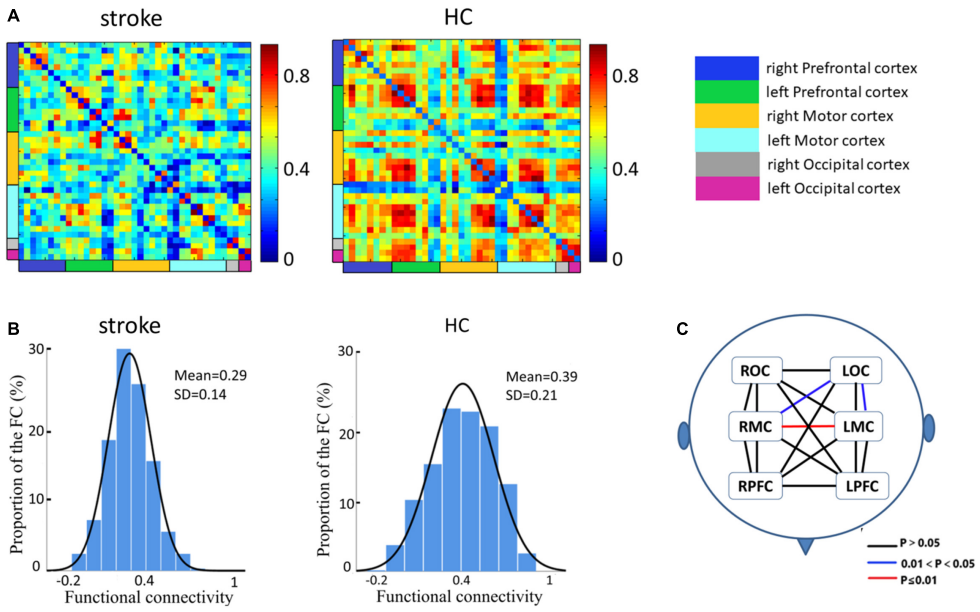

FIGURE 2
Spatial patterns of the functional connectivity in the FNS state and resting state. **(A)** Networks of FNS-related changes in functional connectivity between stroke patients and HCs. **(B)** Histograms of functional connectivity distribution in the two groups. **(C)** Functional connectivity in patients with stroke showed significant decreases in different cerebral regions when compared with HCs.

TABLE 2 Channels with HBO significantly increased when compared with the resting baseline during FNS.

ROI of cortical area	Channels
L-DLPC	9 23 24*
R-DLPC	3 17 19* 28*
L-PT	11 12 25#
R-PT	3 4 18
L-PMC	31 30* 32 33
R-PMC	15 16 34* 35*
L-SMC	13* 14* 26 27
R-SMC	1 2 28* 29
L-VAC	38 39
R-VAC	36 37
Obitorfrontal area	5 6 8
Frontopolar area	7* 9 10 20* 21* 22*

L, left; R, right; DLPC, Dorsolateral Prefrontal Cortex; PT, Pars Triangular; PMC, Primary Motor Cortex; SMC, Supplementary Motor Cortex; VAC, Visual Association Cortex.
*$p < 0.05$ in the stroke group.
#$p < 0.05$ in the stroke group and HCs.

showed that the average connectivity strength in stroke patients was much lower [e.g., in the MC and occipital cortex (OC)] than that in the HCs. The mean values and standard deviations of connectivity strength were 0.29 ± 0.14 for stroke patients, and 0.39 ± 0.21 for HCs (Figure 2B). Figure 2C shows the difference in functional connection strength between the two groups in six ROI. Compared with the HCs, stroke patients showed decreased functional connectivity between RMC and LMC ($t = 4.65$, $p = 0.0007$), RMC and LOC ($t = 2.93$, $p = 0.04$), and LMC and LOC ($t = 2.81$, $p = 0.04$). The results were corrected by FDR.

Analysis of cortical activation

13 of the 39 channels were significantly activated in the 2 groups distributed across the 12 Brodmann regions (Table 2) where distributed according MNI coordination (Supplementary Table 3). In stroke patients, the ΔHBO among several channels in the bilateral PFC (CH7, CH19, CH20, CH21, CH22, CH24) and bilateral MC (CH13, CH14, CH28, CH30, CH34, CH35) regions were significantly increased during the FNS state ($p < 0.05$ FDR correction, the effect size of all channels can be found in Supplementary Table 2) when compared with the resting state. In HCs, the ΔHBO in CH25 of the left Pars Triangular was significantly increased as compared to the resting state. Figure 3 shows brain maps with activation regions during FNS being highlighted by using beta values of GLM analysis in (A) HCs and (B) stroke patients. Figure 4 shows dynamic concentration changes in the average HBO of stroke patients

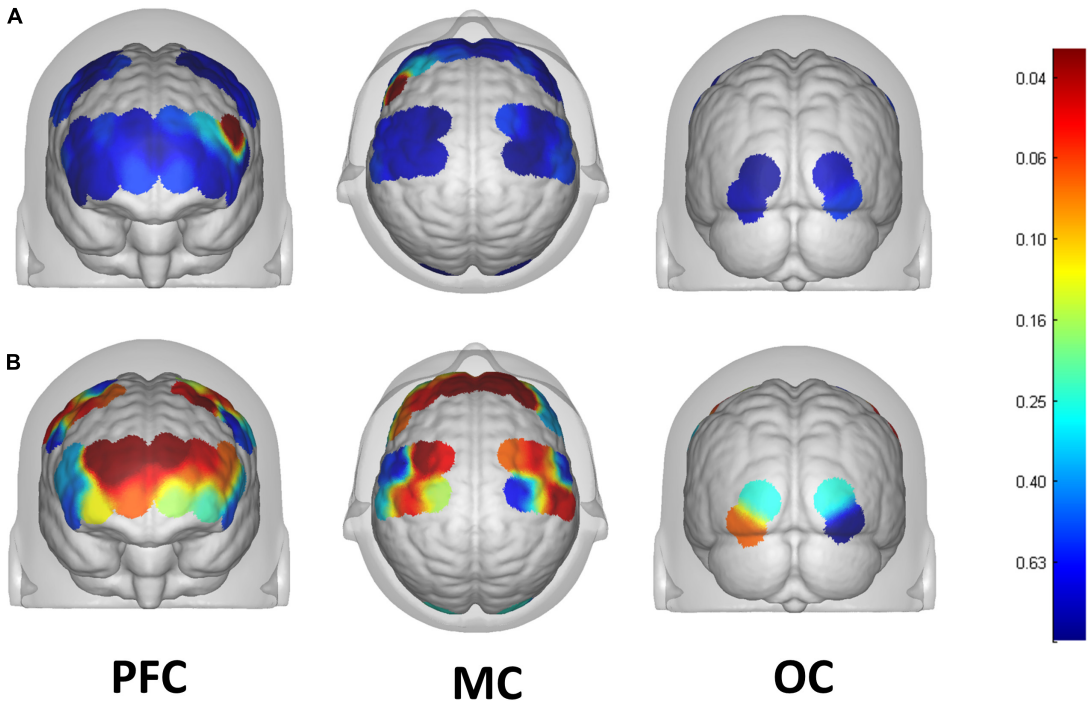

FIGURE 3
Brain map of activation regions during FNS by using beta values of GLM analysis in the **(A)** HCs, and the **(B)** stroke patients. The color bar represents the *P*-value of beta values.

at different Brodmann regions over time (–5 to 60 s, 0–30 s represent the FNS period). The concentration of HBO gradually increased with the initiation of FNS. It reached the peak value after 10 s and then dropped rapidly in the bilateral MC.

Discussion

In this study, the fNIRS approach was used to study cortex functional connectivity and activation characteristics in the stroke patient and HCs. From the functional connectivity perspective, the correlation coefficients between bilateral MC and left OC were found to decrease in stroke patients compared with the HCs during the resting state; from the cortex activation perspective, significant activation was observed in the PFC and MC of stroke patients during FNS. Moreover, FN was also found to activate part of the LPFC in the HCs.

Based on the results of this study, the functional connectivity strength between RMC and LMC, RMC and LOC, and LMC and LOC were significantly decreased in stroke patients compared with participants in the HCs. And the strength of functional connection in both hemispheres decreased asymmetrically. Neural plasticity is an important factor that reflects cortical reorganization after stroke, and functional connection is one of the main indicators of neural plasticity. The MC is the core of the brain that plans and executes volitional movements (Svoboda and Li, 2018), whereas the OC is associated with peripheral sensory information (Song et al., 2017). The results of this study are consistent with previous studies that reported a high correlation between decreased sensorimotor connectivity and clinical motor functional defect assessment (Volz et al., 2016). Studies found that focal cerebral ischemic injury can

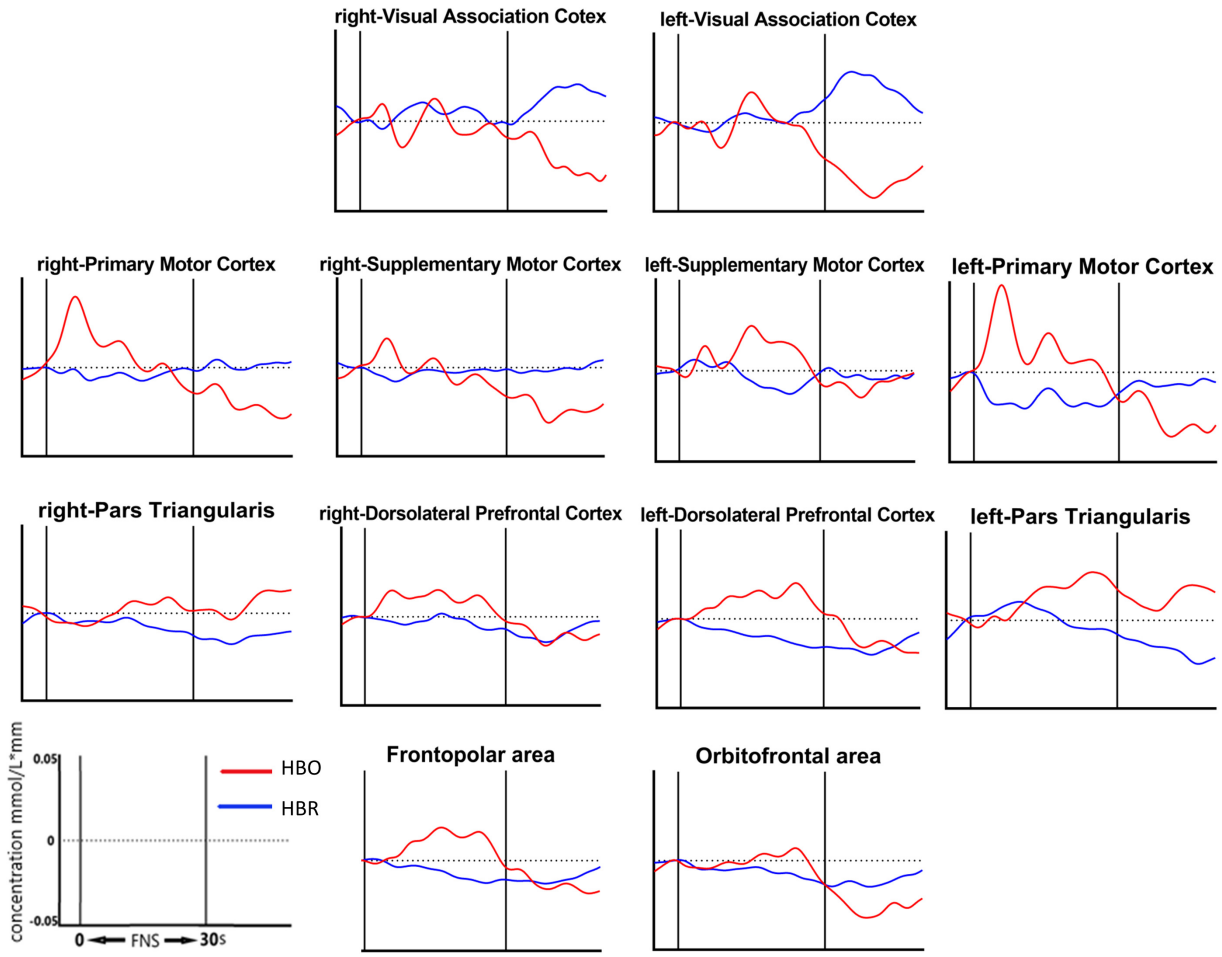

FIGURE 4
Grand average waveforms of HBO changes during FNS in each ROI based on Brodmann in stroke patients. The vertical axis represents concentration changes of HBO and HBR; while the horizontal axis represents the latency. The start time of the FNS period was defined as 0 s. The ROI contained 12 cerebral areas, which include the bilateral Visual Association Cortex, bilateral Primary Motor Cortex, bilateral Supplementary Motor Cortex, bilateral Pars Triangular, bilateral Dorsolateral Prefrontal Cortex, Frontopolar area and Obitorfrontal area.

lead to a decline in the complete network of sensorimotor connections, especially in the early stage of stroke (Park et al., 2011). It can also affect functional connections between the hemispheres of the undamaged lateral cortex (Green et al., 2018). Although all patients in the stroke patient group of this study suffered from long-term unilateral ischemic brain injury and most of the infarcts are located in the left basal ganglia, with only a few patients that had large frontal parietal and temporal lobe infarction on left hemisphere, results showed weakened intra-hemispheric and inter-hemispheric brain functional connectivity. The results of our study suggest that our stroke patients still need rehabilitation therapy to improve the motor function of the affected limbs and improve the level of motor functional connection between the hemispheres.

Results also showed that the HBO of the bilateral PFC and bilateral MC significantly increased during the FNS period in stroke patients and HCs. This outcome indicates that FNS can activate parts of the brain in the PFC and MC. HBO in the MC increased with FNS but gradually returned to baseline when FNS was stopped (**Figure 4**). These results are in line with those of previous studies (Steriade, 1995; Golanov and Reis, 1996; Watson et al., 2009, 2014), where EEG examination showed that the brain-electric activity began to increase after FNS. CBF was also found to increase in 4 s, peaked around 8 s, and then gradually dropped to the baseline level. A plausible explanation to these results may be the ability of FNS in increasing CBF by evoking vasodilation neurons. The HBO signal could reflect the dynamic changes in the neural and functional activity of the cerebral cortex due to the neurovascular coupling mechanism (Claassen et al., 2021). Besides the influence of CBF, FNS also activates the intrinsic neurons in the cerebral cortex through neural pathways (Reis et al., 1997). Fibers from the FNS cross to the opposite side of the cerebellar vermis to form an uncinate cerebellar bundle (Haroian et al., 1981). This nerve bundle projects to the dorsal tegmental area of the midbrain, continues to rise into the thalamus, and finally terminates in the ventromedial nucleus of the thalamus dorsal medial nucleus. Due to the extensive relationship between the dorsal medial thalamic nucleus and the prefrontal cortex (PFC), the FNS could activate the PFC (Steriade, 1995). The present results are significant as the activation of PFC and MC by FNS provides a certain therapeutic basis and plays a guiding role in the rehabilitation of stroke patients.

Conclusion

This study illustrated that FNS induced activation in the brain regions of PFC and MC, with the FC values between bilateral MC and left OC being significantly decreased in stroke patients. The results of this study provide evidence for the clinical application and curative effect guidance of FNS treatment in the rehabilitation of patients with stroke and brain injury.

Limitations

Due to the limitation of the fNIRS technology, it was not possible to measure the subcortical structures and cerebellum. In the future, the mechanisms related to the neural conduction pathways between cerebellar FN and cortex should be further explored to provide more accurate evidence that would be critical for potential clinical application. Besides, the sample size in this study was not large enough as well.

Data availability statement

The raw data supporting the conclusions of this article will be made available by the authors, without undue reservation.

Ethics statement

The studies involving human participants were reviewed and approved by the Sun Yat-sen Memorial Hospital Ethics Committee. The patients/participants provided their written informed consent to participate in this study.

Author contributions

HM and YZ performed the experiment and wrote the manuscript. ZX collected the data. SF and XW contributed significantly to the data analysis. JX contributed to data processing. CM and SW contributed equally to design the experiment. All authors read and approved the final version of the manuscript.

Funding

This work was supported by the National Natural Science Foundation of China (grant no. 81972152), the National Natural Science Foundation of China (grant no. 81901092), and the Guangzhou Science and Technology Project (grant no. 201907010014).

Acknowledgments

We would like to thank the graduate students of Sun Yat-sen Memorial Hospital, Sun Yat-sen University, XW and YZ, and employee, ZX who participated in the experiment. We would also like to thank Hang Liang for their help during the data analysis.

Conflict of interest

The authors declare that the research was conducted in the absence of any commercial or financial relationships that could be construed as a potential conflict of interest.

Publisher's note

All claims expressed in this article are solely those of the authors and do not necessarily represent those of their affiliated organizations, or those of the publisher, the editors and the reviewers. Any product that may be evaluated in this article, or claim that may be made by its manufacturer, is not guaranteed or endorsed by the publisher.

Supplementary material

The Supplementary Material for this article can be found online at: https://www.frontiersin.org/articles/10.3389/fnins.2022.895237/full#supplementary-material

References

Al-Afif, S., Krauss, J. K., Helms, F., Angelov, S., John, N., Schwabe, K., et al. (2019). Long-term impairment of social behavior, vocalizations and motor activity induced by bilateral lesions of the fastigial nucleus in juvenile rats. *Brain Struct. Funct.* 224, 1739–1751. doi: 10.1007/s00429-019-01871-3

Buxton, R. B. (2013). The physics of functional magnetic resonance imaging (fMRI). *Rep. Prog. Phys.* 76:096601.

Claassen, J. A. H. R., Thijssen, D. H. J., Panerai, R. B., and Faraci, F. M. (2021). Regulation of cerebral blood flow in humans: Physiology and clinical implications of autoregulation. *Physiol. Rev.* 101, 1487–1559.

Conceição, N. R., Gobbi, L. T. B., Nóbrega-Sousa, P., Orcioli-Silva, D., Beretta, V. S., Lirani-Silva, E., et al. (2021). Aerobic exercise combined with transcranial direct current stimulation over the prefrontal cortex in parkinson disease: effects on cortical activity. gait, and cognition. *Neurorehab. Neural Repair.* 35, 717–728.

Di Rosa, E., Brigadoi, S., Cutini, S., Tarantino, V., Dell'Acqua, R., Mapelli, D., et al. (2019). Reward motivation and neurostimulation interact to improve working memory performance in healthy older adults: A simultaneous tDCS-fNIRS study. *NeuroImage* 202:116062. doi: 10.1016/j.neuroimage.2019.116062

Dimitrova, A., Weber, J., Redies, C., Kindsvater, K., Maschke, M., Kolb, F. P., et al. (2002). MRI atlas of the human cerebellar nuclei. *NeuroImage* 17, 240–255.

Gao, Z., Davis, C., Thomas, A. M., Economo, M. N., Abrego, A. M., Svoboda, K., et al. (2018). A cortico-cerebellar loop for motor planning. *Nature* 563, 113–116.

Golanov, E. V., and Reis, D. J. (1996). Cerebral cortical neurons with activity linked to central neurogenic spontaneous and evoked elevations in cerebral blood flow. *Neurosci. Lett.* 209, 101–104. doi: 10.1016/0304-3940(96)12611-2

Golanov, E. V., Regnier-Golanov, A. S., and Britz, G. W. (2017). Integrity of cerebellar fastigial nucleus intrinsic neurons is critical for the global ischemic preconditioning. *Brain Sci.* 7:121. doi: 10.3390/brainsci7100121

Golanov, E., and Reis, D. (1999). Neuroprotective electrical stimulation of cerebellar fastigial nucleus attenuates expression of periinfarction depolarizing waves (PIDs) and inhibits cortical spreading depression. *Brain Res.* 818, 304–315. doi: 10.1016/s0006-8993(98)01169-x

Green, C., Minassian, A., Vogel, S., Diedenhofen, M., Beyrau, A., Wiedermann, D., et al. (2018). Sensorimotor functional and structural networks after intracerebral stem cell grafts in the ischemic mouse brain. *J. Neurosci.* 38, 1648–1661. doi: 10.1523/JNEUROSCI.2715-17.2018

Haroian, A. J., Massopust, L. C., and Young, P. A. (1981). Cerebellothalamic projections in the rat: An autoradiographic and degeneration study. *J. Comp. Neurol.* 197, 217–236. doi: 10.1002/cne.901970205

Hooker, J. M., and Carson, R. E. (2019). Human positron emission tomography neuroimaging. *Annu. Rev. Biomed. Eng.* 21, 551–581.

Hou, X., Zhang, Z., Zhao, C., Duan, L., Gong, Y., Li, Z., et al. (2021). NIRS-KIT: A MATLAB toolbox for both resting-state and task fNIRS data analysis. *Neurophotonics* 8:010802. doi: 10.1117/1.NPh.8.1.010802

Hu, S., Shi, J., Xiong, W., Li, W., Fang, L., and Feng, H. (2017). Oxiracetam or fastigial nucleus stimulation reduces cognitive injury at high altitude. *Brain Behav.* 7:e00762.

Huo, C., Li, X., Jing, J., Ma, Y., Li, W., Wang, Y., et al. (2019). Median nerve electrical stimulation-induced changes in effective connectivity in patients with stroke as assessed with functional near-infrared spectroscopy. *Neurorehab. Neural Repair.* 33, 1008–1017. doi: 10.1177/1545968319875952

Kocsis, L., Herman, P., and Eke, A. (2006). The modified beer-lambert law revisited. *Phys. Med. Biol.* 51, N91–N98.

Kozel, F. A., Tian, F., Dhamne, S., Croarkin, P. E., McClintock, S. M., Elliott, A., et al. (2009). Using simultaneous repetitive transcranial magnetic stimulation/functional near infrared spectroscopy (rTMS/fNIRS) to measure brain activation and connectivity. *NeuroImage* 47, 1177–1184. doi: 10.1016/j.neuroimage.2009.05.016

Li, R., Potter, T., Wang, J., Shi, Z., Wang, C., Yang, L., et al. (2019). Cortical hemodynamic response and connectivity modulated by sub-threshold high-frequency repetitive transcranial magnetic stimulation. *Front. Hum. Neurosci.* 13:90. doi: 10.3389/fnhum.2019.00090

Lloyd-Fox, S., Blasi, A., and Elwell, C. E. (2010). Illuminating the developing brain: The past, present and future of functional near infrared spectroscopy. *Neurosci. Biobehav. Rev.* 34, 269–284.

Miura, M., and Reis, D. J. (1969). Cerebellum: A pressor response elicited from the fastigial nucleus and its efferent pathway in brainstem. *Brain Res.* 13, 595–599.

Noda, T., Yoshida, S., Matsuda, T., Okamoto, N., Sakamoto, K., Koseki, S., et al. (2012). Frontal and right temporal activations correlate negatively with depression severity during verbal fluency task: A multi-channel near-infrared spectroscopy study. *J. Psychiatr. Res.* 46, 905–912.

Obrig, H. (2014). NIRS in clinical neurology - a 'promising' tool? *NeuroImage* 85, 535–546.

Park, C. H., Chang, W. H., Ohn, S. H., Kim, S. T., Bang, O. Y., Pascual-Leone, A., et al. (2011). Longitudinal changes of resting-state functional connectivity during motor recovery after stroke. *Stroke* 42, 1357–1362.

Reis, D. J., Golanov, E. V., Galea, E., and Feinstein, D. L. (1997). Central neurogenic neuroprotection: Central neural systems that protect the brain from hypoxia and ischemia. *Ann. N. Y. Acad. Sci.* 835, 168–186. doi: 10.1111/j.1749-6632.1997.tb48628.x

Scholkmann, F., Kleiser, S., Metz, A. J., Zimmermann, R., Mata Pavia, J., Wolf, U., et al. (2014). A review on continuous wave functional near-infrared spectroscopy and imaging instrumentation and methodology. *NeuroImage* 85, 6–27.

Si, X., Xiang, S., Zhang, L., Li, S., Zhang, K., and Ming, D. (2021). Acupuncture with deqi modulates the hemodynamic response and functional connectivity of the prefrontal-motor cortical network. *Front. Neurosci.* 15:693623. doi: 10.3389/fnins.2021.693623

Song, C., Sandberg, K., Andersen, L. M., Blicher, J. U., and Rees, G. (2017). Human occipital and parietal GABA selectively influence visual perception of orientation and size. *J. Neurosci.* 37, 8929–8937. doi: 10.1523/JNEUROSCI.3945-16.2017

Steriade, M. (1995). Two channels in the cerebellothalamocortical system. *J. Comp. Neurol.* 354, 57–70. doi: 10.1002/cne.903540106

Svoboda, K., and Li, N. (2018). Neural mechanisms of movement planning: Motor cortex and beyond. *Curr. Opin. Neurobiol.* 49, 33–41.

Tak, S., and Ye, J. C. (2014). Statistical analysis of fNIRS data: A comprehensive review. *NeuroImage* 85, 72–91. doi: 10.1016/j.neuroimage.2013.06.016

Uga, M., Dan, I., Sano, T., Dan, H., and Watanabe, E. (2014). Optimizing the general linear model for functional near-infrared spectroscopy: An adaptive hemodynamic response function approach. *Neurophotonics* 1:015004.

Volz, L. J., Rehme, A. K., Michely, J., Nettekoven, C., Eickhoff, S. B., Fink, G. R., et al. (2016). Shaping early reorganization of neural networks promotes motor function after stroke. *Cereb. Cortex* 26, 2882–2894. doi: 10.1093/cercor/bhw034

Wang, A. R., Hu, M. Z., Zhang, Z. L., Zhao, Z. Y., Li, Y. B., and Liu, B. (2019). Fastigial nucleus electrostimulation promotes axonal regeneration after experimental stroke *via* cAMP/PKA pathway. *Neurosci. Lett.* 699, 177–183. doi: 10.1016/j.neulet.2019.02.016

Wang, M., Hu, Z., Liu, L., Li, H., Qian, Q., and Niu, H. (2020). Disrupted functional brain connectivity networks in children with attention-deficit/hyperactivity disorder: Evidence from resting-state functional near-infrared spectroscopy. *Neurophotonics* 7:015012. doi: 10.1117/1.NPh.7.1.015012

Watson, T. C., Becker, N., Apps, R., and Jones, M. W. (2014). Back to front: Cerebellar connections and interactions with the prefrontal cortex. *Front. Syst. Neurosci.* 8:4. doi: 10.3389/fnsys.2014.00004

Watson, T. C., Jones, M. W., and Apps, R. (2009). Electrophysiological mapping of novel prefrontal - cerebellar pathways. *Front. Integr. Neurosci.* 3:18. doi: 10.3389/neuro.07.018.2009

Xia, D., Sui, R., Min, L., Zhang, L., and Zhang, Z. (2019). Fastigial nucleus stimulation ameliorates cognitive impairment *via* modulating autophagy and inflammasomes activation in a rat model of vascular dementia. *J. Cell Biochem.* 120, 5108–5117. doi: 10.1002/jcb.27787

Zhang, C., Luo, W., Zhou, P., and Sun, T. (2016). Microinjection of acetylcholine into cerebellar fastigial nucleus induces blood depressor response in anesthetized rats. *Neurosci. Lett.* 629, 79–84. doi: 10.1016/j.neulet.2016.06.063

Zhang, S., Peng, C., Yang, Y., Wang, D., Hou, X., and Li, D. (2021). Resting-state brain networks in neonatal hypoxic-ischemic brain damage: A functional near-infrared spectroscopy study. *Neurophotonics* 8:025007. doi: 10.1117/1.NPh.8.2.025007

Zhang, X. Y., Wang, J. J., and Zhu, J. N. (2016). Cerebellar fastigial nucleus: From anatomic construction to physiological functions. *Cereb. Ataxias.* 3:9.

Zheng, Y. L., Wang, D. X., Zhang, Y. R., and Tang, Y. Y. (2019). Enhancing attention by synchronizing respiration and fingertip pressure: A pilot study using functional near-infrared spectroscopy. *Front. Neurosci.* 13:1209. doi: 10.3389/fnins.2019.01209

frontiers | Frontiers in Neuroscience

TYPE Original Research
PUBLISHED 15 November 2022
DOI 10.3389/fnins.2022.1033155

OPEN ACCESS

EDITED BY
Aleksandra Dagmara Kawala-Sterniuk,
Opole University of
Technology, Poland

REVIEWED BY
Yanlu Wang,
Karolinska Institutet (KI), Sweden
Xiaosu Hu,
University of Michigan, United States

*CORRESPONDENCE
Shaofeng Zhao
zhaoshf6@mail.sysu.edu.cn

SPECIALTY SECTION
This article was submitted to
Brain Imaging Methods,
a section of the journal
Frontiers in Neuroscience

RECEIVED 31 August 2022
ACCEPTED 20 October 2022
PUBLISHED 15 November 2022

CITATION
Deng X, Jian C, Yang Q, Jiang N, Huang Z and Zhao S (2022) The analgesic effect of different interactive modes of virtual reality: A prospective functional near-infrared spectroscopy (fNIRS) study.
Front. Neurosci. 16:1033155.
doi: 10.3389/fnins.2022.1033155

The analgesic effect of different interactive modes of virtual reality: A prospective functional near-infrared spectroscopy (fNIRS) study

Xue Deng[1], Chuyao Jian[1], Qinglu Yang[1], Naifu Jiang[2], Zhaoyin Huang[1] and Shaofeng Zhao[1]*

[1]Department of Rehabilitation Medicine, The Eighth Affiliated Hospital of Sun Yat-Sen University, Shenzhen, China, [2]Key Laboratory of Human-Machine Intelligence-Synergy Systems, Shenzhen Institutes of Advanced Technology, Chinese Academy of Sciences (CAS), Shenzhen, China

Virtual reality has demonstrated its analgesic effectiveness. However, its optimal interactive mode for pain relief is yet unclear, with rare objective measurements that were performed to explore its neural mechanism.

Objective: This study primarily aimed at investigating the analgesic effect of different VR interactive modes *via* functional near-infrared spectroscopy (fNIRS) and exploring its correlations with the subjectively reported VR experience through a self-rating questionnaire.

Methods: Fifteen healthy volunteers (Age: 21.93 ± 0.59 years, 11 female, 4 male) were enrolled in this prospective study. Three rounds of interactive mode, including active mode, motor imagery (MI) mode, and passive mode, were successively facilitated under consistent noxious electrical stimuli (electrical intensity: 23.67 ± 5.69 mA). Repeated-measures of analysis of variance (ANOVA) was performed to examine its pain relief status and cortical activation, with *post hoc* analysis after Bonferroni correction performed. Spearman's correlation test was conducted to explore the relationship between VR questionnaire (VRQ) items and cortical activation.

Results: A larger analgesic effect on the active (−1.4(95%CI, −2.23 to −0.57), $p = 0.001$) and MI modes (−0.667(95%CI, −1.165 to −0.168), $p = 0.012$) was observed compared to the passive mode in the self−rating pain score, with no significant difference reported between the two modes (−0.733(95%CI, −1.631 to.165), $p = 0.131$), associated with diverse activated cortical region of interest (ROI) in charge of motor and cognitive functions, including the left primary motor cortex (LM1), left dorsal−lateral prefrontal cortex (LDLPFC), left primary somatosensory cortex (LS1), left visual cortex at occipital lobe (LOL), and left premotor cortex (LPMC). On the other hand, significant correlations were found between VRQ items and different cortical ROIs ($r = -0.629$ to 0.722, $p < 0.05$) as well as its corresponding channels ($r = -0.599$ to 0.788, $p < 0.05$).

Conclusion: Our findings suggest that VR can be considered as an effective non-invasive approach for pain relief by modulating cortical pain processing. A better analgesic effect can be obtained by exciting and integrating cortical ROIs in charge of motor and cognitive functions. The interactive mode can be easily tailored to be in line with the client's characteristics, in spite of the diverse cortical activation status when an equivalent analgesic effect can be obtained.

KEYWORDS

virtual reality, analgesia, functional near infrared spectroscopy, pain, fNIRS

Introduction

Pain is a complex sensory and emotional experience felt by a person in response to a real or an imaginary tissue injury, which can be largely influenced by personal experience and self-perception (Guarin, 2013). Even though there are a variety of approaches for bringing pain relief in a patient, including pharmacological and non-pharmacological types, there is still a worldwide public concern voiced against any inappropriate pain management (Sinatra, 2010). Considering the unsatisfied side effects caused by pharmacological approaches, we recently witnessed an expansion of research on non-pharmaceutical management (Benyamin et al., 2008; Sostres et al., 2010). The updated rationale behind bringing in such a non-pharmaceutical approach is to modulate both personal and environmental factors (Maral and David, 2017). It is suggested that physical exercise can help alleviate pain by exciting the primary motor cortex (M1), thus inhibiting limbic–cortical–thalamic activities, thereby decreasing the negative impact generated by prolonged immobilization on account of sustained pain (Ambrose and Golightly, 2015). On the other hand, studies have suggested that pain perception can be downgraded by orienting visual attention over the body's painful site, as it can strengthen its functional connectivity between the pain network and visual cortex at the occipital lobes (Longo et al., 2012; Karunakaran et al., 2020). It is speculated that a better analgesic effect can be obtained by incorporating these factors for bringing about innovations in current therapeutic approaches.

Even though traditional non-pharmacological management, such as physical exercise and mindfulness breathing, may bear these factors for pain modulation, it is quite challenging to engage a client at a painful status to sustain his/her engagement in a physically/attentively demanding task, letting alone those clients of older age and/or those who are in a severe painful status. Therefore, a tangible approach, which can address this problem, is keenly required. In recent years, virtual reality (VR) has been slowly expanding its application in health care services (Pillai and Mathew, 2019). The rationale behind such an approach like virtual reality is to immerse the client in a three-dimensional (3D) virtual simulated environment, with an entertaining gaming exercise to distract the client's attention from painful stimuli (Triberti et al., 2014; Rizzo and Bouchard, 2019). Over the past years, successive clinical evidences have demonstrated their promising effectiveness for pain reduction, anxiety, and stress management not only in acute pain management caused by a variety of medical procedures, such as wound dressing changes, dental procedures, and peripheral intravenous catheter placement, but also in chronic pain management (Hoffman et al., 2008; Jones et al., 2016; Alshatrat et al., 2018; Gold et al., 2021). However, these findings were mostly accrued *via* subjective ratings with rare objective measurements. In spite of the VR analgesic effect evidenced by a small number of studies using functional magnetic resonance imaging (fMRI), obvious drawbacks of those studies cannot be ignored (Hoffman et al., 2007). For instance, the fMRI as a neuroimaging technique can have its own constraints when observing the neuronal activities during VR interaction, i.e., poor temporal resolution and constrained testing environment (Hennig et al., 2003). On the other hand, even though the distraction hypothesis also suggests that a better analgesic effect can be achieved when a greater extent of attention is required in the VR environment, its optimal interactive mode and the corresponding neural mechanism are both enigmatic (Li et al., 2011; Lier et al., 2020). To overcome the technical constraints mentioned above, functional near-infrared spectroscopy (fNIRS) has been introduced, as it enables the non-invasive quantification of cortical hemodynamics at the near-infrared spectrum (Boas et al., 2004). A recent fNIRS study on VR-induced analgesia clearly discriminated the unique modulation of anterior prefrontal cortex (aPFC) over the premotor cortex in traditional mindful breathing (interoception) by traditional mindful breathing from VR breathing (exteroception), in which the increased visual–auditory cortical activation was associated with diminished functional connection with primary somatosensory cortex (S1) (Hu et al., 2021). It inspired the applicability of fNIRS in VR-induced analgesia studies. Considering its superior temporal resolution and environmental feasibility in comparison with fMRI and electroencephalography (EEG), fNIRS can be used as an optimal neuroimaging tool for observing neuronal activities during VR interaction in an open and unconstrained

environment bearing its differential optical properties of hemoglobin (Irani et al., 2007; Yücel et al., 2017).

In the present study, we primarily aimed at investigating the analgesic effect of different VR modes under painful stimuli. Secondarily, we aimed at exploring how cortical pain processing is modulated during different VR interactive modes. Based on the distraction theory, our primary hypothesis suggests that VR with a higher requirement of interactive elements can bring in a better analgesic effect by modulating cortical pain processing.

Materials and methods

This prospective study was approved by the Medical Ethics Committee of the hospital, with the clinical trial registered at the Chinese Clinical Trial Registry (Ref. No.: ChiCTR2200061536). The study was performed in line with the principle of the Declaration of Helsinki. Written consent form was obtained from all the participants prior to the beginning of the study.

Participants

Eligible healthy adults aged 18 years or above were enrolled. Participants with disorders enumerated below were excluded: (1) auditory or visual deficit, (2) sensory loss due to peripheral neuropathy or neurological disorders (e.g., peripheral nerve injuries or brain injuries); (3) acute or chronic pain disorders; (4) intake of painkillers or other sensory altering substances (alcohol, etc.) in the recent 2 weeks before the experiment, and (5) motion sickness. Finally, there were 15 young and healthy subjects (4 males, 11 females, age: 21.93 ± 0.59 years) who were recruited.

Study design and procedures

As delineated in Figure 1, this study was basically divided into three rounds, with interval between each round of at least 1 day (24 h) to avoid any carryover effect. After the subjects were enrolled by the convenience sampling method, a briefing session was initiated to introduce the experimental flow, to educate on the use of VR device, and to take safety precautions. A VR questionnaire (VRQ) was provided throughout each experimental round. Prior to each VR session, the participants were asked to report their recent pain status *via* the visual-analog scale (VAS) for pain scores in the VRQ, with those who reported any pain excluded. Immediately after the successful completion of the VR session, the participants were asked to recall their subjective VR experience, including the level of pain status, attention, immersion, and pain distraction as well as their current pain status *via* VAS pain scores.

As shown in Figure 2A, the participant was required to wear a 44-channel fNIRS cap (NirSmart-6000A, Danyang Huichuang Medical Equipment Co. Ltd., China), with a headmounted display (HMD) (HTC VIVE Cosmos, HTC/Valve Co.) placed over his/her head, holding the controllers bilaterally to interact with the VR gaming task. In each round, an electric stimuli equipment (YRKJ-F1002, Yirui Co. Ltd., China) was arranged, with two electrode pads placed on both sides of the participant's lumbar L5/S1 level. The frequency rate was set as 1 Hz, with 1 ms as the frequency width. The intensity of electrical stimuli started from 5 mA upwards, with its intensity fixed when the participant reported that the stimuli were similar to a pinprick sensation (unpleasant, slightly painful). The intensity was constant for every subject throughout each round.

This block study design consists of three parts, including 30-s rest, 190-s VR task, and 60-s recovery. During the 30-s rest period, participants were required to stand still with eyes closed, counting the number in seconds from 1 to 30. In the 190-s task session, subjects were required to interact with the VR gaming task in line with the interactive rules. The last part was a 60-s recovery session. Again, subjects were required to stand still with eyes closed, counting the number in seconds from 1 to 60. The task was conducted under constant electrical stimuli throughout the experiment.

As delineated in Figure 1, the three rounds were composed of active VR mode (R1), motor imagery (MI) mode (R2), and passive VR mode (R3), respectively. A rhythm VR game named < Beat Saber > (Beat Games, Czech) was chosen as the VR task, with the music <pop stars> by K-DA, a virtual K-pop female vocal group that opted for the VR session (Figure 2B). In R1, the participants were required to wield a pair of glowing sabers, slashing a stream of approaching blocks in sync with the song's beats and notes; whereas in R2, the participants were required to track the stream of blocks with their eyes, imaging the correct slashing act without any physical motion; in R3, the participants were required to listen to the music only, with eyes closed and physical motion absent.

Data analysis

fNIRS acquisition

A multichannel portable near-infrared system (NirSmart-6000A, Danyang Huichuang Medical Equipment Co., Ltd., China) was used in this study, taking 11 Hz as the sampling frequency rate with dual near-infrared (near-IR) lights (wavelengths: 730 nm and 850 nm) to detect oxyhemoglobin (HbO) and deoxyhemoglobin (HbR) concentration changes. In accord with the international 10/20 electrode distribution system, the 18 emission sources and 16 detectors (source-detector separation: 3 cm) were arranged over the frontal,

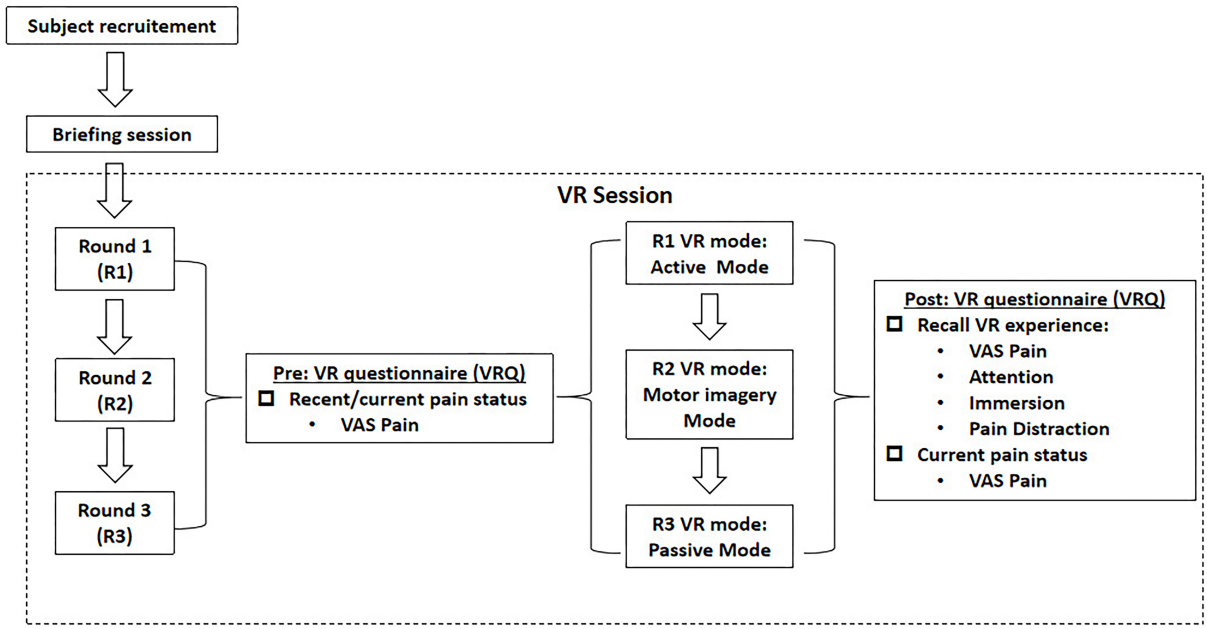

FIGURE 1
Experimental flow.

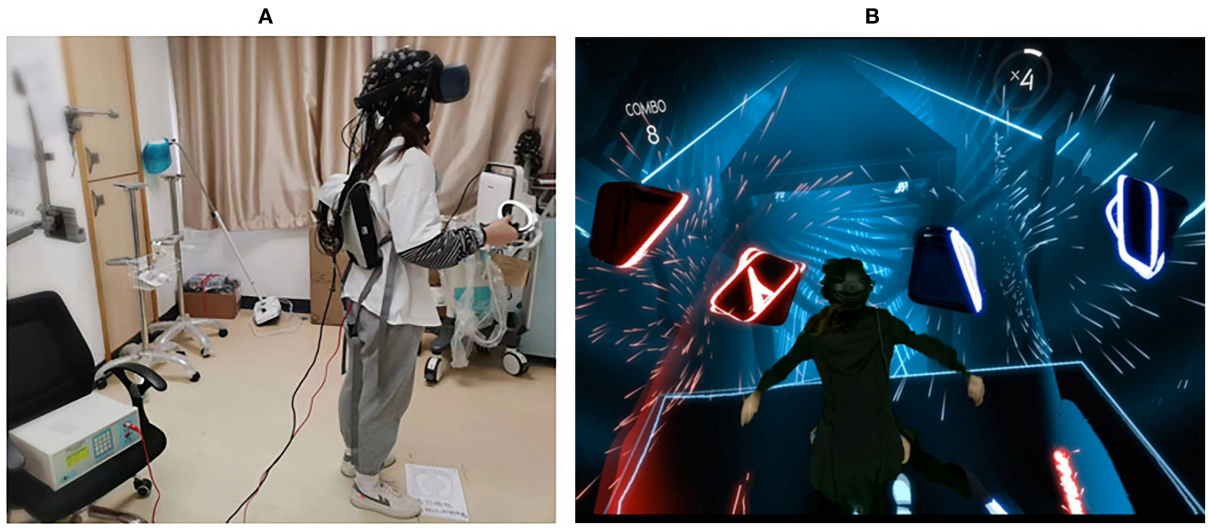

FIGURE 2
Experimental scenario. **(A)** The scenario of real world; **(B)** the scenario of virtual world (Virtual Scenario of Beat Saber, n.d.).

parietal, temporal, and occipital regions at both hemispheres, consisting of 44 channels. The spatial locations of sources and detectors were measured by an electromagnetic 3D digitizer device (Patriot, Polhemus, USA) placed on the head of the subject, with acquired coordinates that are converted into coordinates in line with the Montreal Neurological Institute and Hospital (MNI). These coordinates are further projected to the MNI standard brain template using the spatial registration approach in NirSpace (Danyang Huichuang Medical Equipment Co., Ltd., China). A flexible headgear holder was used for reducing signal noise between the emitter and scalp. During the experiment, the excessive

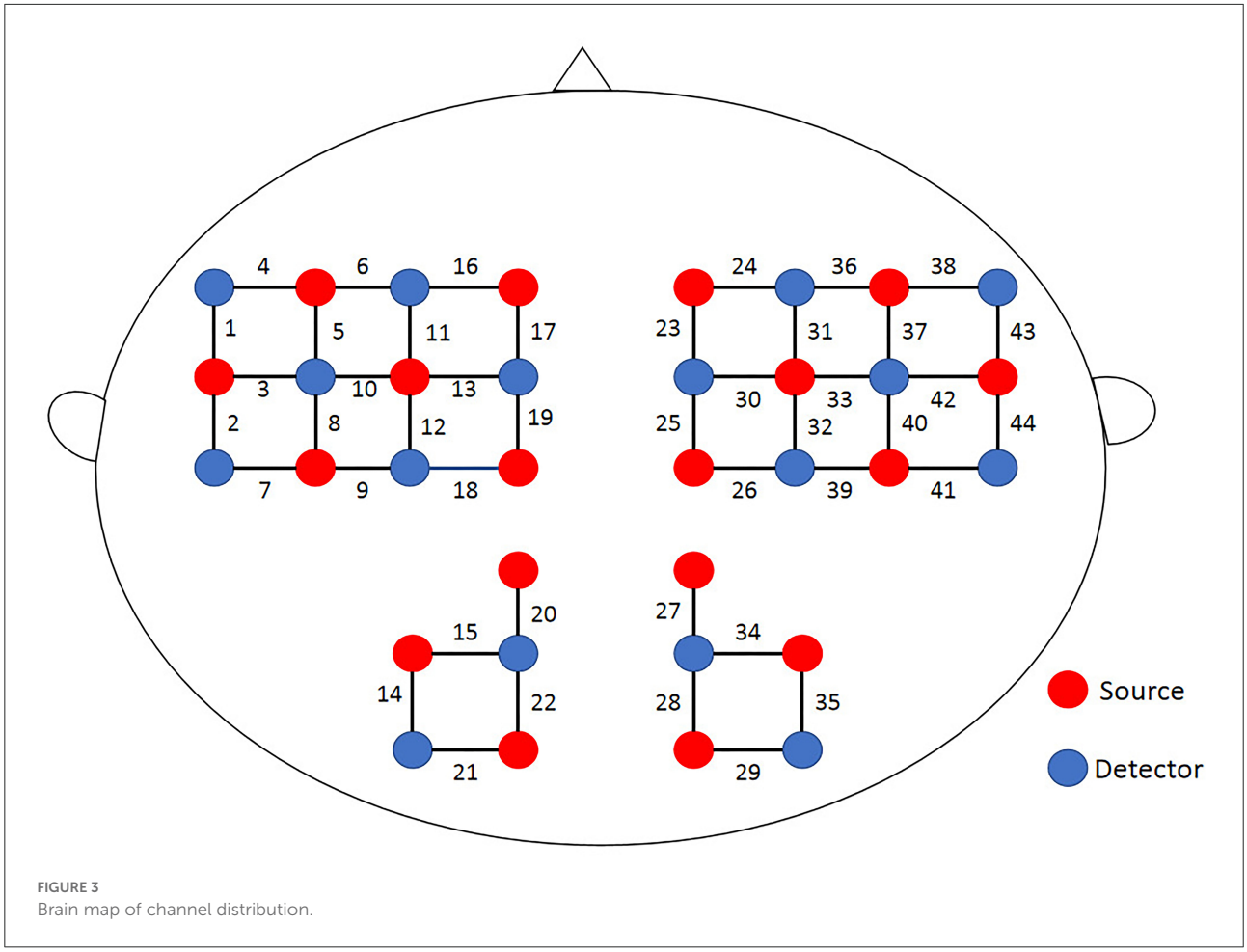

FIGURE 3
Brain map of channel distribution.

light was controlled for better data collection. A brain location map with its distribution of channels is shown in Figure 3.

fNIRS data processing

The NIRspark (v1.7.3, Huichuang, China) based on Matlab (v2021a, Natick, USA) was used to analyze the experimental data collected by the fNIRS system. The data processing was performed in the following steps:

① Elimination of the motion artifact: Spline interpolation was taken for data correction. The time window was set as 0.5s. Those signals with any changes beyond 6 standard deviation (std_thr $>$ 6) and 0.5 amplitude (amp_thr $>$0.5) of the whole time series were considered as the motion artifact (Scholkmann et al., 2010).

② Data conversion: Based on the Beer–Lambert Law, the optical density was converted into HbO and HbR concentrations.

③ Data filter: The raw data were digitally filtered in the bandpass 0.01–0.2 Hz to remove low oscillations, e.g., respiratory and cardiac components.

④ Obtainment of the hemodynamic response function (HRF): The hemodynamic response function's (HRF's) initial time was set to −32 s, and the end time was set to 30 s (with "−32 to −30s" as the reserved baseline state and "−30 to 30s" as the time for a single block paradigm). The HbO concentrations across channels for each subject were superimposed and averaged to compute an average result.

⑤ Calculation of cortical activation: The β value and featured value (FV) were taken as cortical activation in this study. The β values was calculated by employing the Generalized linear model (GLM) as follows:

$$Y = X\beta + \varepsilon, X \epsilon R^{N\times M}, \beta \epsilon R^{M\times L} \quad (1)$$

$$\beta = X*Y, X* = (X^T X)^{-1} X^T \quad (2)$$

where $X \epsilon R^{N\times M}$ denotes the design matrices (where M is the number of data points during the recording period and

TABLE 1 Descriptive characteristics.

Demographics

N		15			
Age (year): Mean ± SD		21.93 ± 0.59			
Gender (Male/Female, N)		4/11			
Hand dominance(Left/Right)		0/15			
Electric stimulus intensity (mA): mean ± SD		23.67 ± 5.69			
VRQ		Pain	Attention	Immersion	Pain Distraction
R1	Pre VR task	4/10	-	-	-
	During VR task	2.33 ± 1.23/10	7.87 ± 2.42	8.73 ± 1.39	6.53 ± 3.36
	Post VR task	0	-	-	-
R2	Pre VR task	4/10	-	-	-
	During VR task	3.07 ± 0.7/10	6.2 ± 2.11	6.53 ± 2.29	6.2 ± 2.27
	Post VR task	0	-	-	-
R3	Pre VR task	4/10	-	-	-
	During VR task	3.73 ± 0.88/10	4.93 ± 2.19	4.87 ± 2.67	4.73 ± 2.4
	Post VR task	0	-	-	-

VRQ, VR questionnaire; R1, active mode R2, motor imagery; R3, passive mode.

N is the number of β dimensions), and $\beta \epsilon R^{M \times L}$ (where L is the number of measurement channels) is the corresponding response signal strength for the HbO parameter. The canonical HRF was chosen as the basic function of GLM. The match between experimental design and HRF values was calculated, then the GLM can derive the β value. The β value represents the intensity of activation triggered by the experimental task in the individual's cerebral cortex. Then, the FV was obtained based on HRF in the rest period (-30 to 0s) being subtracted from that in the task period (0–30 s).

Statistical analysis

SPSS (v24.0, IBM, USA) was used for statistical analysis. The interactive VR mode from R1 to R3 was considered as the within-subject variable, while the mode sequence was incorporated as the between-subjects variable. The Kolmogorov–Smirnov and Shapiro–Wilk tests were used, revealing data were normally distributed. The obtained data were corrected for multiple comparisons across channels by the false discovery rate (FDR). Repeated-measures analysis of variance (ANOVA) was used to examine the cortical activation (β and FV) and VAS pain scores in the VRQ among the three VR modes. Bonferroni's correction was utilized for multiple comparisons. The confidence level a was defined as 0.05. Finally, Spearman's correlation test was used to examine the relationship between VRQ items and cortical activation (ROIs and corresponding channels).

Results

Descriptive characteristics

Finally, there were 15 right-hand dominant participants (number of males/females: 4/11; age: 21.93 ± 0.59 years) who were enrolled, with no one dropped out throughout the experiment. The overall mean intensity of electrical stimuli was 23.67 ± 5.69 mA, equivalent of VAS 4/10 subjectively reported by the enrolled participants during the resting period, with no one reporting any side effect after the experiment. The VAS scores during VR task from R1 to R3 were 2.33/10 (active mode), 3.07/10 (MI mode), and 3.73/10 (passive mode) respectively (Table 1).

VR-induced analgesic effect during different VR interactive modes

The painful status during different modes of VR interaction is presented in Figure 4. A significant effect of VR analgesia was found in the subjectively reported pain scores ($F(1.743, 24.401)=11.47$, $p < 0.0001$). *Post hoc* analysis revealed significant difference between R1 (active mode) and R3 (passive mode) (−1.4 (95%CI, −2.23 to −0.57), $p = 0.001$), R2 (MI mode), and R3 (passive mode) (−0.667 (95%CI, −1.165 to −0.168), $p = 0.012$), whereas no significant difference was found between R1(active mode) and R2 (MI mode) (−0.733 (95%CI, −1.631 to 0.165), $p = 0.131$).

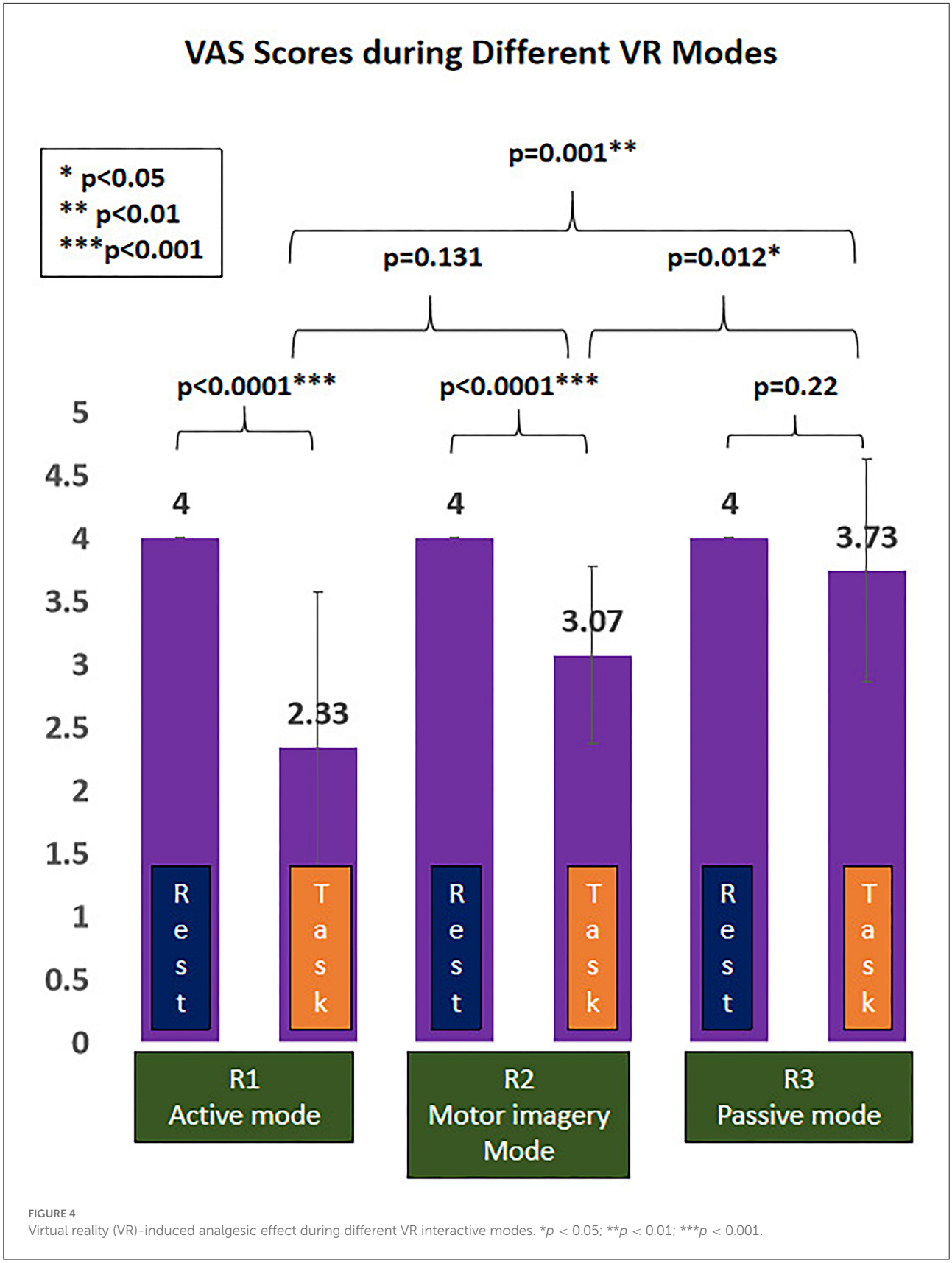

FIGURE 4
Virtual reality (VR)-induced analgesic effect during different VR interactive modes. *$p < 0.05$; **$p < 0.01$; ***$p < 0.001$.

TABLE 2 Cortical activation [β and featured values (FVs)] during different virtual reality (VR) interactive modes.

ROI	BA	Anatomic label	CH	MNI coordinates			Beta			Feature value		
				X	Y	Z	R1	R2	R3	R1	R2	R3
LDLPFC	9	Dorsolateral prefrontal cortex	16	12.45	−3.15	15.75	0.10 ± 0.13	0.03 ± 0.13	−0.03 ± 0.11	0.03 ± 0.07	0.00 ± 0.02	−0.02 ± 0.07
RDLPFC	9	Dorsolateral prefrontal cortex	24	14.7	−4.65	6.8	0.07 ± 0.14	0.02 ± 0.14	−0.04 ± 0.07	0.02 ± 0.07	−0.02 ± 0.08	−0.03 ± 0.05
LOL	18	V2	14	1.25	−9.2	14.55	0.05 ± 0.09	0.00 ± 0.11	−0.05 ± 0.10	0.04 ± 0.05	0.04 ± 0.05	−0.03 ± 0.07
	17,18,19	V1, V2, V3	15	3.2	−10.9	14.45						
	19	V3	20	5.65	−12.05	14.05						
	18	V2	21	0.85	−9.7	13.6						
	17	V1	22	2.8	−11.4	13.5						
ROL	19	V3	27	7.2	−13.35	8.45	0.07 ± 0.07	0.01 ± 0.07	−0.04 ± 0.09	0.04 ± 0.04	0.01 ± 0.05	−0.01 ± 0.06
	17	V1	28	4.25	−12.85	7.7						
	17	V1	29	2.75	−11.65	6.05						
	18	V2	34	5.4	−12.	6.75						
	17,18,19	V1,V2,V3	35	3.9	−11.6	5.1						
LM1	4	Primary motor cortex	13	11.3	−6.1	16.15	0.1 ± 0.11	0.03 ± 0.12	−0.05 ± 0.11	0.04 ± 0.05	0.02 ± 0.06	−0.04 ± 0.06
	4	Primary motor cortex	19	11.6	−8.2	15.25						
RM1	4	Primary motor cortex	25	13.45	−9.3	8.4	0.02 ± 0.1	0.01 ± 0.09	−0.02 ± 0.15	−0.01 ± 0.08	0.01 ± 0.04	0.01 ± 0.10
	4	Primary motor cortex	30	13.7	−7.7	6.75						
LPMC	6	Pre-motor and supplementary motor cortex	11	10.8	−3.9	16.8	0.08 ± 0.09	0.03 ± 0.14	−0.04 ± 0.08	0.03 ± 0.04	0.02 ± 0.06	−0.02 ± 0.06
	6	Pre-motor and supplementary motor cortex	17	12.95	−5.35	15.1						
RPMC	6	Pre-motor and supplementary motor cortex	23	14.75	−6.45	8.3	0.03 ± 0.07	0.02 ± 0.08	−0.02 ± 0.12	0.02 ± 0.06	0.00 ± 0.06	−0.01 ± 0.07
	6	Pre-motor and supplementary motor cortex	31	13.65	−5.9	5.25						
LS1	2	Primary somatosensory cortex	8	6.7	−5.1	17.25	0.06 ± 0.05	−0.03 ± 0.11	−0.02 ± 0.08	0.02 ± 0.05	0.01 ± 0.04	−0.02 ± 0.05
	1, 2, 3	Primary somatosensory cortex	12	9.3	−6.8	16.95						
RS1	1	Primary somatosensory cortex	32	12.3	−8.8	5.35	0.06 ± 0.11	0.02 ± 0.11	−0.01 ± 0.14	0.01 ± 0.07	−0.01 ± 0.06	−0.01 ± 0.07
	2	Primary somatosensory cortex	40	10.1	−7.45	3.25						
LSTG	22	Superior temporal gyrus	3	6.15	−3.05	17	0.09 ± 0.14	0.12 ± 0.11	−0.04 ± 0.18	0.00 ± 0.04	0.03 ± 0.08	0.02 ± 0.04
RSTG	22	Superior temporal gyrus	42	9.45	−5.	2.7	0.04 ± 0.08	0.04 ± 0.1	0.00 ± 0.1	−0.02 ± 0.08	0.01 ± 0.06	0.02 ± 0.05

ROI, Region of interest; BA, Broadmann area; CH, channel; MNI, Montreal Neurological Institute and Hospital (MNI); R1, active mode R2, motor imagery; R3, passive mode; LDLPFC, left dorsal lateral prefropntal cortex; RDLPFC, right dorsal lateral prefrontal cortex; LOL, left occipital lobe; ROL, right occipital lobe; LM1, left primary motor cortex; RM1, right primary motor cortex; LPMC, left premotor cortex; RPMC, right premotor cortex; LS1, left primary somatosensory cortex; RS1, right primary somatosensory cortex; LSTG, left superior temporal gyrus; RSTG, right superior temporal gyrus;V1, primary visual cortex, V2, visual association cortex 2; V3, visual association cortex 3.

10.3389/fnins.2022.1033155

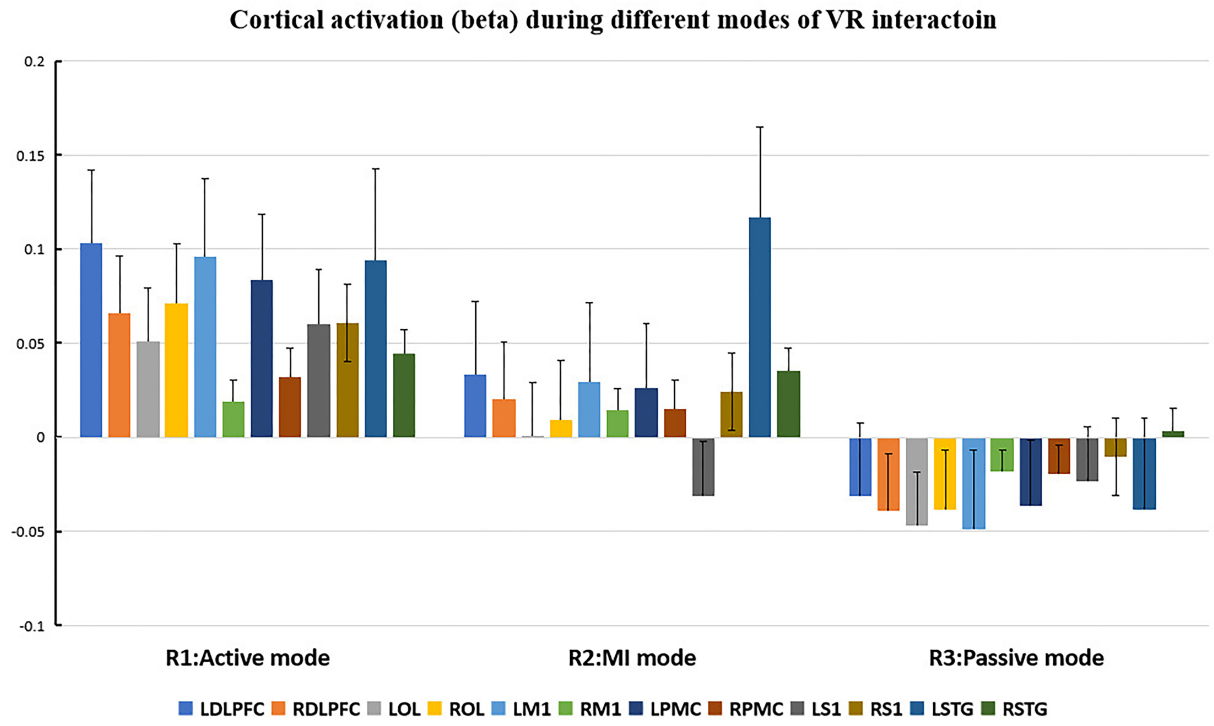

FIGURE 5
Cortical activation (β value) during different modes of virtual reality (VR) interaction. LDLPFC, left dorsal–lateral prefrontal cortex; RDLPFC: right dorsal–lateral prefrontal cortex; LOL, left occipital lobe; ROL, right occipital lobe; LM1, left primary motor cortex; RM1, right primary motor cortex; LPMC, left premotor cortex; RPMC, right premotor cortex; LS1, left primary somatosensory cortex; RS1, right primary somatosensory cortex; LSTG, left superior temporal gyrus; RSTG, right superior temporal gyrus.

Cortical activation during different VR interactive modes

The cortical regions of interest (ROIs) and their corresponding channels, associated with the MNI coordinates, are described in Table 2. The obtained β and featured values (FVs) in each ROI, including dorsal–lateral prefrontal cortex (DLPFC), primary motor cortex (M1), premotor cortex (PMC), primary somatosensory (S1), superior temporal gyrus (STG), and occipital lobe (OL) in both hemispheres, were also delineated, with the numerical analysis for each ROI plotted in Figures 5, 6 correspondingly.

Repeated measures (RM)-ANOVA revealed significant difference in β values of LM1 (F(6.37, 20.3), $p = 0.009$), LS1 (F(3.708, 24.628), $p = 0.041$), and LOL (F(7.973, 22.5), $p = 0.003$) as well as the FV in LPMC (F(8.379, 21.1), $p = 0.002$), LM1 (F(4.356, 22.627), $p = 0.027$), and LOL (F(9.249, 20.725), $p = 0.002$). On the other hand, in terms of the individual channel, it revealed a significant difference in the β values of channel 13 (F(3.963, 15.938), $p = 0.04$) and channel 15 (F(11.274, 14.917), $p = 0.002$) as well as FV in channel 11 (F(5.255, 18.478), $p = 0.017$), channel 17 (F(4.349, 13.85), $p = 0.035$), and channel 19 (F(5.782,23.117), $p = 0.01$).

Even though no significant difference was found in the cortical activation of ROIs between R1 and R2 (Figure 7), there were significant differences of ROIs in comparisons with ROIs and individual channels for R1 and R3 (Figure 8) as well as R2 and R3 (Figure 9). Regarding β values, *post hoc* analysis after Bonferroni correction revealed significant difference between R1 and R3 in channel 13 (0.133(95%CI, 0.028 to 0.238), $p = 0.012$), channel 15 (0.14(95%CI, 0.028 to 0.252), channel 16 (0.025(95%CI, −0.087 to 0.138), $p = 0.017$), and channel 17 (0.17(0.037, 0.304), $p = 0.013$) (Figure 8A); R2 and R3 in LOL (0.103 (95%CI, 0.041 to 0.166) $p = 0.003$) and channel 15 (0.17(95%CI, 0.037 to 0.304), $p = 0.013$) (Figure 9A).

Regarding FV, *post hoc* analysis after Bonferroni correction revealed significant difference between R1 and R3 in channel 11 (0.091(95%CI, 0.004 to 0.177), $p = 0.014$), channel 17 (0.071(95%CI, −0.003 to 0.146), $p = 0.016$), and channel 19 (0.083(95%CI, 0.011 to 0.135), $p = 0.022$) as well as LPMC (0.069(95%CI, 0.027 to.11), $p = 0.003$) (Figure 8B); R2 and R3 in LOL (0.067(95%CI, 0.032 to 0.101), $p = 0.004$) (Figure 9B).

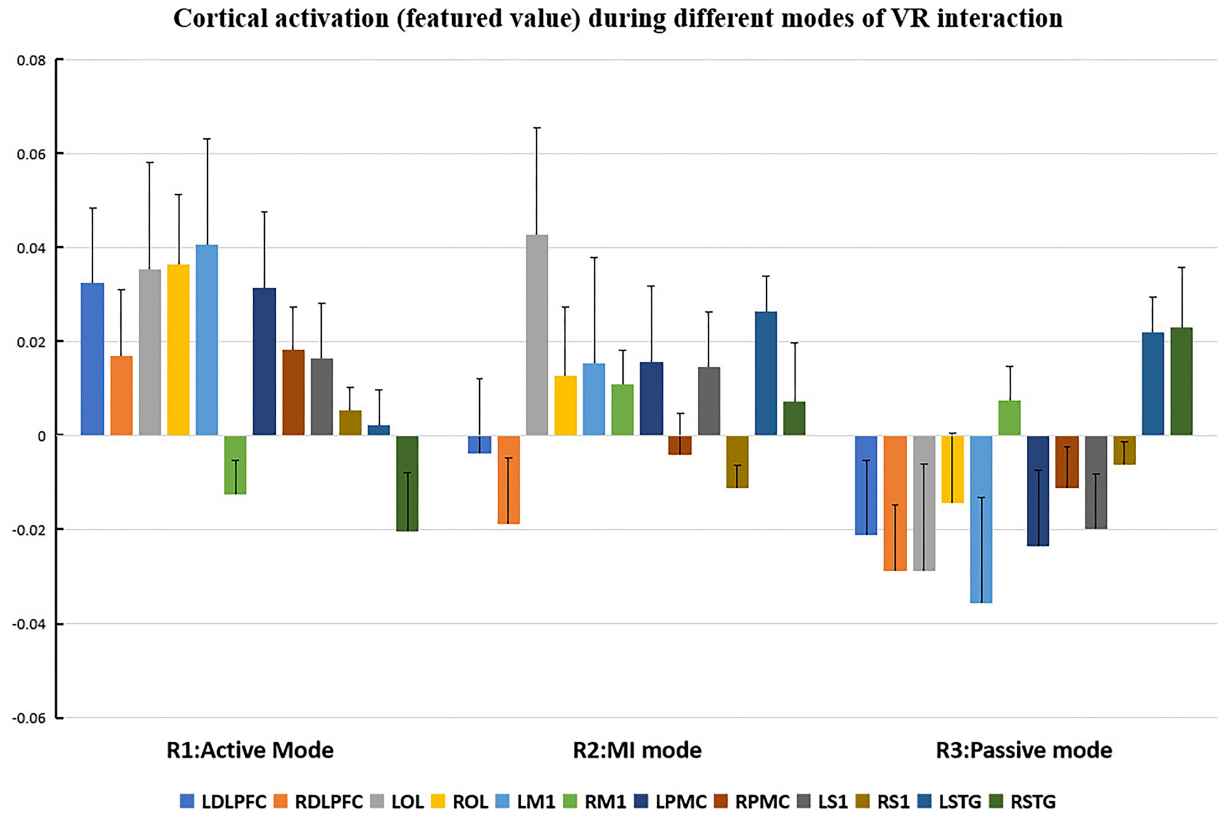

FIGURE 6
Cortical activation (featured value) during different modes of virtual reality (VR) interaction. LDLPFC: left dorsal–lateral prefrontal cortex; RDLPFC, right dorsal–lateral prefrontal cortex; LOL, left occipital lobe; ROL, right occipital lobe; LM1, left primary motor cortex; RM1, right primary motor cortex; LPMC, left premotor cortex; RPMC, right premotor cortex; LS1, left primary somatosensory cortex; RS1, right primary somatosensory cortex; LSTG, left superior temporal gyrus; RSTG: right superior temporal gyrus.

Correlation between VRQ items and cortical roi/channel activation

Regarding correlations between VRQ items and β values, significant correlations were found between attention and LM1 ($r = 0.609$, $p = 0.016$) as well as its corresponding channel 19 ($r = 0.677$, $p = 0.006$), pain and right S1 [right primary somatosensory cortex (RS1)] ($r = -0.588$, $p = 0.021$), pain distraction and right PMC (RPMC) ($r = -0.528$, $p = 0.043$) as well as RDLPFC ($r = -0.668$, $p = 0.009$) in R1; significant correlation was found between pain distraction and RDLPFC in R2 ($r = 0.531$, $p = 0.042$); significant correlations were found between attention and RDLPFC ($r = 0.587$, $p = 0.027$), attention and RS1 ($r=0.543$, $p = 0.045$) as well as between immersion and RS1 ($r = 0.539$, $p = 0.047$) in R3 (Table 3).

On the other hand, regarding correlations between VRQ items and featured values (FVs), a significant correlation was found between attention and LM1 ($r = 0.772$, $p = 0.001$) associated with its corresponding channel 19 ($r = 0.788$, $p < 0.001$), as well as RS1 ($r = 0.543$, $p = 0.036$) in R1; immersion and RDLPFC ($r = 0.574$, $p = 0.032$) in R2; pain and LPMC ($r = 0.539$, $p = 0.047$), attention and RPMC ($r=-0.62$, $p = 0.014$) associated with its corresponding channel 33($r=-0.599$, $p = 0.022$), LOL ($r = 0.557$, $p = 0.039$) as well as RSTG ($r = -0.629$, $p = 0.016$) in R2; correlation was found between attention and RDLPFC ($r = 0.538$, $p = 0.047$) as well as pain distraction and RDLPFC ($r = 7.43$, $p = 0.002$) in R3 (Table 3).

Discussion

To our knowledge, this is the first study which has investigated the effectiveness of different VR interactive modes for pain relief through fNIRS. In terms of the outcome generated through both subjective and objective measurements, we aimed at exploring VR as an analgesic by observing the cortical pain processing during painful stimuli. Throughout each round, the VR context and the electrical stimuli were both consistent, while the interactive mode was particularly designed in terms of its engaged level. According to the distraction theory, it is suggested that not only the interactive element of VR but also the level of attention is paid to the VR environment, which may contribute

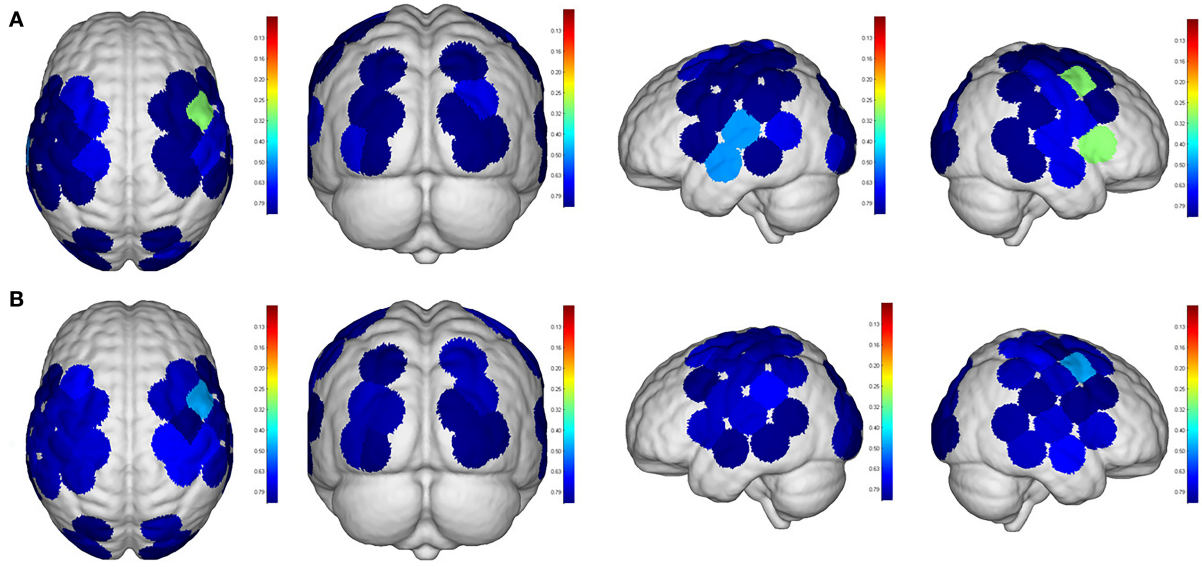

FIGURE 7
Comparisons of cortical activation between R1 and R2. R1: Active mode; R2: motor imagery (MI) mode; **(A)**: β value; **(B)**: featured value; color bar: 0.1 to 0.9.

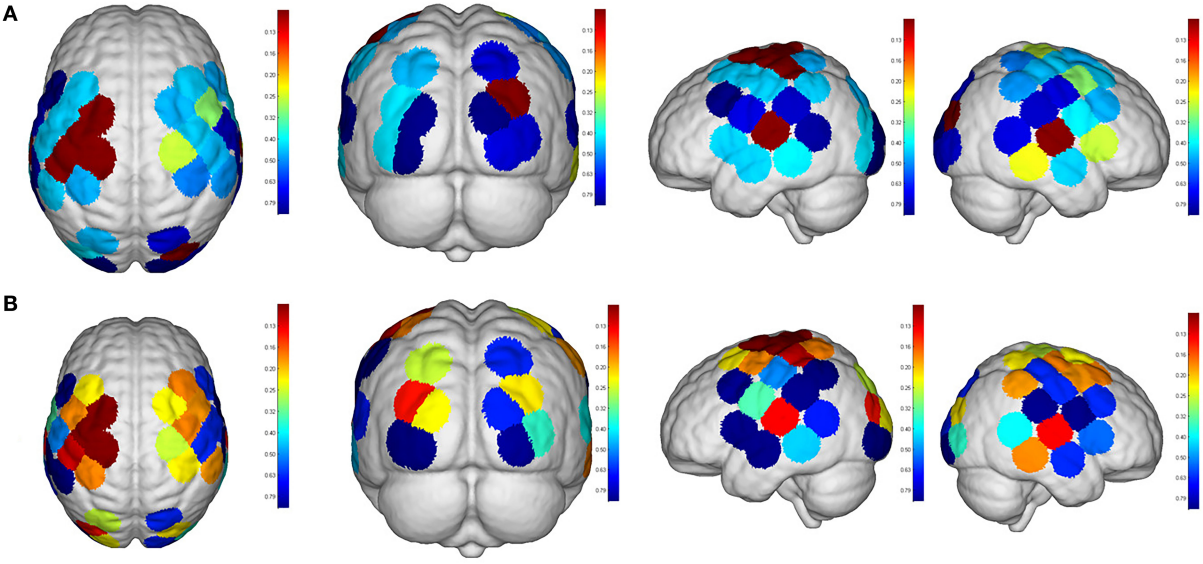

FIGURE 8
Comparisons of cortical activation between R1 and R3. R1: active mode; R3: passive mode; **(A)**: β value; **(B)**: featured value; color bar: 0.1 to 0.9.

to the ultimate analgesic effect (Mccaul and Malott, 1985; Gutierrez-Maldonado et al., 2011). Our finding demonstrated a better analgesic effect can be achieved to be associated with higher attention, immersion, and pain distraction during interaction with the VR context, which was consistent with a prior VR study using EEG, suggesting a better analgesic effect in the active VR mode is associated with reduced amplitudes of N1 and P3 (Lier et al., 2020). In addition, another finding in our studies revealed no significant difference between active and MI mode, implicating equivalent analgesic effect can be attainable when a sufficient level of attention was distracted in the VR context. This finding can be inspiring for those clients who tend to be quite immobile at painful status, as a similar analgesic effect can be achieved when a less active mode can be used.

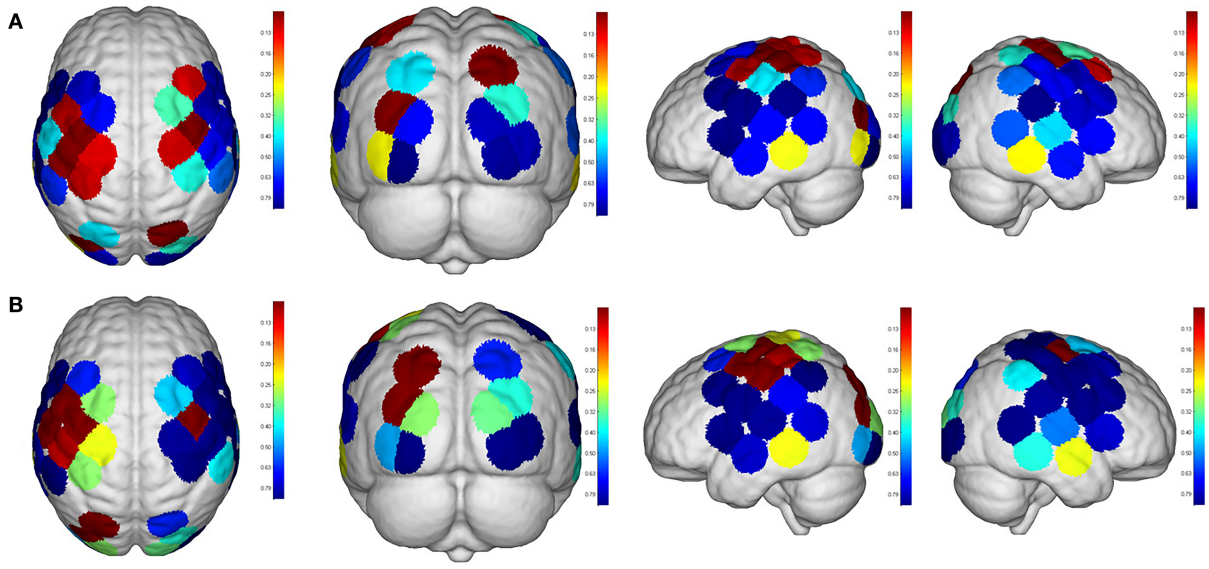

FIGURE 9
Comparisons of cortical activation between R2 and R3. R2: motor imagery (MI) mode; R3: passive mode; **(A)**: β value; **(B)**: featured value; color bar: 0.1 to 0.9.

Pain was processed, based on the sensory stimuli and behavior status by integrating different cortical information from various ROIs (Karunakaran et al., 2020). Therefore, the diverse analgesic effect associated with varied activated cortical area during different VR modes can be indicative of an altered pain perceptual processing. In our experiment, since the intensity of the electrical stimulus was never changed for every subject, the noxious input can be constant from peripheral to the spinal level. In this way, the area that modulates noxious stimuli by VR can only be situated at the thalamal–cortical area, where the correspondent cortical ROIs in charge of motor and cognitive function were involved.

As for the motor-relevant cortical area, significant difference in the activation in LM1 between active and passive mode was found (Figure 8). In addition, a dual positive correlation between attention and LM1 activation, associated with its corresponding channel in the active mode, was also specified (Table 3). M1 was basically in charge of motor planning, initiation, and execution of voluntary movement by processing cortical information from parietal, frontal, and temporal cortical regions (Wei-Ju et al., 2015). Since the corticospinal activation can be inhibited by acute painful stimuli, this ROI has been a critical target for pain relief by exciting it through invasive or non-invasive approaches (Svensson et al., 2003; Lopes et al., 2019). In our experiment, the active VR mode requires the participant's visual attention to identify and track the fast-moving blocks, plan the dimensions of movement, i.e., direction, speed, etc., to initiate and finally execute the slashing act in an appropriate way. It can be analogous to a process of non-invasive stimulation (exercise) to excite the primary motor cortex, meanwhile distracting his/her attention to interact in the VR context. Whereas in the passive VR mode, the level of attention was much less needed, in which the M1 was least activated compared to the other modes (Figures 5, 6). Therefore, M1 can be considered as a critically targeted area in a VR-induced analgesic approach.

Regarding cognition-relevant cortical area, a similar finding was observed in the DLPFC, in which its activation in the active VR mode was higher compared to the less engaged VR modes, bearing a strong correlation with cognitive factors during different modes of VR interaction (Table 3, Figures 5, 6). The DLPFC (Brodmann Area 9) is considered to be relevant to higher-order cognitive processing related to attention, working memory, and inhibition of responses (Karunakaran et al., 2020). Previous fMRI studies reported its role in pain processing, including detection, perception, and suppression of pain (Apkarian et al., 2004). It was found that non-invasive stimulation of the LDLPFC appears to exhibit an anti-nociceptive effect, thus increasing pain tolerance (Brighina et al., 2011). In our study, a higher activation of DLPFC was found in the active VR mode compared to the less engaged modes (Figures 5, 6). Therefore, it can be considered as a non-invasive approach to excite the DLPFC, thus sustaining participant's attention to the VR task during noxious stimuli.

Even though the role of visual cortex at OL in pain processing has not been established, Huff et al. (2022) suggested that visual cortex is critical for the consious perception of visual stimuli, visual-guided attention, and motor action. Previous studies have reported the use of fNIRS in observing the function

TABLE 3 Spearman's correlation between virtual reality questionnaire (VRQ) items and cortical activation (β and featured values).

		LDLPFC	RDLPFC	LOL	ROL	LM1	RM1	LPMC	RPMC	LS1	RS1	LSTG	RSTG
Beta value	P_R1	-	-	-	-	-	-	-	-	-	−0.588*	-	-
	A_R1	-	-		-	0.609*	-	-	-	-	-	-	-
						(Ch19:0.677**)							
	I_R1	-	-	-	-	-	-	-	-	-	-	-	-
	PD_R1	-	0.668**	-	-	-	-	-	−0.528*	-	-	-	-
	P_R2	-	-	-	-	-	-	-	-	-	-	-	-
	A_R2	-	-	-	-	-	-	-	-	-	-	-	-
	I_R2	-	-	-	-	-	-	-	-	-	-	-	-
	PD_R2	-	0.531*	-	-	-	-	-	-	-	-	-	-
	P_R3	-	-	-	-	-	-	-	-	-	-	-	-
	A_R3	-	-	-	-	-	-	-	-	-	0.543*	-	-
	I_R3	-	-	-	-	-	-	-	-	-	0.539*	-	-
	PD_R3	-	-	-	-	-	-	-	-	-	-	-	-
Featured Value	P_R1	-	-	-	-	-	-	-	-	-		-	-
	A_R1	-	-	-	-	0.772**	-	-	-	-	0.543*	-	-
						(Ch19:0.788***)							
	I_R1	-	-	-	-	-	-	-	-	-	-	-	-
	PD_R1	-	-	-	-	-	-	-	-	-	-	-	-
	P_R2	-	-	-	-	-	-	0.539*	-	-	-	-	-
	A_R2	-	-	0.557*	-	-	-	-	−0.62*	-	-	-	−0.629*
									(Ch31:−0.599*)				
	I_R2	-	0.574*	-	-	-	-	-	-	-	-	-	-
	PD_R2	-	-	-	-	-	-	-	-	-	-	-	-
	P_R3	-	-	-	-	-	-	-	-	-	-	-	-
	A_R3	-	0.538*	-	-	-	-	-	-	-	-	-	-
	I_R3	-	-	-	-	-	-	-	-	-	-	-	-
	PD_R3	-	0.743**	-	-	-	-	-	-	-	-	-	-

* $p < 0.05$; ** $p < 0.01$; *** $p < 0.001$.

VRQ, VR questionnaire; R1, active mode; R2, motor imagery mode; R3, passive mode, P, Pain, A, attention; I, immersion; PD, pain distraction; LDLPFC, left dorsal lateral prefropntal cortex; RDLPFC, right dorsal lateral prefrontal cortex; LOL, left occipital lobe; ROL, right occipital lobe; LM1, left primary motor cortex; RM1, right primary motor cortex; LPMC, left premotor cortex; RPMC, right premotor cortex; LS1, left primary somatosensory cortex; RS1, right primary somatosensory cortex; LSTG, left superior temporal gyrus; RSTG, right superior temporal gyrus.

of visual cortex for attention and working memory following mild traumatic brain injury. However, there is yet not any study using fNIRS to evaluate pain-associated changes in the visual cortex (Takahashi et al., 2000). In our experiment, it was found that the visual cortex was correlated with attention (Table 3), with higher increased activation in the active VR mode compared to those less engaged modes, associated with better pain relief status (Figures 4, 5). Even though no casual relationship was found between visual cortex and pain relief in our study, there were animal studies that reported atrophy in visual cortex may occur following intense stress, which is reportedly similar to human beings in painful status (Yoshii et al., 2017).

Similar to visual cortex, a higher activation of PMC was also found in the active mode in comparison with those less engaged VR modes (Figures 4, 5), associated with better analgesic effect. This frontal cortical region is part of Brodmann Area 6 in charge of movement preparation (Chouinard and Paus, 2006). The PMC function in motor activities for planning, imagination, and control of movement was evidenced by previous fNIRS studies but no specific studies relevant to pain processing were reported (Pawan et al., 2017). Nevertheless, PMC was suggested in planning the escape when facing an aversive event such as pain (Haines and Mihailoff, 2018). In this way, a higher level of VR interaction can be considered as a way of better "escaping" from the pain status, which may help to explain the consistent activation.

Nevertheless, several drawbacks cannot be ignored in our study. The participants were all young and healthy, such that the promising analgesic effect can be biased. Regarding the combined use of VR headset and fNIRS equipment, the weight of HMD headset as well as the optode of the fNIRS cap over

the scalp may generate some pain. The HbO collected by fNIRS was not nociceptive specific but reflected an overall response following the noxious stimulation. The head movement may vary in different interactive modes, resulting in various motion artifacts. To reduce the impact, a time window (1–2 min) for adaptation was provided immediately after placing these devices on the head before the experiment. To minimize the possible data interference, a prevalently used data-processing method, which enables semi-automatic detection and reduction of movement artifacts, was taken based on moving standard deviation and spline interpolation (Scholkmann et al., 2010). In addition, multiple channels in the correspondent ROIs were averaged among subjects, which can represent the repeated measures of analyzed ROIs in the time-locked phase. It is believed that a more robust result can be obtainable when the future studies bearing a larger sample size with broader spectrum such as age, gender, and specific pain-related disorder are made accountable.

Conclusion

Conclusively, our findings suggest that the VR mode with a higher level of engagement can bring in a better analgesic effect by modulating motor and cognitive cortical ROIs in charge of pain processing. They further suggest that the VR interactive mode can be easily tailored to be in line with the client's status when the equivalent analgesic effect can be attainable. Our findings have contributed to suggest VR as a non-pharmacological analgesic method for pain management.

Data availability statement

The raw data supporting the conclusions of this article will be made available by the authors, without undue reservation.

Ethics statement

The studies involving human participants were reviewed and approved by Medical Ethics Committee of the Eighth Affiliated Hospital of Sun Yat-Sen University. The patients/participants provided their written informed consent to participate in this study.

Author contributions

XD contributed to study design, data acquisition, and drafting and revision of manuscript. SZ contributed to study concept and methodology design. CJ contributed to data processing. QY and NJ contributed to data analysis. ZH contributed to data collection and data management. All authors contributed to the article and approved the submitted version.

Funding

This study was sponsored by National Natural Science Foundation of China (Ref. No. 82001356), Shenzhen Science and Technology Program (Ref. No. JCYJ20190808102001750, JCYJ20210324115014038, and JCYJ20220818102016034), and Futian Healthcare Research Project (Ref. No. FTWS2021089).

Conflict of interest

The authors declare that the research was conducted in the absence of any commercial or financial relationships that could be construed as a potential conflict of interest.

Publisher's note

All claims expressed in this article are solely those of the authors and do not necessarily represent those of their affiliated organizations, or those of the publisher, the editors and the reviewers. Any product that may be evaluated in this article, or claim that may be made by its manufacturer, is not guaranteed or endorsed by the publisher.

References

Alshatrat, S. M., Alotaibi, R., Sirois, M., and Malkawi, Z. (2018). The use of immersive virtual reality for pain control during periodontal scaling and root planing procedures in dental hygiene clinic. *Int. J. Dent. Hyg.* 17, 71–76. doi: 10.1111/idh.12366

Ambrose, K. R., and Golightly, Y. M. (2015). Physical exercise as non-pharmacological treatment of chronic pain: why and when. *Best Pract. Res. Clin. Rheumatol.* 29, 120–130. doi: 10.1016/j.berh.2015.04.022

Apkarian, AR., Sosa, Y., Sonty, S., Levy, R., Harden, R., Parrish, T., et al. (2004). Chronic back pain is associated with decreased prefrontal and thalamic gray matter density. *J Neurosci.* 24, 10410–5. doi: 10.1523/JNEUROSCI.2541-04.2004

Benyamin, R., Trescot, A. M., Datta, S., Buenaventura, R., Adlaka, R., Sehgal, N., et al. (2008). Opioid complications and side effects. *Pain Physician.* 11, 105–120. doi: 10.36076/ppj.2008/11/S105

Boas, D. A., Dale, A. M., and Franceschini, M. A. (2004). Diffuse optical imaging of brain activation: approaches to optimizing image sensitivity, resolution, and accuracy. *Neuroimage* 23, S275–88. doi: 10.1016/j.neuroimage.2004.07.011

Brighina, F., Tommaso, M. D., Giglia, F., Scalia, S., Cosentino, G., Puma, A., et al. (2011). Modulation of pain perception by transcranial magnetic stimulation of left prefrontal cortex. *J. Headache Pain.* 12, 185–191. doi: 10.1007/s10194-011-0322-8

Chouinard, P. A., and Paus, T. (2006). The primary motor and premotor areas of the human cerebral cortex. *Neuroscientist*. 12, 143–152. doi: 10.1177/1073858405284255

Gold, J. I., Michelle, S. H., Andrea, M. L., Arianna, S. L., and Margaret J. K. (2021). Effect of an immersive virtual reality intervention on pain and anxiety associated with peripheral intravenous catheter placement in the pediatric setting: A randomized clinical trial. *JAMA Netw. Open* 4, e2122569–e2122569. doi: 10.1001/jamanetworkopen.2021.22569

Guarin, P. L. B. (2013). How effective are nerve blocks after orthopedic surgery? A quality improvement study. *Nursing*. 43, 63–66. doi: 10.1097/01.NURSE.0000428334.08731.2e

Gutierrez-Maldonado, J., Gutierrez-Martinez, O., and Cabas-Hoyos, K. (2011). Interactive and passive virtual reality distraction: effects on presence and pain intensity. *Stud. Health Technol. Inform.* 167, 69–73.

Haines, D. E., and Mihailoff, G. A. (2018). *Fundamental Neuroscience for Basic and Clinical Applications*, eds D. E. Haines and G. A. Mihailoff. Philadelphia, PA: Elsevier.

Hennig, J., Speck, O., Koch, M. A., and Weiller, C. (2003). Functional magnetic resonance imaging: a review of methodological aspects and clinical applications. *J. Magn. Reson*. 18, 1. doi: 10.1002/jmri.10330

Hoffman, H. G., Patterson, D. R., Seibel, E., Soltani, M., Jewett-Leahy, L., and Sharar, S. R. (2008). Virtual reality pain control during burn wound debridement in the hydrotank. *Clin. J. Pain* 24, 299–304. doi: 10.1097/AJP.0b013e318164d2cc

Hoffman, H. G., Richards, T. L., Oostrom, T. V., Coda, B. A., Jensen, M. P., Blough, D. K., et al. (2007). The analgesic effects of opioids and immersive virtual reality distraction: evidence from subjective and functional brain imaging assessments. *Anesth. Analg.* 105, 1776–1783. doi: 10.1213/01.ane.0000270205.45146.db

Hu, X.-S., Beard, K., Sherbel, M. C., Nascimento, T. D., Petty, S., Pantzlaff, E., et al. (2021). Brain mechanisms of virtual reality breathing versus traditional mindful breathing in pain modulation: observational functional near-infrared spectroscopy study. *J. Med. Internet Res.* 23, e27298–e27298. doi: 10.2196/27298

Huff, T., Mahabadi, N., and Tadi, P. (2022). *Neuroanatomy, Visual Cortex*. Treasure Island, FL: StatPearls.

Irani, F., Platek, S. M., Bunce, S., Ruocco, A. C., and Chute, D. (2007). Functional near infrared spectroscopy (fNIRS): an emerging neuroimaging technology with important applications for the study of brain disorders. *Clini. Neuropsychol.* 21, 9–37. doi: 10.1080/13854040600910018

Jones, T., Moore, T., Rose, H., and Choo, J. (2016). The impact of virtual reality on chronic pain. *J. Pain* 17, S102–S103.

Karunakaran, K. D., Peng, K., Berry, D., Green, S., and Borsook, D. (2020). NIRS measures in pain and analgesia: fundamentals, features, and function. *Neurosci Biobehav Rev.* 120, 335–353. doi: 10.1016/j.neubiorev.2020.10.023

Li, A., Zorash, M., Chen, V. J., and Gold, J. I. (2011). Virtual Reality and Pain Management: Current Trends and Future Directions. *Pain Manag. (London).* 1, 147–157. doi: 10.2217/pmt.10.15

Lier, E. J., Oosterman, J. M., Assmann, R., Vries, M. D., and Goor, H. V. (2020). The effect of virtual reality on evoked potentials following painful electrical stimuli and subjective pain. *Sci. Rep*. 10, 9067. doi: 10.1038/s41598-020-66035-4

Longo, M. R., Iannetti, G. D., Mancini, F., Driver, J., and Haggard, P. (2012). Linking pain and the body: neural correlates of visually induced analgesia. *J. Neurosci.* 32, 2601–2607. doi: 10.1523/JNEUROSCI.4031-11.2012

Lopes, P., Campos, A., Fonoff, E., Britto, L., Pagona, R. (2019). Motor cortex and pain control: exploring the descending relay analgesic pathways and spinal nociceptive neurons in healthy conscious rats. *Behav. Brain Funct*. 15, 5. doi: 10.1186/s12993-019-0156-0

Maral, T., and David, C. J. (2017). Nonpharmacological interventions in targeting pain-related brain plasticity. *Neural Plasticity*. 2017, 1–10. doi: 10.1155/2017/2038573

Mccaul, K. D., and Malott, J. M. (1985). Distraction and coping with pain. *Psychol. Bull*. 95, 516–533. *Pain* 23(3), 315. doi: 10.1037/0033-2909.95.3.516

Pawan, L., Xian, Z., Adam, N., Hirsch, J. (2017). Neurofeedback-based functional near-infrared spectroscopy upregulates motor cortex activity in imagined motor tasks. *Neurophotonics*. 4, 021107. doi: 10.1117/1.NPh.4.2.021107

Pillai, A. S., and Mathew, P. S. (2019). *Impact of Virtual Reality in Healthcare: a review. Virtual and Augmented Reality in Mental Health Treatment*. doi: 10.4018/978-1-5225-7168-1.ch002

Rizzo, A. S., and Bouchard, S. (2019). *Virtual Reality for Psychological and Neurocognitive Interventions*. New York, NY: Springer. doi: 10.1007/978-1-4939-9482-3

Scholkmann, F., Spichtig, S., Muehlemann, T., and Wolf, M. (2010). How to detect and reduce movement artifacts in near-infrared imaging using moving standard deviation and spline interpolation. *Physiol. Meas.* 31, 649–662. doi: 10.1088/0967-3334/31/5/004

Sinatra, R. (2010). Causes and consequences of inadequate management of acute pain. *Pain Medicine*. 11, 1859–1871. doi: 10.1111/j.1526-4637.2010.00983.x

Sostres, C., Gargallo, C. J., Arroyo, M. T., and Lanas, A. (2010). Adverse effects of non-steroidal anti-inflammatory drugs (NSAIDs, aspirin and coxibs) on upper gastrointestinal tract. *Best Pract. Res. Clin. Gastroenterol.* 24, 121–132. doi: 10.1016/j.bpg.2009.11.005

Svensson, P., Miles, T. S., Mckay, D., and Ridding, M. C. (2003). Suppression of motor evoked potentials in a hand muscle following prolonged painful stimulation. *Eur. J. Pain*. 7, 55–62. doi: 10.1016/S1090-3801(02)00050-2

Takahashi, K., Ogata, S., Yamamoto, R., Shiotsuka, S., Maki, A., Yamashita, Y., et al. (2000). Activation of visual cortex imaged by 24 channel near-infrared spectroscopy. *J. Biomed. Opt.* 5, 93–6. doi: 10.1117/1.429973

Triberti, S., Repetto, C., and Riva, G. (2014). Psychological factors influencing the effectiveness of virtual reality–based analgesia: a systematic review. *Cyberpsychol. Behav. Social Network.* 17, 335. doi: 10.1089/cyber.2014.0054

Virtual Scenario of Beat Saber. (n.d.). [Online]. Available online at: https://ng.d.cn/jiezoukongjian/ (accessed November 7, 2022).

Wei-Ju, C., O'Connell N, Burns, E., Chipchase, L., Liston, M., Schabrun S. (2015). Organisation and function of the primary motor cortex in chronic pain: protocol for a systematic review and meta-analysis. *BMJ Open*. 5, e008540. doi: 10.1136/bmjopen-2015-008540

Yoshii, T., Oishi, N., Ikoma, K., Nishimura, I., Sakai, Y., Matsuda, K., et al. (2017). Brain atrophy in the visual cortex and thalamus induced by severe stress in animal model. *Sci. Rep.* 7, 12731. doi: 10.1038/s41598-017-12917-z

Yücel, M., Selb, J. J., Huppert, T. J., Franceschini, M. A., and Boas, D. A. (2017). Functional near infrared spectroscopy: enabling routine functional brain imaging. *Curr. Opini. Biomed. Eng.* 4, 78. doi: 10.1016/j.cobme.2017.09.011

frontiers | Frontiers in Neuroscience

TYPE Original Research
PUBLISHED 28 November 2022
DOI 10.3389/fnins.2022.1011475

OPEN ACCESS

EDITED BY
Waldemar Karwowski,
University of Central Florida,
United States

REVIEWED BY
Debatri Chatterjee,
Tata Consultancy Services, India
Yanlu Wang,
Karolinska Institutet (KI), Sweden
Yinglei Song,
Jiangsu University of Science and Technology, China

*CORRESPONDENCE
Limin Zhang
lmzhang@hytc.edu.cn

SPECIALTY SECTION
This article was submitted to Brain Imaging Methods, a section of the journal Frontiers in Neuroscience

RECEIVED 04 August 2022
ACCEPTED 18 October 2022
PUBLISHED 28 November 2022

CITATION
Zhang L and Cui H (2022) Reliability of MUSE 2 and Tobii Pro Nano at capturing mobile application users' real-time cognitive workload changes. *Front. Neurosci.* 16:1011475. doi: 10.3389/fnins.2022.1011475

Reliability of MUSE 2 and Tobii Pro Nano at capturing mobile application users' real-time cognitive workload changes

Limin Zhang[1]* and Hong Cui[2]

[1]China School of Fine Arts, Huaiyin Normal University, Huaian, China, [2]USA School of Information, University of Arizona, Tucson, AZ, United States

Introduction: Despite the importance of cognitive workload in examining the usability of smartphone applications and the popularity of smartphone usage globally, cognitive workload as one attribute of usability tends to be overlooked in Human-Computer Interaction (HCI) studies. Moreover, limited studies that have examined the cognitive workload aspect often measured some summative workloads using subjective measures (e.g., questionnaires). A significant limitation of subjective measures is that they can only assess the overall, subject-perceived cognitive workload after the procedures/tasks have been completed. Such measurements do not reflect the real-time workload fluctuation during the procedures. The reliability of some devices on a smartphone setting has not been thoroughly evaluated.

Methods: This study used mixed methods to empirically study the reliability of an eye-tracking device (i.e., Tobii Pro Nano) and a low-cost electroencephalogram (EEG) device (i.e., MUSE 2) for detecting real-time cognitive workload changes during N-back tasks.

Results: Results suggest that the EEG measurements collected by MUSE 2 are not very useful as indicators of cognitive workload changes in our setting, eye movement measurements collected by Tobii Pro Nano with mobile testing accessory are useful for monitoring cognitive workload fluctuations and tracking down interface design issues in a smartphone setting, and more specifically, the maximum pupil diameter is the preeminent indicator of cognitive workload surges.

Discussion: In conclusion, the pupil diameter measure combined with other subjective ratings would provide a comprehensive user experience assessment of mobile applications. They can also be used to verify the successfulness of a user interface design solution in improving user experience.

KEYWORDS

cognitive workload, EEG, eye tracking, eye movement, GUI

Introduction

Portable media devices, such as smartphones, have become an increasingly pervasive part of our lives. In 2020, the number of smartphone users in the United States was estimated to reach 294.15 million and will reach 311.53 million by 2025 (O'Dea, 2021). American adults spent around 3 h and 30 min per day using mobile phones in 2019, with an increase of about 20 min from 2018, according to Zenith (Molla, 2020).

Correspondingly, the number of applications in the App Store has soared from the initial 500 in 2008 to roughly 2.22 million available applications in 2021 (Ceci, 2022). As a result, mobile phone applications receive greater attention from the Human–Computer Interaction (HCI) field, resulting in a surge in the number of publications. We input a query "usability AND phone AND application" with custom time ranges: 1991–2000, 2001–2010, and 2011–2020 in Google Scholar, and get 8,500, 55,500, and 68,200 results.

Researchers in Human–Computer Interaction (HCI) fields have long recognized usability as the core of product design, including the application design of smartphones (Shneiderman, 1986; Nielsen, 1993; Brooke, 1996; Dumas et al., 1999). Previous research has manifested that cognitive workload is an essential aspect of product usability (Harrison et al., 2013; Davids et al., 2015).

Measuring cognitive workload has been recognized as one challenge when taking objectivity and causality into consideration (Brunken et al., 2003; Brünken et al., 2010). Instruments such as the NASA questionnaire (Hart and Staveland, 1988) help solicit *perceived* cognitive workload from users *after* a task is completed. Results obtained through such instruments are tinted with a level of subjectivity and put the causality between stimuli and reported cognitive workload in question.

On the other hand, electroencephalogram (EEG) devices can objectively monitor and record the brain's electrical activities and researchers have successfully identified signals from EEG to measure cognitive workload (Gevins and Smith, 2003; Antonenko et al., 2010a; Makransky et al., 2019). And eye movement data have been collected and analyzed to guide and advise various aspects of product design: navigation, page layout, user interface (UI) visualization style with design elements, advertisement, user viewing behaviors, and user cognitive workload (Goldberg and Wichansky, 2003; Nielsen and Pernice, 2010).

However, most of the studies were not executed in a smartphone setting and they cannot provide direct evidence for the reliability of EEG and eye-tracking devices to measure cognitive workload in a smartphone setting, due to several variabilities between desktop/laptop computer settings and smartphone settings. The screen sizes of desktop/laptop computers and smartphones are different: large vs. small. Users' interactions with these devices are distinct: cursors vs. gestures. The content compositions are not the same either: columns vs. scrolling. Physically, the users interact with their smartphones in different manners, such as: (1) one-handed, (2) two-handed, and (3) cradled, (4) no-handed; and in three body postures: walking, standing, and sitting/lying (Hoober, 2013).

Based on a thorough review of the related literature, we have identified three gaps as follows:

(1) Despite the significance of cognitive workload, it tends to be overlooked in the HCI field (Zhang and Adipat, 2005; Coursaris and Kim, 2006; Harrison et al., 2013).
(2) The majority of studies we reviewed only examine the overall cognitive workload during tasks and fail to study the instantaneous or peak cognitive workload during tasks and its relationship with product interface design and usability.
(3) There is little direct evidence to suggest that EEG and eye-tracking devices are reliable in measuring cognitive workload in a smartphone setting.

To address these gaps, we need to answer the two questions first:

(1) Are EEG data collected by MUSE 2 and eye movement data recorded by Tobii Pro Nano valid, reliable, and feasible as assessment tools for the real-time cognitive workload?
(2) Are measures collected by the two devices (averages of Event-related (de-)synchronization (ERD) of Alpha, Beta, and Event-related synchronization (ERS) of Theta for TP9, TP10, AF7, and AF8; pupil dilation, saccade duration and saccade number, fixation duration, and fixation number) sensitive to the cognitive workload of different N-back tasks in real time when the tasks are completed on a smartphone?

To answer the questions asked above, we employed a low-cost and portable electroencephalogram (EEG) device (MUSE 2, https://choosemuse.com/muse-2-guided-bundle/) and a user-friendly eye-tracking device (Tobii Pro Nano, https://www.tobiipro.com/product-listing/nano/) to detect real-time cognitive workload changes during N-back tasks on a smartphone. Our hypotheses were simple—we predict that the EEG device, MUSE 2, and the eye tracker device, Tobii Pro Nano with smartphone adopters, are reliably quantifying the cognitive workload of users performing tasks on a smartphone by these measures listed above.

Background

Cognitive workload in usability

According to the latest ISO 9241-11 (2018), usability is "the extent to which a system, product, service can be used by specified users to achieve specified goals with effectiveness, efficiency, and satisfaction in a specified context of use." Various standards and models list a range of attributes for usability. Among these attributes, the cognitive workload is defined by Bevan and MacLeod (1994) as the mental effort required to perform tasks and is particularly important in safety-critical applications. It refers to the user's cognitive processing amount to using the application (Harrison et al., 2013).

Cognitive workload measurements in HCI

The cognitive workload measurements can be roughly grouped into three broad categories: subjective self-assessment rating scales, performance measures, and psychophysiological measures (Wilson and Eggemeier, 1991; Cain, 2007; Evans and Fendley, 2017). Here, we only introduce two measures adopted in this research: electroencephalogram (EEG) and eye movement in psychophysiological measures.

Measurement of cognitive workload using electroencephalogram

Electroencephalogram (EEG) is an electrophysiological method of monitoring and recording the brain's electrical activity. Most of the time, an EEG device that comprises non-invasive electrodes is placed along a subject's scalp. These electrodes capture voltage fluctuations resulting from ionic currents within the brain's neurons.

In recent years, researchers have been evaluating the potential of the EEG as a measure of cognitive workload in different task conditions: arithmetic tasks (Anderson et al., 2011; Cirett Galán and Beal, 2012; Kumar and Kumar, 2016; Borys et al., 2017; Chin et al., 2018); cognitive tasks (Trammell et al., 2017); reading tasks (Dimigen et al., 2011; Knoll et al., 2011; Gwizdka et al., 2017); listening to music tasks (Asif et al., 2019); visual search task (Winslow et al., 2013; Hild et al., 2014); learning tasks (Dan and Reiner, 2017; Mazher et al., 2017; Notaro and Diamond, 2018); and vehicle driving task (Cernea et al., 2012). These studies confirm the fact that EEG provides reliable signals for studying cognitive workload in their respective settings.

Event-related (de-)synchronization (ERD/ERS) with Alpha, Theta, and Beta bands is one of the three most popular analysis techniques (Cabañero et al., 2019). Event-related (de)synchronization (ERD) is a recognized rate-of-change metric for oscillatory EEG dynamics, which was originally developed to quantify changes in the Alpha band (Pfurtscheller and Aranibar, 1977). Synchronization is a process where neurons are getting in line (synchronized) to enter an idling state. Desynchronization is a process where individual neurons get ready to perform their parts in a task. The steps of performing a task are: neurons desynchronize (wake up), perform tasks, and neurons synchronize (rest).

To obtain percentage values for ERD/ERS, the power within the frequency band of interest in the period after the event is given by A, whereas that of the preceding baseline or reference period is given by R. The percentage decrease (or increase) from the reference interval (R) to the activation interval (A) (before responding) was defined as

$$ERD/ERS\% = [(R - -A)/R]*100\% \quad (1)$$

(Pfurtscheller and Aranibar, 1977; Pfurtscheller and Lopes da Silva, 1999; Pfurtscheller, 2001).

Negative values computed by Equation 1 indicate power increase and desynchronization (ERD), and positive values indicate power decrease and synchronization (ERS).

Pfurtscheller and Lopes da Silva (1999) recommended that the term ERD is meaningful only if the baseline measured some seconds before the event represents rhythmicity seen as a clear peak in the power spectrum. Similarly, the term ERS only has a meaning if the event results in the appearance of a rhythmic component and therefore in a spectral peak that was initially not detectable (Pfurtscheller and Lopes da Silva, 1999).

The quantification of ERD/ERS was divided into four steps, first, the bandpass filtering was carried out for all Event-related trials; second, the amplitude samples were squared to obtain the power samples; third, the power samples of all trials were averaged; and fourth, the time samples were averaged to make the data smooth and reduce (Pfurtscheller and Lopes da Silva, 1999).

The review articles (Klimesch, 1999; Antonenko and Niederhauser, 2010b) concluded that with increasing task demands Theta synchronizes (decreases), whereas Alpha and Beta desynchronize (increase) (Pfurtscheller and Berghold, 1989; Neubauer and Fink, 2003; Stipacek et al., 2003; Klimesch et al., 2005; Neubauer et al., 2006; Scharinger et al., 2016; Saitis et al., 2018).

Measuring cognitive workload using eye movement data

Multiple kinds of eye movement data related to cognitive workload can be reliably collected using a high-quality eye-tracking device.

Pupil dilation is an involuntary response, in which the pupil diameter changes to protect the retina or to respond to a shift in fixation between objects at different distances. Previous research has shown that users' pupils dilate when the difficulty of the task increases and more cognitive effort has been allocated to solve the task (Granholm et al., 1996; Pomplun and Sunkara, 2003; Klingner et al., 2008; Chen et al., 2011; Porta et al., 2012; Rafiqi et al., 2015; Gavas et al., 2017; Ehlers, 2020). Accounting for individual and environmental differences, it is necessary to measure pupil diameters while referencing an adaptive baseline (Lallé et al., 2016).

According to Purves et al. (2001), saccades are rapid and ballistic movements of eyes that change the fixations abruptly. Previous research has found that growth in saccade velocity indicates a greater task difficulty (Barrios et al., 2004; Chen et al., 2011; Lallé et al., 2016; Zagermann et al., 2018).

Eye fixation refers to a focused state when eyes dwell voluntarily over some time and is the most common type of eye-tracking event (Zagermann et al., 2016). Previous research has proven that the correlation between the duration of fixation and

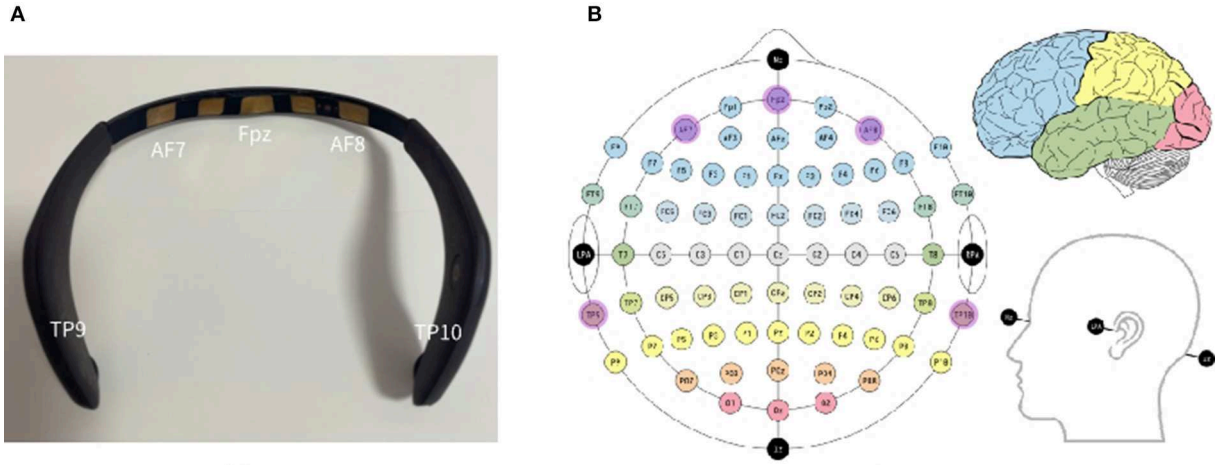

FIGURE 1
(A) MUSE 2 EEG headband; **(B)** EEG electrode positions in the 10-10 system using modified combinatorial nomenclature, along with the fiducials and associated lobes of the brain. Adopted from https://en.wikipedia.org/wiki/10%E2%80%9320_system_%28EEG%29#/media/File:EEG_10-10_system_with_additional_information.svg.

the cognitive processing level is positive (Rudmann et al., 2003; Goldberg and Helfman, 2010; Chen et al., 2011; Wang et al., 2014; Zagermann et al., 2018).

Devices in measuring cognitive workload

As previously reviewed literature shows, the measures of computing from EEG and eye movement data have been proven to be effective for detecting cognitive workload changes. However, most of the studies were conducted in smartphone settings, and the devices adopted in these studies are not suitable for use in smartphone usability testing environment.

Grateful to technology development, there are a wide range of choices in the selection of devices to capture the EEG data and eye-tracking data, respectively. Some examples of the EEG devices, ordered at prices, from low to high include: MUSE 2 headband, Emotiv Insight, OpenBCI, ANT Neuro, BioSemi, etc. (Farnsworth, 2019). A ranking of the top eye-tracking companies, ordered by the number of publications found through Google Scholar, is Tobii, SMI, EyeLink, Smart Eye, LC Technologies, Gazepoint, The Eye Tribe, etc. (Farnsworth, 2020).

Among listed choices, the MUSE 2 headband (Figure 1A, $250) is an easy-to-use, affordable, and portable EEG recording system from InteraXon Inc. It is a four-channel headband with dry electrodes at positions AF7, AF8, TP9, and TP10 (Figure 1B). The headband is connected to the app on phone via Bluetooth, which makes it a great tool for detecting cognitive workload while the user is performing the task on smartphones, especially in some field experiments, of course, after its reliability is verified.

Despite the small number of sensors and the mismatch in the locations of the sensors to the standard 10–20 electrode positioning system, several studies have shown that the MUSE headband has the potential to provide good quality EEG data. Two studies (Arsalan et al., 2019; Asif et al., 2019) adopted MUSE 2 to capture EEG data and adopted classifiers to classify stress levels. Another study (Papakostas et al., 2017) also adopted MUSE EEG to predict the user task performance, and they achieved a maximum accuracy rate of 74%. Krigolson et al. (2017) collected data by MUSE EEG system, and the results showed quantifiable N200 and P300 Event-related potential (ERP) components in the visual oddball task and the reward positivity. However, these studies cannot provide direct evidence on the EEG data captured by the MUSE EEG system is reliable for cognitive workload changes.

Some studies have pointed out MUSE's limitations. Ratti et al. (2017) compared two medical grade (B-Alert, Enobio) and two consumer (MUSE, Mindware) EEG systems in five healthy subjects. Results showed that EEG data can be successfully collected from four devices, yet MUSE showed a broadband increase in power spectra and the highest relative variation across test–retest acquisitions. Another study has also shown that the data collected by MUSE headband were of poor quality under noisy conditions, such as at a public lecture (Przegalinska et al., 2018). To explore MUSE 2's potential as a great tool in smartphone usability testing, we still need direct empirical evidence on the reliability of MUSE 2 in capturing EEG data for measuring cognitive workload.

Having picked an EEG device with its usefulness still under investigation, we selected a well-established eye-tracking device for this study to control the risk. We chose Tobii Pro Nano because it is one of the top eye-tracking companies and has

been used in 20.5 k publications. It is also an accessible and efficient approach to capturing eye movement (Figure 2) and is used by many HCI researchers (Sugaya, 2019; Ehlers, 2020; Lee and Chenkin, 2020). Ehlers (2020) adopted Tobii Pro Nano to capture the pupil diameter and confirmed that it is a valid indicator of cognitive workload. Lee and Chenkin (2020) evaluated Tobii Pro Nano's potential to differentiate between experts and novices in the interpretation of POCUS clips in medical fields. Sugaya (2019) used Tobii Pro Nano to test an assumption about the meaning-making process of adjective expression formation.

Tobii Pro Nano can be mounted on a mobile testing accessory, also manufactured by Tobii (Figure 2). It has a screen capture device connecting directly to smartphones. The screen capture device records a high-definition (HD) video of the mobile device's screen at 60 frames per second with a latency of only 10 milliseconds (Mobile Testing Accessory | Perfect for Usability Tests., 2020). Yet, the mobile testing accessory is just in the market, with no research done on it. The other great device for smartphone experiments is Tobii Pro Glass with a much higher price. If we can provide a piece of evidence on the reliability of Tobii Pro Nano with a mobile testing accessory, it could be a high-performance cost ratio choice for researchers.

FIGURE 2
Tobii Pro Nano with mobile testing accessory.

Methods

The goal of the experiment was to examine the reliability of the MUSE 2 headband and Tobii Pro Nano with a mobile testing accessory for detecting cognitive workload changes during a smartphone task and to select the best measure(s) computed from data collected by the two devices. The measures adopted in the experiment are (1) ERD percentage for Alpha, Beta, and ERS Theta rhythms extracted from EEG data; (2) multiple eye movements: pupil dilation, saccade duration, saccade number in second, fixation duration, and fixation number in second; and (3) user performance data: reaction time and accuracy rate.

Participants

This study was approved by the UA IRB office (Protocol Number: 2101428836) and obtained permission from Qinghe High School, Jiangsu, China.

We recruited 5 students as pilots and 30 students as participants from Qinghe High School, Jiangsu, China. The inclusion criteria were normal vision or correct to normal vision, normal cognitive function, and proficiency in smartphones.

Students who participated either as pilots or as participants were compensated 50 in Chinese currency after they complete the task successfully.

Apparatus

We used the MUSE 2 headband and Tobii Pro Nano as the devices to collect cognitive workload-related measures.

The environment's brightness variations produce changes in the pupil size (Pfleging et al., 2016; Zagermann et al., 2016). Therefore, the experiment was conducted in a room with lightproof curtains down to avoid natural lighting conditions, and electric lights on the room ceiling created a consistent lamination for the experiment. Environment, such as noise, also impacts cognitive load (Örün and Akbulut, 2019). We made sure the experiment room was free of all noise during the experimental sessions. All devices were sanitized before the next participant came.

When using EEG devices, one has to fulfill several other requirements. These include a clean scalp, clean electrodes, minimum participant activities, including head movements, since a small movement could generate muscle-based signals known as artifacts (Pratama et al., 2020). We instructed all participants to stay as still as possible and not to wear any makeup during the experiment. Also, as the electrodes need to be attached to the back of the ears, we encouraged the participants to wear contacts instead of glasses. We also provided a disposable wet cloth for participants to moisturize their foreheads and back of the ears to get a better connection of the EEG headset.

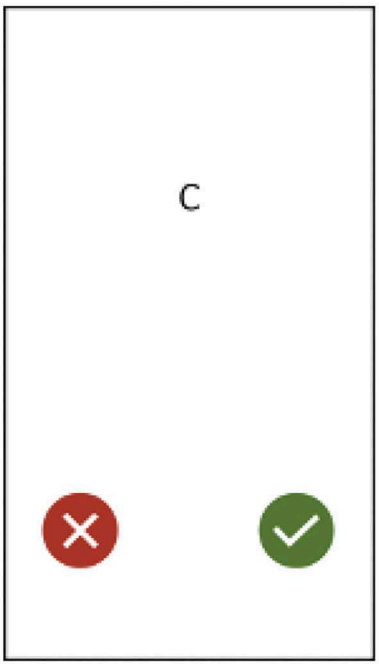

FIGURE 3
A screenshot of the N-back task.

Task: N-back task

N-back tasks are continuous-recognition measures that present stimulus sequences, such as letters or pictures. A sequence of stimuli is presented to the participants one by one. The participants are required to make a decision as to whether the current stimulus is the same as the one presented in N trials ago (Coulacoglou and Saklofske, 2017). The N can be 0, 1, 2, 3, etc. There is an increase in difficulty in tasks while N increases. An N-back task is a useful tool for experimental research on working memory (Jaeggi et al., 2010), and it has been adopted to manipulate cognitive workload (Reimer et al., 2009; Ayaz et al., 2010; Yokota and Naruse, 2015).

In this study, all participants completed an N-back task.When employed in a computer setting, the participants of the experiment can press individual keys on keyboards as "YES" or "NO". To cope with the touch screen of a smartphone, we placed "×" on the left bottom corner, and "√" on the right bottom corner of the smartphone screen (Figure 3).

In this study, we employed a 1 back task and a 2 back task to create a low cognitive workload condition and a high cognitive workload condition. The rationale of only including 1 and 2 levels is to simulate cognitive workload levels that smartphone users would experience in the real world.

The key features of the N-back task implementation were:

- Four sets of letters were created and arranged in two groups for a training block and an experiment block.
  - Training Block:
    - Five trails of one back task (EEIPP) as a training session,
    - Six trails of two back task (OSOMLI) as a training session;
  - Experiment Block:
    - low cognitive workload block: 20 trials of 1 back task (DAABEEDRRODHHRDSSELDD);
    - high cognitive workload block: 21 trails of 2 back (BAEAAEASHSAELEOBBBOSHS).
- These two sets of letters in the experiment block were designed to have an identical "YES" or "NO" response sequential: YNNNYNNNYNNNYNNYNNYN.
- Each stimulus was presented for maximally 3,000 milliseconds.

The low and high cognitive workload blocks were randomly and evenly assigned to participants. More specifically, 15 participants assigned an odd ID completed the task in Order 1: low cognitive workload block, high cognitive workload block; and another 15 participants assigned an even ID completed the task in Order 2: high cognitive workload block, low cognitive workload block.

Procedure

All participants entered the experiment room and performed the experiment once at a time.

First, the participants watched an instructional video of the instruments and experimental procedure (https://youtu.be/_d24CRSwhuQ). They were free to ask any questions after viewing the video.

The experiment started with the participant filling in a demographic questionnaire (Appendix A). This questionnaire covered subjects' age, gender, strong hand, experience with smartphones, and current smartphone usage situation. Then, they wore the MUSE 2 headband and adjusted themselves to a comfortable sitting position. After that, the participants completed an eye-tracking calibration with Tobii Pro Nano followed by 10 s with an eye-open relaxed position and another 10 s with an eye-closed comfortable position.

After the preparation step, the participants completed the training session. They can ask any questions about the N-back task during or after the training section. The training sessions were excluded from data analysis.

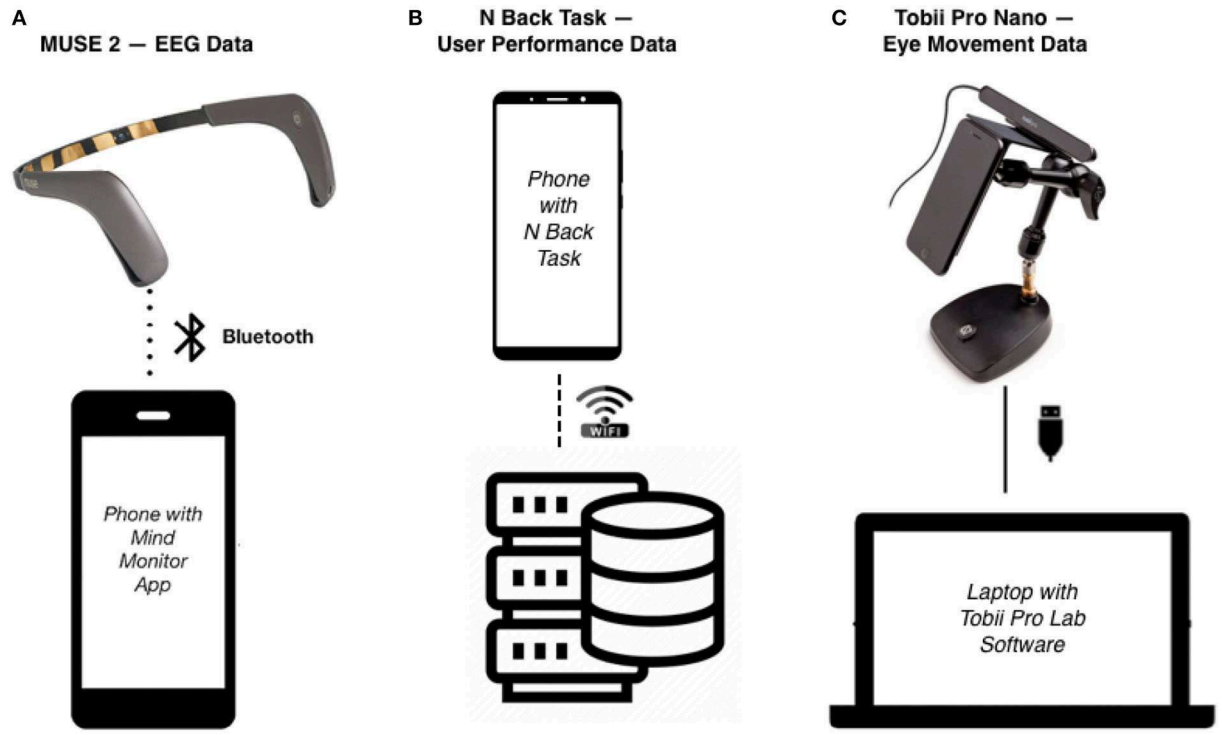

FIGURE 4
(A) The MUSE 2 headband was transmitted over Bluetooth to a phone *via* an application called Mind Monitor for EEG data collection, and the EEG data were uploaded to the research's selected cloud drive after each participant completed the task. **(B)** The N back task was recorded on a website designed by researchers, and the user performance data were collected via the server. **(C)** The Tobii Pro Nano eye tracker was connected to a laptop with Tobii Pro Lab software installed, and the eye movement data were collected by the Tobii Pro Lab software and stored in the hard drive of the laptop.

Then the participants completed the experiment session of the N-back task at the experiment station, wearing the MUSE 2 headband. They first completed 20 trails of 1-back/2-back stimuli, followed by 20 trails of 2-back/1-back stimuli, with intervals of approximately 1–2 s in between each 1-back/2back stimuli (the time between a response and the display of the next stimuli) and a rest period of 5 s in between 1-back and 2-back blocks. The participants were instructed to respond to tasks as accurately and rapidly as possible. The variation of intervals between each 1-back/2back stimuli caused by the internet loading time varied.

The MUSE 2 headband collected raw EEG data of TP9, AF7, AF8, and TP10 through an application called Mind Monitor (iOS Version 2.2.0) (Figure 4A). And the Tobii Pro Nano recorded multiple types of eye movement data: pupil dilation, saccade length, saccade velocity, fixation duration, and fixation number (Figure 4B). The self-developed website for the N-back task collected the reaction time and accuracy rate during the experiment (Figure 4C) (N-back task website: http://n-back.artkey.xin/). It is designed for an experiment on a smartphone, and it works best on a smartphone.

Besides the procedure described above, the procedure described in Appendix B when conducting the experiments as a precaution against COVID-19 was followed as well.

Measures

Data collected from the experiment allow us to examine and compare the following measures:

(1) Event-Related Synchronization percentage (ERS) of Theta, Event-Related Desynchronization percentage (ERD) of Alpha, and Event-Related Desynchronization percentage (ERD) (Equation 1).
(2) Multiple eye movements: pupil dilation, saccade duration, saccade number in second, fixation duration, and fixation number in second.
(3) User performance data: reaction time (RT) and accuracy rate (AR). Reaction time (RT) is the period between the onset of a letter and the response made by a participant. The accuracy rate (AR) is the ratio of the number of correct inputs and the total number of inputs.

TABLE 1 Participants' answers for Questions 4–8 in the demographic questionnaire.

Question	Answer ($n = 30$)
Q4: Smartphone: You are able to operate smartphones proficiently.	Strongly agree – 20 Agree – 10 Neither agree nor disagree – 0 Disagree – 0 Strongly disagree – 0
Q5: Smartphone: Which operating system do you use more frequently and proficiently?	iOS – 3 Android – 22 Both – 5 Other – 0
Q6: Smartphone: How many years have you owned/used a smartphone?	<1 year – 5 1–2 years – 15 3–5 years – 7 5–10 years – 1 >10 years – 2
Q7: Smartphone: How many hours a day on average do you use your smartphone when the school is in session?	0.5–1 h – 28 1–2 h – 2 3–5 h – 0 6–8 h – 0 >8 h – 0
Q8: Smartphone: How many hours a day on average do you use your smartphone when the school is on break?	0.5–1 h – 5 1–2 h – 10 3–5 h – 13 6–8 h – 2 >8 h – 0

Results, analysis, and discussion

The experiment has investigated the feasibility of using data acquired wirelessly from an EEG headband (MUSE 2) and an eye-tracking device (Tobii Pro Nano) to assess cognitive workload in a well-controlled N-back task in a smartphone setting.

Demographic data

A total of 30 high school students from Qinghe High School in Huaian, Jiangsu, China completed the experiment, including the demographic questionnaire (Appendix A). Eleven of the 30 participants were female and 19 were male, and the female and male ratio is 11/19. Their average age was 16.34 years old (SD = 0.61). All participants were from the first year in high school. The right hand was the dominant in 29 participants, and the other participant was ambidextrous. The answers to Questions 4–8 of the demographic questionnaire are presented in Table 1. To summarize the data in Table 1, all participants were frequent and proficient smartphone users.

User performance data

Only 29 participants' user performance data were processed, analyzed, and discussed here. Participant ID 126's experimental data were not recorded due to Internet connection issues.

We analyzed user performance data (reaction time and accuracy rate) in order to confirm that participants perceived the various N-Back conditions as different. User performance data processing, user performance data results, and user performance data analysis are included in this section.

User performance data processing

The N-Back website recorded participants' ID, N-back order, current letter, participants' choices, accuracy (yes/no/null), reaction time, start timestamp in Unix time, and end timestamp in Unix time. Unix time is a system for describing a point in time and it is the number of seconds that have elapsed since the Unix epoch, excluding leap seconds (Ritchie and Thompson, 1978).

I conducted a Shapiro–Wilk test for the reaction time (RT) of all participants for 1 back and 2 back tests to check its normality. The result is significant ($p < 0.001$), which indicates that the data are not normally distributed. Therefore, I conducted a Mann–Whitney–Wilcoxon Test for the reaction time (RT) between 1 and 2 back.

User performance data results

The descriptive statistics and the Mann–Whitney–Wilcoxon Test results for the reaction time (RT) and accuracy rate (AR) between conditions are presented in Table 2.

User performance data analysis

Reaction time

The Mann–Whitney U test was conducted to examine whether the reaction time (RT) had statistically significant differences between 1 and 2 back for all participants, for participants with odd IDs, and for participants with even IDs. The *p*-values (< 0.001) indicate the answer is yes, as expected (Table 2).

Accuracy rate

The Mann–Whitney–Wilcoxon test was conducted to examine whether the accuracy rate (AR) had significant differences between 1 back and 2 back for the 29 participants. The p-value (<0.001) indicates the answer is yes, as expected. The median of 1 back accuracy rate is 1, which is higher than the median of 2 back accuracy rate (0.9) (Table 2).

User performance data discussion

As expected, the reaction time (RT)increased and accuracy rate (AR) decreased with the leveled-up differential of N-Back

TABLE 2 The descriptive statistics and Mann–Whitney–Wilcoxon Test results for reaction time (RT) (unit: second) and accuracy rate (AR) between 1 and 2 back.

Measure	N back	N	Mean	SD	Median	W*	*p*-value
Reaction time	1	580	1.11	0.35	1.06	91,036	< 2.2e-16***
	2	580	1.58	0.65	1.43		
Reaction time with odd IDs	1	300	1.15	0.32	1.13	25,475	< 2.2e-16***
	2	300	1.65	0.67	1.53		
Reaction time with even IDs	1	280	1.06	0.38	0.98	19,302	< 2.2e-16***
	2	280	1.51	0.62	1.33		
Accuracy rate	1	29	0.94	0.14	1	702	6.547e-06***
	2	29	0.85	0.11	0.9		

*W-Value is the sum of the ranks of the first sample. ***$P = 0.001$.

tasks, and 1 and 2 back tasks did create low and high cognitive workload conditions for the experiment's participants.

EEG data

EEG data processing and analysis

Only 29 participants' EEG data were processed, analyzed, and discussed here. Participant ID 126's EEG was not recorded due to Internet connection issues.

During the experiment, participants wore a MUSE 2 headband connected to the Mind Monitor. The Mind Monitor collected their EEG data. According to the Technical Manual from the Mind Monitor website, bandpass filtering was carried out on the raw data with power noise at 50 Hz or 60 Hz. Then, a fast Fourier transform (FFT) calculation (Heckbert, 1995) was applied to the raw data to get Theta, Alpha, and Beta.

The recorded EEG signals were processed using Excel and R to get two baselines:

- baseline_near: Based on the timestamps recorded by the N-back task website, we sectioned the intervals starting from−200 ms to the onset of each letter as the baseline interval for each letter (Xiang et al., 2021).
- baseline_away: According to the timestamps recorded by the N-back task website, we segmented the first 3,000 ms of the 10 s relaxing eyes open relaxing as a baseline.

Computed ERD of Alpha {TP9, AF7, AF8, TP10}, ERD of Beta{TP9, AF7, AF8, TP10}, and ERS of Theta {TP9, AF7, AF8, TP10} with baseline near for each letter interval; and ERD of Alpha AF7, Alpha AF8, Beta AF8, and Beta TP9 with baseline away for each letter interval. The interval starts from the onset of each letter to the time point that a choice is being made by participants, which is definitely ≤ 3 s.

A non-parametric test, the Mann–Whitney–Wilcoxon test, was selected for non-normal data. The Mann–Whitney–Wilcoxon test was conducted for 12 measures (Alpha {TP9, AF7, AF8, TP10}, ERD of Beta{TP9, AF7, AF8, TP10}, and ERS of Theta {TP9, AF7, AF8, TP10} with baseline_near between 1 back and 2 back; and ERD of Alpha AF7, Alpha AF8, Beta AF8, and Beta TP9 with baseline away 1 back and 2 back. See Appendix C for the details.

EEG data results

The average workload is the average value of instantaneous loads within a task duration (Xie and Salvendy, 2000). In this study, the average cognitive workload is represented by the average ERD of Alpha, Beta, and ERS of Theta for TP9, TP10, AF7, and AF8 of the intervals of each letter with baseline_near.

To examine whether there is a difference between 1 and 2 back for averages of ERD of Alpha, Beta, and ERS of Theta for TP9, TP10, AF7, and AF8 with baseline near, we conducted Mann–Whitney–Wilcoxon tests between 1 and 2 back of all participants. The results are included in Table 3. Due to computational problems, the numbers of subjects (N) vary between the analyses.

It is not feasible to have a baseline for each stimulus in scenarios of users experiencing an application on smartphones. Hence, to explore the feasibility of adopting a single baseline away with stimulus, we conducted Mann–Whitney–Wilcoxon tests for averages of ERD of Alpha AF7 and Beta TP9 with baseline away between 1 and 2 back for all participants, participants with odd IDs, and participants with even IDs, respectively. We find no significant results (Table 4).

Analysis of EEG results

Different cognitive workloads evoked associated human brain oscillatory responses (Krause et al., 2000; Pesonen et al., 2007) that made it possible to measure the corresponding cognitive workload levels.

The results in Table 3 show that only Alpha ERD AF7 and Beta ERD TP9 among the 12 measures (TP9, AF7, AF8,TP10 * Alpha, Beta, and Theta) are sensitive to the different

TABLE 3 The descriptive statistics and Mann–Whitney–Wilcoxon test results for averages of ERD of Alpha, Beta, and ERS of Theta for TP9, TP10, AF7, and AF8 with baseline near between 1 and 2 back.

Measure	N Back	N	Mean	SD	Median	W*	*p*-value
Theta_ERS_TP9_near	1	415	0.5103788	2.3437866	0.1606055	81,290	0.05664
	2	424	0.3624826	0.8789823	0.1961127		
Theta_ERS_AF7_near	1	442	1.479168	7.528482	0.3261652	102,550	0.1951
	2	488	40.222121	858.424241	0.3993164		
Theta_ERS_AF8_near	1	463	256.550957	4473.14064	0.4962916	107,560	0.7199
	2	471	1.656752	6.897568	0.4979768		
Theta_ERS_TP10_near	1	402	0.1968689	0.2983741	0.1055942	76,520	0.1935
	2	402	0.4827313	2.7181894	0.1440152		
Alpha_ERD_TP9_near	1	407	−0.2429342	0.6022346	−0.0708803	94,305	0.07823
	2	433	−1.0891115	16.1080866	−0.0994483		
Alpha_ERD_AF7_near	1	417	−0.4870307	1.31401	−0.1177238	89,413	**0.03469****
	2	395	−4.1949784	63.64311	−0.1726443		
Alpha_ERD_AF8_near	1	422	−1.305807	7.191686	−0.1905496	91,227	0.9368
	2	431	−7.442734	122.014022	−0.2087486		
Alpha_ERD_TP10_near	1	382	−0.3358805	1.1701908	−0.0741198	75,913	0.6915
	2	391	−0.2689888	0.5359719	−0.0839877		
Beta_ERD_TP9_near	1	424	−0.0948762	0.1298309	−0.053213	94,695	**0.04122****
	2	413	−0.1438368	0.3410383	−0.0645524		
Beta_ERD_AF7_near	1	398	−0.4218005	1.783285	−0.0801937	86,126	0.8545
	2	436	−0.6272942	3.536376	−0.0829866		
Beta_ERD_AF8_near	1	431	−0.1898465	0.3919714	−0.0811931	99,618	0.1104
	2	435	−0.2896695	0.7094699	−0.1054581		
Beta_ERD_TP10_near	1	259	−0.1434616	0.2283444	−0.0740742	36,067	0.2439
	2	263	−0.1571087	0.1960775	−0.0797461		

*W-Value is the sum of the ranks of the first sample. The bold values are p values smaller than 0.01, so they are statistically significantly. **$P = 0.01$.

TABLE 4 The descriptive statistics and Mann–Whitney–Wilcoxon test results for averages of ERD of Alpha_AF7 and Beta_TP9 with baseline away between 1 back and 2 back.

ID	Measure	N Back	N	Mean	SD	Median	W*	*p*-value
ALL	Alpha_ERD_AF7_away	1	325	−0.707954	0.6306785	−0.548365	56,233	0.2634
		2	364	−0.707059	0.7387755	−0.4852188		
	Beta_ERD_TP9_away	1	179	−0.119261	0.1193088	−0.0843989	20,950	0.1648
		2	205	−0.154169	0.1637146	−0.1034079		

*W-Value is the sum of the ranks of the first sample.

workloads of between 1 and 2 back conditions for all participants ($p < 0.05$).

The magnitudes of Alpha ERD AF7 and Beta ERD TP9 are significantly greater for the 2 back than for the 1 back (Figure 5), indicating that Alpha and Beta increase as tasks demand more cognitive workload. This is in line with previous studies that found with inclining task demands, Alpha and Beta desynchronize (increase) (Klimesch, 1999; Stipacek et al., 2003; Klimesch et al., 2005; Neubauer et al., 2006; Antonenko et al., 2010a; Antonenko and Niederhauser, 2010b; Xiang et al., 2021).

The insensitivity of the six measures (AF8 and TP10 * Alpha, Beta, and Theta) can be explained by the functions of the cerebral cortex.

The TP10 electrode is positioned behind the right ear, which is the right temporal lobe, and the AF8 electrode is on the right forehead, which is the right frontal lobe (Figure 1). The TP9 electrode is positioned behind the left ear, which is the left temporal lobe, and the AF7 electrode is on the left forehead, which is the left frontal lobe (Figure 1).

The left temporal lobe is associated with understanding language, learning, memorizing, forming speech, and

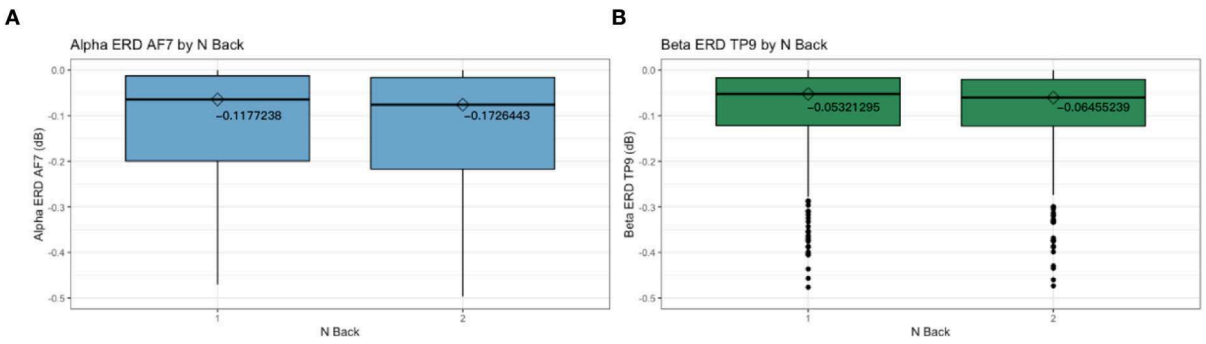

FIGURE 5
Box plots with medians between 1 back and 2 back for Alpha ERD AF7 **(A)** and Beta ERD TP9 **(B)**.

remembering verbal information (Guy-Evans, 2021b). We used English letters as a stimulus in the N-back task and participants' primary language is Chinese, thus it makes sense that Beta ERD TP9 are found to have significant differences between 1 and 2 back.

The AF7 electrode is on the left side of the frontal lobe. The frontal lobe is located behind the forehead, at the front of the brain. Each lobe controls the operations on opposite sides of the body: the left hemisphere controls the right side of the body and vice versa (Guy-Evans, 2021a). It is believed that the left frontal lobe works predominantly with language, logical thinking, and analytical reasoning. The right frontal lobe, on the other hand, is mostly associated with non-verbal abilities, creativity, imagination, musical, and art skills (Guy-Evans, 2021a).

The dominant hands of 29 participants were the right hand, and the remaining one was both hands. We observed all participants only used their right hands to make the choices. This explains that the Alpha ERD AF7 (left forehead) but not AF8 (right forehead) was found to have significant differences between 1 and 2 back. However, the other four measures of TP9 and AF7 shall be sensitive to the difference in cognitive workload, as previous studies prove.

Discussion on EEG data

In summary, MUSE 2 outputs good signals, but these signals may not be readily useful in the studies on the usability of smartphone applications for an entire and consecutive user experience as a result of the difficulty in selecting a sensible baseline due to two rationales.

The first rationale behind the difficulty in the selection of a sensible baseline lies in the fact that only Alpha ERD AF7 and Beta ERD TP9 show sensitivity to the difference in cognitive workload between 1 and 2 back. It is not consistent with that given in previous studies (Klimesch, 1999; Stipacek et al., 2003; Klimesch et al., 2005; Neubauer et al., 2006; Antonenko and Niederhauser, 2010b; Xiang et al., 2021).

Second, according to Pfurtscheller and Lopes da Silva (1999), ERD/ERS is required to have a baseline captured some seconds right before the events. Yet, it is not feasible to have a baseline for each stimulus in the scenarios of users experiencing any applications on smartphones. We had carried out an exploration of adopting a single baseline away with stimulus, but unfortunately it did not show any statistically significant differences for averages of ERD of Alpha AF7 and Beta TP9 between 1 and 2 back.

All in one sentence, although MUSE 2 is of consumer grade, comfortable to wear, and wireless connected, it is a reliable device for researchers to capure stable EEG data for measuring cognitive workload. It does show some promise for detecting cognitive workload elicited by isolated/independent elements in user interface (UI) design, and selective signals may be combined with eye-tracking data to detect UI issues that invoke user errors.

Eye movement data

Eye movement data processing and analysis

During the experiment, participants completed N-back tasks on a smartphone attached to the mobile testing accessory with the Tobii Pro Nano mounted on the top (Figure 2). Eye movement data were collected by the Tobii Pro Nano *via* the Tobii Pro Lab software (version 1.162.32461).

Similar to the EEG data, the recorded eye movement data were processed using Excel and R through several steps to get averaged pupil dilation left, averaged pupil dilation right, averaged fixation duration, averaged fixation number in second, averaged saccade duration, averaged saccade number in second, maximums of pupil dilation left, maximums of pupil dilation right, maximums of fixation duration, and maximums of saccade duration.

A non-parametric test was selected for non-normal data. See Appendix C for data processing and analysis detailed steps.

Eye movement data results

The Tobii Pro Nano was extremely sensitive to angle changes between participant's eyes and the device. Based on the experience we had gathered from pilots, we had a higher chair for the participants to improve the capture rate and adjusted the Tobii Pro Nano angle according to each participant. Despite the higher chair we had employed and the active adjustments made to the mobile testing accessory, the capture rates varied across participants. Eighteen participants' data with relatively higher capture rates were processed and analyzed here.

Averaged cognitive workload is quantified by the averaged pupil dilation left and the averaged pupil dilation right, the averaged fixation duration and the averaged fixation number, and the averaged saccade duration and the averaged saccade number.

To examine whether there were statistically significant differences for averaged pupil dilation changes between low and high cognitive workload conditions, we conducted a Mann–Whitney–Wilcoxon test for averaged pupil dilation left, averaged pupil dilation right, between 1 and 2 back. The results are presented in Table 5.

In this research, the averaged fixation duration and the fixation number in second were adopted as the representative of the averaged cognitive workload during the intervals, starting from the appearance of each letter to the time point that choices were made.

To examine whether there were statistically significant differences for averaged fixation duration and fixation number in second between low and high cognitive workload conditions were observed, we conducted Mann–Whitney–Wilcoxon tests between 1 and 2 back. The results are presented in Table 5.

In this research, the averaged saccade duration and the averaged saccade number in second were adopted as the representative of the averaged cognitive workload during the intervals, starting from the appearance of each letter to the time point that choices were made.

To examine whether there were statistically significant differences for the averaged saccade duration and the averaged saccade number in second between low and high cognitive workload conditions, we conducted Mann–Whitney–Wilcoxon tests between 1 and 2 back. The results are presented in Table 5.

The maximum pupil dilation left and the maximum pupil dilation right were adopted as the representative of the peak cognitive workload during the intervals, starting from the appearance of each letter to the time point that choices were made.

To examine whether statistically significant differences for maximums of pupil dilation changes between low and high cognitive workload condition, we conducted Mann–Whitney–Wilcoxon tests for maximums of pupil dilation left and of pupil dilation right between 1 and 2 back. The results are presented in Table 6.

In this research, the maximums of fixation duration were adopted as the representative of the peak cognitive workload during the intervals, starting from the appearance of each letter to the time point that choices were made.

To examine whether statistically significant differences exist for the maximums of fixation duration between low and high cognitive workload conditions, we conducted Mann–Whitney–Wilcoxon tests between 1 and 2 back. We find no significant results (Table 7).

In this research, the maximum saccade duration was adopted as the representative of the peak cognitive workload during the intervals, starting from the appearance of each letter to the time point that choices were made.

To examine whether statistically significant differences exist for the maximums of saccade duration between low and high cognitive workload conditions, we conducted Mann–Whitney–Wilcoxon tests for it between 1 and 2 back. We find no significant results (Table 7).

Eye movement results' analysis

Overall, the eye movement data collected by the Tobii Pro Nano are valid and reliable. Some measures (pupil dilation, saccade number in second, fixation number in second) are sensitive to the difference of average cognitive workload and peak cognitive workload introduced by the 1 or 2 back tasks.

The averages of pupil dilations of both eyes have been proven to be reactive to the differences of average cognitive workload between 1 and 2 back tasks consistently. As Table 5 reveals, there are statistically significant differences between 1 and 2 back for the averages of pupil dilation of both eyes ($p < 0.05$). The medians of the averages of pupil dilations of both eyes are larger in 2 back than in 1 back. The medians of the averages of pupil dilations of both eyes remain greater in the 2 back and in the 1 back, so that the bigger average of pupil dilations means a higher averaged cognitive workload. This finding is in line with earlier studies (Granholm et al., 1996; Pomplun and Sunkara, 2003; Klingner et al., 2008; Chen et al., 2011; Porta et al., 2012; Rafiqi et al., 2015).

The same pattern is discovered in the maximums of pupil dilation. There are statistically significant differences between 1 back and 2 back for maximums of pupil dilation of both eyes ($p < 0.05$ or < 0.001) (Table 6). The medians of the maximum pupil dilation of both eyes are larger in 2 back than in 1 back for both eyes, which indicates the larger maximum of pupil dilations means a higher peak cognitive workload.

As for fixation and saccade, statistically significant differences were observed between 1 and 2 back in the fixation number in second and saccade number in second (Table 6).

TABLE 5 The descriptive statistics and Mann–Whitney–Wilcoxon test results for the averaged pupil dilation left, the averaged pupil dilation right, the averaged fixation duration, the averaged fixation number, the averaged saccade duration, and the averaged saccade number in second between 1 and 2 back.

Measure [mm]	N back	N	Mean	SD	Median	W*	*p*-value
Averaged pupil dilation left	1	245	0.0776042	0.3685327	0.1129762	24,874	**0.0006402*****
	2	247	0.2135481	0.3894946	0.1967991		
Averaged pupil dilation right	1	255	0.1306679	0.4081041	0.1599511	29,682	**0.005187****
	2	271	0.2631821	0.4403823	0.2407292		
Averaged fixation duration [ms]	1	247	224.4167	186.5857	166.7222	30,689	0.6749
	2	254	217.8477	167.6373	166.4935		
Fixation number in second	1	247	25.89081	15.4502	22.97702	33,166	**0.02676****
	2	254	24.25003	14.94318	22.54331		
Averaged saccade duration[ms]	1	267	27.14384	10.29906	25	37,158	0.9221
	2	277	27.43823	13.47225	25		
Saccade number in second	1	267	11.416636	6.600944	10.673235	41,258	**0.0196****
	2	277	9.862231	5.004347	9.687836		

*W-Value is the sum of the ranks of the first sample. The bold values are *p* values smaller than 0.01, so they are statistically significantly. **$P = 0.01$; ***$P = 0.001$.

TABLE 6 The descriptive statistics and Mann–Whitney–Wilcoxon test results for the maximum pupil dilation left and the maximum pupil dilation right between 1 and 2 back.

Measure [mm]	N back	N	Mean	SD	Median	W*	*p*-value
Maximums of pupil dilation left	1	299	−0.5025064	1.676639	0.1764088	26,852	**0.03083****
	2	300	−0.3933013	1.735202	0.2990345		
Maximums of pupil dilation right	1	300	−0.30043015	1.54833	0.2411331	37,104	**0.0001998*****
	2	300	0.04463652	1.391381	0.397199		

*W-Value is the sum of the ranks of the first sample. **$P = 0.01$; ***$P = 0.001$.

TABLE 7 The descriptive statistics and Mann–Whitney–Wilcoxon test results for the maximums of fixation duration between 1 and 2 back for all selected participants.

Measure	N Back	N	Mean	SD	Median	W*	*p*-value
Maximum of fixation duration [ms]	1	247	290.8664	226.5789	217	30234	0.3964
	2	256	309.6367	247.3612	217		
Maximum of saccade duration[ms]	1	267	42.42697	23.30892	33	36237	0.5242
	2	280	43.71071	24.47466	33		

*W-Value is the sum of the ranks of the first sample.

Irreconcilable with previous findings is that the correlation between the number of fixation and cognitive workload is negative. Previous studies have concluded that an upswing number of fixations correlate with an increased cognitive load level (Goldberg and Helfman, 2010; Chen et al., 2011; Wang et al., 2014; Zagermann et al., 2018). And the higher number of saccades in second (saccade velocity) is also related to lower cognitive workload, opposing the previous research (Barrios et al., 2004; Chen et al., 2011; Lallé et al., 2016; Zagermann et al., 2018).

Discussion on eye movement data

In this study, we found that eye-tracking device, Tobii Pro Nano with mobile testing accessory, appears to be a valid instrument for monitoring the cognitive workload difference in a smartphone setting. This finding along with previous studies (Sugaya, 2019; Ehlers, 2020; Lee and Chenkin, 2020) can provide an initial empirical evidence on the reliability of Tobii Pro Nano with mobile testing accessory. Moreover, the average pupil dilation and the maximum pupil dilation have been ratified as the effective measures of cognitive workload difference in a

TABLE 8 The tasks in the papers.

Paper	Task
Chen et al. (2011)	observing team player positions in basketball game videos
Goldberg and Helfman (2010)	scanning within and between bar, line, and spider graphs
Barrios et al. (2004)	browsing content to learn
Lallé et al. (2016)	retrieve, find, sort, and compute in charts
Wang et al. (2014)	online shopping tasks on a shopping website
Zagermann et al. (2018)	three visual search tasks that represent different levels of difficulty

smartphone setting, and they enlarge along with the difficulty levels of N-back task rising.

One incongruent finding is that the fixation velocity and saccade velocity decline with the increment of cognitive workload, while the previous studies found an upswing number of fixations correlate with an increased cognitive load level (Barrios et al., 2004; Goldberg and Helfman, 2010; Chen et al., 2011; Wang et al., 2014; Lallé et al., 2016; Alonso Dos Santos and Calabuig Moreno, 2018; Zagermann et al., 2018).

One possible justification for this reverse is the different task design. The N-back task only required participants to look at one spot on the screen, while the previous studies required participants to observe, scan, and search during tasks and the gazes were not fixed in one spot (Table 8).

Another obvious concern about the Tobii Pro Nano is the unstable capture rate. Only nearly half of the participants' data was captured enough to be adopted.

One pilot participant's capture rate was 0% and he mentioned that he had a high degree of astigmatism, around 500–600 in both eyes. Astigmatism is an imperfection in the curvature of your eye's cornea or lens (Boyd, 2021). It may be helpful to think of the normal eye as being shaped like a basketball. With astigmatism, it is shaped more like an American football. The Tobii Pro Nano may not effectively recognize the eyes of people with astigmatism. This suggests that the low capture rate for some participants may be caused by astigmatism. Therefore, information about astigmatism was obtained from the participants.

For the astigmatism degree, we averaged two eye degrees. The capture rate was recorded in the Tobii Pro Nano. We adopted Spearman's rho statistic to assess the correlation between capture rate and astigmatism degree, and the correlation coefficients and p values are given in Figure 6. The result shows that there is a statistically significant negative correlation between capture rate and astigmatism degree ($p < 0.05$ or < 0.001). The correlation coefficient is −0.55. The negative correlation between astigmatism and capture rate may have resulted from the changes in the shape of eyeballs.

Overall, the objective of Experiment 1 was to assess the feasibility of using wirelessly acquired EEG (MUSE 2) and eye-tracking device (Tobii Pro Nano) to assess cognitive workload in a well-controlled N-back task in a smartphone setting. And the eye-tracking device, Tobii Pro Nano, can be adopted as a device to collect eye movement data to monitor cognitive workload fluctuations in a smartphone setting with a screen for high astigmatism, and pupil dilation can be measured for cognitive workload differences.

Conclusion and future directions

This study aimed to verify the feasibility of using eye-tracking (i.e., Tobii Pro Nano) and low-cost electroencephalogram (EEG, i.e., MUSE 2) devices to measure real-time cognitive workload changes during mobile application use, and which measures are sensitive to cognitive workload differences. Results from the experiment manifest that the eye-tracking device (Tobii Pro Nano) can be adopted as a device to collect eye movement data to monitor cognitive workload fluctuations in a smartphone setting, and pupil dilations can be used to measure the cognitive workload differences, with a screening test to filter out people with a high astigmatism degree.

There are three main directions for future research. The first one is to adopt pupil dilations as an effective measure to assess users' cognitive workloads while experiencing a smartphone application and to improve the UI design of the application based on the assessment.

The second one is to expand the age range to cover middle-aged and older adults. Only younger users who were born with smartphones were included in the study and we found that they have a high level of endurance for design issues and proficient capability to resolve issues by themselves. While it has been found that cognitive performance declines with age (Deary et al., 2009), it is reasonable to expand research to include middle-aged and older adults to verify the findings in the different age groups to investigate whether experience with smartphones overcomes cognitive ability's recession.

The third one is to test findings in other settings, e.g., virtual reality (VR), wearable devices, etc. Some ubiquitous screens (e.g., smart watches, etc.) and certain brand immersive experience technologies (e.g., VR glasses, etc.) have been winning consumers' heart with acceptable prices and great user experiences. It is necessary to test our findings in these settings as well.

In the far future, one major direction we desire to explore is to establish a multidimensional assessment tool for product usability, including subjective ratings, psychophysiological measures, and performance measures. We understand this

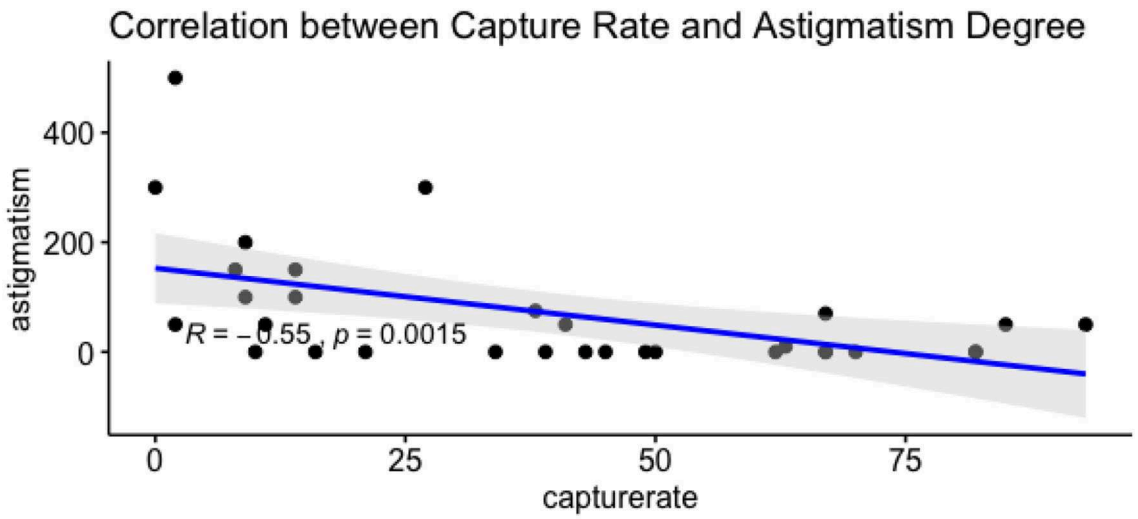

FIGURE 6
The correlation between capture rate and astigmatism degree.

objective is extensive and requires considerable time and human resources to complete.

Another direction is to expand from application-focused studies to include cognitive-focused studies. Instead of studying how to improve the usability of specific kinds of software applications, we aim to study cognitive processes, such as how to help people focus or refocus in different settings.

Data availability statement

The raw data supporting the conclusions of this article will be made available by the authors upon request.

Ethics statement

The studies involving human participants were reviewed and approved by University of Arizona IRB Office (Protocol Number: 2101428836). Written informed consent to participate in this study was provided by the participants' legal guardian/next of kin.

Author contributions

Study conception and design, data collection, and draft manuscript preparation: LZ. Analysis and interpretation of results: LZ and HC. All authors reviewed the results and approved the final version of the manuscript.

Funding

NSF award # 1661485 and University of Arizona SBS summer dissertation fellowship.

Conflict of interest

The authors declare that the research was conducted in the absence of any commercial or financial relationships that could be construed as a potential conflict of interest.

Publisher's note

All claims expressed in this article are solely those of the authors and do not necessarily represent those of their affiliated organizations, or those of the publisher, the editors and the reviewers. Any product that may be evaluated in this article, or claim that may be made by its manufacturer, is not guaranteed or endorsed by the publisher.

Supplementary material

The Supplementary Material for this article can be found online at: https://www.frontiersin.org/articles/10.3389/fnins.2022.1011475/full#supplementary-material

References

Alonso Dos Santos, M., and Calabuig Moreno, F. (2018). Assessing the effectiveness of sponsorship messaging: measuring the impact of congruence through electroencephalogram. *Int. J. Sports Mark. Spons.* 19, 25–40. doi: 10.1108/IJSMS-09-2016-0067

Anderson, E. W., Potter, K. C., Matzen, L. E., Shepherd, J. F., Preston, G. A., and Silva, C. T. (2011). A user study of visualization effectiveness using EEG and cognitive load. *Computer Graphics Forum*. 30, 791–800. doi: 10.1111/j.1467-8659.2011.01928.x

Antonenko, P., Paas, F., Grabner, R., and van Gog, T. (2010a). Using Electroencephalography to measure cognitive load. *Educ. Psychol. Rev.* 22, 425–438. doi: 10.1007/s10648-010-9130-y

Antonenko, P. D., and Niederhauser, D. S. (2010b). The influence of leads on cognitive load and learning in a hypertext environment. *Comput. Human Behav.* 26, 140–150. doi: 10.1016/j.chb.2009.10.014

Arsalan, A., Majid, M., Butt, A. R., and Anwar, S. M. (2019). Classification of perceived mental stress using a commercially available EEG headband. *IEEE J. Biomed. Health Info*. 23, 2257–2264. doi: 10.1109/JBHI.2019.2926407

Asif, A., Majid, M., and Anwar, S. M. (2019). Human stress classification using EEG signals in response to music tracks. *Comput. Biol. Med.* 107, 182–196. doi: 10.1016/j.compbiomed.2019.02.015

Ayaz, H., Willems, B., Bunce, S., Shewokis, P. A., Hah, S., Deshmukh, A. R., et al. (2010). "Cognitive workload assessment of air traffic controllers using optical brain imaging sensors," in *Advances in Understanding Human Performance: Neuroergonomics, Human Factors Design, and Special Populations*. 21–32. doi: 10.1201/EBK1439835012-c3

Bevan, N., and MacLeod, M. (1994). Usability measurement in context. *Behav. Infm.Technol.* 13, 132–145. doi: 10.1080/01449299408914592

Borys, M., Plechawska-Wójcik, M., Wawrzyk, M., and Wesołowska, K. (2017). "Classifying Cognitive Workload Using Eye Activity and EEG Features in Arithmetic Tasks," in Damaševičius, R., and Mikašyte, V. *Information and Software Technologies*. Midtown Manhattan, New York City: Springer International Publishing. p. 90–105. doi: 10.1007/978-3-319-67642-5_8

Boyd, K. (2021). *What Is Astigmatism? - American Academy of Ophthalmology*. Available online at: https://www.aao.org/eye-health/diseases/what-is-astigmatism

Brooke, J. (1996). *SUS: A "Quick and Dirty" Usability Scale. In Usability Evaluation In Industry*. CRC Press. p. 7.

Brunken, R., Plass, J. L., and Leutner, D. (2003). Direct measurement of cognitive load in multimedia learning. *Educ. Psychol.* 38, 53–61. doi: 10.1207/S15326985EP3801_7

Brünken, R., Seufert, T., and Paas, F. (2010). *Measuring cognitive load*. doi: 10.1017/CBO9780511844744.011

Cabañero, L., Hervás, R., González, I., Fontecha, J., Mondéjar, T., and Bravo, J. (2019). Analysis of cognitive load using EEG when interacting with mobile devices. *Proceedings*. 31, 70. doi: 10.3390/proceedings2019031070

Cain, B. (2007). "A Review of the Mental Workload Literature," *Defence Research And Development Toronto (Canada)*. Available online at: https://apps.dtic.mil/docs/citations/ADA474193

Ceci, L. (2022). "Biggest app stores in the world 2021," in *Statista*. Available online at: https://www.statista.com/statistics/276623/number-of-apps-available-in-leading-app-stores/

Cernea, D., Olech, P.-S., Ebert, A., and Kerren, A. (2012). "Controlling In-Vehicle Systems with a Commercial EEG Headset: Performance and Cognitive Load," in Garth, C., Middel, V., and Hagen, H. (Eds.). *Visualization of Large and Unstructured Data Sets: Applications in Geospatial Planning, Modeling and Engineering—Proceedings of IRTG 1131 Workshop 2011*. Schloss Dagstuhl–Leibniz-Zentrum fuer Informatik. p. 113–122

Chen, S., Epps, J., Ruiz, N., and Chen, F. (2011). "Eye activity as a measure of human mental effort in HCI," *Proceedings of the 16th International Conference on Intelligent User Interfaces*. p. 315–318. doi: 10.1145/1943403.1943454

Chin, Z. Y., Zhang, X., Wang, C., and Ang, K. K. (2018). "EEG-based discrimination of different cognitive workload levels from mental arithmetic," in *2018 40th Annual International Conference of the IEEE Engineering in Medicine and Biology Society (EMBC)*. p. 1984–1987. doi: 10.1109/EMBC.2018.8512675

Cirett Galán, F., and Beal, C. R. (2012). "EEG estimates of engagement and cognitive workload predict math problem solving outcomes," in Masthoff, J., Mobasher, B., Desmarais, M. C., and Nkambou, R. (Eds.). *User Modeling, Adaptation, and Personalization*. Springer. p. 51–62. doi: 10.1007/978-3-642-31454-4_5

Coulacoglou, C., and Saklofske, D. H. (2017). "Executive Function, Theory of Mind, and Adaptive Behavior," in *Psychometrics and Psychological Assessment*. Elsevier. p. 91–130. doi: 10.1016/B978-0-12-802219-1.00005-5

Coursaris, C., and Kim, D. (2006). "A qualitative review of empirical mobile usability studies," *Conference: Connecting the Americas*. Acapulco, México: 12th Americas Conference on Information Systems, AMCIS 2006. p. 352.

Dan, A., and Reiner, M. (2017). Real time EEG based measurements of cognitive load indicates mental states during learning. *JEDM*. 9, 31–44. doi: 10.5281/zenodo.3554719

Davids, M. R., Halperin, M. L., and Chikte, U. M. E. (2015). Review: optimising cognitive load and usability to improve the impact of e-learning in medical education. *Afr. J. Health Prof. Educ.* 7, 147–152. doi: 10.7196/AJHPE.569

Deary, I. J., Corley, J., Gow, A. J., Harris, S. E., Houlihan, L. M., Marioni, R. E., et al. (2009). Age-associated cognitive decline. *Br. Med. Bull.* 92, 135–152. doi: 10.1093/bmb/ldp033

Dimigen, O., Sommer, W., Hohlfeld, A., Jacobs, A. M., and Kliegl, R. (2011). Coregistration of eye movements and EEG in natural reading: analyses and review. *J. Exp. Psychol.: General*. 140, 552–572. doi: 10.1037/a0023885

Dumas, J. S., Dumas, J. S., and Redish, J. (1999). *A Practical Guide to Usability Testing*. Intellect Books.

Ehlers, J. (2020). "Exploring the effect of transient cognitive load on bodily arousal and secondary task performance," *Proceedings of the Conference on Mensch Und Computer*. p. 7–10. doi: 10.1145/3404983.3410017

Evans, D. C., and Fendley, M. (2017). A multi-measure approach for connecting cognitive workload and automation. *Int. J. Hum. Comput. Stud.* 97, 182–189. doi: 10.1016/j.ijhcs.2016.05.008

Farnsworth, B. (2019). "EEG Headset Prices – An Overview of 15+ EEG Devices," *Imotions*. Available online at: https://imotions.com/blog/eeg-headset-prices/

Farnsworth, B. (2020). "Top 12 Eye Tracking Hardware Companies (Ranked)," *Imotions*. Available online at: https://imotions.com/blog/top-eye-tracking-hardware-companies/

Gavas, R., Chatterjee, D., and Sinha, A. (2017). "Estimation of cognitive load based on the pupil size dilation," in *2017 IEEE International Conference on Systems, Man, and Cybernetics (SMC)*. p. 1499–1504. doi: 10.1109/SMC.2017.8122826

Gevins, A., and Smith, M. E. (2003). Neurophysiological measures of cognitive workload during human-computer interaction. *Theor. Issues Ergon. Sci.* 4, 113–131. doi: 10.1080/14639220210159717

Goldberg, J., and Helfman, J. (2010). "Comparing information graphics: a critical look at eye tracking," *Conference on Human Factors in Computing Systems - Proceedings*. doi: 10.1145/2110192.2110203

Goldberg, J. H., and Wichansky, A. M. (2003). "Chapter 23 - Eye Tracking in Usability Evaluation: A Practitioner's Guide," in Hyönä, J., Radach, R., and Deubel, H. (Eds.). *The Mind's Eye*. North-Holland. p. 493–516. doi: 10.1016/B978-044451020-4/50027-X

Granholm, E., Asarnow, R. F., Sarkin, A. J., and Dykes, K. L. (1996). Pupillary responses index cognitive resource limitations. *Psychophysiology*. 33, 457–461. doi: 10.1111/j.1469-8986.1996.tb01071.x

Guy-Evans, O. (2021a). *Frontal Lobe Function, Location in Brain, Damage, More | Simply Psychology*. Available online at: https://www.simplypsychology.org/frontal-lobe.html

Guy-Evans, O. (2021b). *Temporal Lobe: Definition, Functions, and Location | Simply Psychology*. Available online at: https://www.simplypsychology.org/temporal-lobe.html

Gwizdka, J., Hosseini, R., Cole, M., and Wang, S. (2017). Temporal dynamics of eye-tracking and EEG during reading and relevance decisions. *J. Assoc. Inf. Sci. Technol.* 68, 2299–2312. doi: 10.1002/asi.23904

Harrison, R., Flood, D., and Duce, D. (2013). Usability of mobile applications: literature review and rationale for a new usability model. *J. Interact. Sci.* 1, 1. doi: 10.1186/2194-0827-1-1

Hart, S. G., and Staveland, L. E. (1988). "Development of NASA-TLX (Task Load Index): results of empirical and theoretical research," in Hancock, P. A.,

and Meshkati, N. (Eds.). *Advances in Psychology*. North-Holland. p. 139–183. doi: 10.1016/S0166-4115(08)62386-9

Heckbert, P. (1995). *Fourier Transforms and the Fast Fourier Transform (FFT) Algorithm*. p. 13.

Hild, J., Putze, F., Kaufman, D., Kühnle, C., Schultz, T., and Beyerer, J. (2014). *Spatio-Temporal Event Selection in Basic Surveillance Tasks using Eye Tracking and EEG*. p. 6.

Hoober, S. (2013). *How Do Users Really Hold Mobile Devices? UXmatters*. Available online at: https://www.uxmatters.com/mt/archives/2013/02/how-do-users-really-hold-mobile-devices.php?

ISO 9241-11. (2018). *Ergonomics of human-system interaction—Part 11: Usability: Definitions and concepts*. Available online at: https://www.iso.org/obp/ui/#iso:std:iso:9241:-11:ed-2:v1:en

Jaeggi, S. M., Buschkuehl, M., Perrig, W. J., and Meier, B. (2010). The concurrent validity of the N-back task as a working memory measure. *Memory*. 18, 394–412. doi: 10.1080/09658211003702171

Klimesch, W. (1999). EEG alpha and theta oscillations reflect cognitive and memory performance: a review and analysis. *Brain Res. Rev*. 29, 169–195. doi: 10.1016/S0165-0173(98)00056-3

Klimesch, W., Schack, B., and Sauseng, P. (2005). The functional significance of theta and upper alpha oscillations. *Exp. Psychol*. 52, 99–108. doi: 10.1027/1618-3169.52.2.99

Klingner, J., Kumar, R., and Hanrahan, P. (2008). "Measuring the task-evoked pupillary response with a remote eye tracker," in *Proceedings of the 2008 Symposium on Eye Tracking Research and Applications*. p. 69–72. doi: 10.1145/1344471.1344489

Knoll, A., Wang, Y., Chen, F., Xu, J., Ruiz, N., Epps, J., et al. (2011). "Measuring Cognitive Workload with Low-Cost Electroencephalograph," in Campos, P., Graham, N., Jorge, J., Nunes, N., Palanque, P., and Winckler, M. (Eds.). *Human-Computer Interaction – INTERACT 2011*. Springer. p. 568–571. doi: 10.1007/978-3-642-23768-3_84

Krause, C. M., Sillanmäki, L., Koivisto, M., Saarela, C., Häggqvist, A., Laine, M., et al. (2000). The effects of memory load on event-related EEG desynchronization and synchronization. *Clini. Neurophysiol.* 111, 2071–2078. doi: 10.1016/S1388-2457(00)00429-6

Krigolson, O. E., Williams, C. C., Norton, A., Hassall, C. D., and Colino, F. L. (2017). Choosing MUSE: validation of a low-cost, portable EEG system for ERP research. *Front. Neurosci*. 11. doi: 10.3389/fnins.2017.00109

Kumar, N., and Kumar, J. (2016). Measurement of cognitive load in HCI systems using EEG power spectrum: an experimental study. *Procedia Comp. Sci*. 84, 70–78. doi: 10.1016/j.procs.2016.04.068

Lallé, S., Conati, C., and Carenini, G. (2016). Prediction of individual learning curves across information visualizations. *User Model. User-adapt. Interact*. 26, 307–345. doi: 10.1007/s11257-016-9179-5

Lee, W. F., and Chenkin, J. (2020). "Exploring Eye-tracking Technology as an Assessment Tool for Point-of-care Ultrasound Training," in *AEM Education and Training*. 5:e10508. doi: 10.1002/aet2.10508

Makransky, G., Terkildsen, T. S., and Mayer, R. E. (2019). Adding immersive virtual reality to a science lab simulation causes more presence but less learning. *Learn. Instruct*. 60, 225–236. doi: 10.1016/j.learninstruc.2017.12.007

Manuel, V., Barrios, G., Gütl, C., Preis, A. M., Andrews, K., Pivec, M., et al. (2004). "AdELE: A framework for adaptive e-learning through eye tracking," in *Proceedings of I-Know'04*. p. 609–616.

Mazher, M., Abd Aziz, A., Malik, A. S., and Ullah Amin, H. (2017). An EEG-based cognitive load assessment in multimedia learning using feature extraction and partial directed coherence. *IEEE Access*. 5, 14819–14829. doi: 10.1109/ACCESS.2017.2731784

Mobile Testing Accessory | Perfect for Usability Tests. (2020). Available online at: https://www.tobiipro.com/product-listing/mobile-testing-accessory/

Molla, R. (2020). "Americans spent about 3.5 hours per day on their phones last year—A number that keeps going up despite the "time well spent" movement," in *Vox*. Available online at: https://www.vox.com/recode/2020/1/6/21048116/tech-companies-time-well-spent-mobile-phone-usage-data

Neubauer, A. C., and Fink, A. (2003). Fluid intelligence and neural efficiency: effects of task complexity and sex. *Pers. Individ. Dif*. 35, 811–827. doi: 10.1016/S0191-8869(02)00285-4

Neubauer, A. C., Fink, A., and Grabner, R. H. (2006). "Sensitivity of alpha band ERD to individual differences in cognition," in Neuper, C., and Klimesch, W. (Eds.). *Progress in Brain Research*. Elsevier. p. 167–178. doi: 10.1016/S0079-6123(06)59011-9

Nielsen, J. (1993). Iterative user-interface design. *Computer*. 26, 32–41. doi: 10.1109/2.241424

Nielsen, J., and Pernice, K. (2010). *Eyetracking Web Usability*. New Riders.

Notaro, G. M., and Diamond, S. G. (2018). Simultaneous EEG, eye-tracking, behavioral, and screen-capture data during online German language learning. *Data in Brief*. 21, 1937–1943. doi: 10.1016/j.dib.2018.11.044

O'Dea, S. (2021). *Number of smartphone users in the U.S. 2025. Statista*. Available online at: https://www.statista.com/statistics/201182/forecast-of-smartphone-users-in-the-us/

Örün, Ö., and Akbulut, Y. (2019). Effect of multitasking, physical environment and electroencephalography use on cognitive load and retention. *Comput. Human Behav*. 92, 216–229. doi: 10.1016/j.chb.2018.11.027

Papakostas, M., Tsiakas, K., Giannakopoulos, T., and Makedon, F. (2017). "Towards predicting task performance from EEG signals," in *2017 IEEE International Conference on Big Data (Big Data)*. p. 4423–4425. doi: 10.1109/BigData.2017.8258478

Pesonen, M., Hämäläinen, H., and Krause, C. M. (2007). Brain oscillatory 4–30 Hz responses during a visual n-back memory task with varying memory load. *Brain Res*. 1138, 171–177. doi: 10.1016/j.brainres.2006.12.076

Pfleging, B., Fekety, D. K., Schmidt, A., and Kun, A. L. (2016). "A model relating pupil diameter to mental workload and lighting conditions," in *Proceedings of the 2016 CHI Conference on Human Factors in Computing Systems*. p. 5776–5788. doi: 10.1145/2858036.2858117

Pfurtscheller, G. (2001). Functional brain imaging based on ERD/ERS. *Vision Res*. 41, 1257–1260. doi: 10.1016/S0042-6989(00)00235-2

Pfurtscheller, G., and Aranibar, A. (1977). Event-related cortical desynchronization detected by power measurements of scalp EEG. *Electroencephalogr. Clin. Neurophysiol*. 42, 817–826. doi: 10.1016/0013-4694(77)90235-8

Pfurtscheller, G., and Berghold, A. (1989). Patterns of cortical activation during planning of voluntary movement. *Electroencephalogr. Clin. Neurophysiol*. 72, 250–258. doi: 10.1016/0013-4694(89)90250-2

Pfurtscheller, G., and Lopes da Silva, F. H. (1999). Event-related EEG/MEG synchronization and desynchronization: basic principles. *Clini. Neurophysiol*. 110, 1842–1857. doi: 10.1016/S1388-2457(99)00141-8

Pomplun, M., and Sunkara, S. (2003). "Pupil dilation as an indicator of cognitive workload in human-computer interaction," in *Human-Centered Computing*, (CRC Press).

Porta, M., Ricotti, S., and Perez, C. J. (2012). "Emotional e-learning through eye tracking," in *Proceedings of the 2012 IEEE Global Engineering Education Conference (EDUCON)*. p. 1–6. doi: 10.1109/EDUCON.2012.6201145

Pratama, S. H., Rahmadhani, A., Bramana, A., Oktivasari, P., Handayani, N., and Haryanto, F., et al. (2020). Signal comparison of developed EEG device and emotiv insight based on brainwave characteristics analysis. *J. Physics: Conference Series*. 1505, 012071. doi: 10.1088/1742-6596/1505/1/012071

Przegalinska, A., Ciechanowski, L., Magnuski, M., and Gloor, P. (2018). "Muse Headband: Measuring Tool or a Collaborative Gadget?" in Grippa, F., Leitão, J., Gluesing, J., Riopelle, K., and Gloor, P. (Eds.). *Collaborative Innovation Networks: Building Adaptive and Resilient Organizations*. Midtown Manhattan, New York City: Springer International Publishing. p. 93–101. doi: 10.1007/978-3-319-74295-3_8

Purves, D., Augustine, G. J., Fitzpatrick, D., Katz, L. C., LaMantia, A.-S., McNamara, J. O., et al. (2001). *Types of Eye Movements and Their Functions. Neuroscience. 2nd Edition*. Available online at: https://www.ncbi.nlm.nih.gov/books/NBK10991/

Rafiqi, S., Wangwiwattana, C., Kim, J., Fernandez, E., Nair, S., and Larson, E. C. (2015). "PupilWare: towards pervasive cognitive load measurement using commodity devices," in *Proceedings of the 8th ACM International Conference on PErvasive Technologies Related to Assistive Environments*. p. 1–8. doi: 10.1145/2769493.2769506

Ratti, E., Waninger, S., Berka, C., Ruffini, G., and Verma, A. (2017). Comparison of medical and consumer wireless EEG systems for use in clinical trials. *Front. Hum. Neurosci*. 11, 398. doi: 10.3389/fnhum.2017.00398

Reimer, B., Mehler, B., Coughlin, J. F., Godfrey, K. M., and Tan, C. (2009). "An on-road assessment of the impact of cognitive workload on physiological arousal in young adult drivers," in *Proceedings of the 1st International Conference on Automotive User Interfaces and Interactive Vehicular Applications*. p. 115–118. doi: 10.1145/1620509.1620531

Ritchie, D. M., and Thompson, K. (1978). The UNIX time-sharing system†. *Bell System Tech. J*. 57, 1905–1929. doi: 10.1002/j.1538-7305.1978.tb02136.x

Rudmann, D. S., McConkie, G. W., and Zheng, X. S. (2003). "Eyetracking in cognitive state detection for HCI," in *Proceedings of the 5th International Conference on Multimodal Interfaces*. p. 159–163. doi: 10.1145/958432.958464

Saitis, C., Parvez, M. Z., and Kalimeri, K. (2018). *Cognitive Load Assessment from EEG and Peripheral Biosignals for the Design of Visually Impaired Mobility Aids [Research Article]*. Hindawi: Wireless Communications and Mobile Computing. doi: 10.1155/2018/8971206

Scharinger, C., Kammerer, Y., and Gerjets, P. (2016). "Fixation-Related EEG Frequency Band Power Analysis: A Promising Neuro-Cognitive Methodology to Evaluate the Matching-Quality of Web Search Results?" in Stephanidis, C. (Ed.). *HCI International 2016 – Posters' Extended Abstracts*. Midtown Manhattan, New York City: Springer International Publishing. p. 245–250. doi: 10.1007/978-3-319-40548-3_41

Shneiderman, B. (1986). Designing menu selection systems. *J. Am. Soc. Inf. Sci.* 37, 57–70. doi: 10.1002/(SICI)1097-4571(198603)37:2<57::AID-ASI2>3.0.CO;2-S

Stipacek, A., Grabner, R. H., Neuper, C., Fink, A., and Neubauer, A. C. (2003). Sensitivity of human EEG alpha band desynchronization to different working memory components and increasing levels of memory load. *Neurosci. Lett.* 353, 193–196. doi: 10.1016/j.neulet.2003.09.044

Sugaya, Y. (2019). *Distributed Pragmatic Processing for Adjective Expression: An Experimental Study*. Available online at: https://www.jcss.gr.jp/meetings/jcss2019/proceedings/area14.html

Trammell, J. P., MacRae, P. G., Davis, G., Bergstedt, D., and Anderson, A. E. (2017). The relationship of cognitive performance and the theta-alpha power ratio is age-dependent: an EEG study of short term memory and reasoning during task and resting-state in healthy young and old adults. *Front. Aging Neurosci.* 9. doi: 10.3389/fnagi.2017.00364

Wang, Q., Yang, S., Liu, M., Cao, Z., and Ma, Q. (2014). An eye-tracking study of website complexity from cognitive load perspective. *Decis. Support Syst.* 62, 1–10. doi: 10.1016/j.dss.2014.02.007

Wilson, G. F., and Eggemeier, F. T. (1991). "Psychophysiological assessment of workload in multi-task environments," in *Multiple-task performance*. CRC Press. doi: 10.1201/9781003069447-15

Winslow, B., Carpenter, A., Flint, J., Wang, X., Tomasetti, D., Johnston, M., et al. (2013). Combining EEG and eye tracking: using fixation-locked potentials in visual search. *J. Eye Mov. Res.* 6, 4. doi: 10.16910/jemr.6.4.5

Xiang, Z., Huang, Y., Luo, G., Ma, H., and Zhang, D. (2021). Decreased event-related desynchronization of mental rotation tasks in young tibetan immigrants. *Front. Hum. Neurosci.* 15, 664039. doi: 10.3389/fnhum.2021.664039

Xie, B., and Salvendy, G. (2000). Review and reappraisal of modelling and predicting mental workload in single- and multi-task environments. *Work and Stress.* 1, 74–99. doi: 10.1080/026783700417249

Yokota, Y., and Naruse, Y. (2015). Phase coherence of auditory steady-state response reflects the amount of cognitive workload in a modified N-back task. *Neurosci. Res.* 100, 39–45. doi: 10.1016/j.neures.2015.06.010

Zagermann, J., Pfeil, U., and Reiterer, H. (2016). "Measuring Cognitive Load using Eye Tracking Technology in Visual Computing," *Proceedings of the Beyond Time and Errors on Novel Evaluation Methods for Visualization – BELIV*. p. 78–85. doi: 10.1145/2993901.2993908

Zagermann, J., Pfeil, U., and Reiterer, H. (2018). "Studying Eye Movements as a Basis for Measuring Cognitive Load," in *Extended Abstracts of the 2018 CHI Conference on Human Factors in Computing Systems.* p. 1–6. doi: 10.1145/3170427.3188628

Zhang, D., and Adipat, B. (2005). Challenges, methodologies, and issues in the usability testing of mobile applications. *Int. J. Human–Computer Interact* 18, 293–308. doi: 10.1207/s15327590ijhc1803_3

Frontiers in Neuroscience

Provides a holistic understanding of brain function from genes to behavior

Part of the most cited neuroscience journal series which explores the brain - from the new eras of causation and anatomical neurosciences to neuroeconomics and neuroenergetics.

Discover the latest Research Topics

See more →

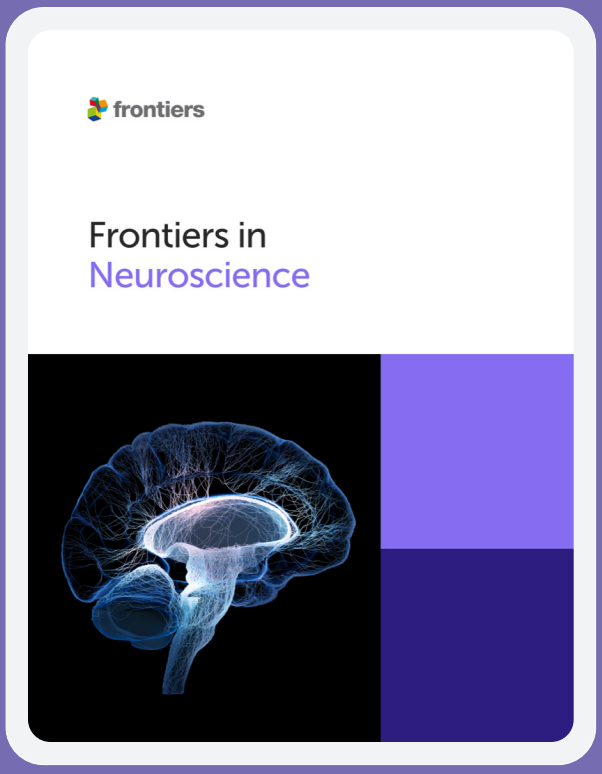

Frontiers

Avenue du Tribunal-Fédéral 34
1005 Lausanne, Switzerland
frontiersin.org

Contact us

+41 (0)21 510 17 00
frontiersin.org/about/contact